# Effects of Dynamic Vegetation and Topography on Hydrological Processes in Semi-Arid Areas

by

Valeriy Yuryevich Ivanov

M.S. Hydrology, Massachusetts Institute of Technology (2002)
Diploma in Hydrology, Moscow State University, Russia (1996)

Submitted to the Department of Civil and Environmental Engineering
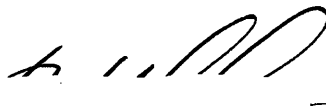in partial fulfillment of the requirements for the degree of

Doctor of Philosophy in the field of Hydrology

at the

MASSACHUSETTS INSTITUTE OF TECHNOLOGY

June 2006
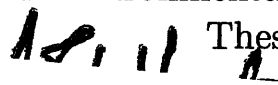
Author . . . . . . . . . . . . . . . . . . . . . . . . . . . . . . . . . . . . . . . . . . . . . . . . . . . . . . . . . . . . . . . . .
Department of Civil and Environmental Engineering
April 28, 2006

Certified by . . . . . . . . . . . . . . . . . . . . . . . . . . . . . . . . . . . . . . . . . . . . . . . . . . . . . . . . . . .
Rafael L. Bras
Edward Abdun-Nur Professor of Civil and Environmental Engineering
Thesis Supervisor

Accepted by . . . . . . . . . . . . . . . . . . . . . . . . . . . . . . . . . . . . . . . . . . . . . . . . . . . . . . . . . . . . . .
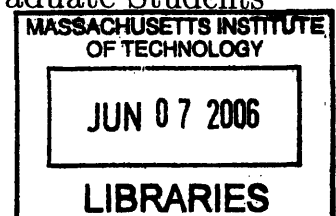Andrew J. Whittle
Chairman, Departmental Committee on Graduate Students

# Effects of Dynamic Vegetation and Topography on Hydrological Processes in Semi-Arid Areas

by

## Valeriy Yuryevich Ivanov

Submitted to the Department of Civil and Environmental Engineering
on April 28, 2006, in partial fulfillment of the
requirements for the degree of
Doctor of Philosophy in the field of Hydrology

## Abstract

Ecosystems of dry climates represent a particularly interesting object for ecohydrological studies, as water is generally considered to be the key limiting resource. This work focuses on vegetation-water-energy dynamics occurring in the complex terrain of a semi-arid area characteristic of central New Mexico. The study constructs a dynamic model of coupled interactions, [tRIBS+VEGGIE], that considers essential water and energy processes over the river basin and links them to the basic plant life regulatory processes. After model calibration, a set of numerical experiments is carried out for two small-scale synthetic domains that exhibit characteristic hillslope curvatures. A weather generator is used to create the long-term series of meteorological forcing. The linkages between terrain attributes and patterns of $C_4$ grass productivity and water balance components are examined for three generic soil types: sand, loam, and clay. It is argued that in conditions of negligible moisture exchange, site aspect and slope are the key determinants of both the hydrologic behavior and the degree of "favorability" to vegetation. As shown, certain topographic locations are more favorable to vegetation development, as compared to a flat horizontal surface not affected by lateral effects such as radiative shading or water transfer. These locations are associated with sites of northerly aspect with surface slopes within a narrow range of magnitudes. Contributions from both the rainfall and radiation forcings are discussed to explain the existence of these niches. The sensitivity of results is investigated relative to modifications in the meteorological forcing and the dominant mechanism of lateral water transfer. The analysis unequivocally demonstrates the critical role of soil texture type in regulating the spatio-temporal aspects of coupling between vegetation-hydrology processes. Two additional controlling topographic features are suggested, corresponding to the local and global terrain convergence levels. Furthermore, it is argued that grass productivity and water fluxes of a site can be characterized as a function combining local and global terrain properties.

Thesis Supervisor: Rafael L. Bras
Title: Edward Abdun-Nur Professor of Civil and Environmental Engineering

# Acknowledgments

The first words of appreciation are devoted to my advisor, Prof. Rafael L. Bras, who has been a truly great person from whom to learn, to work with, and to learn with. I am very grateful for his thorough guidance, support, advice, and for his immense patience during periods of academic "stagnation." His scientific vision and subtle feeling of what *is* indeed important had a huge impact on my professional education, in general, and on this work, in particular. It would also be an understatement of significant proportion to say that he only taught me hydrology. Throughout the last seven and a half years, I was implicitly mentored on how to deal with a wide spectrum of issues associated with academic experience of a faculty. Something that sends a bold statement on CVs of my advisor's students: "Prof. Bras's stock."

I am also very grateful to my Ph.D. Committee members: Prof. Dara Entekhabi, Prof. Elfatih Eltahir, and Prof. Dennis McLaughlin. I cannot express enough joy for the fact that they failed me on my first attempt to defend a research proposal several years ago. Thank you, indeed! Sometimes bad experience leads to a positive outcome, and, well, that failure resulted in new interests for me and, hopefully, a fruitful research agenda for years to come. In particular, I am very grateful to Dara for his sharp remarks and unforeseen angles of view on research I became interested in. I would not be writing these lines without his former student, or should I say my another unofficial committee member, Enrique Vivoni. My colleague, my mentor, my friend. A man of inextinguishable inner flame and spirit.[1] Thank you, Enrique, and I hope that our friendship will continue for many years to come. This work would not also have been completed without a man who "...has become MIT-like more than many who came out of MIT,"[2] Erkan Istanbulluoglu. His deep and sincere friendship, advice, and delicate sense of humor kept me afloat and focused. Erkan, "Kak dela!?,"[3] I do hope that our pathways will intertwine many times more!

The story of mentorship, friendship, support, advice, and sacrifice simply goes on. So many people to thank. What stage would I be at without pin-pointed remarks of Jingfeng Wang [4]? How can I express my gratitude to the entire group of people who listened to, criticized, advised, counseled, and humored me during all these long[5] eight years? My infinite thanks go to Jean Fitzmaurice, Nicole Gasparini, Homero Flores Cervantes, Gautam Bisht, Ryan Knox, Fernando Nardi, Lejo Flores, Daniel Collins, Frédéric Chagnon, Valerio Noto, Hanan Karam, Andrea Adamo, Susan

---

[1] ...focus, efficiency, and organization. I didn't realize such people exist!

[2] A quote from Prof. Bras's speech at Erkan's farewell party, August, 2005.

[3] "How are you!?", in Russian.

[4] ...I cannot help mentioning ski trips we did together, which refreshed our minds so much...

[5] Read also "shortest".

Dunne, Luisa Marcelino, Scott Rybarczyk, Greg Tucker, Jeff Nieman, Steven Lancaster, Vanessa Teles, Giacomo Falorni, Salvatore Grimaldi, Domenico Capolongo, Agnes Fischer, Kai Udert, Sheila Frankel, and Vicky Murphy.[6] I am very grateful to my dearest russian friends, who helped me with math, and to who I occasionally "paid" with devastating spurts in the White Mountains or elsewhere: Dmitriy Pouchine, Roman Barankov, Daniel Kirsanov, Sasha Kochurov, Oleg Logoutov, Mikhail Veshtort, Yulia Yaglovskaya, and Igor Pavlovskiy. I am particularly grateful to the Department of Hydrology at Moscow State University where I spent wonderful years "learning rivers," my former advisor and dear friend Victor Archipovich Zhouk, and all people whose compassion for the science of hydrology was a foundation of every word in this thesis: Nikolay Ivanovich Alexeevskiy, Andrey Valentinovich Christoforov, Valeriy Mikhailovich Evstigneev, Konstantin Konstantinovich Edelstein, Maya Borisovna Zaslavskaya, Vadim Nikolaevich Mikhailov, Natalya Leonidovna Frolova, Roman Sergeevich Chalov, Yuriy Sergeevich Datcenko, and Zinaida Ilyinichna Zhmakina (AKA "BabZina"). My words of sincerest gratitude also go to all people in Russia who made this important step with me, from 17 to 22, while learning what being a "geographer" means, to all those who was bitten by mosquitos, sweated, froze, and sank in marshes with me, to all those who shared their bread, "kil'ka"[7], and vodka during the hard times of 90-s, to all my close friends, with only a small subset listed here: Sashka Agibalov, Dimon Zemtcov, Kostik Kirpichyov, Zheka Postnikov, Vasya Sarana, Tatyana Karimova, Yulianna Babich, Olga Lavruhina, Vladimir Petrovich Lisitcyn, Alik Revzin, Alexey Kozhevnikov, and San Sanych.

In the very first turn, this thesis is devoted to my parents, Galina Afanasyevna Ivanova and Yuriy Iosifovich Ivanov. I can only hope that it will compensate a tiny bit of all the hardships of their youth spent in the devastated by the War country. Mom and Dad, if only I could do more. Thank you very very much for letting me grow so freely, for guiding me in the times of need, and for being so patient every time I got into trouble. I am very grateful to my brother, Stas, who had the wits not to transform his respectable seniority into cruel dictatorship. And yes, brother, I am very happy you did not go to fight that war in Afganistan...

Lastly, and to the greatest extent, I would like to thank my wife Tatyana. No ordinary words can express it. No earthly deeds can heal or reward your sacrifices. I can only promise to carry on.

---

[6]While my message can only be virtual, originating in the realm of innate boldness, I am greatly thankful to the following people, from a "different book", whose genius influenced this work via sound: W.A. Mozart (esp. "Requiem"), F.J. Haydn, S. Rachmaninov, V.S. Vysotckiy, D. Brubeck, D. Gilmour ("Pink Floyd"), M. Knopfler ("Dire Straits"), J. Serrie, K. Schulze, and S. van Hees.

[7]Canned small fish from the Pacific Ocean, in Russian.

# Contents

# List of Figures

14

19

21

23

26

27

31

35

36

40

# List of Tables

# Chapter 1

# Vegetation-Hydrology Studies: Literature Review and Scope of Research

## 1.1 Motivation and scope of work

The processes within the terrestrial biosphere and atmosphere are intrinsically coupled with the hydrological cycle. The coupling is non-linear and multi-directional, implying that an individual component of the system is both under the influence of, as well as impacting upon, the remaining parts of the system (Eagleson, 1978; Eagleson, 2002). Vegetation is one of the essential components that significantly influences the water and energy balances, establishing bi-directional links with the climate (Foley et al., 2000). For instance, Arora and Boer (2002) show that on a global average, the combined evaporation from leaves and transpiration account for about 72% of the total evaporation from the land surface. Interactions and feedbacks between the climate and biosphere have been the subject of a number of studies (e.g., Eltahir, 1996; Hutjes et al., 1998; Dickinson, 2000; Wang and Eltahir, 2000; Pielke, 2001). Recently, a multi-outcome interplay between vegetation, climate, and soil has been illustrated in a series of papers: Rodriguez-Iturbe et al. (1999b), D'Odorico et al.

(2000), Ridolfi et al. (2000), Laio et al. (2001a, 2001b), Guswa et al. (2002), Ridolfi et al. (2000a, 2000b), Van Wijk and Rodriguez-Iturbe (2002), among others.

Understanding the basic processes and feedbacks in the vegetation-hydrology system is the crucial link to characterizing the existence of different biomes and hydrological mechanisms that underlie the coupled dynamics. As pointed out by a number of researchers (e.g., Eagleson, 1978; Protopapas and Bras, 1986; Rodriguez-Iturbe, 2000; Mackay, 2001), the fundamental variables determining the vegetation structure and function are *light*, *soil moisture*, and *nutrient supplies*. Besides vegetation itself, they represent the diagnostic variables of climate, soil, and topography, the key factors affecting their spatio-temporal dynamics. Explicit modeling of one of these factors requires the simultaneous treatment of the others. Significant variations and feedbacks, which may occur over a wide range of temporal and spatial scales, must be considered. If some of the hydrological or vegetation components are prescribed, the lack of dynamic feedbacks could seriously alter the modeled system's behavior (Band et al., 1993). Despite the recognition of the principal factors and their coupled nature, hydrology-vegetation modeling has been extremely simplified in at least one of the following contexts: the effects of climate forcing, soil spatial/vertical heterogeneity, and the impact of topography on lateral fluxes in the system and light exposure. Topography, observed to have a significant influence on vegetation distribution (e.g., Figure 1-1) (e.g., Florinsky and Kuryakova, 1996; Franklin, 1998; Meentemeyer et al., 2001; Dirnbock et al., 2002; Kim and Eltahir, 2004; Ben Wu and Archer, 2005; Dietrich and Perron, 2006), is particularly often disregarded in modeling analysis. Vegetation itself is considered as a static component with prescribed characteristics in most hydrology models. Understanding the impact of climatic disturbances, topography, and soil variability on vegetation, however, requires dynamic vegetation modeling across the watershed.

In this context, coupling of a vegetation model that explicitly considers plant dynamics to a spatially-distributed hydrological model should provide a necessary step towards an integrated approach. The hydrological model will provide the framework to account for the spatial variability of the topography-controlled continuous

52

Figure 1-1: An example of extreme spatial differentiation in the vegetation cover: the north-facing slopes are covered with needle-leaf woody vegetation, the slopes of southerly aspect feature herbaceous species and patches of bare soil, and the convergent areas of the terrain exhibit a mixture of broadleaf shrubs and grasses. The site is located in the Columbia River basin (photo is courtesy of Dr. Enrique R. Vivoni).

rainfall-runoff process, subject to stochastic climatic forcing. In this spatially explicit scheme, vegetation will grow and die, which will reflect its biophysical and biochemical characteristics, seasonal and interannual climate forcing, and the competition for vital resources. Such a framework offers a variety of opportunities to explore the bidirectional interactions between vegetation and hydrological mechanisms and represents an important advance toward integrated ecohydrological modeling. Ecosystems of arid and semi-arid areas represent a particularly interesting object for study, as they comprise some of the major biomes of the world, often exhibiting a delicate equilibrium between their essential constituents. In these systems, soil water is generally considered to be the key resource affecting vegetation structure and organization. The mechanisms through which water limitation affects ecosystems are related to carbon assimilation via the control of photosynthesis and stomatal closure as well as nitrogen assimilation through the control of the nitrogen mineralization rate. Many important issues depend on the quantitative understanding of dynamics inherent to these ecosystems, including human interference, climate change, environmental preservation, and proper management of resources.

The aim of this work, therefore, is: 1) to develop a modeling system that incor-

porates *state-of-the-art* tools to represent vegetation-hydrology interactions in areas of complex terrain; and 2) to address a variety of questions concerning vegetation-hydrology mechanisms in semi-arid zones. In particular, this research addresses the effects of topography on vegetation temporal development and spatial distribution.

The system for modeling dynamic vegetation in the framework of a hydrological model is described in detail in the following chapters. The system is composed of several key components: a climate simulator and a model of plant physiology and spatial dynamics (*VEGetation Generator for Interactive Evolution*, VEGGIE) are coupled to the spatially-distributed physically-based hydrological model *the TIN-based Real-time Integrated Basin Simulator*, tRIBS (Ivanov et al., 2004a, 2004b; most of the tRIBS hydrological components however have been modified in this work and their current formulation is provided in the following chapters). The modeling system thus allows a fully dynamic interaction between the hydrological and vegetation processes occurring at fine space-time scales (10-40 m in space, 10 min.-1 hour in time).

*Chapter 2* of this thesis outlines the climate simulator that generates hourly hydrometeorological variables (rainfall, air and dew point temperatures, cloud cover, and wind speed). The model is based primarily on work of Curtis and Eagleson (1982), with several modifications that improve the performance statistics and simplify the model structure. The model of the shortwave radiative transfer through the atmosphere is also presented in this chapter. The model simulates the surface irradiances both in visible and infra-red bands, which depend on geographic location of a site, its geometric configuration (slope and aspect), and atmospheric conditions (e.g., opacity, water vapor content, and cloudiness).

*Chapter 3* describes the framework of the land-surface vegetation-hydrology model. The chapter provides details on vegetation representation at the level of basic computational elements and outlines routines that estimate canopy and ground-surface radiation budgets. The infiltration model based on the finite-element solution of the Richards equation (Hillel, 1980) is also introduced in this chapter; it emphasizes how the surface and subsurface water exchanges are simulated for a given watershed. The framework for simulating canopy resistance is introduced with reference to the pho-

54

tosynthesis model of Farquhar et al. (1980), as expanded by Collatz et al. (1991, 1992), and the model of stomatal physiology of Ball et al. (1987).

*Chapter 4* describes the model of vegetation dynamics that simulates spatio-temporal changes in vegetation structure and composition, both as explicit and implicit functions of plant properties, hydrometeorological forcing, soils, and position in the landscape. The simulation framework represents the processes of photosynthesis and primary production, stomatal physiology, respiration, allocation, tissue turnover and stress-induced foliage loss, phenology, and plant recruitment. The results of model verification for a field site located in the Sevilleta National Wildlife Refuge (New Mexico) are also presented.

*Chapter 5* addresses the aspects of topographic control on vegetation spatial organization and temporal fluctuations in semi-arid areas. Two synthetic catchment topographies ($\sim4$ $km^2$) with prescribed characteristics of hillslope curvature are used in the experiments. $C_4$ grass model is forced with synthetic hydrometeorological series corresponding to the location of Albuquerque (35.05N, 106.617W). Soils of various generic texture types are considered: sand, loam, and clay. The 50-year simulation periods are assumed to be sufficient to provide representative statistics of vegetation-hydrology dynamics. The chapter further describes topography niches that feature more/less favorable conditions for grass function.

*Chapter 6* discusses the simulation results, addressing the sensitivity of vegetation-hydrology dynamics presented in Chapter 5, referred to as the "*base*" case scenario. The experimental design is subject to modifications in a) the hydrometeorological forcing and b) the processes of lateral moisture transfer. The first set of experiments explores the impact of the random nature of the rainfall vector (i.e., deviation of droplet pathways from the vertical) as well as introduces artificial changes to the seasonal precipitation and radiation regimes. The second group of experiments considers more rapid processes of lateral moisture exchange, as compared to the "*base*" case scenario. The former are implemented through the high soil anisotropy ratios, the runon mechanism allowing for re-infiltration process, and the partial surface sealing during the growing season, leading to higher runoff-runon volumes. The results that

are presented suggest that the combined effect of terrain attributes exhibits scaling properties, which allows one to propose a conceptual relationship linking both the productivity and water balance components at various landscape locations.

*Chapter 7* summarizes this thesis. The chapter outlines the developed modeling components, discusses their critical assumptions as well as the assumptions of the presented study, and provides several topics for future research efforts.

## 1.2 Vegetation-hydrology modeling background

### 1.2.1 Space-time scale issues

Plant intrinsic physiology is what makes the study of vegetation function in terrestrial ecosystems so intriguing. The processes of photosynthesis, respiration, allocation, and phenology, which through the water and energy cycles are strongly dependent on climate, soil, and topography characteristics, make vegetation a dynamic component of the ecosystem. For example, by regulating stomata opening, plants respond to environmental conditions that affect photosynthesis, such as temperature, humidity, radiation, $CO_2$ concentration, and soil moisture (e.g., Eagleson, 2002). Such regulatory processes are rather quick: a characteristic time scale for stomata response to environmental stress is typically 0.01-1 hour (Hutjes et al., 1998). Life cycle processes are therefore strongly coupled to the other components of vegetation-hydrology system at the diurnal scale. In a more passive way, at the time scales of weeks to months, vegetation may affect seasonal magnitude of energy and momentum fluxes via the dynamic changes of the physical properties of its canopy: albedo, leaf area index (LAI), height, and roughness. Vegetation also impacts the biogeochemical cycle (e.g., carbon), thus influencing long-term climate changes (e.g., Walker, 1994; Walker et al., 1997; Hutjes et al., 1998).

Therefore, as pointed out by Rodriguez-Iturbe (2000) and Porporato and Rodriguez-Iturbe (2002), it is extremely important to consider the scale at which the vegetation-hydrology interactions occur in the analysis of coupled systems. The importance of

processes involved in hydrological and vegetation cycles is different when one considers hourly, daily, seasonal, or interannual dynamics, or interactions at the point, hillslope, catchment, or continental scale. For example, at the point scale the fluctuations of hydrometeorological forcing can be considered as an external variable without taking into account feedbacks that vegetation imposes on the atmosphere. For short-term analysis, vegetation structure itself can be considered static, and modeling can be done without dynamic update of its state. Large-scale patterns of vegetation, however, heavily influence the dynamics of the atmospheric boundary layer; and the climatic component of the climate-soil-vegetation system becomes dependent on the feedbacks that the biosphere imposes. At this scale, climate can no longer be considered as an external forcing component and becomes an essential part of the overall dynamics (e.g., Eltahir, 1996; Xue, 1997; Hogg et al., 2000; Pielke, 2001). Analysis of the long-term behavior of the climate-vegetation system at such scale should include the capabilities for dynamic vegetation that include biogeochemical cycling with time dependent carbon and nutrient supply (Peng, 2000; Arora, 2002).

Studying the characteristics of vegetation response to regional water balance, intra/inter-species interactions, vegetation spatial patterns, and the underlying hydrological mechanisms is most revealing when the key factors defining the vegetation structure and function are explicitly accounted for: climate, soils, and topography. Averaging over large spatial scales significantly decreases the spatial variability (topography and soils in particular and, as a result, soil moisture) and increase the temporal scales at which the processes are effectively correlated. Such scales, mostly used in climatologically oriented studies, are not very illuminating for the study of vegetation and hydrologic response that are controlled by the dynamics at much smaller temporal and spatial scales (Rodriguez-Iturbe et al., 2001). While the point analysis is very helpful in recognizing the most important features of vegetation-hydrology dynamics, it usually implies simplifying assumptions that are not always applicable (Guswa et al., 2002). Point analysis does not account for spatial interaction and lateral mass transfer. For instance, temporal fluctuations of the soil moisture, one of the key variables defining vegetation structure, have been shown
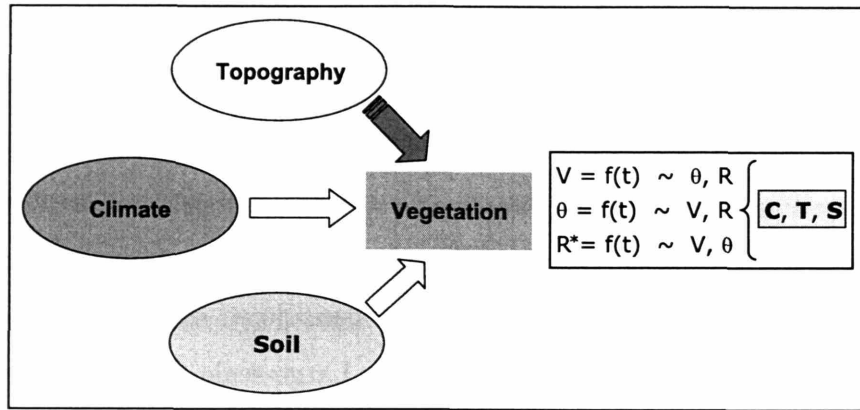
Figure 1-2: A conceptual diagram of the adopted approach, illustrating the relationship among key components contributing to the cycles of energy, water, and elements in natural systems. The arrows indicate the direction of influence. $T$ is topography, $C$ is climate, $S$ is soil, $V$ is vegetation, $R$ is incident solar radiation, $R^*$ is net radiation at the canopy and ground levels, $\theta$ is soil moisture, and $t$ is time. As can be seen, climate, topography, and soil affect the temporal change in vegetation, soil moisture, and net canopy/ground radiation at any given location; all latter variables are inter-related through a variety of coupling mechanisms.

to have topography-controlled properties (Beven and Kirkby, 1979). In addition, one of the largest problems of linking point models to explain ecosystem functioning is the spatial scaling issue (Peng, 2000). Modeling vegetation at the catchment scale, however, should account for interaction among the stochastic fluctuations in precipitation and soil moisture, the basin geometry, and the vegetation structure. Therefore, a spatio-temporal approach that can resolve both the variation of hydrological fluctuations occurring at the hillslope scale and the diurnal variations of plant physiological processes is needed (Figure 1-2).

## 1.3 Hydrology-vegetation studies background

Hydrologic modeling has generally ignored the importance of vegetation as an important spatio-temporal dynamic component in the land-surface hydrological cycle and the existence of topographic controls on plant spatial distribution. Past simplifications are due to the overall extreme complexity of the problem and differences in opinion among ecologists and hydrologists about what simplifications are necessary.

While ecologists tends to over-simplify the hydrological mechanisms involved in vegetation function, hydrologists choose to neglect the dynamic features of vegetation. Nonetheless, a variety of questions related to hydrology-vegetation interactions and ecosystem function have been explored in existing approaches, which range from point studies to spatially-explicit modeling efforts.

## 1.3.1   Hydrological modeling of vegetation

Eagleson (1978) was one of the first who investigated mechanisms underlying the vegetation-hydrology interactions. Eagleson (1982) developed an ecological optimality theory of water-limited systems using a statistical-dynamical model of the average annual water balance. Eagleson (1982) argued that these systems seek a short-term equilibrium state such that the water demand stress is minimized. Long-term equilibrium state is reached by maximization of the minimum stress canopy density. Eagleson and Segarra (1985) tested the ecological optimality hypotheses for two tree-grass savannas, showing that tree-grass coexistence can be explained by minimization of water demand stress. They discussed the stability conditions for such equilibrium showing that it was stable only if the climate was constant. The vegetation monocultures (i.e., grassland and forest) were shown to be in unstable equilibrium. Using a simple physical-conceptual model of infiltration, evapotranspiration, and leakage, Cordova and Bras (1981) developed an analytical probability mass function of soil moisture at the end of a growing season given the soil moisture at the beginning of the season. This represented one of the first attempts to implicitly include plant biophysical characteristics (via the parameterization of evapotranspiration and root zone) into the framework of a statistical distribution of the transient soil moisture. Protopapas and Bras (1986, 1988) developed a point mechanistic model of plant physiology, which took into account moisture and salinity profiles in a soil column. Necessary conditions for optimal plant growth were investigated suggesting the importance of diurnal variability of plant stress, which is a function of climate and soil characteristics. Protopapas and Bras (1993) used the model of Protopapas and Bras (1986) to study the variance of soil- and plant-state variables due to the deviations

of climatic variables and soil parameters. An approximate linear model for the per-turbations was used. It was argued, that only correlated climatic variables create significant effects on biomass production and that the uncertainty of soil parameters is attenuated through the system dynamics. They suggested that natural vegetation systems have the capacity to resist moderate climatic changes and maintain their stability. Rodriguez-Iturbe et al. (1999a) developed a simple point water balance model based on a simplified representation of the processes of infiltration, evapo-transpiration, and leakage dependent on the soil moisture content. The stochastic nature of rainfall forcing was modeled using Poisson arrival process with the daily amounts defined by the exponential distribution. Rodriguez-Iturbe et al. (1999a) derived an analytical solution for the steady-state probability density function of soil moisture for a control volume with its vertical size constrained by the assumed root-ing depth. In an attempt to study aspects of vegetation optimality, Rodriguez-Iturbe et al. (1999b) constructed a spatial model of savanna grass-tree ecosystem. The mean soil moisture, obtained from the model of Rodriguez-Iturbe et al. (1999a) for different fractions of woody plants, was assigned as an initial condition. The spatial competition for water was then allowed to occur, considered as a part of an optimiza-tion problem. Imposing two objectives, the minimization of the global water stress and the maximization of biomass productivity, it was shown that an optimal coex-istence was achievable in relative proportions observed for savannas. D'Odorico et al. (2000) used the statistical model of Rodriguez-Iturbe et al. (1999a) to investigate the impacts of interannual climate fluctuations, soil, and vegetation on the mean soil moisture state during the growing season. The results showed that the frequency distribution of the mean soil moisture can become bimodal under certain conditions, implying two preferential states in the ecosystem function. Ridolfi et al. (2000a) explored the statistical properties of vegetation water stress as a function of climate, soil, and vegetation variability, illustrating the crucial role of hydrologic mechanisms underlying the climate-soil-vegetation dynamics.

In a series of papers Rodriguez-Iturbe et al. (2001), Laio et al. (2001a, 2001b), Porporato et al. (2001), a soil moisture dynamics model similar to Rodriguez-Iturbe

et al. (1999a) was developed, with a more realistic representation of the loss functions (evapotranspiration and root zone leakage). A concept of "dynamic" stress was introduced as a measure of intensity and duration of periods that plants spend in water-stressed conditions. One of the key arguments made was that the optimal conditions for plants are likely to be between low water stress and high productivity (associated with maximum evapotranspiration), which is consistent with previous studies by Eagleson (1982, 1994) and Rodriguez-Iturbe et al. (1999b). Laio et al. (2001b) illustrated applications of the model to African savanna, Texas shrubland, and Colorado steppe, emphasizing the characteristic controlling features for each ecosystem. Fernandez-Illescas et al. (2001) showed vegetation sensitivity to soil texture type and argued that soil texture may play a major role in modulating the impact that inter-annual rainfall fluctuations have on the fitness and coexistence of trees and grasses. Guswa et al. (2002) compared the estimates of evapotranspiration and root zone saturations over a growing season of a bucket model of Rodriguez-Iturbe et al. (1999a) and that of the Richards infiltration model. They showed that substantial differences may arise in model predictions, if the model cannot simulate water extraction from wet regions to make up for roots in dry portions of the soil column. This implies that a simple bucket-filling model may not adequately represent soil moisture conditions for a number of climates and soils.

Even though the role of vegetation dynamics in land surface energy and water balance is well recognized, there still is an on-going debate about at what space-time scales vegetation (static or dynamic) is climatically important. For example, a new study of Williams and Albertson (2005) has confirmed that dynamic vegetation plays a crucial role in transpiration at daily and seasonal scales, but argues that the impact of dynamic vegetation is minimal at annual scales. At the same time, recent studies (Scanlon et al., 2005; Seyfried et al., 2005) show that inter-annual variability of vegetation, linked to fluctuations in climate, and changes in the type of plant communities play a crucial role in groundwater recharge rates.

The above studies, which focused on *point* dynamics, are very insightful as they allow one to distinguish among the key and the less important aspects of system

behavior. They also allow one to isolate certain mechanisms and study system sensitivity with respect to them. Nonetheless, the simplifying assumptions that these approaches impose cannot account for the complexity of natural systems and feedbacks they exhibit, which can be crucial in determining system dynamics. For example, in conditions of non-uniform topography, site aspect and slope control the local net radiation and lateral surface/subsurface fluxes. Such controls may lead to certain locations in the hillslope that exhibit highly dynamic hydrologic behavior by contributing to surface runoff generation during storms, yielding evaporation at potential rates for extended periods, and discharging the groundwater (e.g., Dunne and Black, 1970; Salvucci and Entekhabi, 1995; Levine and Salvucci, 1999). Accounting for the transient effects of soil moisture dynamics, as has been shown by Guswa et al. (2002), i.e., infiltration process, may lead to a different (i.e., from the steady-state approach) rainfall partition. For instance, runoff generation via the infiltration excess mechanism, which has been argued to occur frequently in arid regions (e.g., Martinez-Mena et al., 1998), can substantially modify the local moisture dynamics.

An attempt to explicitly consider the effects of topography was made by Ridolfi et al. (2003) who studied the interplay among vegetation, climate, and soils using hillslopes of different curvatures. Two characteristic regimes were revealed: topography may exert significant or negligible effects on lateral fluxes, which corresponds to humid and dry climates, respectively. The study, however, included neither the terrain features affecting the incoming radiation, nor the groundwater effects. Both could provide evidence of vegetation-hydrology coupling in the hillslope system (Levine and Salvucci, 1999; Kim et al., 1999). Additionally, soil macroporosity (vertical variability of the saturated conductivity) and anisotropy (non-uniformity of soil hydraulic conductivity in the vertical and lateral directions), often observed at the hillslope scale (e.g., Beven and German, 1982; Bronstert, 1999), were neglected in this study. These soil characteristics may have a significant influence on the spatio-temporal moisture dynamics.

Van Wijk and Rodriguez-Iturbe (2002) studied spatio-temporal dynamics of trees and grasses using an individual-based approach in which a single computational cell

was assumed to be occupied either by a single tree or by grass. In this framework, plants faced competition for available space, with water considered as the limiting factor. Death and colonization rates were related to plant biophysical properties and stress magnitude. The simple framework of Van Wijk and Rodriguez-Iturbe (2002) demonstrated a range of interannual rainfall fluctuations over which trees and grass could co-exist in savanna regions. The model results also showed that temporal and spatial fractal structures could be identified in tree-grass ecosystem, implying self-organizing properties operating at a wide range of temporal scales. While the employed model did consider spatial interactions among various vegetation species, their heuristic approach is likely to be oversimplified: "...all (spatial) patterns that do arise...are therefore determined by the biotic part of the model: death and reproduction" (Van Wijk and Rodriguez-Iturbe, 2002). Recently, Caylor et al. (2005) argued that the "feasible optimality" in minimization of plant water stress plays the fundamental role in organization of vegetation patterns in semi-arid river basins.

Two additional comments may be relevant with respect to the discussed studies. Firstly, the steady-state analysis of soil-moisture proposed by Rodriguez-Iturbe et al. (1999a) and extended by Laio et al. (2001a), which was used in all of the discussed studies, is not always suitable. As recognized by these researchers, (Porporato and Rodriguez-Iturbe, 2002), the transient properties of soil moisture can be crucial in systems where the impact of vegetation dynamics is strongest during periods with the least rainfall and initial conditions play an essential role. Also, it may not be suitable for systems where the surface and subsurface lateral moisture redistribution is an important factor in overall moisture dynamics (Rodriguez-Iturbe et al., 2001). In certain conditions, the groundwater dynamics may also play an active role in determining the soil moisture conditions, thus leading to non-steady-state conditions.

Second, and a more general comment, also referring to most hydrologic models that include sophisticated vegetation frameworks (e.g., Wigmosta et al., 1994), is that the dynamic properties of vegetation response are neglected. Parameterizing vegetation by means of constant prescribed interception and transpiration functions implies over-simplification of vegetation behavior and plant response to water stress.

For instance, a tree that has been under moisture stress for a prolonged period of time, resulting in plant physiomorphological changes, will respond to the revival of favorable soil moisture conditions differently than a tree that has been persistently under favorable conditions (Kramer, 1983; Turner et al., 1985). For example, Kramer (1983) discusses tolerance levels to drought and recovery rates that may vary widely among plant species. One may also argue that frequent, although sufficiently short, stress periods may result in inability of the plant to completely recover leading to progressive stress build up in time (e.g., gradual depletion of hydrocarbon reserves and tissue damage). Therefore gradual and substantial changes in plant physiological function may occur (i.e., changes in transpiration and interception). These changes cannot be captured by using prescribed soil-moisture dependent transpiration functions (e.g., Laio et al., 2001a, eq. 12). Such approaches treat vegetation essentially as an abiotic, state-dependent response component.

Catchment scale vegetation-hydrology studies that include a component of dynamic vegetation are quite limited. Nonetheless, a few relevant studies have been recently reported. An attempt to account for topography as well as soil moisture lateral transfer at a catchment scale was done by Band et al. (1993), who coupled the biogeochemical model FOREST-BGC (Running and Coughlan, 1988) with the hydrologic framework of TOPMODEL (Beven and Kirkby, 1979). Data and a simulation framework of the RHESS model (Band et al., 1991) were used to explicitly model forest evapotranspiration and canopy net photosynthesis with a spatially prescribed canopy cover (not dynamic). The approach partitioned the study catchment into a number of representative hillslopes. The internal representation of the hillslopes was provided by the frequency distribution of the TOPMODEL similarity index for which different values of LAI and root zone depth were computed. Based on the analysis of the canopy dynamics simulation for one year that had severe summer drought conditions, Band et al. (1993) stressed the importance of topography in soil water redistribution and its impact on evapotranspiration and canopy net photosynthesis. Band et al. (1993) also discussed the limitations of the TOPMODEL approach, which does not explicitly model soil moisture conditions at any given site

and uses a uniform hillslope recharge rate. Besides these limitations, one may also argue that applying steady-state conditions (i.e., the assumptions of TOPMODEL) for soil water deficit distribution along the hillslope within a single time step (day), limits the current approach to steep catchments with highly conductive soils. Local heterogeneities (e.g., differences in vegetation stand) also cannot be accounted for in the statistical-dynamical method of TOPMODEL.

Vertessy et al. (1996) incorporated a distributed forest growth model into the TO-POG hydrological model (Dietrich et al., 1992) for application in small watersheds to study the forest responses and water balance to clear-felling and regeneration. Using this framework, Watson et al. (1998, 1999) developed a Macaque model that had a similar structure as RHESS (Band et al., 1991), applying the TOPMODEL approach for lateral water distribution. The key difference was in the artificial constraining the water table variations along a hillslope, i.e., differentiating the groundwater dynamics according to the position of a site in the hillslope. Watson et al. (1999) studied the implications of the forest stand LAI dynamics on the annual streamflow. Mackay and Band (1997) used the framework of Band et al. (1993) to study the effects of seasonally dynamic LAI (as opposed to prescribed) with different scenarios of prescribed rooting depth. Slope aspect and the type of vegetation stand were used as the criteria to partition a watershed into hillslopes, with subsequent assigning of wetness intervals for each elevation zone within a particular hillslope. Mackay and Band (1997) concluded that topographic features are an important factor in determining the spatial variability of leaf area index and emphasized the significance of the proper parameterization of rooting depth. Mackay (2001) extended the same simulation framework by including a nitrogen dynamics model as the limiting factor of ecosystem evolution. Mackay (2001) argued that nitrogen availability is one of the key factors determining ecosystem equilibrium. Ludwig et al. (2005) document a dynamic self-enhancing feedback between vegetation growth and local hydrology, modulated by topography, where vegetation harvests runoff water by intercepting overland flow, increasing local soil moisture that promotes vegetation growth and the expansion of vegetation patches on the landscape.

Wigmosta et al. (1994) presented the Distributed-Hydrology-Soil-Vegetation Model (DHSVM) that circumvents most deficiencies of the TOPMODEL method by using an explicit quasi-three dimensional approach for lateral redistribution of soil moisture. The unsaturated and saturated zones are coupled accounting for local transient soil moisture dynamics. The model has a two-layer vegetation structure with separate simulation of radiation and water balances on a pixel-by-pixel basis. Nonetheless, vegetation properties are prescribed with the stomatal resistance as the only dynamic vegetation variable. The model has been used in several studies of climate change impact (Wigmosta et al., 1995; Leung and Wigmosta, 1999) and land use change effect on the catchment hydrologic regime (Storck et al., 1998; Bowling et al., 2000; VanShaar et al., 2002).

A variety of soil-vegetation-atmosphere transfer (SVAT) schemes has been constructed to explicitly account for the vegetation physiological properties and the role of changing vegetation in affecting the land-surface water and energy balances. Although SVAT schemes do include biophysical and biochemical processes, most SVAT models still do not treat vegetation as a dynamic component, i.e., many essential vegetation variables are prescribed (Avissar, 1998; Hutjes, 1998). For instance, the vegetation cover fraction is used as a static parameter that does not respond to environmental conditions. Importantly, typical SVAT applications are of mid- to large-scale, within the frameworks of mesoscale and global circulation atmospheric models, with typical computational elements much larger than a hillslope size. As pointed out above, such scales are not suitable for studying the underlying vegetation response and hydrologic dynamics, which are controlled by the interactions at much smaller spatial scales (Rodriguez-Iturbe et al., 2001). Although topography has been considered to be very important for spatial variability of soil moisture (e.g., Beven, 1986; Sivapalan et al., 1987), many SVAT schemes do not include topography in any explicit fashion assuming "flat Earth". The TOPMODEL treatment of topography, proposed by Famiglietti and Wood (1991, 1994), Stieglitz et al. (1997), Walko et al. (2000), allows one to account for the subgrid variability in soil moisture and runoff production, thus improving the land-surface representation (e.g., Warrach et

al., 2002). Nonetheless, the approach has a number of limitations, as noted above: the statistics rather than the details of the topography are used and the hydrologic response is treated as a series of quasi-steady states. SVAT schemes are not directly discussed here. In Chapters 3 and 4, where vegetation functions in the catchment scale hydrology model are presented, references to a number of SVAT models will be given. A review of vegetation components of common SVAT schemes is provided by Arora (2002).

## 1.3.2 Ecological modeling of vegetation

Plant physiological studies have provided considerable insights into biophysics and biochemistry at the individual leaf or plant level (e.g., Evans, 1972; Levitt, 1980; Farquhar et al., 1980; Jarvis and Mansfield, 1981; Kramer, 1983; Crawley, 1986; Ball et al., 1987; Crawford, 1989; Collatz et al., 1991, 1992). Such studies have contributed substantially to the understanding of plant behavior with respect to the hydrological processes. Point models, that include an explicit representation of key physiological processes (e.g., establishment, growth, competition, death, carbon and nutrient cycling), have been developed to capture the transient response of vegetation to changing environmental conditions. These models do not include spatial components and key feedbacks imposed by the hydrological system; they primarily focus on biophysical and biochemical aspects of plant dynamics. Elements of these models are used in many SVAT schemes and ecological studies.

Spatial modeling of vegetation dynamics in ecological applications has been limited to the "gap"-type models for forest succession or cellular automata models. The former class of models considers ecosystems consisting of spatially independent homogeneous patches, within which several plant forms can be present. Such models (Bugmann, 2001) pay little attention to energy, water, and nutrient fluxes in the system in attempt to provide a simple, rule-based formulations of forest dynamics. Typically, the only state variable used in these models is the tree breast height diameter. For example, Pacala et al. (1993, 1996) presented a temperate forest succession model, SORTIE, intended for forest resource modelers. The model was capable of

simulating the evolution of all individual trees within multiple patches through their competition for light. With the time step of 5 years, the model could not include soil moisture effects. In recent efforts, more sound physiology-based gap models were developed, which provided frameworks to study the ecosystem structure and function by modeling energy and matter fluxes (e.g., FOREST-BGC of Running and Coughlan, 1988; BIOME-BCG of Running and Hunt, 1993; HYBRID of Friend, et al., 1993, 1997; FIRE-BGC of Keane et al., 1996). However, such models extremely simplify hydrologic aspects of the ecosystem function, although several studies for gap-type modeling have shown the profound effects of water budgets on the simulated forest dynamics (e.g., Martin, 1992). An example of an advanced model application is by Peng et al. (2002). They presented a generic model, TRIPLEX, as a hybrid product synthesized from three models of forest production, growth and yield and the soil-carbon-nitrogen model. The model primarily focused on aspects of sustainable forest management. Peng et al. (2002) demonstrated good performance in simulating forest evolution, while accounting for carbon and nitrogen dynamics and considering soil water as one of the limiting resources. Model sensitivity to variability in climatic forcing was also studied. The simple soil water balance model, however, operated at monthly time step with prescribed input and loss functions.

Cellular automata models (Wolfram, 1983, 1984), sub-divide the computational domain into a grid of cells, the size of each cell is determined by some typical biological scale (e.g., 5 $m$ x 5 $m$ is common for individual-based modeling of vegetation dynamics). The necessary biological information for the modeled process is included in the form of heuristic rules, rather than physically-based equations (Balzter et al., 1998). Evolution of state of any cell depends on its current state and state of its neighboring cells. Most of such models operate at time steps larger than one month, usually ranging between 1-5 years. Because vegetation physiological processes, such as seed production, germination, and survival are dependent on the timing of rainfall and its amount, these processes are accounted for in an implicit manner. Cellular automata models thus attempt to recreate complex ecosystem dynamics without explaining the underlying mechanisms of hydrology-vegetation interactions. For ex-

ample, Poiani and Johnson (1993) constructed a model of vegetation dynamics for semi-permanent prairie wetlands that considered seven dynamically evolving species, responding to changes in the hydrologic regime. The study evaluated the potential effects of climate change on wetland resources, with hydrologic components simplified by empirical relationships established for the region of interest. Weigand et al. (1995) presented a "dynamic automata" model (following Jeltsch and Wissel (1994)) that assumed disturbances in the hydrometeorologic forcing to be an additional factor affecting local cell dynamics. The model was applied at a monthly time step to evaluate the temporal and spatial dynamics of a shrub ecosystem driven by the monthly rainfall amounts. Neither topography effects, nor the dynamics of soil moisture were considered. Five plant species were able to co-exist throughout long-term simulation, where quasi-stable periods were interrupted by sudden changes in species composition, in response to extreme events (droughts and precipitation). Jeltsch et al. (1996) developed a more elaborate cellular automata model that considered the moisture availability scenarios in the two-layer soil. Driving the ecosystem processes (e.g., growth, mortality, competition, etc.) with yearly rainfall, the dynamics of tree-grass coexistence was studied. Jeltsch et al. (1996) argued that disturbances are likely to be the key processes driving the dynamics of plant community and plant coexistence. A concurrent conclusion was made later by Van Wijk and Rodriguez-Iturbe (2002) using a more hydrologically sound model. Perry and Enright (2002) developed a grid-based model of vegetation dynamics, applied in particular to maquis. Although the position of vegetation in topography was explicitly considered via simple categories of slope favorability, the role of soil moisture was not explicitly accounted for with the time step of one year.

Overall, the spatial ecological models operate with a set of mechanisms that have little or no objective linkage with the characteristics of soil, climate fluctuations, and site-specific hydrologic response. A more hydrologically sound approach, combined with the strengths of mechanistic understanding of plant physiology and function, would thus provide a unique opportunity for studying a range of ecohydrological problems.

69

## 1.4 Summary

This chapter reviews literature on ecohydrological studies and approaches utilized to address questions related to the non-linear and multi-directional coupling in vegetation-hydrology systems. Space-time scales are also discussed, in the context of their suitability for studying hydrological processes that influence vegetation systems, particularly in areas of complex terrain. As follows from above, the goal of this study is both to develop a modeling system that would incorporate up-to-date mechanistic methodologies to modeling vegetation-hydrology interactions and to address a variety of questions of ecohydrology, applicable to semi-arid regions. In particular, the research will attempt to elucidate the effects of topography on vegetation temporal function and spatial distribution.

The following chapters will present the developed modeling system, referred to above as [tRIBS+VEGGIE], which includes a number of components: a weather generator, a land-surface hydrology scheme, and a model of vegetation dynamics. Most of the model components are based on modern physical / biophysical / biochemical / mechanistic approaches to modeling the water, energy, and element cycles of vegetated and partially vegetated systems. The model will be applied to a semi-arid zone of New Mexico to study the impact of topography on the spatial and temporal dynamics of a generic $C_4$ grass.

# Chapter 2

# Formulation of Weather Generator

## 2.1   Introduction

Climate is one of the major factors determining the regional hydrologic regime and existence of different ecosystems. The forcing of climate and the features of its temporal variability need to be considered in any study that focuses on elucidating the mechanisms of coupled vegetation-hydrology dynamics.

Several hydrometeorological variables are needed by the model discussed in Chapter 3. The *hourly* input required by that model includes incoming *shortwave radiation*, *rainfall, air temperature* and *humidity, total cloud cover,* and *wind speed*. Using series of observed meteorological data as input to the model is always the best option to account for the local climate characteristics. However, such methodology may lead to under-representation of extreme climatological events that may not be well reflected in data series of short duration. Moreover, using observed meteorological data makes it impossible to explore different scenarios of climate, for example by varying characteristics of rainfall arrival and magnitude.

Weather generators have been developed as a technique for simulating time series consistent with observed climate characteristics. A fast point-scale routine is assumed to be a sufficient means for reproducing essential climate features considered at the hillslope - small basin scale, the primary scale used in this study. Wilks and Wilby (1999) provide a review of the most commonly used stochastic weather generators.

In general, it can be noted that most approaches: 1) do not simulate all the required variables in a single framework implying implicit simplifying assumptions; 2) use *daily* time step resulting in different (as compared to hourly time scale) auto- and cross-correlation properties of simulated meteorological variables; 3) have intensive data requirements due to the common Fourier series representation of parameter seasonal cycles. The following sections provide an overview of existing approaches used in simulating each individual component of the weather generator.

Among investigated methodologies, the weather simulator of Curtis and Eagleson (1982) was selected as most suitable for the needs of this work. The simple and efficient approach of Curtis and Eagleson (1982) allows one to capture the essential relationships among the meteorological variables of interest, while modeling the diurnal variation of hydrometeorological conditions. For instance, simulation of rainfall occurrence drives the cloud cover model, the simulated cloudiness affects the incoming and outgoing radiation, the air and dew point temperature are consequently influenced by the simulated radiation balance. Another advantage is that the model is suitable for creating multiple scenarios, e.g., dry and wet climates. The model of Curtis and Eagleson (1982) is used as the core model of the discussed framework with necessary modifications that lead to a better or more efficient representation of simulated statistics. The shortwave radiation model discussed below represents a separate effort of creating a simulation framework of direct and diffuse solar radiation with the capability of accounting for visible and infra-red bands.

## 2.2 Meteorological data

Hydrometeorological data for three weather stations are used to illustrate the procedure of parameter estimation as well as the subsequent simulation of climate quantities and comparison with the statistics derived from the observed data. A short description of climate characteristics for each station location is provided below.

1.) *Albuquerque International Airport* (New Mexico), 35.05N, 106.617W, data availability 01/1961-12/1995. The climate of Albuquerque can be described as arid

72

continental with abundant sunshine, low humidity, scarce precipitation, and a wide seasonal range of temperatures. More than three-fourths of the day-light hours have sunshine, even in the winter months. The air is normally dry and humid days are rare. Nearly half of the annual precipitation in Albuquerque results from afternoon and evening thunderstorms during the summer. Thunderstorm frequency increases rapidly around the beginning of July, peaks during August, then diminishes by the end of September. Thunderstorms are usually brief, sometimes produce heavy rainfall. Small amounts of precipitation fall in the winter. Temperatures in Albuquerque are those characteristic of a dry, high altitude, continental climate. The average daily range of temperature is relatively high, but extreme temperatures are rare. High temperatures during the winter are near 10°C with only a few days on which the temperature is below zero. In summer, day-time maxima are about 32°C. Sustained winds of 5.4 $[m \ s^{-1}]$ or less occur approximately 80% of the time.

2.) *Tucson International Airport* (Arizona), 32.131N, 110.955W, data availability 01/1961-12/1990. The climate of Tucson is characterized by a long hot season, from April to October. Temperatures above 32°C prevail from May through September. Temperatures of 38°C or higher average 41 days annually, including 14 days each for June and July. The daily temperature range is large, averaging 17°C or more. More than 50% of the annual precipitation falls between July 1 and September 15 in the form of scattered convective or orographic showers and thunderstorms. Over 20% of annual precipitation falls from December through March and occurs as prolonged rainstorms characteristic to cyclonic systems. Snow is infrequent, particularly in accumulations exceeding 2 cm in depth. From the first month of the year, the humidity decreases steadily until the summer thunderstorm season, when it shows a marked increase. From mid-September, the end of the thunderstorm season, the humidity decreases again until late November. Cloudless days are common and average cloudiness is low. Surface winds are generally light, with no major seasonal changes in velocity or direction. Usually local winds tend to be in the southeast quadrant during the night and early morning hours, veering to northwest during the day. Highest velocities usually occur with winds from the southwest and east to south.

3.) *Tulsa International Airport* (Oklahoma), 36.197N, 95.886W, data availability 01/1961-12/1990. The climate in Tulsa is essentially continental, characterized by rapid changes in temperature. Temperatures occasionally fall below zero but only for short times. Generally, the winter months are mild. Temperatures of 37.8°C or higher are often experienced from late July to early September, but are usually accompanied by low relative humidity. The fall season is long with a great number of sunny days. The average date of the last 0°C temperature occurrence is late March and the average date of the first 0°C degree occurrence is early November. Rainfall is distributed fairly evenly throughout the year. Spring is the wettest season, having an abundance of rain in the form of showers and thunderstorms. The steady rains of fall are a contrast to the spring and summer showers. The greatest amounts of snow are received in January and early March. The snow is usually light and only remains on the ground for brief periods. Prevailing surface winds are southerly during most of the year.

## 2.3    Simulation of short-wave radiation

### 2.3.1    Model formulation

One of the most important hydrometeorological variables driving the surface energy balance is solar, or shortwave, radiation. The amount of incoming radiation affects the soil moisture budget since the magnitude of the latent heat flux is often controlled by the amount of available energy. A spectral band of the shortwave irradiance $[0.30\,\mu m \div 0.7\,\mu m]$ corresponds to the *Photosynthetically Active Radiation* (PAR), which constitutes one of the principal determinants of biomass production. The spatial and temporal distribution of surface irradiance, therefore, exerts one of the fundamental controls on the land-surface energy, water, and element dynamics.

Solar irradiance is highly variable both daily and seasonally and many factors and processes interact to determine the amount of solar radiation received at a given point on the Earth's surface. At the global scale, the amount of energy that reaches

the Earth's surface is highly dependent on latitude and day of the year (day length). At the mesoscale, the presence of air, water vapor, and particles in the atmosphere leads to the processes of reflection, absorption, and scatter that significantly reduce the amount of energy reaching the ground. The presence of the atmosphere leads to the attenuation of the *direct beam* flux, i.e., the energy flux that comes from the direction of the Sun beam. The degree to which the solar beam is attenuated or scattered depends on the volume of air the beam must travel through, which in turn is determined by the elevation above sea level, the Sun's position in the sky, and local atmospheric conditions (cloudiness, amount of aerosols, and dust) (Figure 2-1). The scattering of the energy beam by the atmosphere and clouds leads to some of the energy striking the ground from directions other than that of the direct beam of the Sun. This is known as the *diffuse* irradiance, which can be broken down further into *isotropic* and *circumsolar* diffuse irradiances. The isotropic diffuse irradiance comes from all directions of the sky, except from within about five degrees of the direct solar beam, which is associated with the circumsolar irradiance. Together, the direct beam and diffuse irradiances make up the total, or often referred as the *global* irradiance (a commonly measured variable at meteorological stations). Landscape topography leads to processes that further modify the actual irradiance received at a given location. Terrain effects such as slope angle, aspect, and topographic shading (Figure 2-1) are extremely important in determining the relative reduction or increase in the amount of received radiation at a site. A surface irradiance model, which is to be used to force the model of vegetation-hydrology interactions, has to be sufficiently flexible to account for all described effects. The developed framework combines both the flexibility and universality allowing to parameterize the model for essentially any geographic location and a wide range of atmospheric conditions.

For all practical purposes, the Sun radiates its energy at a constant rate. Outside the atmosphere, at the mean solar distance, the beam irradiance, also known as the *solar constant*, $S_o$, is 1367 $[W\,m^{-2}]$ (as adopted by the World Meteorological Organization). The Earth's orbit is slightly eccentric and the Sun-Earth distance varies throughout the year. To allow for the varying solar distance, a correction, a
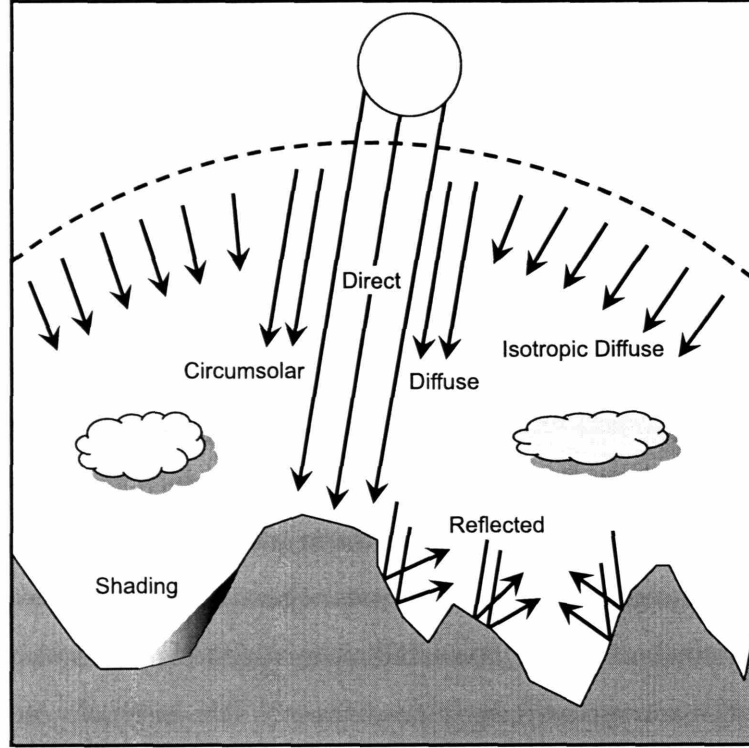
Figure 2-1: Conceptual diagram of the shortwave radiative fluxes.

ratio of the actual Earth-Sun to the mean Earth-Sun Distance, $r$ [−], is introduced so that:

$$S'_o = \frac{S_o}{r^2}, \tag{2.1}$$

$$r = 1.0 + 0.017 \cos\left[\frac{2\pi}{365}(186 - JDay)\right], \tag{2.2}$$

where $JDay$ is the Julian day $[1, \ldots, 365]$.

For further discussion, several variables need to be introduced that define the Sun's position with respect to a location on Earth. The declination of the Sun, $\delta_\oplus$ [$radian$], or the angular distance between the celestial equator plane and the Sun, measured from the former (and positive when the Sun lies north of the Earth's equator) and along the hour circle (Eagleson, 2002) is defined as (Curtis and Eagleson, 1982)

$$\delta_\oplus = \frac{23.45\pi}{180} \cos\left[\frac{2\pi}{365}(172 - JDay)\right]. \tag{2.3}$$

76

The angular distance between the planes of the meridian and the Sun's hour circle (Eagleson, 2002) is known as the hour angle of the Sun, $\tau(T_{ST})$ [radian]:

$$\tau_{\oplus}(T_{ST}) = \frac{15\pi}{180}(T_{ST} + 12 - \Delta T_{SL}), \quad \text{if} \quad T_{ST} < 12 + \Delta T_{SL}, \quad (2.4)$$

$$\tau_{\oplus}(T_{ST}) = \frac{15\pi}{180}(T_{ST} - 12 - \Delta T_{SL}), \quad \text{if} \quad T_{ST} > 12 + \Delta T_{SL}, \quad (2.5)$$

where $T_{ST}$ [hour] is the standard time in the time zone of the observer counted from midnight and $\Delta T_{SL}$ [hour] is the time difference between the standard and local meridian:

$$\Delta T_{SL} = \frac{\xi}{15} \left[ 15|\Delta GMT| - |\Phi'| \right], \quad (2.6)$$

where $\Delta GMT$ [hour] is the time difference between the local time zone and Greenwich Mean Time, $\Phi'$ [angular degree] is the local longitude, and $\xi$ is equal to -1 for west longitude and +1 for east longitude. The solar altitude or an angle of radiation with respect to an observer's horizon plane, $h_{\oplus}$ [radian], is defined as

$$\sin h_{\oplus} = \sin \Phi \sin \delta_{\oplus} + \cos \Phi \cos \delta_{\oplus} \cos \tau(T_{ST}), \quad (2.7)$$

where $\Phi$ [radian] is the local latitude. The mean value of solar altitude over a time interval $\Delta t$ [hour] is often needed in simulation applications. It is provided here for reference:

$$\sin h_{\oplus} = \Delta t \sin \Phi \sin \delta_{\oplus} + \frac{12}{\pi} \cos \Phi \cos \delta_{\oplus}(\sin \tau_{\oplus}(T_{ST} + 1) - \sin \tau_{\oplus}(T_{ST})). \quad (2.8)$$

The Sun's azimuth $\zeta_{\oplus}$ [radian] is obtained from the "hour angle method" as the clockwise angle from north:

$$\zeta_{\oplus} = \arctan\left(\frac{-\sin \tau_{\oplus}}{\tan \delta_{\oplus} \cos \Phi - \sin \Phi \cos \tau_{\oplus}}\right). \quad (2.9)$$

The sunrise time, $T_{H\,rise}$ [local hour], the sunset time, $T_{H\,set}$ [local hour], and the

total day length $D_{LH}$ [*hour*] are often required in applications:

$$T_{H\,rise} = \frac{180}{15\pi}(2\pi - \arccos(-\tan\delta_\oplus \tan\Phi)) - 12\,, \qquad (2.10)$$

$$T_{H\,set} = \frac{180}{15\pi}\arccos(-\tan\delta_\oplus \tan\Phi) + 12\,, \qquad (2.11)$$

$$D_{LH} = \frac{360}{15\pi}\arccos(-\tan\delta_\oplus \tan\Phi)\,. \qquad (2.12)$$

The discussed framework considers two wide bands of solar spectrum: the ultraviolet (UV)/visible (VIS) band, $B_{\Lambda 1}$, $[0.29\,\mu m \div 0.70\,\mu m]$, where ozone absorption and molecular scattering are concentrated, and the infra-red in near and short wavelength range (NIR), $B_{\Lambda 2}$, $[0.70\,\mu m \div 4.0\,\mu m]$, where water and mixed gases absorptions are concentrated. The spectrum separation into two bands facilitates the transmittance modeling of beam and diffuse *clear sky* irradiances because overlaps between scattering and selective absorption is limited (Gueymard, 1989). In the presence of *clouds*, the chosen spectral limits are also convenient due to the above differences in absorption properties by water droplets. Moreover, separate treatment of these two bands allows one to explicitly compute the *photosynthetically active radiation* $[0.30\,\mu m \div 0.7\,\mu m]$ (contained in $B_{\Lambda 1}$), which is used in the process of leaf photosynthesis (Section 4.4.1). According to Slingo (1989), the energy contained in the two considered bands, $[0.29\,\mu m \div 0.7\,\mu m]$ and $[0.70\,\mu m \div 4.0\,\mu m]$, is respectively 46.628316% and 53.371684% of $S'_o$. These fractions are applied to the total extraterrestrial irradiance $S'_o$ to obtain the extraterrestrial flux densities in the two considered bands: $S_{o\Lambda 1}$ and $S_{o\Lambda 2}$ $[W\,m^{-2}]$.

### 2.3.1a Clear sky

**Direct beam irradiance**  It is assumed that direct rays entering the atmosphere encounter extinction processes, which are limited to (Gueymard, 1989): ozone absorption (subscript '$O$' in the following), Rayleigh (molecular) scattering (subscript '$R$'), uniformly mixed gases absorption (subscript '$G$'), water vapor absorption (subscript '$W$'), and aerosol scattering and absorption (subscript '$A$'). Separate extinction layers are considered, so that each band atmospheric transmittance for beam radiation

may be obtained as a product of layer transmittances. Thus, for each of the two considered bands, the beam irradiance at normal incidence, $S^{\mu}_{b\Lambda i}$, is

$$S^{\mu}_{b\Lambda i} = S_{o\Lambda i}T_{Oi}T_{Ri}T_{Gi}T_{Wi}T_{Ai}, \qquad (2.13)$$

where $T$ $[-]$ is transmittance and $i$ $(i = 1, 2)$ is used to denote the considered bands ('1' for $B_{\Lambda 1}$ and '2' for $B_{\Lambda 2}$). The model that derives transmittances for each of the extinction processes is provided in Appendix A.1 and is based on work of Gueymard (1989). For clear skies, the total direct beam flux at the ground at *normal incidence* is

$$S^{\mu}_{b} = S^{\mu}_{b\Lambda 1} + S^{\mu}_{b\Lambda 2}. \qquad (2.14)$$

**Diffuse irradiance** The diffuse irradiance at the ground level is modeled as a combination of three individual components corresponding to the two scattering layers (molecules and aerosols, $I_{dRi}$ and $I_{dAi}$ $[W\,m^{-2}]$, respectively) and to a backscattering process between ground and sky ($I_{dDi}$ $[W\,m^{-2}]$). It is assumed that the fractions

$$B_R = 0.5, \qquad (2.15)$$

$$B_A = 1 - e^{(-0.6931 - 1.8326\sin h_{\oplus})}, \qquad (2.16)$$

of the Rayleigh, $B_R$ $[-]$, and aerosol, $B_A$ $[-]$, scattered fluxes are directed downward (Gueymard, 1989). The diffuse components for band $i$ are written as follows:

$$I_{dRi} = B_R(S_{o\Lambda i}\sin h_{\oplus})T_{Oi}T_{Gi}T_{Wi}T_{Aai}(1 - T_{Ri}), \qquad (2.17)$$

$$I_{dAi} = B_A(S_{o\Lambda i}\sin h_{\oplus})T_{Oi}T_{Gi}T_{Wi}T_{Aai}T_{Ri}(1 - T_{Asi}), \qquad (2.18)$$

$$I_{dDi} = \frac{\rho_g\rho_{si}}{(1 - \rho_g\rho_{si})}(S^{\mu}_{b\Lambda i}\sin h_{\oplus} + I_{dAi} + I_{dRi}), \qquad (2.19)$$

$$S_{d\Lambda i} = I_{dRi} + I_{dAi} + I_{dDi}, \qquad (2.20)$$

where $T_{Aai}$ and $T_{Asi}$ $[-]$ are the aerosol transmittances due to absorption and scattering, respectively, $\rho_g$ $[-]$ is the spatial average regional albedo (assumed to be a

constant value for a considered domain), and $\rho_{si}$ [−] is the sky albedo. The formulation of $T_{Aai}$, $T_{Asi}$, and $\rho_{si}$ is provided in Appendix A.2 and is based on the model of Gueymard (1989). For clear skies, the total diffuse flux at the ground:

$$S_d = S_{d\Lambda 1} + S_{d\Lambda 2}. \qquad (2.21)$$

### 2.3.1b Cloudy sky

The presence of cloud cover significantly modifies the surface irradiance since clouds alter transmission and reflection properties of the atmosphere. Radiative driving of the land-surface systems is thus strongly affected by clouds that exhibit time-varying properties and seasonal dynamics. Therefore, in the framework of a vegetation-hydrology study, the radiative effects of clouds need to be accounted for as accurately as possible.

Cloud parameterizations provided in hydrological literature are often over-simplified since only the global value of the shortwave radiation is required in most hydrological applications. The utilized approaches use empirical formulations that are functions of the total cloud cover (Becker, 2001), or, in a more explicit fashion, that specify fixed bulk properties of the clouds, such as transmissivity and reflectivity. However, it is well known that the radiative effects of clouds vary strongly depending on cloud type, structure, and density. Also, in the framework of the simulation model, a separate treatment of the shortwave bands is needed since cloud reflectivity, absorption, and transmittance vary for different spectral intervals (Slingo and Schrecker, 1982).

The discussed framework for estimating cloudy sky beam and diffuse radiation relies on parameterizations developed by Stephens (1978) and Slingo (1989). Based on both observational and theoretical evidence, these studies assume that the cloud shortwave radiative properties are mainly determined by the cloud total vertical liquid water path, $LWP$ [$g\ m^{-2}$], which is defined as the integral of the liquid water content, $LWC$ [$g\ m^{-3}$], from the cloud base to the cloud top. Stephens (1978) convincingly showed that the broadband optical thickness is essentially the same for clouds of different types (shape and altitude) that have the same $LWP$. Slingo (1989), however,

introduced an additional independent functional relationship between cloud radiative properties and the effective radius of drop size distribution. The advantage of using liquid water path is that $LWP$ can be obtained by satellite microwave radiometry and allows the introduction of seasonality effects in the cloud properties.

The presented approach, described in detail in Appendix B, employs relationships developed by Stephens (1978) to derive the effective radius of drop size distribution based on $LWP$. The four-band model of Slingo (1989) is then used to derive the cloud shortwave radiative properties such as transmittances and reflectances for the incident direct $S^\mu_{b\Lambda i}$ and diffuse $S^\mu_{d\Lambda i}$ fluxes computed in (2.13) and (2.20) (note that although these clear sky fluxes are estimated at the ground level, they are assumed to be incident on the top of clouds).

**Direct beam irradiance**  The model presented here uses the total cloud cover, $N$ [0.0 ÷ 1.0], to differentiate between the clear sky, $(1 - N)$, and cloudy, $N$, fractions of the sky dome. The direct beam flux from the clear sky fraction is assumed to reach the ground surface unaltered, as estimated in (2.13). It is assumed that the cloudy fraction of sky contains a homogeneous layer of clouds characterized by the total vertical liquid water path, $LWP$ [$g\ m^{-2}$]. The total direct beam normal irradiance $S^\mu_{B\Lambda j}$ in each of the bands $j$, $j = 1, \ldots, 4$ of Slingo's (1989) parameterization (Appendix B) is estimated as a linear combination of the fluxes from the clear sky and cloudy fractions of the sky dome:

$$S^\mu_{B\Lambda j} \;=\; S^\mu_{b\Lambda i}\left[(1 - N) + T_{DBj}N\right]\frac{k_j}{K}, \qquad (2.22)$$

where $T_{DBj}$ [−] is the cloud transmissivity for the direct beam flux in band $j$ that depends on the vertical $LWP$ of the sky cloudy fraction, $k_j$ is the respective fraction of solar irradiance at the top of the atmosphere in each band [0.46628316, 0.31963484, 0.180608, 0.033474] (Appendix B.1), and $K = 0.46628316$ if $i = 1$, $K = 0.53371684$ if $i = 2$. The fluxes are then summed to obtain the shortwave radiation values $S^\mu_{B\Lambda i}$ in the two considered bands $B_{\Lambda 1}$ and $B_{\Lambda 2}$. For cloudy sky, the total beam irradiance

at *normal incidence* is

$$S_B^\mu = S_{B\Lambda1}^\mu + S_{B\Lambda2}^\mu. \tag{2.23}$$

**Diffuse irradiance**   As above, in order to account for the incoming diffuse radiation, clear sky and cloudy fractions of the sky dome are considered, and diffuse flux from the clear sky fraction is assumed to reach the ground surface unaltered, as estimated in (2.20). The diffuse radiative flux at the cloud bottom may result from both the diffuse and beam radiation incident at the cloud top. The total diffuse irradiance $S_{D\Lambda j}$ in each of the bands $j$ (Appendix B) is estimated as a linear combination of the fluxes from the clear sky and cloudy fractions of the sky dome:

$$S_{D\Lambda j} = (1-N)S_{d\Lambda i} + N\left[T_{DIRj}S_{b\Lambda i}^\mu + T_{DIFj}S_{d\Lambda i}\right]\frac{k_j}{K}, \tag{2.24}$$

where $T_{DIRj}$ $[-]$ is the diffuse transmissivity for direct incident radiation and $T_{DIFj}$ $[-]$ is the diffuse transmissivity for diffuse incident radiation, both depend on $LWP$ of the sky cloudy fraction. The fluxes are then accordingly summed to obtain the shortwave radiation values $S_{D\Lambda i}$ in the two considered bands $B_{\Lambda1}$ and $B_{\Lambda2}$. For cloudy sky, the total diffuse irradiance is

$$S_D = S_{D\Lambda1} + S_{D\Lambda2}. \tag{2.25}$$

### 2.3.1c Terrain effects

**Direct beam irradiance**   The spatial distribution of solar radiation over the surface is strongly affected by small-scale terrain features such as slope angle, aspect, and screening or reflection effects from the surrounding terrain. A comprehensive vegetation-hydrology model needs to account for the associated effects. The solar angle of incidence, formally defined as the angle between the sun beam and the normal to the slope surface, $\varphi_{\oplus\triangledown}$ $[radian]$, uniquely determines orientation of the irradiated

surface with respect to the Sun:

$$\cos\varphi_{\oplus\triangledown} = \cos\alpha_{\triangledown}\sin h_{\oplus} + \sin\alpha_{\triangledown}\cos h_{\oplus}\cos(\zeta_{\oplus} - \zeta_{\triangledown}), \qquad (2.26)$$

where $\alpha_{\triangledown}$ [radian] is the slope of the surface and $\zeta_{\triangledown}$ [radian] is its aspect (in the clockwise direction from north). The above expression is given by the cosine law of spherical trigonometry (e.g., Sellers, 1965). Omitting in the following the subscripts that denote the considered spectral bands $B_{\Lambda1}$ and $B_{\Lambda2}$, the direct beam flux, $S_{atm}\downarrow_{\Lambda}^{\mu}$ [$Wm^{-2}$], at the ground surface oriented in space can be estimated in general as

$$S_{atm}\downarrow_{\Lambda}^{\mu} = S_{b\Lambda}^{\mu}\cos\varphi_{\oplus\triangledown}W_{BH}, \quad if \quad N = 0, \qquad (2.27)$$

$$S_{atm}\downarrow_{\Lambda}^{\mu} = S_{B\Lambda}^{\mu}\cos\varphi_{\oplus\triangledown}W_{BH}, \quad if \quad N > 0, \qquad (2.28)$$

where $W_{BH}$ [0.0 ÷ 1.0] is the hourly sun view factor defined as the ratio of maximum sun shine duration during which the sun can be seen above the actual horizon to that of unobscured horizon (Olseth et al., 1995). The term $\cos\varphi_{\oplus\triangledown}$ accounts for "self-shading" of the surface and $W_{BH}$ is a factor accounting for "distant-shading" from the surrounding topography. $W_{BH}$ can be significantly different from '1' in mountainous terrain. The factor $W_{BH}$ is included in the above equations for the purposes of generality, and it is assumed to be equal to '1' in this work.

**Diffuse irradiance**  The diffuse sky irradiance on a surface oriented in space is composed of three components: the circumsolar, isotropic, and ground reflected diffuse radiation. The circumsolar component of diffuse radiation on a surface oriented in space (the subscript '$B$', which refers to cloudy sky conditions, is used in the notation of the beam flux $S_B^{\mu}$ to indicate a generally wider range of applicability of the equation) is

$$S_{DC\Lambda} = S_{D\Lambda}\left[\frac{S_B^{\mu}}{S_o'}\right]\frac{\cos\varphi_{\oplus\triangledown}}{\sin h_{\oplus}}. \qquad (2.29)$$

83

The isotropic component of the diffuse radiation is

$$S_{DI\Lambda} \;=\; S_{D\Lambda}\left[1 - \frac{S_B^\mu}{S_o'}\right]\frac{1 + \cos\alpha_\nabla}{2}\,. \qquad (2.30)$$

The diffuse radiation reflected from other sites is

$$S_{DR\Lambda} \;=\; \rho_g'\left[\frac{S_{B\Lambda}^\mu}{S_B^\mu}\sin h_\oplus + S_{D\Lambda}\right]\frac{1 - \cos\alpha_\nabla}{2}\,, \qquad (2.31)$$

where $\rho_g'$ [$-$] is the ground albedo, which is assumed to be wavelength independent with typical values 0.10 - 0.25 for snow-free environments. Although $\rho_g'$ is assumed to be space-time constant in the discussed framework, its temporal variability can be introduced by using simulated spatially-averaged albedos for a considered domain (Section (3.5.2)).

The total diffuse irradiance for a surface oriented in space is finally estimated as (Olseth et al., 1995)

$$S_{atm}\downarrow_\Lambda \;=\; [S_{DC\Lambda} + S_{DI\Lambda}]\,W_D + S_{DR\Lambda}\,, \qquad (2.32)$$

where $W_D$ [0.0 $\div$ 1.0] is the sky-view factor for diffuse radiation (fraction of sky visible at a specific grid point). It is approximated as $W_D = 0.5(1 + \cos\alpha_\nabla)$ (Olseth et al., 1995). One may note that if the considered surface is horizontal, i.e., $\alpha_\nabla = 0$, equations (2.29) - (2.32) simply result in $S_{atm}\downarrow_\Lambda = S_{D\Lambda}$.

Figures 2-2 - 2-3 provide illustrative examples of how aspect and slope modify the amount and timing of the incoming shortwave radiation.

## 2.3.2 Parameter estimation

The parameters of the described shortwave radiation model include: the ozone amount in a vertical column $u_o$ [$cm$], the Angström turbidity parameter $\beta$ (assumed to be the same for both VIS and NIR bands), the aerosol single-scattering albedo $\omega_{Ai}$ [$-$], and the spatial average regional albedo $\rho_g$ [$-$] (Appendices A.1 - A.2). The liquid water path, $LWP$ [$g\ m^{-2}$], is a measurable state variable of cloud thickness, however, it is
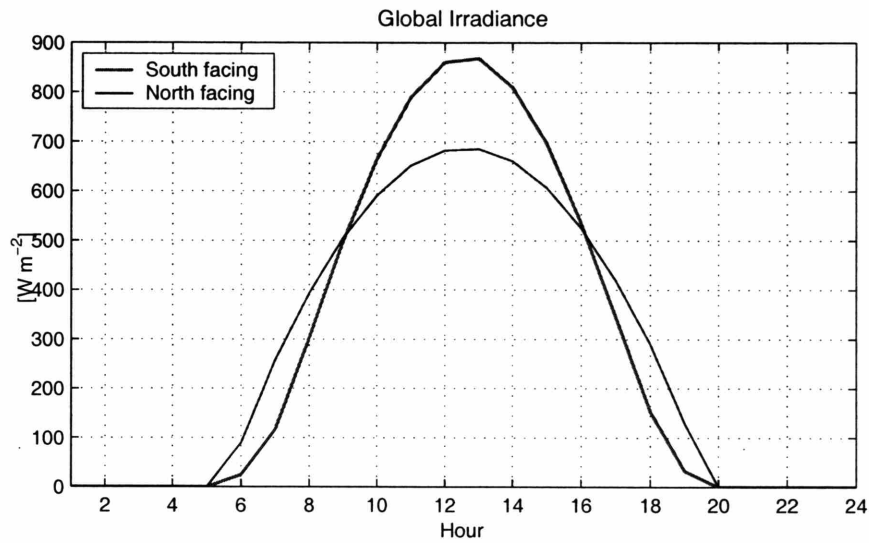
Figure 2-2: The daily cycle of the global irradiance on a 30° slope that has either southerly or northerly aspect (August, Albuquerque, NM).
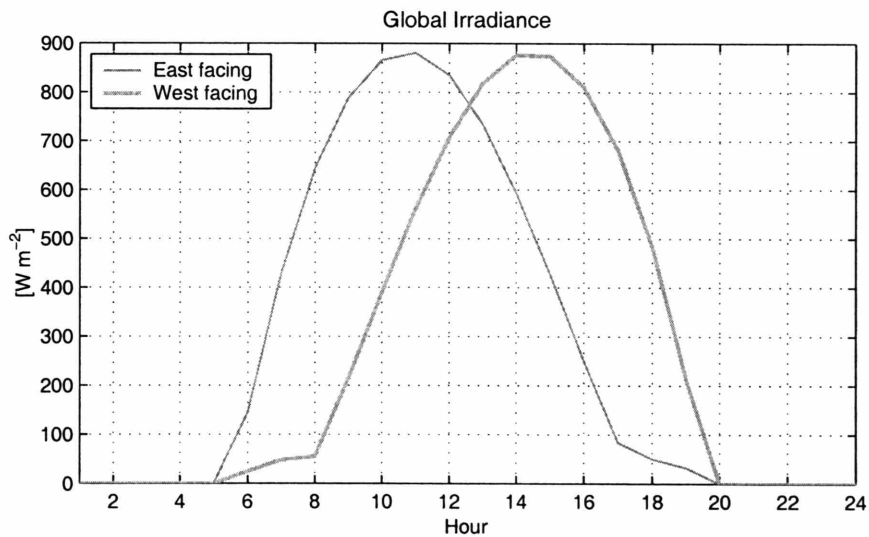


Figure 2-3: The daily cycle of the global irradiance on a 30° slope that has easterly or westerly aspect (August, Albuquerque, NM).

not easily available. Furthermore, if the radiative transfer model is used along with the stochastic climate simulator (Sections 2.4 - 2.8), it is a reasonable approach to generate $LWP$ based on the regional climatology. All subsequent illustrations refer to the observed data for Albuquerque (NM), the only location for which radiation data were available.

The parameters $u_o$, $\beta$, $\omega_{Ai}$, and $\rho_g$ are derived for clear sky atmospheric conditions. As specified in Appendix A, $u_o$ is assumed to be a seasonally constant value (0.34 is used in this study). The radiative transfer model is very sensitive to the parameter $\beta$, which is calibrated based on the measured direct beam irradiance data. The procedure consists in adjusting $\beta$ via the comparison of observed and simulated using (2.13)-(2.14) clear sky direct beam flux. For example, Figure 2-4 illustrates the annual cycle of the mean observed and simulated irradiances for a number of hours of a given Julian day (Albuquerque, NM). By tuning the seasonally-invariant $\beta$ parameter, the magnitude of the simulated direct beam flux can be increased or decreased with respect to the observed flux (in Figure 2-4, $\beta = 0.017$). Similarly, the aerosol single-scattering albedo $\omega_{Ai}$ and the spatial average regional albedo $\rho_g$ are adjusted to obtain the proper seasonal cycle of the clear sky diffuse radiation. In this study, the values are assumed to be seasonally-invariant with $\rho_g = 0.1$ and $\omega_{A1} = 0.920$, $\omega_{A2} = 0.833$. The seasonal invariance of these parameters can partly contribute to the smaller than observed variability of the simulated clear sky diffuse radiation throughout the year (Figure 2-4).

Once the clear sky radiative fluxes are reproduced at a satisfactory level, $LWP$ is considered as the model parameter to account for overcast and partially cloudy sky conditions in the radiative transfer model. Note, however, that the parameters of both the rainfall (Section 2.4) and cloudiness model (Section 2.5) have to be estimated at that time. A seasonally-varying value (on a monthly basis) of $LWP_o$ for *overcast* conditions is used in this study to account for the different cloud structure and origin during different periods of the year. Furthermore, it is assumed that the liquid water path for any sky condition is $LWP_N = e^{N \ln(LWP_o)} - 1$, where $N$ is the total cloudiness bounded by values '0' (clear sky) and '1' (overcast). This non-parametric relationship
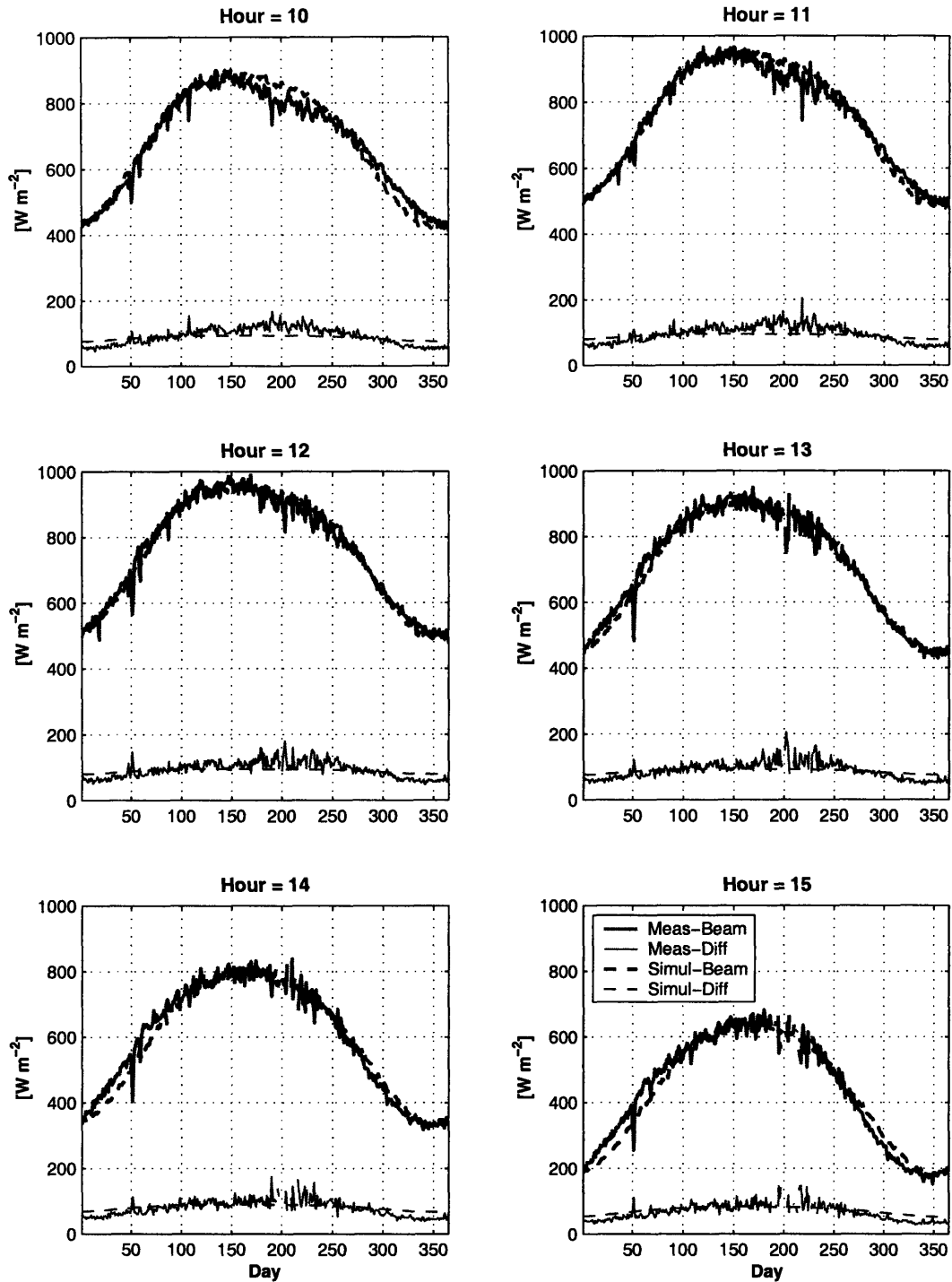
Figure 2-4: Seasonal cycles of the observed and simulated direct beam and diffuse flux on a horizontal surface in *clear sky* conditions for hours 10-15 (on a 24-hour basis, Albuquerque, NM).
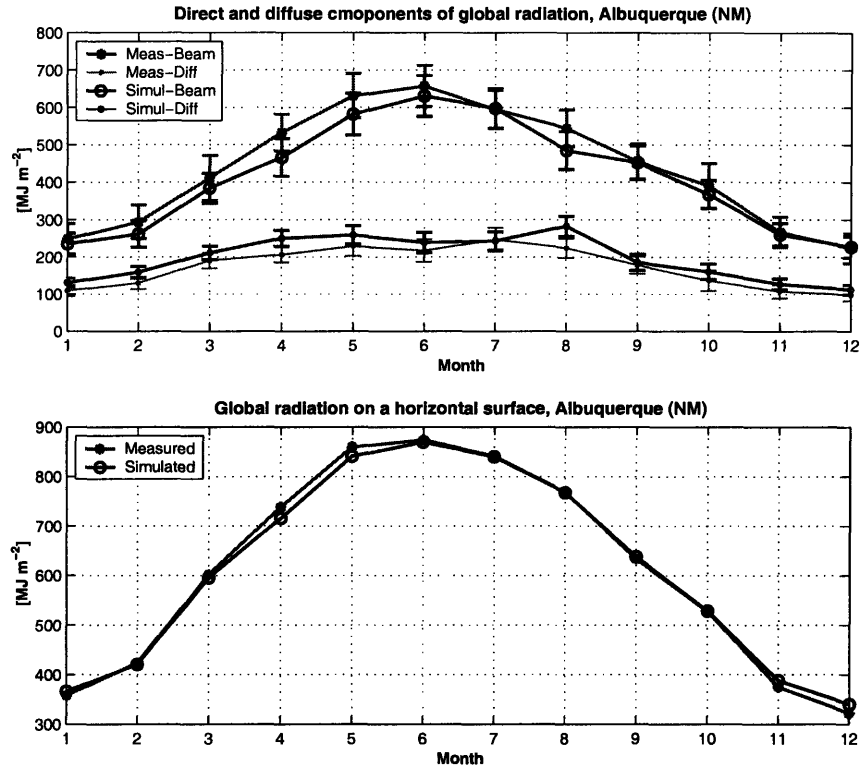
Figure 2-5: Seasonal cycles of mean monthly observed and simulated direct beam flux, diffuse flux, and global radiation on a horizontal surface for all sky conditions (Albuquerque, NM).

introduces a decrease of $LWP$ for *any sky condition* with respect to the overcast value $LWP_o$. The monthly values of $LWP_o$ are adjusted based on comparison between the simulated and observed direct beam and diffuse fluxes for all sky conditions. Figure 2-5 illustrates the annual cycles of the radiative fluxes for Albuquerque (NM) with $LWP_o = $ [Jan: 110, Feb: 80, Mar: 80, Apr: 60, May: 65, Jun: 75, Jul: 95, Aug: 60, Sep: 100, Oct: 100, Nov: 130, Dec: 150] $[g \ m^{-2}]$.

## 2.4 Simulation of rainfall

### 2.4.1 Model formulation

A variety of stochastic models of precipitation has been developed over the past years (Buishand, 1978; Chin, 1977; Gabriel and Neuman, 1962; Smith and Schreiber, 1973;

Woolhiser, 1992). Not only is precipitation the most crucial meteorological variable for many applications, but the presence or absence of precipitation also affects statistics of many other hydrometeorological variables. Since in stochastic simulations precipitation is conventionally considered as an independent hydrometeorological variable, in principle any model that satisfies conditions of efficiency and feasibility can be used to simulate precipitation occurrence. Among the widely used models, perhaps the most known are the seasonally varying first-order two-state Markov model and the "renewal" model, also referred as the *spell-length* model (Wilks and Wilby, 1999).

The first type of rainfall models, such as the commonly used precipitation generator of Richardson (1981), assumes the Markov chain model, which is fully described by the transition probabilities of precipitation occurrence for any given period. A decision is made first if a wet or dry period occurs following a dry or wet period. If a wet period occurs, the amount of precipitation for that period is generated. The model incorporates a continuous Fourier representation of the rainfall parameters that are obtained from long-term precipitation records. As a rule, most of the precipitation models of this type simulate the occurrence of daily precipitation. The number of parameters required by these models is quite high.

Rather than simulating precipitation occurrences day by day, the "renewal" models generate random numbers from the fitted dry and wet spell-length distributions. This implies that a new spell length of wet/dry period is generated only after a spell of the opposite type (wet or dry) has come to an end. The renewal model is often represented by the Poisson arrival model (Todorovic, 1968; Todorovic and Yevjevich, 1969) that assumes the exponential distribution for dry spell (interstorm) periods. A Poisson arrivals process has the ability to represent the distribution of the precipitation process in any time period in terms of just a few parameters. The relatively large number of storms in even a few years, make the estimation of such parameters feasible (Eagleson, 1978). It can conveniently represent both the distribution of inter-arrival time (length of the interstorm period) as well as storm duration. Benjamin and Cornell (1970) point out that "the Poisson process seems to provide the best compromise between the conflicting demands of simplicity and generality". Another advantage of

the approach is that by using distributions that have seasonally-varying parameters (Todorovic and Yevjevich, 1969; Rodriguez-Iturbe et al., 1999b), the rainfall process that exhibit temporal non-uniformity of characteristics (storm arrival rates, durations and intensities) can be accounted for. The Poisson storm arrival model is selected for the purposes of the presented research.

Grayman and Eagleson (1969) showed that storm durations and interstorm times could be treated as independent events. Thus, the precipitation model can be expressed by successive sampling from the fitted probability density functions. E.g., time between two successive storms $t_b$ [$hour$] follows the exponential distribution (by definition of the Poisson arrival process):

$$f(t_b) \quad = \quad \frac{1}{\mu_b}e^{-\frac{1}{\mu_b}t_b}, \tag{2.33}$$

where $\mu_b$ [$hour$] is the mean time between storms. The storm duration $t_r$ [$hour$] is also simulated using the exponential distribution (Grayman and Eagleson, 1969):

$$f(t_r) \quad = \quad \frac{1}{\mu_r}e^{-\frac{1}{\mu_r}t_r}, \tag{2.34}$$

where $\mu_r$ [$hour$] is the mean storm duration. Grayman and Eagleson (1969) showed that storm depths were highly dependent on storm durations. Storm depths $h$ [$mm$] were found to follow a gamma distribution conditioned by storm duration:

$$f\left(h \mid \frac{t_r}{\mu_r}\right) \quad = \quad \frac{1}{\mu_d}\frac{\left(\frac{h}{\mu_d}\right)^{\frac{t_r}{\mu_r}-1}e^{-\frac{h}{\mu_d}}}{\Gamma\left(\frac{t_r}{\mu_r}\right)}, \tag{2.35}$$

where $\mu_d$ [$mm$] is the mean storm depth. The two-parameter gamma distribution has been shown to satisfactorily preserve the rainfall statistical characteristics (Curtis and Eagleson, 1982).

The following procedure is used to simulate rainfall. At some initial time $t_0$ an interstorm duration $t_b$ is generated from the distribution (2.33). The period [$t_0$, $t_0 + t_b$] is considered dry. When the time reaches [$t_0 + t_b$], the storm duration $t_r$ is gener-

ated from (2.34). Using the value set for $t_r$, a storm depth $h$ is generated from the distribution described by (2.35). The period $[t_0 + t_b, \ t_0 + t_b + t_r]$ is then considered wet. When time reaches $[t_0 + t_b + t_r]$ the process is repeated to determine the next storm-interstorm sequence. The procedure follows the model of *rectangular pulses* that considers a *uniform* rainfall intensity throughout the whole $t_r$. The advantage of this modeling approach is in knowledge of the time limits of a current hydrometeorological period (dry or wet spell) at any time. As will be shown later, this facilitates an explicit coupling of the precipitation model and other components of the weather generator, such as cloud cover and air and dew point temperature.

## 2.4.2 Parameter estimation

The required parameters for the precipitation components include the mean time between storms $\mu_b$, the mean storm duration $\mu_r$, and the mean storm depth $\mu_d$. The major challenge in estimating these parameters, as indicated by Restrepo-Posada and Eagleson (1982), is separating point-precipitation records into statistically-independent storms. Multiple mesoscale precipitation events are embedded in a single synoptic scale disturbance and each mesoscale event may produce intervals of rainfall followed by periods without rainfall before the next event arrives. Since it is practically impossible to define independence criteria based on the physics of storm generation when operating with series of point precipitation data, a statistical method is required.

The following procedure was proposed by Restrepo-Posada and Eagleson (1982). They argued that time between storms can be used to test the independence of successive rainfall events. Since rainfall arrival is assumed to be a Poisson process, then the interstorm times are assumed to follow the exponential distribution and, therefore, the mean and standard deviation of interstorm times have to be equal (resulting in the coefficient of variation $C_v$ equal to one). The procedure, therefore, is to choose such a duration of time between storms, $t_{b\,\text{min}}$ [$hour$], at which $C_v$ passes through one. The $t_{b\,\text{min}}$ would thus represent the minimum separation time of independent events, i.e., when the rainless period separating two rainy periods has a duration less than $t_{b\,\text{min}}$, the two rainy periods belong to the same storm.

91

Restrepo-Posada and Eagleson (1982) applied the procedure to a number of precipitation records at various locations having different climate characteristics. They found $t_{b\,min}$ times ranging between 8 and 76 hours. In general, dry climates had higher values, while more humid climates were found to have lower values. The estimates were also shown to produce Poisson distributions of annual precipitation, which agreed well with observed distributions at several arid climate sites. Restrepo-Posada and Eagleson (1982), however, concluded that for precipitation models, similar to the one within the framework of stochastic weather generator, such a strict requirement of independence is operationally impractical and probably unnecessary: "...for dynamic purposes, the distributions of the constituent storm variables are more appropriately and conveniently determined from the raw storm data without concern for independence". If such long separation intervals (e.g., 8-76 hours) are imposed, long storm durations would result and storms would contain many periods without precipitation. This would produce unrealistically low average storm intensities. As a result, Restrepo-Posada and Eagleson (1982) suggested that for problems where the dynamic response of hydrologic system to precipitation inputs is of major interest, the rainfall model parameters should be estimated from the raw storm data without concern for event independence.

Grace and Eagleson (1967) and Sariahmed and Kisiel (1968) used autocorrelation of successive storm depths to identify independent storm events (which is only a *necessary* condition for independence, according to Restrepo-Posada and Eagleson (1982)). The time lag at which autocorrelation was not significantly different from zero (at significance level 0.90-0.95, corresponding to the autocorrelation values $\leq 0.15 - 0.20$) was used as the $t_{b\,min}$. Grace and Eagleson (1967) and Sariahmed and Kisiel (1968) found such durations to be between 2 and 3 hours (for convective storms). Curtis and Eagleson (1982) used the value of 2 hours.

The same procedure is used for estimation of parameters of the rainfall model used in this work. Figure 2-6 illustrates the autocorrelation functions of storm depths estimated for precipitation records in Tucson (AZ), Tulsa (OK), and Albuquerque (NM) used in the following analysis. The minimum lull durations are taken to be

92
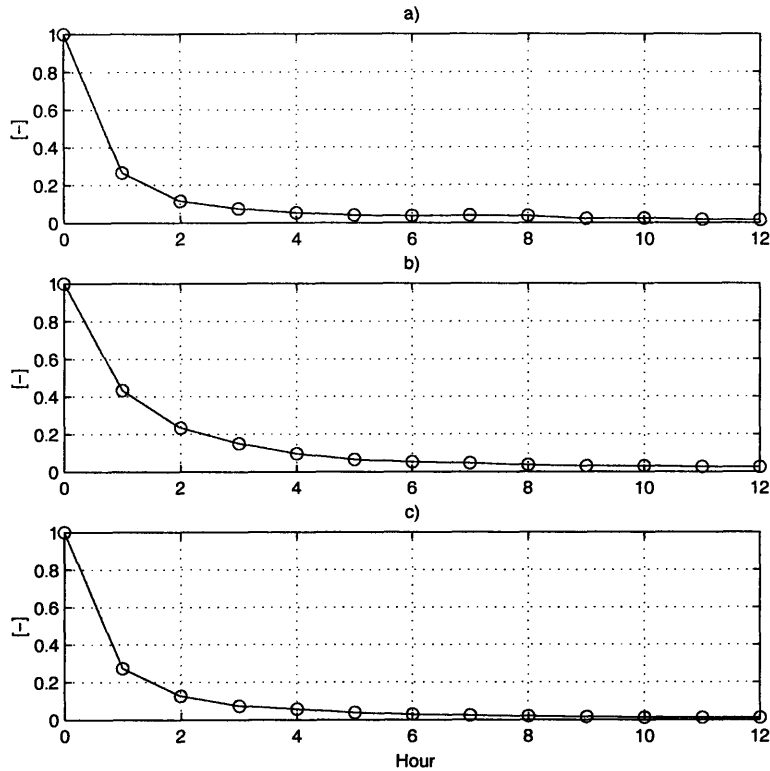
Figure 2-6: Autocorrelation functions of hourly rainfall depths: a.) Tucson (AZ); b.) Tulsa (OK); and c.) Albuquerque (NM)

3 hours (Table 2.1). The estimation procedure, therefore, assumes that a storm duration includes both hours with recorded precipitation and any non-precipitation separation intervals less or equal than the value determined for each station (3 hours in this case).

For climates with pronounced precipitation seasonality, the parameters $\mu_b$, $\mu_r$, and $\mu_d$ have to account for the intra-annual variability. Precipitation seasons are identified by analyzing the mean monthly distribution of precipitation. Figures 2-7 - 2-9 illustrate the mean monthly values of number of storms and the total precipitation amounts based on data of stations in Tucson (AZ), Tulsa (OK), and Albuquerque (NM). As can be seen, for example, in Figure 2-8, some areas exhibit a sharply marked intra-annual variability in precipitation. The rainfall model parameters are estimated to account for such a seasonality (Table 2.1).
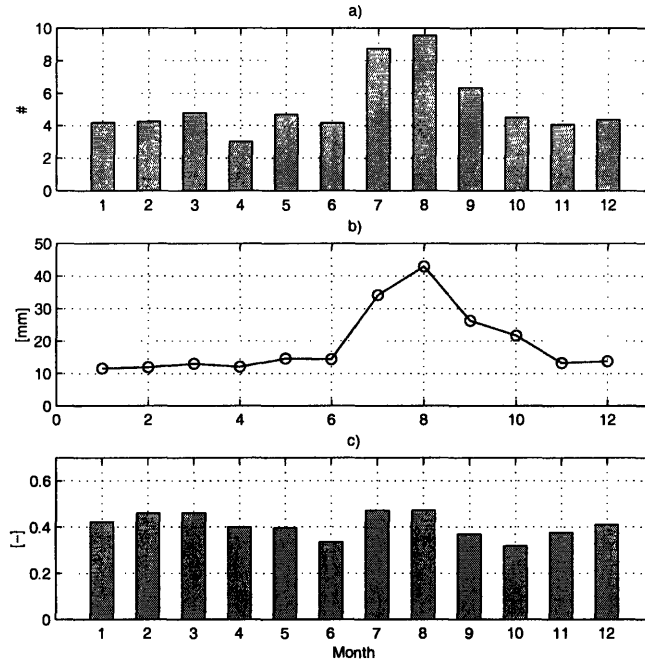
Figure 2-7: The mean monthly distribution of precipitation and cloud cover (Albuquerque, NM): a.) number of storms; b.) total amount of precipitation; and c.) cloudiness.
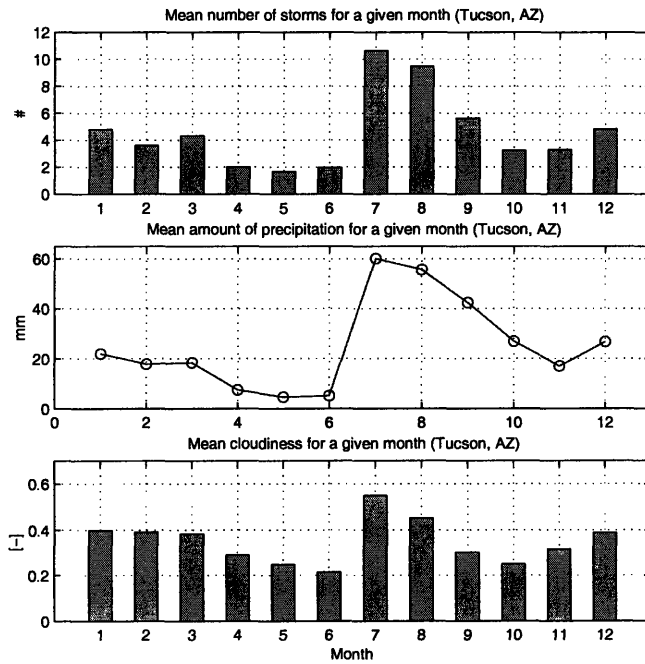


Figure 2-8: The mean monthly distribution of precipitation and cloud cover (Tucson, AZ): a.) number of storms; b.) total amount of precipitation; and c.) cloudiness.
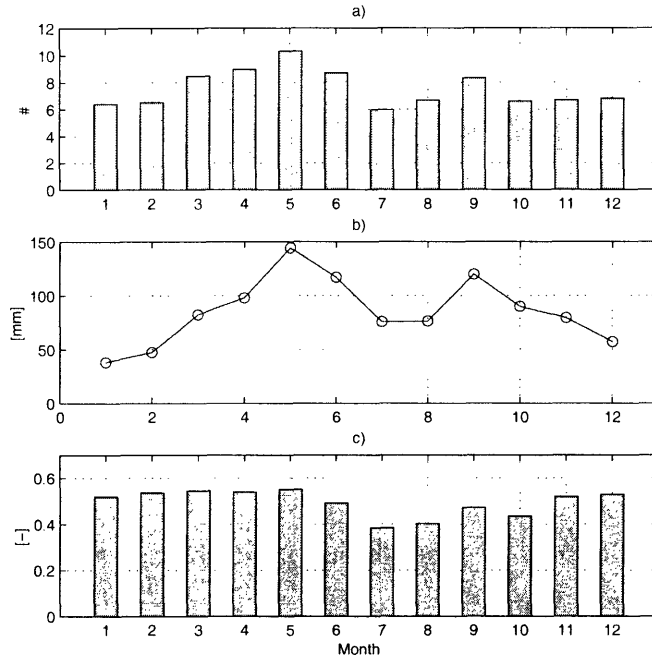
Figure 2-9: The mean monthly distribution of precipitation and cloud cover (Tulsa, OK): a.) number of storms; b.) total amount of precipitation; and c.) cloudiness.

Table 2.1: Rainfall statistics: the mean values of precipitation rate $(\mu_d/\mu_r)$ [$mm\ hour^{-1}$] and storm $(\mu_r)$ and interstorm $(\mu_b)$ durations [$hour$] (parameters have the same respective order in the table).

| Meteostation / Season | Albuquerque (NM) 35.05N 106.617W | Tucson (AZ) 32.131N 110.955W | Tulsa (OK) 36.197N 95.886W |
|---|---|---|---|
| Min. lull dur. | 3 [hour] | 3 [hour] | 3 [hour] |
| Season #1 | (mo.11-6): 0.778/3.61/152.7 | (mo.12-3): 0.775/5.16/142.6 | (mo.12-2): 0.981/6.82/107.4 |
| Season #2 | (mo.7-8): 1.661/2.44/70.3 | (mo.4-6): 1.15/2.86/315.6 | (mo.3-4): 1.953/5.46/75.2 |
| Season #3 | (mo. 9): 1.161/3.197/85.9 | (mo.7-9): 2.03/ 2.83/ 74.9 | (mo. 5): 3.03/4.06/60.0 |
| Season #4 | (mo.10): 1.048/3.96/122.7 | (mo.10-11): 1.13/5.03/176.3 | (mo. 6): 3.41/3.86/69.5 |
| Season #5 | - | - | (mo. 7-8): 3.01/3.91/102.2 |
| Season #6 | - | - | (mo. 9): 2.61/4.86/73.1 |
| Season #7 | - | - | (mo. 10-11): 1.91/6.66/104 |
| **Year** | 1.091/ 3.25/ 125.8 | 1.438/ 3.83/ 143.8 | 2.244/ 5.285/ 93.3 |

## 2.5  Simulation of cloudiness

### 2.5.1  Model formulation

Cloud cover significantly affects radiation balance by altering transmission and re-
flection properties of the atmosphere, as seen in Section 2.3. Cloud cover, therefore
plays, an important role in regulating moisture and heat fluxes at the land surface.
When one has to explicitly consider the components of the energy balance, their tem-
poral dynamics, and dependence on occurrence of precipitation events, simulating
cloudiness is necessary.

Simulation of cloud cover as a stochastic process has received little attention in
the hydrological literature. The cloud cover is not explicitly modeled by most of the
weather generator models. The problem is circumvented by simulating net solar ra-
diation that implicitly accounts for daily cloudiness (e.g., as in two commonly used
models USCLIMATE and CLIGEN) (Richardson, 1981; Nicks and Gander, 1993,
1994). Where studies have been performed (e.g., Falls, 1974; Chia and Hutchinson,
1991; Aguiar and Collares-Pereira, 1992), the cloud cover is treated independently
of other hydrometeorological variables (daily time scale), which is not a suitable ap-
proach for this study. Only two models were found that provide frameworks for hourly
cloudiness simulation. A study by Remund et al. (1999) reports the derivation of
cloud cover based on simulation of the daily clearness index (it represents the ratio of
radiation for a horizontal surface to the solar radiation at the top of the atmosphere).
Curtis and Eagleson (1982) provide a framework for hourly cloud cover simulation
using information on precipitation occurrence. Their model couples cloudiness de-
velopment to the occurrence of intra- and interstorm periods simulated within the
framework of the Poisson arrival process of precipitation events. The model of Curtis
and Eagleson (1982) serves as a basis for the cloud cover model implemented within
the discussed climate simulator. The description below provides only key aspects of
the model along with the added modifications. For details, the reader is referred to
the original work of Curtis and Eagleson (1982).

Cloud cover simulated by the weather generator can be defined as the fraction of

the celestial dome covered by clouds. The cloudiness process, $N(t)$ $[-]$, is therefore bounded by '0' (clear sky) and '1' (overcast). Intermediate values can define a variety of hydrometeorological conditions, e.g., '0.2' - scattered,..., '0.7' - broken, etc. Curtis and Eagleson (1982) consider $N(t)$ as a random non-stationary process composed of intra- and interstorm periods. During the *intra-storm* period, the expected value of the mean of the process is close to 1.0, while if $N(t)$ is examined near the middle of sufficiently long *interstorm* period, the expected value is usually quite different from 1.0. The central assumption made in the model of Curtis and Eagleson (1982) is that there is a loosely centered sub-region, $R_0$, around the midpoint of the interstorm period in which the process $N(t)$ can be assumed stationary. By examining the first and second moment properties of the process, they conclude that the "fairweather" cloud cover process in this sub-region is unaffected by approaching or receding precipitation systems:

$$E(N(t) \mid t_b)_{t \in R_0} = E(N(t))_{t \in R_0} = M_0,$$

$$Var(N(t) \mid t_b)_{t \in R_0} = Var(N(t))_{t \in R_0} = \sigma_m^2, \qquad (2.36)$$

where $t$ is time, $t \in R_0$, $M_0$ $[-]$ is the "fairweather" mean value of $N(t)$, and $\sigma_m^2$ $[-]$ is the "fairweather" variance of $N(t)$. Another major assumption made in the model is that there is a smooth transition of moment properties (mean and variance) from the boundaries, i.e., from the end of a precipitation event to "fairweather" and from the end of "fairweather" period to the beginning of the following rainfall event. The process is therefore assumed to be of the form:

$$N(t) = M_0 + (1 - M_0)(1 - J(t)) + m(t)J(t), \qquad (2.37)$$

where $J(t)$ is an assumed transition function and $m(t)$ is the stationary sequence of correlated deviations with $E(m(t)) = 0$ and $Var(m(t)) = \sigma_m^2$, and autocorrelation function $\rho_N(\tau)$, where $\tau$ $[hour]$ is the lag. The time varying conditional expectation and variance of cloud cover under this assumption are obtained as (Curtis and

Eagleson, 1982)

$$
\begin{aligned}
E(N(t) \mid t_b) &= M_0 + (1 - M_0)(1 - J(t)) , \\
Var(N(t) \mid t_b) &= \sigma_N^2(t) = \sigma_m^2 P^2(t) ,
\end{aligned}
\tag{2.38}
$$

where $t \in t_b$. The autocorrelation structure of the cloud cover process (2.37), as shown by Curtis and Eagleson (1982), is not affected by $J(t)$ and is identical to the autocorrelation function of the process $m(t)$: $\rho_N(\tau) = \rho_m(\tau)$. The transition function $J(t)$ is assumed to be of an exponential form:

$$
J(t) = (1 - e^{-\varsigma(t - t_0)})(1 - e^{-\gamma(t_0 + t_b - t)}) ,
\tag{2.39}
$$

where $\varsigma$ and $\gamma$ $[hour^{-1}]$ are decay coefficients controlling the transition rates from the boundaries (end/beginning of precipitation events) to/from the region $R_0$. These rates are assumed to be equal in this model implementation, although different values can also be imposed. As follows from (2.39), when $t \in R_0$ and $t_b \to \infty$:

$$
\lim_{t_b \to \infty} J(t) = 1 .
\tag{2.40}
$$

$J(t)$ reaches a value close to 1.0 for all reasonable values of the decay coefficients and, therefore, the "fairweather" cloudiness is essentially simulated as

$$
\lim_{t_b \to \infty} N(t) = M_0 + m(t) .
\tag{2.41}
$$

The stationary deviations process, $m(t)$, is taken to be a first order Markov process:

$$
m(t) = \rho_m(1) m(t - 1) + \varepsilon(t) \sigma_m \sqrt{1 - \rho_m^2(1)} ,
\tag{2.42}
$$

where $\varepsilon(t)$ is a random deviate. In the model of Curtis and Eagleson (1982), $\varepsilon(t)$ is assumed to be a normally distributed variable, $N(0, 1^2)$. However, as admitted by the authors, this leads to the cloud cover values in (2.37) that can be negative or

exceed '1'. Therefore, a truncation of $N(t)$ is necessary in such cases, in order to keep cloudiness values within the realistic range, i.e., between 0 and 1. The first and second moments of the cloud cover distribution, therefore, become biased. Another issue, is that the model (2.37) leads to frequency distributions of the cloud cover that are more uniform than those that are usually observed, i.e., primarily 'U-shaped'. Curtis and Eagleson (1982) argued that "...if histogram of observed cloudiness is expanded into ranges of values lower than 0 and higher than 1, the broader causative atmospheric conditions can be better represented and a better match between simulated and observed distributions can be achieved". However, the procedure is purely artificial and does not satisfy the requirement of cloud cover simulation to be as close as possible to the observations. To account for the above problems, a modification is introduced in this work and $\varepsilon(t)$ is simulated as a random deviate from the *Beta* probability distribution:

$$Beta(y) = \frac{\Gamma(a+b)}{\Gamma(a)\Gamma(b)} \frac{1}{(y_2 - y_1)^{a+b-1}} (y - y_1)^{a-1} (y_2 - y)^{b-1}, \qquad (2.43)$$

where $y_1$ and $y_2$ are the lower and upper bounds of the *Beta* distribution for independent variable $y$ and $a$ and $b$ are the distribution shape parameters ($a > 0, b > 0$). The lower and upper bounds $(y_1, y_2)$ are found from (2.37) and (2.42) at every simulation step, i.e., the knowledge of $m(t-1)$ and $J(t)$ at every time $t$ allows one to derive $y_1$ and $y_2$ by imposing the requirement for the cloud cover $N(t)$ to be in the range $[0, 1]$. The *Beta* distribution shape parameters $a$ and $b$ are estimated based on conditioning by the cloudiness value at $(t-1)$ (see Section 2.5.2). Sampling of the deviate $\varepsilon(t)$, performed in this manner, allows one to avoid the truncation of values of $N(t)$ and preserve the moments and shape of the cloud cover distribution.

## 2.5.2 Parameter estimation

Major parameters used by the cloud cover model are $M_0$, $\sigma_m^2$, $\rho_m(1)$, $\gamma$, $a$, and $b$. The general procedure of parameter estimation follows the one of Curtis and Eagleson (1982). An outline is presented here along with additional comments that concern

implemented modifications.

The existence of *stationary* interstorm "fairweather" cloud cover process is the central assumption of the model. The identification of sequences of the fairweather periods in series of meteorological data therefore becomes essential. The methodology proposed by Curtis and Eagleson (1982) employs an iterative approach that uses records of the total cloud cover during periods *between successive* precipitation events. The essence of the method is in estimating the mean value of cloud cover for some sub-region $\Delta t$ within an interstorm period (Figure 2-10).

Each interstorm period of length $T_{is} = \Delta t_0$ [*hour*] (Figure 2-10) is considered to be constrained by the last hour of the first rainfall event and the first hour of the following rainfall event. By successively eliminating one hour from both ends of any given interstorm period ($\Delta \tau_1 = 1$ *hour*, $\Delta \tau_2 = 2$ *hours*, ...), a number of sub-regions, not exceeding in total ($T_{is}/2 - 1$), can be defined for each interstorm period. For any given sub-region, $\Delta t_k$, corresponding to $k$ number of eliminated hours from each end (Figure 2-10), a mean value of the cloud cover is estimated over all interstorm periods in the considered precipitation record whose duration exceeds $2k$ hours. Since $k \in [0, T_{is\,\max}/2 - 1]$, where $T_{is\,\max}$ is the maximum duration of an interstorm period in the considered record, a vector of the mean values of cloud cover of length ($T_{is\,\max}/2 - 1$) is obtained.

Curtis and Eagleson (1982) argue that with the increasingly larger number of eliminated hours, the estimated mean value stabilizes, reaching some constant, or the fairweather mean value, $M_0$. The number of hours, $T_r$, eliminated from both ends of all interstorm periods (whose duration exceeds $2T_r$) after which there is no significant change in the mean cloudiness value, is considered to be the length of the *transition* period. Consequently, a necessary condition for an interstorm period to contain a fairweather cloud cover sequence is to be of duration $T_{is} > 2T_r$ [*hour*].

A note has to be made regarding a particular case of sub-regions within certain interstorm periods for which the described approach fails. Sometimes, passing atmospheric precipitation systems do not necessarily result in rainfall at a given location. However, the cloud cover process is obviously non-stationary during such periods
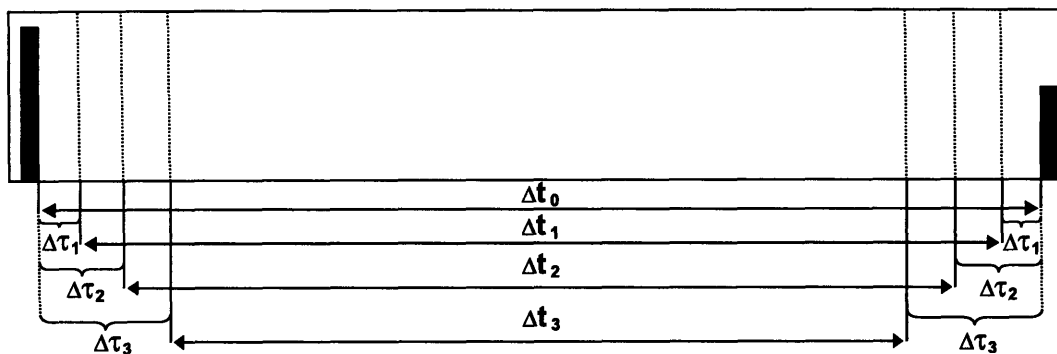
Figure 2-10: An illustration of the procedure used to identify the "fairweather" cloud cover period.

and the estimated mean value can be significantly affected. The discussed approach cannot identify such periods, which would, perhaps, require auxiliary information about cloud vertical structure and spatial information about the precipitation process. Nonetheless, the procedure is efficient for most of interstorm periods and results in reasonable estimates of the transition period as long as the above situation does not occur often. Caution has to be taken when interpreting the results of this method.

Figures 2-11 - 2-13 illustrate the outlined procedure. In addition to the mean values, the standard deviation of the mean estimate is plotted. Although the standard deviation does not have as clear dependence on the length of transition period as the mean value, it allows one to critically evaluate the estimates of mean values. For the selected values of $T_r$, both the analytical and observed transition function $J(t)$ are plotted in Figures 2-14 - 2-16. As one can see, the exponential form of $J(t)$ fits the observed cloud cover transition quite well most of the months. The chosen values of the transition period length after which the fairweather conditions can be assumed are shown in Table 2.2.

Once $T_r$ is established, the fairweather sequences contained in the interstorm periods of length $T_{is} > 2T_r$ are combined in a new time series containing only fairweather cloud cover values. For these series, created for each month or the whole period of analysis, the parameters $M_0$, $\sigma_m^2$, and $\rho_m(1)$ are determined by conventional methods. Estimated values of the parameters are given as a reference in Table 2.3. As can be seen, the mean value of the fairweather cloudiness varies throughout the year some-

101
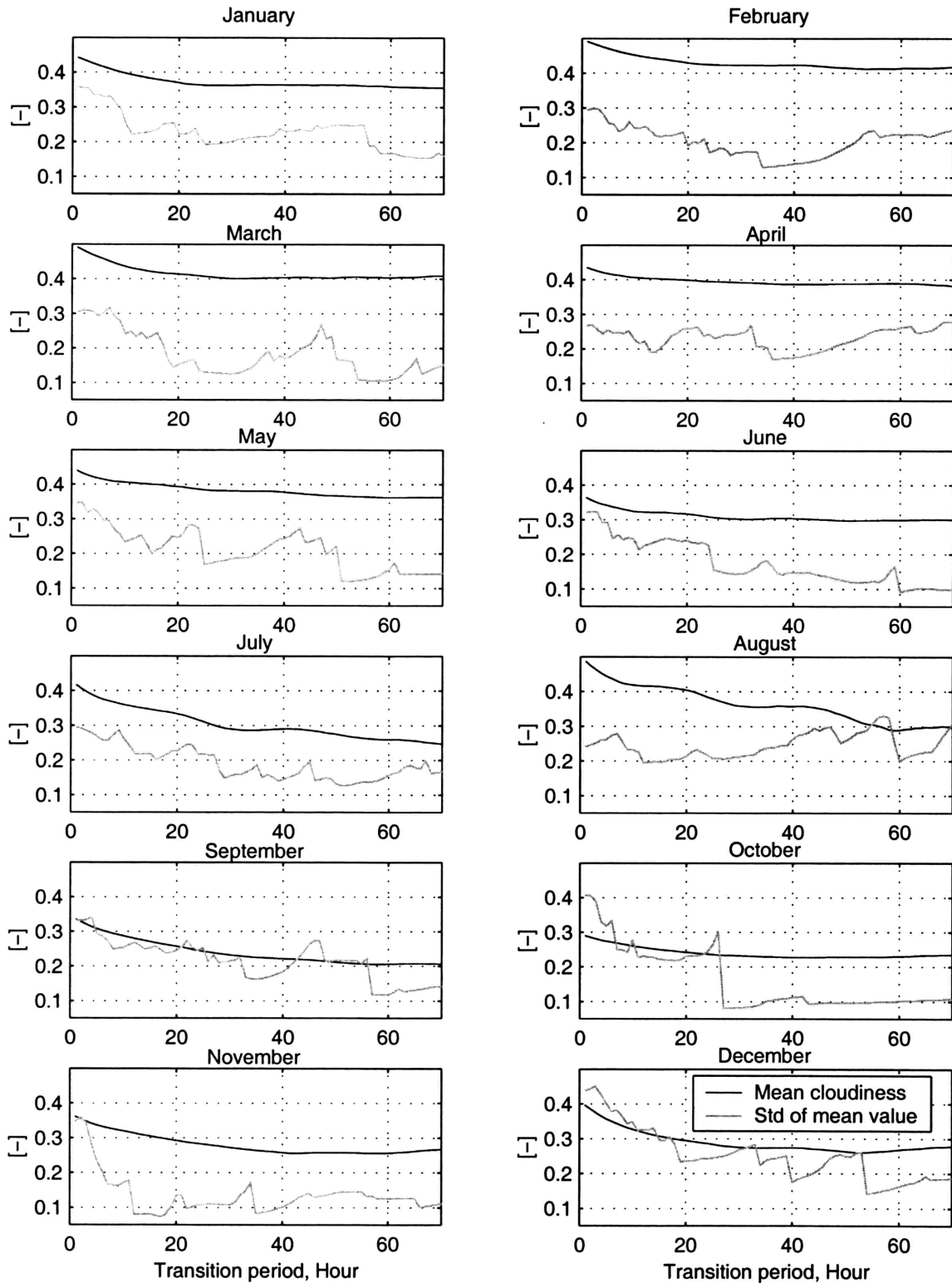
Figure 2-11: The estimated mean cloud cover value and standard deviation of the estimate as a function of the length of transition period (Albuquerque, NM).
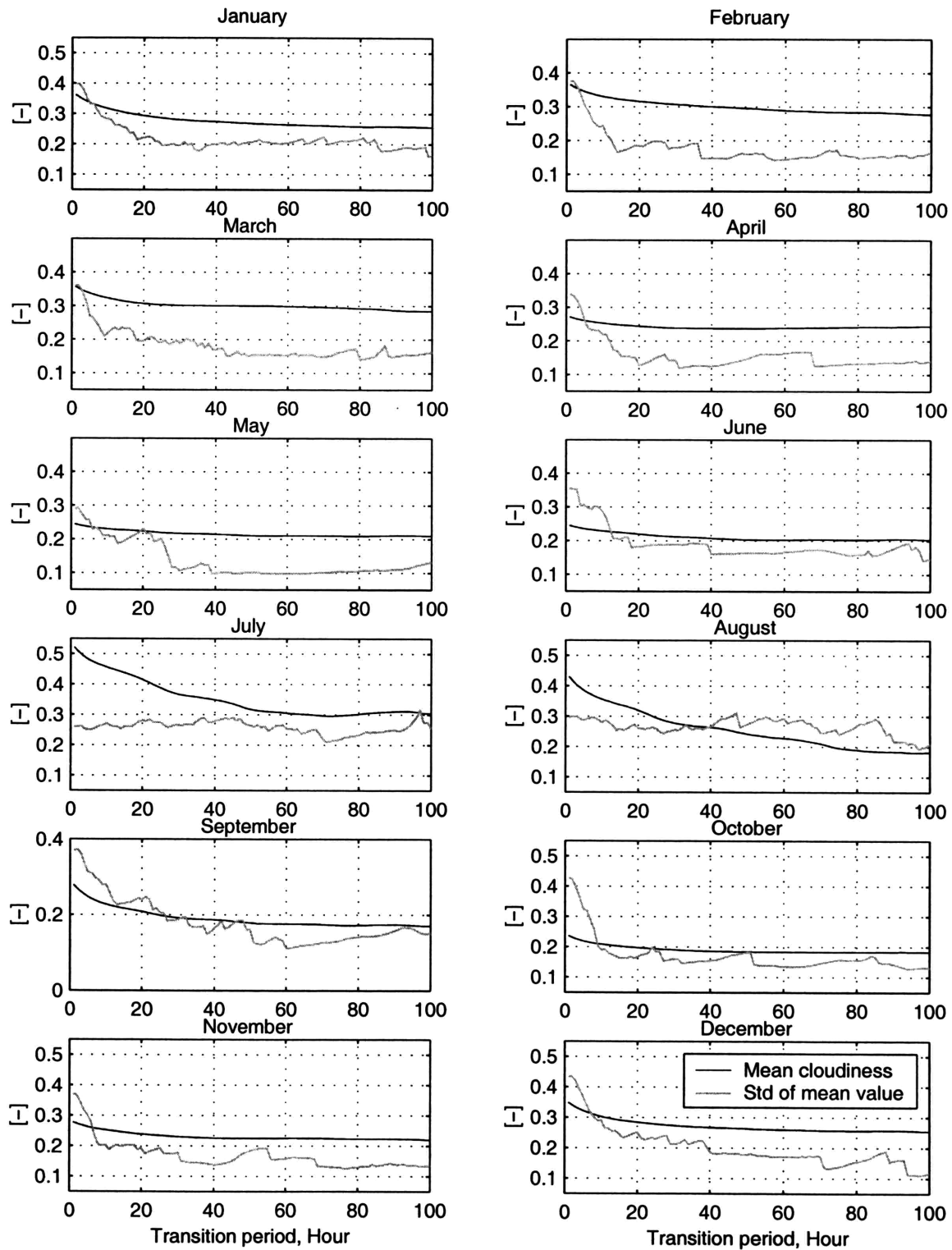
Figure 2-12: The estimated mean cloud cover value and standard deviation of the estimate as a function of the length of transition period (Tucson, AZ).
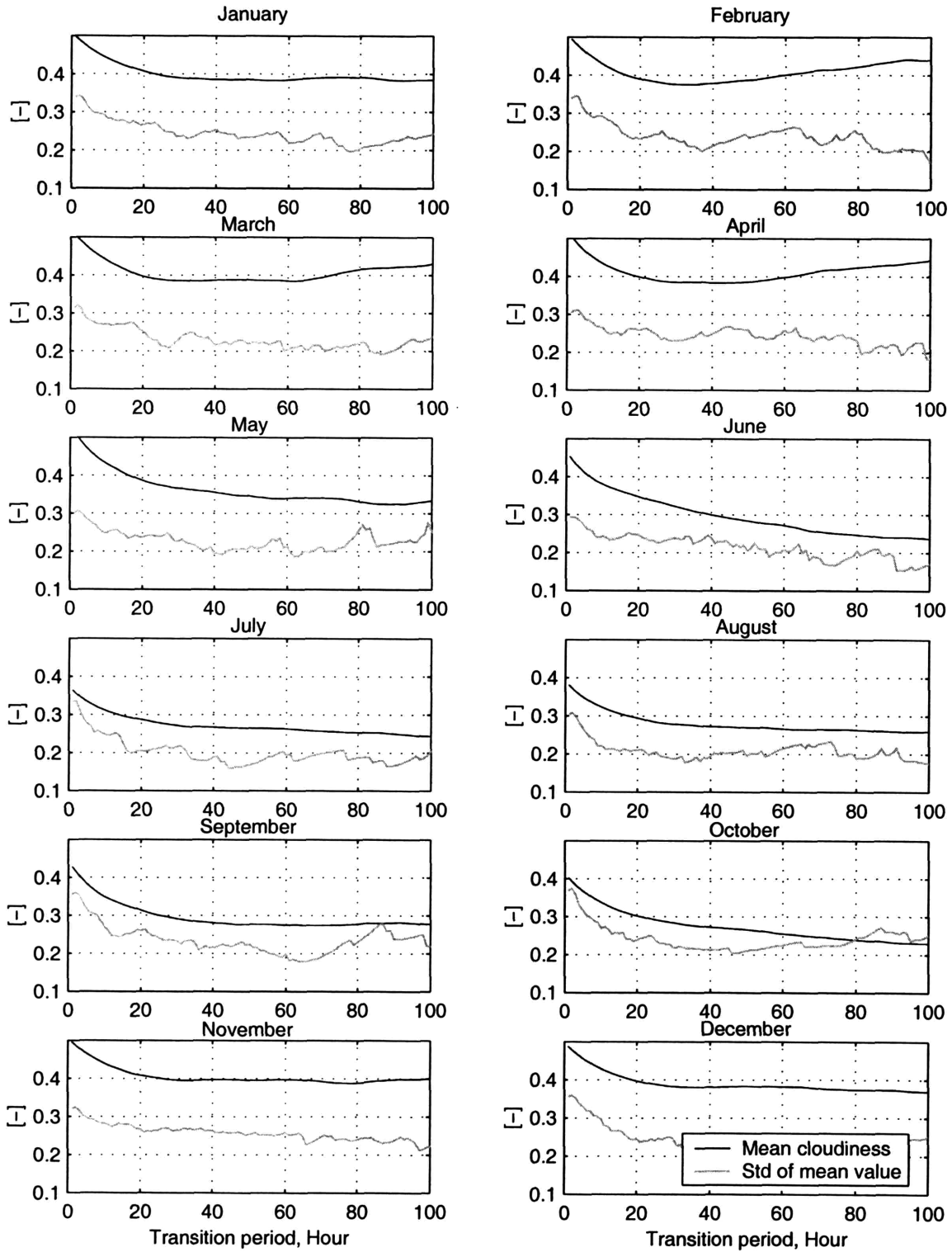
Figure 2-13: The estimated mean cloud cover value and standard deviation of the estimate as a function of the length of transition period (Tulsa, OK).

104
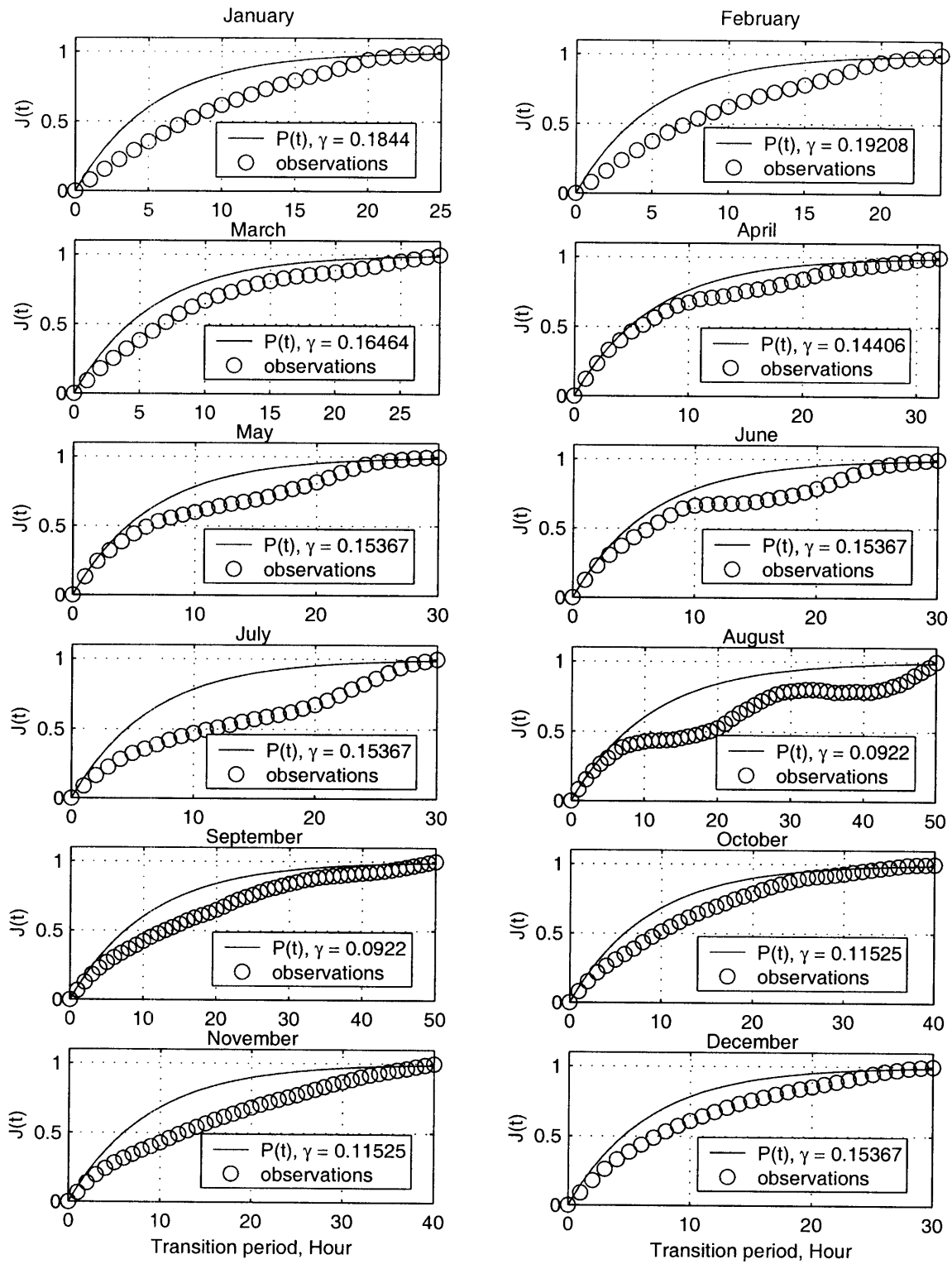
Figure 2-14: The analytical and observed transition functions $J(t)$ corresponding to the estimated transition period lengths (Albuquerque, NM).
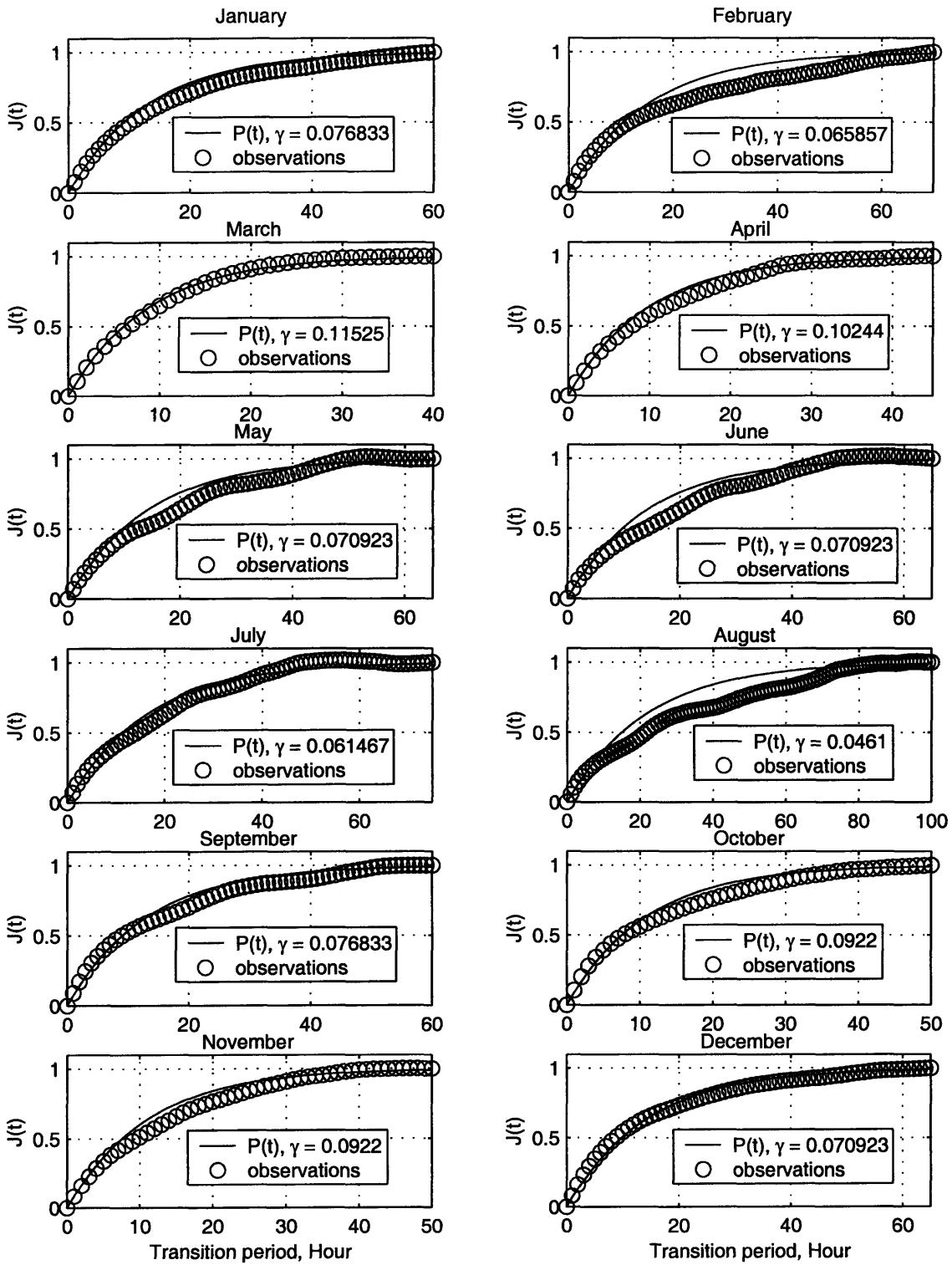
Figure 2-15: The analytical and observed transition functions $J(t)$ corresponding to the estimated transition period lengths (Tucson, AZ).
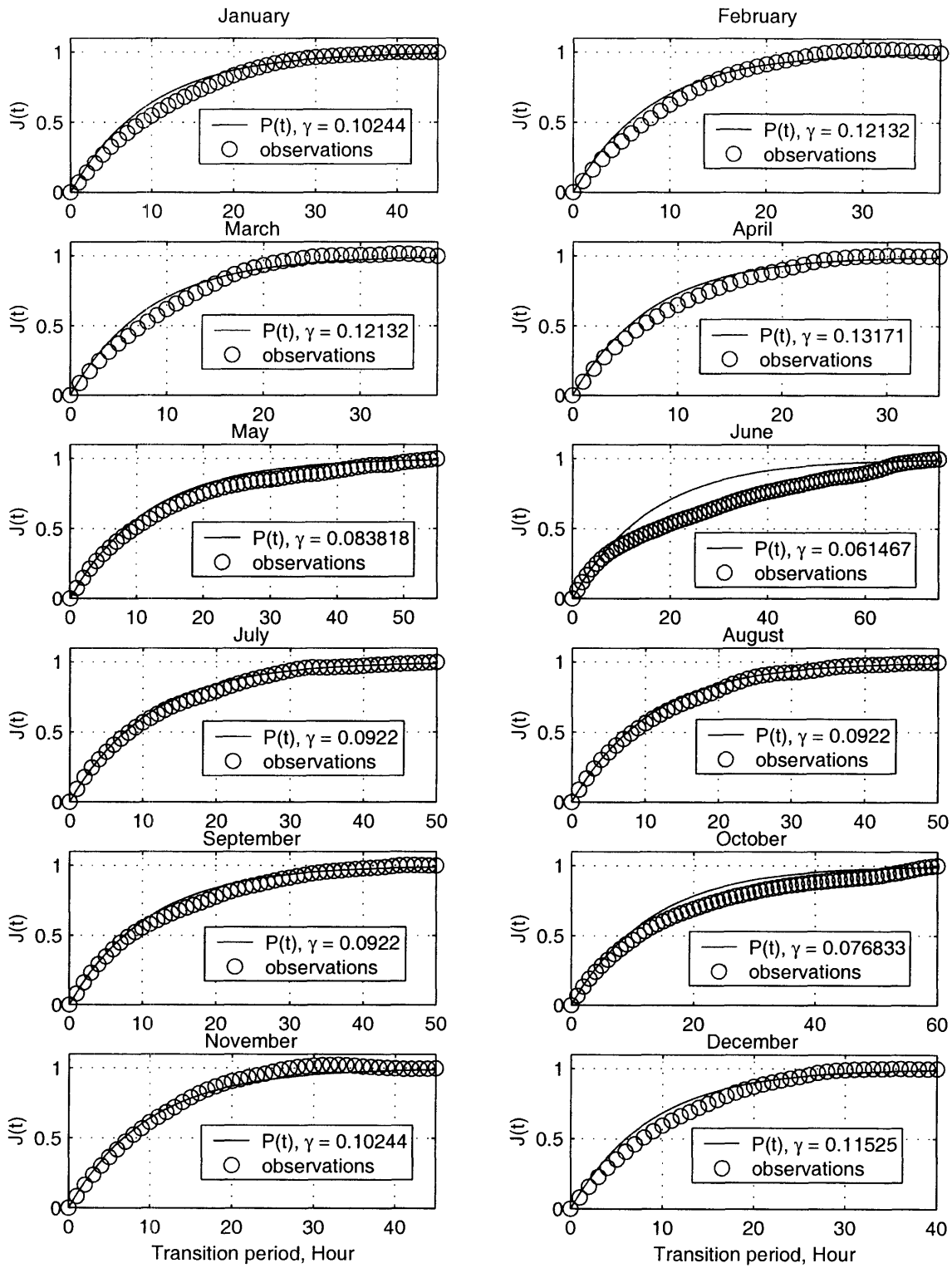
Figure 2-16: The analytical and observed transition functions $J(t)$ corresponding to the estimated transition period lengths (Tulsa, OK).

Table 2.2: The estimated length of the cloud cover transition period [*hour*] for different months and meteorological stations.

| Meteostation / Month | ALB[a] | TCS[b] | TLS[c] |
|---|---|---|---|
| January | 25 | 60 | 45 |
| February | 24 | 70 | 38 |
| March | 28 | 40 | 38 |
| April | 32 | 45 | 35 |
| May | 30 | 65 | 55 |
| June | 30 | 65 | 75 |
| July | 30 | 75 | 50 |
| August | 50 | 100 | 50 |
| September | 50 | 60 | 50 |
| October | 40 | 50 | 60 |
| November | 40 | 50 | 45 |
| December | 30 | 65 | 45 |

[a]Albuquerque (NM) 35.05N 106.617W
[b]Tucson (AZ) 32.131N 110.955W
[c]Tulsa (OK) 36.197N, 95.886W

times changing in magnitude by a factor of two (e.g., for Albuquerque, NM). The standard deviation also changes throughout the year, although the magnitude of its variability is much smaller as compared to the mean value. Fairweather cloudiness usually exhibits high autocorrelation at lag one hour ($\sim 0.9$). The parameter $\gamma$, with $\gamma = \varsigma$, is estimated according to Curtis and Eagleson (1982) as

$$\gamma = \frac{4.61}{T_r}.$$ (2.44)

The parameters $a$ and $b$ are estimated by analyzing random deviates $\varepsilon(t)$, which are computed from the observed cloud cover series by inverting (2.37) and (2.42). The estimation of $\varepsilon(t)$ is conditioned by the cloud cover at time $(t - 1)$. Therefore, 11 vectors of deviates are composed from the could cover records for every month, each vector corresponds to one of the values of $N(t-1)$: $0.0, 0.1, \ldots, 1.0$. For each $N(t-1)$, the corresponding distribution of deviates is approximated by the *Beta* distribution with parameters $a$ and $b$ estimated from these deviates. Figures 2-17 - 2-18 illustrate the procedure for the months of January and July (Albuquerque, NM). The last plot in both figures shows the first two moments scaled to be in the range [0, 1] as well as skewness of the deviates. The behavior of these variables with respect to $N(t - 1)$ is similar for all months (not only for the months illustrated in Figures 2-17 - 2-18): while the mean and standard deviation are essentially constant throughout the entire range of $N(t - 1)$ values, the skewness of the deviates varies significantly, changing its sign from positive to negative. As can also be seen in the figures, the probability density functions of the *Beta* distribution, corresponding to the same $N(t - 1)$, can be quite different for different months. An illustration of the variability of parameter values throughout the year is provided in Figures 2-19 - 2-20. Since the variability is quite substantial for most months (for all stations), the values of $a$ and $b$ are estimated on a monthly basis.

Table 2.3: The parameter values of $M_0$, $\sigma_m^2$, and $\rho_m(1)$ of the cloud cover model (parameters have the same respective order in the table).

| Meteostation / Month | ALB[a] | TCS[b] | TLS[c] |
|---|---|---|---|
| January | 0.363/ 0.407/ 0.916 | 0.263/ 0.378/ 0.943 | 0.385/ 0.412/ 0.928 |
| February | 0.424/ 0.410/ 0.909 | 0.285/ 0.381/ 0.940 | 0.378/ 0.408/ 0.925 |
| March | 0.402/ 0.400/ 0.893 | 0.301/ 0.388/ 0.936 | 0.387/ 0.401/ 0.925 |
| April | 0.391/ 0.389/ 0.896 | 0.237/ 0.356/ 0.943 | 0.386/ 0.393/ 0.928 |
| May | 0.381/ 0.376/ 0.896 | 0.210/ 0.340/ 0.944 | 0.339/ 0.357/ 0.907 |
| June | 0.302/ 0.349/ 0.908 | 0.203/ 0.331/ 0.945 | 0.250/ 0.318/ 0.925 |
| July | 0.288/ 0.321/ 0.879 | 0.298/ 0.358/ 0.922 | 0.264/ 0.319/ 0.919 |
| August | 0.323/ 0.354/ 0.853 | 0.182/ 0.297/ 0.939 | 0.270/ 0.324/ 0.916 |
| September | 0.210/ 0.329/ 0.918 | 0.176/ 0.294/ 0.931 | 0.277/ 0.354/ 0.928 |
| October | 0.228/ 0.345/ 0.922 | 0.184/ 0.319/ 0.944 | 0.254/ 0.366/ 0.933 |
| November | 0.257/ 0.357/ 0.904 | 0.225/ 0.349/ 0.946 | 0.397/ 0.411/ 0.927 |
| December | 0.275/ 0.384/ 0.911 | 0.259/ 0.370/ 0.935 | 0.382/ 0.417/ 0.926 |

[a]Albuquerque (NM) 35.05N 106.617W
[b]Tucson (AZ) 32.131N 110.955W
[c]Tulsa (OK) 36.197N, 95.886W
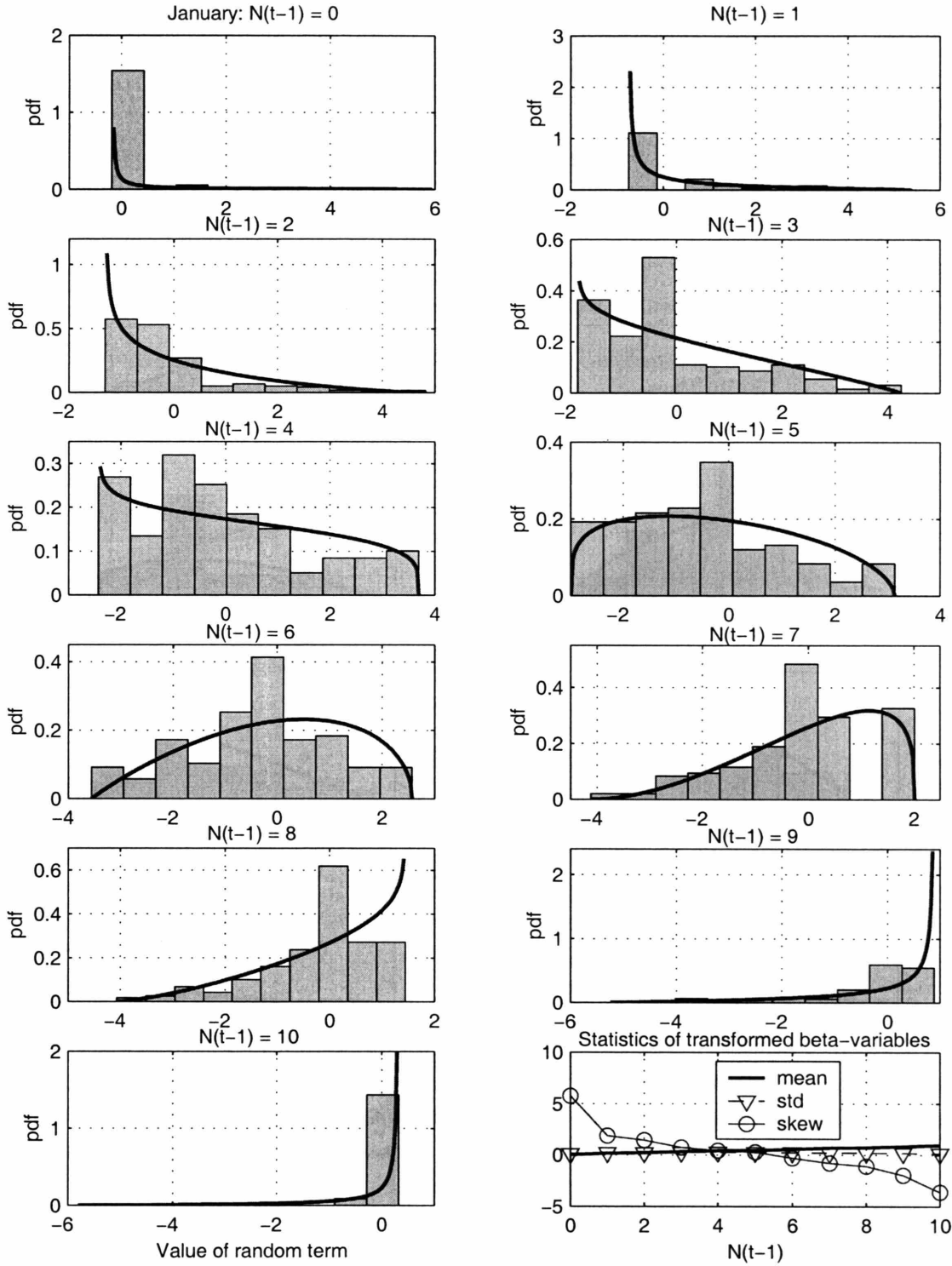
Figure 2-17: A histogram of deviates $\varepsilon(t)$ in the cloud cover model and the corresponding probability density function (solid line) approximated with the *Beta* distribution. The cloud cover $N(t-1)$ for the month of *January* is given on a $[0, 10]$ basis (Albuquerque, NM).
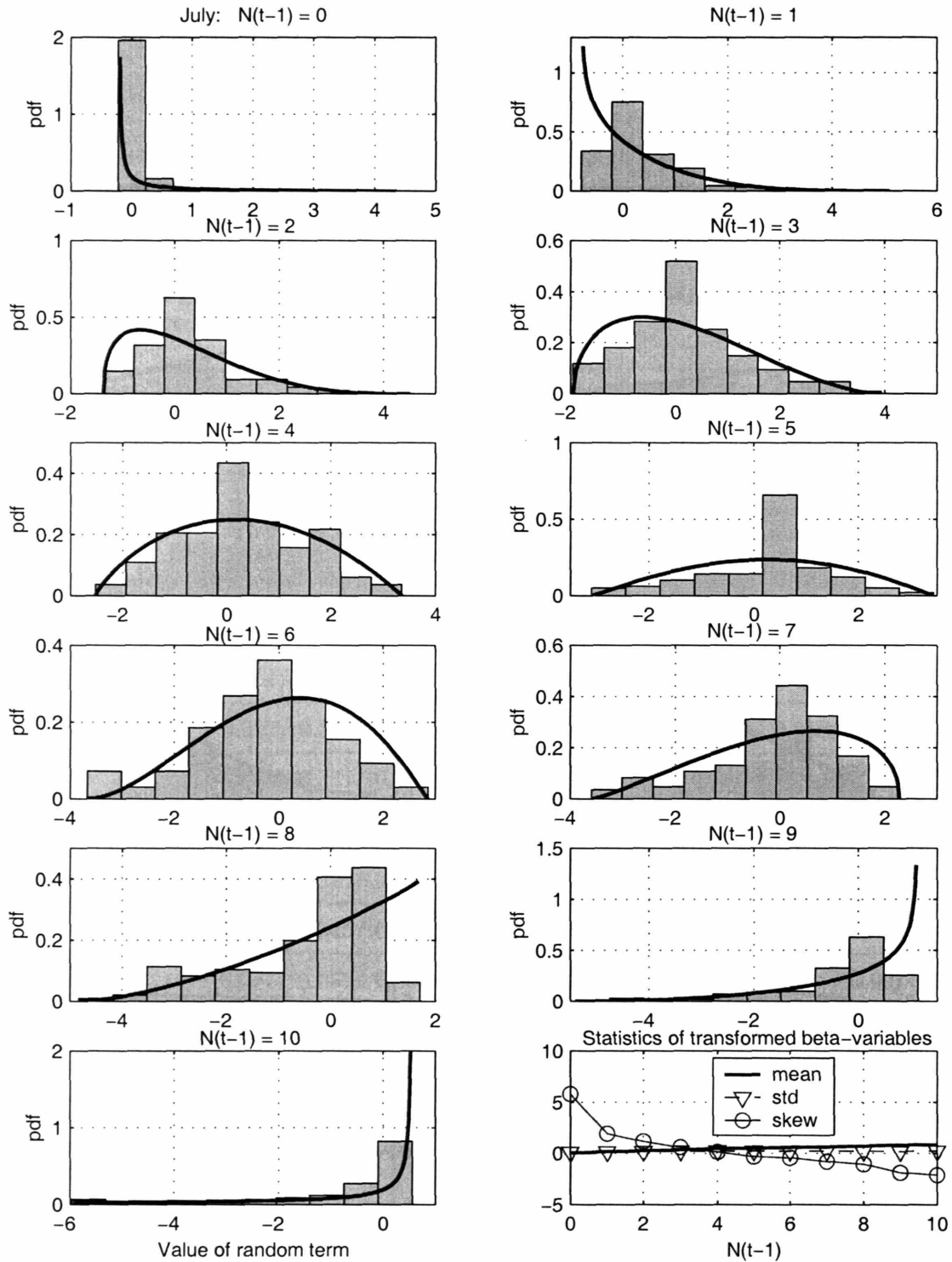
Figure 2-18: A histogram of deviates $\varepsilon(t)$ in the cloud cover model and the corresponding probability density function (solid line) approximated with the *Beta* distribution. The cloud cover $N(t-1)$ for the month of *July* is given on a $[0, 10]$ basis (Albuquerque, NM).

a) Parameter "a" of the Beta distribution (random term in AR(1) model of cloudiness)

Computed after conditioning by cloudiness at (t-1) hour for each month (different curves)

Means and stds of the parameter for all curves are shown

b) Parameter "a" of the Beta distribution (random term in AR(1) model of cloudiness)
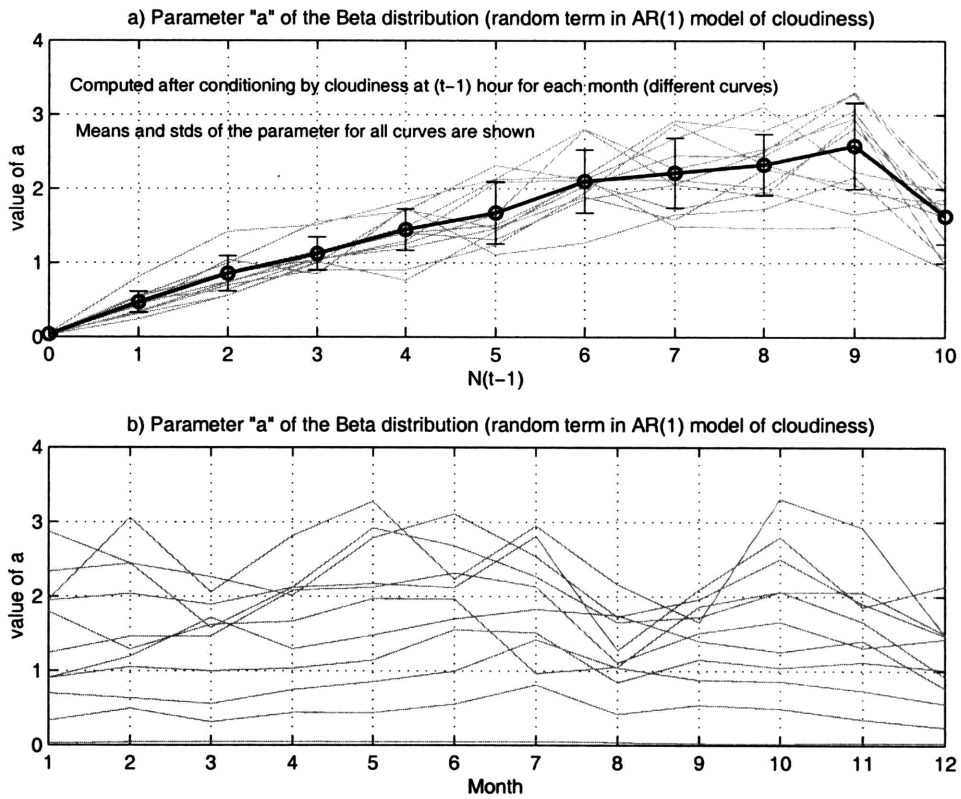
Figure 2-19: The parameter $a$ of the *Beta* distribution for different months (Albuquerque, NM) as a function of a.) $N(t-1)$ and b.) month of the year. The mean parameter values and the corresponding standard deviations are shown as the error bar plot.

**a.) Parameter "b" of the Beta distribution (random term in AR(1) model of cloudiness)**

Computed after conditioning by cloudiness at (t-1) hour for each month (different curves)

Means and stds of the parameter for all curves are shown

value of b

$N(t-1)$

**b.) Parameter "b" of the Beta distribution (random term in AR(1) model of cloudiness)**

value of b
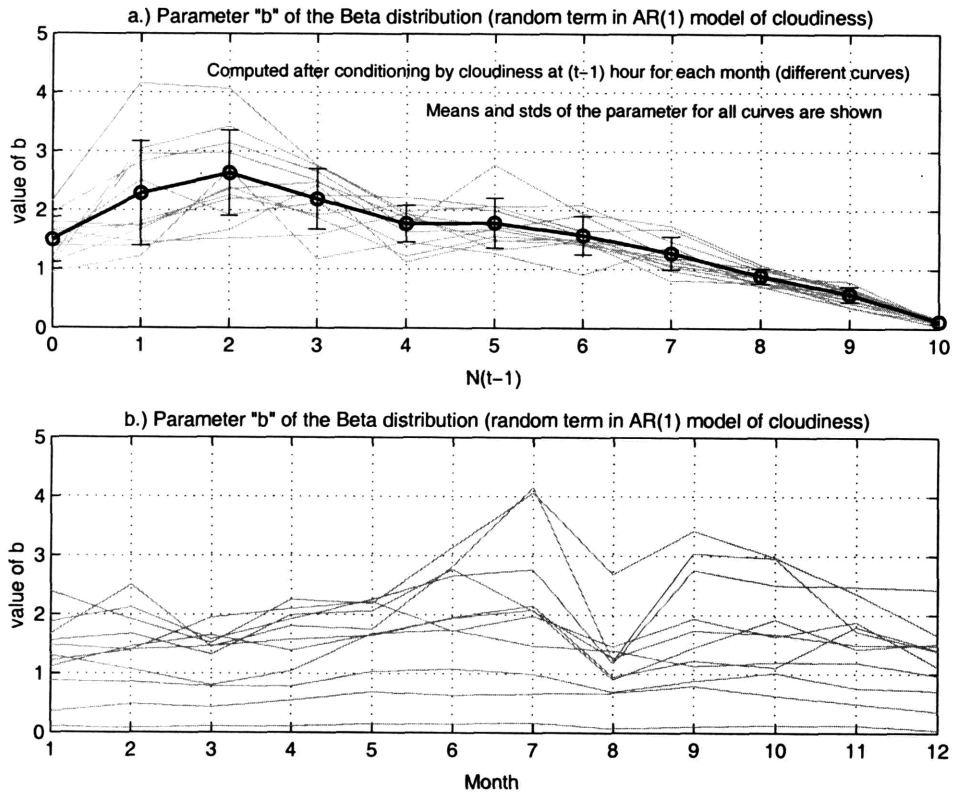
Month

Figure 2-20: The parameter $b$ of the *Beta* distribution for different months (Albuquerque, NM) as a function of a.) $N(t-1)$ and b.) month of the year. The mean parameter values and the corresponding standard deviations are shown as the error bar plot.

114

## 2.6 Simulation of air temperature

### 2.6.1 Model formulation

Air temperature is an important hydrometeorological state variable that affects a variety of natural phenomena. A number of stochastic weather generators that include capabilities of modeling air temperature have been proposed for agricultural simulations and climate studies (Richardson and Wright, 1984; Hanson et al., 1994; Nicks and Gander, 1993, 1994). These models typically simulate daily maximum and minimum temperature. The majority of these models are based on the multivariate stationary process that permits autocorrelation in the individual time series and cross-correlations between the time series of air temperature and precipitation (USCLIMATE model, Richardson and Wright, 1984, Hanson et al., 1994). Generally, temperature simulations are conditioned by the wet or dry day occurrence. The common problem with these approaches, however, is that the temperature diurnal variation is neglected. Moreover, these approaches are seriously handicapped because they do not consider the effects of other variables (e.g., cloud cover) on a continuous basis. The model of Curtis and Eagleson (1982) deals with both problems and provides a convenient method for hourly temperature simulation.

Curtis and Eagleson (1982) consider the air temperature, $T(t)$ [$°C$], to be a sum of two variables: a deterministic air temperature component $\tilde{T}(t)$ and a random variate $\delta T(t)$:

$$T(t) = \tilde{T}(t) + \delta T(t).$$ (2.45)

The following outlines the approach in modeling both terms of equation (2.45).

### 2.6.1a Definition of the deterministic component

The deterministic component is built on an empirical method of Bryan (1964) that attributes temporal variation of the air temperature to the divergence of radiative heat flux and the divergence of eddy heat flux. In essence, an assumption is made

that hourly temperature increments can be regressed on several hydrometeorological variables:

$$\frac{d\widetilde{T}(t)}{dt} = b_0 - b_1\widetilde{T}(t) + b_2 K(t)s(t) + b_3 K(t)r(t) + b_4 q(t), \qquad (2.46)$$

where $b_i$-s ($i = 0, 1, \ldots, 4$) are the regression coefficients, $s(t)$ and $r(t)$ are the variables of the Sun position and geographic location, $K(t)$ is the radiation attenuation factor, $K(t) = 1 - 0.65 N^2(t)$, and $q(t)$ is the estimate of incoming longwave radiation. Expression (2.46) does not include all the terms of the air temperature model of Curtis and Eagleson (1982). The excluded terms contain the ground temperature $T_g(t)$, wind speed $W_s(t)$, and wind direction $W_d(t)$. These terms were not used because the ground temperature is not a standard measurement variable and is not readily available for many meteorological data sets, the wind direction and speed exhibit high temporal variability and are assumed to have minimal contribution in modifying the air temperature.

The longwave radiation is modeled using the gray-body theory as

$$q(t) = \sigma K_c(t) T'^4(t), \qquad (2.47)$$

where $\sigma = 5.67 10^{-8}$ $[W\,m^{-2}\,K^{-4}]$ is the Stefan-Boltzmann constant, $T'$ $[K]$ is air temperature, $K_c(t) = 1 + 0.17 N^2(t)$. The variables $s(t)$ and $r(t)$ are defined as

$$
\begin{aligned}
s(t) &= \sin\delta_\oplus \sin\Phi - \cos\delta_\oplus \cos\Phi \cos\frac{\pi t}{12}, & T_{H\,rise} \le t \le T_{H\,set}, \\
s(t) &= 0, & \text{otherwise}, \\
r(t) &= \frac{ds(t)}{dt} = \frac{\pi}{12}\cos\delta_\oplus \cos\Phi \sin\frac{\pi t}{12}, & T_{H\,rise} \le t \le 12, \\
r(t) &= 0, & \text{otherwise}, & (2.48)
\end{aligned}
$$

where $\delta_\oplus$ is the solar declination, $\Phi$ is the local latitude, $T_{H\,rise}$ is the local time of sunrise and $T_{H\,set}$ is the local time of sunset (Section 2.3.1). Equation (2.46) relates the change in temperature to a number of factors that affect the air temperature

116

throughout the daily and seasonal cycle. For example, higher values of cloud cover associated with precipitation systems result in lower amplitude of the daily temperature because of the terms containing $s(t)$ and $r(t)$. The term containing $q(t)$ is non-zero throughout the whole day and should explain some of the differences in cooling observed on clear nights as opposed to cloudy nights. Absolute magnitudes of $s(t)$ and $r(t)$ are different for different seasons and geographic locations.

Equation (2.46) is a first order differential equation, the solution to which can be found if the initial condition, i.e., the initial temperature, $\tilde{T}(t^*)$, is given. Curtis and Eagleson (1982) provide the following expression:

$$\tilde{T}(t) = \tilde{T}(t^*)e^{-b_1(t-t^*)} + e^{-b_1 t}G(t, t^*), \tag{2.49}$$

where

$$
\begin{aligned}
G(t, t^*) &= b_0 \int_{t^*}^{t} e^{b_1 \tau} d\tau + b_2 \int_{t^*}^{t} e^{b_1 \tau} K(\tau) s(\tau) d\tau + \\
& \quad b_3 \int_{t^*}^{t} e^{b_1 \tau} K(\tau) r(\tau) d\tau + b_4 q(t-1) \int_{t^*}^{t} e^{b_1 \tau} d\tau \\
&= I_1(t) + I_2(t) + I_3(t) + I_4(t).
\end{aligned}
\tag{2.50}
$$

By using the *full*, non-zero expressions for $s(t)$ and $r(t)$ (the system of equations (2.48)) Curtis and Eagleson (1982) derive the following expressions evaluating the term $G(t, t^*)$:

$$I_1(t) = b_0 \int_{t^*}^{t} e^{b_1 \tau} d\tau = \frac{b_0}{b_1} \left[ e^{b_1 t} - e^{b_1 t^*} \right], \tag{2.51}$$

$$
\begin{aligned}
I_2(t) &= b_2 \int_{t^*}^{t} e^{b_1 \tau} K(\tau) s(\tau) d\tau \\
&= K(t) \left[ K_2 \left( e^{b_1 t} - e^{b_1(t-1)} \right) - K_3 e^{b_1 t} \cos \frac{\pi t}{12} - K_4 e^{b_1 t} \sin \frac{\pi t}{12} + \right. \\
& \quad \left. K_3 e^{b_1(t-1)} \cos \frac{\pi(t-1)}{12} + K_4 e^{b_1(t-1)} \sin \frac{\pi(t-1)}{12} \right] + I_2(t-1), \tag{2.52}
\end{aligned}
$$

117

$$I_3(t) = b_3 \int_{t^*}^{t} e^{b_1 \tau} K(\tau) r(\tau) d\tau$$

$$= K(t) \left[ K_6 \sin \frac{\pi t}{12} - K_5 e^{b_1 t} \cos \frac{\pi t}{12} - \right.$$

$$\left. K_6 e^{b_1(t-1)} \sin \frac{\pi(t-1)}{12} + K_5 e^{b_1(t-1)} \cos \frac{\pi(t-1)}{12} \right] + I_3(t-1), \quad (2.53)$$

$$I_4(t) = b_4 \int_{t^*}^{t} e^{b_1 \tau} q(\tau) d\tau = \frac{b_4}{b_1} q(t-1)(1 - e^{b_1}) e^{b_1 t} + I_4(t-1), \quad (2.54)$$

where

$$p = \frac{\pi}{12}, \qquad K_1 = \frac{b_0}{b_1}, \qquad K_2 = \frac{b_2}{b_1} \sin \delta_\oplus \sin \Phi,$$

$$K_3 = \frac{b_1 b_2}{b_1^2 + p^2} \cos \delta_\oplus \cos \Phi, \qquad K_4 = \frac{p b_2}{b_1^2 + p^2} \cos \delta_\oplus \cos \Phi,$$

$$K_5 = \frac{p^2 b_3}{b_1^2 + p^2} \cos \delta_\oplus \cos \Phi, \qquad K_6 = \frac{p b_1 b_3}{b_1^2 + p^2} \cos \delta_\oplus \cos \Phi. \quad (2.55)$$

Expression (2.54) linearizes the integral $I_4(t)$ containing $q(t)$, which is a non-linear function of the temperature, by using the value from the previous hour $q(t-1)$. Besides, the one-hour integration interval is considered short enough to allow variables $K(t)$ and $q(t-1)$ to be brought outside their respective integrals (eq. (2.52) - (2.54)).

The full, non-zero expressions for $s(t)$ and $r(t)$ (the system of equations (2.48)) were used to obtain the above general equations (2.52) - (2.53). Since $s(t)$ and $r(t)$ can be equal to zero during certain periods of the day, it can be seen that the integrals $I_2(t)$ and $I_3(t)$ may have different forms depending on time of the day. The ranges over which each form is valid are delimited by several critical times. Curtis and Eagleson (1982) identify five critical times: 1) $t_0$ is the value of $t$ in local time corresponding to midnight in standard time; 2) $t_R$ is the earliest standard hour that does not precede local sunrise $T_{Hrise}$, $(t_R \geq T_{Hrise})$; 3) $t_{12}$ is the value of $t$ at the earliest standard hour that does not precede local noon $(t_{12} \geq 12)$; 4) $t_S$ is the value of $t$ at the earliest standard hour that does not precede local sunset, $T_{Hset}$ $(t_S \geq T_{Hset})$; 5) $t_{23}$ is the value corresponding to 23.00 local standard time. The integrals $I_2(t)$ and $I_3(t)$ are evaluated according to the above time ranges using the system of equations (2.48),

which leads to different forms for $G(t, t*)$.

**2.6.1b Definition of the random deviate component $\delta T(t)$**

The deterministic component in the model of Curtis and Eagleson (1982) essentially represents the expected temperature value. It cannot explain all of the temperature variability and therefore the random deviate $\delta T(t)$ $[°C]$ is introduced. It is defined as

$$\delta T_o(t) = T_o(t) - \tilde{T}(t), \tag{2.56}$$

where $T_o(t)$ $[°C]$ is the observed air temperature and $\tilde{T}(t)$ $[°C]$ is the deviation component. The deviations are assumed to be approximated by a first order Markov process:

$$\delta T(t) = \overline{\delta T} + \rho_{\delta T}(1)(\delta T(t-1) - \overline{\delta T}) + \varepsilon_T(t)\sigma_{\delta T}\sqrt{1 - \rho_{\delta T}^2(1)}, \tag{2.57}$$

where $\overline{\delta T}$, $\sigma_{\delta T}^2$, and $\rho_{\delta T}(1)$ are the mean, variance, and lag-1 value of autocorrelation of random temperature deviates, respectively, and $\varepsilon_T(t)$ is the standard normal deviate.

## 2.6.2 Parameter estimation

The parameters of the air temperature model that have to be estimated from data are: the regression coefficients $b_i$-s $(i = 0, 1, \ldots, 4)$, $\overline{\delta T}$, $\sigma_{\delta T}^2$, and $\rho_{\delta T}(1)$. The general procedure of parameter estimation follows the one described by Curtis and Eagleson (1982) and only an outline is presented below.

According to Curtis and Eagleson (1982), equation (2.49) can be re-written to obtain:

$$\tilde{T}(t) = e^{-b_1}\tilde{T}(t-1) + e^{-b_1 t}G(t, t-1). \tag{2.58}$$

The hourly temperature change $Y(t)$ is obtained if temperature $T(t-1)$ is subtracted from both sides of equation (2.58). Curtis and Eagleson (1982) show that an equation

for $Y(t)$ can be represented in the regression form:

$$Y(t) = a_0 + a_1 X_1(t) + \ldots + a_4 X_4(t) , \tag{2.59}$$

where the coefficients $a_i$-s $(i = 0, 1, \ldots, 4)$ are

$$a_1 = -(1 - e^{-b_1}) ,$$
$$a_i = \frac{a_1}{b_1} b_i , \qquad i = 0, 2, \ldots, 4 , \tag{2.60}$$

and the predictors $X_i(t)$ are

$$X_1(t) = \tilde{T}(t - 1) ,$$
$$X_2(t) = K(t) \int_{t-1}^{t} s(\tau) d\tau ,$$
$$X_3(t) = K(t) \int_{t-1}^{t} r(\tau) d\tau ,$$
$$X_4(t) = q(t - 1) . \tag{2.61}$$

As above, the one-hour integration interval is considered to be short enough to allow variables $K(t)$ and $q(t-1)$ to be brought outside their respective integrals. Similarly to the previous discussion, the terms $X_2(t)$ and $X_3(t)$ containing $s(t)$ and $r(t)$ have different form depending on time of the day. From a set of linear equations (2.59), the regression coefficients $a_i$-s $(i = 0, 1, \ldots, 4)$ can be found by conventional methods. Once $a_i$-s $(i = 0, 1, \ldots, 4)$ have been estimated, the regression parameters $b_i$ can be easily found from (2.60). The $b_i$-s are developed for each period of interest. As an example, the parameters can be estimated on a monthly or seasonal basis, or as representative values for the whole period. Tables 2.4 - 2.5 provide estimates of the regression parameters for air temperature data in Albuquerque (NM) and Tulsa (OK).

Once the regression parameters have been estimated, equation (2.49) can be used to simulate the deterministic component of the hourly temperature model. Equa-

Table 2.4: The regression parameters $b_i$-s of the air temperature model (Albuquerque, NM).

| Month | $b_0$ | $b_1$ | $b_2$ | $b_3$ | $b_4$ |
|---|---|---|---|---|---|
| January | -5.5203 | 0.138942 | 3.7006 | 18.0189 | 14.5135 |
| February | -5.3184 | 0.144578 | 3.5558 | 17.3492 | 14.2234 |
| March | -4.7566 | 0.146556 | 3.1645 | 16.4153 | 13.1644 |
| April | -4.0284 | 0.146684 | 2.7356 | 15.9645 | 12.0318 |
| May | -2.8657 | 0.156073 | 2.7392 | 14.8671 | 10.4074 |
| June | -0.7758 | 0.155488 | 2.9915 | 13.2796 | 6.7334 |
| July | 2.5994 | 0.168031 | 3.3570 | 10.2081 | 0.76313 |
| August | 2.3131 | 0.182750 | 3.4410 | 10.2988 | 1.7927 |
| September | -0.4032 | 0.156095 | 3.1506 | 12.8382 | 5.6238 |
| October | -2.6586 | 0.147337 | 3.2063 | 17.1321 | 9.2895 |
| November | -4.3010 | 0.149007 | 3.3970 | 17.9837 | 12.3253 |
| December | -5.0664 | 0.145371 | 3.5374 | 19.8933 | 13.4403 |

Table 2.5: The regression parameters $b_i$-s of the air temperature model (Tulsa, OK).

| Month | $b_0$ | $b_1$ | $b_2$ | $b_3$ | $b_4$ |
|---|---|---|---|---|---|
| January | -3.0184 | 0.057963 | 2.3679 | 17.3769 | 7.4718 |
| February | -2.9205 | 0.063544 | 2.3707 | 15.4241 | 7.1971 |
| March | -3.0549 | 0.072282 | 1.9315 | 15.5443 | 7.9302 |
| April | -2.9210 | 0.092812 | 1.7068 | 15.0982 | 8.6095 |
| May | -1.9909 | 0.093586 | 1.4074 | 15.3078 | 6.9842 |
| June | -0.6312 | 0.102220 | 1.5354 | 13.7160 | 5.0429 |
| July | 0.1837 | 0.109034 | 1.7566 | 13.1594 | 4.0661 |
| August | 0.2812 | 0.108134 | 1.9591 | 13.5815 | 3.6354 |
| September | -1.2637 | 0.079379 | 1.5523 | 15.4662 | 5.1255 |
| October | -2.1254 | 0.093813 | 1.7459 | 18.4586 | 7.1137 |
| November | -2.5561 | 0.067231 | 1.6084 | 19.9932 | 6.9136 |
| December | -2.8513 | 0.058512 | 1.9429 | 19.2813 | 7.2249 |

Table 2.6: The parameters $\overline{\delta T}$, $\sigma_{\delta T}^2$, and $\rho_{\delta T}(1)$ of the air temperature model (parameters have the same respective order in the table).

| Meteostation / Month | ALB[a] | TCS[b] | TLS[c] |
|---|---|---|---|
| January | 0.0059/ 2.947/ 0.930 | 0.0111/ 2.813/ 0.943 | -0.0439/ 4.416/ 0.975 |
| February | 0.0161/ 3.032/ 0.928 | 0.0139/ 2.868/ 0.946 | 0.0302/ 4.263/ 0.973 |
| March | 0.00048/ 3.188/ 0.926 | 0.0072/ 3.032/ 0.949 | -0.0664/ 4.00/ 0.968 |
| April | -0.0064/ 3.184/ 0.924 | -0.0008/ 2.979/ 0.940 | -0.0189/ 3.416/ 0.961 |
| May | -0.0208/ 3.018/ 0.918 | -0.0326/ 2.642 0.928 | -0.042/ 2.854/ 0.955 |
| June | -0.0455/ 2.901/ 0.913 | -0.0410/ 2.436/ 0.922 | -0.076/ 2.668/ 0.952 |
| July | -0.0063/ 2.638/ 0.903 | -0.0045/ 2.696 0.925 | -0.0218/ 2.483/ 0.949 |
| August | -0.0185/ 2.366/ 0.891 | -0.0165/ 2.559/ 0.927 | -0.0096/ 2.778/ 0.954 |
| September | 0.0013/ 2.7752/ 0.923 | -0.0004/ 2.727/ 0.944 | 0.0743/ 3.344/ 0.962 |
| October | 0.0018/ 3.125/ 0.925 | 0.0184/ 3.081/ 0.949 | -0.0229/ 3.612/ 0.961 |
| November | 0.0246/ 3.133/ 0.925 | 0.0154/ 3.091/ 0.945 | 0.1056/ 4.048/ 0.970 |
| December | 0.0154/ 2.891/ 0.924 | -0.0020/ 3.018/ 0.946 | 0.1048/ 4.33/ 0.974 |

[a]Albuquerque (NM) 35.05N 106.617W
[b]Tucson (AZ) 32.131N 110.955W
[c]Tulsa (OK) 36.197N, 95.886W

tion (2.49) is applied each day to compute temperatures for each hour starting from midnight ($t = 0$). The initial temperature, $\tilde{T}(t^*)$, is taken as the deterministic temperature component estimated for 11pm of the previous day. According to (2.56), the difference between the observed and estimated deterministic temperature components defines the temperature random deviate. Consequently, series of deviates can be estimated for each period of interest, e.g., for each month or season. The parameters $\overline{\delta T}$, $\sigma_{\delta T}^2$, and $\rho_{\delta T}(1)$ are then obtained using conventional estimation techniques. Estimated values of the parameters for the test meteorological stations are provided for a reference in Table 2.6. As can be seen from the table, the mean of the deviates is around zero, the standard deviation is of the order of $2.5 - 3°C$ for all months of the year. The random deviates have high correlation at lag one hour ($\sim 0.9$).

## 2.7　Simulation of air humidity

### 2.7.1　Model formulation

Traditionally, most weather generators have been limited to modeling precipitation and extreme temperatures only. Because many physically-based models of natural phenomena require some measure of atmospheric moisture in the meteorological input, some stochastic weather generators do include simulation of variables that can be translated into air humidity. Ahmed (1974) generated air humidity within the framework of a multivariate model by using the observed mean weekly relative humidities. Hanson and Johnson (1998) used the weather generator GEM to simulate the daily dew point, assuming that it is normally distributed. Parlange and Katz (2000) extended the model of Richardson (1981) to include the dew point temperature as a component of multivariate stochastic process. Curtis and Eagleson (1982) developed a framework that allowed to simulate dew point temperatures for two cases. When dew point temperature was considered as an independent process, a first-order Markov model was applied. A multiple linear regression was applied to simulate dew point temperatures during months when stronger cross-correlation properties with the other hydrometeorological variables were revealed. The latter model used 11 additional parameters. While the model of Curtis and Eagleson (1982) allows one to reproduce the dew point temperatures sufficiently well at an hourly scale, a simpler model requiring less parameters is sought. For example, dew point temperatures have been found to stay relatively constant during the day (e.g., Glassy and Running, 1994), which provides a sufficient motivation for developing a simple model. The desired approach is required to account for the climate characteristics of a particular region in a simple and efficient way.

Observations have shown that nightly minimum temperatures, $T_{mind}$ [$°C$], tend to come into equilibrium with daily dew point temperatures, $T_{dew}$ [$°C$] (Running et al., 1987). Because of these characteristics $T_{mind}$ is often used as an indirect measure of $T_{dew}$, due to generally greater accuracy and frequency of air temperature observations. However, Kimball et al. (1997) showed that there can be substantial

differences between these two variables, especially in arid and semi-arid climates. Based on long-term records, Kimball et al. (1997) proposed a simple empirical model that allows for the adjustment of daily dew point temperature with respect to the minimum daily air temperature using information on daily potential evaporation and degree of aridity of the region:

$$T_{dew} = T_{mind}[-0.127 + 1.121(1.003 - 1.444EF +$$
$$12.312EF^2 - 32.766EF^3) + 0.0006\Delta T_d] - 273.15\,, \qquad (2.62)$$

where $\Delta T_d$ $[°C]$ is the amplitude of daily air temperature and $EF$ $[-]$ is the evaporative factor, $0 \leq EF \leq 1$ that Kimball et al. (1997) define as

$$EF = \frac{1}{P_{ann}}\left[\frac{E_p}{\rho_w}D_{LH}\right]\,, \qquad (2.63)$$

where $E_p$ $[kg\,m^{-2}\,s^{-1}]$ is the daily average potential evapotranspiration, $\rho_w$ $[kg\,m^{-3}]$ is the density of water, $D_{LH}$ $[sec]$ is the day length, and $P_{ann}$ $[m]$ is the annual precipitation. The variable $D_{LH}$ is defined as the time interval between sunrise and sunset (Section 2.3.1). The potential evapotranspiration is estimated using the formulation of Priestley-Taylor (Priestley and Taylor, 1972):

$$E_p = \frac{1.26}{\lambda}\frac{\Delta}{\Delta + \gamma}(R_n - G)\,, \qquad (2.64)$$

where $\lambda$ $[J\,kg^{-1}]$ is the latent heat of vaporization, $\Delta$ $[Pa\,K^{-1}]$ is the rate of change of saturation vapor pressure with temperature, $\gamma$ $[Pa\,K^{-1}]$ is the psychrometer constant, $R_n$ $[W\,m^{-2}]$ is the average daily net energy flux, and $G$ $[W\,m^{-2}]$ is the average daily ground heat flux. Kimball et al. (1997) show that the model (2.62) allows one to improve estimates of daily dew point temperatures based on daily minimum temperatures. A substantial improvement can be obtained for stations in arid and semi-arid climates. The approach of Kimball et al. (1997) is attractive since it does not require extensive observed data input and does not introduce a significant number of new parameters. The following is a description of implementation of formulation

124

(2.62) in the presented modeling framework.

## 2.7.2 Model implementation

The major difficulty in estimating $T_{dew}$ using (2.62) is in computing daily values of $E_p$ and obtaining $\Delta T_d$ from the air temperature model. The estimates of daily values of $E_p$ and $\Delta T_d$ have to be available each time $T_{dew}$ is computed since the latter variable is estimated on a daily scale at the *beginning* of each day. Both $E_p$ and the air temperature, however, are defined by a number of variables simulated at the hourly scale that cannot be easily estimated or predicted for the whole day at the time when $T_{dew}$ is estimated. For instance, the hourly cloudiness affects temperature estimation and since both models (the cloud cover and air temperature) use random deviates, there is no suitable way to predict the exact daily air temperature amplitude.

It is assumed that *adjusted* values of $E_p$ and $\Delta T_d$ from the previous day, $(d-1)$, can be used for estimation of $T_{dew}$ on the current day $d$. Since the cloud cover significantly affects incoming radiation and, therefore, the amount of energy available for evapotranspiration, it is proposed to use an adjustment factor based on the radiation attenuation factor, $K(t)$ (Section 2.6.1) in the form:

$$\tilde{A}(d) \;=\; \frac{\widetilde{K}(d)}{\overline{K}(d-1)} \;=\; \frac{1 - 0.65^2 \widetilde{N}(d)}{1 - 0.65^2 \overline{N}(d-1)}, \tag{2.65}$$

where is $\overline{K}(d-1)$ the average value of the attenuation factor for the previous day and $\widetilde{K}(d)$ is the mean *expected* value for the day of estimation. The possibility to estimate the latter quantity comes from using the Poisson process as the rainfall arrival model: at every time point between successive storms, both the end time of the previous storm and beginning time of the next storm are known. The cloud cover model (2.37) can be used to estimate the expected value of cloudiness for the following day, from which the factor $\tilde{A}(d)$ is then estimated. Once $\tilde{A}(d)$ has been estimated, $E_p$ and $\Delta T_d$ that appear in expressions (2.62) - (2.63) can be approximated as

$$\tilde{E}_p(d) \;=\; \tilde{A}(d)\overline{E}_p(d-1),$$

125
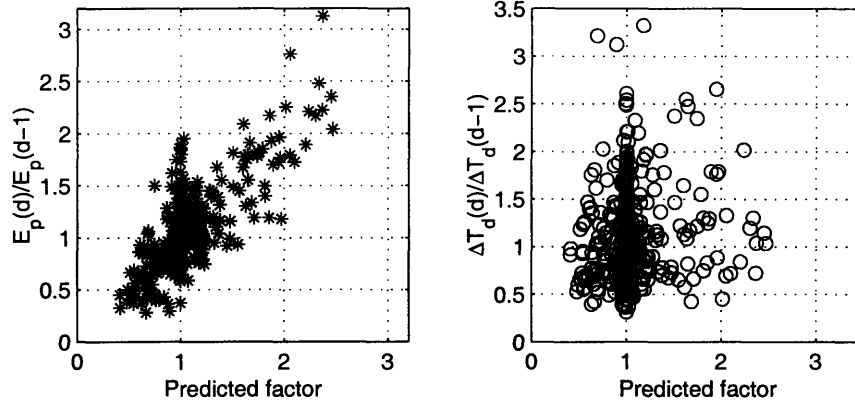
Figure 2-21: Comparison of $\tilde{A}(d)$, the predicted factor, as defined in (2.65) and the factor obtained from the simulated data when both $\overline{E}_p(d)$ and $\Delta T_d$ become known (Albuquerque, NM).

$$\Delta \tilde{T}_d(d) = \tilde{A}(d) \Delta T_d(d-1).\qquad(2.66)$$

Kimball et al. (1997) used the Priestley-Taylor model (Priestley and Taylor, 1972) to estimate the daily potential evapotranspiration (equation (2.64)). Although the discussed framework contains a more physically-based model for estimation of the evaporative demand (Chapter 3), the formulation (2.64) is used here to obtain the daily average potential evapotranspiration for the preceding day $\overline{E}_p(d-1)$. This is justified by the need for the climate simulator to generate variables (such as $\overline{E}_p(d-1)$) *independent* from the states of the soil surface and vegetation, which would not be true if $R_n$ and $G$ were computed using a fully-dynamic, state-dependent model. The model (2.64) assumes that the ground surface has a seasonally constant albedo, $R_n$ can be estimated based on the air temperature, and that $G$ is 10% of $R_n$ (Kimball et al., 1997). A comparison of the factors approximated with (2.65) and factors computed from the simulated daily data (i.e., when both $\overline{E}_p(d)$ and $\Delta T_d$ are known) is shown in Figure 2-21. As can be seen, the use of $\tilde{A}(d)$ is satisfactory for estimating $\overline{E}_p(d)$. However, the definition of $\tilde{A}(d)$ is not quite suitable for adjusting the air temperature amplitude for the previous day $\Delta T_d(d-1)$. $\tilde{A}(d)$ is therefore not used for this adjustment.

Two other variables are required for estimation of $T_{dew}$ using (2.62): $T_{mind}$ and

Table 2.7: The precipitation factor $P^*_{ann}$ estimated for different months of the year.

| Meteostation / Month | ALB[a] | TCS[b] | TLS[c] |
|---|---|---|---|
| January | 65 | 87 | 100 |
| February | 60 | 87 | 132 |
| March | 60 | 84 | 170 |
| April | 55 | 45 | 280 |
| May | 70 | 41 | 505 |
| June | 70 | 46 | 520 |
| July | 120 | 185 | 525 |
| August | 160 | 225 | 520 |
| September | 105 | 160 | 430 |
| October | 60 | 103 | 270 |
| November | 50 | 84 | 150 |
| December | 55 | 88 | 95 |

[a]Albuquerque (NM) 35.05N 106.617W
[b]Tucson (AZ) 32.131N 110.955W
[c]Tulsa (OK) 36.197N, 95.886W

$P_{ann}$. The problem of estimating the minimum daily air temperature, $T_{mind}$, is similar to the problem of estimating $E_p$ and $\Delta T_d$: the value of $T_{mind}$ is not known unless all hourly temperatures have been simulated for the current day $d$. Since the value of the air temperature at the hour preceding sunrise can be usually associated with $T_{mind}$, the simulation of daily $T_{dew}$ occurs at this hour and $T_{mind}$ is taken as the air temperature simulated according to (2.45). Kimball et al. (1997) used the mean value of annual precipitation $P_{ann}$ for all days throughout the year. However, it is assumed in the presented framework, that a monthly basis is more appropriate since different months/seasons have different degree of dryness (e.g., Figure 2-8). Therefore, $P_{ann}$ is considered as a precipitation parameter for each month, $P^*_{ann}$, rather than the amount of annual precipitation. The monthly values of $P^*_{ann}$ depend on wetness of any particular month and are determined iteratively by comparing the mean observed and simulated monthly dew point temperatures. Table 2.7 provides the parameter $P^*_{ann}$ estimated on a monthly basis for several meteorological stations.

## 2.8 Simulation of wind speed

### 2.8.1 Model formulation

Wind speeds are required as input into the radiation model to characterize turbulent mechanisms of moisture and heat transport from evaporating surfaces. The statistical structure of the wind speed series has been extensively studied within individual stochastic models (e.g., Brown et al., 1984; Carlin and Haslett, 1982; Haslett and Raftery, 1989). The simulation of wind speed within the framework of a stochastic climate simulator has been attempted in a few studies (Curtis and Eagleson,1982; Nicks et al., 1990; Hanson and Johnson, 1998; Parlange and Katz, 2000). Typically, the cross-correlation coefficients between wind speed and other hydrometeorological variables are small. Curtis and Eagleson (1982) provide estimates of the cross-correlation with the maximum values of 0.35, typically around 0.1(for hourly weather data in Massachusetts and Kansas including: air and dew point temperature and cloud cover). Parlange and Katz (2000) used daily weather data from Oregon and reported cross-correlation values not exceeding 0.2 (daily maximum and minimum air temperatures, dew point). Wind speed has been therefore typically simulated as an independent variable (Curtis and Eagleson, 1982; Nicks et al., 1990; Hanson and Johnson, 1998). The approach of Curtis and Eagleson (1982) for simulating hourly wind speed is used in the presented framework.

It is well known that the distribution of both hourly and daily wind speed is positively skewed, with theoretical distributions such as the squared normal distribution (Carlin and Haslett, 1982), the Weibull (Hennessey, 1977) having been fitted. The Weibull distribution appears to be the most popular. To generate skewed hourly wind speed data, while preserving the first two moments of its distribution, Curtis and Eagleson (1982) employed the Thomas-Fiering method (Maass et al., 1962), i.e., the $AR(1)$ model where the random term forces skewness on the results of the autoregressive model:

$$W_s(t) \;\; = \;\; \overline{W}_s + \rho_s(1)(W_s(t-1) - \overline{W}_s) + \varepsilon_t \sigma_s \sqrt{1 - \rho_s^2(1)}, \qquad (2.67)$$

Table 2.8: The parameters $\overline{W}_s$ $[m\ s^{-1}]$, $\sigma_s^2$ $[m^2\ s^{-2}]$, $\rho_s(1)$ $[-]$, and $\gamma_s$ $[-]$ of the wind speed model

| Parameter / Meteostation | ALB[a] | TCS[b] | TLS[c] |
|---|---|---|---|
| $\overline{W}_s$ | 3.491 | 3.897 | 4.594 |
| $\sigma_s$ | 2.452 | 2.028 | 2.472 |
| $\rho_s(1)$ | 0.755 | 0.608 | 0.709 |
| $\gamma_s$ | 1.688 | 1.145 | 0.516 |

[a]Albuquerque (NM) 35.05N 106.617W
[b]Tucson (AZ) 32.131N 110.955W
[c]Tulsa (OK) 36.197N, 95.886W

where $\overline{W}_s$ $[m\ s^{-1}]$, $\sigma_s^2$ $[m^2\ s^{-2}]$, and $\rho_s(1)$ $[-]$ are the mean, variance, and lag-1 value of autocorrelation of wind speed, respectively. The term $\varepsilon_t(t)$ is defined as (Wilson and Hillerty, 1931)

$$\varepsilon_t = \frac{2}{\gamma_\varepsilon}\left[1 + \frac{\gamma_\varepsilon \psi_t}{6} - \frac{\gamma_\varepsilon^2}{36}\right]^3 - \frac{2}{\gamma_\varepsilon}, \qquad (2.68)$$

where $\gamma_\varepsilon(t)$ is the skewness of $\varepsilon_t(t)$ and $\psi_t$ is a standard normal deviate. The skewness of $\gamma_\varepsilon(t)$, in turn, is defined as

$$\gamma_\varepsilon = \frac{(1 - \rho_s^3)\gamma_s}{(1 - \rho_s^2)^{1.5}}, \qquad (2.69)$$

where $\gamma_s(t)$ is the skewness determined from the wind speed data. Curtis and Eagleson (1982) considered variation of wind speed mean and variance with time of the day (notation '$(t)$' above). This was important for the application of their weather generator since it was used for simulating input to a land-surface model. Such variation is of less concern for the current work and therefore no diurnal variation of parameters $\overline{W}_s$ and $\sigma_s^2$ is considered. The parameters are assumed to be time-invariant over the entire simulation period. The parameters $\overline{W}_s$, $\sigma_s^2$, $\rho_s(1)$, and $\gamma_s$ are estimated from wind speed data using conventional methods. The estimated values of the parameters for the test meteorological stations are provided for reference in Table 2.8.
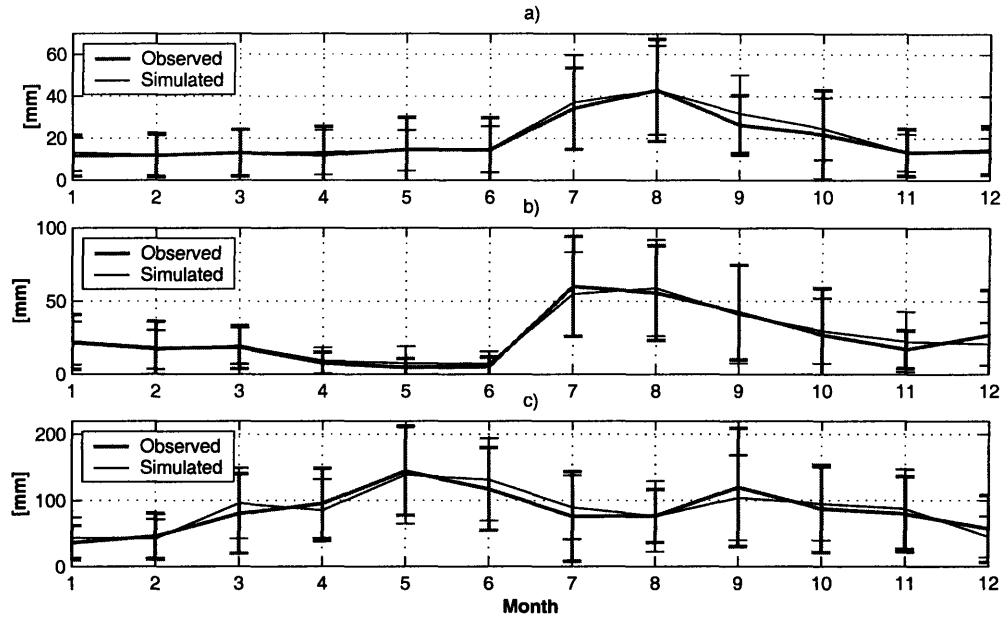
Figure 2-22: Observed and simulated mean monthly rainfall for: a.) Albuquerque (NM); b) Tucson (AZ); c) Tulsa (OK). The vertical bars denote the estimated standard deviation of the monthly value.

## 2.9 Verification of weather generator

The performance of the weather generator is illustrated in the following with the statistics derived from the *hourly* hydrometeorological data simulated for a 100-year period. The results are based on complete weather simulations that involve synthetic modeling of the entire set of climate variables, accounting for all previously discussed linkages among them.

### 2.9.1 Simulation of rainfall

Since the parameters of the rainfall model (the storm arrival rate, duration, and depth) are sampled from the assumed analytical distributions, the statistical properties of the corresponding parameters are inherently preserved. Precipitation intra-annual seasonality is introduced by considering different model parameters for different months (Table 2.1). Figure 2-22 illustrates the annual cycle of the rainfall process for the three sites in New Mexico, Arizona, and Oklahoma.

130

## 2.9.2 Simulation of cloud cover

Along with the first two moments of the cloudiness distribution, the model has to preserve the shape of the cloud cover frequency histogram. In general, the frequency distributions of fairweather cloudiness tend to be U-shaped with spikes at zero and one. Figures 2-23 - 2-25 illustrate the results of hourly cloud cover simulation using the model described in Section 2.5.1. As can be seen, there is a generally good agreement between the observed and simulated data. A note has to be made concerning the cloud cover during consecutive months that have highly different cloudiness statistics (e.g., Figure 2-24, Tucson, AZ: July and August). The cloud cover model considers monthly values of the parameters. Cloudiness of an interstorm period that overlaps two months is therefore simulated using parameters for both months. The procedure that identifies the fairweather cloud cover sequences considers an interstorm period starting in one month and ending in a subsequent month as belonging to one month only, depending on the relative duration of the dry spell within each month. Consequently, the cloud cover statistics derived for any given month can be affected by the presence of interstorm periods during which cloudiness is simulated using two parameter sets. This is reflected in statistics, for example, for July and August in Figure 2-24.

## 2.9.3 Simulation of air temperature

When simulating hourly temperature, it is important to reproduce both its mean daily cycle and average daily variability. Figures 2-26 - 2-28 illustrate the daily cycles of the mean air temperature and its standard deviation computed separately for each month. As the figures show, the model (2.45) produces quite satisfactory results that mimic the daily air temperature fluctuations very well. At a longer, monthly scale, the air temperature statistics are also well reproduced, as is shown in Figures 2-29 - 2-31 (subplots a, b, and c). Table 2.9 summarizes the results of simulation for the test stations. As can be concluded from the table and Figures 2-26 - 2-31, the model described in Section 2.6 generally produces lower root mean square error estimates
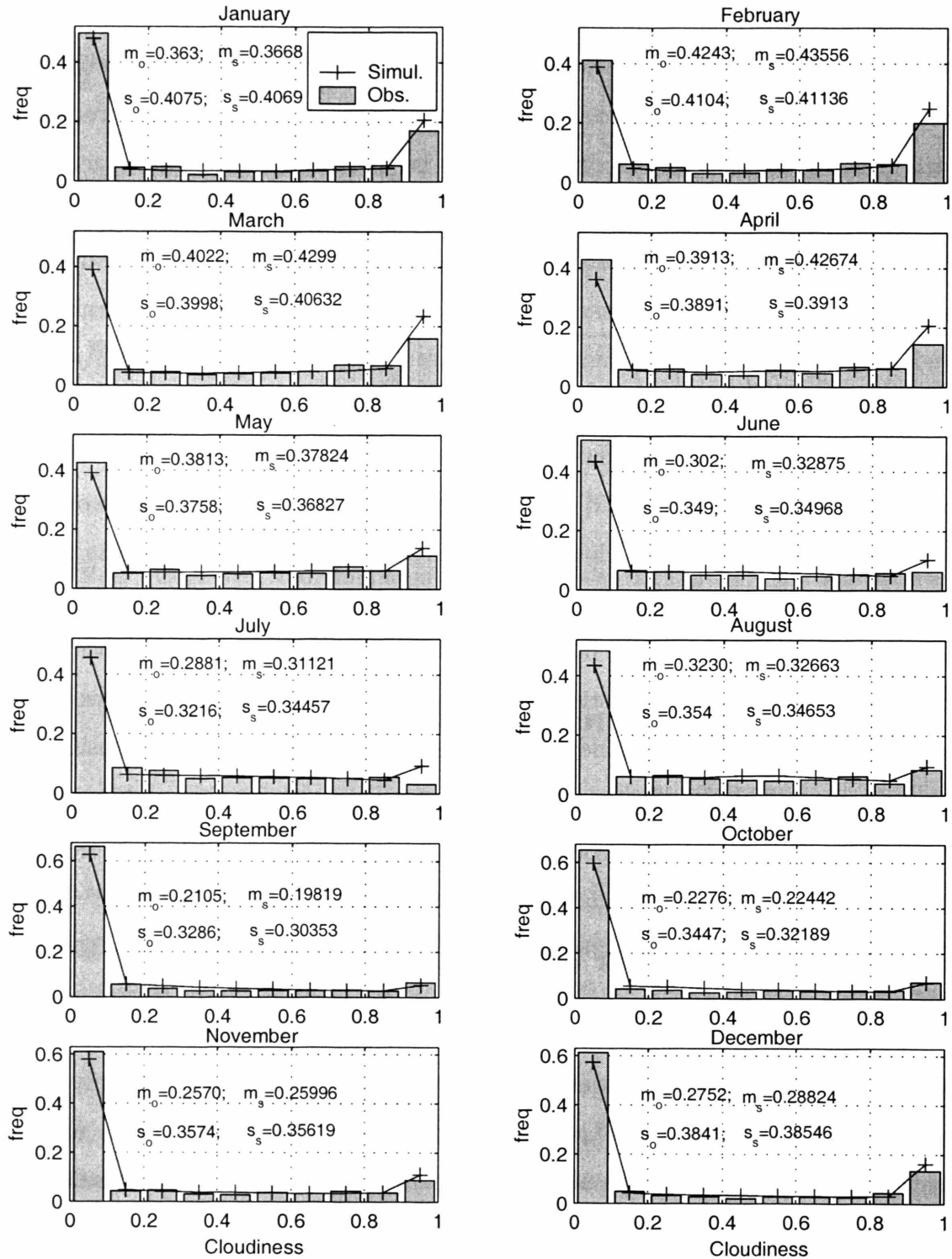
Figure 2-23: Observed and simulated cloud cover distribution (Albuquerque, NM). Symbols $m$ and $s$ are the mean and standard deviation values, correspondingly, for the observed (sub-index "o") and simulated (sub-index "s") data.
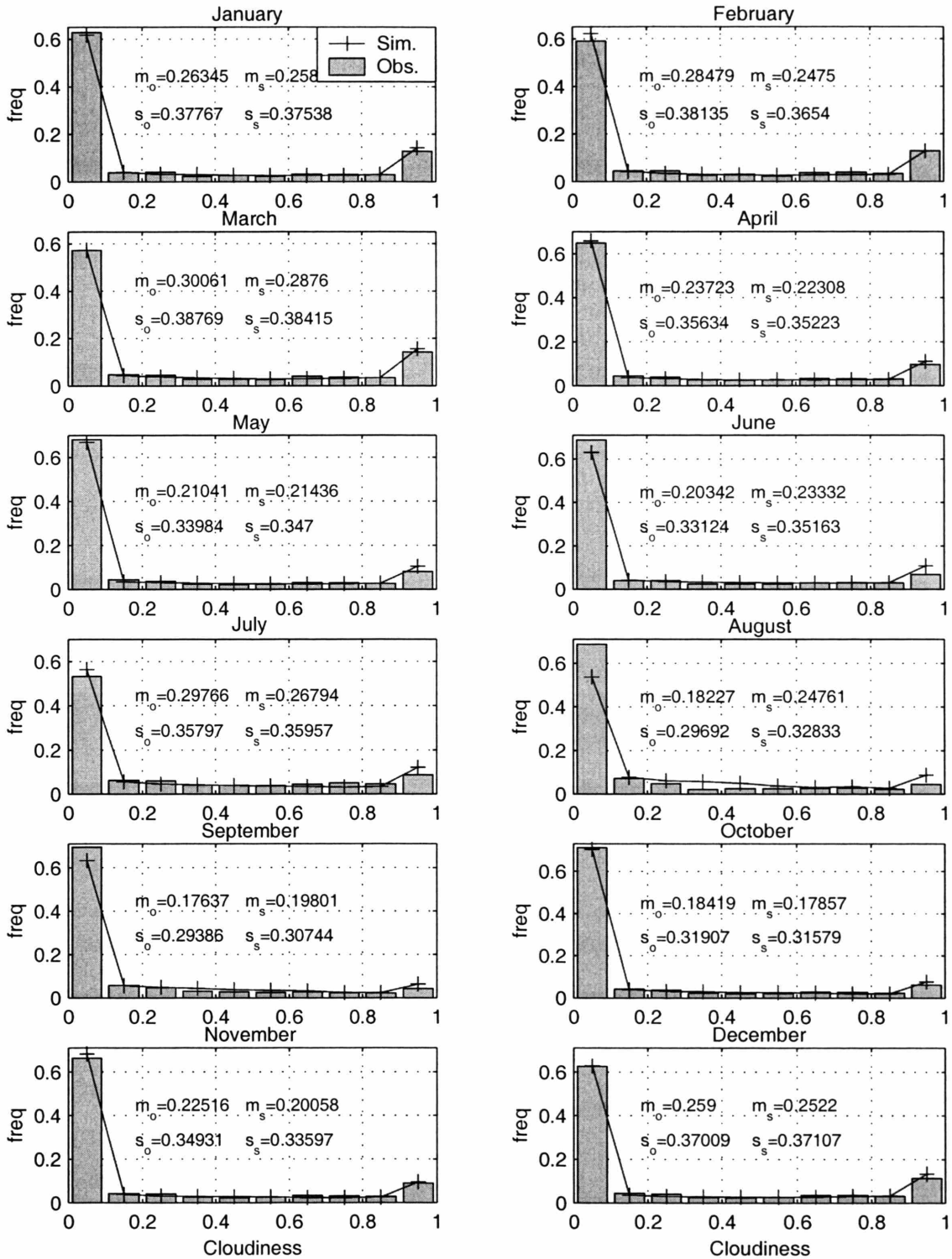
Figure 2-24: Observed and simulated cloud cover distribution (Tucson, AZ). Symbols $m$ and $s$ are the mean and standard deviation values, correspondingly, for the observed (sub-index "o") and simulated (sub-index "s") data.

133
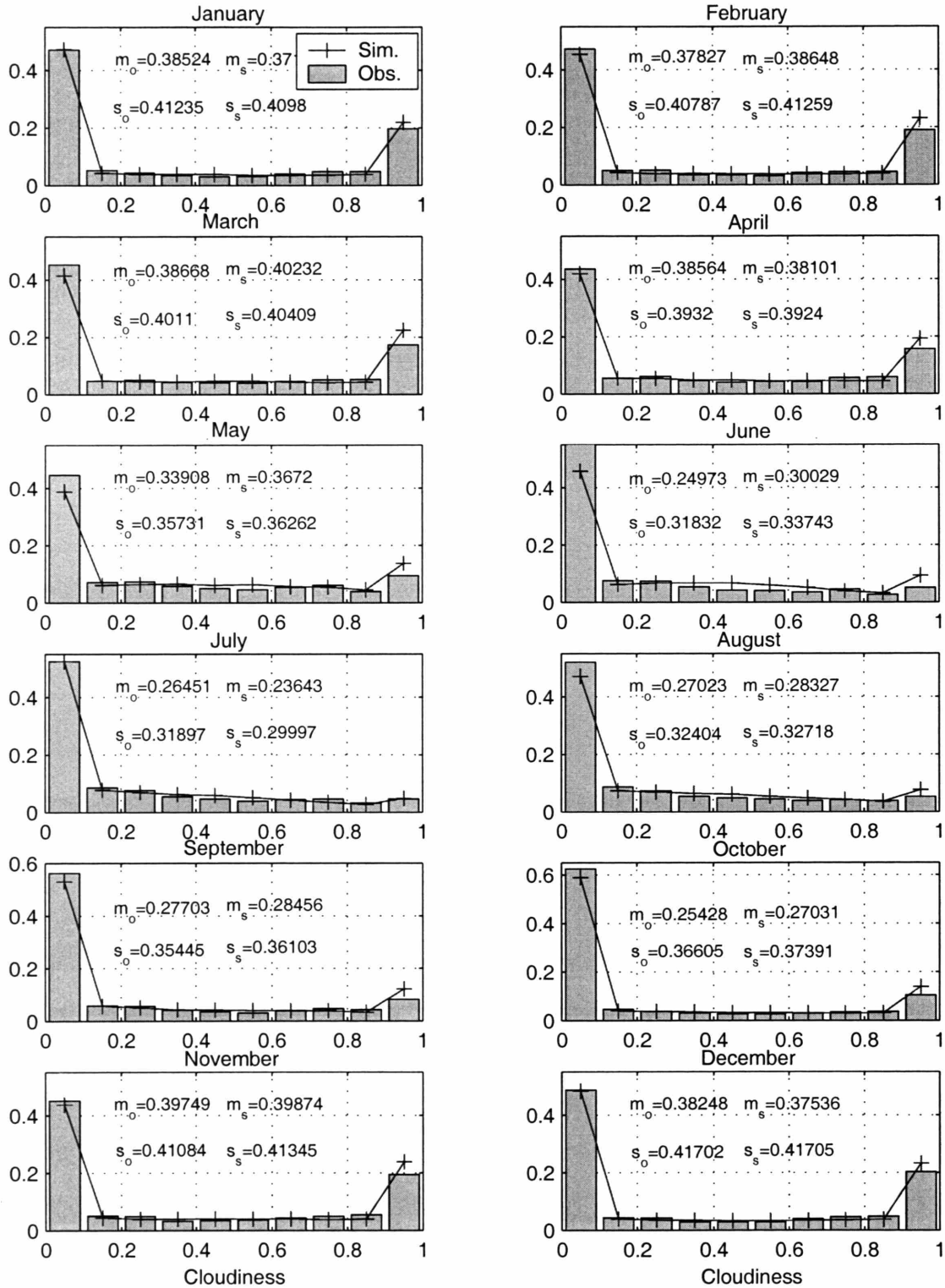
Figure 2-25: Observed and simulated cloud cover distribution (Tulsa, OK). Symbols $m$ and $s$ are the mean and standard deviation values, correspondingly, for the observed (sub-index "o") and simulated (sub-index "s") data.

Table 2.9: The estimates of the root mean square error (RMSE, °C) for the simulated daily cycle of air temperature.

| Meteostation / Month | ALB[a] | TCS[b] | TLS[c] |
|---|---|---|---|
| January | 5.450 | 5.636 | 6.881 |
| February | 5.136 | 5.816 | 5.813 |
| March | 5.556 | 5.789 | 8.879 |
| April | 6.018 | 7.531 | 4.558 |
| May | 5.266 | 7.112 | 3.787 |
| June | 5.278 | 6.358 | 3.938 |
| July | 4.344 | 4.123 | 3.418 |
| August | 4.781 | 5.046 | 3.697 |
| September | 4.832 | 6.185 | 7.269 |
| October | 5.746 | 7.385 | 6.243 |
| November | 6.167 | 7.195 | 6.617 |
| December | 4.760 | 6.558 | 10.789 |

[a]Albuquerque (NM) 35.05N 106.617W
[b]Tucson (AZ) 32.131N 110.955W
[c]Tulsa (OK) 36.197N, 95.886W

during summer periods. A somewhat better performance can also be attributed to warmer climates.

### 2.9.4 Simulation of dew point temperature

Since dew point temperature exhibits little variability on any given day, only monthly statistics are presented. Figures 2-29 - 2-31 (subplots d, e, and f) show the mean daily dew point temperatures as well as the mean daily maximum and minimum dew point temperatures simulated for each month. Since the model that generates hourly dew point temperatures is quite simple, the simulated and observed series are in less agreement as compared to the results of the air temperature simulation.
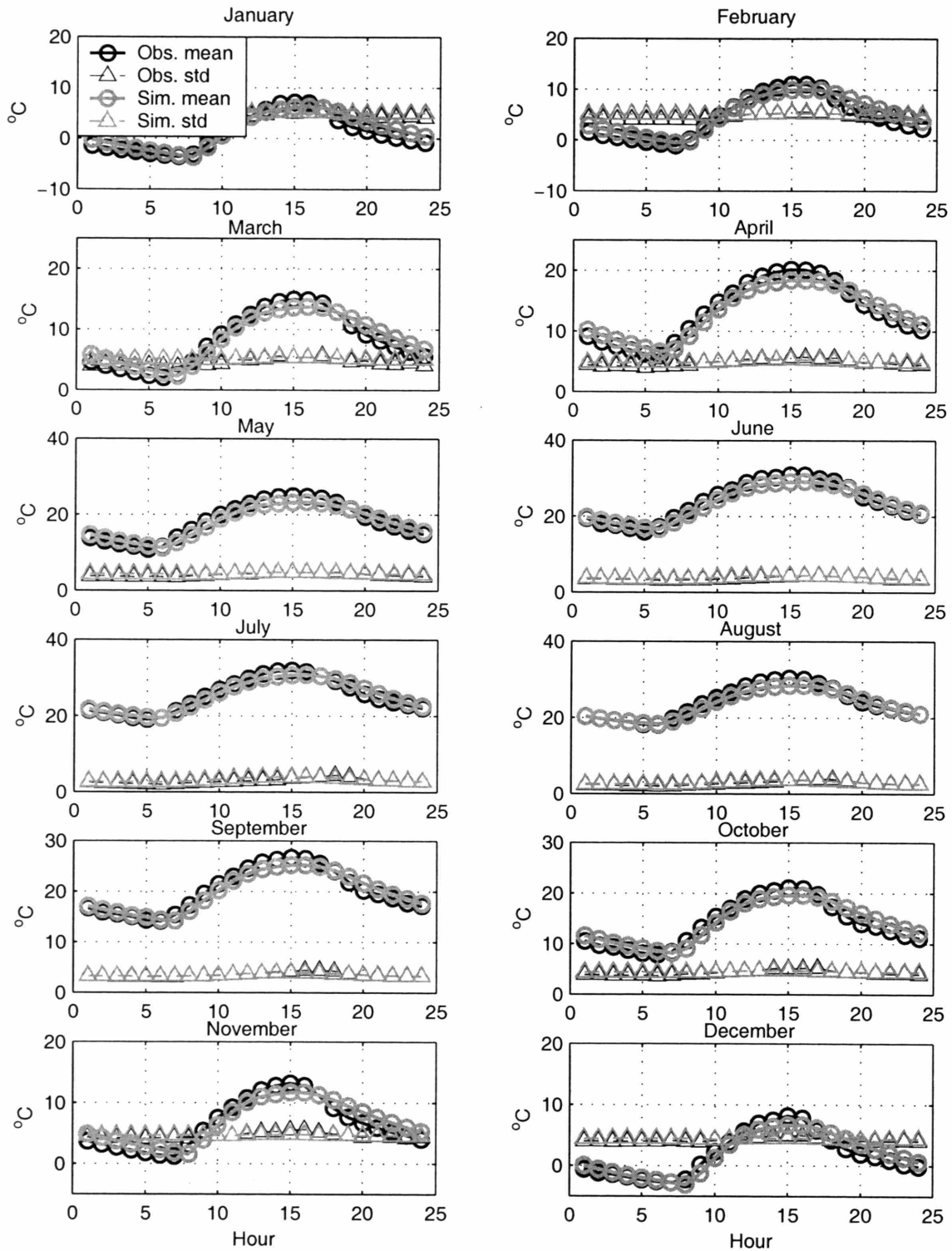
Figure 2-26: Observed and simulated daily cycles of air temperature and its standard deviation (Albuquerque, NM).

136
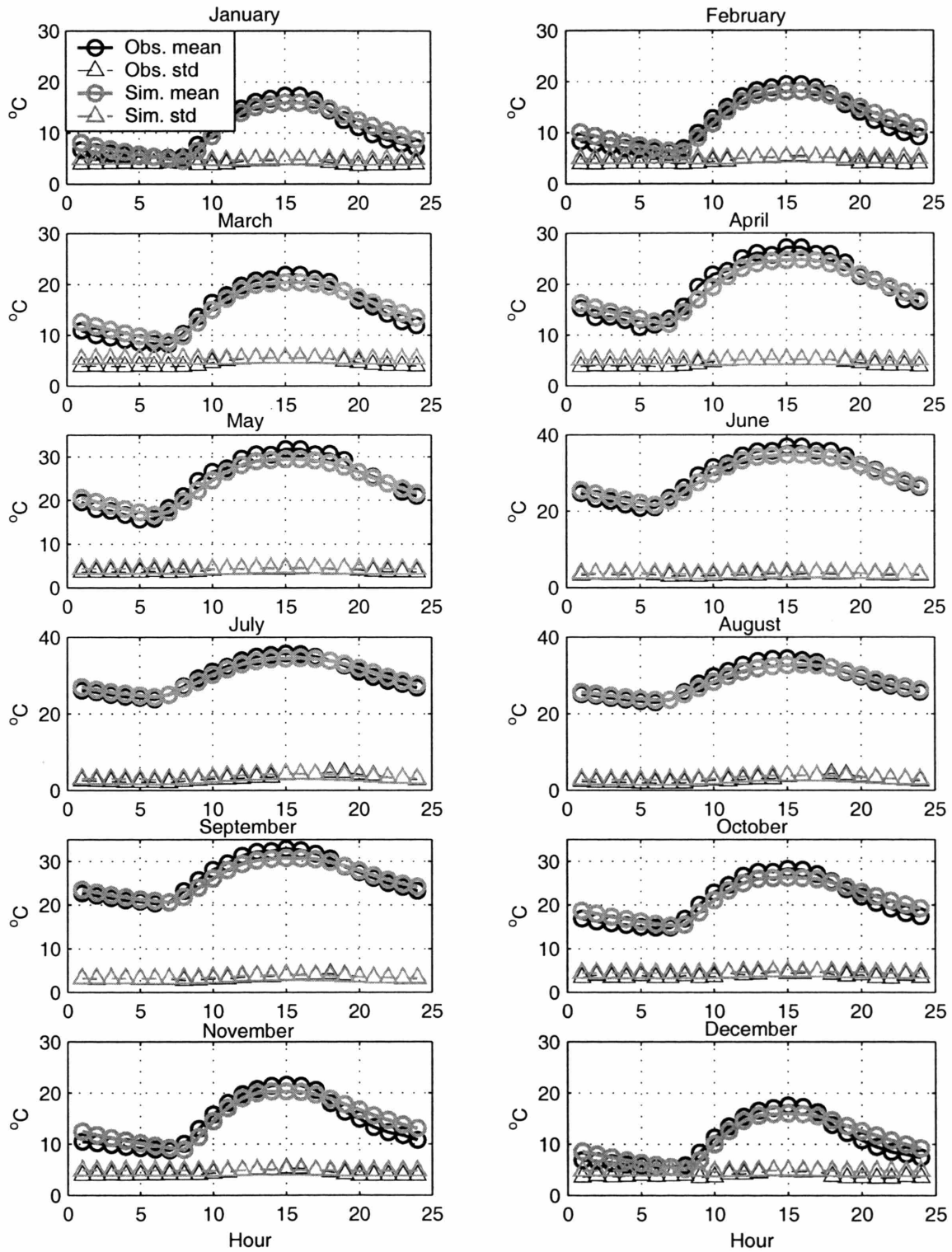
Figure 2-27: Observed and simulated daily cycles of air temperature and its standard deviation (Tucson, AZ).
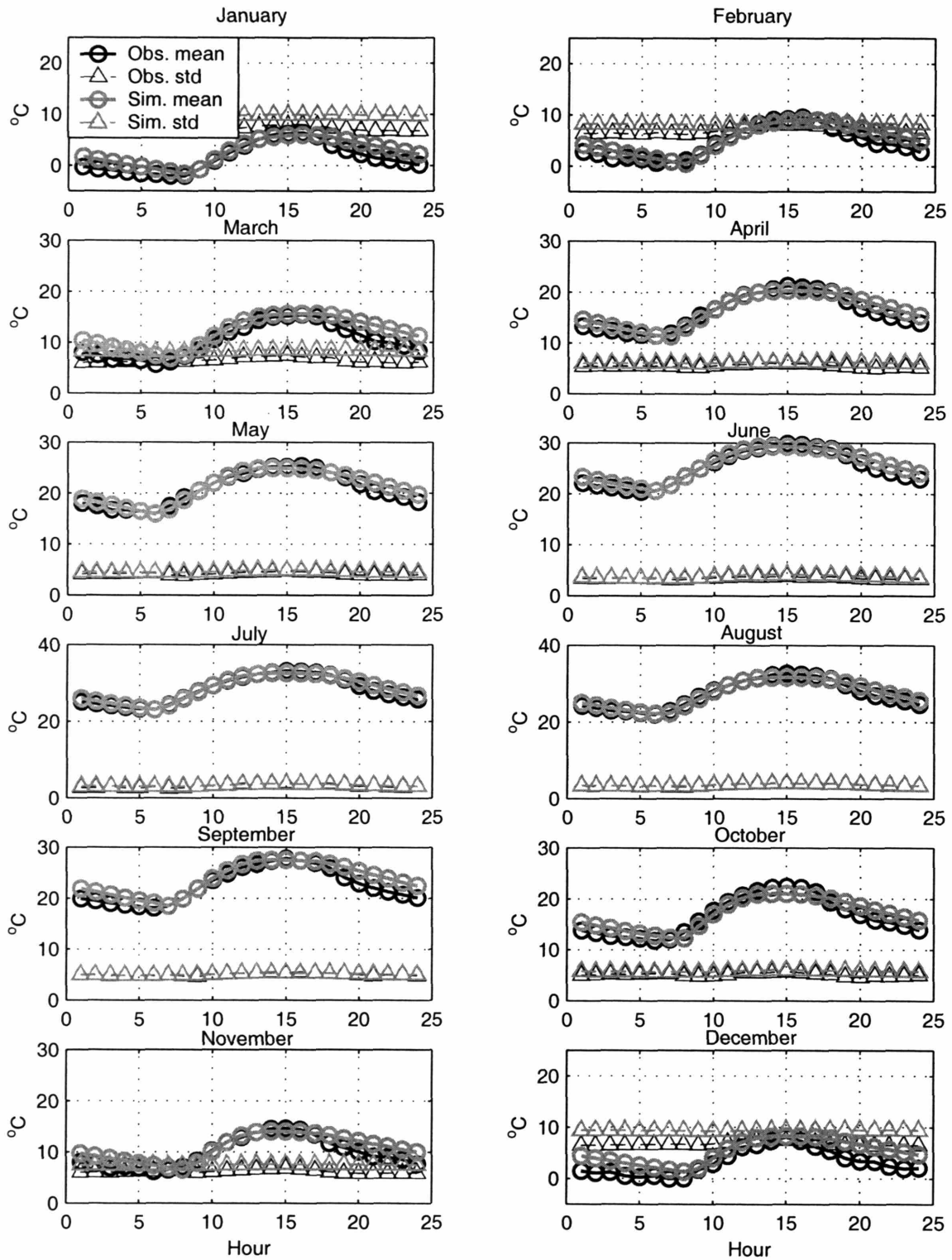
Figure 2-28: Observed and simulated daily cycles of air temperature and its standard deviation (Tulsa, OK).
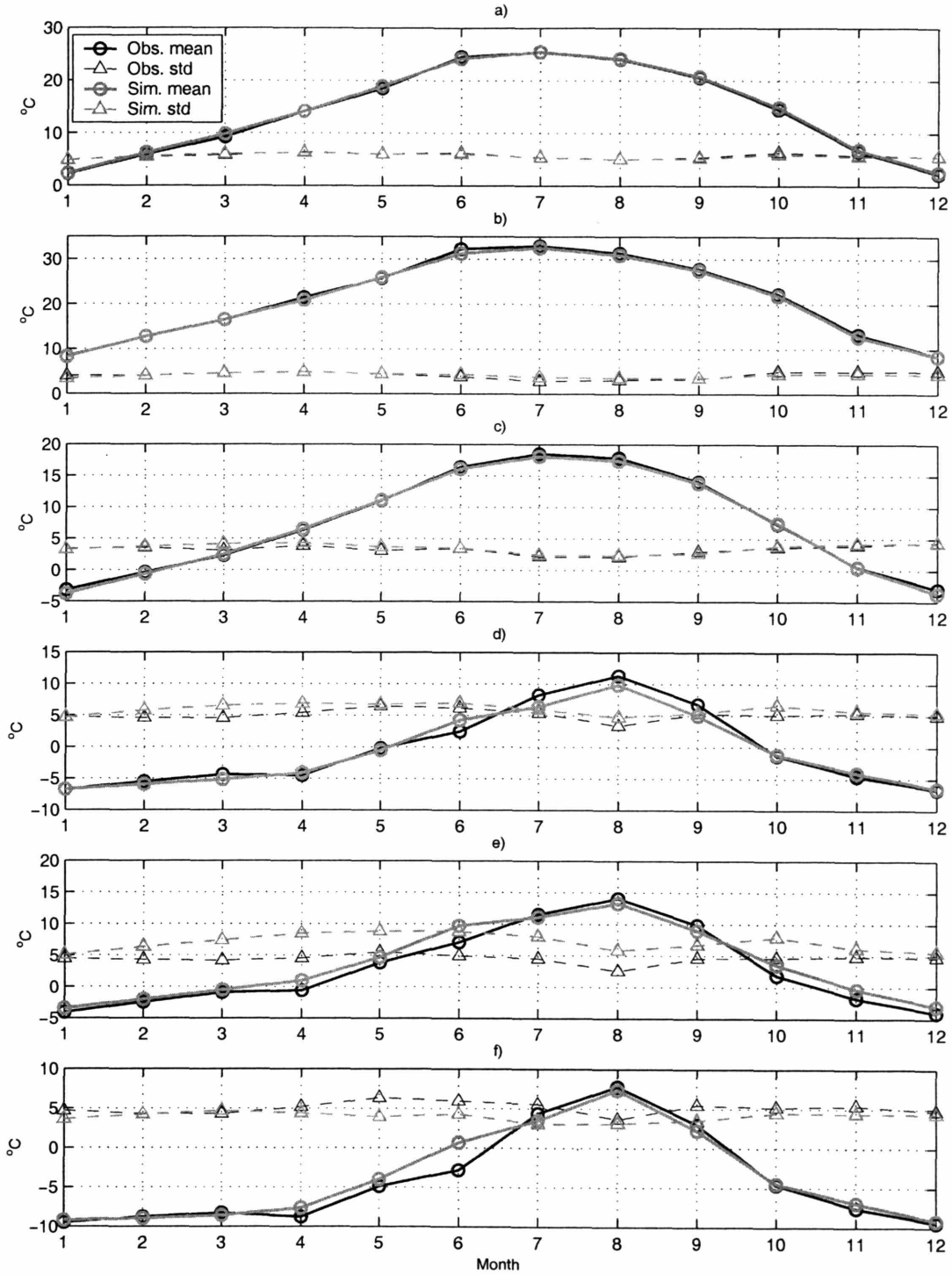
Figure 2-29: Observed and simulated mean values of air and dew point temperature and their standard deviations (Albuquerque, NM). Mean monthly values and daily standard deviation of: a.) air temperature; b.) maximum air temperature; c.) minimum air temperature; d.) dew point temperature; e.) maximum dew point temperature; and f.) minimum dew point temperature.

139
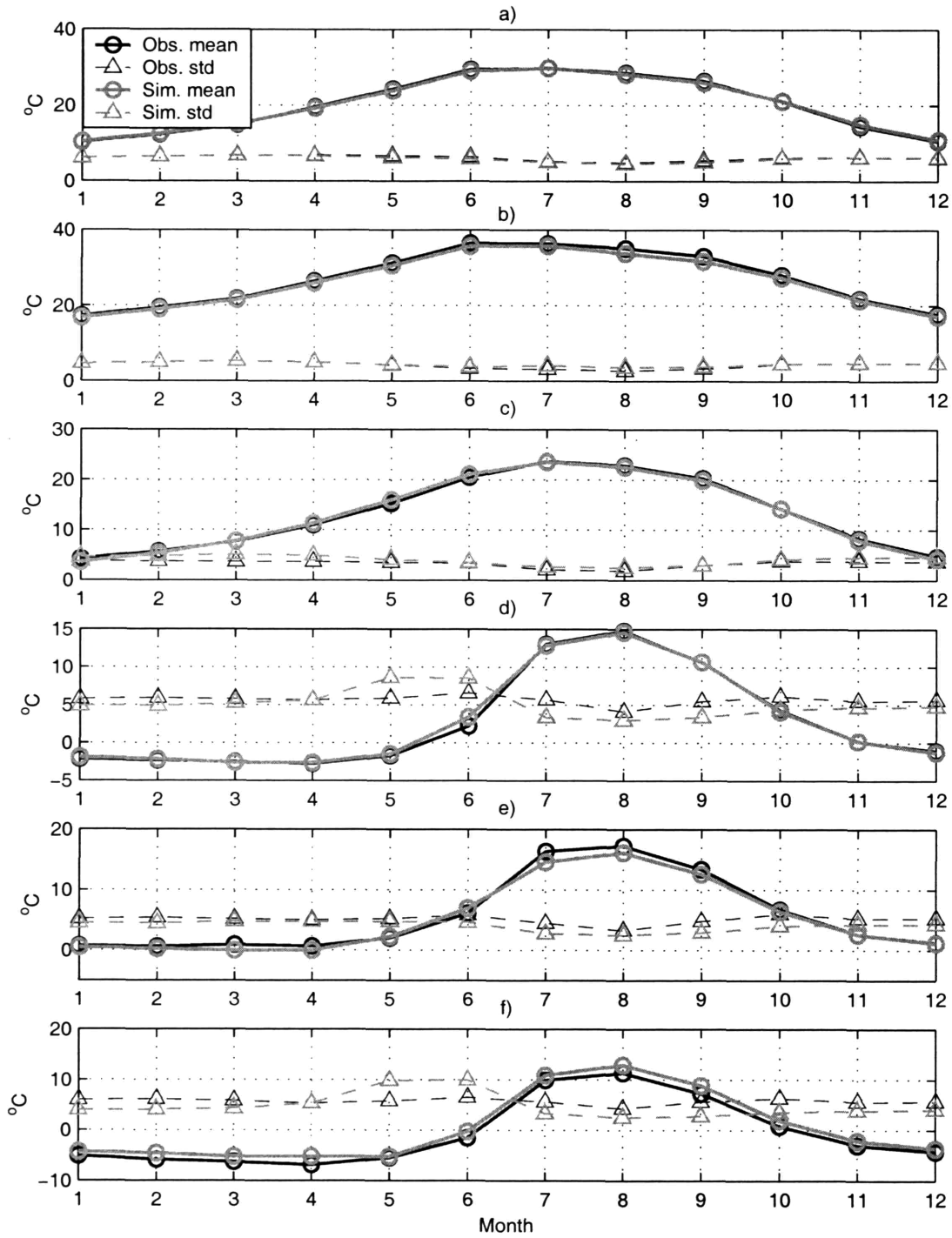
Figure 2-30: Observed and simulated mean values of air and dew point temperature and their standard deviations (Tucson, AZ). Mean monthly values and daily standard deviation of: a.) air temperature; b.) maximum air temperature; c.) minimum air temperature; d.) dew point temperature; e.) maximum dew point temperature; and f.) minimum dew point temperature.
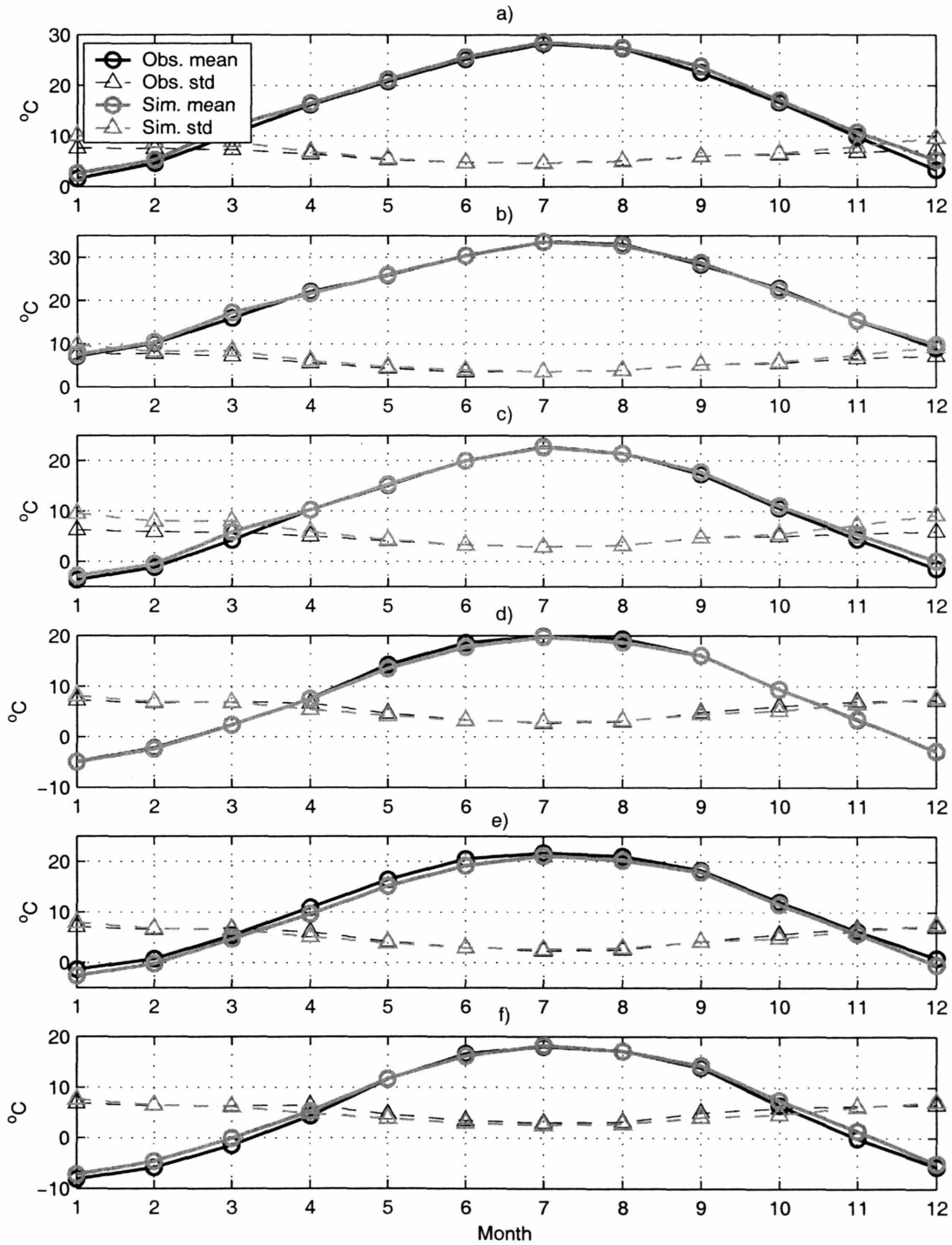
Figure 2-31: Observed and simulated mean values of air and dew point temperature and their standard deviations (Tulsa, OK). Mean monthly values and daily standard deviation of: a.) air temperature; b.) maximum air temperature; c.) minimum air temperature; d.) dew point temperature; e.) maximum dew point temperature; and f.) minimum dew point temperature.

141
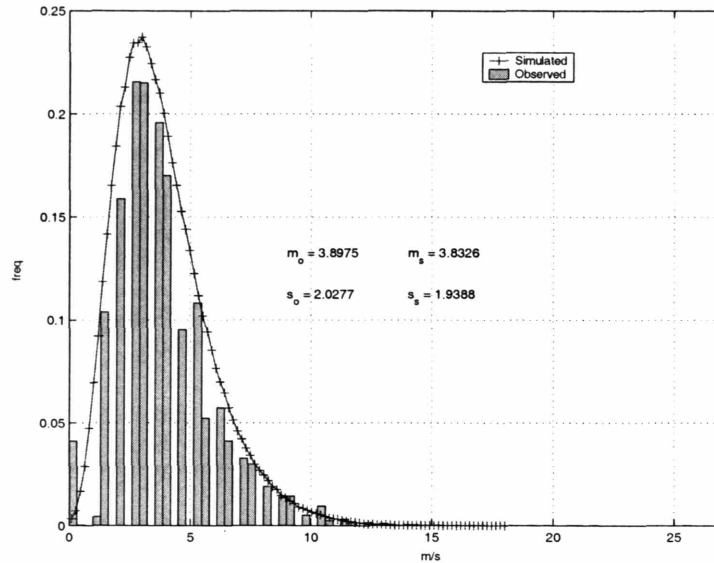
Figure 2-32: The histogram of hourly wind speed from the observed and simulated data (Tucson, AZ). Symbols $m$ and $s$ are the mean and standard deviation values, correspondingly, for the observed (sub-index "o") and simulated (sub-index "s") data.

### 2.9.5 Simulation of wind speed

As was discussed in Section 2.8, the frequency distribution of wind speed data is positively skewed. Both the skewness properties and the first two moments of the distribution are preserved with the model (2.67). Figure 2-32 illustrates the wind speed histograms computed from the observed and simulated data.

## 2.10 Co-variation of hydrometeorological variables

The weather generator explicitly couples a number of simulated variables. Although the cross-correlation properties are not directly accounted for as, for example, in the model of Richardson (1981), it can be expected that all major weather variables should exhibit consistent co-variation. Figure 2-33 illustrates such interdependencies in a qualitative manner, using the results of simulation of the weather generator calibrated for the location of Albuquerque (NM). Simulations start in August and extend through half of September. As can be seen in the figure, the cloudiness dynamics correspond to precipitation events and the incoming shortwave is correspondingly

142

affected by the presence of clouds. The air temperature series exhibit both lower magnitude and diurnal variability during the days with precipitation. The dew point temperatures become less differentiated from the air temperatures during wet periods and show a substantial deviation from the minimum daily temperatures during dry hot periods.

Figures 2-34 - 2-36 illustrate the dependence of the mean monthly cloud cover on rainfall occurrence. As can be seen in the figures, there is a good correspondence between the simulated and observed data. The cloud cover model slightly overestimates the mean observed values, which can be attributed to both: a) overestimation of the rainfall occurrence for some months due to the introduced seasonality in rainfall model parameters; and b) some inadequacy of the exponential form of the transition function $J(t)$ to describe the cloud cover dynamics during transition to/from fairweather periods.

Figures 2-37 - 2-39 show the mean maximum and minimum air temperatures on rainy and rainless days for different months, derived from the simulated and observed data. While the air temperature model accounts for precipitation occurrence only implicitly (via the factors $K(t)$ and $K_c(t)$ applied to the various terms of (2.46)), a generally good agreement can be observed between the simulated results and observed data.

Figure 2-40 shows sample cross-correlation functions between the mean daily cloud cover and air temperature amplitude $(\Delta T_d)$, derived from both the observed and simulated data. As can be seen, the cross-correlation structure is well preserved by the weather generator at the lag 0-1 *day*.

## 2.11  Summary

This chapter discusses a weather generator that allows one to synthetically generate several hydrometeorological variables: the *incoming shortwave radiation, rainfall, air temperature* and *humidity, total cloud cover*, and *wind speed*. These variables represent input for the hydrology model discussed in Chapter 3 at the hourly time step.
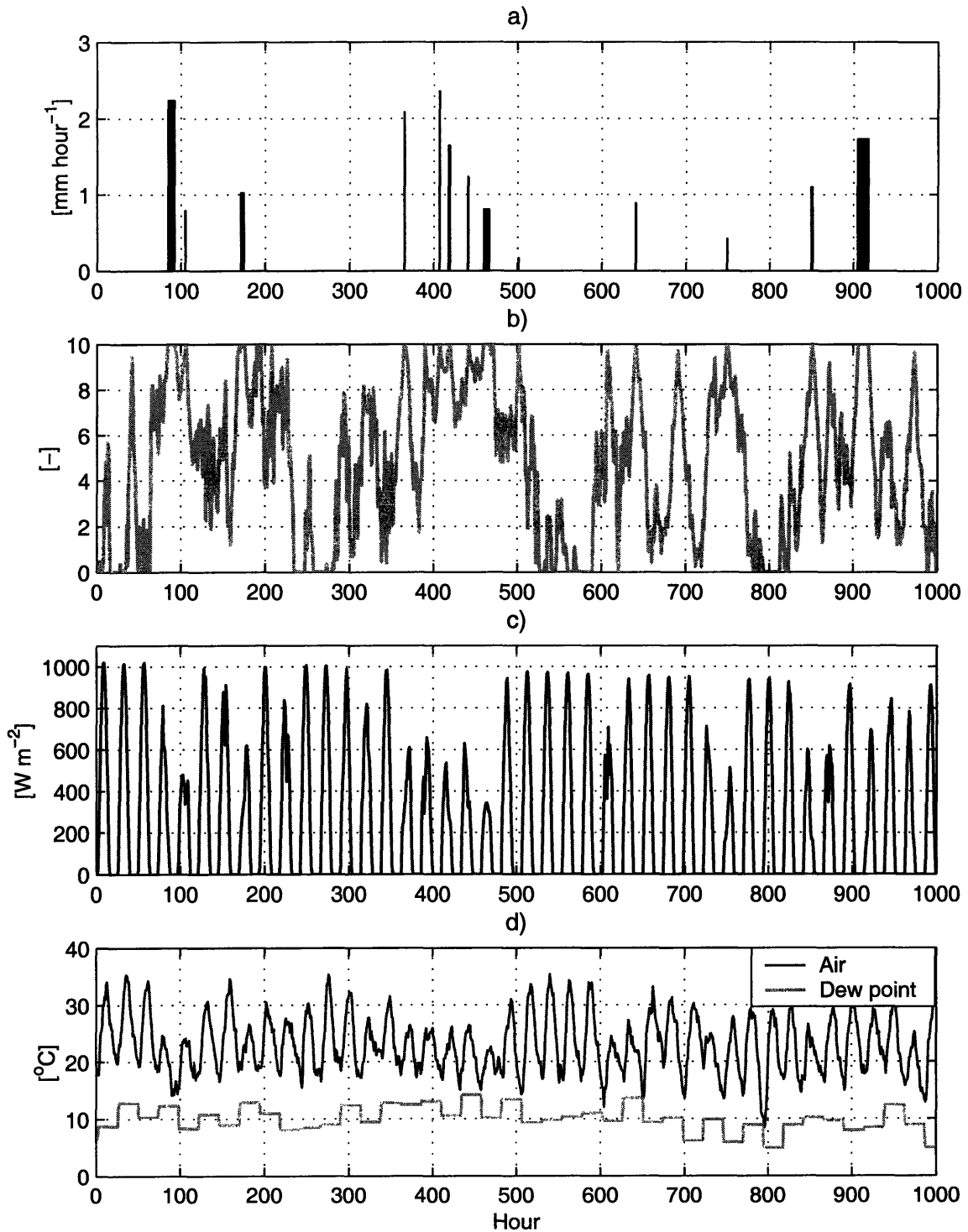
Figure 2-33: Simulated hourly hydrometeorological variables based on parameters derived for the location of Albuquerque (NM) (August): a.) rainfall; b.) cloud cover; c.) incoming shortwave radiation; and d.) air and dew point temperature.

144
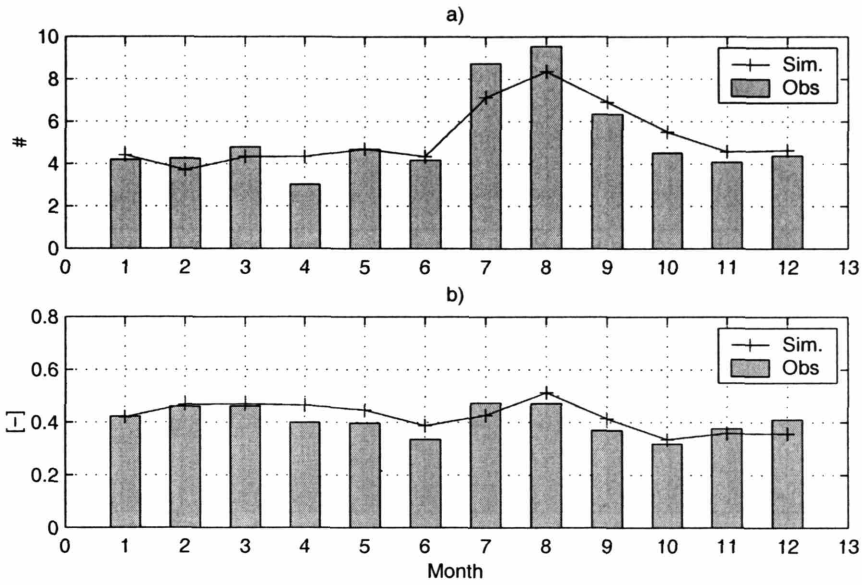
Figure 2-34: Observed and simulated mean monthly precipitation occurrence and cloud cover (Albuquerque, NM): a.) mean number of storms; and b.) mean cloudiness.
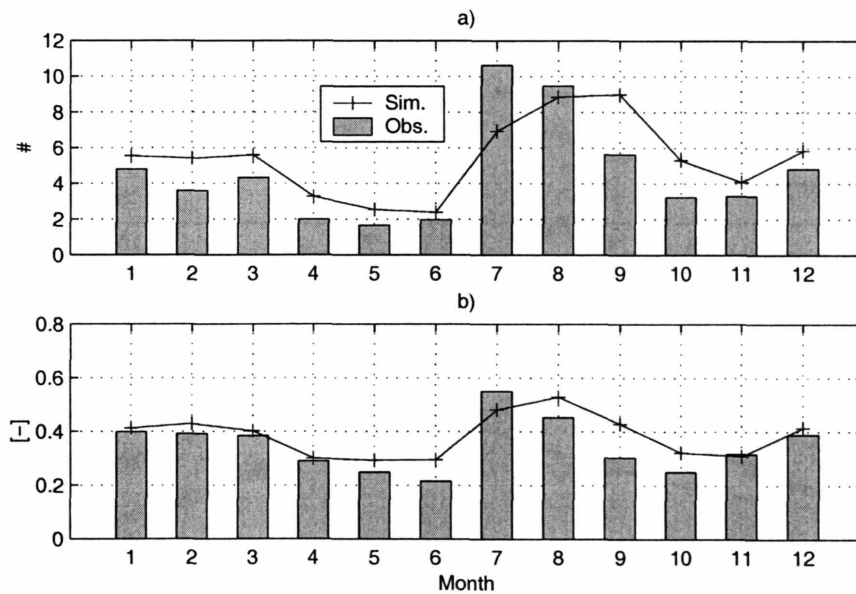


Figure 2-35: Observed and simulated mean monthly precipitation occurrence and cloud cover (Tucson, OK): a.) mean number of storms; and b.) mean cloudiness.
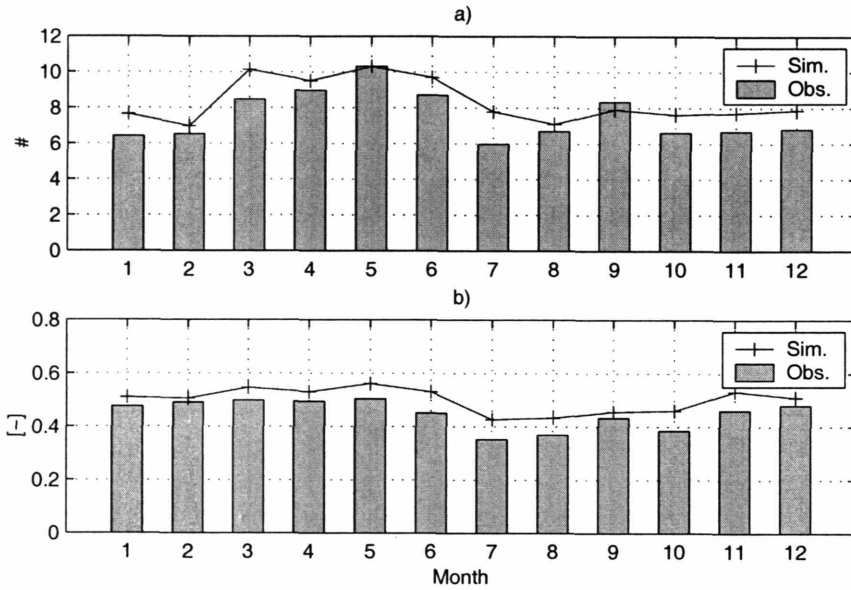
Figure 2-36: Observed and simulated mean monthly precipitation occurrence and cloud cover (Tulsa, OK): a.) mean number of storms; b.) mean cloudiness.
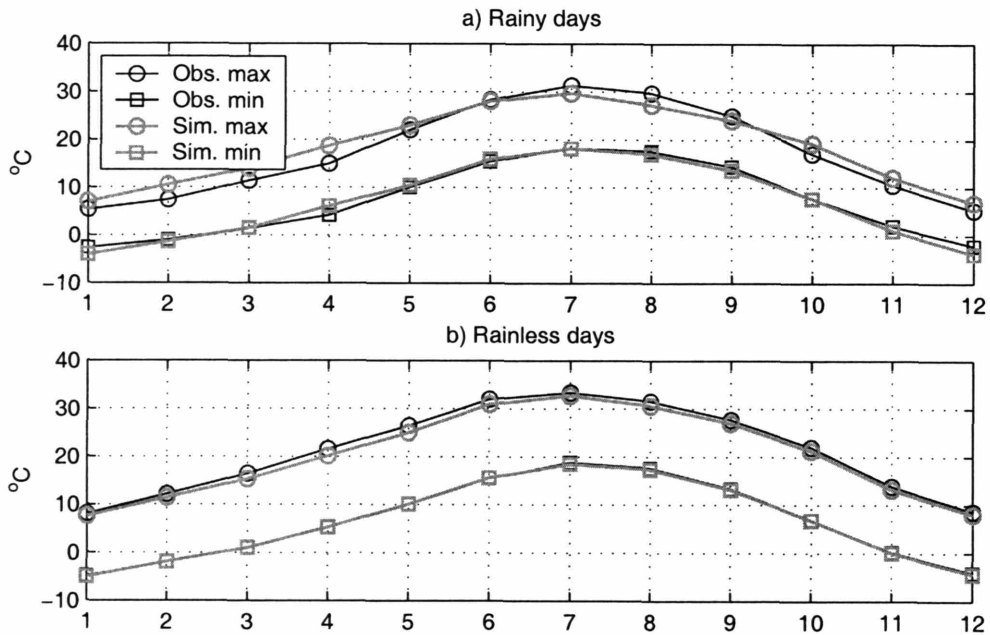


Figure 2-37: Mean maximum and minimum air temperatures derived from the observed and simulated data (Albuquerque, NM) on: a.) rainy days; and b.) rainless days.
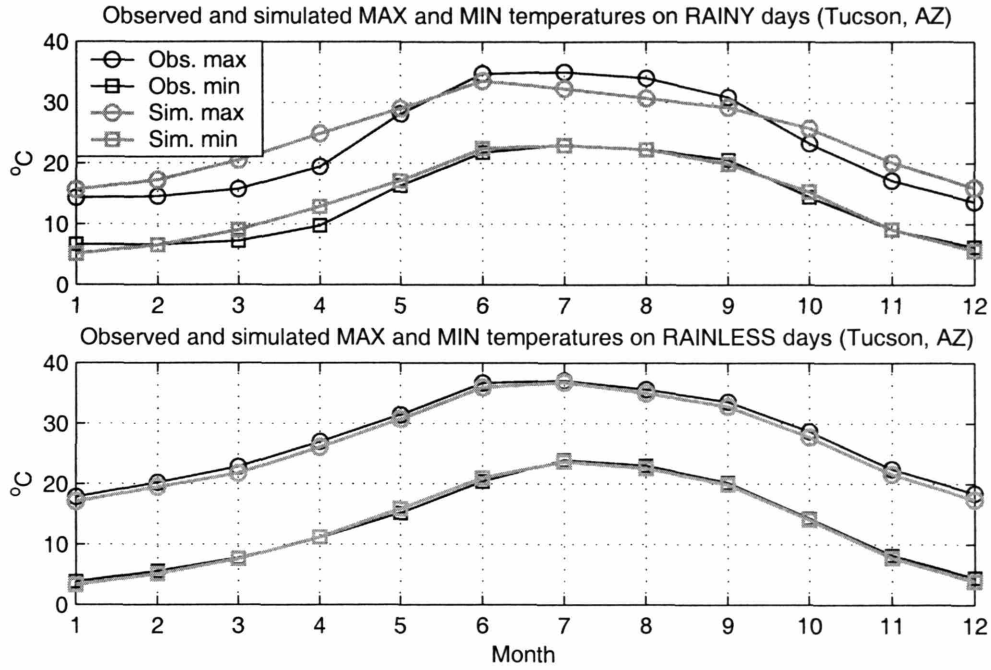
Figure 2-38: Mean maximum and minimum air temperatures derived from the observed and simulated data (Tucson, AZ) on: a.) rainy days; and b.) rainless days.
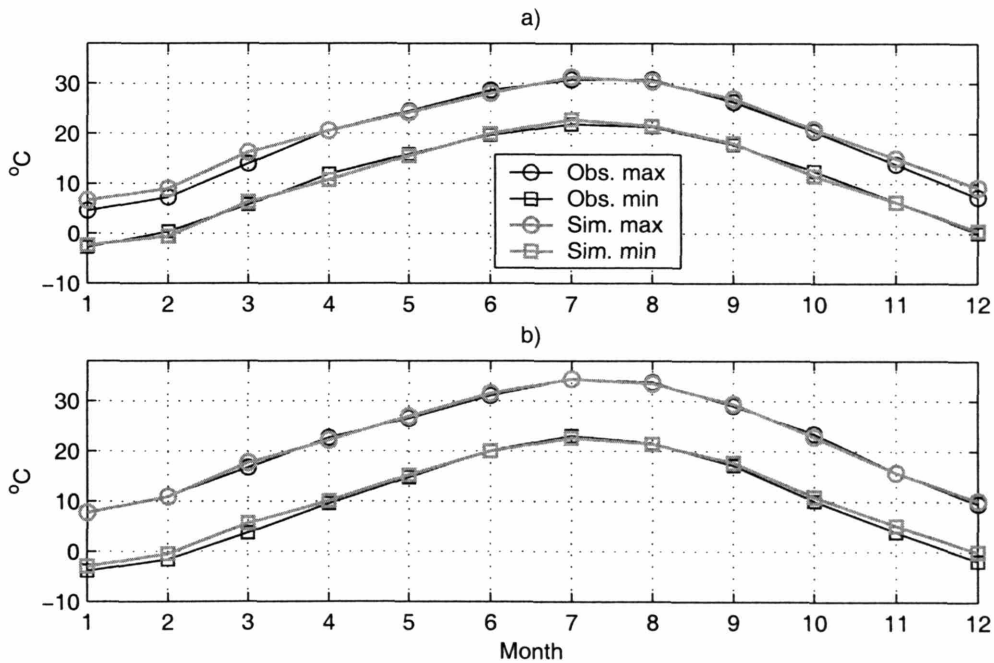


Figure 2-39: Mean maximum and minimum air temperatures derived from the observed and simulated data (Tulsa, OK) on: a.) rainy days; and b.) rainless days.

147
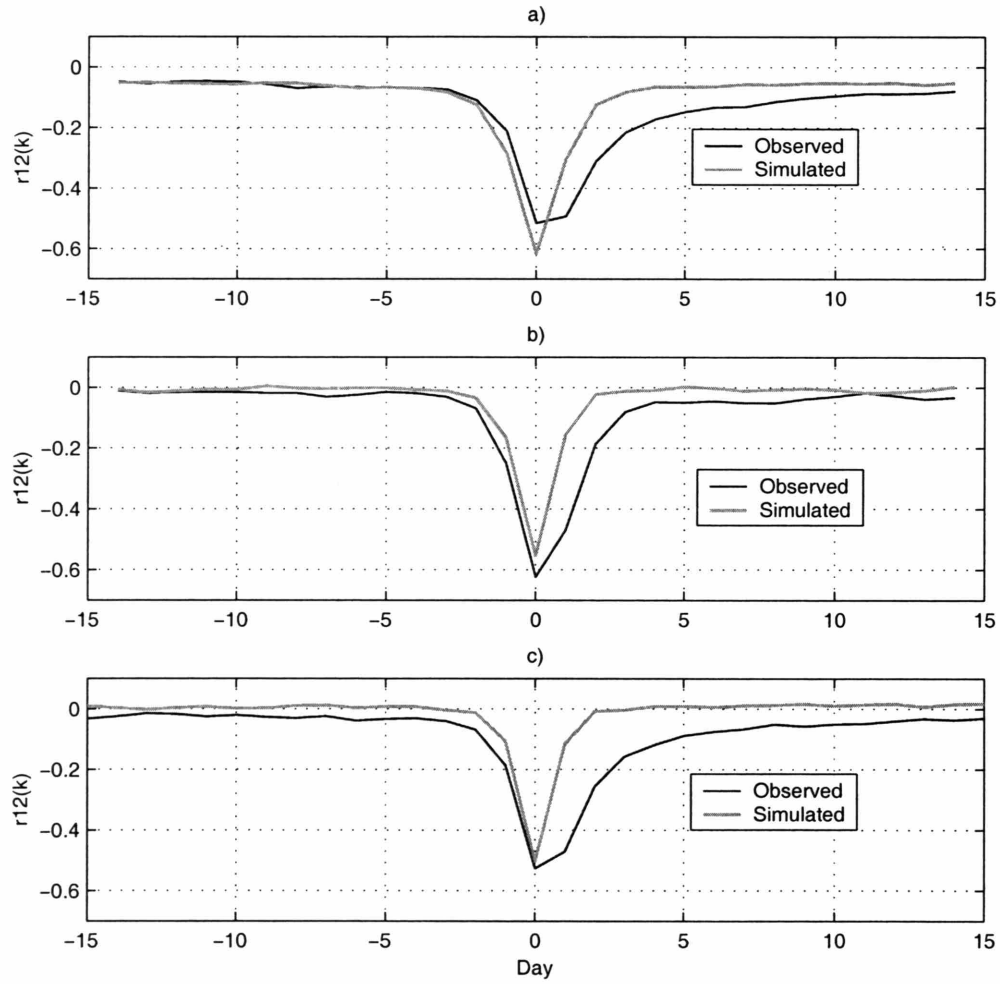
Figure 2-40: Sample cross-correlation functions derived between the mean daily cloud cover and mean daily air temperature amplitude derived from the observed and simulated data: a.) Tucson (AZ); b.) Tulsa (OK); and c.) Albuquerque (NM).

The weather simulator of Curtis and Eagleson (1982) was selected as the core framework for the presented model. A new shortwave radiation model is introduced, allowing one to represent separately the atmospheric radiative transfer for the two essential bands, VIS and NIR. Other necessary modifications have also been implemented, which lead to a better or more efficient representation of the simulated statistics.

Overall, the simulator of Curtis and Eagleson (1982) allows one to capture the essential relationships among the meteorological variables of interest, while modeling the diurnal variation of hydrometeorological conditions. Consistent time-series of hydrometeorological quantities are thus obtained: although the cross-correlation properties are not directly accounted for, all major weather variables exhibit an agreed co-variation. Another advantage of the discussed framework is that the model is suitable for creating consistent multiple climate scenarios (e.g., dry and wet climates). In such scenarios, changes in the dynamics of a certain meteorological quantity trigger corresponding changes in other related variables.

The discussed model is used in the following chapters to create synthetic hydrometeorological series used as the input for vegetation-hydrology model. In Chapter 5, the climate of New Mexico, corresponding to the location of Albuquerque (NM), is selected as representative of a typical semi-arid area. The weather generator is used to create consistent time-series of variables of hydrometeorological forcing for a 50-year simulation period. Additionally, in Chapter 6, the monsoonal precipitation regime is artificially modified to create alternative forcing scenarios.

# Chapter 3

# Coupled Model of Energy and Water Budgets

## 3.1   Introduction

This chapter discusses a coupled model of energy and water budgets for vegetated surfaces. The following is a description of the model structure and mathematical formulation of moisture and energy fluxes. When applied to a basic computational element, the model is one-dimensional; however, lateral moisture exchange can occur in the system. The formulation offers a solution for the canopy and ground energy fluxes resulting from the lateral flux boundary conditions. The estimation of energy fluxes is related to the *soil moisture state* that can be strongly affected by the dynamics of lateral exchange of soil water. Consequently, when applied to a catchment system, the model offers a quasi-three-dimensional framework in which lateral moisture transfers may lead to the spatio-temporal variability of states. By considering physically-based governing equations, the model accounts for the hydraulic and thermal properties of different soil types. The framework explicitly considers the morphological and biophysical differences among multiple vegetation types that can be present within a given element. Overall, the presented framework links in a unique way the hydrological and ecophysiological features of vegetated surfaces in natural catchment systems.

## 3.2  Model overview

The model simulates the energy and water budgets of both vegetated and non-vegetated surfaces that can be simultaneously present within a given element. In a domain of study, the dynamics of each computational element are simulated separately. Spatial dependences are introduced by considering the surface and subsurface moisture transfers among the elements (Section 3.7.2), which affect the local dynamics via the coupled energy-water interactions. Soil effects are accounted for by parameterizing the thermal and hydraulic properties that depend on soil's sand and clay content. Soils also differ in color, which is reflected in the values of soil albedo.

The framework simulates a number of processes that manifest numerous dynamic feedbacks among various components of the coupled vegetation-hydrology system:

1. **Biophysical processes**

   - absorption, reflection, and transmittance of solar shortwave radiation (Section 3.5.2);

   - absorption, reflection, and emission of longwave radiation (Section 3.6.2);

   - sensible and latent heat fluxes, partition of latent heat into canopy and soil evaporation, and transpiration (Section 3.6.3);

   - stomatal physiology (Section 3.6.3b, see also Chapter 4, Section 4.4.1);

   - ground heat flux (Sections 3.6.4);

2. **Hydrological processes**

   - interception, throughfall, and stem flow (Section 3.7.1);

   - infiltration in a multi-layer soil (Section 3.7.2, Appendix D.1);

   - lateral water transfer in the unsaturated zone (Section 3.7.2, Appendix D.2);

   - runoff and runon (Section 3.7.2).

While the models of biophysical processes operate at an *hourly* time scale, the routines simulating the processes of infiltration, lateral moisture transfer, and runoff (runon) use a finer time step (7.5-15 min.) due to numerical requirements of the infiltration scheme used (Section 3.7.2).

## 3.3 Topographic representation and basic computational element

### 3.3.1 Terrain representation

In a watershed model, topography can be represented utilizing a number of computational structures, including contour-based streamtubes, raster or grid domains, and triangulated irregular networks (TIN). The TIN data structure is a piece-wise linear interpolation of a set of points that results in a group of non-overlapping triangular elements of varying dimensions (Kumler, 1994). Hydrologic models based on triangular elements are well documented in the literature (e.g., Goodrich et al., 1991; Palacios-Vlez and Cuevas-Renaud, 1992; Tucker et al., 2001).

Various factors motivate the use of triangular elements to represent topography. The primary advantage is the multiple resolutions offered by the irregular domain, which can translate directly to computational savings as the number of nodes is significantly reduced. A second advantage is that the TIN representation permits linear features to be precisely preserved in the model mesh, as opposed to the rasterized representation of a grid model. This allows one to mimic natural terrain breaklines, stream networks or boundaries between heterogeneous regions. The construction of a triangular irregular network model for distributed hydrologic modeling has been detailed by Vivoni et al. (2004). The utilized methodology for reconstructing the flow pathways and drainage networks, both stream and overland, is briefly described in Ivanov et al. (2004a).

### 3.3.2 Basic computational element

The presented model uses a mixture of finite-element and finite-difference control-volume approach to estimate the state variables of the soil profile. The hydrological variables are computed for the control volumes of mesh nodes (see below). They do not represent two-dimensional continuous fields defined for mesh triangles (e.g., Vieux, 1988). The model's computational framework thus relies heavily both on the

(a)                              (b)
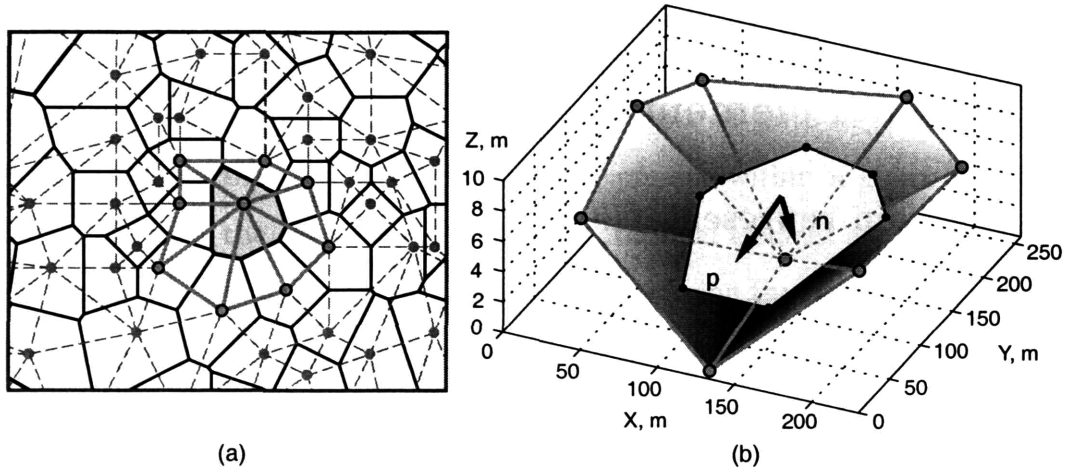
Figure 3-1: Voronoi diagram and Voronoi polygon: a.) An example of Voronoi diagram constructed for the TIN of a real basin. The dashed lines define the edges that connect nodes of the TIN (grey circles). The solid lines depict boundaries of Voronoi regions associated with the TIN nodes. b.) Geometry of a Voronoi cell in three dimensions. The shaded triangles depict TIN facets, the polygon inside is the constructed Voronoi cell sloped along the steepest direction $n$. The $n$-direction is orthogonal to the $p$-direction.

basic geometry of control volumes defined for mesh nodes and node connectivity.

One of the steps in the mesh generation process in the model is to construct a *Voronoi diagram*, also known as *Dirichlet tessellation* (Green and Sibson, 1978). The Voronoi diagram, also referred below as *Voronoi Polygon Network* (VPN), is a set of convex polygons formed by connecting the perpendicular bisectors of the triangles of the mesh (Figure 3-1a). A polygon, built around a mesh node, represents its control volume and is called the *Voronoi region* (same as *Thiessen polygon*). The boundaries between Voronoi polygons, formed by the bisectors of the mesh edges, define the interfaces between adjoining cells (Figure 3-1a). When a mass flux is computed into a neighboring Voronoi region, the length of a given interface is used as the flux window width.

The reference system of a Voronoi cell is defined by the axes $p$ and $n$, where $p$ follows the direction parallel to the plane of the maximum slope $\alpha_\nabla$ (positive downslope) and $n$ follows the direction normal to that plane (positive downward) (Figure 3-1b). The maximum slope direction is chosen among all edges that connect a Voronoi cell

154

to its neighbors. The state variables of the one-dimensional mass flow equations (e.g., soil moisture profile), when applied to a Voronoi cell, are a function of the direction $n$. The surface and subsurface (in the unsaturated zone) mass flux exchange between the contiguous elements is assumed to occur in the plane parallel to the direction $p$.

## 3.4 Vegetation composition and structure

The material of this section is an overview of vegetation representation at the element scale. The level of detail of presented information is the minimum required for the discussion of energy and moisture fluxes, which are formulated in the following sections. A more thorough discussion of vegetation structure, composition, and processes that dynamicly update vegetation attributes is provided in Chapter 4.

It is assumed that vegetated surfaces are comprised of multiple *plant functional types* (PFT, see Bonan et al. (2002)) that differ in life form (tree, shrub, grass), vegetation physiology (e.g., leaf optical properties, stomatal physiology, leaf photosynthetic characteristics) and structural attributes (e.g., height, leaf dimension, roughness length, root profile). A single computational element can contain a fraction of bare soil and, for instance, patches of deciduous forest and grass (Figure 3-2). The total number of PFTs that can be present within the same element is not limited to any particular value; however, it may be restricted by issues of computational performance. Each patch, while co-occurring in the same Voronoi element, constitutes a separate column upon which energy and water calculations are performed. Accordingly, differences in plant properties strongly affect estimation of the surface fluxes. *Fractional areas* that represent vegetated patches (Section 4.4.8) and bare soil are used to weight the relative contribution of each PFT/bare soil to the element-scale flux values (e.g., Sections 3.6.6, 3.7.1, 3.7.2).

Vegetation structure is defined by the *time-varying* leaf and stem areas and canopy height (Chapter 4) and the *time-invariant* root profile and leaf dimension. The time-invariant vegetation properties are obtained from literature: Jackson et al. (1996) provide a comprehensive study of the root distributions for a variety of species, Bonan
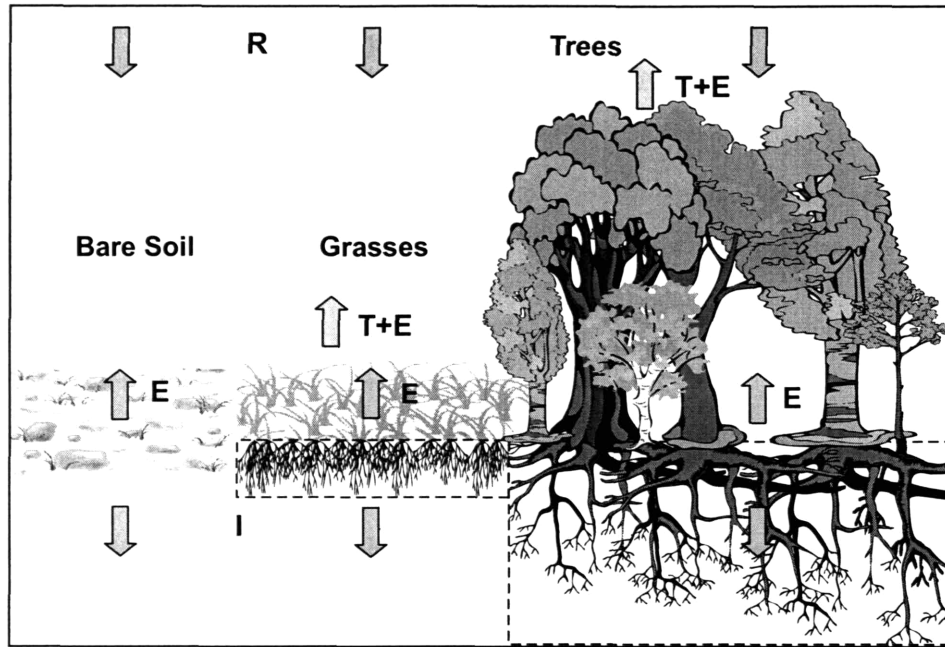
Figure 3-2: An illustration of vegetation representation at the element scale. The area is divided into patches of bare soil, soil covered with herbaceous (grass) and woody vegetation. $R$ is rainfall, $I$ is infiltration, $T$ is transpiration, and $E$ is evaporation.

(1995, 1996) provide typical values of leaf dimension for various plant types. The relative root abundance in each soil layer $R_{root}$ [$-$] is calculated from an exponential root profile (Jackson et al., 1996):

$$R_{root}(z) = 1 - e^{-\eta z},\qquad(3.1)$$

where $z$ [$mm$] is soil depth and $\eta$ [$mm^{-1}$] is the decay rate of distribution of the root biomass with the soil depth. This formulation allows one to adjust the profile so that different vegetation types can have different distributions of the root biomass.

## 3.5  Surface albedos

Two types of surfaces are considered within a computational element: *ground* and *canopy*. The ground surface can be present as both bare soil and under-canopy soil. Ground albedos are parameterized based on the soil surface moisture content. The

reflectance properties of the canopy depend on both the biophysical properties of a considered vegetation type (e.g., leaf and stem reflectances and transmittances, leaf orientation, canopy total biomass, etc.) as well as the characteristics of the incident direct shortwave radiation (angle of incidence).

### 3.5.1  Ground albedos

The overall direct beam $\alpha_{g\Lambda}^{\mu}$ and diffuse $\alpha_{g\Lambda}$ [$-$] ground albedos depend on soil color class and moisture content at the soil surface (Dickinson et al., 1993):

$$\alpha_{soi\,\Lambda}^{\mu} \;=\; \alpha_{soi\,\Lambda} \;=\; \alpha_{sat\,\Lambda} + \Delta \leq \alpha_{dry\,\Lambda}\,, \tag{3.2}$$

where $\Delta$ [$-$] depends on the volumetric water content $\theta_1$ [$mm^3\ mm^{-3}$] of the soil surface (Section 3.7.2) as $\Delta = 0.11 - 0.40\,\theta_1 > 0$, $\alpha_{sat\,\Lambda}$ and $\alpha_{dry\,\Lambda}$ [$-$] are the albedos for saturated and dry soil color classes (assigned as in Dickinson et al., 1993). The $\Lambda$ symbol refers to differentiation between the two considered wavebands: *visible* [$0.29\,\mu m \,\div\, 0.70\ \mu m$] and *near-infrared* [$0.70\ \mu m \,\div\, 4.0\ \mu m$]. The $\mu$ symbol is used to denote a quantity corresponding to the direct beam (directional) incident radiation. As seen above, the ground albedos are assumed to be independent of the type of incident radiation (direct beam or diffuse), while can be different for different wavebands.

### 3.5.2  Canopy radiative transfer

Radiative transfer within vegetative canopies is calculated from the two-stream approximation of Dickinson (1983) and Sellers (1985):

$$-\bar{\mu}\frac{dI\uparrow}{d(L+S)} + [1 - (1-\beta)\omega]I\uparrow -\omega\beta I\downarrow \;=\; \omega\bar{\mu}K\beta_0 e^{-K(L+S)}\,, \tag{3.3}$$

$$\bar{\mu}\frac{dI\downarrow}{d(L+S)} + [1 - (1-\beta)\omega]I\downarrow -\omega\beta I\uparrow \;=\; \omega\bar{\mu}K(1-\beta_0)e^{-K(L+S)}\,, \tag{3.4}$$

where $I \uparrow$ and $I \downarrow$ [−] are the upward and downward diffuse radiative fluxes per unit incident flux, $K = G(\mu)/\mu$ [−] is the optical depth of direct beam per unit leaf and stem area, $\mu$ is the cosine of the zenith angle of the incident beam $\mu = \cos(\pi/2 - h_\oplus)$ ($h_\oplus$ is the solar altitude or an angle of radiation with respect to an observer's horizon plane, Section 2.3.1), $G(\mu)$ [−] is the relative projected area of leaf and stem elements in the direction $cos^{-1}\mu$, $\bar{\mu}$ [−] is the average inverse diffuse optical depth per unit leaf and stem area, $\omega$ [−] is a scattering coefficient, $\beta$ and $\beta_0$ [−] are the upscatter parameters for diffuse and direct beam radiation, respectively, $L$ [$m^2\ leaf\,area\ m^{-2}\ ground\,area$] is the leaf area index section and $S$ [$m^2\ m^{-2}$] is the stem area index (Chapter 4, Section 4.4.8). Given the direct beam albedo $\alpha_{g\Lambda}^\mu$ and diffuse albedo $\alpha_{g\Lambda}$ of the ground (Section 3.5.1), these equations are solved to calculate the fluxes, per unit incident flux, absorbed by the vegetation, reflected by the vegetation, and transmitted through the vegetation for *direct* and *diffuse* radiation and for *visible* [$0.29\,\mu m \div 0.70\,\mu m$] and *near-infrared* [$0.70\,\mu m \div 4.0\,\mu m$] wavebands. The optical parameters $G(\mu)$, $\bar{\mu}$, $\omega$, $\beta$, and $\beta_0$ are calculated based on work in Sellers (1985) as follows.

The relative projected area of leaves and stems in the direction $cos^{-1}\mu$ is

$$G(\mu) \;=\; \phi_1 + \phi_2\mu, \tag{3.5}$$

where $\phi_1 = 0.5 - 0.633\chi_L - 0.33\chi_L^2$ and $\phi_2 = 0.877(1 - 2\phi_1)$ for $-0.4 < \chi_L < 0.6$. $\chi_L$ is the departure of leaf angles from a spherical angle distribution, i.e., random (Ross, 1975; Goudriaan, 1977), and equals +1 for horizontal leaves, 0 for a spherical leaf angle distribution, and −1 for vertical leaves.

The average inverse diffuse optical depth per unit leaf and stem area is

$$\bar{\mu} \;=\; \int_0^1 \frac{\mu'}{G(\mu')}d\mu' \;=\; \frac{1}{\phi_2}\left[1 - \frac{\phi_1}{\phi_2}\ln\left(\frac{\phi_1 + \phi_2}{\phi_1}\right)\right], \tag{3.6}$$

where $\mu'$ is the direction of the scattered flux.

158

The optical parameters $\omega$, $\beta$, and $\beta_0$ vary with wavelength and are defined as

$$\omega_\Lambda = \omega_\Lambda^{veg},$$

$$\omega_\Lambda \beta_\Lambda = \omega_\Lambda^{veg} \beta_\Lambda^{veg}, \qquad (3.7)$$

$$\omega_\Lambda \beta_{0,\Lambda} = \omega_\Lambda^{veg} \beta_{0,\Lambda}^{veg}.$$

For vegetation, $\omega_\Lambda^{veg} = \alpha_\Lambda + \tau_\Lambda$. $\alpha_\Lambda$ [$-$] is a weighted combination of the leaf and stem reflectances ($\alpha_\Lambda^{leaf}, \alpha_\Lambda^{stem}$):

$$\alpha_\Lambda = \alpha_\Lambda^{leaf} w_{leaf} + \alpha_\Lambda^{stem} w_{stem}, \qquad (3.8)$$

where $w_{leaf} = L/(L+S)$ and $w_{stem} = S/(L+S)$. $\tau_\Lambda$ [$-$] is a weighted combination of the leaf and stem transmittances ($\tau_\Lambda^{leaf}, \tau_\Lambda^{stem}$):

$$\tau_\Lambda = \tau_\Lambda^{leaf} w_{leaf} + \tau_\Lambda^{stem} w_{stem}. \qquad (3.9)$$

The upscatter for diffuse radiation is

$$\omega_\Lambda^{veg} \beta_\Lambda^{veg} = \frac{1}{2} \left[ \alpha_\Lambda + \tau_\Lambda + (\alpha_\Lambda - \tau_\Lambda) \left( \frac{1 + \chi_L}{2} \right)^2 \right] \qquad (3.10)$$

and the upscatter for direct beam radiation is

$$\omega_\Lambda^{veg} \beta_{0,\Lambda}^{veg} = \frac{1 + \bar{\mu} K}{\bar{\mu} K} a_s(\mu)_\Lambda, \qquad (3.11)$$

where the single scattering albedo is

$$\alpha_s(\mu)_\Lambda = \frac{\omega_\Lambda^{veg}}{2} \int_0^1 \frac{\mu' G(\mu)}{\mu G(\mu') + \mu' G(\mu)} d\mu'$$

$$= \frac{\omega_\Lambda^{veg}}{2} \frac{G(\mu)}{\mu \phi_2 + G(\mu)} \left[ 1 - \frac{\mu \phi_1}{\mu \phi_2 + G(\mu)} \ln \left( \frac{\mu \phi_1 + \mu \phi_2 + G(\mu)}{\mu \phi_1} \right) \right]. \qquad (3.12)$$

The upward diffuse fluxes per unit incident direct beam and diffuse flux, i.e., the

surface albedos are

$$I \uparrow_\Lambda^\mu = \frac{h_1}{\sigma} + h_2 + h_3 \,, \qquad (3.13)$$

$$I \uparrow_\Lambda = h_7 + h_8 \,. \qquad (3.14)$$

The downward diffuse fluxes per unit incident direct beam and diffuse radiation, respectively, are

$$I \downarrow_\Lambda^\mu = \frac{h_4}{\sigma} e^{-K(L+S)} + h_5 s_1 + \frac{h_6}{s_1} \,, \qquad (3.15)$$

$$I \downarrow_\Lambda = h_9 s_1 + \frac{h_{10}}{s_1} \,. \qquad (3.16)$$

The estimation of parameters $h_1$ to $h_{10}$, $\sigma$, and $s_1$ follows Sellers (1985) and is provided in Appendix C.

# 3.6    Radiative fluxes

For a vegetated surface, the net radiation is estimated at two levels. At the *canopy* level, the net radiation is $R_{nv} = \vec{S}_v + \vec{L}_v$, at the *ground* level, $R_{ng} = \vec{S}_g + \vec{L}_g$, where $\vec{S}$ and $\vec{L}$ [$W\ m^{-2}$] are the net solar and longwave fluxes, respectively, absorbed by the vegetation ("$v$") and ground ("$g$"). At the canopy level, the net radiation $R_{nv}$ is partitioned into sensible heat $H_v$ and latent heat $\lambda E_v$ fluxes [$W\ m^{-2}$]. At the ground level, $R_{ng}$ is partitioned into sensible heat $H_g$, latent heat $\lambda E_g$, and ground heat $G$ fluxes. If no vegetation is present, only the ground level fluxes are estimated.

## 3.6.1    Shortwave solar fluxes

At the element scale, solar radiation is conserved as

$$\sum_\Lambda [S_{atm} \downarrow_\Lambda^\mu + S_{atm} \downarrow_\Lambda] = \vec{S}_v + \vec{S}_g + \sum_\Lambda [S_{atm} \downarrow_\Lambda^\mu I \uparrow_\Lambda^\mu + S_{atm} \downarrow_\Lambda I \uparrow_\Lambda] \,, \ (3.17)$$

where $S_{atm} \downarrow_\Lambda^\mu$ and $S_{atm} \downarrow_\Lambda$ $[W \ m^{-2}]$ are the incident direct beam and diffuse solar fluxes (Section 2.3.1) and the summation term is the total reflected solar radiation.

### 3.6.1a Non-vegetated surface

The total solar radiation absorbed by bare soil is

$$\vec{S}_g^{bare} = \sum_\Lambda \left[ S_{atm} \downarrow_\Lambda^\mu (1 - \alpha_{g\Lambda}^\mu) + S_{atm} \downarrow_\Lambda (1 - \alpha_{g\Lambda}) \right] . \tag{3.18}$$

### 3.6.1b Vegetated surface

With reference to Figure 3-3a, the direct beam flux transmitted through the canopy per unit incident flux is $e^{-K(L+S)}$ and the direct beam and diffuse fluxes absorbed by the vegetation per unit incident flux are

$$\vec{I}_\Lambda^\mu = 1 - I \uparrow_\Lambda^\mu - (1 - \alpha_{g\Lambda})I \downarrow_\Lambda^\mu - (1 - \alpha_{g\Lambda}^\mu)e^{-K(L+S)} , \tag{3.19}$$

$$\vec{I}_\Lambda = 1 - I \uparrow_\Lambda - (1 - \alpha_{g\Lambda})I \downarrow_\Lambda . \tag{3.20}$$

$I \uparrow_\Lambda^\mu$ and $I \uparrow_\Lambda^\mu$ $[-]$ are the upward diffuse fluxes per unit incident direct beam and diffuse flux (Section 3.5.2). $I \downarrow_\Lambda^\mu$ and $I \downarrow_\Lambda^\mu$ $[-]$ are the downward diffuse fluxes per unit incident direct beam and diffuse radiation (Section 3.5.2). $\alpha_{g\Lambda}^\mu$ and $\alpha_{g\Lambda}$ are the direct beam and diffuse ground albedos (Section 3.5.1).

The total solar radiation absorbed by the vegetation $\vec{S}_v^{veg}$ and under-canopy ground $\vec{S}_g^{veg}$ $[W \ m^{-2}]$ are

$$\vec{S}_v^{veg} = \sum_\Lambda \left[ S_{atm} \downarrow_\Lambda^\mu \vec{I}_\Lambda^\mu + S_{atm} \downarrow_\Lambda \vec{I}_\Lambda \right] , \tag{3.21}$$

$$\vec{S}_g^{veg} = \sum_\Lambda [S_{atm} \downarrow_\Lambda^\mu e^{-K(L+S)}(1 - \alpha_{g\Lambda}^\mu) +$$
$$(S_{atm} \downarrow_\Lambda^\mu I \downarrow_\Lambda^\mu + S_{atm} \downarrow_\Lambda I \downarrow_\Lambda)(1 - \alpha_{g\Lambda})] . \tag{3.22}$$

The visible and near-infrared reflectances $r_{vis}$ and $r_{nir}$ $[-]$ are estimated as

$$r_\Lambda = \frac{S_{atm} \downarrow_\Lambda^\mu I \uparrow_\Lambda^\mu + S_{atm} \downarrow_\Lambda I \uparrow_\Lambda}{S_{atm} \downarrow_\Lambda^\mu + S_{atm} \downarrow_\Lambda} \tag{3.23}$$
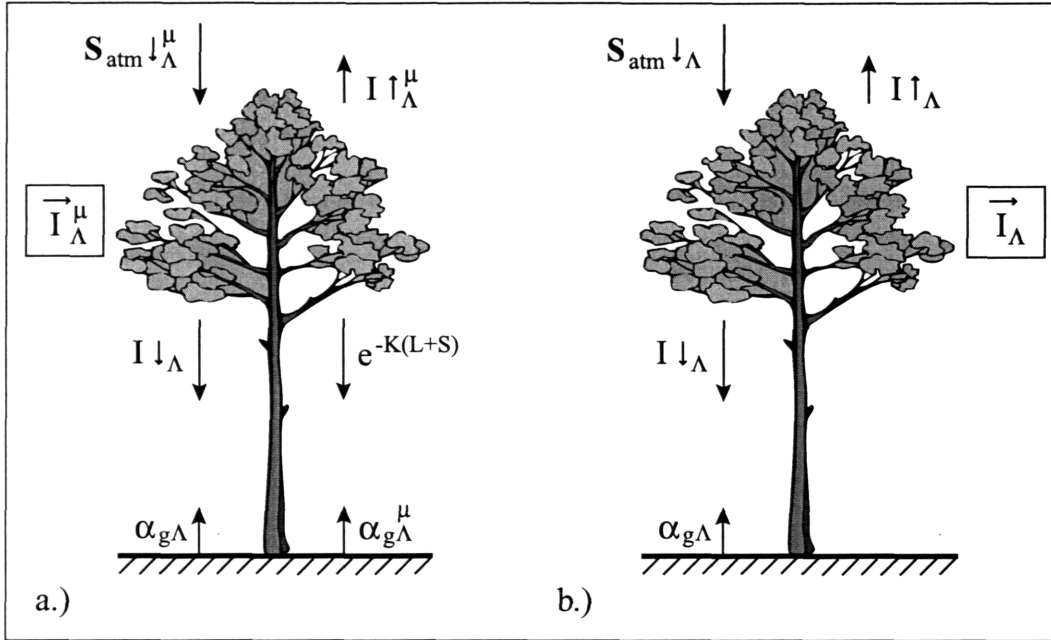
Figure 3-3: A schematic diagram of the a.) direct beam and b.) diffuse solar radiation absorbed, transmitted, and reflected by vegetation and under-canopy ground.

They are used to calculate the *Normalized Difference Vegetation Index* (NDVI) for a given vegetation type: $NDVI = \frac{r_{nir} - r_{vis}}{r_{nir} + r_{vis}}$. The formulation for the *element-scale* estimate of $NDVI$ is provided in Section 3.6.5.

### 3.6.1c Canopy fractions

Canopy photosynthesis models are generally formulated to describe the fluxes of both $CO_2$ and water vapor at the *leaf* level (Section 4.4.1). Some method is required to scale these quantities to the canopy level. Both multilayer and "big-leaf" approaches have been used for such scaling (Dai et al., 2004). A multilayer model integrates the fluxes from each canopy layer to give the total flux (e.g., Wang and Jarvis, 1990; Leuning et al., 1995); while the big-leaf approach maps properties of the whole canopy onto a single leaf to calculate the flux (e.g., Sellers et al., 1996a; Bonan, 1996; Oleson et al., 2004). The multilayer models can use parameters that are measured at the leaf level, however, such approaches are highly computationally demanding. The big-leaf models require some plausible assumption about the vertical profile of leaf properties.

162

The most often used hypothesis assumes that the limiting rate of carbon uptake varies with canopy depth in the same manner as the time-mean profile of *Photosynthetically Active Radiation* (PAR) (e.g., Sellers et al., 1992). However, as argued by Norman (1993), de Pury and Farquhar (1997), and Wang and Leuning (1998), it is theoretically incorrect to ignore the instantaneous distribution of radiation in the canopy due to strong non-linearities in the leaf biochemical processes that depend on PAR and leaf temperature. For instance, the photosynthesis of shaded leaves has an essentially linear response to absorbed PAR, while photosynthesis of sunlit leaves is often light saturated, i.e., independent of absorbed PAR. Direct sun shine heats leaves more than the scattered light in the shade, and hence sunlit leaves can be several degrees warmer than shaded leaves. Therefore, if the differences in PAR and temperatures between sunlit and shaded leaves are neglected, the estimates of photosynthesis and energy/water fluxes for the canopy may be incorrect.

Wang and Leuning (1998) have demonstrated that two-leaf approach, i.e., the one that divides canopy into *sunlit* and *shaded* leaves, leads to assimilation rates and energy/water fluxes comparable to those of a multilayer model. The averaging of PAR in each of these two classes of leaves is appropriate and introduces little error in the final predicted canopy photosynthesis (Dai et al., 2004). The discussed model uses the two-level canopy assumption to account for PAR. However, the same leaf temperature is assumed for both layers, similarly to Bonan (1996) and Dickinson et al. (1998). The separate treatment of the assimilation rates and stomatal conductances for sunlit and shaded leaves is assumed to be a sufficient measure to account for the principal differences between the two canopy layers. The estimation of separate canopy temperatures for the two levels would result in an extremely high computational overhead due to the highly non-linear coupling between the energy budget and the photosynthesis/stomatal conductance models (as demonstrated in Sections 3.6.7 and 3.8.2). The framework, however, can be easily extended to compute separate temperatures in future implementations less concerned with the performance issues.

The sunlit fraction of the canopy $f_{sun}$ [−] is estimated assuming that penetration of the direct beam radiation in the canopy decays exponentially and is controlled by

the light extinction parameter $K'$ (according to the Beer's law):

$$f_{sun} = \frac{1}{(L+S)} \int_0^{L+S} e^{-K'x} dx = \frac{1}{(L+S)} \frac{1-e^{-K'(L+S)}}{K'}, \qquad (3.24)$$

where $e^{-K'(L+S)}$ is the fractional area of the direct beam radiation (sunflecks) on a horizontal plane below the leaf and stem area index $(L+S)$. The shaded fraction is $f_{shd} = 1 - f_{sun}$ and the sunlit and shaded leaf area indices are $L_{sun} = f_{sun}L$ and $L_{shd} = f_{shd}L$ $[m^2\ m^{-2}]$. In calculating $f_{sun}$, $K' = G(\mu)/\mu\sqrt{1-\omega_{vis}^{veg}}$, where $\sqrt{1-\omega_{vis}^{veg}}$ accounts for scattering within the canopy (Sellers, 1985). To prevent numerical instabilities $f_{sun} = 0$ when the sunlit fraction is less than 1% (e.g., hours with significant cloudiness or periods of early morning and late evening).

The solar radiation absorbed by the vegetation in the visible waveband [0.29 $\mu m$ ÷ 0.70 $\mu m$] is partitioned to sunlit and shaded leaves to calculate the average absorbed PAR for sunlit $\phi_{sun}$ and shaded $\phi_{shd}$ $[W\ m^{-2}]$ leaves for a given hour. For $f_{sun} > 0$:

$$\phi^{sun} = \left(S_{atm}\downarrow_{vis}^{\mu}\ \vec{I}_{vis}^{\mu} + f_{sun}S_{atm}\downarrow_{vis}\ \vec{I}_{vis}\right)\frac{L}{L+S}, \qquad (3.25)$$

$$\phi^{shd} = \left(f_{shd}\,S_{atm}\downarrow_{vis}\ \vec{I}_{vis}\right)\frac{L}{L+S}. \qquad (3.26)$$

$\phi_{sun}$ and $\phi_{shd}$ $[W\ m^{-2}]$ are used in the estimation of photosynthesis and stomatal resistance (Chapter 4, Section 4.4.1). The above equations assume the sunlit leaves absorb the direct beam radiation, that all leaves absorb diffuse radiation, and that leaves absorb $\frac{L}{L+S}$ of the radiation absorbed by the vegetation. If $f_{sun} = 0$ all radiation is absorbed by the shaded leaves.

## 3.6.2   Longwave fluxes

The net longwave radiation (positive towards the atmosphere) for any type of surface $[W\ m^{-2}]$ is

$$\vec{L} = -L_{atm}\downarrow +L\uparrow, \qquad (3.27)$$

where $L_{atm} \downarrow$ $[W\ m^{-2}]$ is the downward atmospheric longwave radiation and $L \uparrow$ $[W\ m^{-2}]$ is the upward longwave radiation (Bras, 1990):

$$L \uparrow = \sigma T_{rad}^4 , \tag{3.28}$$

where $T_{rad}$ $[K]$ is the radiative temperature of a surface and $\sigma = 5.67 10^{-8}$ $[W\ m^{-2}\ K^{-4}]$ is the Stefan-Boltzmann constant.

### 3.6.2a Non-vegetated surface

For *non-vegetated* surfaces, formulation (3.27) for the net longwave radiation takes the form:

$$\vec{L}_g^{bare} = -\alpha_g L_{atm} \downarrow +\epsilon_g \sigma T_g^4 , \tag{3.29}$$

where $\alpha_g$ $[-]$ is the ground absorptivity, $\epsilon_g$ $[-]$ is the ground emissivity, and $T_g$ $[K]$ is the ground temperature (Section 3.6.7). The upward longwave radiation is

$$L_g^{bare} \uparrow = (1 - \alpha_g) L_{atm} \downarrow +\epsilon_g \sigma T_g^4 . \tag{3.30}$$

The above equation assumes that the fraction $(1 - \alpha_g)$ of the atmospheric longwave flux is reflected by the ground.

### 3.6.2b Vegetated surface

With reference to Figure 3-4, the downward longwave radiation below the vegetation canopy is

$$L_v^{veg} \downarrow = (1 - \alpha_v) L_{atm} \downarrow +\epsilon_v \sigma T_v^4 . \tag{3.31}$$

The upward longwave radiation from the ground is

$$L_g^{veg} \uparrow = (1 - \alpha_g) L_v^{veg} \downarrow +\epsilon_g \sigma T_g^4 . \tag{3.32}$$

The upward longwave radiation above the vegetation canopy is

$$L_v^{veg} \uparrow \; = \; (1 - \alpha_v)L_g^{veg} \uparrow + \epsilon_v \sigma T_v^4 . \tag{3.33}$$

According to formulation (3.27), the net radiation fluxes (positive towards the atmosphere) for canopy $\vec{L}_v^{veg}$ and understory ground $\vec{L}_g^{veg}$ are

$$\begin{aligned}
\vec{L}_v^{veg} &= -\alpha_v(L_{atm} \downarrow + L_g^{veg} \uparrow) + 2\epsilon_v \sigma T_v^4 \\
&= -\alpha_v \left[1 + (1 - \alpha_v)(1 - \alpha_g)\right] L_{atm} \downarrow - \\
&\quad \alpha_v \epsilon_g \sigma T_g^4 + \epsilon_v \sigma \left[2 - \alpha_v(1 - \alpha_g)\right] T_v^4 , \tag{3.34} \\
\vec{L}_g^{veg} &= -\alpha_g L_v^{veg} \downarrow + \epsilon_g \sigma T_g^4 \\
&= -\alpha_g(1 - \alpha_v)L_{atm} \downarrow - \alpha_g \epsilon_v \sigma T_v^4 + \epsilon_g \sigma T_g^4 . \tag{3.35}
\end{aligned}$$

$T_v$ and $T_g$ $[K]$ are the vegetation and ground temperatures (Section 3.6.7), respectively, $\epsilon_v$ and $\epsilon_g$ are the vegetation and ground emissivities, and $\alpha_v$ and $\alpha_g$ are the vegetation and ground absorptivities.

In the above equations, it is assumed that leaves emit longwave radiation from both sides. The equations also assume that the fraction $(1 - \alpha_v)$ of either the atmospheric longwave radiation or the upward longwave radiation from the ground is transmitted through the canopy; the fraction $(1 - \alpha_g)$ of the downward longwave radiation below the canopy is reflected by the understory ground. The emissivity of the ground is assumed to be $\epsilon_g = 0.96$. The vegetation emissivity is $\epsilon_v = 1 - e^{-(L+S)/\bar{\mu}}$, where $L$ and $S$ are the one-sided leaf and stem area indices and $\bar{\mu} = 1$ is the average inverse optical depth for longwave radiation (Bonan, 1996).

### 3.6.3 Sensible and latent heat fluxes

The estimation of the sensible and latent heat fluxes employs a commonly used "resistance" formulation (e.g., Shuttleworth, 1979; Bras, 1990; Arya, 2001, pp. 369). The approach parameterizes the vertical fluxes based on an analogy with Ohm's law

166
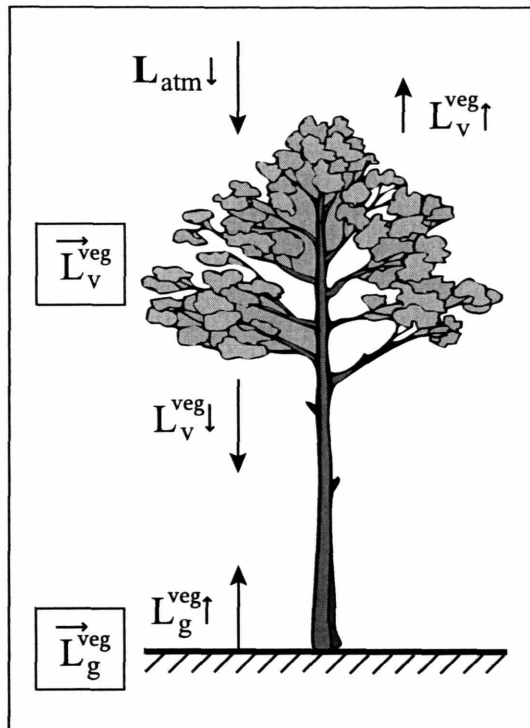
Figure 3-4: A schematic diagram of the longwave radiation absorbed, transmitted, reflected, and emitted by vegetation and under-canopy ground. $L_{atm} \downarrow$ is the downward atmospheric longwave radiation, $L_v^{veg} \downarrow$ is the downward longwave radiation below the vegetation canopy, $L_g^{veg} \uparrow$ is the upward longwave radiation from the ground, and $L_v^{veg} \uparrow$ is the upward longwave radiation above the vegetation canopy. $\vec{L}_v^{veg}$ and $\vec{L}_g^{veg}$ are the net radiation fluxes (positive towards the atmosphere) for canopy and understory ground, respectively.

by using resistance terms for the transfer of heat and moisture. The resistances have dimensions of inverse of velocity and depend on many factors including surface roughness (e.g., canopy structure and leaf dimensions), wind speed, and atmospheric stability. The description below provides a framework for estimation of fluxes from both bare soil and vegetated patches that can be present within a given computational element at the same time.

### 3.6.3a Non-vegetated surface

For bare soil, the sensible heat $H_g^{bare}$ $[W\ m^{-2}]$ and the latent heat $\lambda E_g^{bare}$ $[W\ m^{-2}]$ fluxes between the atmosphere at a reference height $z_{atm}$ $[m]$ and the soil surface are estimated as

$$H_g^{bare} = -\rho_{atm} C_p \frac{(T_{atm} - T_g)}{r_s^h}, \tag{3.36}$$

$$\lambda E_g^{bare} = -\rho_{atm} \frac{C_p}{\gamma} \frac{(e_{atm} - e^*(T_g)\, h_{soil})}{r_s^w}, \tag{3.37}$$

where the following variables are defined at elevation $z_{atm}$: the air temperature $T_{atm}$ $[K]$, the density of moist air $\rho_{atm}$ $[kg\ m^{-3}]$, and the vapor pressure $e_{atm}$ $[mb]$. The ground "skin" temperature $T_g$ $[K]$ and the saturated vapor pressure in soil pores $e^*(T_g)$ $[mb]$ are defined at the ground surface level (see below). $C_p = 1013$ $[J\ kg^{-1}\ K^{-1}]$ is the air heat capacity, $\lambda$ $[J\ kg^{-1}]$ is the latent heat of vaporization, $\gamma$ $[mb\ K^{-1}]$ is the psychrometric constant, $r_s^h$ and $r_s^w$ $[s\ m^{-1}]$ are the resistances to the sensible and latent heat flux, respectively (see discussion below), and $h_{soil}$ $[-]$ is the relative humidity of the soil pore space (after Sellers et al., 1996a):

$$h_{soil} = e^{\frac{\psi_1 g}{R T_g}}, \quad \text{if} \quad e^*(T_g) \geq e_{atm}, \tag{3.38}$$

$$h_{soil} = 1, \quad \text{if} \quad e^*(T_g) < e_{atm}, \tag{3.39}$$

where $\psi_1$ $[m]$ is the soil moisture potential of the top soil layer (first 10 $mm$, see Section 3.7.2), $g = 9.8$ $[m\ s^{-2}]$ is the acceleration due to gravity, and $R = 8.314$ $[J\ kg^{-1}\ K^{-1}]$ is the gas constant.

**Resistances** Assuming a simple linear combination of resistances for the sensible and latent heat fluxes (e.g., Arya, 2001; Taiz and Zeiger, 2002) and with reference to Figure 3-5:

$$r_s^h = r_{ah} , \tag{3.40}$$

$$r_s^w = r_{aw} + r_{srf} , \tag{3.41}$$

where $r_{ah}$ and $r_{aw}$ $[s\ m^{-1}]$ are the bulk resistances to sensible heat and water vapor fluxes between the ground surface and the atmosphere due to the transfer mechanisms involved and $r_{srf}$ $[s\ m^{-1}]$ is the soil surface resistance, an empirical factor that is intended to take into account the impedance of the soil pores to exchanges of water vapor between the first soil layer (first 10 $mm$, see Section 3.7.2) and the immediately overlying air. Following Sellers et al. (1996a):

$$r_{srf} = e^{8.206 - 4.255\,\beta_E^w} , \tag{3.42}$$

where $\beta_E^w$ is in Bonan (1996):

$$\beta_E^w = \frac{\theta_1 - \theta_r}{a'\theta_s - \theta_r} , \tag{3.43}$$

where $\theta_1$ $[mm^3\ mm^{-3}]$ is the soil surface water content (first 10 $mm$, Section 3.7.2), $\theta_s$ and $\theta_r$ $[mm^3\ mm^{-3}]$ are the saturation and residual soil moisture contents, respectively (Section 3.7.3) and $a'$ is assumed to be 0.75.

Since the state of the atmosphere above the soil surface can strongly vary, the dominant physical mechanisms involved in transfer of the heat fluxes away from the ground surface can differ. Highly turbulent, windy conditions lead to **forced convection**, and $r_{ah}$ and $r_{aw}$ in (3.36) - (3.37) thus represent the aerodynamic resistances to heat transfer between the atmosphere at reference height $z_{atm}$ and the heights $z_{0h} + d$ and $z_{0w} + d$ $[m]$, corresponding to the apparent sinks for heat and water vapor, respectively (e.g., Shuttleworth, 1979). Under assumed *neutral* atmospheric conditions

169
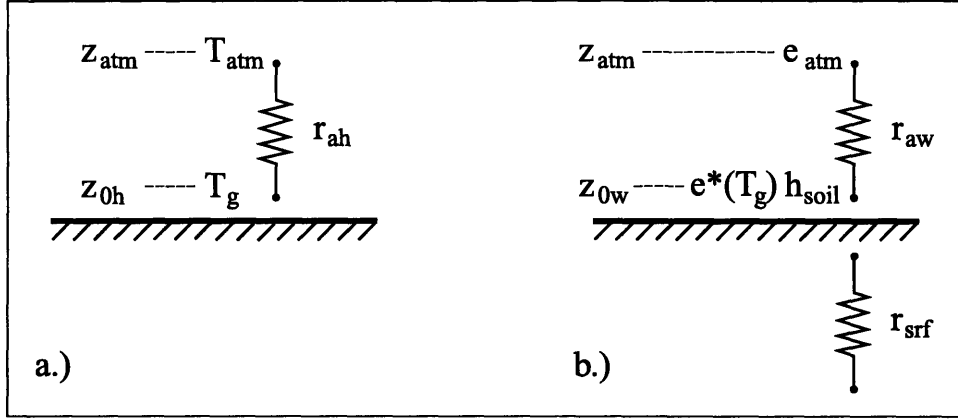
Figure 3-5: A conceptual diagram of resistances for a) sensible and b) latent heat fluxes for *non-vegetated* surfaces.

(Bonan, 1996):

$$r_{ah} = \frac{1}{\kappa^2 u_{atm}} \ln\left(\frac{z_{atm} - d}{z_{0m}}\right) \ln\left(\frac{z_{atm} - d}{z_{0h}}\right), \tag{3.44}$$

$$r_{aw} = \frac{1}{\kappa^2 u_{atm}} \ln\left(\frac{z_{atm} - d}{z_{0m}}\right) \ln\left(\frac{z_{atm} - d}{z_{0w}}\right), \tag{3.45}$$

where $\kappa = 0.41$ is the von Karman constant, $u_{atm}$ [$m\ s^{-1}$] is the wind speed at $z_{atm}$ (for standard meteorological measurements, $z_{atm} = 2\ m$), $d$ [$m$] is the zero plane displacement, $z_{0m} + d$ [$m$] is the height corresponding to the apparent sink for momentum. For bare soil: $d = 0$, $z_{0m} = 0.05\ m$, $z_{0h} = z_{0w} = 0.1z_{0m}$ (Bonan, 1996).

In calm, windless conditions, **free convection** is the dominant mechanism of heat transfer away from the ground surface. In the presented framework, an empirical approach of Kondo and Ishida (1997) is used for $u_{atm} < 1.0\ m\ s^{-1}$ to parameterize $r_{ah}$ and $r_{aw}$ as the reciprocal of an empirically obtained bulk transfer coefficient:

$$r_{ah} = \frac{1}{b' \Delta T_V^{\frac{1}{3}}} = \frac{1}{b'}[(T_g - T_{atm}) + 0.11(e^*(T_g)h_{soil} - e_{atm})]^{-\frac{1}{3}}, \tag{3.46}$$

and $r_{aw} = r_{ah}$. The empirical equation (3.46) assumes that with no wind, the virtual temperature difference $\Delta T_V$ [$K$] creates natural convection, i.e., the air buoyancy is

both due to the surface heating as well as due to water vapor pressure difference between the soil pores and the atmosphere. From experiments of Kondo and Ishida (1997) the value of $b'$ was determined empirically and for rough surfaces is assumed to be $b' = 0.0038\ m\ s^{-1}\ K^{-1/3}$.

### 3.6.3b Vegetated surface

In the more complicated case of a vegetated surface, the sensible and latent heat fluxes are partitioned into vegetation and ground (under-canopy) fluxes that depend on vegetation $T_v$ and ground $T_g$ $[K]$ temperatures. Assuming the canopy air has negligible capacity to store heat, the sensible heat flux between the surface at height $z_{0h} + d$ and the atmosphere at height $z_{atm}$ is partitioned into vegetation and ground fluxes:

$$H^{veg} = H_v^{veg} + H_g^{veg} , \tag{3.47}$$

$$H_v^{veg} = -\rho_{atm} C_p \frac{(T_s - T_v)}{r_v^h} , \tag{3.48}$$

$$H_g^{veg} = -\rho_{atm} C_p \frac{(T_{atm} - T_g)}{r_s^h} , \tag{3.49}$$

where $T_s$ $[K]$ is the surface temperature at height $z_{0h} + d$ (see discussion of resistances below), $r_v^h$ and $r_s^h$ $[s\ m^{-1}]$ are the bulk resistances to sensible heat flux between the vegetation/ground surface and the atmosphere due to the transfer mechanisms involved (see discussion below). The above equations are obtained assuming that the canopy and ground (under-canopy) sensible heat fluxes are independent.

Assuming the canopy air has negligible capacity to store water vapor, the latent heat flux between the surface at height $z_{0h} + d$ and the atmosphere at height $z_{atm}$ is partitioned into vegetation and ground fluxes:

$$\lambda E^{veg} = \lambda E_v^{veg} + \lambda E_g^{veg} , \tag{3.50}$$

$$\lambda E_v^{veg} = -\frac{\rho_{atm} C_p}{\gamma} \frac{(e_s - e^*(T_v))}{r_v^w} , \tag{3.51}$$

$$\lambda E_g^{veg} = -\frac{\rho_{atm} C_p}{\gamma} \frac{(e_{atm} - e^*(T_g) h_{soil})}{r_s^w} , \tag{3.52}$$

where $e_s$ [$mb$] is the surface vapor pressure at height $z_{0h} + d$ (see discussion of resistances below), $r_v^w$ and $r_s^w$ [$s \ m^{-1}$] are the bulk resistances to latent heat flux between the vegetation or ground surface and the atmosphere due to the transfer mechanisms involved (see discussion below). The above equations are obtained assuming that the canopy and ground (under-canopy) latent heat fluxes are independent.

**Resistances**  Resistances used in equations (3.48) - (3.49) and (3.51) - (3.52) can be expressed as

$$
\begin{aligned}
r_v^h &= \frac{1}{c_v^h}, \\
r_s^h &= \frac{1}{c_s^h}, \\
r_v^w &= \frac{1}{c_e^w + c_t^w}, \\
r_s^w &= \frac{1}{c_s^w}.
\end{aligned}
\tag{3.53}
$$

As in Section 3.6.3a, the formulation of resistances in (3.48) - (3.49) and (3.51) - (3.52) depends on the dominant physical mechanisms involved in the transfer of the sensible and latent heat fluxes away from the vegetated areas. In conditions of **forced convection**, the conductances $c_a^h$, $c_a^w$, $c_v^h$, $c_s^h$, $c_e^w$, $c_t^w$, and $c_s^w$ [$m \ s^{-1}$] are defined as (with reference to the system of equations (3.53) and Figure 3-6)

$$
\begin{aligned}
c_a^h &= \frac{1}{r_{ah}}, \\
c_a^w &= \frac{1}{r_{aw}}, \\
c_v^h &= \frac{2(L+S)}{r_b}, \\
c_s^h &= \frac{1}{r_{ah}' + r_{ah}}, \\
c_e^w &= f_{wet}\frac{(L+S)}{r_b}, \\
c_t^w &= (1 - f_{wet})\left(\frac{1}{r_b^{sun} + r_s^{sun}} + \frac{1}{r_b^{shd} + r_s^{shd}}\right), \\
c_s^w &= \frac{1}{r_{aw}' + r_{srf} + r_{aw}},
\end{aligned}
\tag{3.54}
$$

172
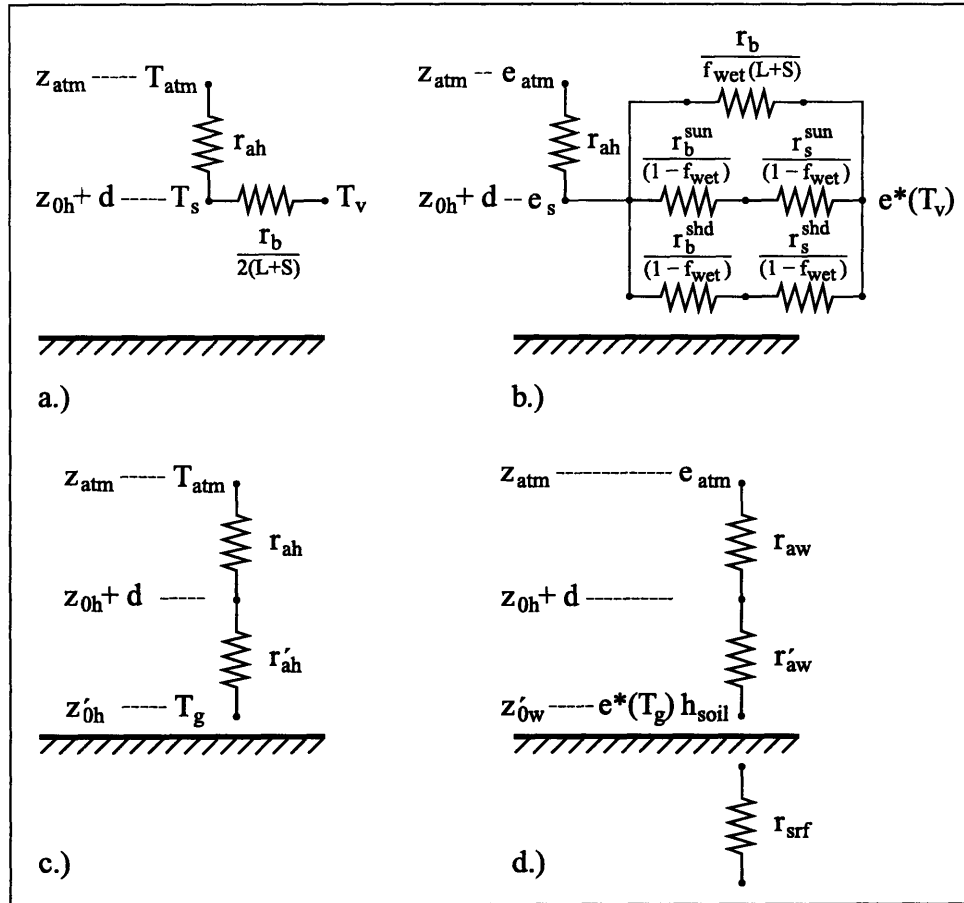
Figure 3-6: A conceptual diagram of resistances for *canopy* a.) sensible heat and b.) latent heat fluxes and for *under-canopy* c.) sensible heat and d.) latent heat fluxes.

where $r'_{ah}$ and $r'_{aw}$ [$s\ m^{-1}$] are the aerodynamic resistances to sensible and latent heat flux, correspondingly, between the ground levels $z'_{0h}$ and $z'_{0w}$ and the heights $z_{0h} + d$ and $z_{0w} + d$ [$m$], $r_b$ [$s\ m^{-1}$] is the one-sided bulk leaf boundary resistance (see below) with the appropriate partitioning between sunlit $r_b^{sun}$ and shaded $r_b^{shd}$ fractions of the canopy, $r_s^{sun}$ and $r_s^{shd}$ [$s\ m^{-1}$] are the sunlit and shaded canopy stomatal resistances (Chapter 4, Section 4.4.1), and $f_{wet}$ [$-$] is the wetted fraction of the canopy (Section 3.7.1, $c_e^w$ is therefore used to parameterize evaporation of intercepted water from the canopy). Note that the soil moisture state affects the latent heat flux magnitude through the stomatal resistances $r_s^{sun}$ and $r_s^{shd}$, which are estimated explicitly accounting for the soil moisture distribution within the root zone (Section 3.7.2).

The roughness lengths $z_{0m}$, $z_{0h}$, and $z_{0w}$ and the displacement height $d$, which are used to calculate $r_{ah}$ and $r_{aw}$, generally vary with leaf and stem area as well as canopy height (Brutsaert, 1982; Sellers et al., 1996a). Here, however, they are considered to be dependent on vegetation roughness height only, according to Shuttleworth (1992, pp. 4.12): $d = 0.67H_v$, $z_{0m} = 0.123H_v$, $z_{0h} = z_{0w} = 0.1z_{0m}$, and $z_{atm} = H_M + H_v$, where $H_v$ $[m]$ is the vegetation height and $H_M$ $[m]$ is the standard measurement height (typically $H_M = 2\ m$). The heights $z'_{0h}$ and $z'_{0w}$ $[m]$ are the ground roughness lengths used in calculation of the aerodynamic resistances within the canopy, $z'_{0h} = z'_{0w} = 0.005\ m$.

The aerodynamic resistances to sensible and latent heat transfer within the canopy $r'_{ah}$ and $r'_{aw}$, respectively, are parameterized according to Choudhury and Monteith (1988). Assuming the exponential profile of the eddy diffusivity $K_h(z)$ $[m^2\ s^{-1}]$ within the canopy, $K_h(z) = K_h(H_v)e^{-a(1-z/H_v)}$ ($z$ $[m]$ is the distance from the ground, positive upward, $0 \leq z \leq H_v$, $a$ is an empirical parameter and $a = 3$, according to Bonan (1996):

$$r'_{ah} = \int_{z'_{0h}}^{z_{0h}+d} \frac{1}{K_h(z)}dz = \frac{H_v}{aK_h(H_v)}\left[e^{a(1-z'_{0h}/H_v)} - e^{a(1-(z_{0h}+d)/H_v)}\right]. \quad (3.55)$$

It is assumed that $r'_{ah} = r'_{aw}$ because the roughness lengths for sensible heat and water vapor are identical and $K_h(H_v) = u_*\kappa(H_v - d)$, where the effects of atmospheric stability are ignored and $K_h(H_v)$ is obtained for neutral conditions. The friction velocity $u_*$ $[m\ s^{-1}]$ is calculated as in Shuttleworth (1979):

$$u_* = \frac{\kappa u_{atm}}{\ln\left(\frac{z_{atm}-d}{z_{0m}}\right)}. \quad (3.56)$$

The one-sided bulk leaf boundary resistance $r_b(z)$ depends on a typical leaf dimension $d_{leaf}$ $[m]$ and wind profile in the canopy as (Choudhury and Monteith, 1988)

$$\frac{1}{r_b(z)} = 0.01\sqrt{\frac{u(H_v)e^{-a(1-z/H_v)}}{d_{leaf}}}, \quad (3.57)$$

where $u(H_v)$ $[m \ s^{-1}]$ is the wind speed at the canopy top and the wind profile within the canopy is consistent with an exponential $K_h(z)$ profile. Integrating $r_b(z)$ over height in the canopy,

$$\frac{1}{r_b} = \frac{\int_0^{H_v} \frac{1}{r_b(z)} dz}{\int_0^{H_v} dz} = \frac{0.02}{a} \sqrt{\frac{u(H_v)}{d_{leaf}}} \left[ 1 - e^{-a/2} \right]. \tag{3.58}$$

To account appropriately for the latent heat transfer from sunlit and shaded fractions of the canopy: $r_b^{sun} = \frac{r_b}{L_{sun}}$, $r_b^{shd} = \frac{r_b}{L_{shd}}$. In this formulation, these resistances refer to one side of the leaf.

The expressions for $T_s$ in (3.48) - (3.49) and $e_s$ in (3.51) - (3.52) are derived from the assumed equality of fluxes among different levels considered within the canopy. Note that the ground and canopy heat fluxes are assumed to be independent (both sensible heat and latent heat fluxes), which is different from the formulation of Bonan (1996) and Oleson et al. (2004). With reference to Figure 3-6:

$$-\rho_{atm} C_p (T_{atm} - T_s) \frac{1}{r_{ah}} = -\rho_{atm} C_p (T_s - T_v) \frac{2(L + S)}{r_b}, \tag{3.59}$$

and

$$-\frac{\rho_{atm} C_p}{\gamma} \frac{(e_{atm} - e_s)}{r_{aw}} = -\frac{\rho_{atm} C_p}{\gamma} \frac{(e_s - e^*(T_v))}{r_b + r_s}, \tag{3.60}$$

from which one can obtain:

$$T_s = \frac{c_a^h T_{atm} + c_v^h T_v}{c_a^h + c_v^h}, \tag{3.61}$$

$$e_s = \frac{c_a^w e_{atm} + (c_e^w + c_t^w) e^*(T_v)}{c_a^w + c_e^w + c_t^w}. \tag{3.62}$$

As in Section 3.6.3a, in calm, windless conditions, **free convection** is the dominant mechanism of the heat transfer away from vegetated areas. In the presented framework, for $u_{atm} < 1.0 \ m \ s^{-1}$, an empirical approach of Kondo and Ishida (1997) is used to parameterize the resistances as functions of empirically obtained bulk transfer

coefficients.

$$
\begin{aligned}
c_v^h &= b' \left[ T_v - T_{atm} \right]^{\frac{1}{3}} , \\
c_s^h &= b' \left[ (T_g - T_{atm}) + 0.11(e^*(T_g)h_{soil} - e_{atm}) \right]^{\frac{1}{3}} , \\
c_e^w &= f_{wet} c_v^h , \\
c_t^w &= (1 - f_{wet}) \left( \frac{c_v^h f_{sun}}{1 + c_v^h f_{sun} \, r_s^{sun}} + \frac{c_v^h f_{shd}}{1 + c_v^h f_{shd} \, r_s^{shd}} \right) , \\
c_s^w &= \frac{c_s^h}{1 + c_s^h \, r_{srf}} .
\end{aligned}
$$

For free convection conditions $T_s = T_{atm}$ and $e_s = e_{atm}$.

## 3.6.4   Ground heat flux

The ground heat flux is an important component of the land-surface energy balance, particularly in arid areas where high shortwave radiation may lead to significant soil heat flux. Since no analytical formulation is available for heat flux for arbitrary boundary conditions, approximate methods are typically used. The discussed framework employs the method of Wang and Bras (1999), which is based on one-dimensional heat diffusion equation with a constant diffusivity parameter. By relating the soil surface temperature to the ground heat flux through a half-order derivative/integral operator, Wang and Bras (1999) give:

$$
G(t) = \sqrt{\frac{k_s C_s}{\pi}} \int_0^t \frac{dT_g(s)}{\sqrt{t-s}} , \tag{3.63}
$$

where $G(t)$ $[W \; m^{-2}]$ is the ground heat flux at time $t$, $k_s$ $[J \; m^{-1} \; s^{-1} \; K^{-1}]$ is the volumetric heat conductivity, $C_s$ $[J \; m^{-3} \; K^{-1}]$ is the heat capacity of the soil, and $s$ is the integration variable. $k_s$ and $C_s$ are well documented parameters for a variety of common soils (e.g., De Vries, 1963). Both $k_s$ and $C_s$ depend on the soil moisture state. From Farouki (1981):

$$
k_s = K_e k_{s,sat} + (1 - K_e) k_{s,dry} , \quad \text{if } \theta_d/\theta_s > 10^{-7} , \tag{3.64}
$$

176

$$k_s = k_{s,dry}, \qquad\qquad \text{if } \theta_d/\theta_s \leq 10^{-7}, \qquad (3.65)$$

where $k_{s,dry}$ and $k_{s,sat}$ are the dry and saturated soil thermal conductivities, respectively, $\theta_d$ is the soil moisture value over depth $z_d$ $[m]$, and $K_e$ $[-]$ is the Kersten number. In this work, the depth $z_d$ is defined as the maximum possible diurnal penetration depth for a given soil:

$$z_d = \left[ \frac{2k_{s,sat}}{\omega_D\, C_{s,soi}(1 - \theta_s)} \right]^{\frac{1}{2}}, \qquad (3.66)$$

where $\omega_D = 2\pi/86400$ $[s^{-1}]$ is the daily frequency and $C_{s,soi}$ is the heat capacity of the soil solid (De Vries, 1963). $\theta_d$ is obtained by integration of the soil moisture profile (Section 3.7.2). The Kersten number is a function of the relative saturation:

$$K_e = \ln\left( \frac{\theta_d}{\theta_s} \right) + 1 \geq 0. \qquad (3.67)$$

The soil heat capacity is estimated as a function of soil moisture as

$$C_s = C_{s,soi}(1 - \theta_s) + \theta_d C_{liq}, \qquad (3.68)$$

where $C_{liq} = 4.188 \times 10^6$ $[J\,m^{-3}\,K^{-1}]$ is the specific heat capacity of water.

Expression (3.63) indicates that the ground heat flux is completely determined by the history of the surface soil temperature, given the soil thermal properties. A numerical integration procedure is implemented in the discussed model that estimates $G$ based on a stored vector of soil surface temperature values $\mathbf{T_g}$ estimated prior to time $t$. The accuracy of estimation depends on the length of the integration period, i.e., the size of $\mathbf{T_g}$, which, however, has to be limited due to computational constraints. The approach consists in storing an additional vector of temperatures, $\mathbf{T'_g}$, starting from the sun set time of a given day until the sun rise time of the next day, when vector $\mathbf{T'_g}$ is used to replace $\mathbf{T_g}$.

$T_g$ represents the "skin" soil temperature, i.e., the value at the very surface of soil. For several estimation procedures it is also important to have the soil temperature

$T_{soil}$ $[K]$ averaged over a certain depth, e.g., root zone. While numerically feasible, the estimation of $T_{soil}$ would introduce a significant computational overhead. It is assumed that $T_{soil}$ can be computed approximately, using available information on $T_g$. Two principal features need to be represented in the dynamics of $T_{soil}$: 1.) the smaller diurnal variability and absolute magnitudes with respect to the diurnal cycle of $T_g$, which mimics dampening of the heat flux with depth; and 2.) the seasonal phases of gradual soil warming and cooling that reflect average conditions for soil biochemical and biophysical processes. To ensure the above characteristics, the current implementation uses the mean value of the vector of surface temperatures $\mathbf{T_g}$ as a surrogate estimate of $T_{soil}$. The length of the vector $\mathbf{T_g}$ varies between 10 and 36 hours, depending on time of the year and location. Future model implementations will certainly require a more rigorous estimation of temperature distribution with soil depth.

### 3.6.5   Element scale quantities

In general, almost any variable estimated separately for vegetated and bare soil fractions of a given element can be expressed as a quantity at the *element-scale*. The latter is composed through a linear combination of the relative contributions (proportional to the corresponding fractional areas) from all PFTs and bare soil present in the element. For instance, the element-scale quantity of the *Normalized Difference Vegetation Index*, previously estimated at the scale of a given PFT (Section 3.6.1), can be obtained as

$$\overline{NDVI} = \frac{\bar{r}_{nir} - \bar{r}_{vis}}{\bar{r}_{nir} + \bar{r}_{vis}}, \qquad (3.69)$$

with

$$\bar{r}_\Lambda = \frac{S_{v,\Lambda} \uparrow + S_{g,\Lambda} \uparrow}{S_{atm} \downarrow_\Lambda^\mu + S_{atm} \downarrow_\Lambda}, \qquad (3.70)$$

$$S_{v,\Lambda} \uparrow = \sum_k^{N_V} (S_{atm} \downarrow_\Lambda^\mu I \uparrow_{k,\Lambda}^\mu + S_{atm} \downarrow_\Lambda I \uparrow_{k,\Lambda}) f_{v,k}, \qquad (3.71)$$

178

$$S_{g,\Lambda} \uparrow \;=\; \left( \alpha_{g,\Lambda}^{\mu} \, S_{atm} \downarrow_{\Lambda}^{\mu} + \alpha_{g,\Lambda} \, S_{atm} \downarrow_{\Lambda} \right) \left( 1 - \sum_{k}^{N_V} f_{v,k} \right) , \qquad (3.72)$$

where $f_{v,k}$ $[-]$ is the vegetation fraction of the $k$th plant functional type present in a given element (Chapter 4, Section 4.4.8), $N_V$ is the total number of vegetation types present in the element. The element-scale quantities are useful for model verification/calibration, e.g., the $NDVI$ values estimated using (3.69) can be used to relate the model output to observations from remote sensing platforms.

### 3.6.6  Net radiation

The net radiation for computational elements that are composed of *bare* soil only is expressed as

$$R_{ng} = \vec{S}_g^{\,bare} - \vec{L}_g^{\,bare} \;=\; H_g^{bare} + \lambda E_g^{bare} + G . \qquad (3.73)$$

If vegetation is present, two levels are considered when estimating the net radiation: the canopy and the ground level. At the *canopy* level, no distinction is made among various PFTs that can be present within a given computational element at the same time. The net radiation is composed for the total vegetated part of the element by linearly combining the contributions from all PFTs currently present (see Section 3.6.5):

$$R_{nv} \;=\; \sum_{k}^{N_V} \left( \vec{S}_{v,k}^{\,veg} - \vec{L}_{v,k}^{\,veg} \right) f_{v,k} \;=\; \sum_{k}^{N_V} \left( H_{v,k}^{veg} + \lambda E_{v,k}^{veg} \right) f_{v,k} , \qquad (3.74)$$

where $f_{v,k}$ $[-]$ is the vegetation fraction of the $k$th plant functional type present in a given element (Chapter 4, Section 4.4.8), $N_V$ is the total number of vegetation types present in the element and the flux components in (3.74) are computed separately for each vegetation type.

The same approach is used for estimating the *ground* level net radiation: the contributions from all PFTs present in the element are lumped together with the

179

contributions from the fraction of bare soil:

$$R_{ng} = \sum_k^{N_V} \left( \vec{S}_{g,k}^{veg} - \vec{L}_{g,k}^{veg} \right) f_{v,k} + \left( 1 - \sum_k^{N_V} f_{v,k} \right) \left( \vec{S}_g^{bare} - \vec{L}_g^{bare} \right) =$$

$$\sum_k^{N_V} \left( H_{g,k}^{veg} + \lambda E_{g,k}^{veg} \right) f_{v,k} + \left( 1 - \sum_k^{N_V} f_{v,k} \right) \left( H_g^{bare} + \lambda E_g^{bare} \right) + G \quad (3.75)$$

While the separate treatment of each plant type would allow one to differentiate the characteristic features of responses of individual species to water-energy conditions at a given location, the above approach attempts to avoid the associated computational expenses (although the implemented scheme is flexible for such an extension). The model aims to address the spatial heterogeneity of hydrology-vegetation dynamics within a complex terrain. Site-specific characteristics such as geometry, location in the landscape, and soil properties should lead to inherently distinct regimes of radiation, soil moisture, and, therefore, spatial differences in vegetation dynamics.

### 3.6.7 Vegetation and ground temperatures

The formulation of net radiation in (3.73), (3.74), and (3.75) depends on the ground temperature $T_g$ and, if vegetation is present, vegetation temperature $T_v$. Both $T_g$ and $T_v$ are state variables that have to be estimated iteratively since (3.73)-(3.75) are highly non-linear equations and analytical solutions are not available.

#### 3.6.7a Non-vegetated surface

Equation (3.73) is the basis for iterative scheme used to close the ground surface energy budget. The Newton method is used with the iteration equation written as

$$-\vec{S}_g^{bare} - \vec{L}_g^{bare}(T_g) + H_g^{bare}(T_g) + \lambda E_g^{bare}(T_g) + G(T_g) +$$

$$\left[ \frac{\partial \vec{L}_g^{bare}(T_g)}{\partial T_g} + \frac{\partial H_g^{bare}(T_g)}{\partial T_g} + \frac{\partial \lambda E_g^{bare}(T_g)}{\partial T_g} + \frac{\partial G(T_g)}{\partial T_g} \right] \Delta T_g = 0, \quad (3.76)$$

where $\Delta T_g$ is the ground temperature iteration step. The partial derivatives $\frac{\partial \vec{L}_g^{bare}(T_g)}{\partial T_g}$, $\frac{\partial H_g^{bare}(T_g)}{\partial T_g}$, and $\frac{\partial \lambda E_g^{bare}(T_g)}{\partial T_g}$ are obtained analytically from (3.29), (3.36), and (3.37).

The derivative the ground heat flux $\frac{\partial G(T_g)}{\partial T_g}$ is estimated numerically. Note that since the dominant heat transfer mechanism is recognized before the iteration, the derivatives $\frac{\partial r_{ah}}{\partial T_g}$ and $\frac{\partial r_{aw}}{\partial T_g}$ can be determined analytically from (3.44), (3.45), or (3.46).

### 3.6.7b Vegetated surface

The estimation of fluxes and temperatures for vegetated surfaces is more complex than for bare ground because of: a) the relative dependence of the vegetation and ground temperatures through (3.34) - (3.35); b) the highly non-linear stomatal response to change in the vegetation temperature (Section 4.4.1). The canopy and ground surface energy budgets thus constitute a system of equations, which are strongly non-linear functions of $T_v$ and $T_g$:

$$F_1(T_v, T_g) = \sum_k^{N_V} \left( -\vec{S}_{v,k}^{veg} + \vec{L}_{v,k}^{veg}(T_v, T_g) + H_{v,k}^{veg}(T_v) + \lambda E_{v,k}^{veg}(T_v) \right) f_{v,k}, \quad (3.77)$$

$$F_2(T_v, T_g) = \sum_k^{N_V} \left( -\vec{S}_{g,k}^{veg} + \vec{L}_{g,k}^{veg}(T_v, T_g) + H_{g,k}^{veg}(T_g) + \lambda E_{g,k}^{veg}(T_g) \right) f_{v,k} +$$

$$(1 - \sum_k^{N_V} f_{v,k})(-\vec{S}_g^{bare} + \vec{L}_g^{bare}(T_g) + H_g^{bare}(T_g) + \lambda E_g^{bare}(T_g)) +$$

$$+ G(T_g). \quad (3.78)$$

The Newton-Raphson iteration method is used to simultaneously solve for $T_v$ and $T_g$ that balance the vegetation and ground surface energy budgets. A set of linear equations for the temperature corrections $\delta \mathbf{T}$ that move functions of (3.77) and (3.78) closer to the solution can be written in the vector form as

$$\mathbf{J} \, \delta \mathbf{T} = -\mathbf{F}, \quad (3.79)$$

where $\mathbf{F} = [F_1, F_2]$, $\delta \mathbf{T} = [\Delta T_v, \Delta T_g]$, and $\mathbf{J}$ is the Jacobian matrix:

$$\mathbf{J} = \begin{bmatrix} \frac{\partial F_1}{\partial T_v} & \frac{\partial F_1}{\partial T_g} \\[2mm] \frac{\partial F_2}{\partial T_v} & \frac{\partial F_2}{\partial T_g} \end{bmatrix}, \quad (3.80)$$

181

and

$$\frac{\partial F_1}{\partial T_v} = \sum_k^{N_V} \left( \frac{\partial \vec{L}_{v,k}^{veg}(T_v, T_g)}{\partial T_v} + \frac{\partial H_{v,k}^{veg}(T_v)}{\partial T_v} + \frac{\partial \lambda E_{v,k}^{veg}(T_v)}{\partial T_v} \right) f_{v,k} , \qquad (3.81)$$

$$\frac{\partial F_1}{\partial T_g} = \sum_k^{N_V} \frac{\partial \vec{L}_{v,k}^{veg}(T_v, T_g)}{\partial T_g} f_{v,k} , \qquad (3.82)$$

$$\frac{\partial F_2}{\partial T_v} = \sum_k^{N_V} \frac{\partial \vec{L}_{g,k}^{veg}(T_v, T_g)}{\partial T_v} f_{v,k} , \qquad (3.83)$$

$$\frac{\partial F_2}{\partial T_g} = \sum_k^{N_V} \left( \frac{\partial \vec{L}_{g,k}^{veg}(T_v, T_g)}{\partial T_g} + \frac{\partial H_{g,k}^{veg}(T_g)}{\partial T_g} + \frac{\partial \lambda E_{g,k}^{veg}(T_g)}{\partial T_g} \right) f_{v,k} +$$

$$\left( 1 - \sum_k^{N_V} f_{v,k} \right) \left( \frac{\partial \vec{L}_g^{bare}(T_g)}{\partial T_g} + \frac{\partial H_g^{bare}(T_g)}{\partial T_g} + \frac{\partial \lambda E_g^{bare}(T_g)}{\partial T_g} \right) +$$

$$+ \frac{\partial G(T_g)}{\partial T_g} . \qquad (3.84)$$

The partial derivatives with respect to the ground temperature $\frac{\partial \vec{L}_v^{veg}(T_v, T_g)}{\partial T_g}$, $\frac{\partial \vec{L}_g^{veg}(T_v, T_g)}{\partial T_g}$, $\frac{\partial H_g^{veg}(T_g)}{\partial T_g}$, $\frac{\partial \lambda E_g^{veg}(T_g)}{\partial T_g}$, $\frac{\partial \vec{L}_g^{bare}(T_g)}{\partial T_g}$, $\frac{\partial H_g^{bare}(T_g)}{\partial T_g}$, and $\frac{\partial \lambda E_g^{bare}(T_g)}{\partial T_g}$ are obtained analytically from (3.34), (3.35), (3.49), (3.52), (3.29), (3.36), and (3.37) and the derivative of the ground heat flux $\frac{\partial G(T_g)}{\partial T_g}$ is estimated numerically. The partial derivatives with respect to the canopy temperature $\frac{\partial \vec{L}_v^{veg}(T_v, T_g)}{\partial T_v}$, $\frac{\partial \vec{L}_g^{veg}(T_v, T_g)}{\partial T_v}$, and $\frac{\partial H_v^{veg}(T_v)}{\partial T_v}$ are obtained analytically from (3.34), (3.35), and (3.48). The partial derivative of the canopy latent heat flux $\frac{\partial \lambda E_v^{veg}(T_v)}{\partial T_v}$ involves evaluation of the derivatives of the stomatal resistance $\frac{\partial r_s^{sun}}{\partial T_v}$ and $\frac{\partial r_s^{shd}}{\partial T_v}$, which cannot be obtained analytically. $\frac{\partial \lambda E_v^{veg}(T_v)}{\partial T_v}$ is therefore estimated numerically.

Since the Newton-Raphson iteration method has poor global convergence properties, it is used in combination with the *line searches and backtracking* algorithm (Press et al., 1999) that ensures the convergence of the above scheme.

## 3.7 Moisture fluxes

The model parameterizes the processes of canopy interception, drainage, through-fall, evapotranspiration, infiltration, surface runoff and runon, and lateral sub-surface

moisture transfer. On one hand, the moisture fluxes strongly depend on the energy partition within a given computational element since the latent heat flux determines the amount of water extracted from the system (or added, via dew). On the other hand, the moisture state of the canopy and soil within the element affects the energy budget by modulating the amount of absorbed radiation (through $\alpha_{g\Lambda}$ in (3.22)), the latent heat partition into canopy and soil evaporation and transpiration (through $h_{soil}$ and $r_{srf}$ in (3.37) and (3.51), and through $r_s$ and $f_{wet}$ in (3.51) and (3.52)), and the magnitude of the ground heat flux (through $k_s$ and $C_s$ in (3.63)). The framework, therefore, represents a strongly coupled system of water-energy interactions.

### 3.7.1 Interception and canopy moisture fluxes

Precipitation is either intercepted by the canopy or falls to the ground as throughfall and stem flow. Interception is estimated from the Rutter et al. (1971, 1975) canopy water balance model:

$$\frac{dC}{dt} = (1-p)R - D - \frac{C}{S}E_E^{veg}, \tag{3.85}$$

where $C$ $[mm]$ is the canopy storage, $E_E^{veg}$ $[mm\ hour^{-1}]$ is the evaporation rate from the wetted fraction of the canopy (see below), $R$ $[mm\ hour^{-1}]$ is the rainfall rate (if there is dew, it is added to $R$), and $D$ $[mm\ hour^{-1}]$ is the canopy drainage:

$$D = K_c e^{g_c(C-S)}, \tag{3.86}$$

where $K_c$ $[mm\ hour^{-1}]$ and $g_c$ $[mm^{-1}]$ are the drainage rate coefficient and exponential decay parameter (Rutter et al., 1971, 1975). The parameters $S$ $[mm]$ and $p$ $[-]$ of (3.85) are the canopy capacity and free throughfall coefficient, respectively. $S$ and $p$ depend on the amount of biomass of a particular PFT present in a given element (Dickinson et al., 1993):

$$S = 0.1(L+S), \tag{3.87}$$

$$p = e^{-0.5(L+S)}.$$
(3.88)

where, as above, $L$ and $S$ are the one-sided leaf and stem area indices. Since equation (3.85) is a non-linear ODE that cannot be solved analytically for $C$, the Runge-Kutta integration method is used to obtain $C$ given the instantaneous values of $R$ and $E_E^{veg}$.

The wetted fraction of the canopy is calculated using the current canopy storage (Dickinson et al., 1993):

$$f_{wet} = \left[\frac{C}{S}\right]^{\frac{2}{3}} \leq 1.$$
(3.89)

The total canopy evapotranspiration flux $E_v^{veg}$ [$mm\ hour^{-1}$] from (3.51) is partitioned into the canopy evaporation $E_E^{veg}$, transpiration $E_T^{veg}$, and canopy dew $E_{Dc}^{veg}$ as

$$E_E^{veg} = E_v^{veg} \frac{c_e^w}{c_e^w + c_t^w},$$
(3.90)

$$E_T^{veg} = E_v^{veg} \frac{c_t^w}{c_e^w + c_t^w},$$
(3.91)

$$E_{Dc}^{veg} = E_v^{veg}, \quad \text{if} \quad E_v^{veg} < 0.$$
(3.92)

From (3.85) and (3.86), the net precipitation reaching the ground within a vegetated patch of $k$th PFT is simply $q_{NR,k} = p_k R + D_k$. At the *element scale*, the net precipitation is obtained by summing the contributions of net precipitation from all PFTs currently present and rainfall on bare soil:

$$q_{NR} = \sum_k^{N_V} (p_k R + D_k) f_{v,k} + \left(1 - \sum_k^{N_V} f_{v,k}\right) R.$$
(3.93)

Similarly, the total canopy evapotranspiration at the *element scale* is composed as in (3.74)

$$E_v = \sum_k^{N_V} E_{v,k}^{veg} f_{v,k}.$$
(3.94)

The element scale quantities for each of the components of $E_v^{veg}$, i.e., canopy evapo-

184

ration, transpiration, and canopy dew, are estimated in a similar manner.

## 3.7.2 Infiltration and soil moisture fluxes

The water influx at the soil surface,

$$q_{infl} = q_{NR} + q_{dew} + q_{runon} , \qquad (3.95)$$

originates from the direct rainfall and throughfall $q_{NR}$, dew $q_{dew}$, and runon $q_{runon}$ [$mm$ $hour^{-1}$]. The runon for a given element is estimated as the sum of surface runoff produced in neighboring elements that have their direction of steepest descent towards the considered element. The soil dew is estimated at the element scale as

$$q_{dew} = \sum_{k}^{N_V} E_{Dg,k}^{veg} f_{v,k} + \left(1 - \sum_{k}^{N_V} f_{v,k}\right) E_{Dg}^{bare} , \qquad (3.96)$$

$$E_{Dg}^{veg} = E_g^{veg}, \quad \text{if} \quad E_g^{veg} < 0 , \qquad (3.97)$$

$$E_{Dg}^{bare} = E_g^{bare}, \quad \text{if} \quad E_g^{bare} < 0 . \qquad (3.98)$$

The water flux $q_{infl}$ can either infiltrate into the soil column or become runoff. The infiltration and runoff production are simulated by numerically solving the one-dimensional Richards equation (Hillel, 1980) that governs the fluid flow into the unsaturated soil. When moisture content $\theta$ [$mm^3$ $mm^{-3}$] is used as a dependent variable, the Richards equation for a sloped surface with balanced subsurface fluxes and negligible evapotranspiration is expressed as

$$\frac{\partial \theta}{\partial t} = \frac{\partial}{\partial z}\left(D(\theta)\frac{\partial \theta}{\partial z} - K(\theta)\cos\alpha_\nabla\right) , \qquad (3.99)$$

where $K(\theta)$ [$mm$ $hour^{-1}$] is the unsaturated hydraulic conductivity, $D(\theta)$ [$mm^2$ $hour^{-1}$] is the unsaturated diffusivity, $\alpha_\nabla$ [$radian$] is the slope of the soil surface (Section 2.3.1), $t$ [$hour$] is time, and $z$ [$mm$] denotes the *normal* to the soil's surface coordinate assumed to be positive downward (direction $n$ in Figure 3-1). The finite-element, backward Euler time-stepping numerical approximation used to solve equation (3.99)

is described in detail in Appendix D.1. When one needs to consider a domain of an arbitrary geometrical configuration, subject to a variety of possible hydrometeorological and vegetation states, the subsurface lateral exchange in the unsaturated zone and the evapotranspiration flux have to be accounted for. This can be achieved by adding the corresponding sinks/sources terms into the formulation (3.99). The corresponding formulation and its numerical solution for a one-dimensional soil column are provided in Appendix D.2. The solution permits lateral moisture redistribution in the direction of steepest decent (direction $p$ in Figure 3-1) as well as the surface and subsurface influx of water from multiple sources (elements) located directly above a given element. The solution also allows for water losses from the soil surface and root zone via the evapotranspiration process with the following possible components: evaporation from the fraction of bare ground $E_g^{bare}$ (from (3.37)), evaporation from the under-canopy soil surface $E_g^{veg}$ (from (3.52)), and transpiration $E_T^{veg}$ (from (3.91)). The numerical implementation also evaluates the moisture loss from the root zone due to drainage to deeper layers, when there is water excess, or gain due to capillary rise, when the root zone is drier than deeper soil horizons. The corresponding net flux is estimated in (D.40). The details of the numerical implementation of how the fluxes $q_{infl}$, $E_g^{veg}$, $E_g^{bare}$, and $E_T^{veg}$ are combined from multiple possible sources and applied to different depths of one-dimensional soil column are given in Appendix D.2.

The numerical solution provided in Appendices D.1 - D.2 operates on mesh that resolves the vertical variability of soil moisture. Since the finite-element method permits multiple resolution, the soil profile is resolved at a high detail near the surface, which allows one to account for the high-frequency variability in the atmospheric forcing. The mesh has a coarser resolution at greater depths for computational efficiency. An example of the typical mesh is shown in Figure 3-7. For a number of estimation procedures, one needs to know the volumetric water content of the soil surface. This value is approximated with the soil moisture $\theta_1$ $[mm^3\ mm^{-3}]$ contained in the first 10 $mm$ of the soil column.

Since the soil column is resolved at multiple number of points, the root biomass profile (3.1) can be explicitly represented in the numerical scheme. If $z_i$ $[mm]$ is

**Finite–element mesh**
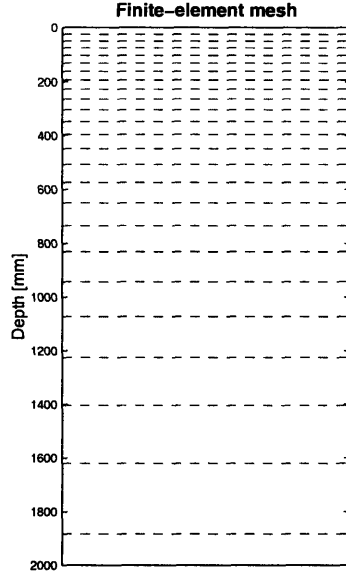
Figure 3-7: An illustration of the finite-element mesh assumed in the soil profile. The dashed lines are located at depths corresponding to the location of mesh nodes.

a depth in the soil profile, the corresponding fraction of the root biomass $r_i$ $[-]$ , $i = 1 \ldots I_{root}$ (note that $\sum_i^{I_{root}} r_i = 0.95$) attributed to that depth is

$$r_i = 1 - e^{-\eta 0.5 \Delta z_i}, \qquad\qquad \text{if} \quad i = 1, \qquad\qquad (3.100)$$

$$r_i = e^{-\eta(z_i - 0.5\Delta z_{i-1})} - e^{-\eta(z_i + 0.5\Delta z_i)}, \quad \text{if} \quad z_i + 0.5\Delta z_i \leq Z_{root}, \quad (3.101)$$

$$r_i = e^{-\eta(z_i - 0.5\Delta z_{i-1})} - e^{-\eta Z_{root}}, \qquad \text{if} \quad z_i + 0.5\Delta z_i \geq Z_{root}, \quad (3.102)$$

where $\Delta z_i$ $[mm]$ is the positive difference between $z_{i+1}$ and $z_i$, $Z_{root}$ $[mm]$ is the depth that contains 95% of root biomass, and $\eta$ $[mm^{-1}]$ is the decay rate of root biomass distribution with the soil depth (equation (3.1)).

### 3.7.3 Soil hydraulic properties

The Brooks and Corey (1964) parameterization scheme is adopted to relate the unsaturated hydraulic conductivity and soil water potential to the moisture content. The Brooks and Corey (1964) model uses Burdine's theory (Burdine, 1953) to relate the

187

unsaturated hydraulic conductivity $K_n(S_e)$ $[mm\ hour^{-1}]$ and the moisture content:

$$K_n(S_e) = K_{sn}S_e \left[ \int_0^{S_e} \frac{1}{\psi^2(S)}dS \right] \left[ \int_0^1 \frac{1}{\psi^2(S)}dS \right]^{-1}, \qquad (3.103)$$

where $K_{sn}$ $[mm\ hour^{-1}]$ is the saturated hydraulic conductivity in the normal to the soil's surface direction (direction $n$ in Figure 3-1), $\psi(S)$ is the soil water retention curve and $S_e$ $[-]$ is the effective saturation:

$$S_e = \frac{\theta - \theta_r}{\theta_s - \theta_r}, \qquad (3.104)$$

where $\theta_s$ $[mm^3\ mm^{-3}]$ is the saturation moisture content and $\theta_r$ $[mm^3\ mm^{-3}]$ is the residual moisture content defined as is the amount of soil water that cannot be removed from soil by drainage or evapotranspiration. Brooks and Corey (1964) proposed the following empirical model for soil water retention curve (assuming isotropic media, drainage cycle, and neglecting hysteresis):

$$\psi(\theta) = \psi_b \left( \frac{\theta - \theta_r}{\theta_s - \theta_r} \right)^{-\frac{1}{\lambda_o}}, \qquad (3.105)$$

where $\psi_b$ $[mm]$ is the air entry bubbling pressure and $\lambda_o$ $[-]$ is the pore-size distribution index. An expression relating the unsaturated conductivity and soil moisture content is obtained from (3.103) and (3.105) as

$$K_n(\theta) = K_{sn} \left( \frac{\theta - \theta_r}{\theta_s - \theta_r} \right)^{\frac{2+3\lambda_o}{\lambda_o}}. \qquad (3.106)$$

From (3.105) and (3.106) one can get an expression for the unsaturated diffusivity $D(\theta)$ $[mm^2\ hour^{-1}]$:

$$D(\theta) = K_n(\theta)\frac{d\psi}{d\theta} = K_{sn}\frac{-\psi_b}{\lambda_o(\theta_s - \theta_r)} \left( \frac{\theta - \theta_r}{\theta_s - \theta_r} \right)^{2+\frac{1}{\lambda_o}}. \qquad (3.107)$$

The parameterization is applicable only for the range of $\psi$ satisfying $\psi < \psi_b$ (since soil water is under tension, the pressure $\psi$ has a negative sign).

In the model, the soil anisotropy $a_r$ [$-$] is defined as the ratio between the hydraulic conductivities in the directions parallel to the slope $K_{sp}$ and normal to the slope $K_{sn}$:

$$a_r = \frac{K_{sp}}{K_{sn}}. \tag{3.108}$$

See Figure 3-1 for a reference on orientation of the characteristic directions $n$ and $p$.

# 3.8 Model testing

The material of this section illustrates the various coupling mechanisms captured by the simulation framework in modeling the energy and water budgets of vegetated surfaces. First, the energy partition and soil moisture dynamics are illustrated for surfaces vegetated with broadleaf deciduous trees and $C_4$ grass, for initially saturated soil. Second, the sensitivity of energy partition to wind speed, i.e., to the relative strength of driving mechanisms responsible for the heat transfer away from vegetated surfaces, is illustrated for fully saturated soil conditions (no soil water control). Third, both the simulation of soil moisture dynamics and the vertical structure of transient soil water distribution are illustrated for typical loamy sand and clayey soils for a rainfall forcing that includes two events. Fourth, the effect of topography on lateral water transfer in the unsaturated zone is illustrated for soils with different anisotropy characteristics for a domain of synthetic configuration, exhibiting flow convergence. Finally, the effect of runon on soil moisture dynamics is shown for clayey soils. In all of the following examples, the properties of vegetation are assigned at the beginning and do not change throughout the simulation.

Four generic soil types are used in the material of the following sections. Their hydraulic properties are parameterized according to Rawls et al. (1982). The heat transfer and albedo parameters are from Dickinson et al. (1993) and Bonan (1996). Table 3.1 provides the corresponding values of the soil hydraulic, heat transfer, and albedo parameters.

Table 3.1: The soil hydraulic, heat transfer, and albedo parameters of generic soil types. The hydraulic parameterization follows Rawls et al. (1982). The heat transfer and albedo parameters are from Dickinson et al. (1993) and Bonan (1996). $K_{sn}$ [$mm\ hour^{-1}$] is the saturated hydraulic conductivity in the normal to the soil's surface direction, $\theta_s$ [$mm^3\ mm^{-3}$] is the saturation moisture content, $\theta_r$ [$mm^3\ mm^{-3}$] is the residual moisture content, $\lambda_o$ [$-$] is the pore-size distribution index, $\psi_b$ [$mm$] is the air entry bubbling pressure, $k_{s,dry}$ and $k_{s,sat}$ [$J\ m^{-1}\ s^{-1}\ K^{-1}$] are the dry and saturated soil thermal conductivities, respectively, and $C_{s,soi}$ [$J\ m^{-3}\ K^{-1}$] is the heat capacity of the soil solid. The soil albedo[a] parameters are assumed to be uniform across all considered soil types.

| Parameter | $K_{sn}$ | $\theta_s$ | $\theta_r$ | $\lambda_o$ | $\psi_b$ | $k_{s,dry}$ | $k_{s,sat}$ | $C_{s,soi}$ |
|---|---|---|---|---|---|---|---|---|
| **Sand**[b] | 235.0 | 0.417 | 0.020 | 0.592 | -73 | 0.214 | 2.689 | 1202632 |
| **Loamy sand**[c] | 61.0 | 0.401 | 0.035 | 0.474 | -87 | 0.214 | 2.639 | 1209573 |
| **Loam**[d] | 15.0 | 0.434 | 0.027 | 0.220 | -111 | 0.196 | 2.250 | 1184138 |
| **Clay**[e] | 1.0 | 0.385 | 0.090 | 0.150 | -370 | 0.189 | 1.706 | 1218393 |

[a] The values of the shortwave albedos for *saturated* soil ($\alpha_{sat\Lambda}^{\mu} = \alpha_{sat\Lambda}$) are assigned as 0.11 for visible and 0.225 for near-infrared spectral bands, respectively. The values of the shortwave albedos for *dry* soil ($\alpha_{dry\Lambda}^{\mu} = \alpha_{dry\Lambda}$) are assigned as 0.22 for visible and 0.45 for near-infrared spectral bands, respectively.

[b] 92% sand, 3% clay.

[c] 81% sand, 7% clay.

[d] 42% sand, 18% clay.

[e] 20% sand, 60% clay.

### 3.8.1 Energy partition and soil water dynamics of a flat vegetated surface

The climate simulator parameterized for the location of Albuquerque (NM) (Chapter 2) is used in the following to force the hydrological simulations that assume August 1st as the starting date. To simplify the illustrative examples, rainless periods with zero cloudiness are assumed in all cases. The corresponding simulated time-series of the shortwave radiation are shown in Figure 3-8a. Another simplification is that the air temperature is simulated with $\delta T(t) = 0$ (Section 2.6.1), which results in smooth time-series (Figure 3-8b), and the dew point temperature is assumed to be constant $T_{dew} = 12.8 \,^{\circ}C$ (corresponding to 30-70% daily variability of humidity typical for the location of Albuquerque (NM) for the considered period). Furthermore, the wind speed is also assumed to be constant throughout the entire course of the simulation, $u_{atm} = 3 \, m \, s^{-1}$.

As an initial condition, it is assumed that a *loamy sand* soil column of 1.8 $m$ depth is completely saturated. Free drainage is assumed as the lower boundary flux condition (Appendix D) throughout the course of simulation. A flat horizontal element is considered, which is not affected by the lateral effects such as radiative shading, moisture transfer in the unsaturated zone, or runon.

Figures 3-8 - 3-11 show the simulation results for a surface vegetated with broadleaf deciduous trees that have LAI = 3.0, SAI = 0.75, $H_v = 5.0 \, m$, $d_{leaf} = 4.0 \, cm$, and vegetation fraction equal to one (i.e., trees occupy the entire area of the element and there is no bare soil). Vegetation structural attributes and the fractional area do not change within the simulation period. The root zone extends down to approximately 1 $m$ depth with the biomass distribution parameterized as in (3.1) and $\eta = 0.003046$ $mm^{-1}$. Water uptake properties, i.e., the soil matric potentials $\Psi^*$ and $\Psi_w$ [$MPa$] at which, respectively, the stomatal closure or plant wilting begins (Section 4.3) are taken as $\Psi^* = -0.5 \, MPa$ and $\Psi_w = -2.80 \, MPa$. Note that these values correspond to characteristic relative soil moisture values $\theta^*$ and $\theta_w$ [$mm^3 \, mm^{-3}$], respectively, used in the estimation of transpiration flux (formulation (4.17) of Section 4.4.1).
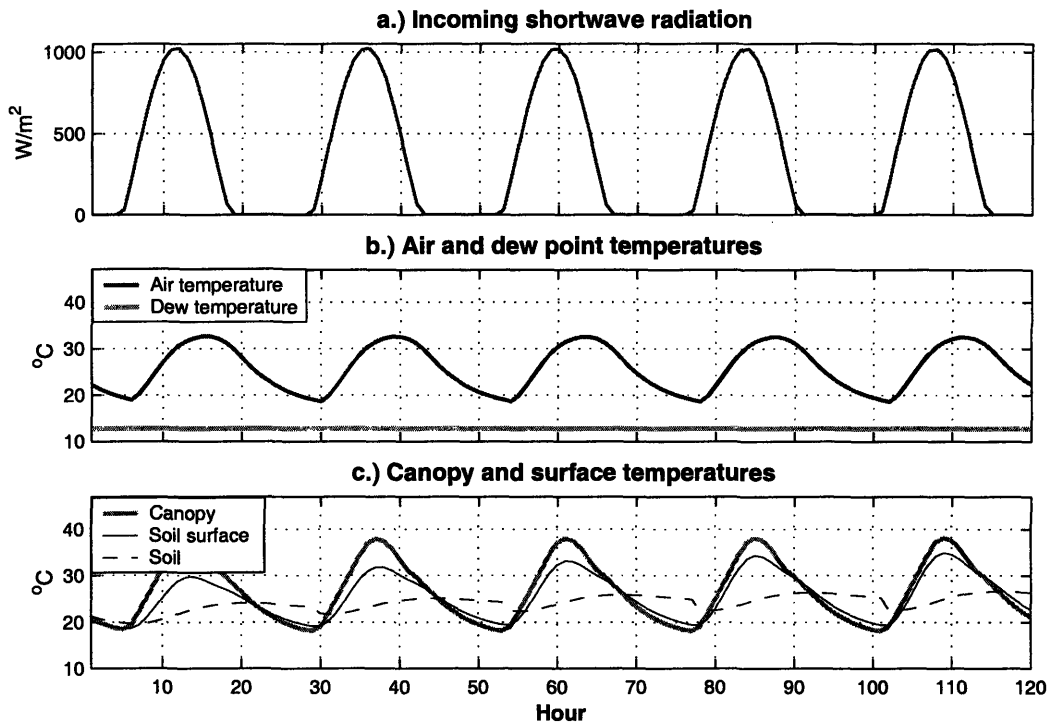
Figure 3-8: Time-series of synthetic hydrometeorological forcing: a.) global shortwave radiation and b.) air and dew point temperatures. Plot c.) illustrates temperatures of the tree canopy $T_v$ ("canopy"), soil surface $T_g$ ("soil surface"), and soil $T_{soil}$ ("soil") estimated from the energy balances.

The radiative transfer and the photosynthesis parameters, required for estimation of the canopy radiative fluxes (Section 3.5.2) and stomatal resistance (Section 4.4.1) are assigned according to a typical parameterization for broadleaf deciduous trees employed by most land-surface schemes (e.g., Sellers et al., 1996b). These values are provided for reference in Table 3.2.

The time-series of estimated canopy and soil surface temperatures that balance the canopy and ground surface energy budgets (Section 3.6.6) are shown in Figure 3-8c. As can be seen in the figure, the soil daily maximum temperatures exhibit a gradual increase throughout the simulation, while the daily course of the canopy temperature remains essentially unchanged. This is attributed to the differences in the dynamics of soil moisture at the ground surface and in the root zone as explained in the following.

As the soil gradually desaturates (Figure 3-9a), the evaporative fraction correspondingly decreases. While the transpiration flux experiences only a minor reduction over the considered period of time, the change in soil evaporation is more substantial and corresponds to a significant decrease of the surface soil moisture (Figure 3-9b - 3-9c).

Figure 3-10 illustrates all of the components of the canopy and ground surface energy balances. One may notice that the dense tree canopy intercepts most of the incoming shortwave radiation (Figure 3-10c) with relatively small fraction reaching the understory ground. This results in much lower magnitudes of net radiation at the ground surface (Figure 3-10b). The root zone is relatively wet throughout the simulation and the canopy day-light latent heat flux is therefore constantly high (mid-day depressions in the time series are attributed to the partial stomatal closure and will be explained later). Since vegetation exhibits some "leakage" conductance (attributed to the uncontrolled water loss through leaf cuticles, Section 4.4.1), the night-time latent heat flux is somewhat above zero. The soil surface layer quickly dries, which leads to a smaller latent heat flux and higher sensible heat flux as well as gradual heating of the surface (Figure 3-10a, f, g). The progressive desaturation of soil also leads to a reduction in the ground heat flux (Figure 3-10e).

Table 3.2: Vegetation biophysical, photosynthesis, and interception parameters. $\chi_L$ is the departure of leaf angles from a random distribution and equals $+1$ for horizontal leaves, 0 for random leaves, and $-1$ for vertical leaves, $\alpha_\Lambda^{leaf}$ and $\tau_\Lambda^{leaf}$ $[-]$ are the leaf reflectances and transmittances, respectively, $\alpha_\Lambda^{stem}$ and $\tau_\Lambda^{stem}$ $[-]$ are the stem reflectances and transmittances, respectively, "VIS" and "NIR" are used to denote the visible and near-infrared spectral bands, respectively, $V_{max\,25}$ $[\mu mol\ CO_2\ m^{-2}\ s^{-1}]$ is the maximum catalytic capacity of Rubisco at 25°C, $\bar{K}$ $[-]$ is the time-mean PAR extinction coefficient used to parameterize decay of nitrogen content in the canopy, $m$ $[-]$ is an empirical parameter used as a slope factor in (4.1), $b$ $[\mu mol\ m^{-2}\ s^{-1}]$ is the minimum stomatal conductance, $\epsilon_{3,4}$ $[\mu mol\ CO_2\ \mu mol^{-1}\ photons]$ is the intrinsic quantum efficiency for $CO_2$ uptake for $C_3$ and $C_4$ plants, $K_c$ $[mm\ hour^{-1}]$ is the canopy water drainage rate coefficient, $g_c$ $[mm^{-1}]$ is the exponential decay parameter of canopy water drainage rate, and $S_{la}$ $[m^2\ leaf\ area\ kg\ C^{-1}]$ is the specific leaf area.

| Parameter / PFT | Broadleaf deciduous tree | C$_4$ grass |
| --- | --- | --- |
| $\chi_L$ | 0.01 | -0.30 |
| $\alpha_\Lambda^{leaf}$ - VIS | 0.10 | 0.11 |
| $\alpha_\Lambda^{leaf}$ - NIR | 0.45 | 0.58 |
| $\alpha_\Lambda^{stem}$ - VIS | 0.16 | 0.36 |
| $\alpha_\Lambda^{stem}$ - NIR | 0.39 | 0.58 |
| $\tau_\Lambda^{leaf}$ - VIS | 0.05 | 0.07 |
| $\tau_\Lambda^{leaf}$ - NIR | 0.25 | 0.25 |
| $\tau_\Lambda^{stem}$ - VIS | 0.001 | 0.22 |
| $\tau_\Lambda^{stem}$ - NIR | 0.001 | 0.38 |
| $V_{max\,25}$ | 90.0 | 25.0 |
| $\bar{K}$ | 0.5 | 0.3 |
| $m$ | 9 | 4 |
| $b$ | 10,000 | 40,000 |
| $\epsilon_{3,4}$ | 0.08 | 0.053 |
| $K_c$ | 0.18 | 0.10 |
| $g_c$ | 3.9 | 3.2 |
| $S_{la}$ | 0.041 | 0.020 |

The simulated resistances, used to compute heat fluxes from the ground and canopy surfaces, are illustrated in Figure 3-11. The stomatal resistances, shown in Figure 3-11a for sunlit and shaded fractions of the canopy, are estimated using the biochemical model described in Section 4.4.1. As can be seen in the figure, the daily cycle of stomatal resistance exhibits a mid-day peak. This model behavior has been previously observed (Collatz et al., 1991) and is associated with partial stomatal closure caused by an increasingly high day-light time air moisture deficit ($T_{dew}$ is constant throughout the day) as well as significant shortwave irradiance of the leaves (Figure 3-10c). The increase in the stomatal resistance causes the mid-day depressions in the photosynthesis and latent heat flux (Figure 3-10g), experimentally observed in leaves (Beyschlag et al., 1986) and open canopies (Tan and Black, 1976; Campbell, 1989; Kinyamario and Imbamba, 1992). The decrease in the surface soil moisture leads to a high surface resistance to the ground latent heat flux (Figure 3-11d). An apparent cyclicity in the time-series is due to the day-time depletion of the surface moisture and night-time capillary rise that replenishes soil water in the surface layer.

Figures 3-12 - 3-15 illustrate the simulated dynamics for a surface vegetated with $C_4$ grass that has LAI = 3.0, SAI = 0.15, $H_v = 0.75\ m$, $d_{leaf} = 0.5\ cm$, and vegetation fraction equal to one (i.e., grass occupies the entire area of the element and there is no bare soil). The vegetation structural attributes and the fractional area do not change during the considered period of time. The root zone extends down to approximately 0.33 $m$ depth, with the biomass distribution parameterized as in (3.1) and $\eta = 0.009$ $mm^{-1}$. Water uptake properties, i.e., the soil matric potentials $\Psi^*$ and $\Psi_w$ [$MPa$] at which, respectively, the stomatal closure or plant wilting begins (Section 4.3) are taken as $\Psi^* = -0.1\ MPa$ and $\Psi_w = -4.0\ MPa$. As above, these values correspond to characteristic relative soil moisture values $\theta^*$ and $\theta_w$ [$mm^3\ mm^{-3}$], respectively, used in the estimation of transpiration flux (formulation (4.17) of Section 4.4.1). The radiative transfer and the photosynthesis parameters, required for estimation of the canopy radiative fluxes (Section 3.5.2) and stomatal resistance (Section 4.4.1) are assigned according to a typical parameterization for $C_4$ grass employed by most land-surface schemes. These values are provided for reference in Table 3.2.
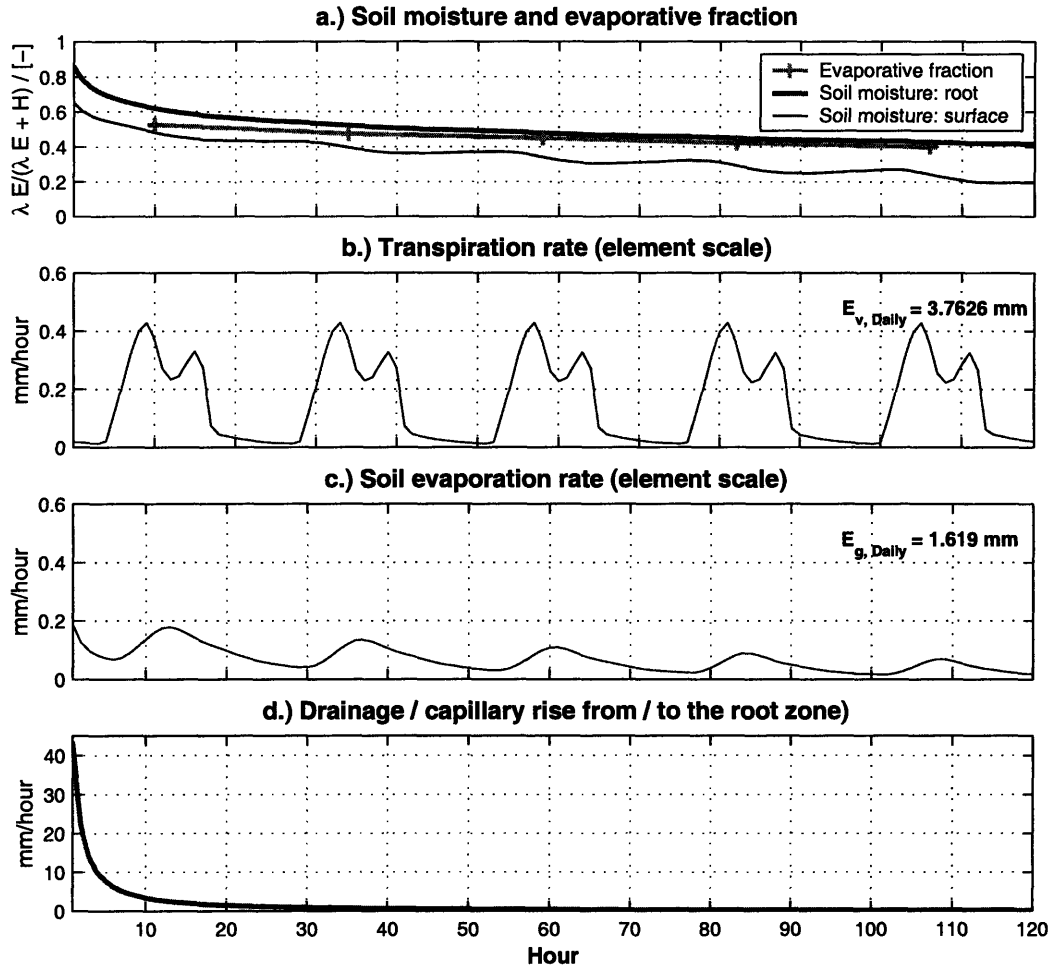
Figure 3-9: The simulated soil water contents, evaporative fraction, and moisture fluxes for an area vegetated with broadleaf deciduous trees: a.) surface $\theta_1$ and root zone $\theta_{root}$ soil moisture and evaporative fraction $\lambda E/(\lambda E + H)$; b.) transpiration rate $E_T^{veg}$; c.) under-canopy soil evaporation rate $E_g^{veg}$; d.) drainage from the root zone to deeper layers $Q_{D\,out}$. "$E_{v,\,Daily}$" and "$E_{g,\,Daily}$" are the mean values of daily transpiration and soil evaporation, respectively, over the considered period of time.
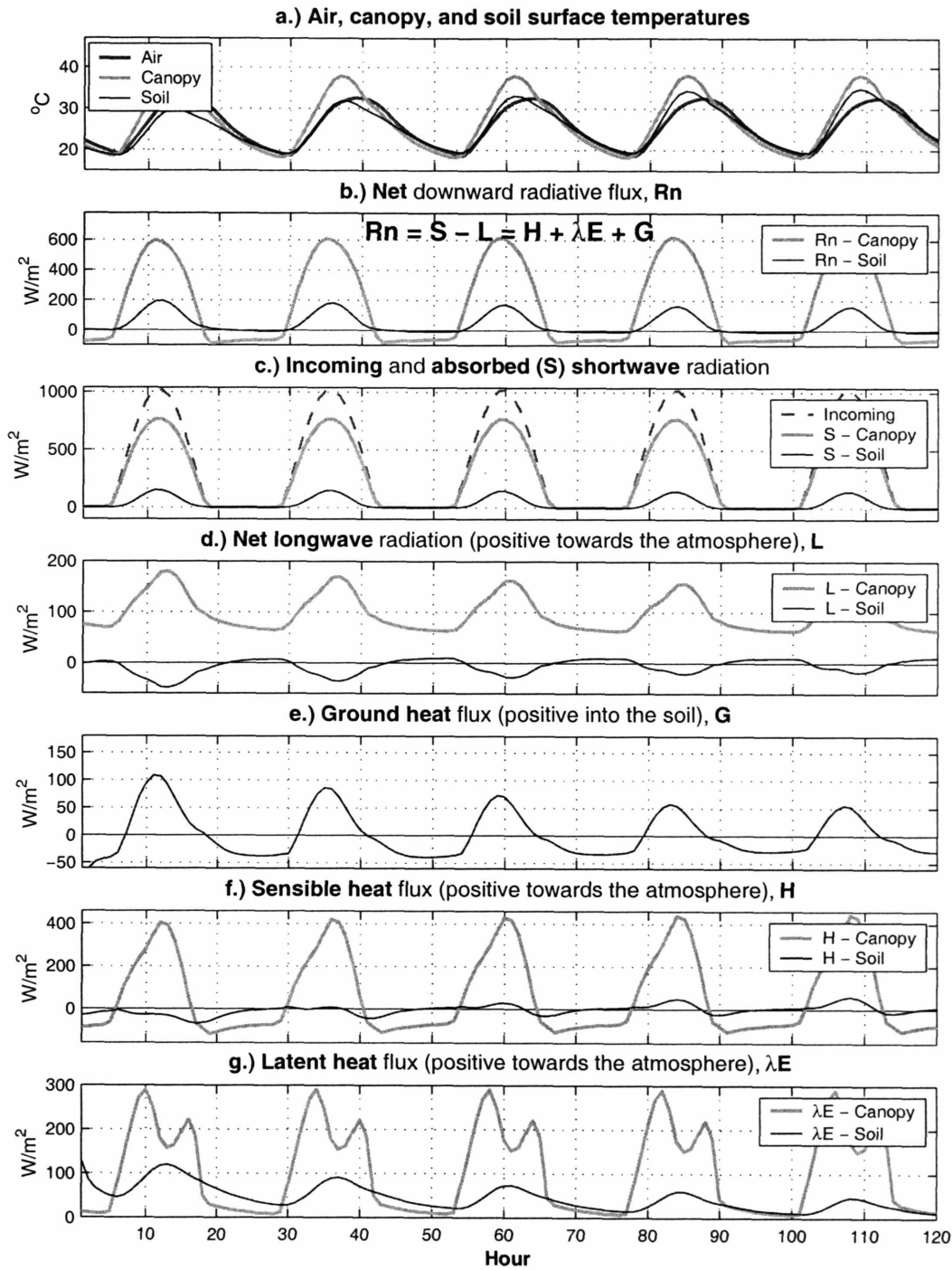
Figure 3-10: The simulated temperatures and components of canopy and ground surface energy budgets for an area vegetated with broadleaf deciduous trees: a.) air $T_{atm}$, canopy $T_v$, and soil surface $T_g$ temperatures; b.) net radiation ($R_{nv}$ and $R_{ng}$); c.) incoming global and absorbed shortwave radiation (($S_{atm}\downarrow_\Lambda^\mu +S_{atm}\downarrow_\Lambda$) and ($\vec{S}_v^{veg}$ and $\vec{S}_g^{veg}$)); d.) net longwave radiation ($\vec{L}_v^{veg}$ and $\vec{L}_g^{veg}$); e.) ground heat flux $G$; f.) sensible heat flux ($H_v^{veg}$ and $H_g^{veg}$); g.) latent heat flux ($\lambda E_v^{veg}$ and $\lambda E_g^{veg}$).

197
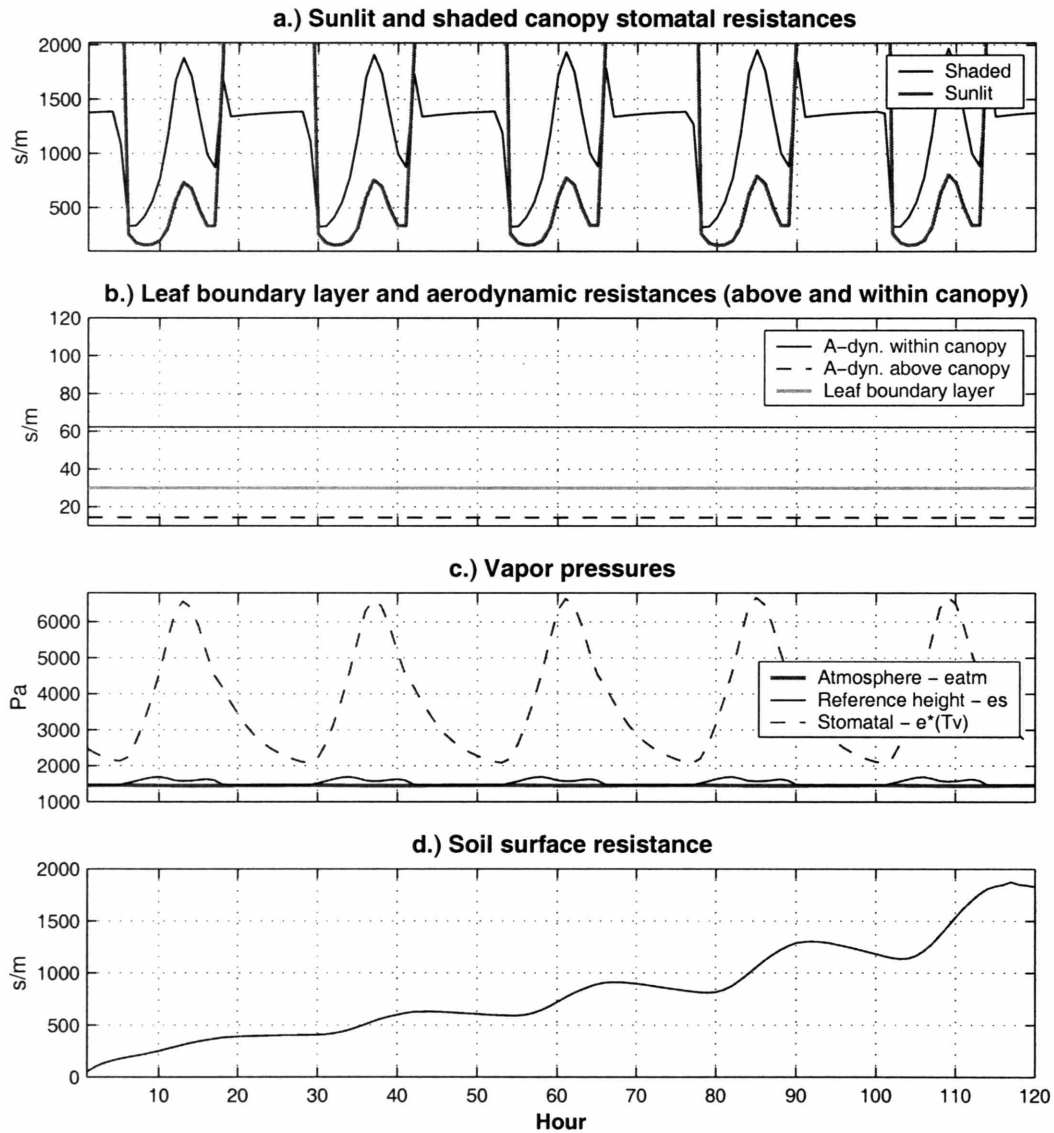
Figure 3-11: Vapor pressures and the simulated resistances used to estimate canopy and ground surface energy fluxes for an area vegetated with broadleaf deciduous trees: a.) sunlit and shaded canopy stomatal resistances ($r_s^{sun}$ and $r_s^{shd}$); b.) leaf boundary layer $r_b$ and aerodynamic resistances ($r_{ah}$ and $r'_{ah}$); c.) atmospheric $e_{atm}$, reference height $e_s$, and stomatal $e^*(T_v)$ water vapor pressures; d.) soil surface resistance $r_{srf}$.

Similar to Figure 3-8c, Figure 3-12c shows the time-series of the simulated grass canopy and soil surface temperatures that balance the corresponding energy budgets (Section 3.6.6). While the estimated canopy temperatures show essentially the same pattern as in Figure 3-8c, the understory ground temperatures exhibit a more significant increase of the daily amplitude. This is related to faster (relative to the previous case with broadleaf woody vegetation) drying of the soil surface as illustrated in Figure 3-13a. The more rapid depletion of the surface soil moisture is related to a higher amount of the shortwave radiation that reaches the ground surface and, as a result, the higher amount of the net radiation (Figures 3-14b - 3-14c). While both trees (discussed previously) and grass have the same amount of foliage biomass, i.e., the same LAI, the orientation of grass leaves is closer to the vertical (expressed through the parameter $\chi_L$), which leads to a smaller amount of radiation absorbed by the leaves and a higher amount of radiation penetrating through the canopy. As a result of the higher available energy for evaporation, combined with the higher fraction of the grass root biomass located in the soil top layers, the soil surface moisture is rapidly depleted.

The $C_4$ photosynthesis of grass does not lead to the same sensitivity of the latent heat flux to air humidity deficit and high shortwave irradiance as was the case of $C_3$ photosynthesis of trees. For approximately the same canopy temperature time-series (Figures 3-10a and 3-14a), the mid-day depressions are not observed in the time series of the grass latent heat flux (Figure 3-14g). The simulated stomatal resistances (Figure 3-15a) clearly have a different daily cycle exhibiting smaller sensitivity to the hydrometeorological conditions.

## 3.8.2 Sensitivity of energy partition to wind speed

Figures 3-16 - 3-17 illustrate the sensitivity of components of the canopy and understory ground energy budgets to wind speed that determines canopy aerodynamic and leaf boundary layer resistances ($r_{ah}$, $r'_{ah}$, and $r_b$). For each given wind speed value, ranging from 0.01 to 10.0 $m\ s^{-1}$, a 24-hour cycle of water-energy dynamics is simulated with the same hydrometeorological forcing as in simulations described in

**a.) Incoming shortwave radiation**

**b.) Air and dew point temperatures**

**c.) Canopy and surface temperatures**
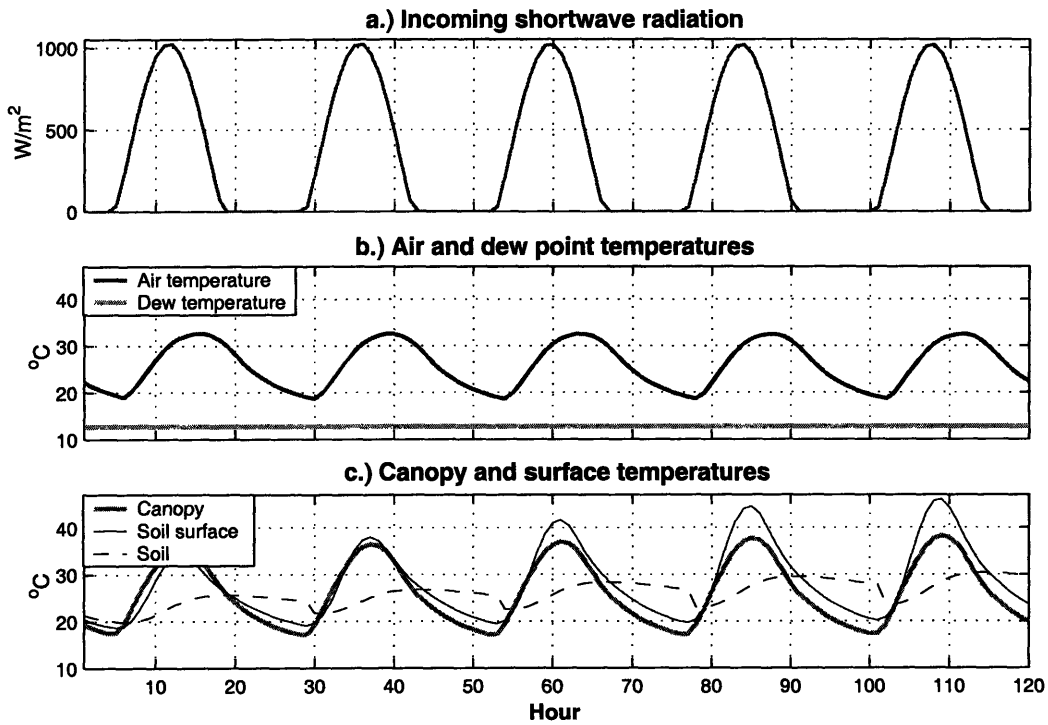
Figure 3-12: Time-series of synthetic hydrometeorological forcing: a.) global short-wave radiation and b.) air and dew point temperatures. The plot c.) illustrates temperatures of the $C_4$ grass canopy $T_v$ ("canopy"), soil surface $T_g$ ("soil surface"), and soil $T_{soil}$ ("soil") estimated from the energy balances.

200
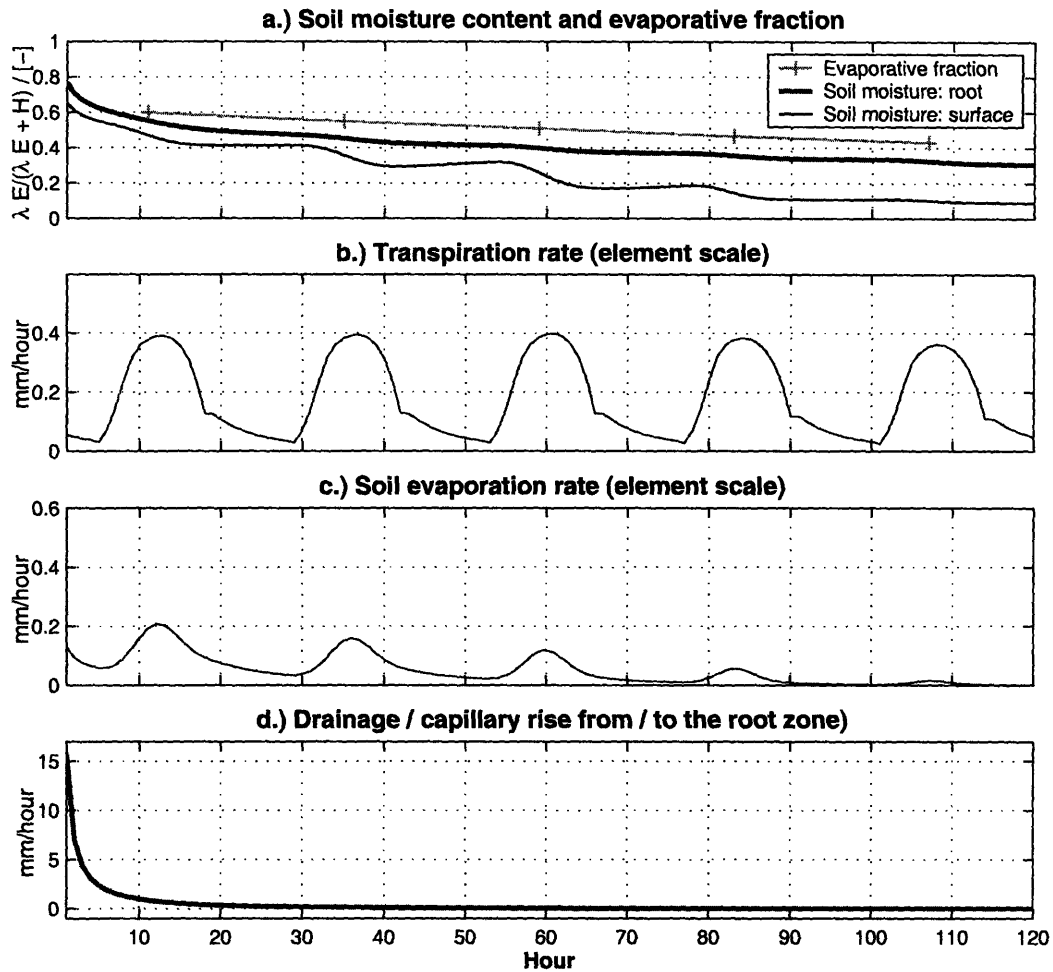
Figure 3-13: The simulated soil water contents, evaporative fraction, and moisture fluxes for an area vegetated with $C_4$ grass: a.) surface $\theta_1$ and root zone $\theta_{root}$ soil moisture and evaporative fraction $\lambda E/(\lambda E + H)$; b.) transpiration rate $E_T^{veg}$; c.) under-canopy soil evaporation rate $E_g^{veg}$; d.) drainage from the root zone to deeper layers $Q_{D\,out}$. "$E_{v,\,Daily}$" and "$E_{g,\,Daily}$" are the mean values of daily transpiration and soil evaporation, respectively, over the considered period of time.
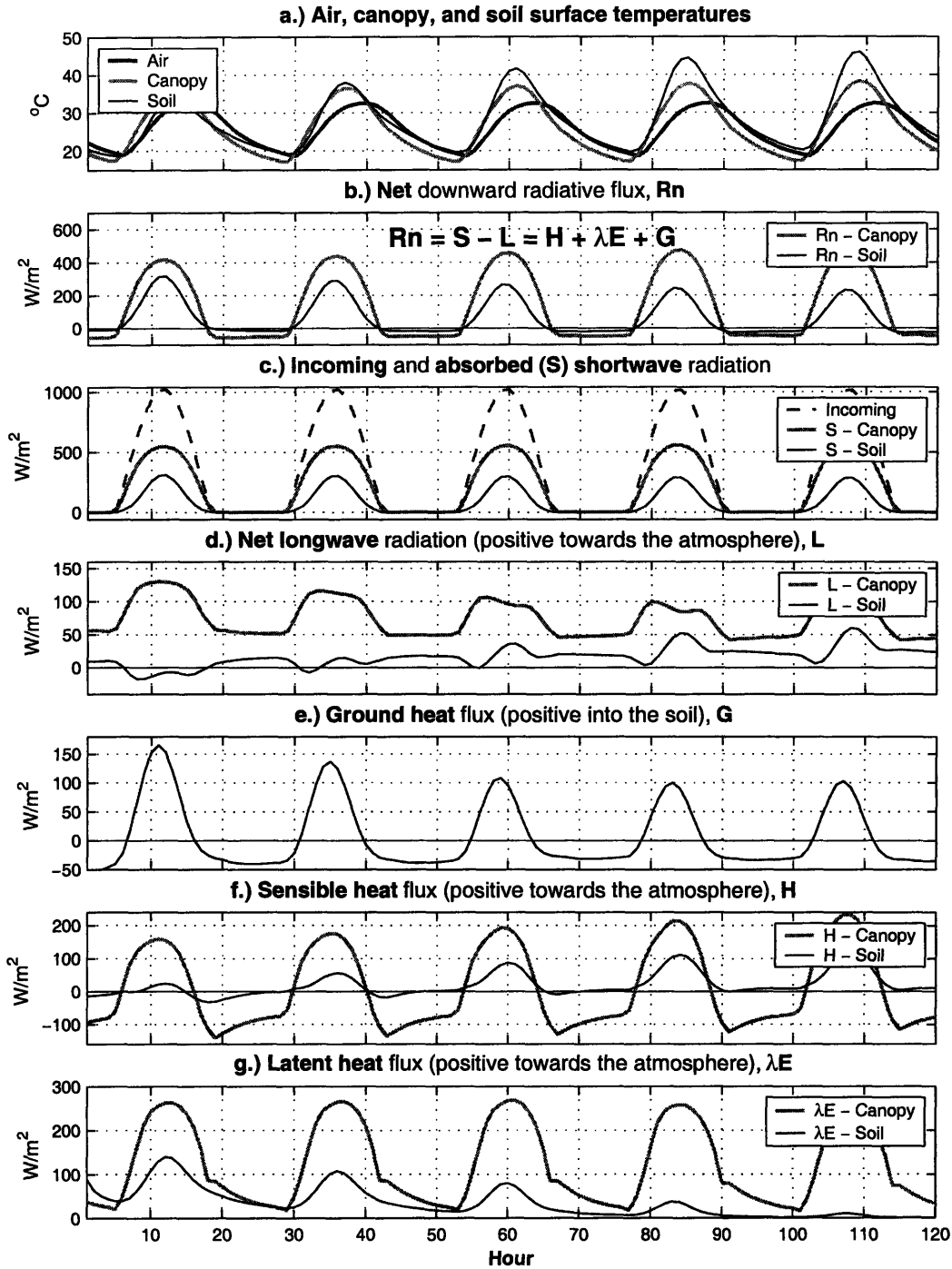
Figure 3-14: The simulated temperatures and components of canopy and ground surface energy budgets for an area vegetated with $C_4$ grass: a.) air $T_{atm}$, canopy $T_v$, and soil surface $T_g$ temperatures; b.) net radiation ($R_{n\,v}$ and $R_{n\,g}$); c.) incoming global and absorbed shortwave radiation (($S_{atm} \downarrow_\Lambda^\mu + S_{atm} \downarrow_\Lambda$) and ($\vec{S}_v^{veg}$ and $\vec{S}_g^{veg}$)); d.) net longwave radiation ($\vec{L}_v^{veg}$ and $\vec{L}_g^{veg}$); e.) ground heat flux $G$; f.) sensible heat flux ($H_v^{veg}$ and $H_g^{veg}$); g.) latent heat flux ($\lambda E_v^{veg}$ and $\lambda E_g^{veg}$).
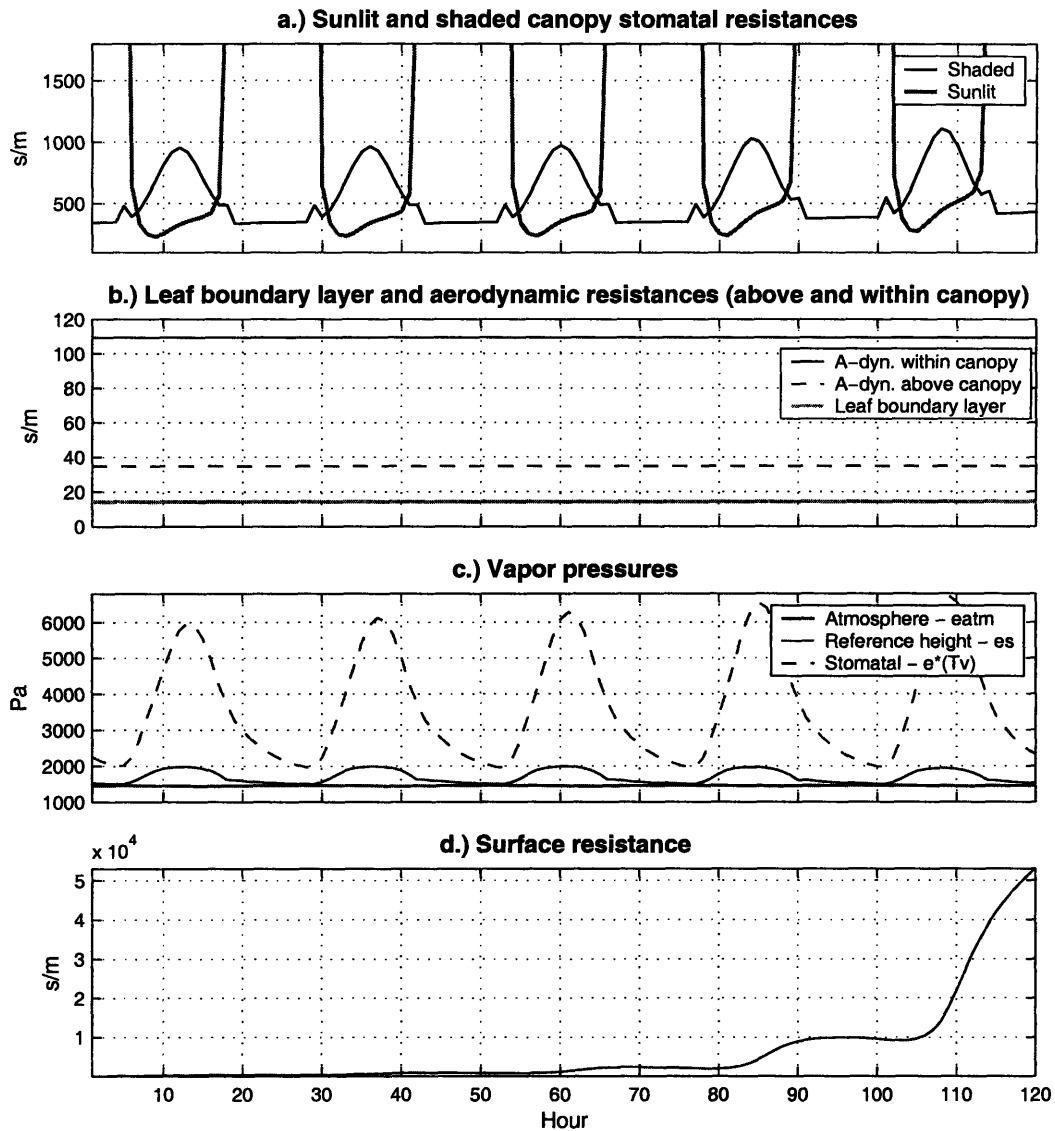
Figure 3-15: Vapor pressures and the simulated resistances used to estimate canopy and ground surface energy fluxes for an area vegetated with $C_4$ grass: a.) sunlit and shaded canopy stomatal resistances ($r_s^{sun}$ and $r_s^{shd}$); b.) leaf boundary layer $r_b$ and aerodynamic resistances ($r_{ah}$ and $r'_{ah}$); c.) atmospheric $e_{atm}$, reference height $e_s$, and stomatal $e^*(T_v)$ water vapor pressures; d.) soil surface resistance $r_{srf}$.

Section 3.8.1. The only difference in conditions for the considered example is that the soil profile is artificially kept saturated throughout the entire simulation. This ensures that the simulated latent heat fluxes are not soil-water limited. Soil is parameterized as a generic loamy sand soil type (Table 3.1). Plots on the left side refer to the quantities estimated for canopy, while plots on the right side refer to the understory ground quantities.

According to Section 3.6.3, wind speed determines which physical mechanism dominates in the transfer of the sensible heat and latent heat fluxes away from a surface. It is assumed that **free convection** is the dominant mechanism in calm, windless conditions with $u_{atm} < 1.0 \ m \ s^{-1}$. As can be observed in Figure 3-16, in these conditions the tree canopy temperature (Figure 3-16d) grows significantly during the day-light hours resulting in high longwave radiative flux (Figure 3-16c) with the sensible heat flux as the primary component of the energy budget (Figure 3-16b). For these windless conditions, a mid-day depression develops during the daily course of the latent heat flux, as a result of partial stomatal closure (Figure 3-16a). The energy partition for the understory ground surface depends on the radiative fluxes of the canopy through the net longwave radiation (Section 3.6.2). Since the canopy emits the longwave flux of high magnitude, the latter strongly affects the amount of available energy at the soil surface. This leads to the net longwave flux directed into soil during the day time (negative values in Figure 3-16g). The resulting available energy is partitioned into the latent heat (Figure 3-16e) and ground heat (not shown) fluxes, with negligible sensible heat flux.

The highly turbulent, windy conditions lead to **forced convection** as the dominant mechanism of the heat transfer. As the magnitude of wind speed grows from 1.0 to 10.0 $m \ s^{-1}$, both the latent heat and sensible heat fluxes become the largest components of the canopy energy budget. In the range of wind speeds 5-10 $m \ s^{-1}$ (Figure 3-16a - 3-16b), the daily courses of both fluxes experience only a minor change when compared for different wind speed values. The day time canopy temperature nears the air temperature. In the case of understory soil, strong wind conditions lead to the radiative cooling of the surface (the ground temperature drops below the air

temperature) and sensible heat flux becomes negative. Figure 3-16e illustrates that in these artificial conditions the latent heat flux is very efficient as a mechanism of removing available energy from the soil surface and grows significantly with decreasing canopy aerodynamic resistances (increasing wind speed).

Figure 3-17 presents the results of a similar simulation for an area vegetated with $C_4$ grass. The same forcing and simulation setting are assumed. Features of the energy partition for the **free convection** conditions are somewhat different from the previous case: growth of the canopy temperature leads to very high values of the latent heat flux (Figure 3-17a), which becomes the primary component of the energy balance. Correspondingly, the canopy temperature does not grow as high and the sensible heat flux and the longwave radiation are not as significant as in the case of the surface vegetated with trees. Same features can be observed for the under-canopy ground surface as for the case discussed above (surface vegetated with trees): the latent heat flux is the principal component of the energy budget, with the net longwave flux directed into the soil. In the case of **forced convection**, the day-time latent heat flux dominates the canopy energy budget with relatively small sensitivity for values of the wind speed exceeding 5 $m$ $s^{-1}$. As in the above example of surface vegetated with trees, strong wind conditions lead to radiative cooling of the soil surface and highly efficient latent heat flux.

### 3.8.3 Soil moisture dynamics

Figures 3-18 - 3-20 illustrate the estimation of the soil moisture vertical profiles and drainage from the root zone for generic loamy sand (Figure 3-19) and clay (Figure 3-20) soils (the hydraulic parameters are provided in Table 3.1). As the initial condition, it is assumed that both soil columns (loamy sand and clay) are relatively dry at a uniform -0.242 $MPa$ tension pressure throughout the 1.8 $m$ depth of the profile. Free drainage is assumed as the boundary condition at the bottom of the soil profile (Appendix D) throughout the course of simulation. A flat horizontal element is considered, which is not affected by the lateral effects such as radiative shading, moisture transfer in the unsaturated zone, or runon.

205
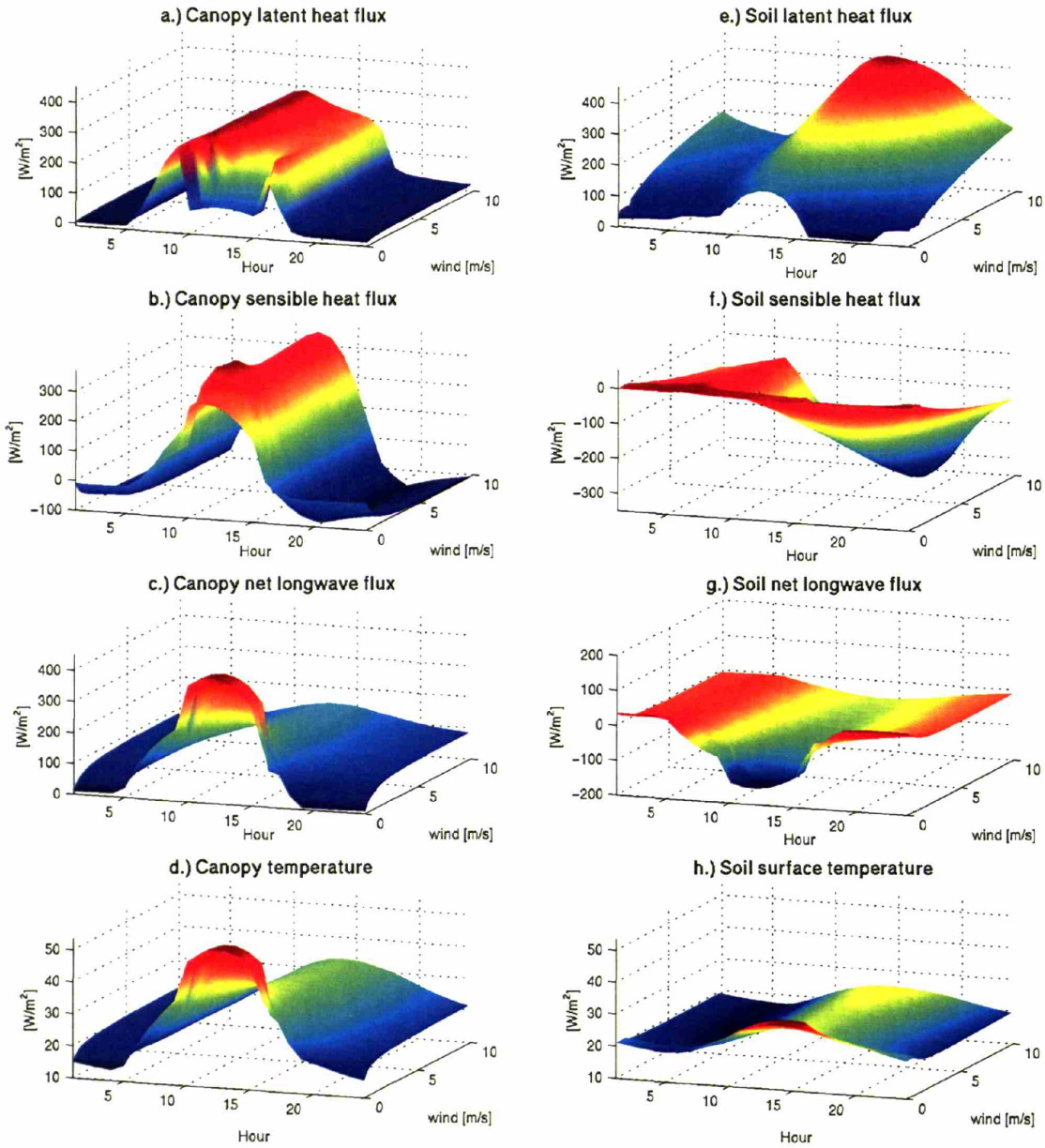
Figure 3-16: An illustration of sensitivity of the energy partition and simulated temperatures to wind speed for an area vegetated with broadleaf deciduous trees: a.) canopy latent heat flux $\lambda E_v^{veg}$; b.) canopy sensible heat flux $H_v^{veg}$; c.) canopy net longwave flux $\vec{L}_v^{veg}$; d.) canopy temperature $T_v$; e.) under-canopy soil latent heat flux $\lambda E_g^{veg}$; b.) under-canopy soil sensible heat flux $H_g^{veg}$; c.) under-canopy soil net longwave flux $\vec{L}_g^{veg}$; d.) ground surface temperature $T_g$.
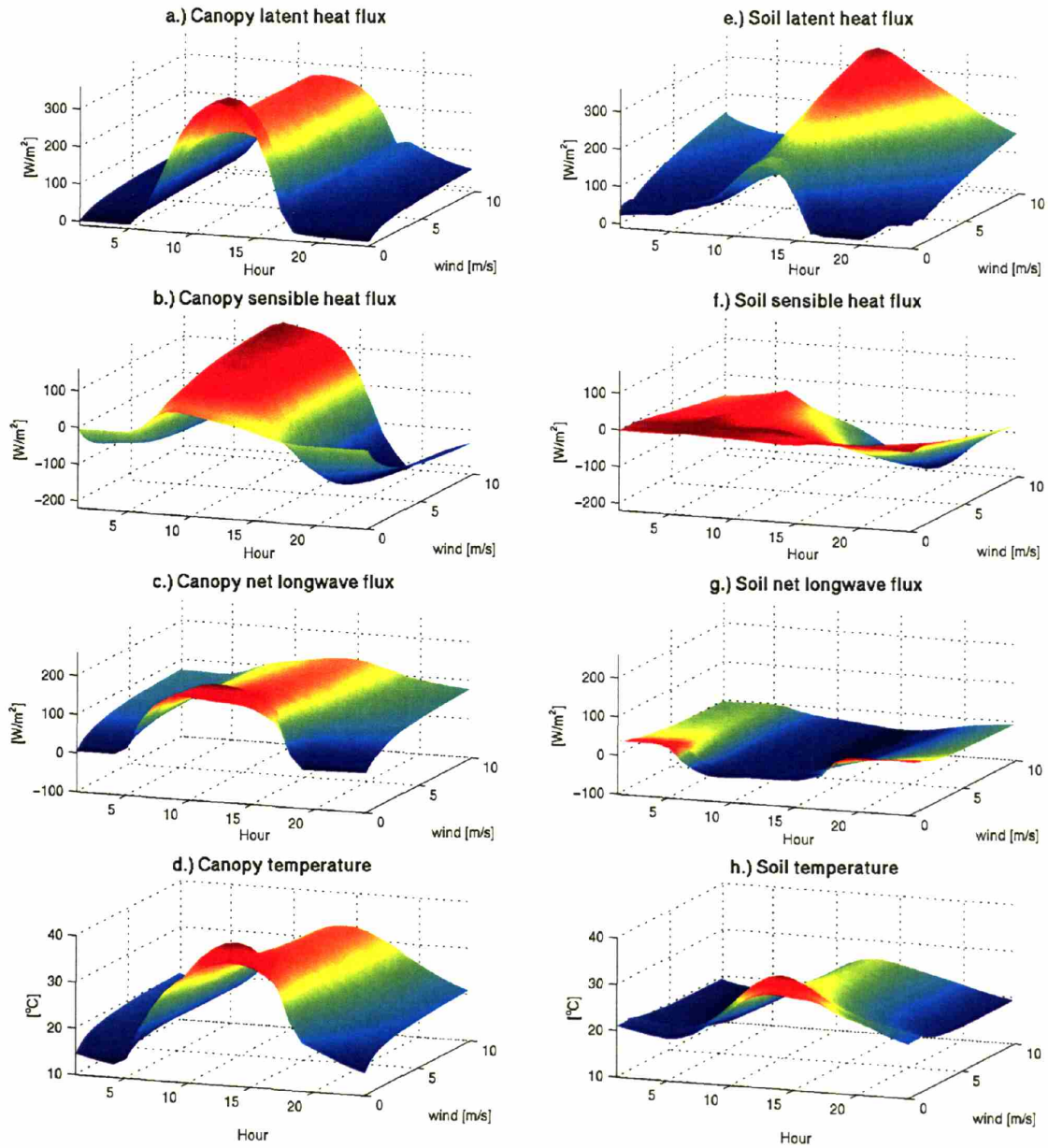
Figure 3-17: An illustration of sensitivity of the energy partition and simulated temperatures to wind speed for an area vegetated with $C_4$ grass: a.) canopy latent heat flux $\lambda E_v^{veg}$; b.) canopy sensible heat flux $H_v^{veg}$; c.) canopy net longwave flux $\vec{L}_v^{veg}$; d.) canopy temperature $T_v$; e.) under-canopy soil latent heat flux $\lambda E_g^{veg}$; b.) under-canopy soil sensible heat flux $H_g^{veg}$; c.) under-canopy soil net longwave flux $\vec{L}_g^{veg}$; d.) ground surface temperature $T_g$.

207

For both soil type cases, the actual record of hydrometeorological observations for Albuquerque (NM) is used to force the simulations, with June 10th, 1991 as the starting date. Note, however, that the rainfall rates were artificially amplified by a factor of $\sim 5$ to ensure substantial amounts of infiltration volume. The first 72 hours of the time-series illustrated in Figure 3-18 are used in the following examples.

Figures 3-19 - 3-20 show the simulation results for a surface vegetated with broadleaf deciduous trees. The latter are parameterized in exactly the same manner as described in Section 3.8.1 and Table 3.2. The structural attributes of vegetation and the fractional area do not change during the considered period of time.

Instantaneous moisture profiles for *loamy sand* soil type are shown in Figure 3-19b - 3-19c for different simulation times. The first rainfall event leads to the soil surface saturation and subsequent runoff generation (Figure 3-19e). The redistribution period (hours 15-35), which follows the first rainfall event, leads to an elongation of the wetted profile and evapotranspiration depleting soil water from the entire wetted portion of the soil column (the root zone extends down to 1 $m$ depth). The second rainfall event leads to a second wetted wedge building up on the moisture profile from the first precipitation event. Both the surface and root zone soil moisture contents change substantially during the considered period of time (Figure 3-19d). The infiltration moisture wave reaches the bottom of the root zone at hour 45, after which water slowly diffuses to deeper soil layers (Figure 3-19e). One may notice, that the drainage from the root zone is delayed by the amount of time required for the moisture wave to travel through the entire rooting depth, determined by both the soil hydraulic properties and the magnitude of co-occurring evapotranspiration outflux. This contrasts conventional parameterizations used in the "bucket"-type vegetation-hydrology models that diffuse soil water from the root zone immediately after the soil reaches its field capacity.

Instantaneous moisture profiles for *clay* soil type are shown in Figure 3-20b - 3-20c for different simulation times. Since the soil's infiltration capacity is strongly limited (Table 3.1), a significant amount of runoff is generated (Figure 3-20e) and the moisture wave does not propagate far from the soil surface. Consequently, the soil

water is more readily available for evaporation. The corresponding changes in the root zone soil water content are small. Since the considered period of time is relatively short, the moisture wave does not reach the root zone bottom, which implies zero losses to drainage.

### 3.8.4 Effects of topography on subsurface water exchange

A synthetic domain is constructed to illustrate the effects of topography on lateral soil water redistribution. Four contributing elements are sloped at the same angle towards a receiving element, which is flat (i.e., has zero inclination, Figure 3-21). Four various angle magnitudes are considered: $10°$, $20°$, $30°$, and $40°$. As the initial condition, it is assumed that all soil columns are relatively dry at a uniform -0.242 $MPa$ tension pressure throughout the 1.8 $m$ depth of the profile. During the entire course of the simulation, free drainage is assumed as the boundary condition at the bottom of soil profiles of all elements, the lateral drainage in the unsaturated zone is estimated for the contributing elements, and lateral influx is computed for the receiving element as the sum of all subsurface influxes. The water-energy dynamics simulation setting as well as the vegetation parameterization are assumed to be the same as in Section 3.8.3. The entire period of hydrometeorological observations illustrated in Figure 3-18 is used in the following examples.

Figure 3-22 illustrates the time-series of the root zone (1-$m$ deep) soil moisture content for broadleaf deciduous trees on loamy sand soil. As can be seen in the figure, there is a pronounced effect of slope magnitude on differences in the root zone soil moisture between the contributing and receiving elements. The time scale, at which these differences are significant, is also a function of slope of the contributing elements. For *isotropic* soil ($a_r = 1$, Figures 3-22a - 3-22d), the shallow slopes of $10°$ - $20°$ have a relatively small effect in the considered semi-dry environment, even for the considered high infiltration volumes. The most substantial difference in the magnitude and duration is apparently observed for $\alpha_\nabla = 40°$. The effect of soil *anisotropy* is shown in Figures 3-22e - 3-22h. As can be observed, the considered soil anisotropy leads to much more pronounced changes in the root zone moisture, both
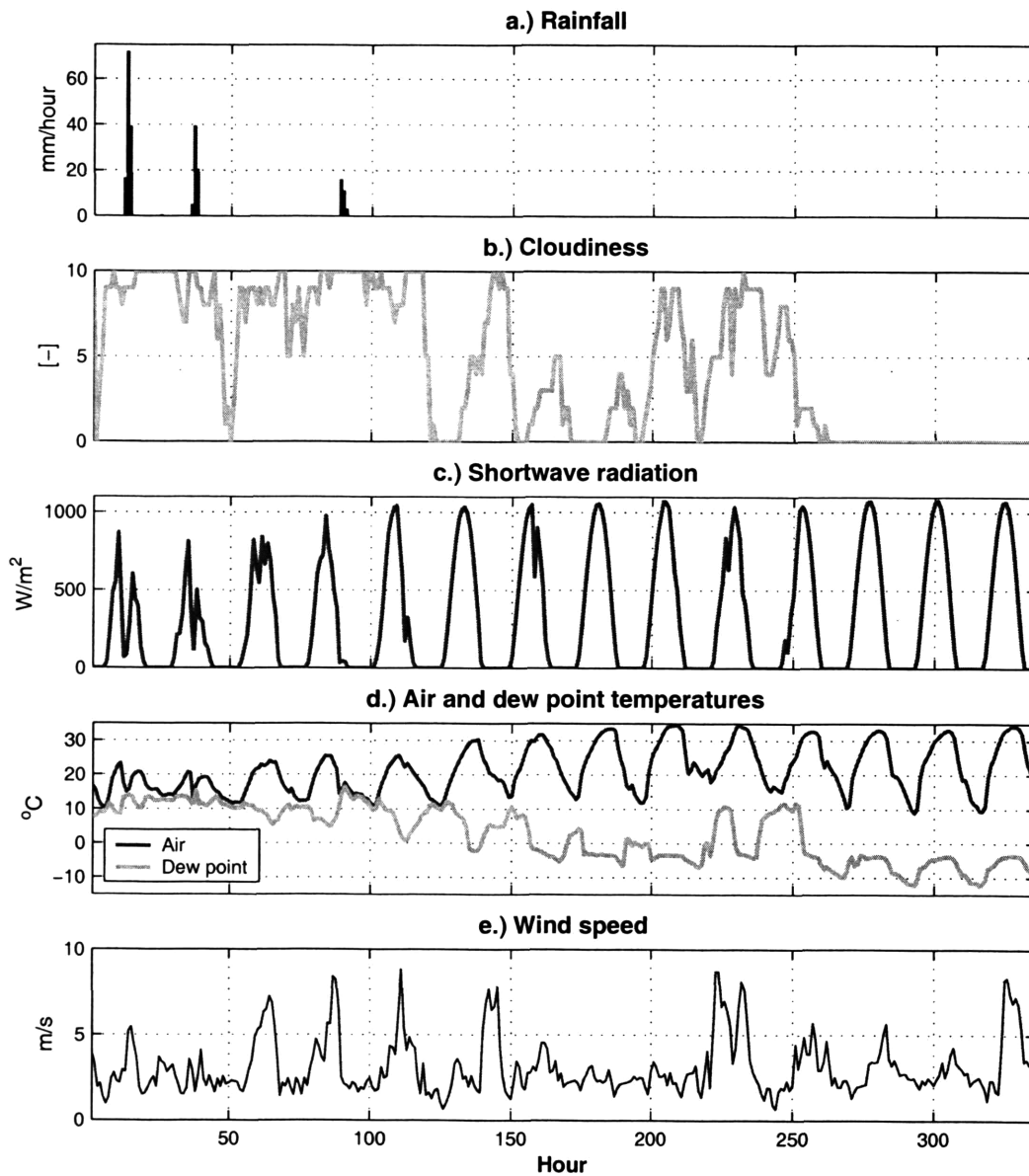
Figure 3-18: Hydrometeorological observations for Albuquerque (NM), with June 10th, 1991 as the starting date. Note that the rainfall rates are artificially amplified by a factor of ~ 5: a.) rainfall rate; b.) cloudiness; c.) global shortwave radiation; d.) air and dew point temperatures; e.) wind speed.
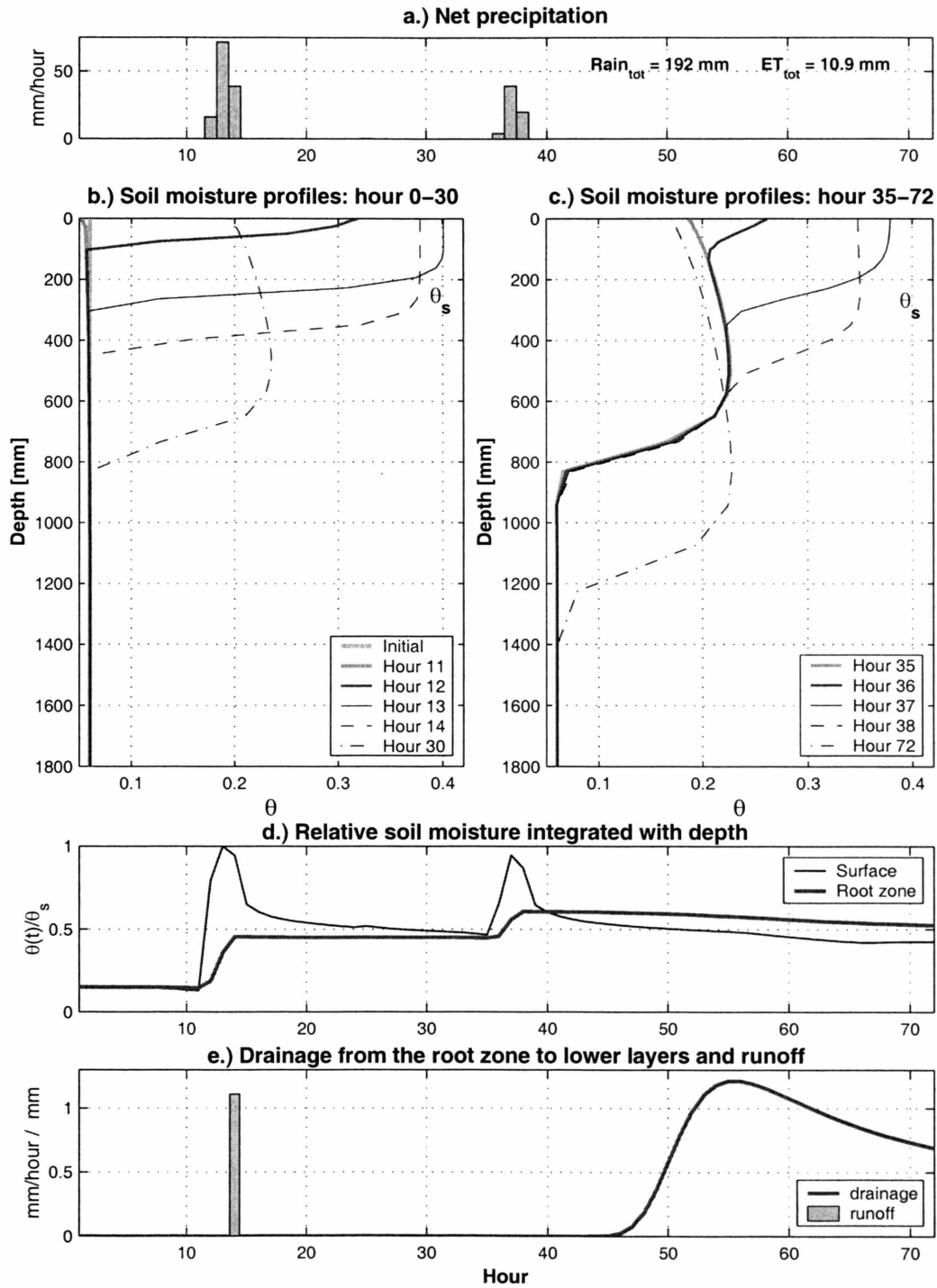
Figure 3-19: Soil moisture dynamics and drainage from the root zone for *loamy sand* soil (surface is vegetated with broadleaf deciduous trees): a.) net precipitation (rainfall less interception losses); b.) instantaneous soil moisture profiles for hour 0 - 30; c.) instantaneous soil moisture profiles for hour 35 - 72; d.) relative soil moisture content at the surface and root zone; e.) drainage from the root zone to lower soil layers and runoff.
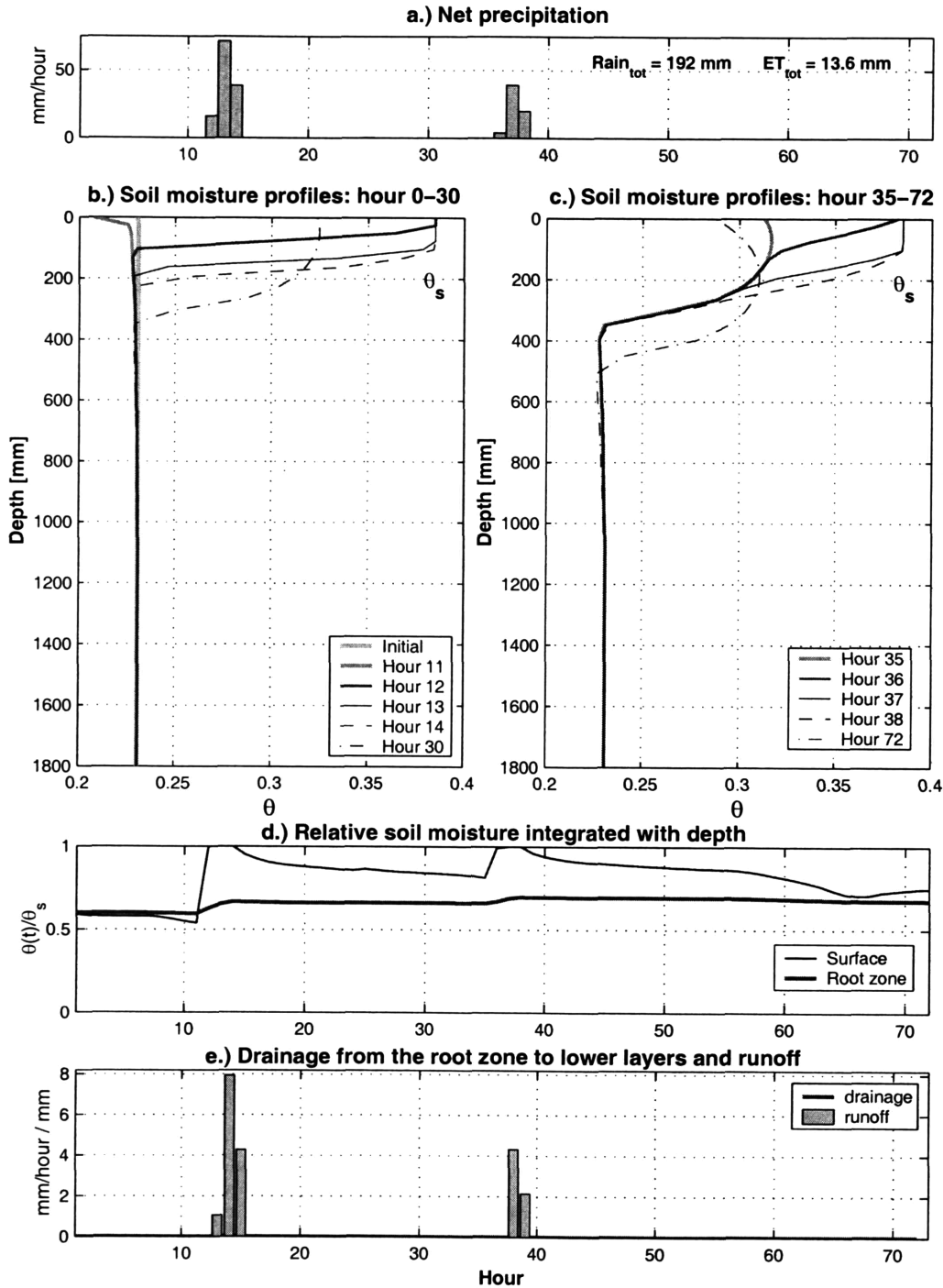
Figure 3-20: Soil moisture dynamics and drainage from the root zone for *clayey* soil (surface is vegetated with broadleaf deciduous trees): a.) net precipitation (rainfall less interception losses); b.) instantaneous soil moisture profiles for hour 0 - 30; c.) instantaneous soil moisture profiles for hour 35 - 72; d.) relative soil moisture content at the surface and root zone; e.) drainage from the root zone to lower soil layers and runoff.
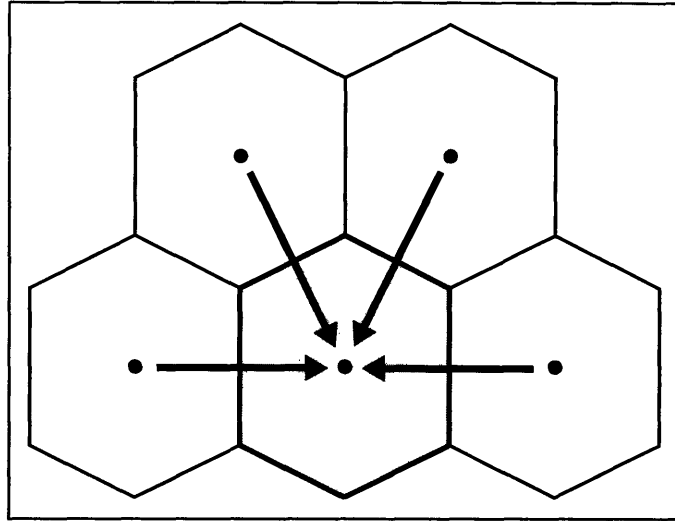
Figure 3-21: An illustration of a synthetic domain used in the experiments on lateral moisture transfer in the unsaturated zone. Four Voronoi elements (the empty polygons) are sloped at the same angle towards one element (the shaded polygon). The former are the *contributing* elements, while the latter is the *receiving* element located in the convergent area. The arrows indicate directions of the surface and subsurface flow. The circles are the centers of the Voronoi polygons.

in the contributing and receiving elements. The rapid lateral drainage of soil water from the sloped elements leads to quick accumulation of water in the downstream receiving element. The direct implication of these dynamics is the higher magnitude and a prolonged period of substantial difference in the soil water content between the receiving and contributing elements.

Figures 3-23 - 3-25 illustrate the time-series of the root zone ($0.33\text{-}m$ deep) soil moisture content for $C_4$ grass on clayey, loamy, and sandy soils, respectively. For clayey soil, that has small saturated hydraulic conductivity, the effect of slope is only pronounced for the case of high soil anisotropy (Figures 3-23f - 3-23h) that leads to somewhat higher root moisture content in the receiving element. Similar results can be observed for loamy soil in Figure 3-24, where in the isotropic case the slope angle of the contributing elements leads to visible differences only for $\alpha_\nabla = 40°$.

For shallow rooted grass in sandy soil, the assumptions made in the model result in an opposite to the previously considered behavior. For high rainfall amount and, therefore, significant lateral fluxes in highly conductive sandy soil, the root moisture

213

of the receiving element is about the same or even somewhat smaller than that of the contributing elements (Figures 3-25d - 3-25h). Figure 3-26 illustrates the soil moisture profiles for hours 30, 37, 70, 150 corresponding to the simulation shown in Figure 3-25d. As the figure shows, at the early stages of infiltration (e.g., hour 30), the wetted wedge of the receiving element in a far more developed state and contains substantially more moisture than the contributing element. This profile is more elongated and has less moisture in the soil surface layers where the grass root zone is located. Two combined effects lead to this result. Firstly, an increase of moisture content in the soil matrix leads to a non-linear growth of the unsaturated hydraulic conductivity (equation (3.106)), which implies a more rapid advancement of the wetting front and, therefore, elongation and thinning of the wetted wedge. Secondly, the subsurface influx is added to a receiving element in accordance with its profile of the hydraulic conductivity, which attempts to mimic the preferential pathflows in the soil slab (Appendix D.2). With evapotranspiration depleting the soil water store of surface layers and moisture located mostly in deeper layers (e.g., Figure 3-26), this leads to further growth of both the moisture content and the unsaturated conductivity in soil's deeper horizons. The simulation effect explained above can only occur in the conditions of very conductive soil, substantial rainfall amount, and significant lateral moisture transfer in the unsaturated zone.

### 3.8.5    Lateral water exchange through runon

The following examples employ the same simulation setting as described in the material of preceding sections. Since clayey soil has the smallest saturated conductivity, it would lead to the highest local runoff/runon production and, therefore, is used for illustrative purposes. Both broadleaf deciduous trees and $C_4$ grass vegetation types are used in the subsequent simulations.

The simple runon scheme, introduced in Section 3.7.2, implies adding runoff generated in upstream cells as an additional influx at the soil's surface. In the considered synthetic domain (Figure 3-21), all four contributing elements produce runoff during the rainfall events of high intensity. The total of runoff instantaneous values is ac-
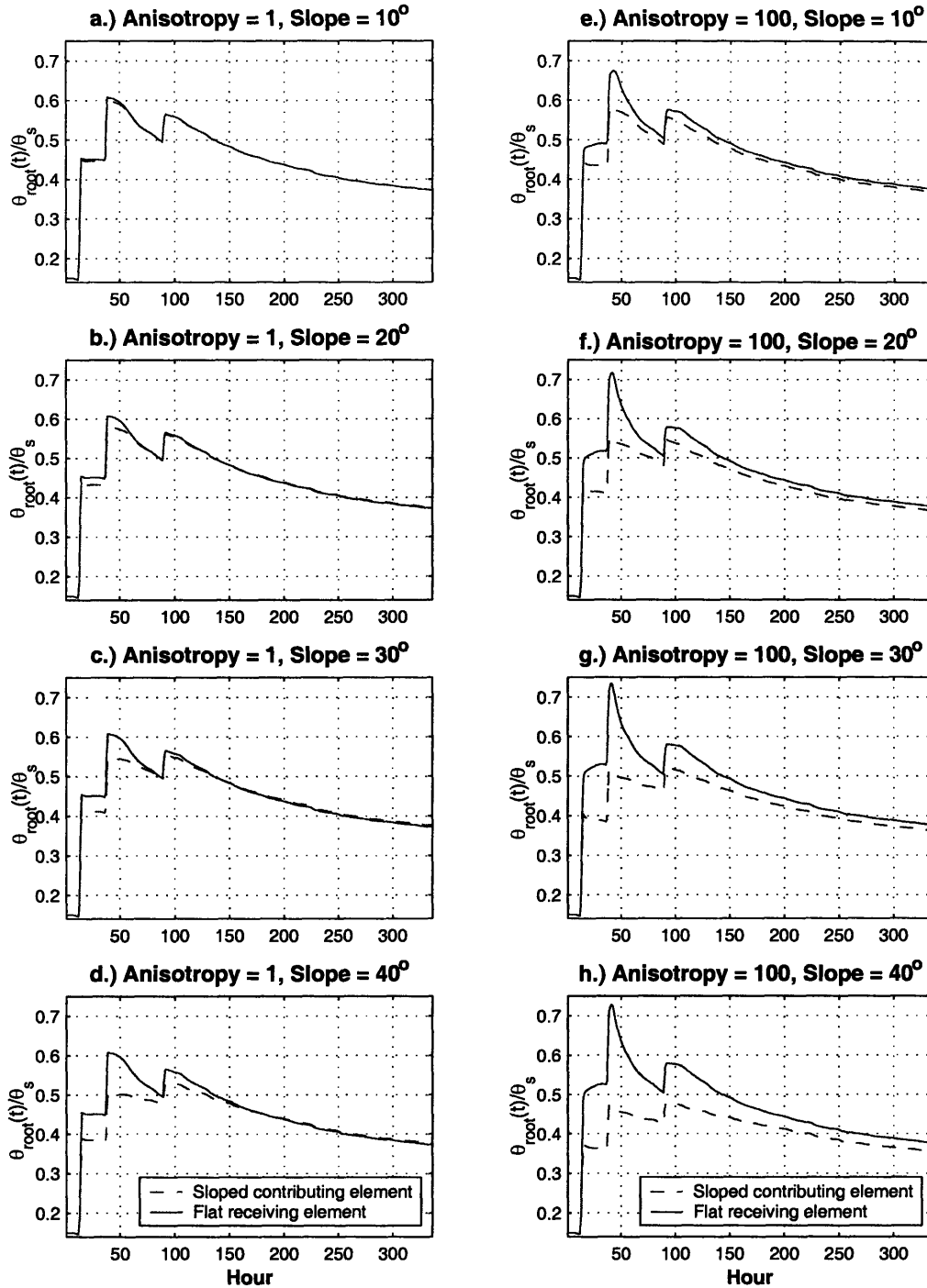
Figure 3-22: The time-series of the relative root zone soil moisture content for broadleaf deciduous trees on *loamy sand* soil. Only one *contributing* and the downslope *receiving* elements are illustrated. Four slope angle magnitudes are considered for the contributing elements: $\alpha_{\nabla} = 10°$, $20°$, $30°$, and $40°$. Two soil anisotropy (Section 3.7.3) values are used: $a_r = 1$ (the left column of plots, a-d) and $a_r = 100$ (the right column of plots, e-h).

215
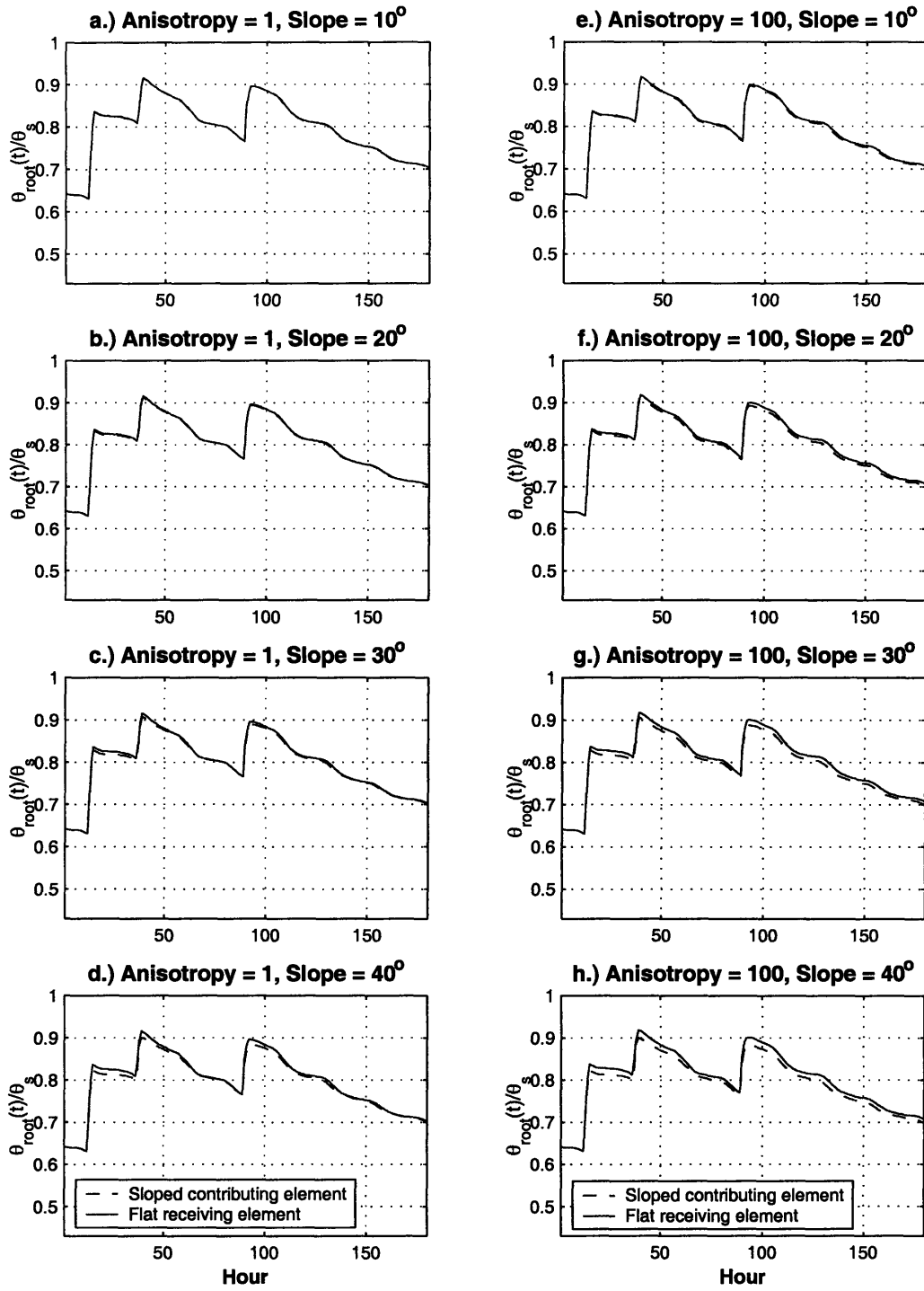
Figure 3-23: The time-series of the relative root zone soil moisture content for $C_4$ grass on *clayey* soil. Only one *contributing* and the downslope *receiving* elements are illustrated. Four slope angle magnitudes are considered for the contributing elements: $\alpha_\triangledown = 10°$, $20°$, $30°$, and $40°$. Two soil anisotropy (Section 3.7.3) values are used: $a_r = 1$ (the left column of plots, a-d) and $a_r = 100$ (the right column of plots, e-h).
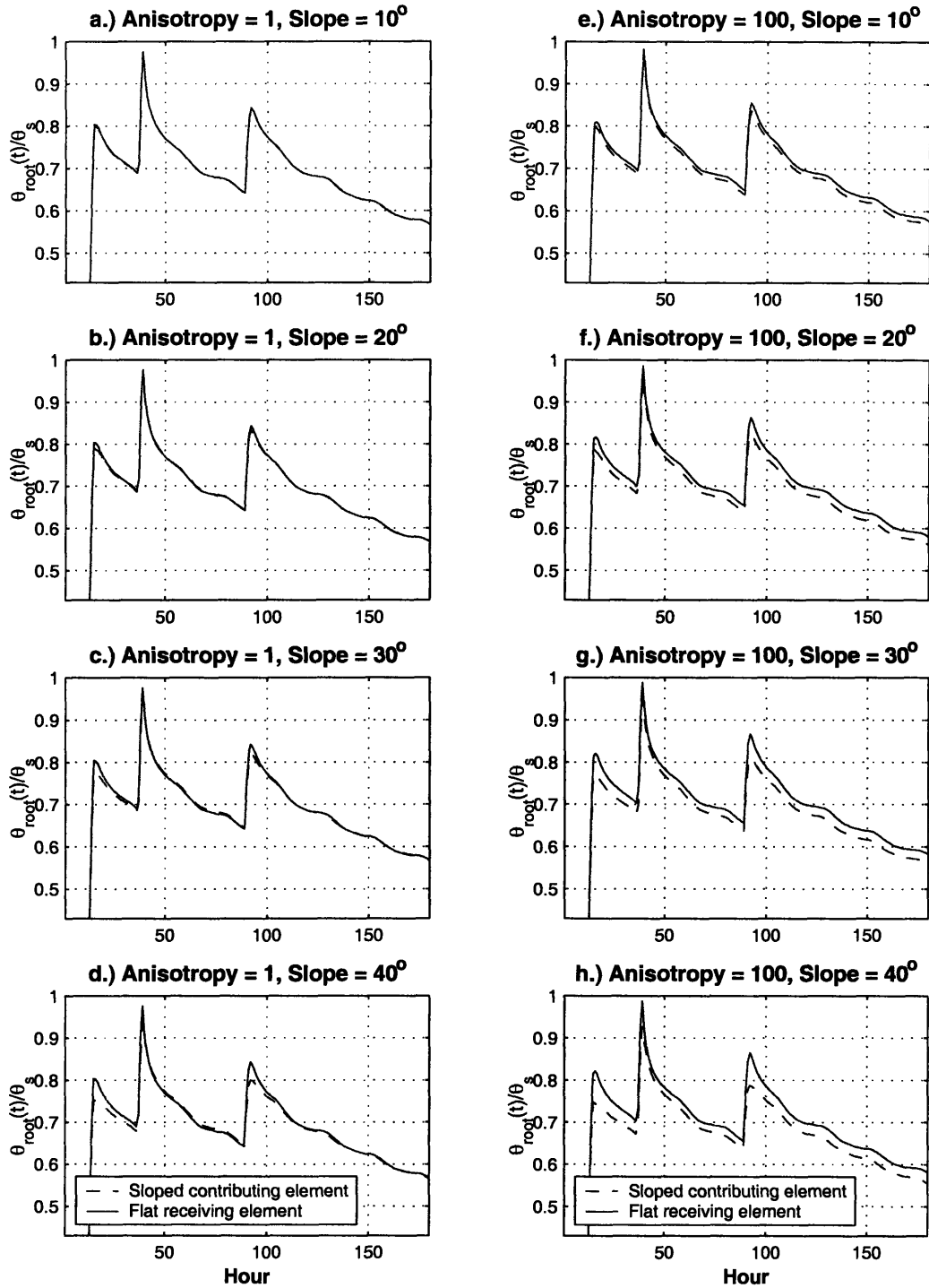
Figure 3-24: The time-series of the relative root zone soil moisture content for $C_4$ grass on *loamy* soil. Only one *contributing* and the downslope *receiving* elements are illustrated. Four slope angle magnitudes are considered for the contributing elements: $\alpha_\nabla = 10°$, $20°$, $30°$, and $40°$. Two soil anisotropy (Section 3.7.3) values are used: $a_r = 1$ (the left column of plots, a-d) and $a_r = 100$ (the right column of plots, e-h).
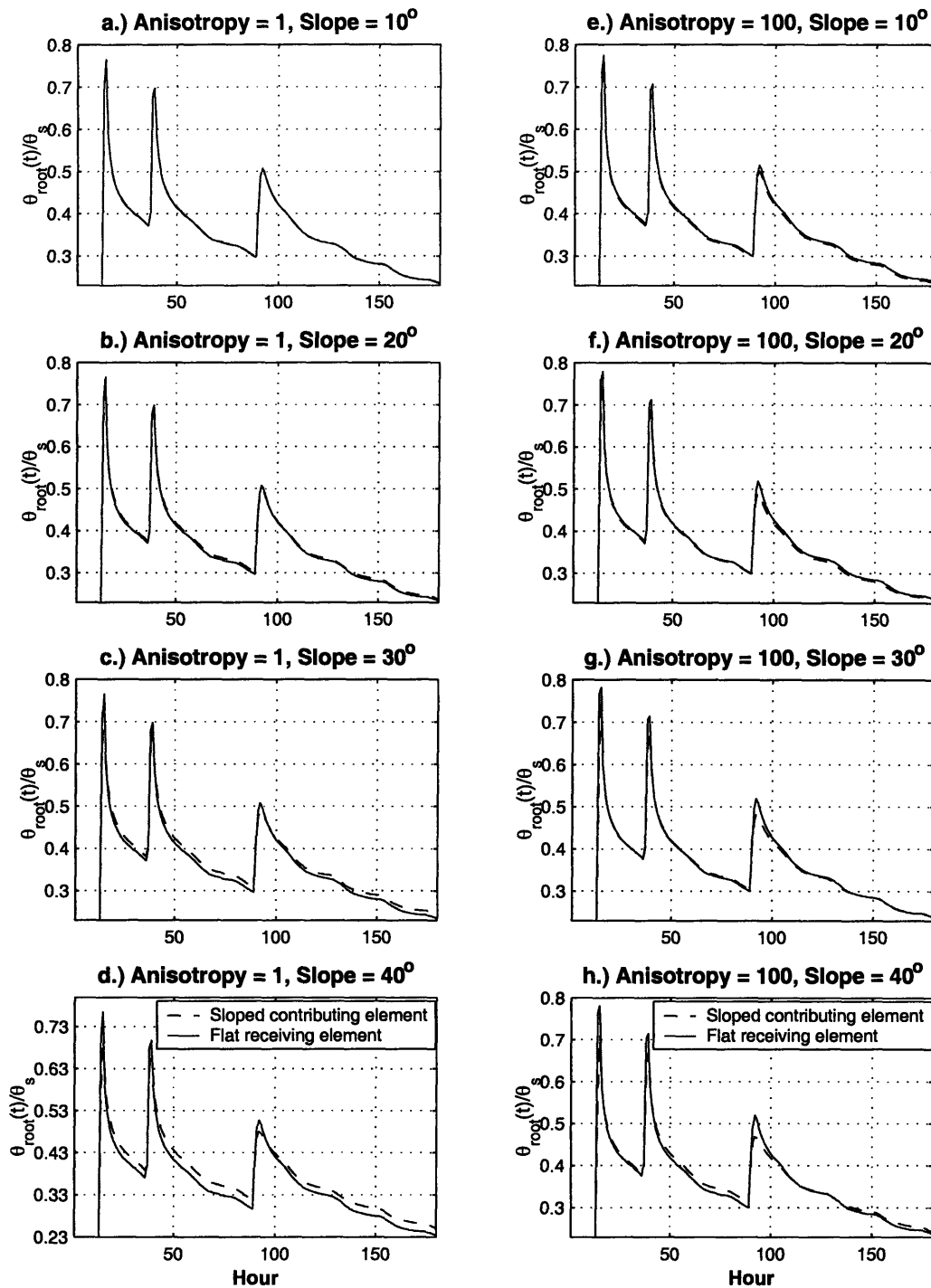
Figure 3-25: The time-series of the relative root zone soil moisture content for $C_4$ grass on *sandy* soil. Only one *contributing* and the downslope *receiving* elements are illustrated. Four slope angle magnitudes are considered for the contributing elements: $\alpha_\nabla = 10°$, $20°$, $30°$, and $40°$. Two soil anisotropy (Section 3.7.3) values are used: $a_r = 1$ (the left column of plots, a-d) and $a_r = 100$ (the right column of plots, e-h).

counted for as the influx onto surface of the receiving element (Figure 3-27a, 3-27c). The runon can re-infiltrate in the receiving element or can be added to its runoff and move to another downslope element. In the examples, runon results in higher root zone moisture throughout the entire simulation for both the contributing and receiving elements in comparison to a case with no runon (Figure 3-27b, 3-27d). This example is an additional illustration of how topography may facilitate water redistribution in the terrain, creating more permanent zones of higher moisture storage.

## 3.9 Summary

This chapter discusses a coupled model of energy and water budgets for both vegetated and non-vegetated surfaces that can be simultaneously present within a given element. The dynamics of each computational element are simulated separately. Spatial dependencies are introduced by considering the surface (runoff-runon) and subsurface (in the unsaturated zone) moisture transfers among the elements, which affect the local dynamics via the coupled energy-water interactions. Soil effects are accounted for by parameterizing the thermal and hydraulic properties that depend on soil's sand and clay content. Soils also differ in color, which is reflected in the values of soil albedo.

The framework explicitly considers the morphological and biophysical differences among multiple vegetation types that can be present within a given element. A variety of biophysical (canopy radiative transfer, energy budget, etc.) and hydrological (rainfall interception, infiltration, runoff production and runon, etc.) processes are considered. It is assumed that vegetated surfaces can be comprised of multiple *plant functional types* that differ in life form (tree, shrub, grass), vegetation physiology (e.g., leaf optical properties, stomatal physiology, leaf photosynthetic characteristics) and structural attributes (e.g., height, leaf dimension, roughness length, root profile). Each patch, while co-occurring in the same Voronoi element, constitutes a separate column upon which energy and water calculations are performed. Accordingly, differences in plant properties strongly affect estimation of the surface fluxes. Fractional
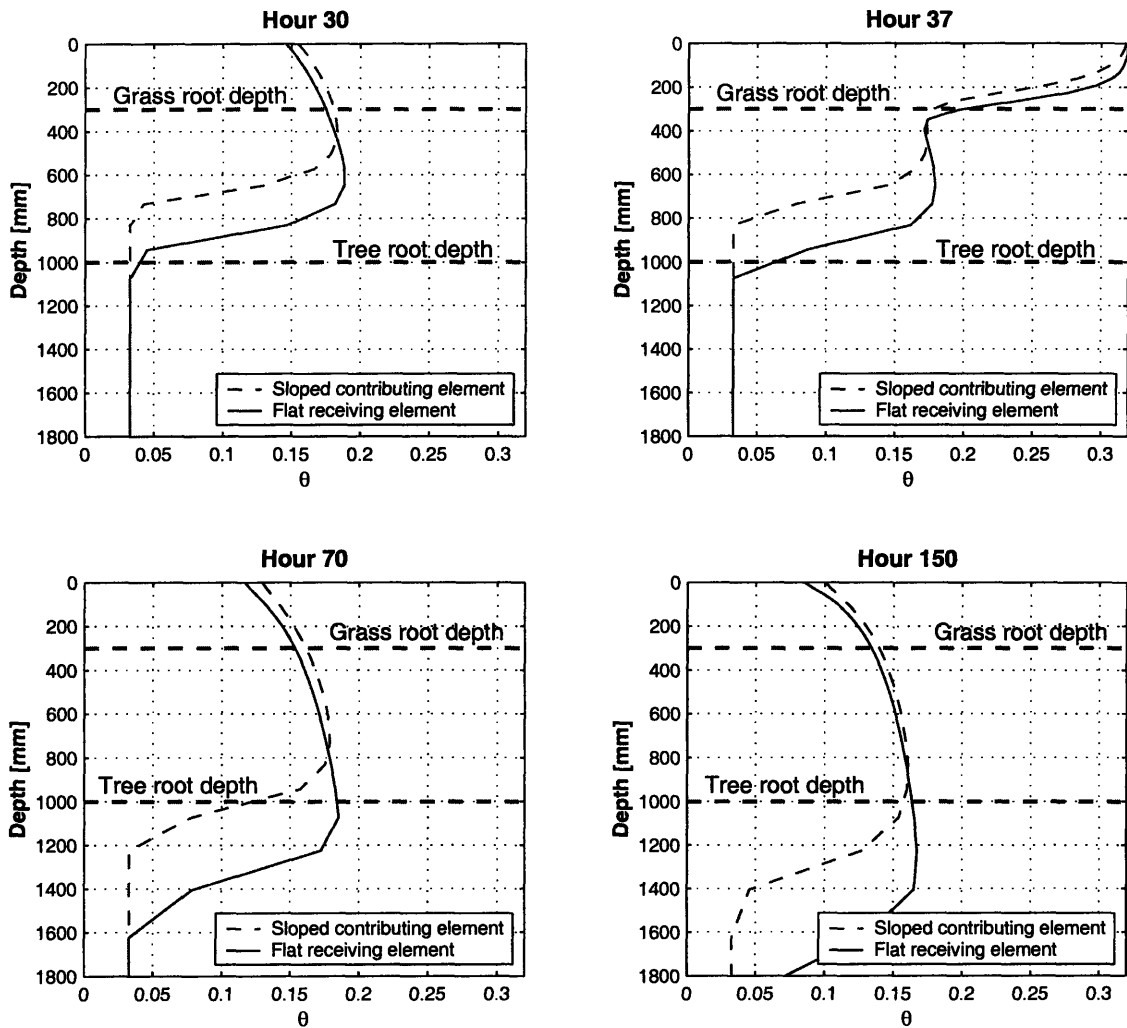
Figure 3-26: The soil moisture profiles of the contributing and receiving elements for hours 30, 37, 70, and 150 of simulation shown in Figure 3-25d: $C_4$ grass on *sandy* soil, $a_r = 1$, all contributing elements are sloped at an angle $\alpha_\nabla = 40°$. The dashed lines show the grass and tree maximum root depth.
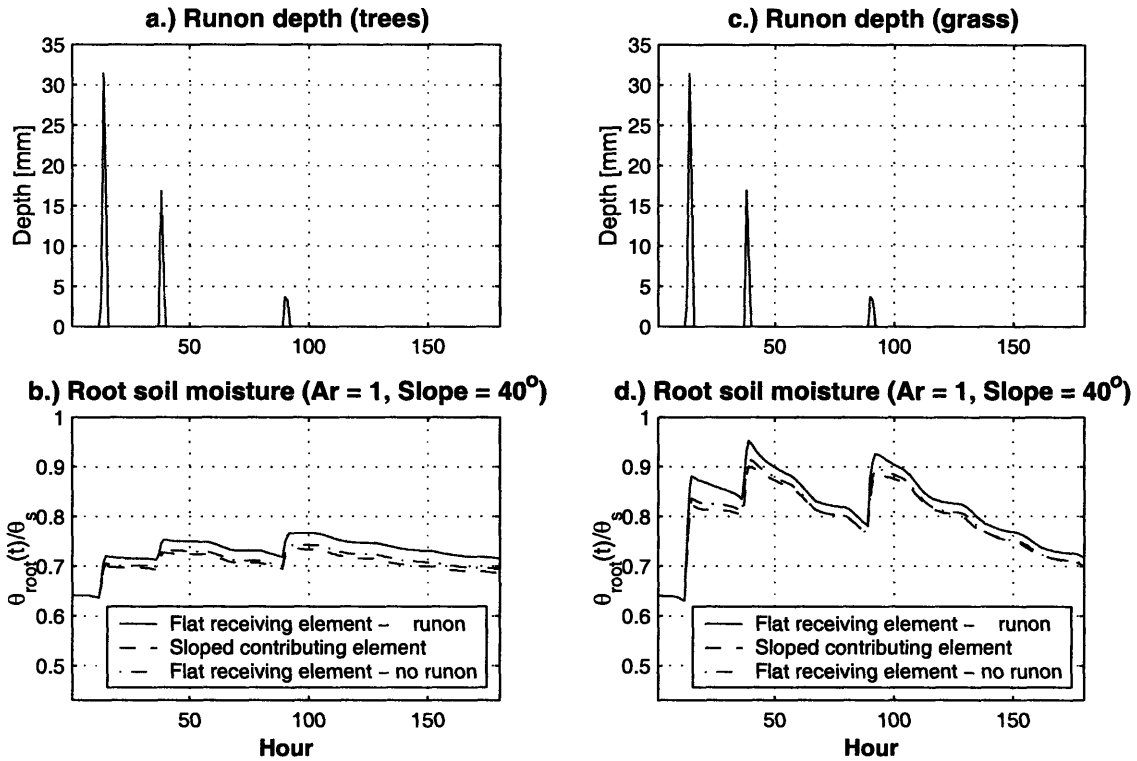
Figure 3-27: An illustration of effect of the runon process on vegetation-hydrology dynamics for isotropic *clayey* soil: runon depth and root zone soil moisture for broadleaf deciduous trees (plots a, b) and $C_4$ grass (plots c, d). All contributing elements are sloped at $\alpha_\nabla = 40°$ angle.

areas that represent vegetated patches and bare soil are used to weight the relative contribution of each PFT/bare soil to the element-scale flux values.

Vegetation characteristics (e.g., leaf and stem areas and canopy, height, and fractional area) are treated in this chapter as the *time-invariant*, prescribed quantities. A detailed discussion of the simulation framework that allows one to dynamicly update these vegetation attributes is provided in the following Chapter 4.

# Chapter 4

# Model of Vegetation Dynamics

## 4.1 Introduction

The developed model simulates the transient response of vegetation to hydrome-
teorological forcing and moisture redistribution in a natural system. A mechanistic
approach is used to describe major life regulatory vegetation processes. This provides
a consistent means for exploring the various biophysical and biochemical linkages that
relate different components of the vegetation development cycle. The model utilizes
the concept of an "average" individual residing in a given computational element as-
sociated with a particular landscape location. In order to represent the differences
among various plants, the model is designed to operate with general life forms or,
in a more detailed way, with *plant functional types* (PFT). However, the presented
mechanistic approach can be readily extended to describe actual vegetation species.

## 4.2 Model overview

A variety of "fast" vegetation processes that update states and fluxes at an *hourly*
time scale are represented in the model:

**Biochemical processes**

- photosynthesis and primary productivity (Section 4.4.1);

223

- stomatal physiology (Section 4.4.1);

- plant respiration (Section 4.4.2);

- tissue turnover and stress-induced foliage loss (Section 4.4.3);

- carbon allocation (Section 4.4.4);

- vegetation phenology (Section 4.4.7);

- plant recruitment (Section 4.4.5).

At the *hourly* time scale, the stomatal response to environmental conditions is the only vegetation process that affects the water and energy budgets estimated using the model of Chapter 3. At the *daily* time scale, vegetation affects state of the land-surface through the change of its structural attributes (such as leaf area index and height) and vegetation fraction (Section 4.4.8). The latter determines the relative contribution of a given PFT to the element-scale fluxes, as discussed in Chapter 3. Although several vegetation types can be present within the same computational element with common hydrometeorological forcing and soil water status, the equations formulated in the following refer to the *vegetation fraction* scale only, i.e., they operate on an individual PFT.

## 4.3 Vegetation composition and structure

### 4.3.1 Vegetation composition and representation at the element scale

In order to represent the differences among various plants, the model operates with the concept of *plant functional types*. This concept allows combining of species with similar characteristics into the same groups (e.g., Smith et al., 1997). The framework assumes that vegetated surfaces can be comprised of multiple plant functional types that differ in physiology (e.g., leaf optical properties, stomatal physiology, leaf photosynthetic characteristics) and structure (e.g., height, leaf dimension, roughness length, displacement height, root profile) (Figure 3-2). Each vegetation patch, while

co-occurring in the same Voronoi cell, constitutes a separate column upon which energy, water, and carbon calculations are performed. Accordingly, the differences in plant characteristics strongly affect estimation of surface fluxes. Water uptake properties of each PFT are controlled by the soil matric potentials $\Psi^*$ and $\Psi_w$ [$MPa$] at which, respectively, the stomatal closure or plant wilting begins. Based on the soil hydraulic parameterization of Section 3.7.3, $\Psi^*$ and $\Psi_w$ are translated into their corresponding relative soil moisture contents $\theta^*$ and $\theta_w$ [$mm^3\ mm^{-3}$], respectively, for a given soil type. Values of $\theta^*$ and $\theta_w$ are used in parameterizing the stomatal resistance as a function of soil moisture in the root zone (equation (4.17) in the following).

Vegetation composition and respective fractional areas are time-dependent (Section 4.4.8). The model assumes that plants do not *explicitly* compete for light and water, i.e., the respective location of PFTs to each other and the effects of shading are not explicitly considered. Instead, these effects are considered *implicitly*. Aboveground competition for light is treated as the competition for available space and is determined from PFT's success to produce biomass (Section 4.4.8). Plant water uptake properties and the characteristic features of the rooting profiles translate into PFT's differences in ability to access soil moisture and, therefore, impose the competition for available water. Evidently, the former form of interaction among PFTs is only applicable to ecosystems with sparse vegetation, where the effects of plant shading are minimal. A more comprehensive approach to representing the competition for light in densely vegetated areas would need to explicitly consider the vertical structure of vegetation organization, i.e., representing the foliage layers of upperstory and understory species.

## 4.3.2 Vegetation structure, carbon, and nutrients

Each vegetation type is represented by carbon stored in leaves, fine roots, and stems/sapwood (for woody species). Given these carbon pools, vegetation structure is defined by *time-varying* leaf and stem areas and canopy height (Section 4.4.8) and *time-invariant* root profile and leaf dimension (Section 3.4). The time-varying vegetation characteristics are determined by using PFT-specific allometric relationships from the

225

size of corresponding carbon pools of each of the compartments: foliage, sapwood, and fine root. Since the model development is tailored to applications in *arid* and *semi-arid* areas, where water constitutes the major limiting resource (e.g., Scholes and Walker, 1993, p. 110; Rodriguez-Iturbe et al., 2001), mineralization rates/nutrient supply are assumed to be directly dependent on water availability. Nutrients (nitrogen) are therefore not tracked in the vegetation compartments. Nonetheless, the maximum catalytic capacity of Rubisco, used as a parameter in the photosynthesis module (Section 4.4.1), and an assumption of vertical decay of leaf nitrogen throughout the canopy are both used to adjust the rates of photosynthesis for nutrient limitations experienced by a given PFT at various stages of growth (Section 4.4.1).

## 4.4 Vegetation function

As stated above, each plant type is represented by carbon/biomass stored in three major compartments corresponding to leaves, fine roots, and sapwood (for woody species). Various biochemical processes affect plant carbon balance. Figure 4-1 illustrates the principal fluxes of carbon and the corresponding vegetation biochemical processes reproduced by the model (the notation style is explained in the figure caption). The following provides a brief outline of how coupling among various plant life regulatory mechanisms is represented in the discussed modeling framework.

Atmospheric carbon dioxide is fixed into carbohydrates and other organic compounds through the processes of photosynthesis. At any given instant, the total amount of uptake is constrained both by biotic (i.e., the amount of foliage expressed as LAI, leaf photosynthetic capacity, etc.) and abiotic (i.e., hydrometeorological conditions, soil water, radiation, etc.) factors. Two carbon uptake levels are considered within the vegetation foliage: sunlit and shaded canopy fractions, which are treated as "big leaves" with the subsequent scaling of obtained quantities to the canopy scale (Section 4.4.1). The model of photosynthesis estimates the Gross Primary Production $GPP$ and, simultaneously, the plant canopy respiration. The following step involves calculation of the other two components of plant autotrophic respiration correspond-
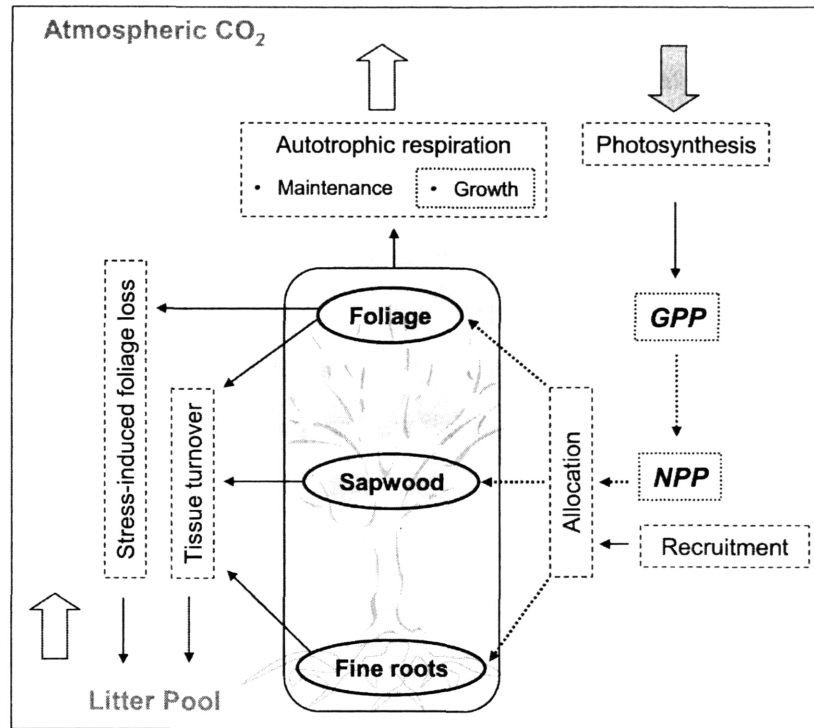
Figure 4-1: A conceptual diagram of carbon fluxes simulated by the model and an outline of the processes involved. The three major carbon pools are leaves, fine roots, and sapwood (woody species). Boxes outlined with dashed lines illustrate processes that affect the carbon balance. The dotted-line boxes represent intermediate quantities, whose magnitude impacts the occurrence of processes that are assumed to follow. The solid-line arrows show carbon fluxes, while dotted-line arrows depict an intermediate partition of carbon fluxes, which depends on the outcome of carbon balance at the preceding stage. The filled downward arrow depicts carbon uptake from $CO_2$, while the filled upward arrows show carbon loss by vegetation.

ing to the fluxes from sapwood and fine root carbon pools. The sum of all respiration fluxes (i.e., for canopy, sapwood, and fine roots) constitutes the maintenance respiration, which refers to the $CO_2$ emission from plants as the result of protein repair and replacement and the respiratory processes that provide energy for the maintenance of ion gradients across cell membranes (Penning De Vries, 1975). If the difference between $GPP$ and maintenance respiration is positive, growth respiration is estimated as a constant fraction of that difference. The growth respiration represents the construction cost (i.e., expended metabolic energy) for new tissue synthesis from mineral and glucose (the product of dark reactions of photosynthesis).

The difference between $GPP$ and the sum of *all* respiration fluxes (i.e., both maintenance and growth) is the Net Primary Production $NPP$. If $NPP$ is positive (note that only in this case the growth respiration can be non-zero), the assimilated carbon is allocated to vegetation compartments: canopy, sapwood, and fine roots (Figure 4-1). The implemented allocation scheme uses information about the states of plant canopy and water availability in the root zone. For woody species, allocation is also related to vegetation phenological status (Section 4.4.7). Such an approach permits dynamic, state-, and stress-dependent allocation patterns as opposed to constant, prescribed allocation fractions.

Tissue senescence, i.e., the process of turnover of plant tissues that exhibit a certain life-span, is considered as the production of "normal" litter (for leaves and fine roots) and non-living heartwood pool (for sapwood). Both production rates depend on sizes of the corresponding plant carbon compartments. The amount of living carbon that enters the above and below ground litter and the amount of sapwood that turns to heartwood are calculated using PFT-specific longevity values for various types of plant tissue. Foliage senescence due to hydrometeorological conditions, which may impose additional controls on the deciduous characteristics of trees and grasses, is also considered. The root zone soil moisture affects the rate of the *drought*-induced canopy loss, while the air temperature is used to parameterize the foliage loss due to *cold* conditions. In the current implementation, heterotrophic respiration is not considered by the model and the dynamics of litter pools are thus not accounted for.

### 4.4.1 Photosynthesis and stomatal resistance model

Canopy photosynthesis is coupled to the stomatal resistance parameterization and, therefore, is an integral part of the framework that estimates the surface energy fluxes (Section 3.6.3). The coupling scheme follows work of Farquhar et al. (1980), Collatz et al. (1991) for $C_3$ plants and Collatz et al. (1992) for $C_4$ plants:

$$\frac{1}{r_s} = m\frac{A_n\, e_{atm}}{c_s\, e^*(T_v)}P_{atm} + b,$$ (4.1)

228

where $r_s$ [$s$ $m^2 leaf$ $\mu mol^{-1}$] is the leaf stomatal resistance, $m$ [$-$] is an empirical parameter, $A_n$ [$\mu mol$ $CO_2$ $m^{-2} leaf$ $s^{-1}$] is the net assimilation rate, $c_s$ [$Pa$] is the $CO_2$ concentration at the leaf surface, $e_{atm}$ [$Pa$] is the vapor pressure at the leaf surface approximated with atmospheric water vapor pressure, $e^*(T_v)$ [$Pa$] is the saturation vapor pressure inside the leaf at the vegetation temperature $T_v$, $P_{atm}$ [$Pa$] is the atmospheric pressure, and $b$ [$\mu mol\, m^{-2} leaf$ $s^{-1}$] is the minimum stomatal conductance when $A_n = 0$. Note that formulation (4.1) is relevant to a *single leaf* scale. For a vegetation-hydrology model, the required step is to integrate equation (4.1) to describe the *canopy* photosynthesis and resistance. Since the canopy shortwave albedos, the sunlit and shaded fractions, as well as the amount of absorbed radiation are provided by the radiative transfer model (Sections 3.5.2 and 3.6.1), this information is used for scaling the photosynthesis and resistance quantities. The utilized approach is described below.

Leaf photosynthesis strongly depends on the type of incident radiation (direct beam or diffuse) and sunlit and shaded fractions of the canopy can substantially differ in magnitudes of carbon uptake (e.g., Saeki, 1961; Spitters, 1986; Norman, 1993; Wang and Leuning, 1998). It is theoretically correct, therefore, to differentiate between the photosynthetic activities of the sunlit and shaded fractions of the canopy. The model thus considers two "big leaves", one sunlit and the other shaded. The penetration of the direct beam radiation in the canopy is assumed to decay exponentially and controlled by the light extinction parameter $K' = \frac{G(\mu)}{\mu}\sqrt{1 - \omega_{vis}^{veg}}$ (Section 3.6.1), which is a function of the Sun's zenith angle, leaf angle distribution, and leaf and stem areas. Since the maximum photosynthetic rate, Rubisco, electron transport rates, and respiration rate have been shown to co-vary with leaf nitrogen content (Ingestad and Lund, 1986; Field and Mooney, 1986), the canopy nitrogen profile also needs to be accounted for to scale photosynthesis to the two considered canopy levels. The central assumption of the hypothesis used by many land-surface models (e.g., Sellers et al., 1996a) is that the leaf nitrogen content acclimates fully to prevailing light conditions within a canopy and is proportional to the radiation-weighted time-mean profile of PAR. A simple exponential description of radiation attenuation is used

to describe the profile of PAR with the time-mean PAR extinction coefficient $\bar{K}$ [–]. Taking into account both extinction coefficients, $K'$ and $\bar{K}$, the following scaling coefficients are obtained separately for the sunlit $F^{sun}$ and shaded $F^{shd}$ canopy fractions $[m^2\,leaf\,m^{-2}\,PFT\,ground\,area]$ (the units refer to a vegetated area of the element occupied by a given PFT; in the following, $[m^{-2}\,PFT\,ground\,area]$ is equivalent to $[m^{-2}\,PFT]$):

$$F^{sun} = \int_0^L e^{-\bar{K}x}e^{-K'x}dx = \frac{1 - e^{-(\bar{K}+K')L}}{\bar{K} + K'}, \tag{4.2}$$

$$F^{shd} = \int_0^L e^{-\bar{K}x}(1 - e^{-K'x})dx = \frac{1 - e^{-\bar{K}L}}{\bar{K}} - \frac{1 - e^{-(\bar{K}+K')L}}{\bar{K} + K'}. \tag{4.3}$$

Note that the term $e^{-K'x}$ gives the sunlit canopy fraction under the LAI equal to $x$ (according to the Beer's law, equation (3.24)). The above coefficients are used to obtain estimates photosynthesis quantities (e.g., net assimilation rate, stomatal resistance, etc.) scaled to either sunlit or shaded canopy fractions. Each fraction is considered separately and, correspondingly, the following equations refer to a particular big leaf. The bulk canopy estimates are obtained by combining the quantities from the two levels (see below).

For each of the levels, formulation (4.1) can be re-written as

$$\frac{1}{r_s^{CL}} = m\frac{A_n^{CL}\,e_{atm}}{c_s\,e^*(T_v)}P_{atm} + F^{CL}\,b', \tag{4.4}$$

where index "$CL$" refers to either sunlit or shaded canopy levels and $b' = \beta_T b$ takes into account the soil moisture effects on the minimum stomatal conductance (see below).

Collatz et al. (1991) describes leaf photosynthesis for $C_3$ species as the minimum of three limiting rates, $J_c$, $J_e$, and $J_s$ [$\mu mol$ $CO_2$ $m^{-2}\,leaf$ $s^{-1}$] that describe assimilation rates as limited by the efficiency of the photosynthetic enzyme system (Rubisco-limited), the amount of photosynthetically active radiation captured by the leaf chlorophyll, and the capacity of the leaf to export or to utilize the products of photosynthesis, respectively. For $C_4$ species, the terms $J_c$ and $J_e$ still refer to Rubisco and

light limitations, respectively, but $J_s$ refers to a PEP-carboxylase limitation (Collatz et al., 1992). The RuBP-carboxylase (Rubisco enzyme) limited carboxylation rate is formulated as

$$J_c = F^{CL} V_{max} \left[ \frac{c_i - \Gamma^*}{c_i + K_c(1 + O_i/K_o)} \right] , \quad \text{for } C_3 , \qquad (4.5)$$

$$J_c = F^{CL} V_{max} , \qquad \qquad \text{for } C_4 . \qquad (4.6)$$

The maximum rate of carboxylation allowed by the capacity to regenerate RuBP (i.e., the light limited rate) is

$$J_e = 4.56 \, \phi^{CL} \epsilon_3 \left[ \frac{c_i - \Gamma^*}{c_i + 2\Gamma^*} \right] , \quad \text{for } C_3 , \qquad (4.7)$$

$$J_e = 4.56 \, \phi^{CL} \epsilon_4 , \qquad \qquad \text{for } C_4 . \qquad (4.8)$$

The export limited rate of carboxylation (for $C_3$ plants) and the PEP-carboxylase limited rate of carboxylation (for $C_4$ plants) are

$$J_s = F^{CL} 0.5 \, V_{max} , \qquad \qquad \text{for } C_3 , \qquad (4.9)$$

$$J_s = F^{CL} 1.8 \times 10^4 \, V_{max} \frac{c_i}{P_{atm}} , \quad \text{for } C_4 . \qquad (4.10)$$

In the above equations, $c_i$ and $O_i$ [$Pa$] are the partial pressures of $CO_2$ and $O_2$, respectively, in leaf interior, $\phi^{CL}$ [$W \, m^{-2}$] is the amount of the visible wave-band solar radiation absorbed by either sunlit or shaded leaves (Section 3.6.1), which is converted to photosynthetic photon flux assuming 4.56 [$\mu mol \, photon \ m^{-2} \, s^{-1}$] per unit absorbed [$W \, m^{-2}$], and $\epsilon_{3,4}$ [$\mu mol \ CO_2 \ \mu mol^{-1} \, photons$] is the intrinsic quantum efficiency for $CO_2$ uptake for $C_3$ and $C_4$ plants (subscript "3"or "4", respectively). $\Gamma^*$ [$Pa$] is the $CO_2$ compensation point:

$$\Gamma^* = \frac{1}{2} \frac{K_c}{K_o} 0.21 O_i , \qquad (4.11)$$

where $K_c$ and $K_o$ [$Pa$] are the Michaelis-Menten constants for $CO_2$ and $O_2$, respectively, expressed as functions of leaf temperature $T_v$ (note that below $T_v$ is expressed

in units of $[K]$:

$$K_c = K_{c25} \, a_{kc}^{0.1(T_v - 298.15)} \, , \tag{4.12}$$

$$K_o = K_{o25} \, a_{ko}^{0.1(T_v - 298.15)} \, . \tag{4.13}$$

The term 0.21 in (4.11) represents the ratio of maximum rates of oxygenation to carboxylation, and is assumed to be constant with temperature following Farquhar and von Caemmerer (1982). Bernacchi et al. (2001), however, noted that this ratio may generally vary within a range of $0.16 \div 0.31$. $K_{c25} = 30$ and $K_{o25} = 3 \times 10^4$ $[Pa]$ are values of constants at 25°C and $a_{kc} = 2.1$ and $a_{ko} = 1.2$ are the temperature sensitivity parameters. The parameter $V_{max}$ $[\mu mol \; CO_2 \; m^{-2} \, leaf \; s^{-1}]$ is the maximum catalytic capacity of Rubisco:

$$V_{max} \quad = \quad V_{max\,25} \, a_{vmax}^{0.1(T_v - 298.15)} \, f_1(T_v) \, \beta_T \, , \tag{4.14}$$

where $V_{max\,25}$ $[\mu mol \; CO_2 \; m^{-2} \, leaf \; s^{-1}]$ is the value at 25°C, $a_{vmax} = 2.4$ for $C_3$ species and $a_{vmax} = 2.0$ for $C_4$ species is a temperature sensitivity parameter, and $f(T_v)$ is a function that mimics thermal breakdown of metabolic processes (Farquhar et al., 1980; Collatz et al., 1991):

$$f_1(T_v) \quad = \quad \left[ 1 + e^{\frac{-220000 + 703 \, T_v}{8.314 \, T_v}} \right]^{-1} , \qquad \text{for } C_3, \tag{4.15}$$

$$f_1(T_v) \quad = \quad \left[ \left( 1 + e^{0.3 \, (T_v - 309.15)} \right) \left( 1 + e^{0.3 \, (286.15 - T_v)} \right) \right]^{-1} , \quad \text{for } C_4. \tag{4.16}$$

The expression for a heuristic function $\beta_T$ $[-]$ that limits canopy photosynthesis based on the soil moisture availability in the root zone is accepted from Bonan (1996) (other formulations are provided in Sellers et al. (1996a) and Cox et al. (1998)):

$$\beta_T \quad = \quad \sum_i^{I_{root}} \beta_{T,i}(z_i) \, r_i(z_i) \, , \tag{4.17}$$

$$\beta_{T,i}(z_i) \quad = \quad \max \left[ 0, \, \min \left( 1, \, \frac{\theta_i(z_i) - \theta_w}{\theta^* - \theta_w} \right) \right] , \quad \text{if } T_{soil} > 273.15 \, , \tag{4.18}$$

$$\beta_{T,i}(z_i) \quad = \quad 0.01 \, , \qquad\qquad\qquad\qquad\qquad \text{if } T_{soil} \leq 273.15 \, , \tag{4.19}$$

232

where index $i$, $i = 1 \ldots I_{root}$ refers to a depth $z_i$ of the soil profile with an associated accumulated root biomass fraction $r_i(z_i)$, $\sum_i^{I_{root}} r_i = 0.95$, $\theta_w$ $[mm^3 \ mm^{-3}]$ is the wilting point and $\theta^*$ $[mm^3 \ mm^{-3}]$ is the threshold soil moisture contents for a given vegetation type (Section 4.3). $T_{soil}$ is estimated according to Section 3.6.4 and is used to constrain transpiration if soil temperature drops below the freezing point. As can be seen from (4.17), $\beta_T \in [0, 1]$ and takes into account the soil moisture variability within the root profile since explicit weights of the root biomass with depth, $r_i$-s, are considered.

Observations indicate that the transition from one limiting rate ($J_c$, $J_e$, and $J_s$) to another is not abrupt and that coupling between the three processes leads to smooth curves rather than superposition of straight lines. Collatz et al. (1991) describe this effect by combining the rate terms into two quadratic equations, which are then solved for their smaller roots:

$$
\begin{aligned}
\alpha_{ce} J_p^2 - J_p(J_c + J_e) + J_e J_c &= 0 \,, \\
\alpha_{ps}(A^{CL})^2 - A^{CL}(J_p + J_s) + J_p J_s &= 0 \,,
\end{aligned}
\tag{4.20}
$$

where $J_p$ $[\mu mol \ CO_2 \ m^{-2} \ leaf \ s^{-1}]$ is a "smoothed" minimum of $J_c$ and $J_e$, $A^{CL}$ $[\mu mol \ CO_2 \ m^{-2} \ s^{-1}]$ is the **gross** assimilation rate of sunlit or shaded canopy fraction, $\alpha_{ce}$ and $\alpha_{ps}$ are the coupling coefficients. From Sellers et al. (1996b): $\alpha_{ce} = 0.98$, $\alpha_{ps} = 0.95$ for $C_3$ species; from Cox et al. (1998): $\alpha_{ce} = 0.83$, $\alpha_{ps} = 0.90$ for $C_4$ species.

The **net** foliage assimilation rate $A_n^{CL}$ is then given by

$$
A_n^{CL} = A^{CL} - F^{CL} R_d \,,
\tag{4.21}
$$

where $R_d$ $[\mu mol \ CO_2 \ m^{-2} \ leaf \ s^{-1}]$ is leaf mitochondrial ("dark") respiration estimated following Collatz et al. (1991, 1992) as

$$
R_d = 0.015 \, V_{max \, 25} \, a_{rmax}^{0.1(T_v - 298.15)} f_2(T_v) \,, \quad \text{for } C_3 \,,
\tag{4.22}
$$

233
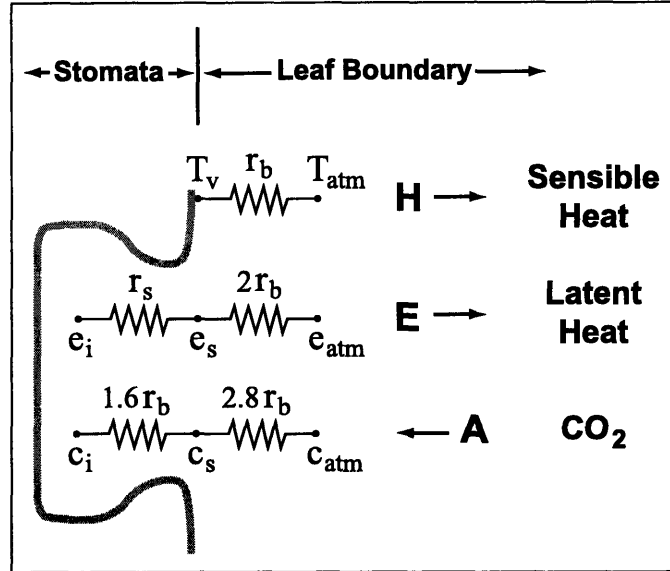
Figure 4-2: A conceptual diagram of state variables, resistances, and fluxes in stomata and at the leaf surface (explanation of the variables is provided in the text).

$$R_d = 0.025\,V_{max\,25}\,a_{rmax}^{0.1(T_v-298.15)}\,f_2(T_v)\,, \quad \text{for } C_4\,, \tag{4.23}$$

where $a_{vmax} = 2.0$ is a temperature sensitivity parameter and $f_2(T_v)$ is a temperature inhibition function:

$$f_2(T_v) = \left[1 + e^{1.3\,(T_v-328.15)}\right]^{-1}\,. \tag{4.24}$$

The $CO_2$ concentration at the leaf surface $c_s$ $[Pa]$ and the internal leaf $CO_2$ concentration $c_i$ $[Pa]$ are assumed to be representative for a considered canopy level (sunlit or shaded) and calculated assuming that the capacity to store $CO_2$ at the leaf surface is negligible, so that, with reference to Figure 4-2

$$\frac{c_a - c_s}{1.37\,r_b^{CL}\,P_{atm}} = \frac{c_s - c_i}{1.65\,r_b^{CL}\,P_{atm}}\,, \tag{4.25}$$

where $c_a = 340 \times 10^{-6}\,P_{atm}$ $[Pa]$ is the background atmospheric $CO_2$ concentration, the coefficients 1.37 and 1.65 are the ratios of diffusivity of $CO_2$ to $H_2O$ for the leaf boundary layer resistance and stomatal resistance (Landsberg, 1986), and $r_b^{CL}$

234

$[s\,m^2\,\mu mol^{-1}]$ is the one-sided bulk leaf boundary resistance estimated for sunlit or shaded fraction of the canopy (Section 3.6.3):

$$r_b^{CL} = r_b^{sun,\,shd}\frac{0.0224\,(1.013\times 10^5)\,T_{atm}}{P_{atm}\,273.15}\times 10^{-6}\,,\qquad (4.26)$$

where $r_b^{sun,\,shd}$ is given in $[s\,m^{-1}]$. Given an initial guess of $c_i$, expressions (4.4) and (4.25) can be combined to obtain the following quadratic equation:

$$\left(m\frac{A_n^{CL}\,e_{atm}}{c_s\,e^*(T_v)}P_{atm} + F^{CL}\,b'\right)(r_s^{CL})^2 +$$
$$\left(m\frac{A_n^{CL}\,r_b^{CL}}{c_s}P_{atm} + F^{CL}\,r_b^{CL}\,b'\right)r_s^{CL} - r_b^{CL} = 0\,,\qquad (4.27)$$

from which the stomatal resistance is estimated as the larger root satisfying (4.27). An updated value of $c_i$ can then be estimated as $c_i = c_s - 1.65\,r_s^{CL}\,A_n^{CL}\,P_{atm}$. Since the productivity $A_n^{CL}$ cannot be expressed as a function of $c_i$ in a closed form, the solution for $r_s^{CL}$ is obtained iteratively. While some land-surface schemes iterate a fixed number of times (e.g., Bonan, 1996), it can be demonstrated that the success of finding the stomatal resistance strongly depends on an initial guess of $c_i$, which is a function of leaf temperature, atmospheric moisture deficit, etc. Here, the search of $r_s^{CL}$ is formulated as a problem of finding root of a non-linear equation, which guarantees convergence of the scheme:

$$\left(c_s(c_i) - 1.65\,r_s^{CL}(c_i)\,A_n^{CL}(c_i)\,P_{atm}\right) - c_i = 0\,.\qquad (4.28)$$

The Newton method is used to find the solution.

The night time stomatal resistance is a function of the minimum stomatal conductance and soil water stress. Taking $r_s^{sun} \to \infty$, the night time stomatal resistance is formulated as $r_s^{shd} = \frac{1}{\beta_T\,b\,L}$, where $L$ is the canopy total leaf area index.

The stomatal resistances for different canopy levels are explicitly used in the estimation of the latent heat flux (Section 3.6.3). The bulk values of canopy net uptake $A_{nC}$ and respiration $R_{dC}$ $[\mu mol\ CO_2\ m^{-2}\ PFT\ s^{-1}]$ are obtained by summing the

values for sunlit and shaded canopy fractions:

$$A_{nC} = A_n^{sun} + A_n^{shd}, \tag{4.29}$$

$$R_{dC} = F^{sun} R_d + F^{shd} R_d. \tag{4.30}$$

## 4.4.2 Net primary production and vegetation respiration

The net primary production $NPP$ $[gC\ m^{-2}\ PFT\ hour^{-1}]$ can be defined as the gross plant photosynthesis, or gross primary production $GPP$ $[gC\ m^{-2}\ PFT\ hour^{-1}]$, minus autotrophic respiration $R_a$ $[gC\ m^{-2}\ PFT\ hour^{-1}]$:

$$NPP = GPP - R_a, \tag{4.31}$$

$$GPP = k_{co2c}(A_{nC} + R_{dC}), \tag{4.32}$$

where $k_{co2c} = 0.0432$ $[gC\ s\ \mu mol\ CO_2^{-1}\ hour^{-1}]$ is the unit conversion coefficient. Vegetation autotrophic respiration $R_a$ is estimated as a sum of maintenance $R_m$ and growth $R_g$ $[gC\ m^{-2}\ PFT\ hour^{-1}]$ respiration rates:

$$R_a = R_m + R_g, \tag{4.33}$$

$$R_m = R_{dC} + R_{dS} + R_{dR}, \tag{4.34}$$

$$R_g = \omega_{grw}(GPP - R_m), \quad \text{if } GPP > R_m, \tag{4.35}$$

$$R_g = 0, \quad\quad\quad\quad \text{if } GPP \leq R_m, \tag{4.36}$$

where $\omega_{grw}$ $[-]$ is a constant $(0.25 \div 0.33)$, and $R_{dS}$ and $R_{dR}$ $[gC\ m^{-2}\ PFT\ hour^{-1}]$ are the respiration rates for sapwood and fine roots, respectively. As can be seen from (4.31), the net primary productivity is positive when carbon uptake from photosynthesis exceeds autotrophic respiration, a situation characteristic for favorable, well-watered conditions. NPP is negative during night time or when soil moisture deficit does not allow vegetation to effectively photosynthesize and maintenance costs are higher than gross carbon uptake.

The foliage day respiration $R_{dC}$ is estimated along with photosynthesis and stom-

atal resistance (Section 4.4.1). Note that $R_{dC}$ depends on the soil moisture state in the root zone via the parameter $\beta_T$ in (4.22) - (4.23). Canopy respiration rate during night time (maintenance respiration of mitochondria) is parameterized in a similar manner:

$$R_{dC} = k_{co2c} F^{shd} R_d , \qquad (4.37)$$

where $R_d$ is from (4.22) or (4.23) with $F^{sun} = 0$. The maintenance respiration for sapwood $R_{dS}$ and root biomass $R_{dR}$ is approximated using the first-order kinetics reaction rates:

$$R_{dS} = r_{sapw} C_{sapw} f_3(T_{atm}) , \qquad (4.38)$$

$$R_{dR} = r_{root} C_{root} f_3(T_{soil}) , \qquad (4.39)$$

where $T_{soil}$ $[K]$ is from Section 3.6.4, $C_{sapw}$ and $C_{root}$ $[g\,C\ m^{-2}\ PFT]$ are pools of carbon of sapwood and fine root, respectively, for a given vegetated fraction of considered element (note that these quantities refer only to the area occupied by a given PFT), and $r_{sapw}$ and $r_{root}$ $[g\,C\ g\,C^{-1}\ hour^{-1}]$ are the tissue respiration coefficients at 10°C that can be generally defined as

$$r_{sapw} = \frac{r\,\vartheta}{cn_{sapw}} , \qquad (4.40)$$

$$r_{root} = \frac{r\,\vartheta}{cn_{root}} , \qquad (4.41)$$

where $\vartheta$ is a rate of $22.824 \times 10^{-4}\ hour^{-1}$, $cn_{sapw} = 330$ and $cn_{root} = 29$ are sapwood and fine root C:N mass ratios $[g\,C\ g\,N^{-1}]$ (Sitch et al., 2003), and $r$ $[g\,C\ g\,N^{-1}]$ is a vegetation type dependent coefficient. The temperature dependence function $f_3(T)$ is defined as

$$f_3(T) = e^{308.56 \left( \frac{1}{56.02} - \frac{1}{T-227.13} \right)} , \qquad (4.42)$$

where $T$ $[K]$ is either $T_{atm}$ or $T_{soil}$.

237

### 4.4.3 Stress-induced foliage loss and tissue turnover

The amount of living carbon that enters the above and below ground litter and the amount of sapwood that turns to heartwood are calculated using PFT-specific longevity values for various types of plant tissue. The turnover and stress-induced foliage loss $D_{leaf}$, sapwood $D_{sapw}$, and root $D_{root}$ $[g\,C\ m^{-2}\,PFT\ hour^{-1}]$ turnover rates are parameterized as (Levis et al., 2004; Arora and Boer, 2005)

$$D_{leaf} = d_{leaf}C_{leaf} + (\gamma_W + \gamma_C)C_{leaf}, \tag{4.43}$$

$$D_{sapw} = d_{sapw}C_{sapw}, \tag{4.44}$$

$$D_{root} = d_{root}C_{root}, \tag{4.45}$$

where $d_{leaf}$, $d_{sapw}$, and $d_{root}$ $[hour^{-1}]$ are the "normal" turnover rates for foliage, sapwood, and fine roots, respectively, and represent the inverse values of corresponding tissue longevities.

Foliage senescence due to hydrometeorological conditions, which may impose additional controls on the canopy dynamics of trees and grasses, is also considered. The foliage loss due to the *drought* stress controls the deciduous characteristics of trees and grasses in semi-arid areas. Since there are no available mechanistic models, a conceptual parameterization is used in the following. The drought-induced foliage loss rate $\gamma_W$ $[hour^{-1}]$ is parameterized as a function of the PFT-dependent maximum drought loss rate $\gamma_{W\,max}$ $[hour^{-1}]$ and the root zone soil moisture factor $\beta_T$ (equation (4.17)):

$$\gamma_W = \gamma_{W\,max}(1 - \beta_T)^{b_W}, \tag{4.46}$$

where $b_W$ $[-]$ is the shape parameter reflecting the sensitivity of canopy to drought. As can be seen from the above formulation, the foliage loss due to drought stress is zero when root zone contains a sufficient amount of moisture ($\beta_T = 1$) and is at maximum when $\beta_T \to 0$ (equation (4.17)).

Parameterization of foliage loss due to *cold* is parameterized in a similar fashion

(Arora and Boer, 2005):

$$\gamma_C = \gamma_{Cmax}(1 - \beta_C)^{b_C}, \tag{4.47}$$

where $\gamma_{Cmax}$ $[hour^{-1}]$ is the PFT-dependent maximum cold foliage loss rate and $b_C$ $[-]$ is the shape parameter reflecting the sensitivity of canopy to cold:

$$b_C = 1.0, \qquad \text{if } T_{atm} \geq T_{cold}, \tag{4.48}$$

$$b_C = \frac{1}{5.0}(T_{atm} - (T_{cold} - 5.0)), \quad \text{if } T_{cold} > T_{atm} > (T_{cold} - 5.0), \tag{4.49}$$

$$b_C = 0.0, \qquad \text{if } T_{atm} \leq (T_{cold} - 5.0), \tag{4.50}$$

where $T_{cold}$ $[K]$ is a PFT-dependent temperature threshold below which cold-induced leaf loss begins ($b_C < 1.0$).

## 4.4.4 Carbon allocation

If the net primary production estimated for a given hour is positive (Section 4.4.2), the assimilated carbon has to be allocated to different vegetation compartments: canopy, fine roots, and sapwood (woody vegetation). In the presented model, the allocation scheme is related to state of the plant canopy, water availability in the root zone, and vegetation phenological status (for woody plant species only, Section 4.4.7). The implemented approach follows the conceptual methodology of Friedlingstein et al. (1999), Salter et al. (2003), and Arora and Boer (2005). The methodology is based on the premises that: 1) plants allocate more carbon to roots when soil moisture is limiting, so that the below ground biomass increases; 2) plants allocate more carbon to canopy when leaves are few in order to increase the photosynthetic carbon gain; and 3) plants allocate more carbon to stem/sapwood when foliage significantly limits light penetration to lower levels of the canopy in order to increase the canopy supporting structure as well as plant height and lateral spread. Such an approach permits *dynamic*, state-, and stress-dependent allocation patterns as opposed to constant allocation fractions assumed in most models of vegetation dynamics. Following

Arora and Boer (2005), for *woody* plant species:

$$a_{sapw} = \frac{e_{sapw} + \varpi(1 - \beta_L)}{1 + \varpi(2 - \beta_L - \beta_T)}, \tag{4.51}$$

$$a_{root} = \frac{e_{root} + \varpi(1 - \beta_T)}{1 + \varpi(2 - \beta_L - \beta_T)}, \tag{4.52}$$

$$a_{leaf} = \frac{e_{leaf}}{1 + \varpi(2 - \beta_L - \beta_T)} = 1 - a_{sapw} - a_{root}, \tag{4.53}$$

$$\beta_L = e^{-0.5\,L}, \tag{4.54}$$

where $\beta_L$ [−] is a scalar index used to measure the availability of light depending on the plant leaf area index $L$, $a_{sapw}$, $a_{root}$, and $a_{leaf}$ [0 ÷ 1] are the dynamic allocation fractions for sapwood, roots, and canopy, respectively, estimated using base allocation values $e_{sapw}$, $e_{root}$, and $e_{leaf}$ [0 ÷ 1] for vegetation state that corresponds to $\beta_L = \beta_T = 1$, $e_{sapw} + e_{root} + e_{leaf} = 1$. As can be inferred from the above formulation, a decrease in water availability in the root zone shifts allocation to roots, while a decrease in available light shifts allocation to stem. When both water and light are available, the allocation is at maximum to leaves. The parameter $\varpi$ [−] in (4.51) - (4.53) controls the sensitivity of allocation to changes in $\beta_L$ and $\beta_T$. As $\varpi$ increases, the allocation is to a greater extent controlled by light or soil water limitations, on the contrary, for $\varpi = 0$, constant allocation fractions $e_{sapw}$, $e_{root}$, and $e_{leaf}$ are assumed.

For *grasses*:

$$a_{root} = \frac{e_{root} + \varpi(1 - \beta_T)}{1 + \varpi(1 + \beta_L - \beta_T)}, \tag{4.55}$$

$$a_{leaf} = \frac{e_{leaf} + \varpi\beta_L}{1 + \varpi(1 + \beta_L - \beta_T)}, \tag{4.56}$$

$$\beta_L = \max\left(0, 1 - \frac{L}{4.5}\right), \tag{4.57}$$

with $e_{root} + e_{leaf} = 1$. The above allocation fractions may change to satisfy the assumed plant structural relationships (see below). Arora and Boer (2005) provide more details on the above scheme of dynamic allocation.

The dynamic allocation fractions estimated using (4.51)-(4.53) or (4.55)-(4.56) can be modified under three additional conditions. First, for deciduous trees and

shrubs all NPP is allocated to leaves at the time of leaf onset, i.e., the beginning of vegetation season when plants transit from a dormant state, as explained in Section 4.4.7. The second condition requires that a sufficient woody and root biomass have to be present to support the mass of leaves. The employed relationship between the foliage and the remaining biomass (sapwood and roots) is

$$(C_{sapw} + C_{root}) \geq \varepsilon_s C_{leaf}^{\xi} , \qquad (4.58)$$

where $\varepsilon_s$ and $\xi$ [−] are PFT-dependent constants (Ludeke et al., 1994). The third imposed condition is intended to maintain a minimum *root:shoot* ratio, i.e., the ratio of below ground to above ground biomass observed for most vegetation species (e.g., Kramer, 1983). Roots uptake water and nutrients, however, they also provide mechanical support and stability to plants. Carbon is allocated to roots at the expense of stem and leaves in order to maintain this structural feature. Note that for grasses, the condition (4.58) corresponds to the third condition of minimum root:shoot ratio.

## 4.4.5 Recruitment

Photosynthesis is the primary mechanism of production of plant leaf biomass, which is initialized with an assumed LAI at the beginning of growing season (Section 4.4.7a). The initial LAI corresponds to either: 1.) some fraction of the maximum LAI that the current carbon pools of sapwood and roots can support (trees and shrubs only), or 2.) a certain LAI value corresponding to initial biomass from vegetative reproduction (grasses). An additional mechanism to carbon uptake by existing canopy, recruitment from seeds introduces new photosynthesizing foliage biomass into the vegetation system.

One of the current limitations of this model version is that only *herbaceous* species can regenerate through seeds. Both seed germination and seedling establishment require favorable temperature and sufficient amounts of water at appropriate depths in the soil profile and at certain times during the year (e.g., Peters, 2000). The following conditions need to be met for a recruitment event to occur:

241

1. The mean daily soil temperature $\overline{T}_{soil}$ has to exceed a certain threshold value $T_{cold}$;

2. Soil moisture in the top 1/3 of the root maximum depth (Section 3.4) must be higher than $\theta^*$;

3. The Julian day of recruitment event must be within a certain period of the year (for instance, between March and July).

If all above conditions are *continuously* met for a certain number of days (e.g., 3 days), the biomass corresponding to leaf area index $L = 0.0025$ is added to the foliage pool of a given grass type. The recruitment root biomass is calculated from the allometric relationship (4.58) and is added to the grass root pool.

### 4.4.6 Carbon pool dynamics

The simulated carbon compartments for leaves, sapwood (woody species), and fine roots are updated every vegetation time step based on the estimated carbon fluxes discussed previously. If the net primary production is positive, the carbon change in the pools is obtained as

$$\frac{dC_{leaf}}{dt} = a_{leaf}NPP - D_{leaf}, \tag{4.59}$$

$$\frac{dC_{sapw}}{dt} = a_{sapw}NPP - D_{sapw}, \tag{4.60}$$

$$\frac{dC_{root}}{dt} = a_{root}NPP - D_{root}, \tag{4.61}$$

$$ANPP = \frac{dC_{leaf}}{dt} + \frac{dC_{sapw}}{dt}, \tag{4.62}$$

where $ANPP$ $[g\,C\;m^{-2}\,PFT\;hour^{-1}]$ is the Above-Ground Net Primary Production, and $D_{leaf}$, $D_{sapw}$, $D_{root}$ are the turnover rates (Section 4.4.3). When summed over the duration of vegetation season, $ANPP$ represents a characteristic of plant performance at a given location. Note that above $a_{sapw}$, $a_{root}$, and $a_{leaf}$ are the *adjusted* values of dynamic allocation fractions. These fractions are first estimated using (4.51)-(4.53)

or (4.55)-(4.56) and subsequently corrected, if necessary, by applying the three conditions of Section 4.4.4, which are intended to maintain the structural dependencies between sizes of various compartments.

If NPP is negative:

$$\frac{dC_{leaf}}{dt} = -\left(R_{dC} + D_{leaf}\right), \qquad (4.63)$$

$$\frac{dC_{sapw}}{dt} = -\left(R_{dS} + D_{sapw}\right), \qquad (4.64)$$

$$\frac{dC_{root}}{dt} = -\left(R_{dR} + D_{root}\right), \qquad (4.65)$$

$$ANPP = -\left(R_{dC} + R_{dS}\right). \qquad (4.66)$$

## 4.4.7 Vegetation phenology

Since the discussed model is applied to arid and semi-arid areas, where ecosystem dynamics are mostly driven by moisture availability, the problem of proper parameterization of plant phenology is intriguing and difficult. Within a simulation framework, vegetation *phenology* refers to the timing of onset (leaf out) and offset (leaf loss) of leaves, i.e., when plants transit from/to the state of dormancy. Leaf onset and offset mark the bounds of the growing season, the period during which the surface albedo, roughness, and surface water and energy fluxes are modulated by the adaptive vegetation dynamics. In the simplest case, the leaf phenology is specified as fixed onset and offset dates (e.g., Running and Hunt, 1993). More complicated schemes involve certain threshold functions of absolute daily soil or air temperature (Verseghy et al., 1993; Dickinson et al., 1993; Knorr, 2000), growing degree days (the sum of positive differences between daily mean air temperature and some threshold temperature) (Sitch et al., 2003), or chilling requirement (the number of days the temperature is below a certain threshold). None of these approaches, however, include the soil moisture control on vegetation phenology. Consequently, a dynamic, state-dependent approach is needed, amenable to a variety of possible hydrometeorological situations.

A semi-empirical "carbon-gain" parameterization, as first discussed by Ludeke et al. (1994), extended by Arora and Boer (2005), and slightly modified here, is used in

243

the following to model vegetation phenology. The essential assumption of the carbon-gain approach is that leaf onset starts when it is beneficial, in carbon terms, for a plant to produce leaves. In the considered process, the carbon *gains* are associated with photosynthesis and the *costs* are associated with canopy respiration and drought/cold induced foliage losses. Similarly, leaf offset is initiated when environmental conditions are unfavorable and disadvantageous for a plant to retain leaves in terms of its carbon balance. The carbon-gain approach, therefore, directly includes the effects of both temperature and soil moisture since photosynthetic activity, respiration, and foliage losses depend on historical (through the soil water dynamics) and current environmental conditions (temperature, radiation, and rainfall). The approach is therefore amenable to any combination of key forcing variables.

The transition from one growth state to another is triggered when a set of environmental conditions or a certain vegetation state are met. Leaf phenology differs for woody vegetation and grasses. For deciduous *trees and shrubs* (evergreen species are not currently considered), there are three leaf phenology stages that determine plant dynamics and allocation patterns: 1) dormancy; 2) maximum growth; 3) normal growth. During winter or drought periods, woody vegetation is in dormant/no-leaf state until the arrival of favorable weather when trees/shrubs enter the maximum growth state and the preferred allocation is made to leaves. When a critical amount of foliage is attained, vegetation is in normal growth stage and assimilated carbon is also allocated to sapwood and roots. The arrival of unfavorable weather conditions triggers the transition to the dormant state until the subsequent arrival of favorable weather conditions. For *herbaceous* species, there is no stage of maximum growth and from the dormant stage grasses transit directly to the normal growth phenology state. The conditions for transition between the subsequent phenology stages are described in more detail below.

### 4.4.7a Dormant state to maximum/normal growth

The transition from the state of dormancy to maximum (for woody species) or normal (for herbaceous plants) growth state occurs on the arrival of favorable weather con-

ditions, subject to moisture availability in the root zone. The overall favorability is signaled by a positive net primary production from a "virtual" foliage. The "virtual" canopy represents a certain amount of foliage biomass *temporarily* assigned to a given PFT during its dormant state. The "virtual" canopy is assumed to represent the amount of foliage a plant would have at the leaf onset. It is assigned at every time step of the vegetation model to check if a given PFT can photosynthesize effectively. For woody species, the virtual canopy is assumed to be proportional to the amount of non-structural carbohydrate reserves since a plant with larger reserves would have a larger initial amount of leaves: the leaf area index value is set to either $L = 0.3$ or LAI corresponding to 7.5% of the maximum canopy biomass the current sapwood and root pools can support (equation (4.58)). For grasses, the virtual canopy corresponds to $L = 0.2$ (an assumed maximum of leaf biomass from the vegetative reproduction). The daily values of $[A_{nC} - D_{leaf}]$ $[g\,C\,m^{-2}\,PFT\,hour^{-1}]$ are accumulated from the hourly estimates. The following conditions have to be met for a given PFT on a daily basis:

1. The total daily net photosynthesis $[A_{nC} - D_{leaf}]$ must be positive (this involves evaluation of $D_{leaf}$ during night time with possible freezing conditions);

2. The ratio of day light hours with zero or negative assimilation rate $A_{nC}$ to the total number of day light hours is less than 1/3;

3. The mean daily soil temperature $\overline{T}_{soil}$ has to exceed the threshold value $T_{cold}$ (Section 4.4.3);

4. The day length $D_{LH}$ has to exceed a certain threshold value $D_{LH}^{C}$;

5. For grass only: soil moisture in the top 1/3 of the maximum root depth (Section 3.4) must be above the wilting point defined for a given grass type.

If all above conditions are *continuously* met for a given PFT for a certain number of days (for instance, 7 days for woody species, 5 days for herbaceous species), PFT transits to the subsequent phenology state (maximum or normal growth). As an initial condition for that state, the canopy biomass is set to the value corresponding

245

to the "virtual" leaf area index (for conversion, see Section 4.4.8) specified above. If there is a break in the sequence of days favorable to a considered vegetation type (e.g., it becomes too dry or too cold), the counter of favorable days is re-set to zero.

### 4.4.7b Maximum to normal growth

During the stage of plant maximum growth (woody species only), all assimilated carbon is allocated to leaves. The transition from the maximum growth to normal growth state occurs when a biomass dependent LAI has been attained. According to Arora and Boer (2005), this LAI is approximately 40-50% of the maximum LAI a given stem and root biomass can support according to equation (4.58) (see also Figure 4 in Arora and Boer (2005)).

### 4.4.7c Normal growth to dormant state

In the normal growth state, a PFT allocates to leaves, sapwood (woody species), and fine roots according to the allocation rules of Section 4.4.4. Every hour a value of $[NPP - D_{leaf}]$ $[g\,C\ m^{-2}\,PFT\ hour^{-1}]$ is evaluated and subsequently accumulated over the day. The following conditions have to be met on a daily basis for a given PFT as a necessary element of transition to a dormant state:

1. The total daily value of $[NPP - D_{leaf}]$ is negative;

2. The ratio of day light hours with zero or negative $NPP$ to the total number of day light hours is higher than 2/3.

A PFT transits to the dormant state if all above conditions are *continuously* met for a given PFT for a certain number of days (for instance, 7 days for woody species, 5 days for herbaceous species) *and* 1) for woody species, the amount of foliage biomass is less than 1% of the maximum value a given stem and root biomass can support according to equation (4.58); and 2) for herbaceous species, the above ground biomass is close to the value (within 10% of it) used for initialization when vegetation season starts (Section 4.4.7a).

246

## 4.4.8 PFT structural attributes and fractional area

Allocation to, and the litter losses from the three vegetation compartments make their biomass time-varying. Changes in biomass of these components is reflected in the structural vegetation attributes used in the energy and water balance calculations (Chapter 3).

### 4.4.8a Woody species

For trees and shrubs, an approach of the LPJ model (Sitch et al., 2003) is used that relates the concept of allometry at the plant individual level with the concept of the "average" individual at the element scale level. For each individual, the average *individual's* leaf area index $L_{ind}$ [$m^2$ *leaf area* $m^{-2}$ *element area*] is estimated as the following:

$$L_{ind} = C_{leaf} \frac{f_v}{P_{ind}} \frac{S_{la}}{C_A}, \qquad (4.67)$$

where $f_v$ [$m^2$ *PFT* $m^{-2}$ *element area*] is the vegetation fraction of a given plant functional type present in the considered element, $P_{ind}$ [# *of individ.* $m^{-2}$ *element area*] is the population density or the number of individuals per unit area of the computational element (note that $C_{leaf}$ is the carbon content for a unit area occupied by a given PFT), $S_{la}$ [$m^2$ *leaf area kg* $C^{-1}$] is the specific leaf area, and $C_A$ [$m^2$ *element area individal*$^{-1}$] is the average individual's crown projective area. From (4.67), the leaf area index of vegetated fraction is $L = \frac{L_{ind}P_{ind}}{f_v}$. The stem area index $S$ [$m^2$ *leaf area* $m^{-2}$ *element area*] of an "average" individual is assumed to be 25% of $L_{ind}$.

Foliage relative projective cover of an average individual $f_{v\,ind}$ and the vegetation fraction of a given PFT $f_v$ are

$$f_{v\,ind} = 1 - e^{-0.5\,(L_{ind}+S_{ind})}, \qquad (4.68)$$

$$f_v = f_{v\,ind}C_A P_{ind}. \qquad (4.69)$$

Note that the product $(C_A P_{ind})$ specifies the fraction of a unit ground area of an

element that contains the projected area of canopy crown. As can be seen, the vegetation fraction for woody species is the same as the *fractional projective cover* of an "average" individual, scaled to the population level for a given element. Since the vegetation fraction is also used in estimating the element-scale hydrological quantities, such as the latent heat flux and evapotranspiration, the same fraction is simultaneously associated with the below-ground fraction of lateral spread of roots.

Plant height $H_v$ [$m$] can be estimated from allometric functions specific for a given PFT (e.g., Shinozaki et al., 1964; Waring et al., 1982). Several suitable approaches exist. Since the module has not been validated (for woody species), the methodology for estimating $H_v$ is not provided here and is considered to be a necessary development component in future studies.

### 4.4.8b Herbaceous species

For grasses, only one "average" individual can be present within a given computational element and

$$L_{ind} \;=\; L \;=\; C_{leaf}S_{la}\,, \tag{4.70}$$

with $P_{ind} = f_v$. $C_A$ for grasses is assumed to be 1.0 [$m^2$ *element area individal*$^{-1}$] (which assumes that grass is uniformly distributed within a given element) and the vegetation fraction is defined as

$$f_v \;=\; 1 - e^{-0.5\,(L+S)}\,. \tag{4.71}$$

The above expression essentially assumes that the grass vegetation fraction $f_v$ in a given element is the same as the *fractional projective cover* of its canopy in the area that grass occupies within the element. The same fraction is also used for the below-ground fraction of lateral spread of roots.

Plant height $H_v$ [$m$] is estimated as (Levis et al., 2004)

$$H_v \;=\; 0.25L\,. \tag{4.72}$$

# 4.5 Model testing

This section illustrates the dynamic aspects of vegetation that adaptively responds to environmental conditions and adjusts its biomass to both favorable and unfavorable situations. As discussed above, it is assumed that water is the principal limiting factor and that nutrient supply is available at all times. These assumptions have been shown to be applicable in arid and semi-arid environments (e.g., Scholes and Walker, 1993, p. 110; Rodriguez-Iturbe et al., 2001). In the following, the vegetation biophysical and biochemical processes are illustrated for surfaces vegetated with $C_4$ grass for initially saturated or dry soil. The dynamic response in terms of carbon assimilation, $CO_2$ respiration, and turnover fluxes are discussed. Next, a model verification study is presented in which the simulated above-ground biomass of a generic $C_4$ grass is compared against field measurements for Black Grama grass (*Bouteloua Eriopoda*, $C_4$ grass) for a site located in a semi-dry environment of central New Mexico.

The model parameters used in the description of processes of photosynthesis, respiration, turnover, and phenology are assigned according to typical parameterizations for broadleaf deciduous tree (examples of the stomatal response were previously illustrated in Chapter 3) and $C_4$ grass employed by most land-surface schemes (e.g., Bonan, 1996; Sellers et al., 1996b; Foley et al., 1996; Haxeltine and Prentice, 1996; Friend et al., 1997; Cox et al., 1999; Kucharik, et al., 2000; Levis et al., 2004; Arora and Boer, 2005; Krinner et al., 2005). The parameter values are provided for reference in Table 4.1 and Table 4.2.

## 4.5.1 Vegetation processes of $C_4$ grass for favorable and unfavorable soil moisture conditions

The climate simulator parameterized for Albuquerque (NM) (Chapter 2) is used in the following to force the hydrology-vegetation simulations, which assume August 1st as the starting date. To simplify the illustrative examples, a rainless period with zero cloudiness is assumed in all cases. The corresponding simulated time-series of the shortwave radiation are shown in Figure 3-8a. Another simplification is that the

Table 4.1: Parameters of biochemical processes for generic broadleaf deciduous trees and $C_4$ grass. $V_{max\,25}$ [$\mu mol$ $CO_2$ $m^{-2}\,leaf\,s^{-1}$] is the maximum catalytic capacity of Rubisco at 25°C; $\bar{K}$ [−] is the time-mean PAR extinction coefficient parameterizing decay of nitrogen content in the canopy; $m$ [−] is an empirical parameter used as a slope factor in (4.1); $b$ [$\mu mol$ $m^{-2}$ $s^{-1}$] is the minimum stomatal conductance; $\epsilon_{3,4}$ [$\mu mol$ $CO_2$ $\mu mol^{-1}$ $photons$] is the intrinsic quantum efficiency for $CO_2$ uptake for $C_3$ and $C_4$ plants; $r_{sapw}$ and $r_{root}$ [$g\,C$ $g\,C^{-1}$ $s^{-1}$] are the sapwood and fine root tissue respiration coefficients at 10°C; $\omega_{grw}$ [−] is the fraction of canopy assimilation less maintenance respiration utilized for tissue growth; $d_{leaf}$, $d_{sapw}$ and $d_{root}$ [$year^{-1}$] are the "normal" turnover rates for foliage, sapwood, and fine roots, respectively, representing the inverse values of tissue longevities.

| Parameter / PFT | Broadleaf deciduous tree | $C_4$ grass |
|---|---|---|
| | *Photosynthesis parameters* | |
| $V_{max\,25}$ | 90.0 | 30.0 |
| $\bar{K}$ | 0.5 | 0.3 |
| $m$ | 9 | 4 |
| $b$ | 10,000 | 40,000 |
| $\epsilon_{3,4}$ | 0.08 | 0.053 |
| | *Respiration parameters* | |
| $r_{sapw}$ | $9.61 \times 10^{-10}$ | - |
| $r_{root}$ | $109 \times 10^{-10}$ | $400 \times 10^{-10}$ |
| $\omega_{grw}$ | 0.25 | 0.25 |
| | *Turnover parameters* | |
| $d_{leaf}$ | 1 | 1 |
| $d_{sapw}$ | 1/25 | - |
| $d_{root}$ | 1/3 | 1 |

Table 4.2: Parameters of vegetation allocation, phenology, and water uptake processes. $\gamma_{W\,max}$ and $\gamma_{C\,max}$ $[day^{-1}]$ are the maximum drought and cold induced foliage loss rates, respectively; $b_W$ and $b_C$ $[-]$ are the shape parameters reflecting the sensitivity of canopy to drought and cold, respectively; $T_{cold}$ [°C] is the temperature threshold below which cold-induced leaf loss begins; $e_{leaf}$, $e_{sapw}$, and $e_{root}$ $[-]$ are the base allocation fractions for canopy, sapwood, and roots respectively; $\varpi$ $[-]$ is the sensitivity parameter of allocation fractions to changes in light and soil water availability; $\varepsilon_s$ and $\xi$ $[-]$ are the constant and exponent in (4.58), respectively, controlling the relation between carbon content in the above and below-ground stores; $\overline{T}_{soil}$ [°C] and $D_{LH}^C$ $[hour]$ are the mean daily soil temperature and day length, respectively, that have to be exceeded for vegetation season to start; $\Delta T_{min,Fav}$ $[day]$ is the minimum duration of period for which the conditions of transition from/to the dormant season have to be continuously met; $f_{C,init}$ and $LAI_{init}$ $[-]$ are the fraction of the structural biomass and the leaf area index, respectively, used to initiate the leaf onset; $\Psi^*$ and $\Psi_w$ $[MPa]$ are the soil matric potentials at which, respectively, the stomatal closure or plant wilting begins.

| Parameter / PFT | Broadleaf deciduous tree | C$_4$ grass |
|---|---|---|
| | *Stress-induced foliage loss parameters* | |
| $\gamma_{W\,max}$ | 1/40 | 1/50 |
| $b_W$ | 3.0 | 4.0 |
| $\gamma_{C\,max}$ | 1/6.7 | 1/10 |
| $b_C$ | 3.0 | 3.0 |
| $T_{cold}$ | 5.0 | 3.0 |
| | *Allocation parameters* | |
| $e_{leaf}$ | 0.25 | 0.45 |
| $e_{sapw}$ | 0.10 | - |
| $e_{root}$ | 0.65 | 0.55 |
| $\varpi$ | 0.80 | 0.70 |
| $\varepsilon_s$ | 30.0 | 1.25 |
| $\xi$ | 1.60 | 1.0 |
| | *Phenology parameters* | |
| $\overline{T}_{soil}$ | 10.0 | 5.0 |
| $D_{LH}^C$ | 10 | 10 |
| $\Delta T_{min,Fav}$ | 7 | 5 |
| $f_{C,init}$ / $LAI_{init}$ | 0.075 / 0.20 | - / 0.20 |
| | *Water uptake parameters* | |
| $\Psi^*$ | -0.5 | -0.1 |
| $\Psi_w$ | -2.8 | -4.0 |

air temperature is simulated with $\delta T(t) = 0$ (Section 2.6.1), which results in smooth time-series (Figure 3-8b), and the dew point temperature is assumed to be constant $T_{dew} = 12.8\ °C$ (corresponding to 30-70% daily variability of humidity, typical for the location of Albuquerque (NM) for the considered period). Furthermore, the wind speed is also assumed to be constant throughout the entire course of the simulation, $u_{atm} = 3\ m\ s^{-1}$.

Dynamics of a generic $C_4$ grass are simulated with the following assumed initial state: LAI = 3.0, SAI = 0.15, $H_v = 0.75\ m$, $d_{leaf} = 0.5\ cm$, and vegetation fraction estimated based on (4.71). Vegetation structural attributes and the fractional area correspondingly change throughout the simulation. The root zone extends down to approximately $0.33\ m$ depth with the biomass distribution parameterized as in (3.1) and $\eta = 0.009\ mm^{-1}$. The root profile remains constant throughout the simulation. Water uptake properties (Table 4.2, the soil matric potentials $\Psi^*$ and $\Psi_w$ $[MPa]$ at which, respectively, the stomatal closure or plant wilting begins, Section 4.3) are taken as $\Psi^* = -0.1\ MPa$ and $\Psi_w = -4.0\ MPa$. These values correspond to characteristic relative soil moisture values $\theta^*$ and $\theta_w$ $[mm^3\ mm^{-3}]$, respectively, used in the estimation of transpiration flux (formulation (4.17) of Section 4.4.1).

In the first numerical experiment, it is assumed that *loamy sand* soil column of 1.8 $m$ depth is initially completely saturated. Free drainage is assumed as the lower boundary flux condition throughout the course of the simulation. Only the unsaturated zone soil water dynamics are simulated and groundwater effects are not accounted for. A flat horizontal surface is considered, which is not affected by the lateral effects such as radiative shading, moisture transfer in the unsaturated zone, or runon. Figure 4-3 illustrates the estimated canopy and ground temperatures, soil water state, and biochemical rates of carbon assimilation and release of $CO_2$. As soil dries from the initially saturated state via the processes of transpiration, soil evaporation, and drainage at the lower boundary, one can observe a substantial growth in the daily amplitude of the ground surface temperature (Figure 4-3a). The transpiration factor $\beta_T$ and, correspondingly, the foliage assimilation (Figure 4-3b, c), are not significantly affected until hour 82, after which one can observe a slight

decrease in the assimilation rates and productivity (more apparent during hours 100-115). The NPP, estimated as the difference between the photosynthetic assimilation and respiration rates, is positive during the day light hours throughout the entire simulation period. This implies that the soil water store and the amount of incoming PAR are in sufficient quantities and grass can support both its existing biomass and produce new photosynthesizing material. The maintenance respiration rates for the grass canopy and root biomass (Figure 4-3d) during the day light hours are around 15-20% of the gross $CO_2$ assimilation and exhibit the diurnal variability associated with the changes in canopy and soil temperatures. Note that the total respiration (both maintenance and growth) over the simulation period is around 50% of the total gross $CO_2$ uptake.

Figure 4-4 illustrates the estimated variables characterizing the canopy and root zone states. As the soil surface and root zone become drier (Figure 4-4a), the canopy state changes slightly during the considered period of time (Figure 4-4b, 4-4c, 4-4d). The characteristics (e.g., maximum and minimum values, their timing, etc.) of the daily cycle of air humidity at the reference level $z_{0h} + d$ do not noticeably change. The canopy exhibits higher water vapor content than the atmosphere above the canopy throughout the entire simulation. The canopy stomatal resistances, sunlit and shaded, exhibit a relatively minor growth on the last day of simulation, associated with the change in $\beta_T$. Since the simulation spans only a period of favorable conditions, the canopy biomass slightly grows, which is reflected in the maximum magnitude of sunlit and shaded leaf area index (Figure 4-4d). Note that the total LAI is shown as the shaded LAI during night time hours.

In the second experiment, initially *dry* soil conditions are assumed for the same initial vegetation state (Figures 4-5 - 4-6). As can be seen in Figure 4-5b, the soil is initially very dry with $\beta_T$ close to zero. The soil surface becomes slightly wetter due to dew on the soil surface during night hours. The daily amplitudes of the estimated ground surface and canopy temperature are substantially higher than those of the previously discussed case since transpiration and evaporation fluxes, i.e., cooling energy fluxes, are near zero. The insufficiency of soil water in the root zone results in the

stomatal closure and, consequently, zero foliage $CO_2$ assimilation rates. Since artificially high biomass is initially assigned, the maintenance respiration rate is also high. Consequently, the NPP is negative throughout the simulation (Figure 4-5c). The outcome of the combined effect of water-stressed conditions and high initial biomass is a high drought-induced carbon loss of foliage biomass (Figure 4-6a). Due to the overall negative carbon balance, the canopy and fine root carbon pools rapidly reduce within the considered period of time (Figure 4-6b). As a consequence, the vegetation fraction, parameterized in (4.71) as a function of the above-ground biomass, also rapidly decreases.

## 4.5.2 Verification of $C_4$ grass model

This section outlines a model verification study based on field measurements of the above-ground biomass of Black Grama grass (*Bouteloua Eriopoda*) for a site located in a semi-dry environment of central New Mexico, specifically, in Sevilleta National Wildlife Refuge. The Sevilleta Refuge is one of the sites of the Long-Term Ecological Research Program of the National Science Foundation (NSF) to study climate change in a biome transition zone as well as habitat diversity and biodiversity characteristics of semi-arid environments. The research area encompasses approximately 3,600 $km^2$ and is located at the intersection of four major biomes including the Great Plains Grassland, Great Basin Shrub-steppe, Chihuahuan Desert, and Montane Woodland. Long-term records from nearest weather station in Socorro (NM) show that the annual precipitation ranges from less than 100 $mm$ to over 500 $mm$, with a mean value of 244 $mm$. Summer precipitation occurs as intense thunderstorms often accounting for over half of the annual moisture, while *El Niño* (wet) and *La Niña* (dry) events markedly influence regime and magnitudes of winter precipitation. Mean monthly temperatures range from 2.5°C to 25.1°C.

In 1989, a study was initiated to examine the effect of fertilization on grassland vegetation productivity in the Sevilleta Refuge. Plots were established on the east and west sides of the Sevilleta (Figure 4-7) at elevations of 1521 $m$ and 1622 $m$, respectively. Both sites were gridded into 30 $m$ x 30 $m$ plots within a rectangular area

254
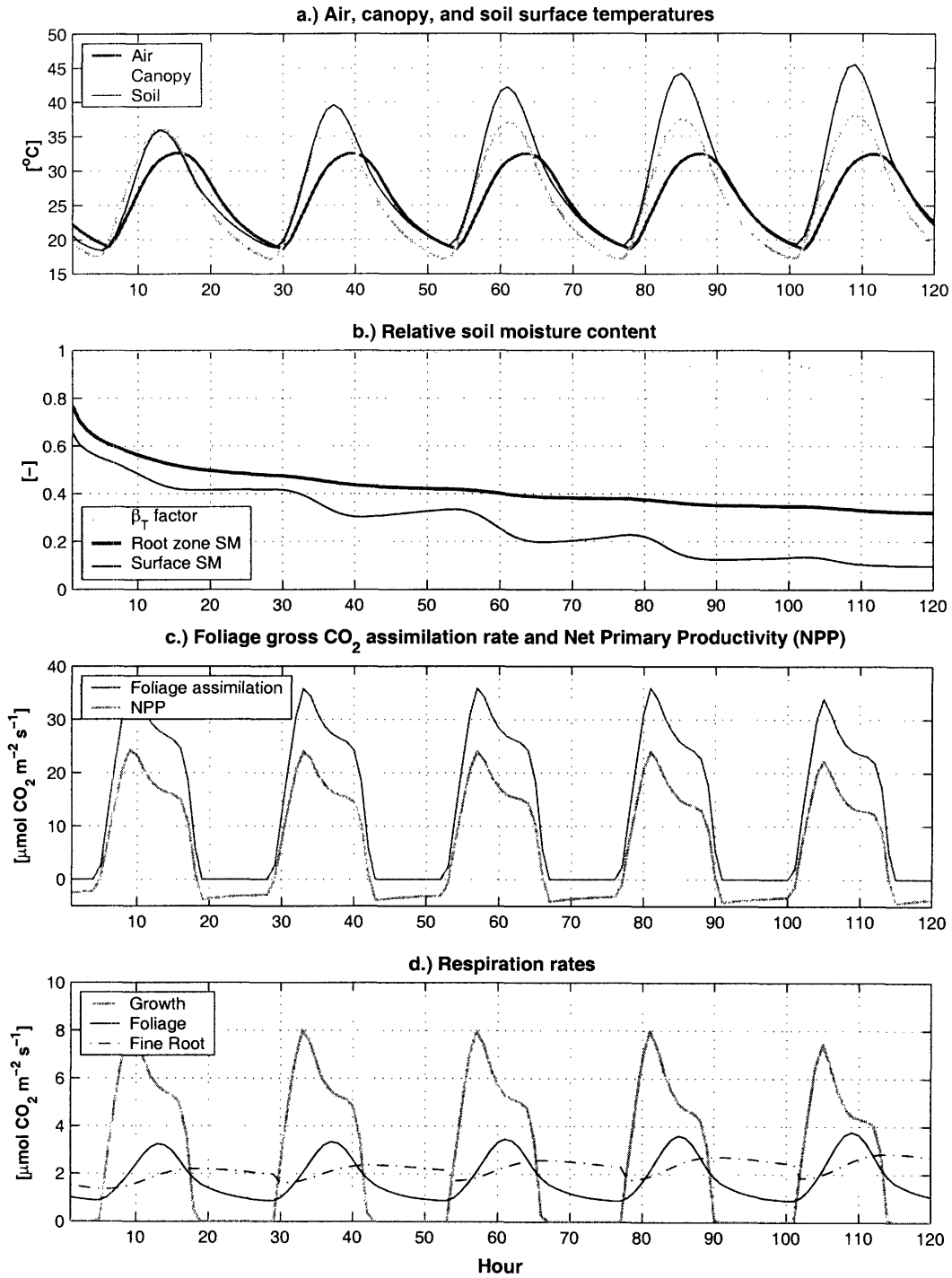
Figure 4-3: The time-series of environmental characteristics and grass biochemical $CO_2$ fluxes for *initially wet* soil: a.) air, canopy, and soil surface temperatures; b.) relative soil moisture contents and transpiration factor $\beta_T$; c.) foliage gross $CO_2$ assimilation rate and Net Primary Productivity (NPP); d.) growth, foliage, and root respiration flux rates. The rates are provided for a unit area of vegetated fraction of the computational element.
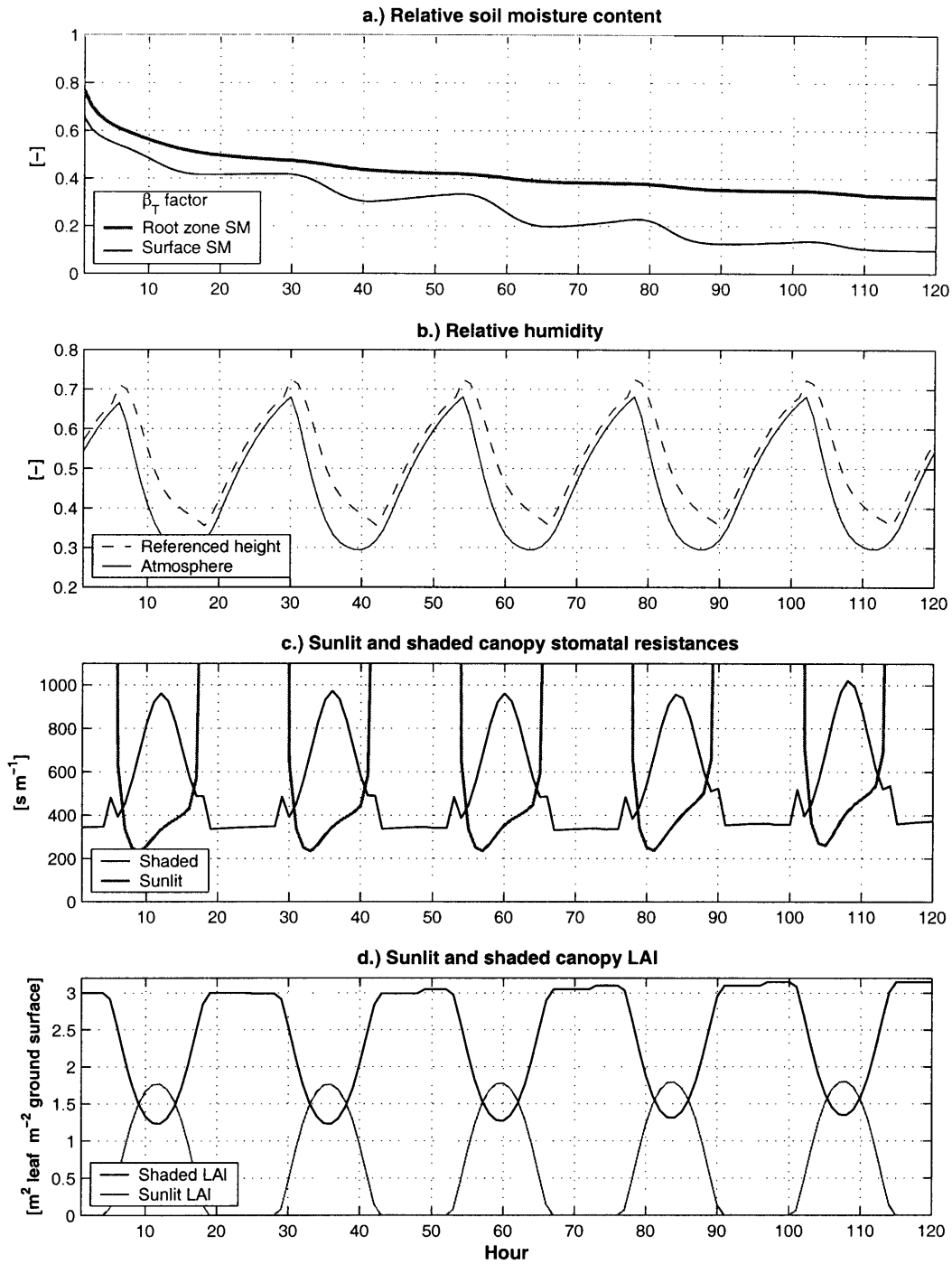
Figure 4-4: The time-series of environmental and biophysical characteristics for *initially wet* soil: a.) relative soil moisture contents and transpiration factor $\beta_T$; b.) relative humidity of the atmosphere and canopy-space air (at the reference height $z_{0h} + d$, Section 3.6.3); c.) sunlit and shaded canopy stomatal resistances; d.) sunlit and shaded canopy LAI. Note that the shaded LAI equals to the total LAI during night time hours.

256
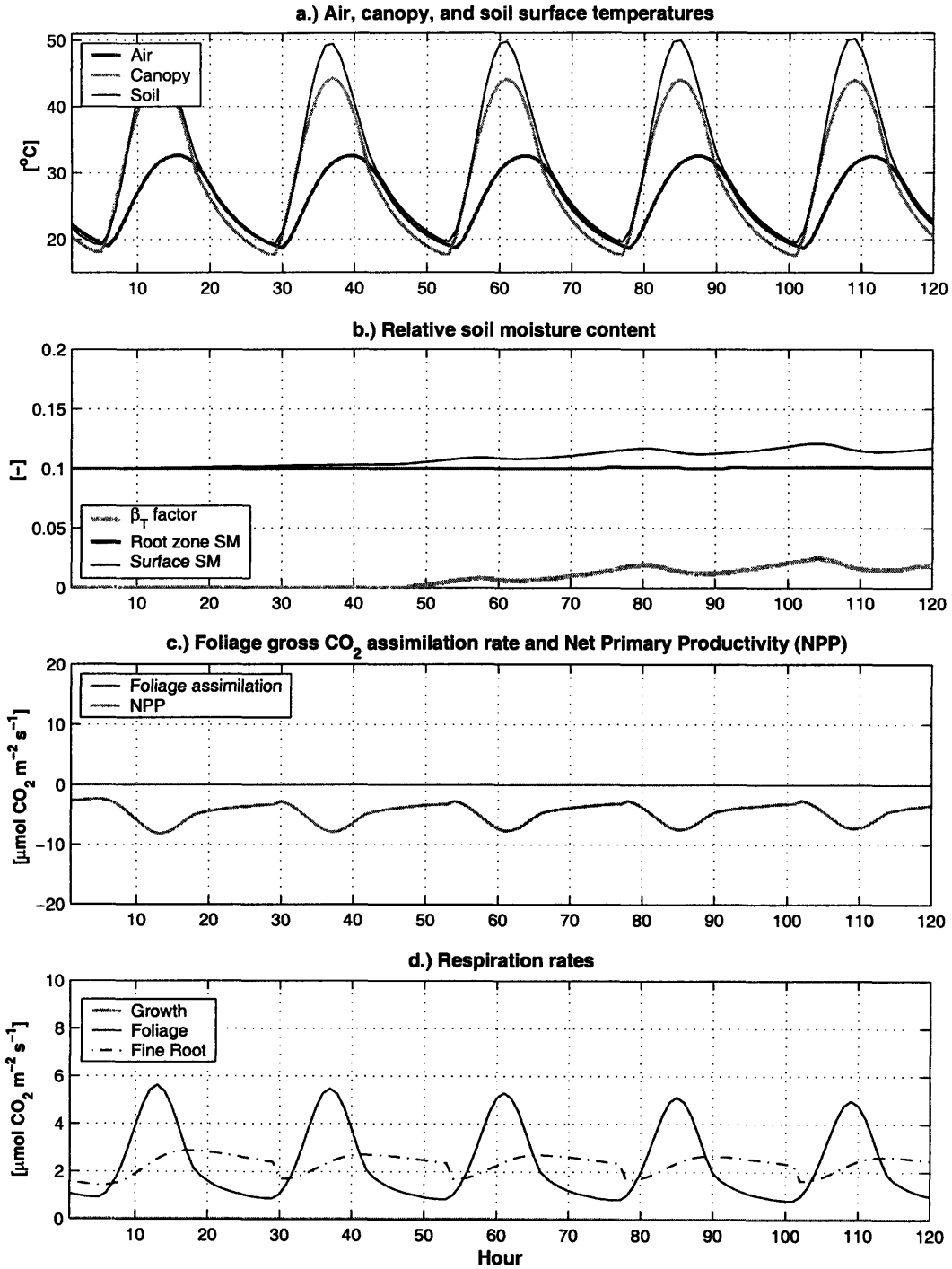
Figure 4-5: The time-series of environmental characteristics and grass biochemical $CO_2$ fluxes for *initially dry* soil: a.) air, canopy, and soil surface temperatures; b.) relative soil moisture contents and transpiration factor $\beta_T$; c.) foliage gross $CO_2$ assimilation rate and Net Primary Productivity (NPP); d.) growth, foliage, and root respiration flux rates. The rates are provided for a unit area of vegetated fraction of the computational element.
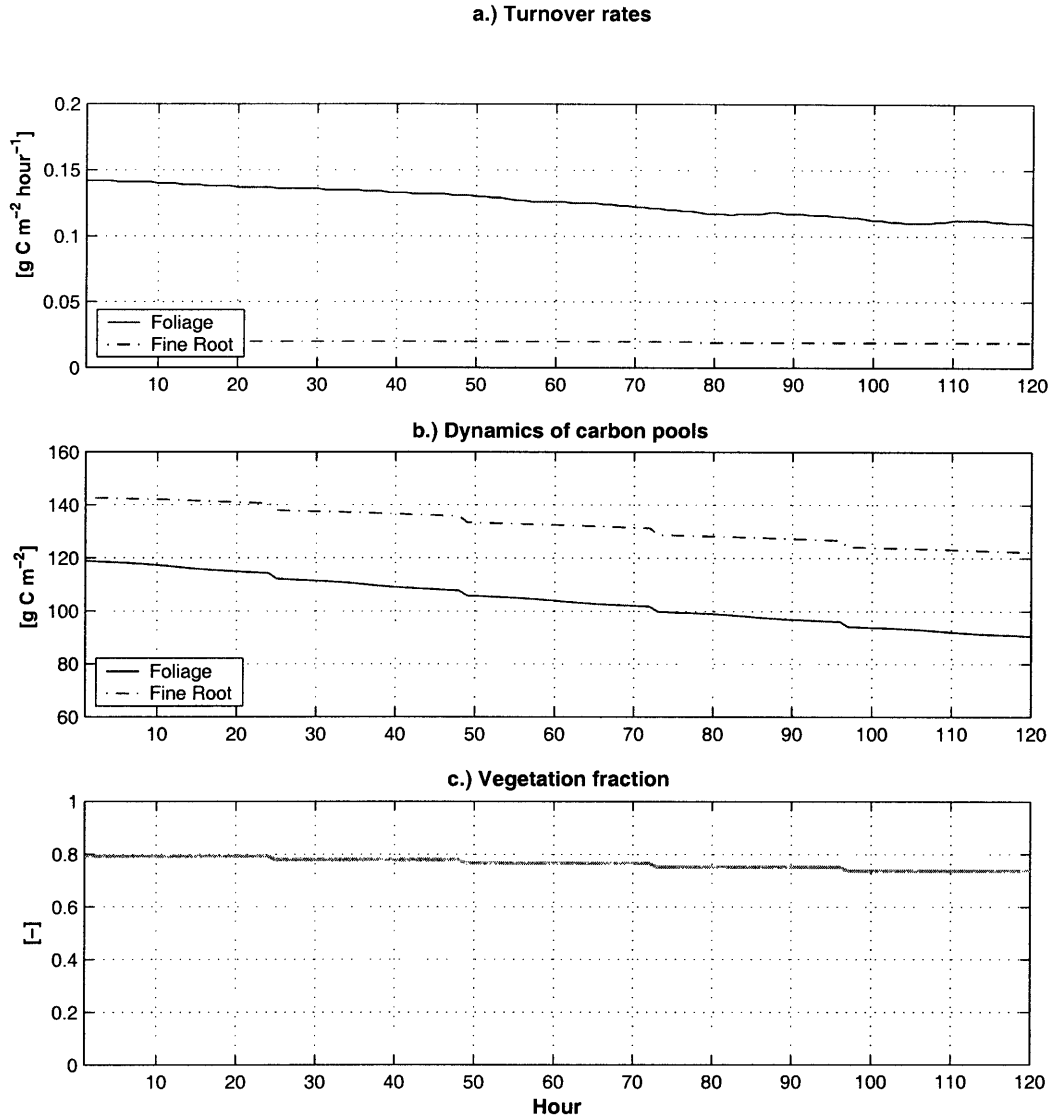
Figure 4-6: The time-series of grass water stress induced foliage loss, dynamics of carbon pools and vegetation fraction for *initially dry* soil: a.) foliage and root turnover rates (vegetated fraction scale); b.) foliage and root carbon pool dynamics (computational element scale); c.) vegetation fraction dynamics (estimated based on the carbon pool size).

of approximately 300 $m$ on a side. The east side ("McKenzie Flats" site) is more characteristic of mixed Chihuahuan Desert and Great Plains Grasslands, dominated by warm season $C_4$ grasses, such as Black Grama (*Bouteloua Eriopoda*) with lesser amounts of other $C_4$ grasses, such as Blue Grama (*Bouteloua gracilis*) and Hilaria Jamesii. The west side is more characteristic of the Great Basin shrub-steppe, dominated by cool season $C_3$ grasses, such as Indian Ricegrass (*Oryzopsis hymenoides*) mixed with other grasses, such as Drop Seeds and Hilaria. Both sites are located on *Turney Loamy Sand* soil. Chemical fertilizer in the form of $NH_4$ - $NO_3$ was applied to a set of plots on both the east and west sides. In 1989, two levels of fertilizer treatment were applied, while in 1990 only a single treatment level was applied. In 1989, 9 plots and, in 1990, 8 plots were randomly selected among the 30 $m$ x 30 $m$ treatment and control plots both during the late spring (early June) and late summer (late September - October). Within each randomly chosen plot, three 1 $m$ x 0.5 $m$ quadrats were randomly selected and clipped to estimate the plant biomass as a measure of grass growth during the cool and warm seasons. A subsequent laboratory procedure consisted in sorting the clipped plant material into live (green) and dead material by species for each quadrat. The samples were oven dried and weighed, and the weights from the 3 quadrats are then averaged and linearly scaled to provide live and dead biomass estimates in $[g \ m^{-2}]$ of the plot (note that the density refers to the quadrat scale). Two years (1989-1990) of sampling showed that there was no any significant measurable effect of fertilization on productivity on either side. Significant differences were found among years and sites. The fertilization aspect of the study was discontinued after 1990 but biomass samples from the plots continued to be collected through 1992 to monitor annual vegetation production of the grasslands.

Since the $C_4$ photosynthesis pathway represents a typical form of carbon assimilation for grass in dry and semi-dry environments, the data for the *east* side of Sevilleta Refuge were used in the following verification study. The above-ground biomass data and the collection dates for the *control* quadrats were obtained from the Sevilleta Web-site (*http://sevilleta.unm.edu/research/local/plant/fertilizer/data/wt_summary*) and are provided for reference in Table 4.3. The period of 1989-1992 appears to be

259

Table 4.3: Live above-ground biomass harvested from the *control* quadrats on the *east* side of the Sevilleta National Wildlife Refuge from 1989 to 1992. The east side was predominantly occupied by Black Grama (*Bouteloua Eriopoda*) grass.

| Year | Date | Above-Ground Biomass [$g\ m^{-2}$] |
|------|------|----------------------------------|
| **1989** | June 9 | 13.1 |
| | September 21 | 91.8 |
| **1990** | June 5 | 99.4 |
| | October 5 | 111.0 |
| **1991** | June 5* | 75.3 |
| | October 5* | 91.4 |
| **1992** | June 5* | 76.7 |
| | October 5* | 104.0 |

*The exact dates are unknown (only month). The specified dates were assigned to correspond to those of the year 1990.

particularly suitable for model verification since the annual precipitation recorded at the nearest weather station involved two contrasting cases of below-average 156 *mm* in 1989 and above-average 335 *mm* in 1991 (1990 - 244 *mm*, 1992 - 240 *mm*).

A complete set of time-series of hydrometeorological variables discussed in Chapter 2 is required to force the vegetation-hydrology model. Several weather stations were installed in the Sevilleta Refuge area during the period of 1989-1992, differing in their starting date of operation (Figure 4-7). Station 40 ("Deep Well" site, latitude 34.3556°, longitude 106.6914°) was the first weather station put into operation in the Sevilleta Refuge and the closest to the McKenzie Flats site, the fertilization study site of interest. The observed hydrometeorological variables involved: precipitation, air temperature, vapor pressure, wind speed, and global solar radiation. Since cloudiness data and partition of the shortwave radiation into the direct beam and diffuse components in VIS and NIR bands are also required, the observational data at the airport of Albuquerque (Chapter 2) were additionally used to synthesize a complete set of the forcing data. Due to the relative proximity of Albuquerque to the Sevilleta Refuge, the following routine was used: 1) the cloudiness data for Albuquerque were used without changes; 2) the measured global solar radiation at Station 40 was partitioned

260
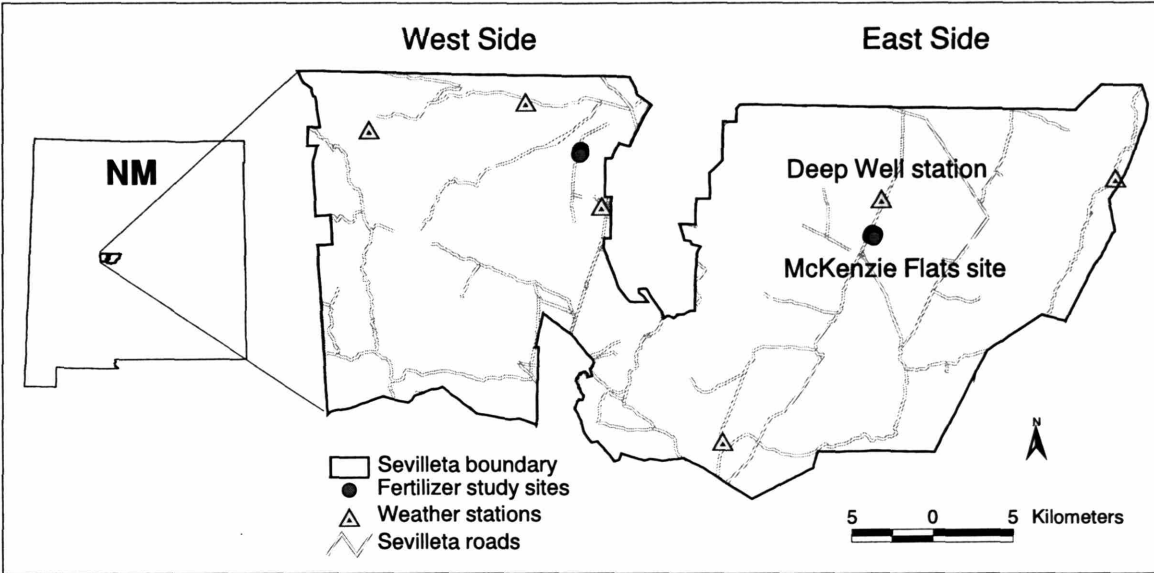
Figure 4-7: Map of the Sevilleta National Wildlife Refuge, illustrating the location of weather stations and fertilization study sites.

into the direct beam and diffuse components using the same fractional composition as the measured radiation at the station in Albuquerque; 3) to further partition the direct beam and diffuse radiation fluxes into the VIS and NIR bands, the calibrated radiative transfer model of Section 2.3 was utilized to obtain the corresponding fractional composition, which was then used for the observed data. In addition to the above procedure, when a period of missing data was encountered for Station 40, the gap was filled with the data corresponding to a nearest station in Sevilleta containing non-void data.

Inspection of digital elevation data for the area of McKenzie Flats site reveals that its topography can be characterized as flat surface situated in a non-convergent terrain location. Therefore, vegetation-hydrology dynamics can be assumed one-dimensional with negligible lateral effects such as radiative shading or mass transfer from adjacent areas. A single flat element is used for simulations and mass fluxes are restricted to be in the vertical direction only.

Since no data are available on the hydraulic properties of *Turney Loamy Sand* soil, the soil type typical for the area of study, a generic loamy sand soil type (Rawls

261

et al.,1982) is used. Its hydraulic parameters are provided in Table 3.1.

The soil water profile is initialized with a uniform depth-averaged value of $0.1\,\theta_s$, corresponding to approximately -7 $MPa$ of the suction pressure head. In order to reduce the effect of the initialization soil moisture conditions on results, one year of spin-up period is introduced. Therefore, the simulation spans the period of 1988-1992 with all vegetation-hydrology dynamics driven by deterministic forcing from the observed (and partially synthesized) meteorological data.

Figure 4-8 illustrates the observed time-series of daily precipitation and the simulated time-series of soil moisture, LAI, and vegetation fraction. One can clearly observe the relative difference in terms of precipitation and soil wetness among the illustrated years. As can be inferred from the figure, winter and spring of 1989 were relatively drier than in the other years of the simulation period. Correspondingly, the pre-growing season root zone soil water content was lower and the grass development was essentially delayed until the arrival of monsoon in July. Precipitation during the monsoon period was also relatively smaller and, consequently, the total produced grass biomass was smaller for 1989. In contrast to 1989, the hydrometeorological conditions of 1991 favored grass development since there was a substantial soil water content at the beginning of the growing season and precipitation during the monsoon period was higher than in the other years. In 1991, the simulated biomass exhibits rapid development during spring period and subsequent significant accumulation. Consequently, the soil water partition into transpiration, soil evaporation, and drainage show significant differences between 1989 and 1991 (Figure 4-9). For instance, the amount of soil evaporation in 1989 is almost equal to that of 1991 (Figure 4-9), while the amount of transpiration is substantially smaller in 1989. The drainage from the root zone is rare and can be attributed to either large precipitation events of monsoon periods or accumulated soil water from the storms of non-growing seasons.

It is also worth noting that with the arrival of favorable conditions, after a prolonged stress period, grass does not immediately transpire at the maximum potential rates (illustrated here at the *element* scale). This case is most apparent for summer of the year of 1992 (Figures 4-8c - 4-9b), although the time-scale is too coarse to

262

clearly observe that. An initial period of biomass growth exists during which the grass fractional area increases. During such a period, soil water is depleted primarily through soil evaporation at rates relatively smaller than the maximum potential transpiration rates, due to the control imposed by the highly variable moisture at the soil surface. Only after attaining a certain cover fraction can grass transpiration reach the potential rates, e.g., 2-3 $mm\ day^{-1}$. Such a situation thus illustrates the case where some ecohydrological models may fail to properly estimate the soil water dynamics. These models typically assume more rapid depletion rates, which are near the potential transpiration, immediately after the arrival of favorable conditions (e.g., Rodriguez-Iturbe et al., 1999a; Laio et al., 2001a, etc.).

Figure 4-10 illustrates the corresponding simulated biochemical fluxes of carbon uptake and loss. As discussed in Section 4.4.7, the growing season starts only when the imposed conditions for leaf onset are met with the positive daily NPP assumed to be the key criterion (Figure 4-10a). The simulated respiration fluxes depend on the amount of biomass present and environmental conditions (Figure 4-10b). The drought-induced foliage loss (combined with the turnover rates in Figure 4-10c) also depends on the amount of biomass, exhibiting higher rates during dry spells of the growing season. Finally, Figure 4-11 compares the simulated and measured above-ground biomass (note that a factor of 0.5 is applied to the data values in Table 4.3 to convert the measured dry biomass to a corresponding carbon content).

While the input meteorological data and the experimental set-up have certain problems (e.g., missing data, the artificial partition procedures of the global radiation, soil moisture initialization, generic soil hydraulic parameterization), the simulated $C_4$ grass biomass does exhibit the same pattern and consistency as the observational data. One can observe a delay in growth during the driest year (1989) and a faster accumulation during favorable periods. The minimum *root:shoot* ratio (assumed to be $\varepsilon_s = 1.25$) is always maintained. Overall, the discussed results provide sufficient evidence that the presented coupled vegetation-hydrology model is capable of producing consistent results that corroborate field-observed data.
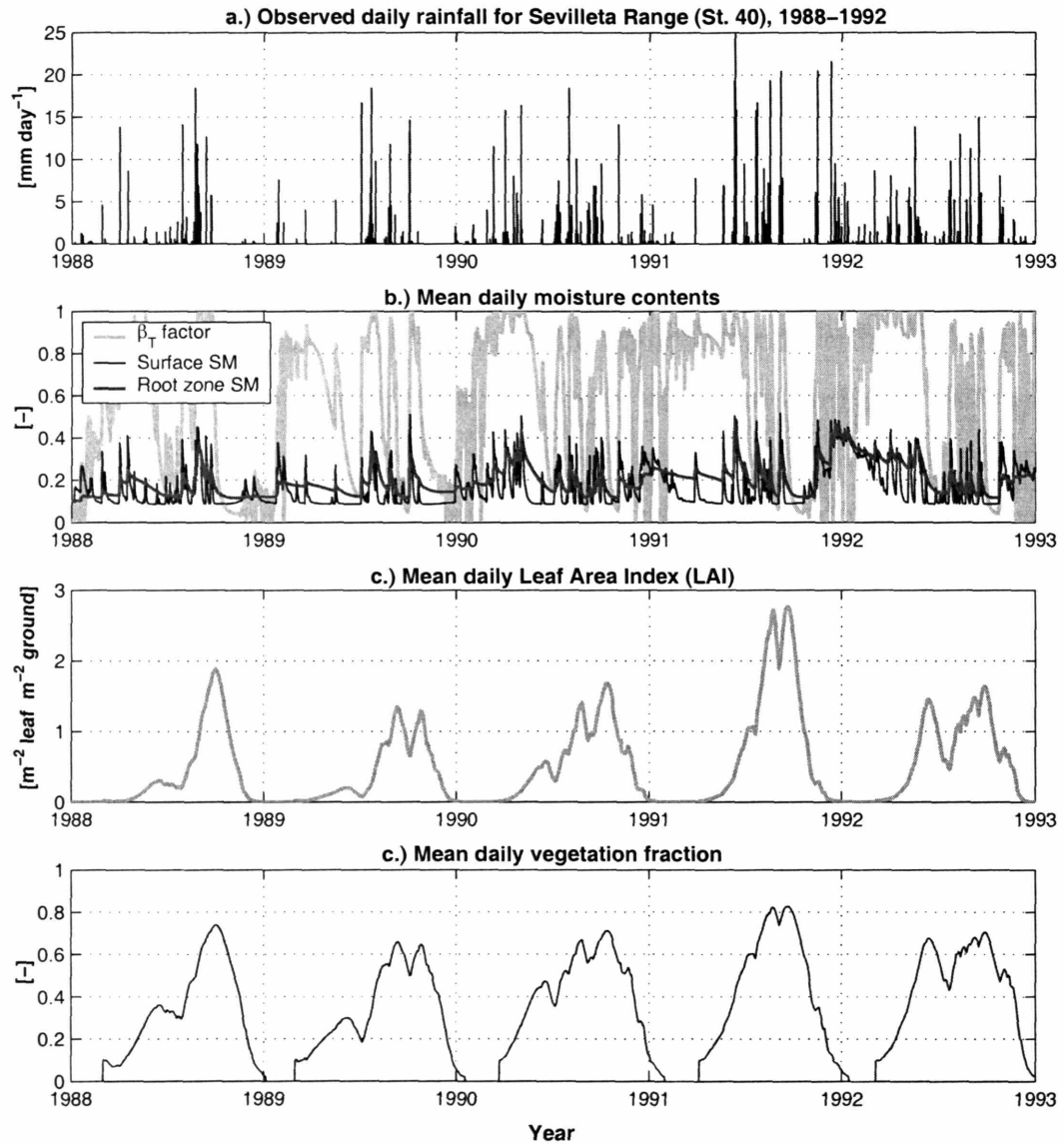
Figure 4-8: The time-series of a.) the total daily *observed* precipitation and the *simulated* time-series of the mean daily b.) relative soil moisture contents and transpiration factor $\beta_T$, c.) leaf-area index (LAI), and d.) vegetation fraction for McKenzie Flats site in the Sevilleta National Wildlife Refuge. The considered period is 1988-1992.
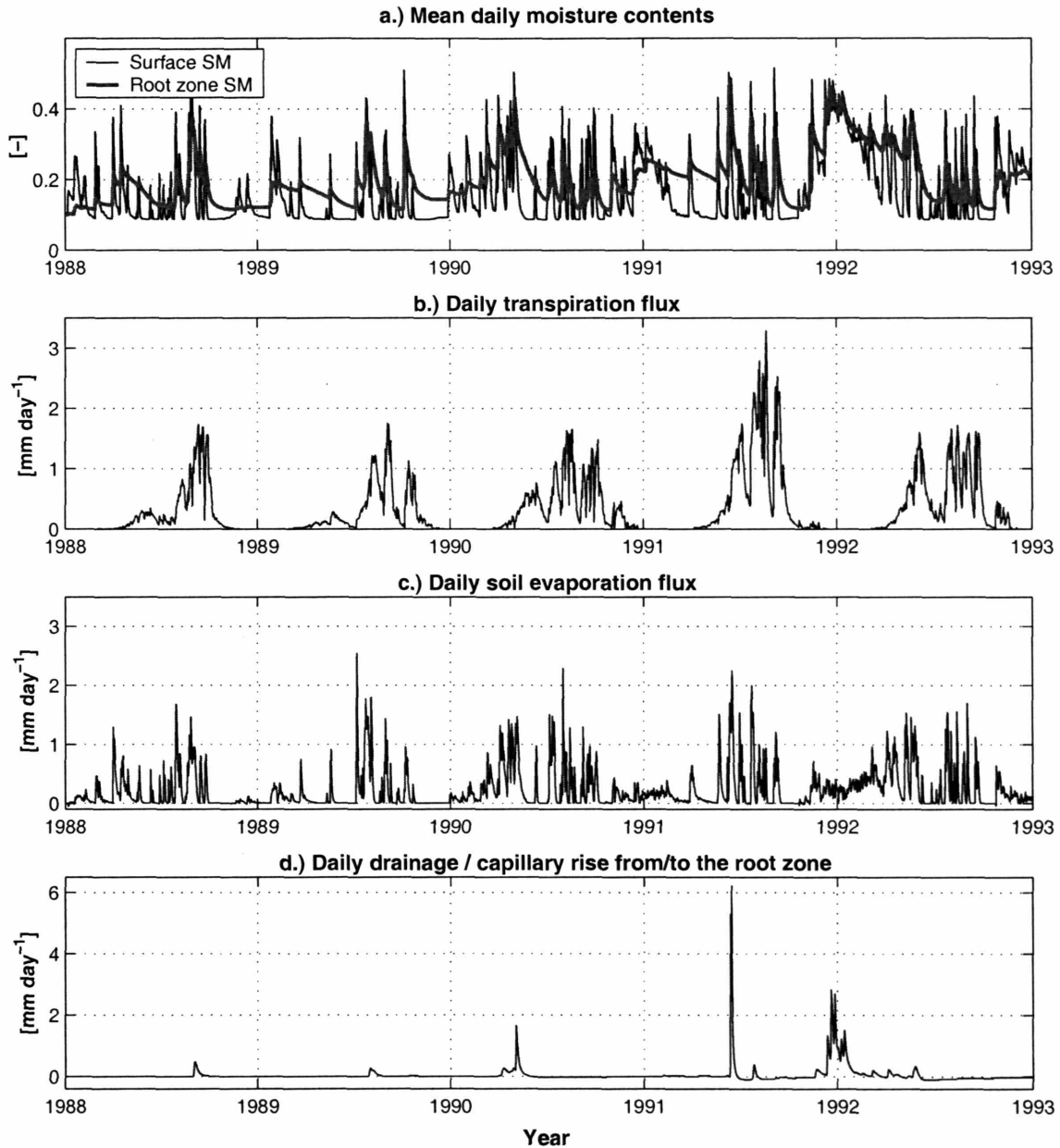
Figure 4-9: The time-series of the mean daily a.) relative soil moisture contents and total daily b.) transpiration c.) soil evaporation, and d.) drainage / capillary rise from / to the grass root zone simulated for McKenzie Flats site in the Sevilleta National Wildlife Refuge. The flux rates are provided as the element scale quantities. The considered period is 1988-1992.
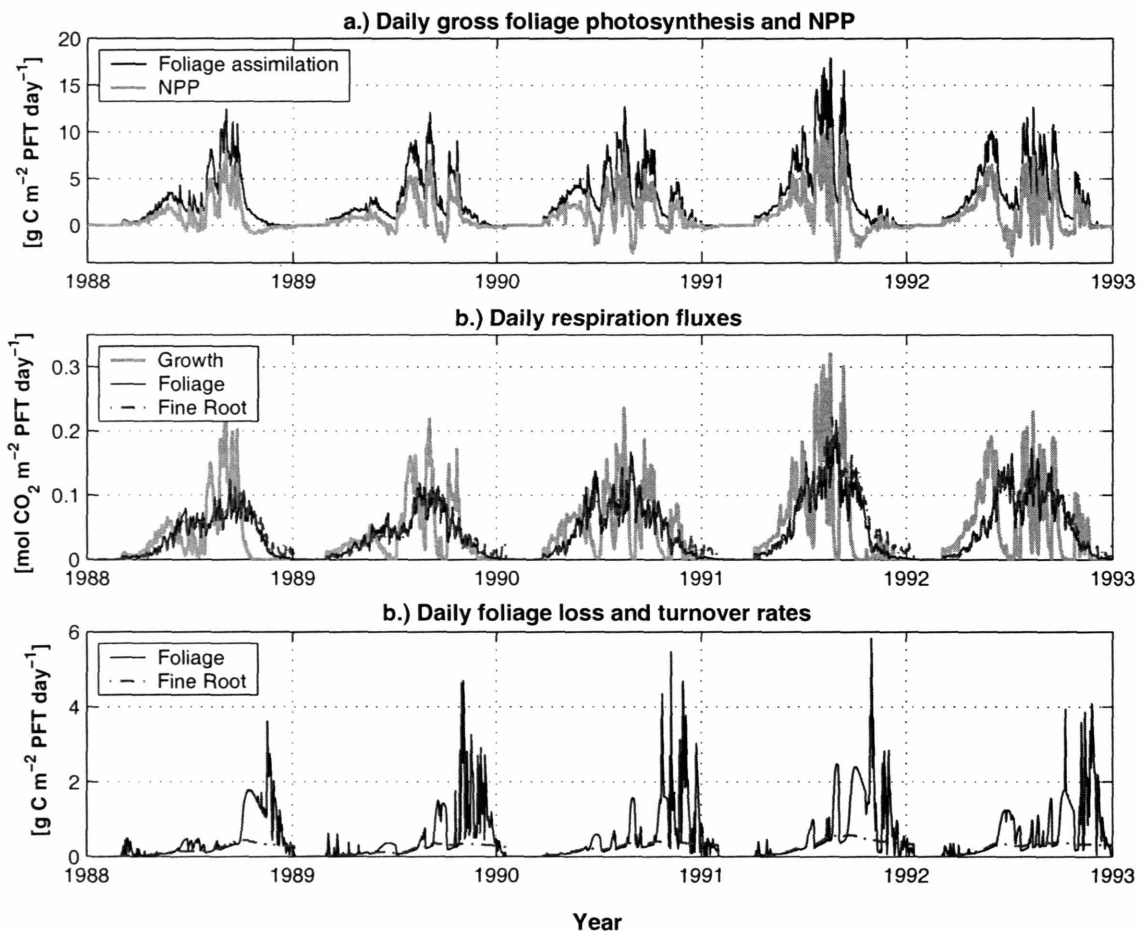
Figure 4-10: The time-series of the total daily $CO_2$ and carbon fluxes simulated for McKenzie Flats site in the Sevilleta National Wildlife Refuge: a.) gross foliage assimilation and Net Primary Productivity (NPP); b.) respiration fluxes; and c.) turnover and foliage loss. The flux rates are provided as the vegetated fraction scale quantities (PFT scale). The considered period is 1988-1992.

**a.) Mean daily moisture contents and transpiration factor**

**b.) Mean daily carbon content of canopy and fine root biomass**
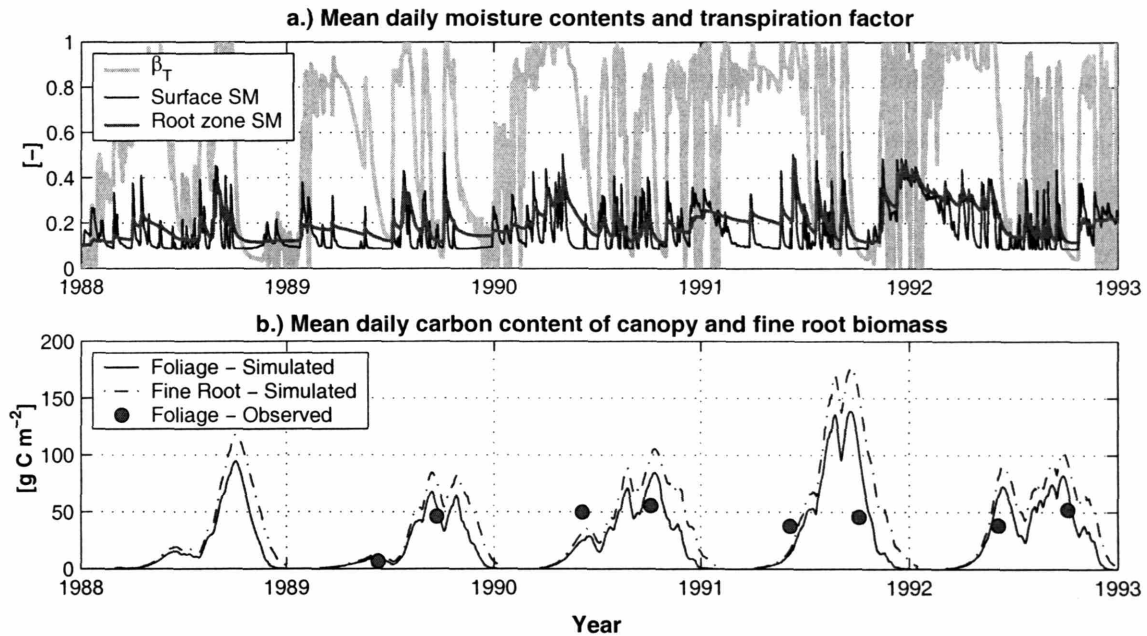
Figure 4-11: The time-series of a.) the simulated mean daily relative soil moisture contents and transpiration factor $\beta_T$ and b.) simulated and observed above ground carbon content in grass biomass (note that a factor of 0.5 was applied to the data values in Table 4.3 to convert the measured dry biomass to approximate carbon contents) for McKenzie Flats site in the Sevilleta National Wildlife Refuge. The density is provided as the element scale quantity. The considered period is 1988-1992.

# 4.6 Summary

The material of this chapter presents the model of vegetation dynamics that allows one to reproduce the transient response of vegetation to hydrometeorological forcing and moisture redistribution in a natural system. Building on the physically-based formulation of hydrological processes of Chapter 3, the description of major life regulatory processes, such as photosynthesis, respiration, tissue turnover and stress-induced foliage loss, carbon allocation, phenology, and recruitment, is primarily based on *mechanistic* models. In order to represent the differences among various plants, the model operates with the concept of plant functional types (PFTs), that allows combining of species with similar characteristics into the same simulation groups. Several PFTs can be simultaneously present in a given computational element. The above-ground competition for light is treated as the competition for available space, while the below-ground competition for water is described through the differences in plant water uptake properties and features of rooting profiles.

The consistency of the model behavior is illustrated with a series of synthetic numerical experiments for $C_4$ grass. The model parameterization is verified against field observations for semi-arid environment of central New Mexico. The results provide sufficient evidence that the coupled vegetation-hydrology model is capable of producing consistent results that corroborate field-observed data. This same parameterization of $C_4$ grass is used in the following Chapter 5 that considers the spatial aspects of vegetation-hydrology dynamics and addresses the effects of topography on vegetation dynamics in semi-arid areas.

# Chapter 5

# Dynamic Vegetation in Complex Terrain

## 5.1   Introduction

This chapter describes simulations addressing the effects of topography on vegetation dynamics in semi-arid areas. The climate corresponding to Albuquerque (NM) is used. The weather generator, described in Chapter 2, is employed to generate the long-term time-series of hydrometeorological forcing variables. The experiments are done on two small-scale synthetic domains (each is $\sim 4\ km^2$ in area) that exhibit significant differences in the hillslope characteristics. A full range of transient vegetation dynamics (Chapter 4) is simulated for a typical annual $C_4$ grass assumed to grow in three different soil types.

## 5.2   Experimental design

The simulations involve modeling vegetation dynamics in synthetic domains that exhibit characteristic self-similar organization subject to stochastic realizations of hydrometeorological forcing. Two synthetic domains are used: one exhibits longer diverging hillslopes and low drainage density. The other has shorter converging hillslopes and higher drainage density. In the former case, a larger proportion of the
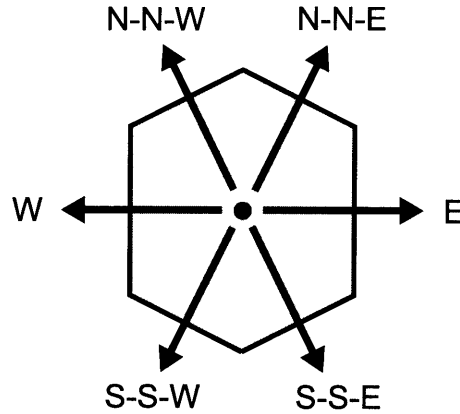
Figure 5-1: An illustration of Voronoi element, the basic computational unit for the considered domains, and its six cardinal flow directions: north-north-east (N-N-E), north-north-west (N-N-W), east (E), west (W), south-south-east (S-S-E), and south-south-west (S-S-W). A single direction is used for surface and subsurface flow routing. Its aspect is used in estimation of the incident shortwave irradiance.

landscape is dominated by *convex* hillslopes, while in the latter case most hillslopes exhibit *concave* profiles. In the following, the two landscapes will be respectively referred to as the "CX" and "CV" domains. In total, 2,400 computational elements are used to represent each of the synthetic topographies covering a wide range of slope magnitudes and aspects. Each element has six cardinal aspects (Figures 5-1, 5-2, and 5-3). The dimensions of a typical element are approximately $30\,m \times 40\,m$ (Figure 5-1). A generic annual $C_4$ grass is used to study the effects of terrain on vegetation spatio-temporal function for three different soil types. No groundwater effects are considered. The total duration of simulation is 50 years for both domains, which makes the experiments computationally feasible. The duration of the simulation period is also assumed to be sufficiently long to provide consistent statistics of vegetation-hydrology dynamics.

The described experimental design constitutes the "*base*" case scenario. For this scenario, soils are considered to be isotropic (i.e., they have a unit anisotropy ratio $a_r = 1$, Section 3.7.3) and the subsurface moisture exchange is assumed to be the only mechanism of water transfer in the domain. Rainfall is assumed to strictly follow the direction of the gravitational force (i.e., strictly vertical direction).

270
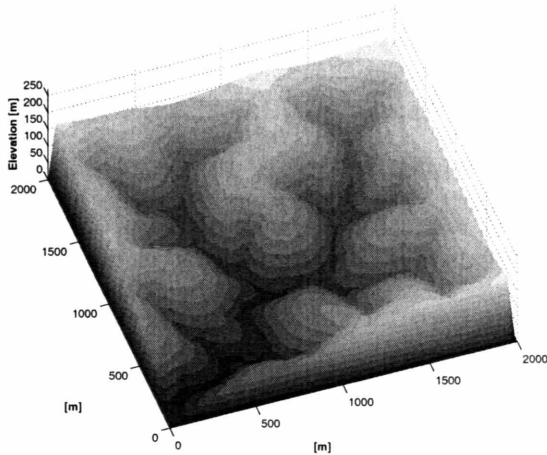
Figure 5-2: Diffusion erosion dominated landscape ("CX" domain) exhibiting longer hillslopes and lower drainage density.
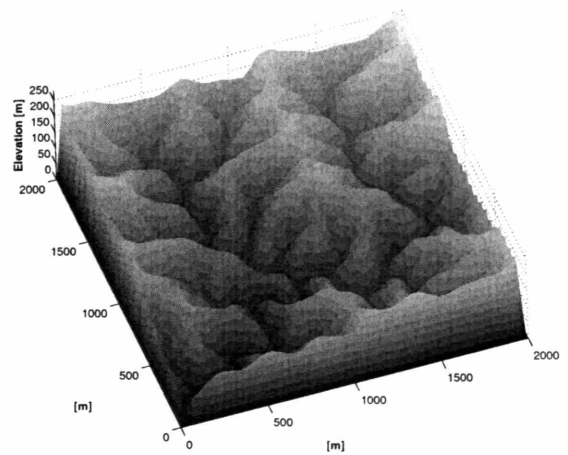


Figure 5-3: Fluvial erosion dominated landscape ("CV" domain) exhibiting shorter hillslopes and higher drainage density.

## 5.2.1 Terrain representation

The topographies of the two synthetic domains used in this study were obtained using CHILD (*the Channel-Hillslope Integrated Landscape Development*) landscape evolution model (Tucker et al., 2001). The following is a brief outline of the corresponding simulation methodology. More details on the utilized approach can be found in Tucker and Bras (2000).

For both topographies, the initial domain represents a flat rectangular surface, which is subsequently seeded with random perturbations in elevation. An outlet of the domain is placed in the lower left (south-west) corner and has an elevation that is kept fixed throughout the simulation. A given landscape is uplifted at a rate of $2.5 \cdot 10^{-5}$ $m\ yr^{-1}$, which represents a conservative value for fluvial landscapes. Each of the landscapes evolves under the action of two major erosion processes: slope dependent soil creep and runoff erosion. Soil creep is often observed in the absence of erosive runoff due to various soil disturbances such as freeze-thaw, rain-splash, bioturbation due to growth and death of vegetation, tree-throw, and soil animal activities. The process of soil creep is usually represented by a linear sediment transport model

271

(McKean, 1993):

$$Q_s = k_d |\nabla Z_E|, \tag{5.1}$$

where $Q_s$ $[m^2\ yr^{-1}]$ is the unit sediment transport rate, $k_d$ $[m^2\ yr^{-1}]$ is the hillslope diffusion constant, and $Z_E$ $[m]$ is the local elevation. The runoff erosion model represents a detachment-limited erosion rule, often used for vegetated landscapes where downslope accumulation of sediment is usually smaller than the carrying capacity of channel flow (Howard, 1994). The detachment-limited erosion can be formulated as a heuristic non-linear function of local discharge and slope:

$$Q_f = k_f Q^a S^b, \tag{5.2}$$

where $Q_f$ $[m^2\ yr^{-1}]$ is the rate of surface lowering by runoff erosion, $k_f$ $[yr^v\ m^{-w}]$ (where $v = 0.6b - 1$, $w = 1.2b - 1$) is the soil erodibility, $Q$ $[m^3\ yr^{-1}]$ is the local runoff discharge, and $S$ $[-]$ is the local slope. The parameters $a$ and $b$ may vary between 1 and 2. Combining the above erosion formulations with a source term for rock uplift, $U$ $[m\ yr^{-1}]$, provides the rate of change in elevation as

$$\frac{\partial Z_E}{\partial t} = U - k_f Q^a S^b + k_d \nabla^2 Z_E. \tag{5.3}$$

In calculating discharge $Q$, steady-state conditions are assumed and runoff at each model element is estimated as the difference between rainfall rate and infiltration capacity $Q = (R - I_c)A_V$, where $I_c$ is assumed infiltration capacity and $A_v$ is the area of Voronoi element.

In both simulations the formation of hollows is due to the simultaneous action and competition between runoff processes and soil creep. Hollow and valley formation occurs where runoff erosion, that tends to form concave valleys, outcompetes soil creep. The latter tends to fill discontinuities on the landscape (i.e., channels) due to its dependence on the hillslope gradient. The resulting landscapes are in the state of dynamic equilibrium, in which erosion is in balance with tectonic uplift everywhere

in the basin. This suggests steady-state basin topographies where over long-term $dZ_E/dt = 0$.

For the experimental domains, the uplift rate $U = 2.5 \cdot 10^{-5}\ m\ yr^{-1}$, the diffusion parameter $k_d = 0.01\ m^2\ yr^{-1}$ for the CX domain (Figure 5-2) and $k_d = 0.002\ m^2\ yr^{-1}$ for the CV domain (Figure 5-3); $a = 1$, $b = 2$, and $k_f = 0.453\ yr^{1/5}\ m^{-7/5}$.

## 5.2.2 Soil types

Three generic soil types corresponding to different hydraulic regimes are used in the experiments: sandy, loamy, and clayey soils. Their parameterization is based on soil pedo-transfer functions of Rawls et al. (1982) and provided in Table 3.1 of Section 3.8. The scenarios for each topography assume *isotropic* soil, i.e., the ratio between the saturated conductivities in the parallel and normal to the slope directions $a_r = 1$ (Section 3.7.3).

## 5.2.3 Hydrometeorological forcing

The climate of New Mexico, corresponding to the location of Albuquerque (35.05N, 106.617W), is selected as representative of a typical semi-arid area with a pronounced monsoon season driving most of the annual vegetation dynamics. The weather generator described in Chapter 2 is used to create consistent time-series of variables of hydrometeorological forcing for a 50-year simulation period. All relevant parameter values are provided in Chapter 2. In the following, the treatment of two most important forcing variables, i.e., solar radiation and precipitation, is discussed.

### 5.2.3a Shortwave radiation

Figure 5-4 shows the annual cycle of spatially lumped global shortwave radiation and a characteristic of its spatial variability. Note that the spatially integrated radiation accounts for the actual geometry of the terrain, as discussed in Section 2.3.1c. Since the CV domain features more rugged terrain with steeper slopes, as compared to the CX domain (Figure 5-3), the corresponding incident shortwave radiation is relatively

273
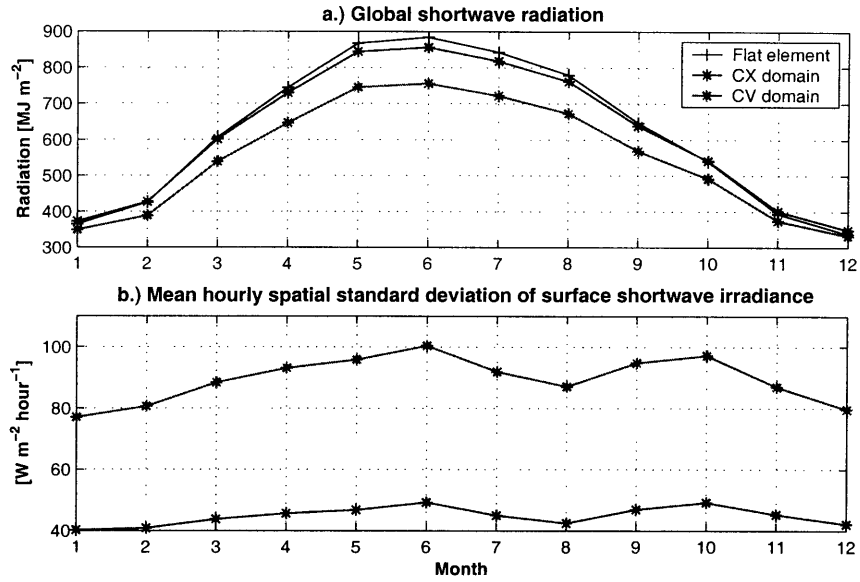
Figure 5-4: The mean simulated annual cycles of: a.) the spatially lumped global shortwave radiation for a unit inclined ground surface area; b.) the mean hourly spatial standard deviation of surface shortwave irradiance (estimated based on the hourly values). Note that the units of $[MJ \ m^{-2} \ year^{-1}]$ can be converted to $[MWh \ m^{-2} \ year^{-1}]$ by dividing the corresponding irradiance values by 3600.

smaller, while its spatial variability is higher. The decrease in the spatial variability of surface irradiance, simulated for both domains during the monsoon months of July through September, can be attributed to higher cloudiness during this period, which leads to a higher proportion of diffuse radiation. Terrain effects on incident radiation are more homogeneous in this case.

Figure 5-5 illustrates the spatial distribution of the annual global shortwave irradiance estimated as the mean value for the 50-year simulation period. Note that the hourly irradiance is computed for elements of both domains based on geometric considerations that explicitly include aspect and slope of any given site (Section 2.3.1). The mean annual irradiance in Figure 5-5 accounts for the cloudiness process, which exhibits a pronounced seasonality, since it is related to the occurrence of precipitation events. As the figure clearly shows, the annual irradiance of the south-facing elements is significantly higher than that of the north-facing sites. While the geometry of basic computational element features six cardinal aspects (Figure 5-1), the simulated

total annual radiation is distinct only for three groups of principal directions due to their symmetry with respect to the north-south axis: 1) N-N-E and N-N-W, 2) S-S-E and S-S-W, and 3) E-W (Figure 5-6a, 5-6b). In the following, unless otherwise specified, these aspects will be simply referred to as north-facing, south-facing, and east-west-facing aspects, respectively. One may notice, that the dependence of surface irradiance on slope magnitude is different for each aspect and that the slope increase for south-facing slopes initially results in growth of the incident annual shortwave radiation (Figure 5-6b). A point on the plot, denoted as "Flat element", corresponds to a flat horizontal site, which is not affected by the lateral effects such as radiative shading, moisture transfer in the unsaturated zone, or runon. The lighter color denotes the data points for the CV domain and the darker color corresponds to the data points for the CX domain. The same plotting style and notation are used in most of the following material. Additionally, Figure 5-7 illustrates the mean estimated fraction of the total annual global irradiance for direct beam and PAR radiation components, corresponding to slopes of various magnitudes and aspects.

## 5.2.3b Rainfall

Since this study attempts to mimic actual vegetation-hydrology processes accounting for the three-dimensional structures of the considered domains, the treatment of precipitation with regard to the terrain surface geometry needs to be discussed in more detail. The mean total depth of annual precipitation for the location of interest is 244 *mm* with more than 50% of it falling during the monsoon months of July through September. The Poisson arrival model of the weather generator reproduces the seasonality of this precipitation regime (Section 2.4). Note that the specified annual rainfall depth refers to a unit area of a *horizontal* surface. This depth is measured with a conventional rain-gauge that has its orifice lying in a strictly horizontal plane. The resulting measured quantity is invariant for any given site orientation irrespective of whether it is inclined or horizontal (Sharon and Arazi, 1997). This quantity is sometimes referred to as "meteorologic rainfall" (e.g., Sharon, 1980; Ambroise, 1995).

In general, the amount of rain flux intercepted on the ground depends on the angle

a.) Diffusion

b.) Fluvial

Topography contours
Contributing area [km^2]
. 0.001478 - 0.08365
. 0.08365 - 0.3216
• 0.3216 - 0.7868
• 0.7868 - 1.872
● 1.872 - 3.845
Shortwave irradiance [MJ / m^2 year]
3290 - 5274
5274 - 6134
6134 - 6697
6697 - 7109
7109 - 7400
7400 - 7683
7683 - 7886
7886 - 8124

200   0   200   Meters
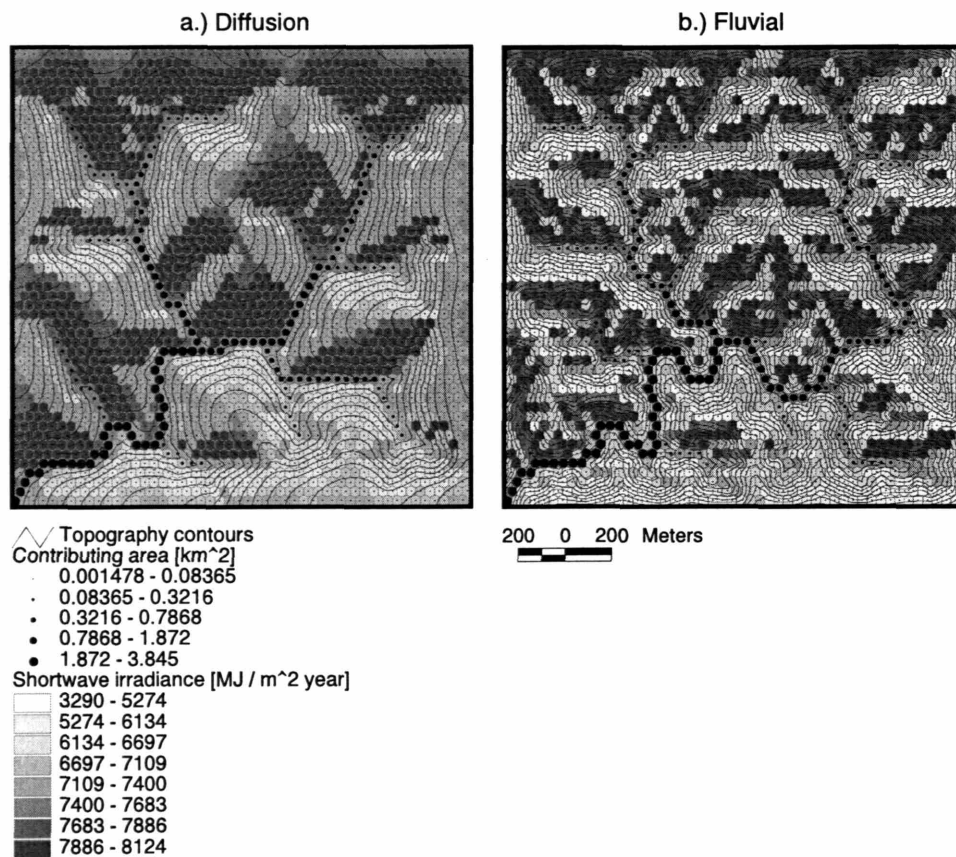
Figure 5-5: Spatial distribution of the 50-year mean annual global shortwave irradiance for the a.) CX domain and b.) CV domain. Note that the units of $[MJ\ m^{-2}\ year^{-1}]$ can be converted to $[MWh\ m^{-2}\ year^{-1}]$ by dividing the corresponding irradiance values by 3600.

**a.) Irradiance on slopes of different aspect**

**b.) Surface slope**
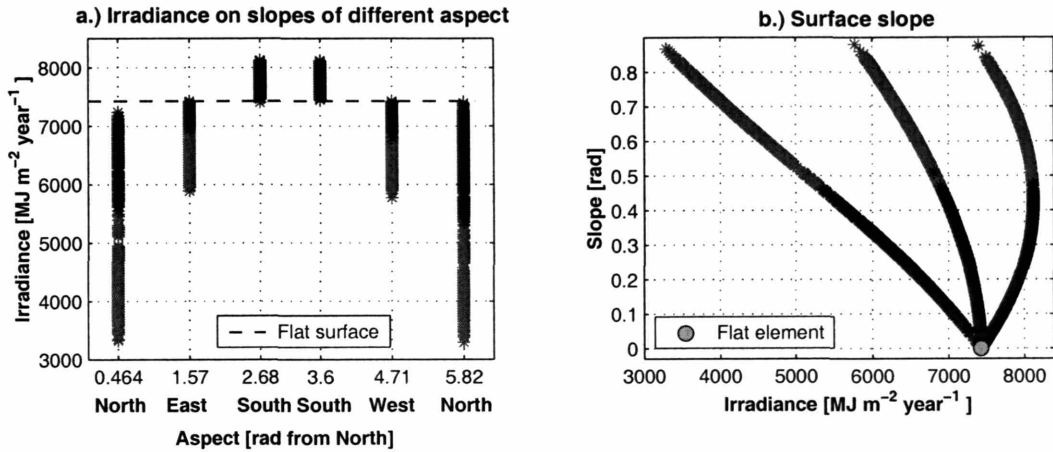
Figure 5-6: Simulated 50-year mean annual site shortwave irradiance relative to a.) six cardinal aspects and b.) site slope magnitude (the left-most curve corresponds to N-N-E and N-N-W aspects, the curve in the middle corresponds to E-W aspects, and the right-most curve is for S-S-E and S-S-W aspects). The lighter color denotes data points for the CV domain and the darker color corresponds to the data points for the CX domain.
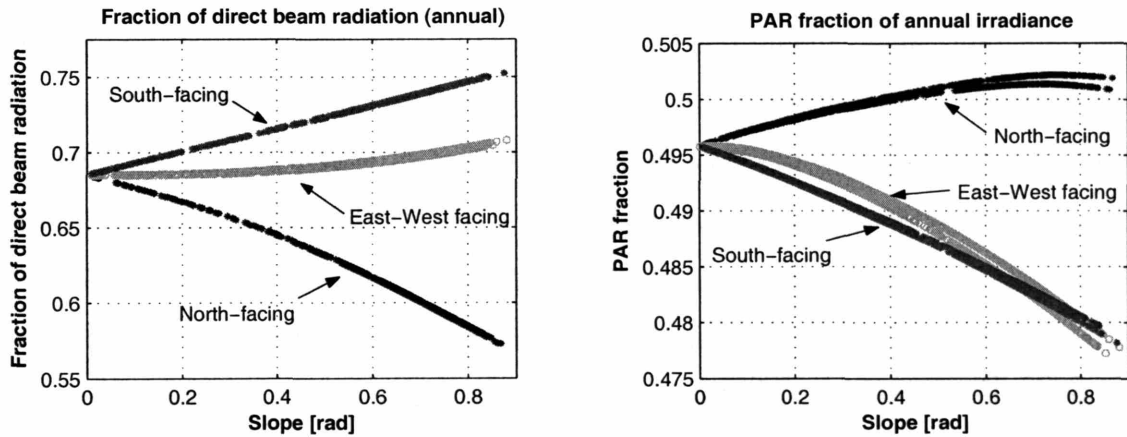


(a) Fraction of direct beam radiation

(b) Fraction of PAR radiation

Figure 5-7: Diagrams illustrating the mean estimated fraction of the total annual global irradiance for direct beam and PAR radiation components for slopes of various magnitudes and aspects. The data points for both the CV and CX domains are combined.

of incidence. It is highest when rain falls normal to a surface and decreases to zero for rain falling parallel to it, such as vertical rainfall near a wall. This implies that any surface may exhibit a *self-shading* effect. Since the rainfall direction and angle change with wind speed, wind direction and rain-water drop size, the proportion of rain actually intercepted on the ground may strongly depend on site spatial orientation (i.e., aspect and inclination). It is this quantity that is significant for rain-dependent processes of hydrology and ecology since it can have a great influence on the local water balance. It is sometimes referred to as "hydrologic rainfall" (e.g., Sharon, 1980; Ambroise, 1995). It has long been neglected in hydrologic research since most of the studies have disregarded the actual watershed topography considering only its horizontally projected area (e.g., in lumped rainfall-runoff modeling). Such an approach contains an implicit assumption that a local precipitation excess on exposed sites is compensated by rainfall deficiency on sheltered sites.

Hydrologic rainfall has been measured by means of inclined rain-gauges that have the orifice lying in a plane exactly parallel to the sloping ground (e.g., Fourcade, 1942; Storey and Hamilton, 1943; Hamilton, 1954). Since in this case the orifice constitutes a truly representative sample of the ground surface, some researchers have argued that standard rain-gauges should be exposed normally to the ground-slope (i.e., with the orifice parallel to the ground), particularly in areas of complex terrain (e.g., Storey and Hamilton, 1943; Hamilton, 1954). A number of studies have illustrated that windward surfaces may intercept up to $1.5 \div 2.0$ times more of precipitation (in the horizontal projection equivalent) than measured by a conventional rain-gauge with horizontal orifice (Sharon, 1980; Ambroise, 1995; Sharon and Arazi, 1997; Ragab et al., 2003; Blocken et al., 2005).

A simple trigonometric model was suggested to relate local topography and rainfall at the ground level (Fourcade, 1942; Sharon, 1980). An implicit assumption was that the geometric consideration used for the solar radiation incident on sloping surfaces can be equally applied to the trajectories of obliquely falling rain drops. The applicability of the model in real situations has been confirmed (Sharon, 1980) and exploited to study the distribution of wind-driven rainfall in natural catchments

(Ambroise, 1995; Sharon and Arazi, 1997). The model utilizes the same cosine law of spherical trigonometry as presented in (2.26) of Section 2.3.1c:

$$\cos\varphi_{\bullet\triangledown} \;=\; \cos\varrho_{\bullet}\cos\alpha_{\triangledown} + \sin\varrho_{\bullet}\sin\alpha_{\triangledown}\cos(\zeta_{\bullet}-\zeta_{\triangledown}), \qquad (5.4)$$

where $\varrho_{\bullet}$ [$radian$] is the inclination of the rainfall vector, measured from the zenith in the direction $\zeta_{\bullet}$ [$radian$] (the clockwise direction from north) from which rain is falling, $\alpha_{\triangledown}$ [$radian$] is the slope of the ground surface, and $\zeta_{\triangledown}$ [$radian$] is its aspect (in clockwise direction from north). The resulting cosine of the incidence angle $\varphi_{\bullet\triangledown}$ of rainfall on an intercepting surface is used to obtain an estimate of the rainfall rate that refers to a unit ground area of an *inclined* surface:

$$R \;=\; R_{\perp}\cos\varphi_{\bullet\triangledown}, \qquad (5.5)$$

where $R_{\perp}$ [$mm\ hour^{-1}$] is the intensity of rainfall with respect to a plane normal to the storm vector. As can be seen from above, for a horizontal surface $R = R_{\perp}\cos\varrho_{\bullet}$ and for vertically falling rain $R = R_{\perp}\cos\alpha_{\triangledown}$. The rate $R$ [$mm\ m^{-2}\ ground\ area$] in (5.5) is therefore expressed in a consistent system of coordinates, which is considered by the model of soil moisture dynamics for specifying the upper boundary condition (Section 3.7.2).

While theoretically sound, the above formulation cannot be directly used in this study unless additional information or a new simulation module providing "storm vectors" (Hamilton, 1954), i.e., rain directions and angles, are available. Indeed, if rainfall depth for a unit area of horizontal surface is the only known rain variable, which is the case for most hydrological studies, the relationship between its causative components is inconclusive. For instance, a rainfall rate $R_o$ attributed to a time interval $\Delta T$ can result from strictly vertical trajectories of the rain water droplets (i.e., $R_o = R_{\perp}$) or represent an "effective" mean rate as a consequence of random perturbations of the wind-driven rain field during the period $\Delta T$. In the latter situation, the total rainfall depths (per unit actual ground area) for a horizontal and certain inclined surfaces can be equal. For example, it can be shown that if $R_{\perp} = const$

279

throughout $\Delta T$ and $\varrho_{\bullet}$ switches for equal periods of time between being equal to zero (vertical rain) and some angle $\alpha_{\triangledown}$ in a certain direction $\zeta_{\triangledown}$, then the horizontal plane and ground surface at the angle $\alpha_{\triangledown}$ and aspect $\zeta_{\triangledown}$ would receive the same amount precipitation per unit ground area. Alternatively, if $R_{\perp} \neq const$, while the observed $R_o = const$, and the orientation of rain switches between being vertical and corresponding to a vector $(\alpha_{\triangledown}, \zeta_{\triangledown})$ for certain respective periods $\Delta t_1$ and $\Delta t_2$, such that $\Delta t_1 + \Delta t_2 = \Delta T$, it can be shown that the horizontal plane and ground surface at $(\alpha_{\triangledown}, \zeta_{\triangledown})$ would intercept equal rain amounts per unit ground area if $t_2 = t_1 \cos \alpha_{\triangledown}$.

In this study, rainfall depths are generated by means of the stochastic simulator (Chapter 2). The development of a suitable model of wind-driven rain would constitute a significant effort, which is beyond the scope of this research. In simulations of the *base* case scenario, all rainfall is assumed to fall *vertically*, and therefore the self-shading effect of inclined sites will be accounted for by using a factor of $\cos \alpha_{\triangledown}$. Figure 5-8a shows an approximate (since interception by vegetation is not taken into account) dependence of the total precipitation depth per unit ground area on site slope magnitude. Figure 5-8b combines the projected precipitation with information on site surface irradiance. Both the total rainfall and incident radiation refer to the actual, not horizontally projected, ground surface area. Note that while sites with the same slope magnitude receive equal precipitation depths (Figure 5-8a), the amount of incident shortwave radiation is different (Figure 5-8b). As will be discussed below, this has a significant effect on vegetation-hydrology dynamics.

As can be seen in Figure 5-8, the assumed projection procedure with the factor $\cos \alpha_{\triangledown}$ leads to a significant rainfall decrease for slopes of higher magnitude, when compared to a horizontal surface. However, as argued above, random perturbations in the wind-driven rain may lead to equality of the hydrological rainfall on horizontal and inclined surfaces. Surprisingly, the amount of research that could verify the above conceptualizations is scarce. A study by Ragab et al. (2003) addressed the effect of roof slope and aspect in the experimental study of water fluxes in a residential area. Figure 5-9a illustrates the precipitation data from this study, collected during the period of June 29, 2000 through June 30, 2001 for roofs of different orientation,

**a.) Annual rainfall depth (sloped surface)**

**b.) Annual rainfall depth (slope and aspect)**
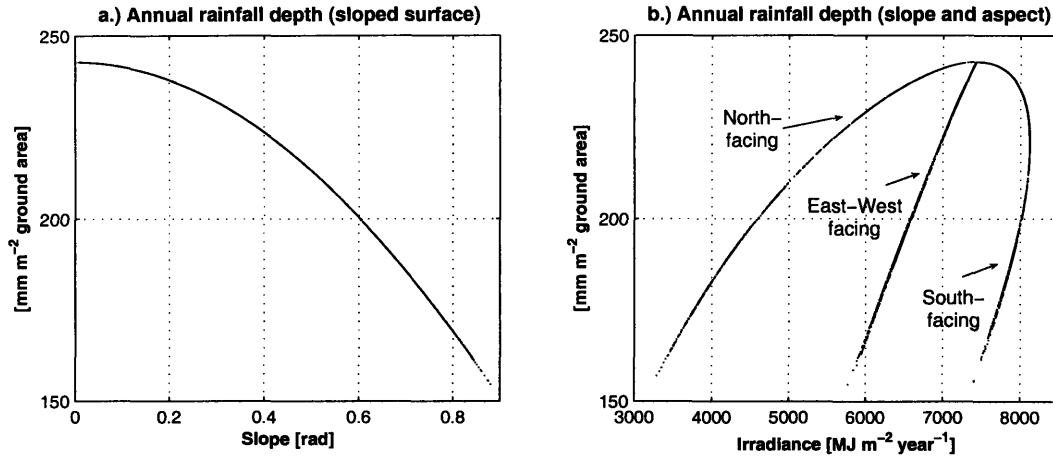
Figure 5-8: Annual rainfall depth per unit ground surface area relative to a.) site slope and b.) annual site surface irradiance (involves both site aspect and slope). Note that the units refer to the actual ground surface area of the computational element. The curves are obtained by applying a factor of $\cos \alpha_\nabla$ to the annual rainfall depth for a horizontal surface thus assuming that all rain falls in the vertical direction (the effects of interception by the canopy are not accounted for).

located in Wallingford (UK). The solid line in the figure corresponds to the rainfall depth collected for a horizontal roof, multiplied by the cosine of slopes in the range $[0 \div 60°]$. While the effect of roof aspect (windward or leeward) with respect to the dominant wind direction is evident, it can also be concluded from the figure that the data points of the observed hydrologic rainfall are in approximate agreement with the utilized $\cos \alpha_\nabla$ reduction factor. The data point for the 50° slope corresponds to a roof that was oriented somewhat leeward $(10 \div 20°)$, as can be inferred from the wind direction rose for that site (Ragab et al., 2003), and therefore collected even less precipitation than predicted by the analytical curve. A study by Sharon and Arazi (1997) addressed the differences in wind-driven rainfall in a small catchment in Israel by using 19 paired 6.75 $cm^2$ rain-gages, each pair consisting of a gage with horizontal orifice and a gage with orifice parallel to site slope. As follows from the results shown in Figure 5-9b, the site location (windward or leeward) and wind speed strongly affected the rainfall catch, resulting in local increases of up to 260% of the value for a horizontal surface. The relative reduction of rainfall depth per unit area of inclined surface, however, appears to be less apparent than in Figure 5-9a. This

281
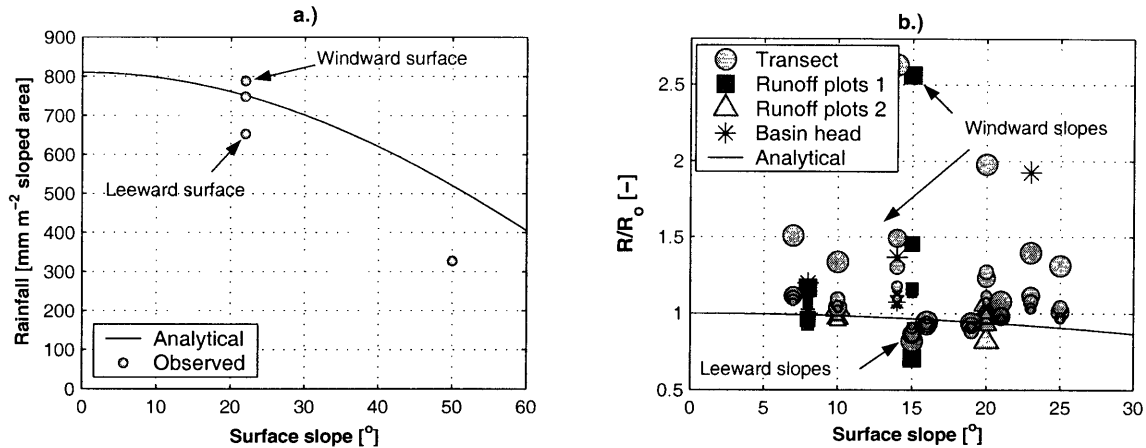
Figure 5-9: "Hydrologic rainfall" on inclined surfaces: a.) Cumulative rainfall depths relative to a unit inclined surface area observed over period of June 29, 2000 to June 30, 2001 for roofs of different orientation located in Wallingford (UK) (after Ragab et al., 2003); b.) Ratio of hydrologic rainfall to meteorologic rainfall for selected rainfall events over period of January 5, 1991 to February 26, 1992 at 19 sites of Nahal Aleket basin (Israel) (after Sharon and Arazi, 1997). The symbol size represents the grouping of storms according to prevailing wind conditions: 3-5 $m$ $s^{-1}$ (smallest symbol), 5-7, 7-9, 9-12, 17-20 $m$ $s^{-1}$ (largest symbol).

confirms that random perturbations of the rain field may lead to spatial averaging of precipitation on inclined surfaces, at least within the considered range of slope magnitudes (0 ÷ 25°).

## 5.2.4 Vegetation

A generic annual $C_4$ grass is used in the following set of experiments. Grass is used due to the following reasons: 1.) biomass of herbaceous species is very responsive to the hydrometeorological conditions of a given year and can be highly dynamic during a single vegetation season and, therefore, grass dynamics simulated over a relatively short period of time can be used as representative indicators of site characteristic conditions; 2.) the initialization of carbon pools does not affect simulated dynamics since biomass is not transferred between vegetation seasons (nutrient pools are not considered); 3.) the physical consistency of the model has been satisfactorily verified based on data of $C_4$ grass productivity for the area of interest (Section 4.5.2); 4.) the

assumption of time-invariant root distribution profile (Section 3.4) is less restrictive for the shallower depths of the rooting zone, which develops during a single growing season. It is worthwhile to elaborate on the last statement. It is recognized that root biomass distribution reflects the adaptive properties of grass dynamics to soil water and temperature stress, which are characteristic for a given soil type. Therefore, it is acknowledged that the assumption of invariant root distribution is rather strong. It is consequently expected that the grass dynamics will be affected, exhibiting distinct differences among the soil types. Nonetheless, the goal of the presented study is to elucidate the principal mechanisms through which the terrain features affect vegetation dynamic behavior and, in particular, grass primary productivity. While the assumption of the root profile invariance in time and among the soil types will limit the results of this study, nonetheless, generality of the discovered mechanisms should still hold.

Grass transits from dormant state to active growth phase every year, when soil and weather conditions become favorable (Section 4.4.7). For all computational elements in both domains, the same minimum initial value of LAI is assumed to define the initial vegetated fraction of the element area (Section 4.4.8). Grass adaptively responds to conditions of a given season by increasing or decreasing the foliage and fine root biomasses. The end of a growing season is also determined by vegetation-hydrology conditions and thus season durations may vary between different sites in a given domain. Figure 5-10 illustrates the mean simulated growing season duration for the *base* case scenario for the three soil types used in the experiments, relative to slope magnitude and site mean annual surface irradiance. Note that the three curves in the upper plots correspond to slopes of different aspect: north-facing is at the top, east-west facing is in the middle, and south-facing is at the bottom. As one can observe, the total annual irradiance is one of the key factors affecting the growing season duration. The solar radiation is the primary determinant of the annual energy budget, which, mediated by vegetation-hydrology processes, affects the initial and final soil water and temperature conditions of growing season, thereby determining its duration.
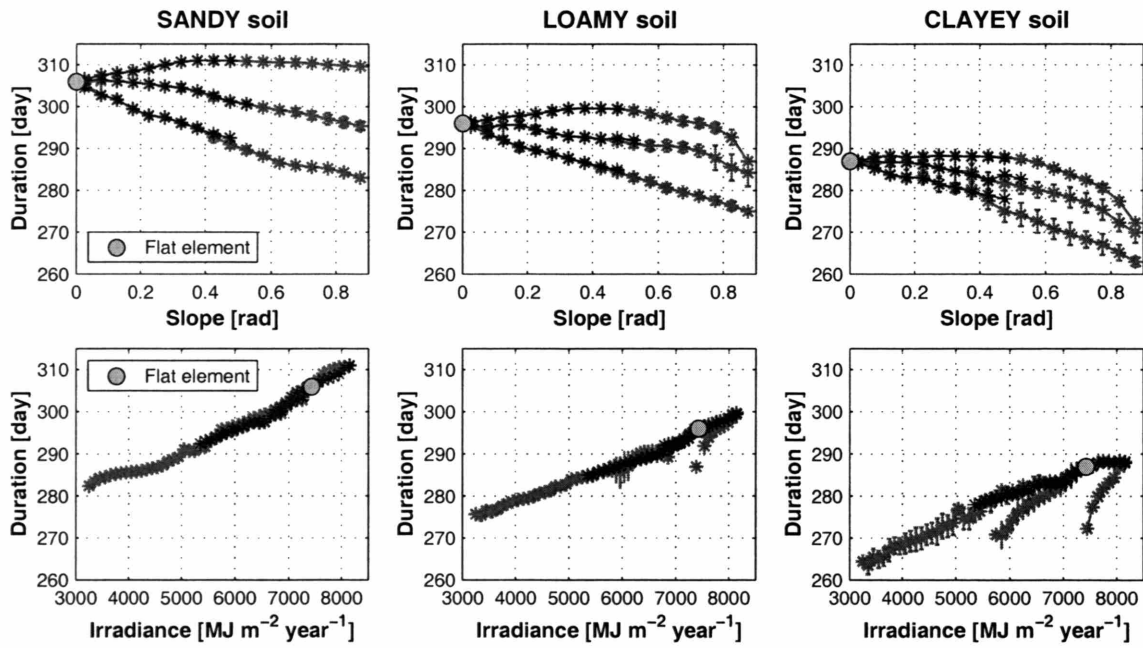
Figure 5-10: Mean simulated durations of growing season for the *base* case scenario for the three soil types used in the experiments, relative to slope magnitude and site mean annual surface irradiance. Note that the three curves in the upper plots correspond to slopes of different aspect: north-facing are at the top, east-west facing are in the middle, and south-facing are at the bottom.

# 5.3   Base case scenario

The following analysis discusses both the spatially-*lumped* and spatially-*distributed* variables of vegetation-hydrology dynamics. The analysis of spatially-lumped quantities addresses the simulated probability distributions of soil moisture and characteristic annual cycles of water fluxes and vegetation variables. A number of quantities are compared that characterize the space-time integrated dynamics for the CX and CV domains as well as for a flat horizontal surface, not affected by lateral interactions or topographic shading. The succeeding analysis of spatially-distributed variables addresses the features of terrain that exert most significant impact on the coupled vegetation-hydrology dynamics. Topographic regions that favor the grass life cycle are identified.

## 5.3.1   Analysis of spatially-lumped variables

### 5.3.1a Probability density function of root soil water content

The probability density function of the root zone soil water content is an important descriptor of the soil-vegetation-climate system. Figure 5-11 illustrates distributions of the mean *daily* spatially-lumped soil moisture content in the root zone. The distributions include the simulated data for both growing and non-growing season periods. As can be observed, the difference between the two terrain types is rather minor, with the CV domain exhibiting somewhat drier states. A drastic difference can be observed among the three soil types: the distribution switches from the bimodal to the unimodal type, when considering soils of coarser and finer texture, respectively. The feature of bimodality has important implications for plant dynamics since it shows that vegetation systems may tend to remain in states deviating significantly from average conditions.

Several mechanisms that may lead to the bimodality property of soil water states have been discussed in literature. Rodriguez-Iturbe et al. (1991) developed a statistical-dynamical model of surface hydrology that included a parameterization for the local recycling of precipitation. It was shown that stochastic fluctuations in the precipita-
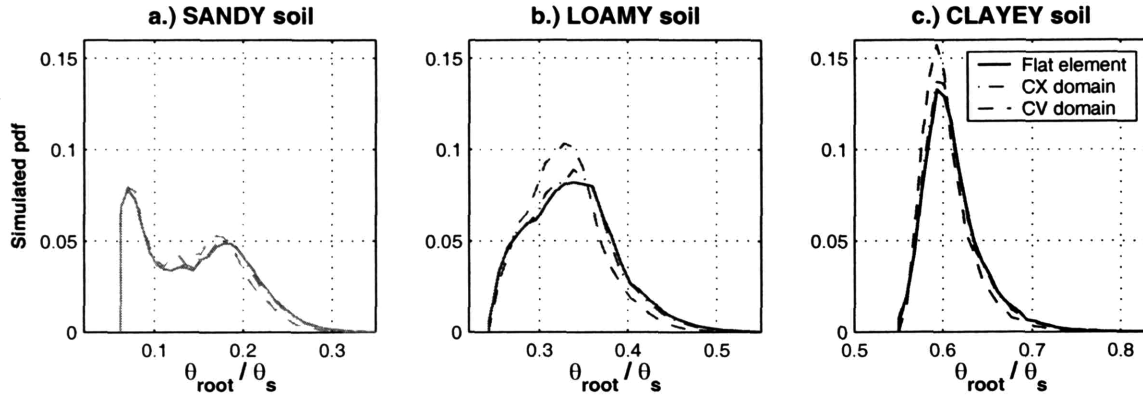
Figure 5-11: The probability density function of the mean *daily* spatially-lumped root soil water content (as $\theta_{root}/\theta_s$ for the first 30 $cm$ of soil) estimated over the 50-year simulation period for both the CX and CV domains: a.) sandy soil; b.) loamy soil; c.) clayey soil. The data involve both growing and non-growing season periods.

tion forcing may lead to two maxima in the steady-state probability density function of the surface soil moisture (top 10 $cm$). Building on the analytical framework of Rodriguez-Iturbe et al. (1999a), D'Odorico et al. (2000) showed that bimodality of the growing season root soil moisture may emerge under highly fluctuating climate. D'Odorico et al. (2000) illustrated the sensitivity of the bimodality property to various parameters of their model concluding that: "The bimodal character of the probability distribution of the average soil moisture ... results from the non-linear dynamics operating in the system, arising primarily because of non-linearity of the losses".

Apparently, the simulated situation is analogous to the one addressed by D'Odorico et al. (2000), since it is the interplay between the various hydrology processes that leads to two preferential states in the system. It is necessary to note that bimodality of the soil water content of the root zone is not present in soils of finer texture (Figure 5-11b, 5-11c). In these soil types, as will be shown later, soil evaporation is the dominant water balance component. It is therefore plausible that the emergence of two distinct statistical modes for sandy soil is actively modulated by the vegetation processes. On the other hand, bimodality does emerge for clayey soil when the probability density function is constructed for water content in the top 1 $cm$ of the

286
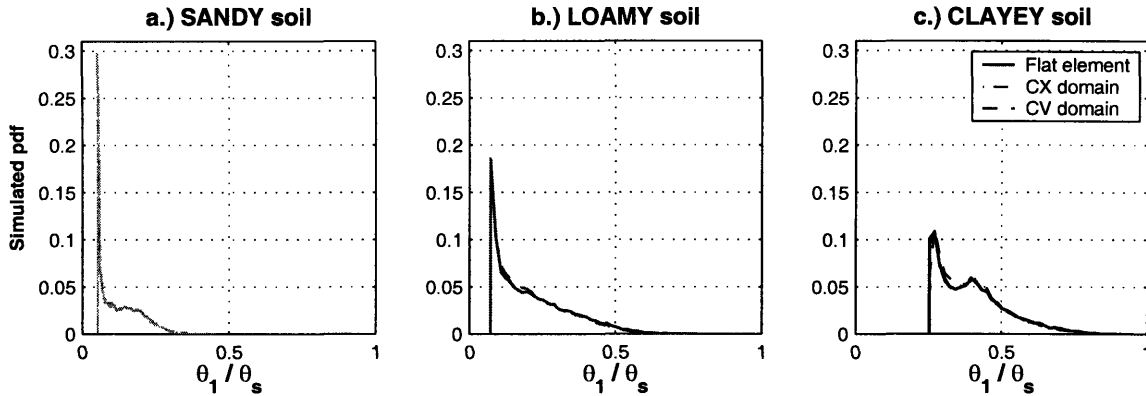
Figure 5-12: The probability density function of the mean *daily* spatially-lumped surface soil water content (as $\theta_1/\theta_s$ for the first 1 *cm* of soil) estimated over the 50-year simulation period for both the CX and CV domains: a.) sandy soil; b.) loamy soil; c.) clayey soil. The data involve both growing and non-growing season periods.

soil column (Figure 5-12). It thus leaves the question open. It is unclear whether the bimodality is associated with vegetation processes or soil texture effects alone contribute to its emergence (with a certain associated integration depth range). Also, since data for the entire year are used, the soil moisture conditions of non-growing season may have a notable impact on the simulated distributions. More research is needed to elucidate the above effects, which may have an important implication on soil water sampling practices.

## 5.3.1b Annual cycles of water fluxes and vegetation variables

In the following, the time-series of spatially-lumped variables are averaged over the 50-year simulation period to obtain their corresponding mean annual cycles. The time-series for a flat horizontal surface, which is not affected by lateral interactions, such as subsurface fluxes and runon, or topographic shading, are also discussed as the benchmark case.

Figures 5-13 - 5-15 illustrate the mean monthly values of the root zone principal water balance components estimated for the two domains and the three soil types. Note that as previously, the units refer to the actual ground surface area and not its horizontal projection equivalent. As can be observed in the figures, the difference

between the annual cycles for the flat domain and the CX domain is minor, and the difference between the cycles for the CX domain and the CV domain is moderate. The CV domain has the largest actual ground surface area due to steeper hillslopes (Section 5.2.1). The most significant discrepancies among the annual cycles of the water balance components can be attributed to soil's effects on the simulated dynamics. As can be inferred from the figures, transpiration is the essential mechanism through which water escapes the grass root zone in sandy soils, while soil evaporation is a more efficient mechanism of moisture removal in clayey soils. Consistently with the imposed forcing, the periods of the highest monthly water fluxes coincide with the monsoon months of July, August, and September. It is worth noting that the maximum of the transpiration flux for clayey soils is somewhat shifted toward later months. This appears to be related to a delay in the grass development, since the high soil water potential during early spring months prevents rapid development of biomass, as opposed to the case of grass dynamics on sandy soils. As can be observed, runoff production is infrequent for all considered scenarios. All soil types exhibit drainage from the root zone during cooler winter months. Capillary rise is characteristic for periods of moisture shortage during the months of higher shortwave radiation (May-June-July).

One of the apparent shortcomings of the modeling approach is that runoff is produced only on clayey soils: the rectangular pulse rainfall model, used to force the simulated dynamics, rarely generates precipitation events of high intensity. In addition to that, the discussed *base* case scenario does not consider soil surface sealing, which is a typical effect for soils of arid and semi-arid regions (Howes and Abrahams, 2003). As will be shown in Chapter 6, soil sealing may lead to significant runoff and remarkable spatial redistribution of water in the domains, thereby strongly affecting local water fluxes and grass productivity.

Figure 5-16 compares the spatial variability of the moisture fluxes in the two domains. The mean *hourly* spatial standard deviation of moisture fluxes within the CV and CX domains is discussed (it is zero for the flat domain). The primary purpose of Figure 5-16 is to contrast the magnitudes of variability in the two domains. As can

288

be seen in the figure, the spatial variability of the hourly moisture fluxes for the CV domain is almost twice higher that of the CX domain. Accordingly, the difference in variability can be attributed to the difference in geometry of the two domains. The underlying mechanisms will be elucidated in Section 5.3.2.

The mean annual cycles of vegetation fraction, the Above-ground Net Primary Productivity (ANPP), and the root moisture transpiration factor $\beta_T$ (determines the departure of transpiration rate from a potential value)are given in Figures 5-17 - 5-19. Similar to the cycles of the moisture fluxes, the differences between the two domains are rather moderate and the major differences are due to the soil's effects. As can be seen, the grass dynamics on sandy soil type lead to a bimodal cycle of productivity. The winter soil water storage is sufficiently high for grass to initiate photosynthesis in the early spring, leading to a rapid biomass accumulation (subplots (a.)). Before the monsoon arrival in July, a die-back phenomenon can be observed: in order to support the accumulated biomass, the grass requires moisture, however, the soil water storage is depleted at that time. Consequently, both the vegetation fraction and the productivity somewhat decrease at that time. The grass dynamics on loamy and clayey soil types are impeded at the beginning of the growing season due to insufficient soil moisture, which does not accumulate over the cooler winter months in sufficient quantities. The slower biomass accumulation leads to a relatively more stable vegetation state during the month of June, since the grass does not die-back during that period for these soil types. A gradual growth and biomass accumulation can be observed throughout the monsoon period. It is worth noting that the monsoon period coincides with the period of maximum incoming solar radiation. Since both the higher energy input and larger amount of biomass lead to growing rates of evapotranspiration, the soil water reservoir is rapidly depleted and grass is under significant stress during this period in all considered scenarios (subplots c.) in all figures).

Figure 5-20 illustrates the spatial variability of the above variables. The mean *hourly* spatial standard deviations are shown. Corroborating the preceding analysis, the spatial variability is twice as high for the CV domain. While the highest spatial

289

variability for vegetation variables (fraction and ANPP) can be evidently attributed to the months of the growing season and monsoon period, the indicator of the soil water state, the factor $\beta_T$, exhibits highest variability during cooler winter months. The latter fact can be probably related to an essential elimination of vegetation as a regulating medium. Therefore, incident radiation that is highly variable in space is the key factor affecting the soil water dynamics.

## 5.3.2 Analysis of spatially-distributed variables

The following analysis of spatially-distributed variables identifies terrain features that influence the coupled vegetation-hydrology dynamics of the *base* case scenario. The first two moments of state and derived variables at any given site are assumed to be representative indicators of these dynamics. Correspondingly, key physical estimates, such as ANPP, moisture fluxes, and soil water states, are averaged over the 50-year simulation period at every computational element and used in the following comparative analysis. Regions of topography that favor grass life cycle are consequently identified.

### 5.3.2a Grass productivity

Figures 5-21a - 5-21b illustrate the spatial distribution of the mean growing season Above-ground Net Primary Productivity (ANPP) simulated for $C_4$ grass on *sandy* soil type in the two domains. Overall, ANPP can be used as one of the representative characteristics of vegetation performance associated with a certain topographic location. One can observe evident differences between the spatial distribution of the mean ANPP in the domains. While maximum values are approximately the same, the productivity is more variable in space for the CV domain and is quite homogeneous for the CX domain. Clearly, topography exerts a distinctive effect on grass dynamics. In the following, an attempt is made to identify terrain features that have a predominant contribution to these simulated patterns. The corresponding hydrological implications are consequently discussed.

290
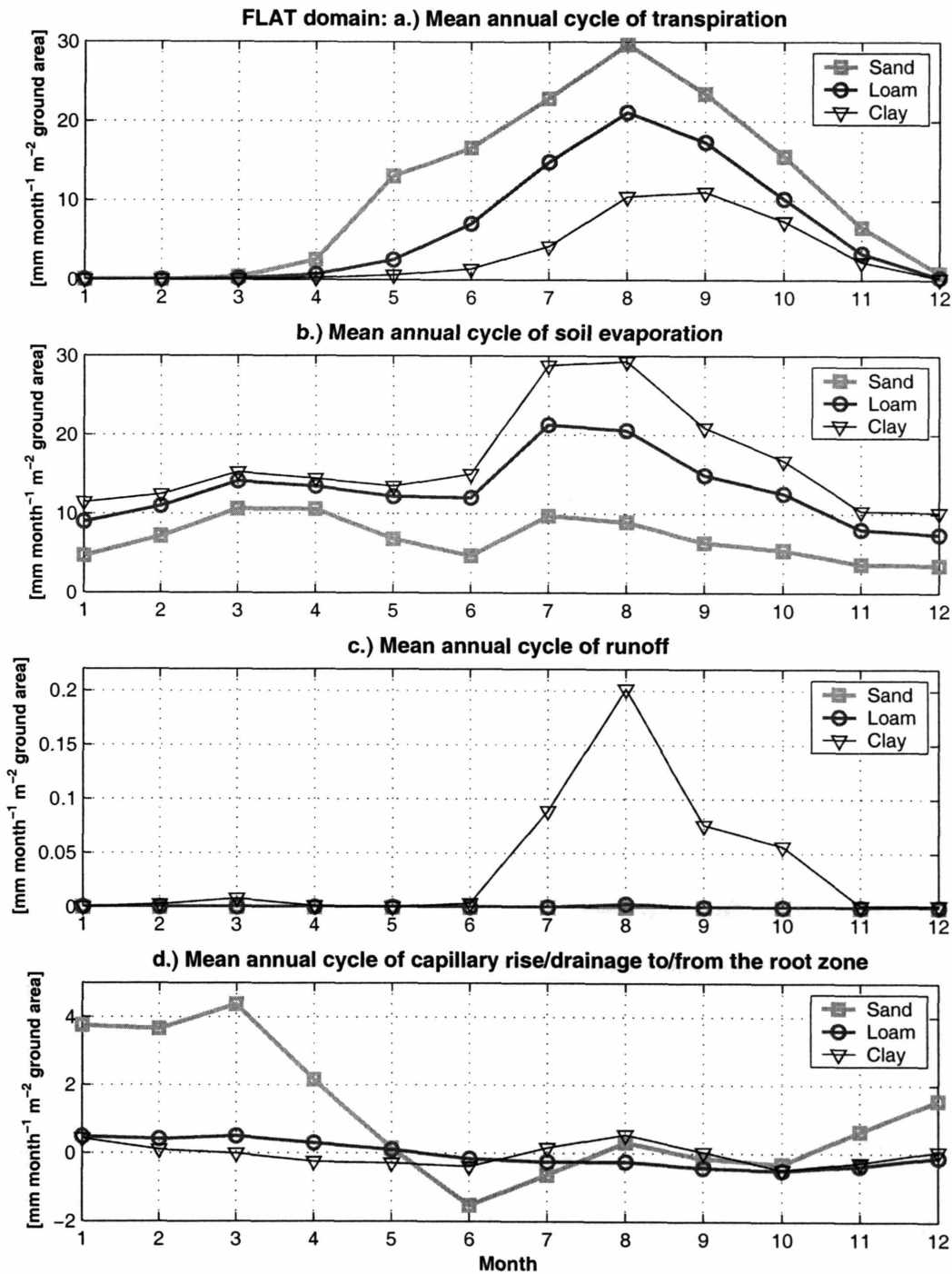
Figure 5-13: The mean annual cycles of components of the root zone water balance for the *flat* domain: a.) transpiration; b.) soil evaporation; c.) runoff; d.) capillary rise / drainage to / from the root zone. Note that the fluxes are given in units of depth per unit actual ground surface area.
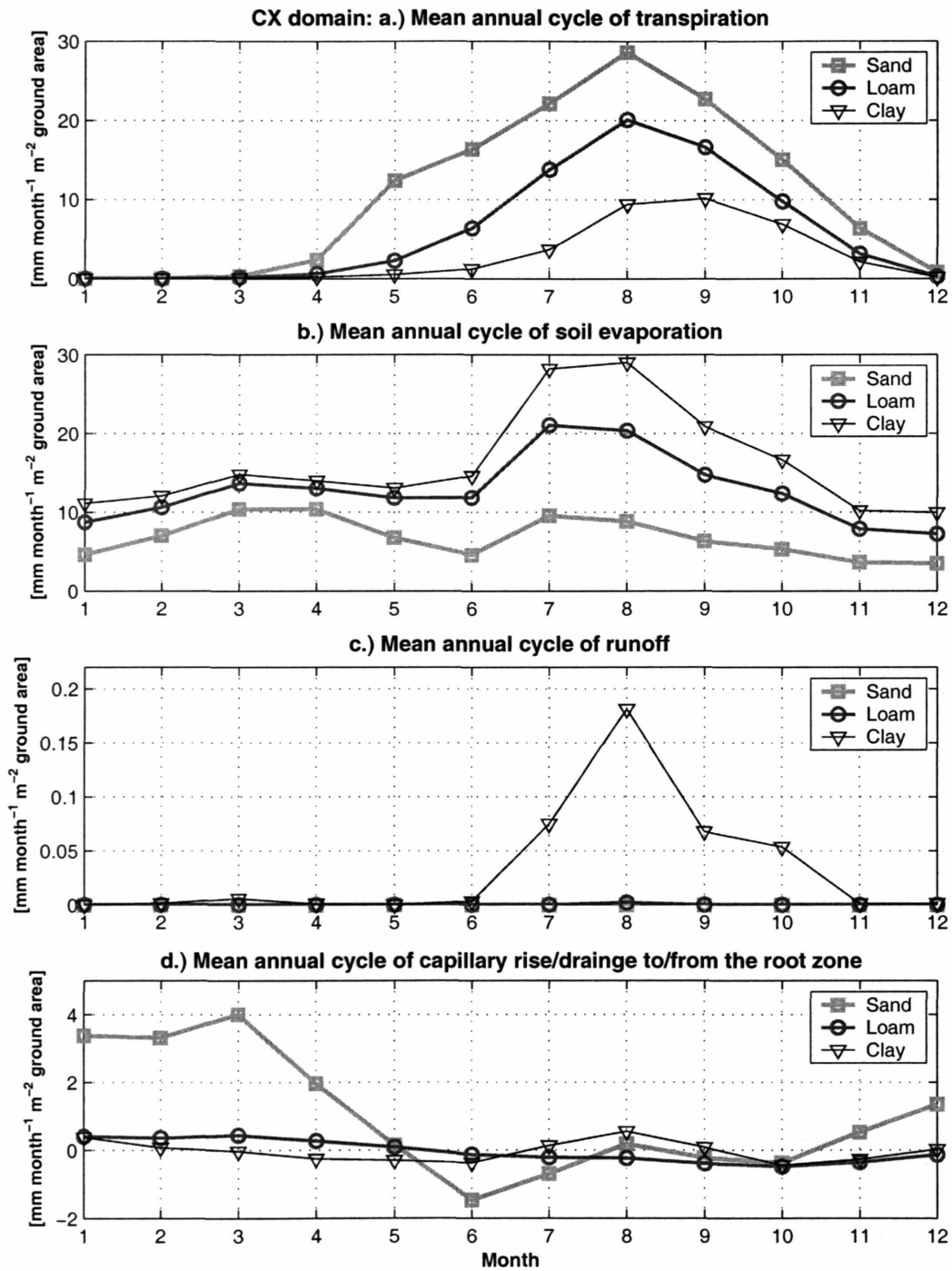
Figure 5-14: The mean annual cycles of major components of the root zone water balance for the *CX* domain: a.) transpiration; b.) soil evaporation; c.) runoff; d.) capillary rise / drainage to / from the root zone. Note that the fluxes are estimated in units of depth per unit actual ground surface area.
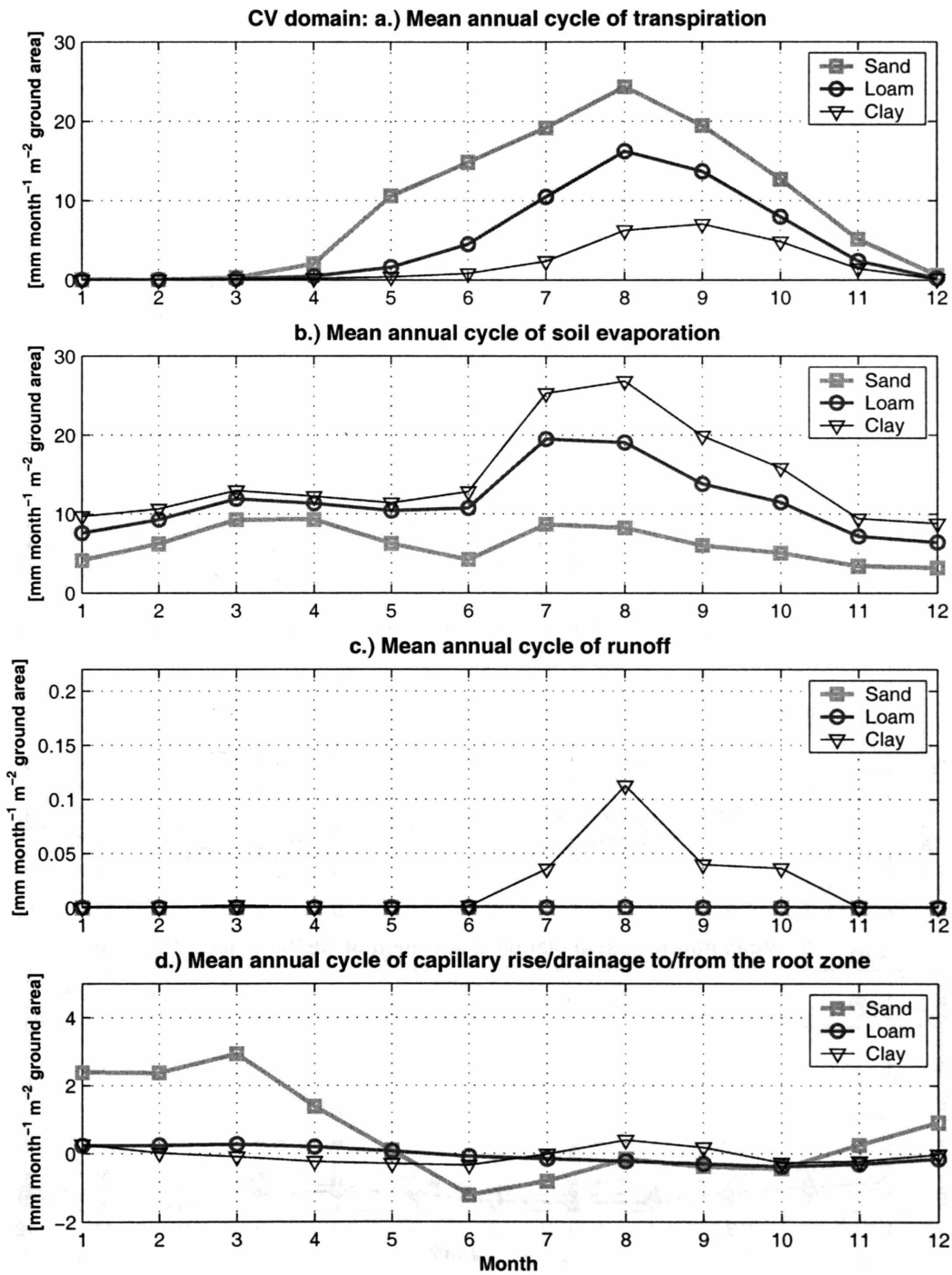
Figure 5-15: The mean annual cycles of major components of the root zone water balance for the *CV* domain: a.) transpiration; b.) soil evaporation; c.) runoff; d.) capillary rise / drainage to / from the root zone. Note that the fluxes are estimated in units of depth per unit actual ground surface area.
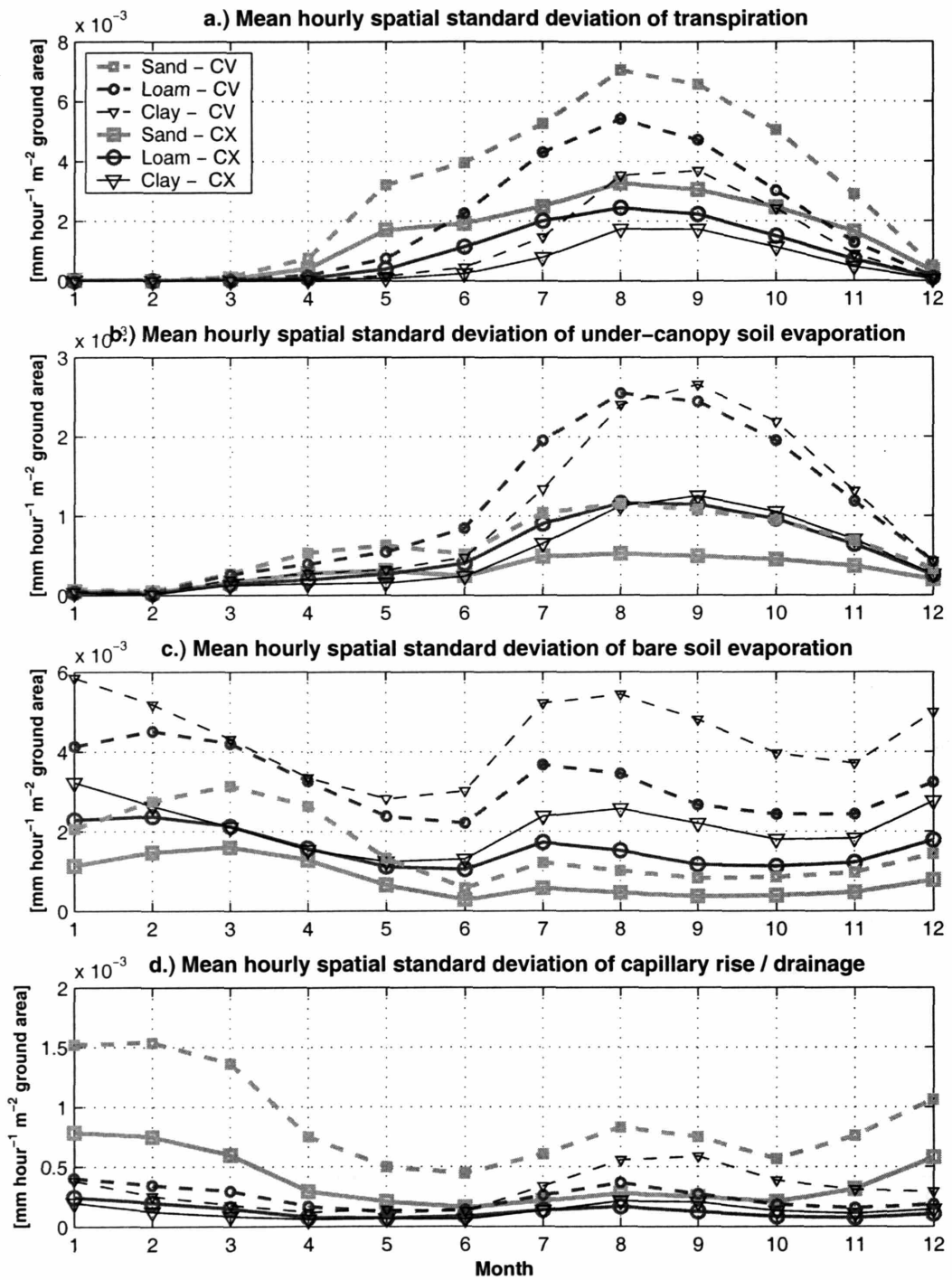
Figure 5-16: The mean annual cycle of *hourly* spatial standard deviation of moisture fluxes within the *CV* and *CX* domains: a.) transpiration; b.) under-canopy soil evaporation; c.) bare soil evaporation; d.) capillary rise / drainage to / from the root zone. Note that the fluxes are estimated in units of depth per unit actual ground surface area.
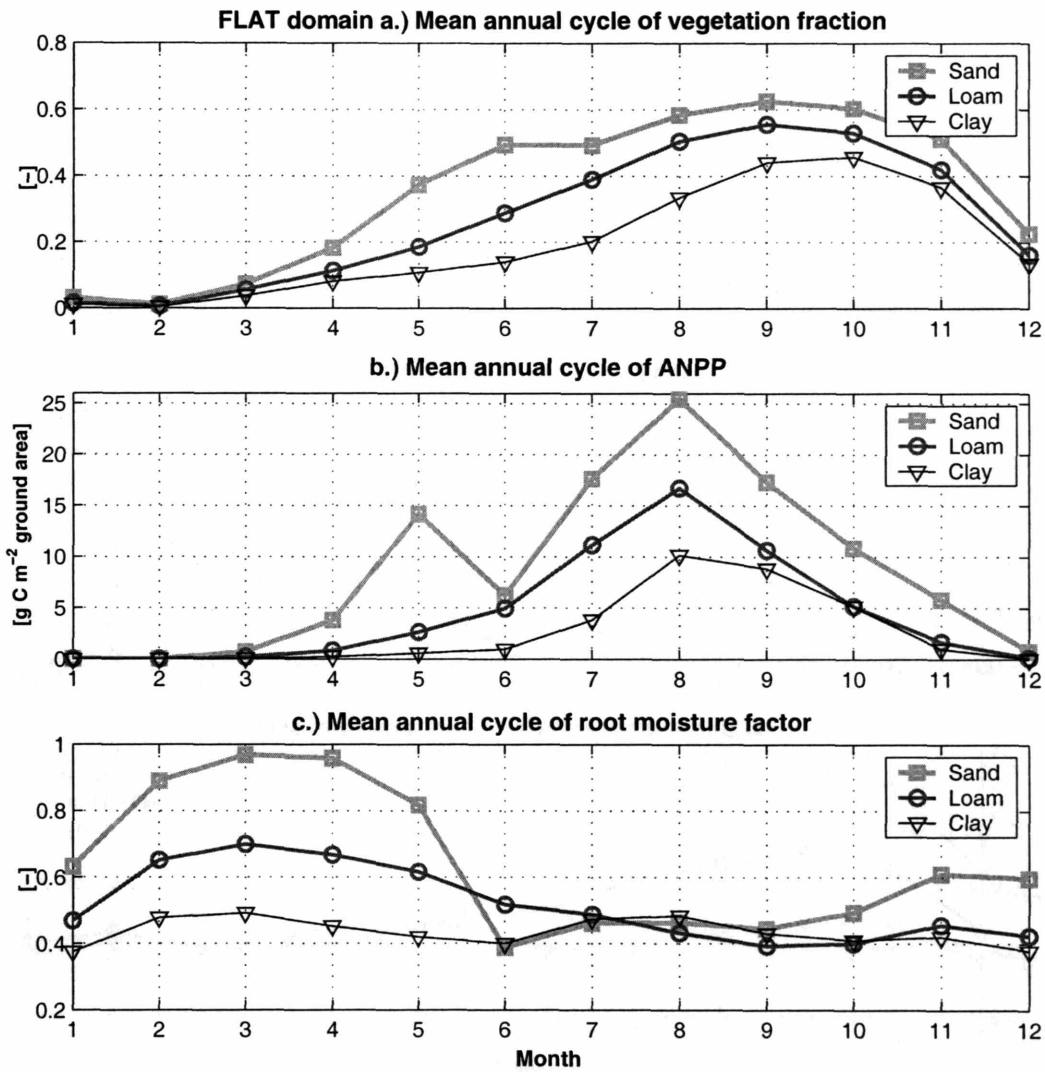
Figure 5-17: The mean annual cycles of: a.) vegetation fraction; b.) Above-ground Net Primary Productivity (ANPP); c.) root moisture transpiration factor $\beta_T$ for the *flat* domain.
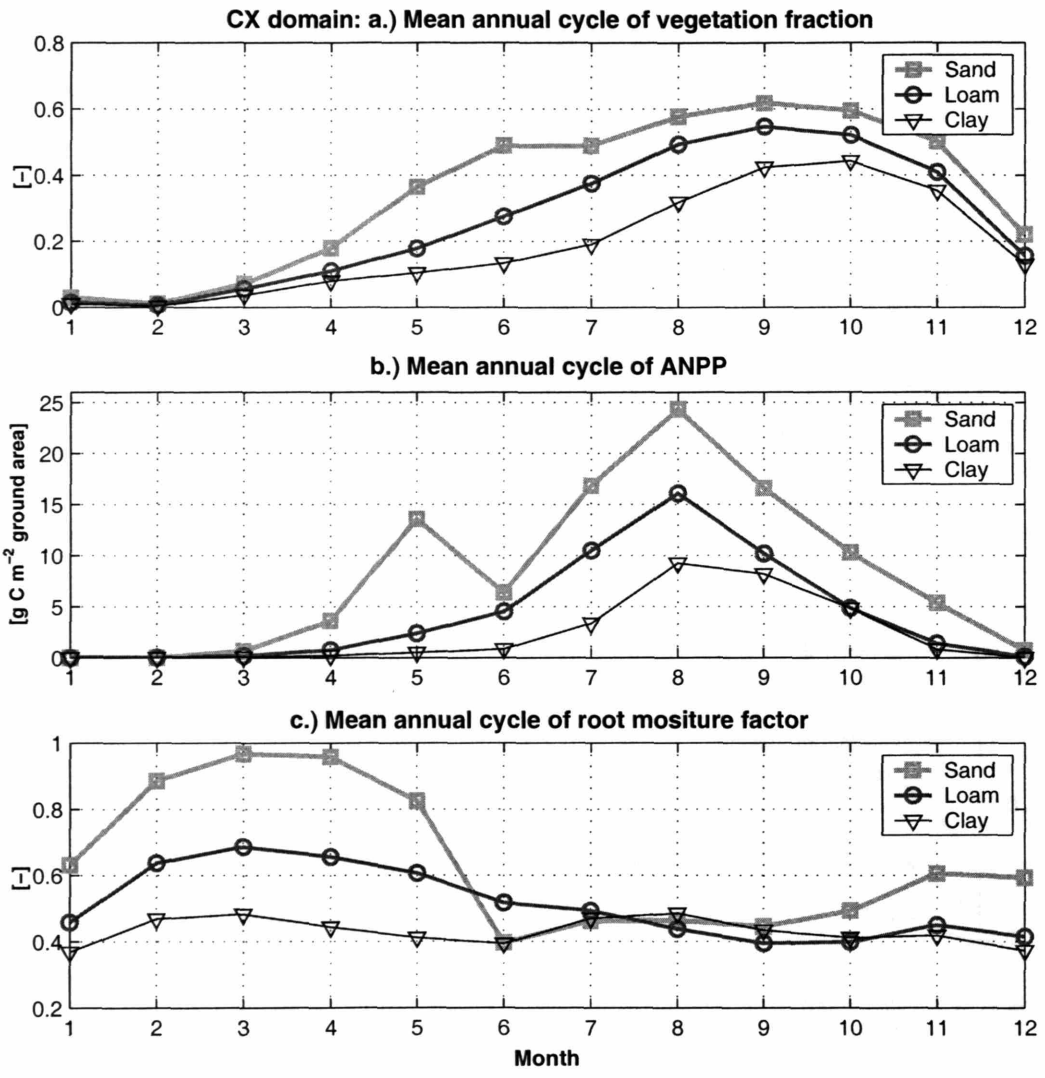
Figure 5-18: The mean annual cycles of: a.) vegetation fraction; b.) Above-ground Net Primary Productivity (ANPP); c.) root moisture transpiration factor $\beta_T$ for the *CX* domain.
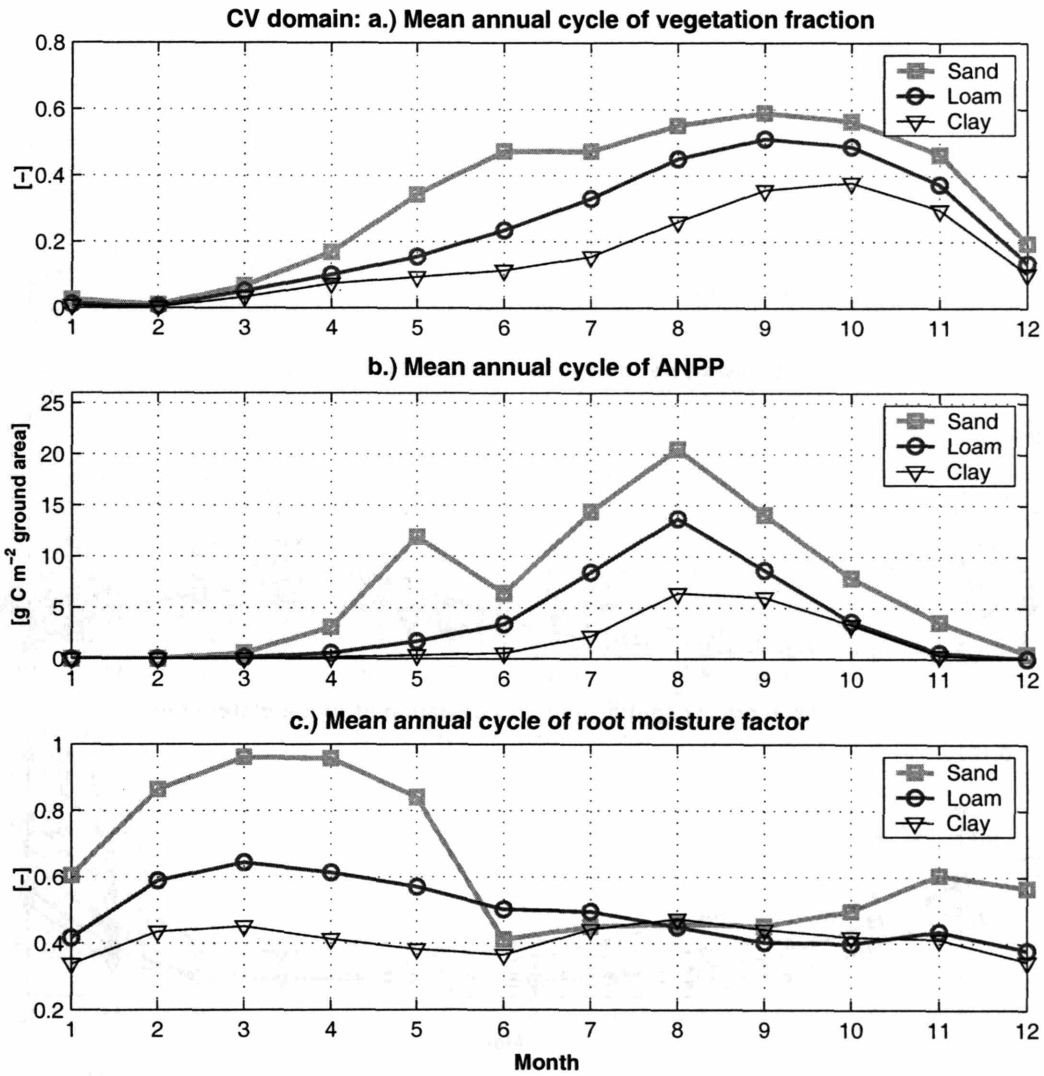
Figure 5-19: The mean annual cycles of: a.) vegetation fraction; b.) Above-ground Net Primary Productivity (ANPP); c.) root moisture transpiration factor $\beta_T$ for the *CV* domain.
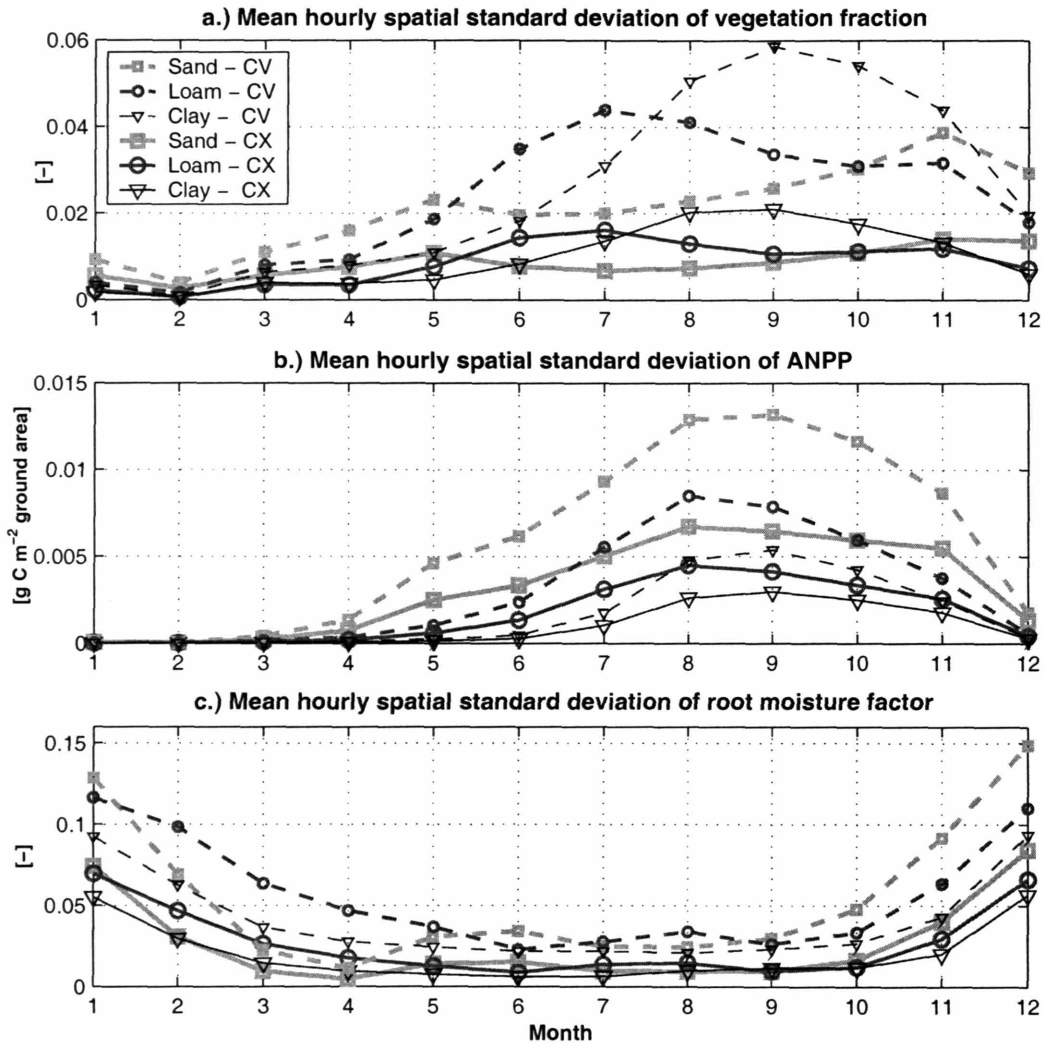
Figure 5-20: The mean annual cycle of *hourly* spatial standard deviation of: a.) vegetation fraction; b.) Above-ground Net Primary Productivity (ANPP); c.) root moisture transpiration factor $\beta_T$ within the $CV$ and $CX$ domains.

a.) CX domain          b.) CV domain

ANPP [g C / sq. m ground area]
50.8 - 54.49
54.49 - 58.18
58.18 - 61.87
61.87 - 65.56
65.56 - 69.26
69.26 - 72.95
72.95 - 76.64
76.64 - 80.33
80.33 - 84.02
84.02 - 87.71

200    0    200   Meters
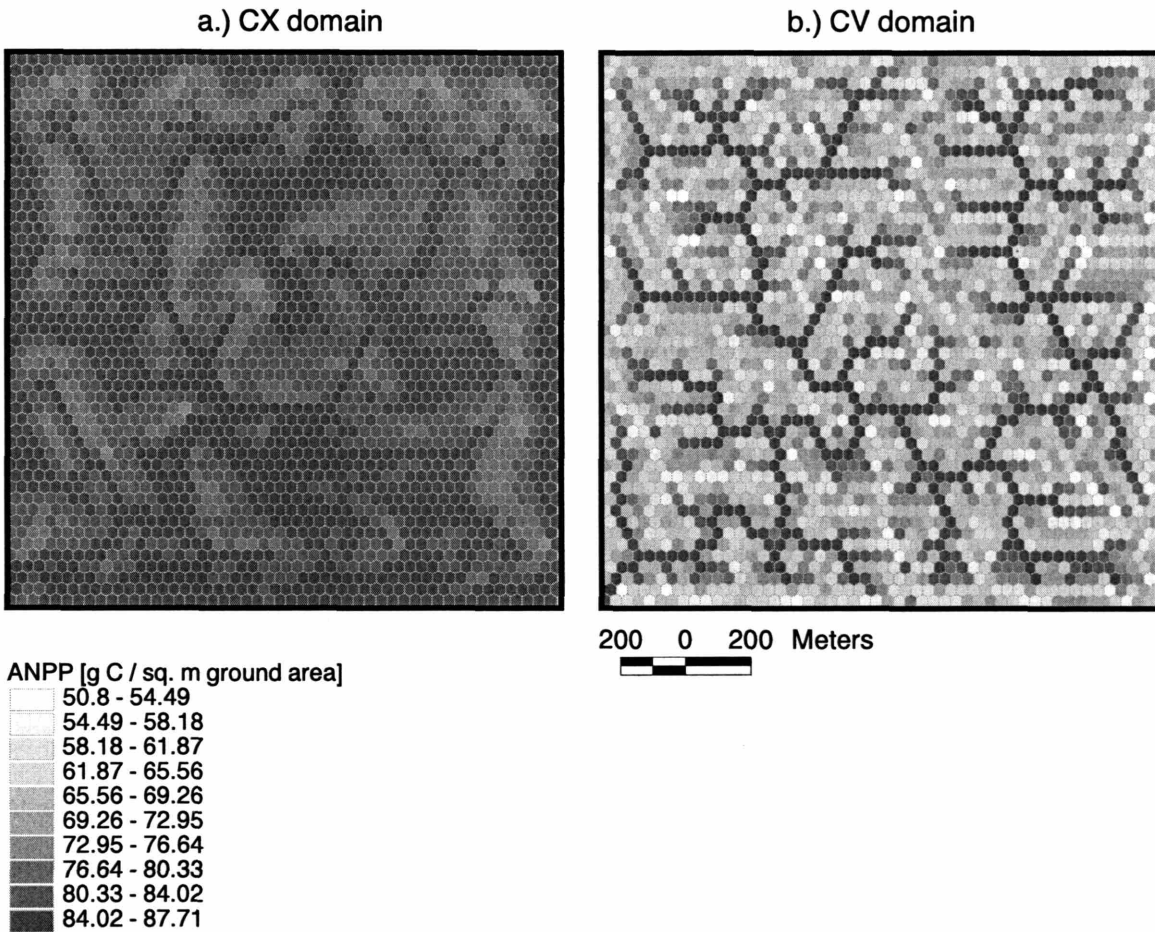
Figure 5-21: The mean annual Above-ground Net Primary Productivity (ANPP) simulated for $C_4$ grass on sandy soil type: a.) CX domain; b.) CV domain. The units are given at the element scale and refer to the actual inclined ground surface area.
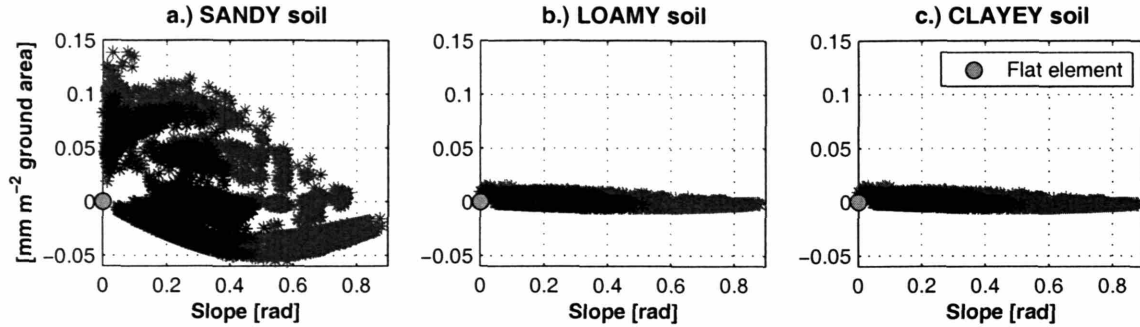
Figure 5-22: The mean simulated net lateral exchange in the root zone during a growing season for three considered soil types. Positive values imply moisture gain, while negative values imply moisture loss.

Before proceeding further, it is important to pre-determine if any of the processes of spatial interaction in the two domains are significant under the imposed hydrometeorological forcing and soil-topography characteristics. This should elucidate whether the dynamics in certain terrain locations can be considered as independent from those of the rest of the landscape. Since the subsurface lateral exchange in the unsaturated zone is the only form of spatial interaction between the elements allowed in the *base* case scenario, it would be relevant to evaluate the magnitude of the net subsurface flux in the systems during a growing season. It should be noted that the net flux does not provide information on how much moisture coming from upstream elements is used for transpiration. The net flux rather represents only an approximate measure of the significance of lateral effects on vegetation dynamics. Figure 5-22 illustrates the 50-year mean net flux in the grass root zone during a growing season for different slope magnitudes and soil types. As compared to the total amount of annual rainfall, 244 *mm*, the maximum of the total net subsurface flux does not exceed 0.06% (for sandy soil). Consequently, it appears that under the imposed conditions of the *base* case scenario, the subsurface lateral moisture exchange should not significantly affect the vegetation-hydrology dynamics. Therefore, it is appropriate for the following analysis to consider dynamics at the element scale as *spatially-independent*. The *local* terrain features, such as aspect and slope, are the key determinants of the overall dynamics at a given site. Discussion in the following will corroborate this statement.

Following the above conclusion, the growing season productivity needs to be attributed to both site aspect and slope. Figures 5-23a, 5-24a, and 5-25a show the total growing season ANPP for sandy, loamy, and clayey soil types, respectively, in a manner similar to Figure 5-8. Curves on the left correspond to the north-facing sites, while curves on the right illustrate data for the southerly slopes, and points corresponding to the east-west-facing sites are located in the middle. As previously, the annual shortwave irradiance on the horizontal axis is used to illustrate the differences between slopes of different orientation. The data points from both the CV and CX domains are combined in the figures as the symbols of lighter and darker colors, respectively. In each of the plots, the data points for the two domains overlap in the area of higher productivity. This area corresponds to a flatter terrain: the location of data points for the CX domain, relative to site irradiance, corresponds exactly to elements with relatively shallow slopes in Figure 5-6b. Alternatively, if the ANPP values were plotted against slope magnitudes separately for each aspect in a manner similar to the upper plots of Figure 5-10, it would become clear that the grass productivity for sites of a given aspect *in both domains* is completely determined by site slope. This explains why there is only a partial overlap of the data points for the two landscapes in Figures 5-23 - 5-25: the CX domain exhibits a narrower range of terrain slopes.

The above suggests that in the two simulation scenario, watershed geomorphological structure and organization of the drainage network do not represent an important factor in affecting the spatial distribution of ANPP. As stated above, the *local* terrain features have the primary significance. To verify the statement, an artificial experiment was carried out in which, for any given computational element, the outflux from the unsaturated zone was estimated as in the *base* case scenario, while the influx was always assigned to zero. Such a scenario constitutes a strong test of the significance of the lateral subsurface influx for grass productivity. As Figure 5-26 shows, the obtained results are essentially identical to the results of the *base* case scenario for all soil types.

Note that the same values of ANPP for sites of different orientation in Figures 5-
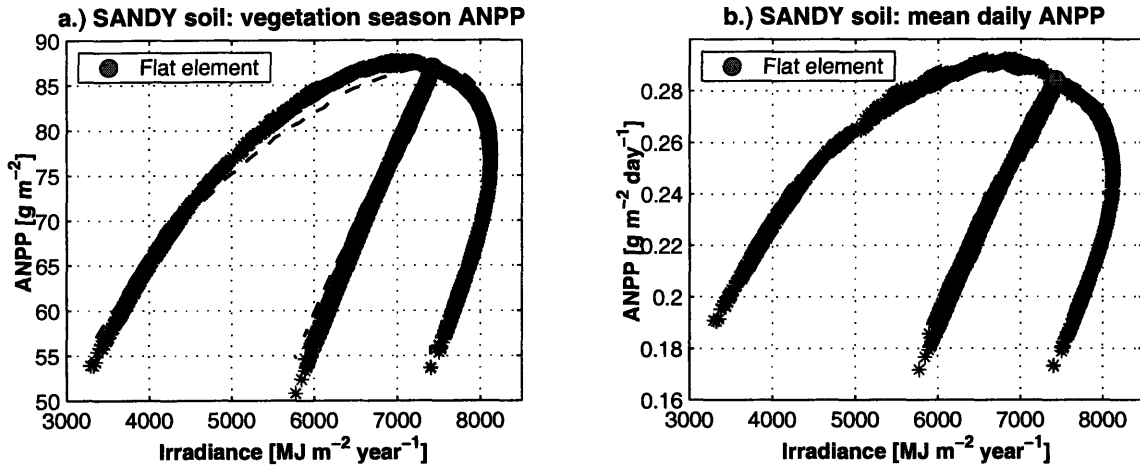
Figure 5-23: The mean simulated Above-ground Net Primary Productivity for *sandy* soil type: a.) ANPP accumulated over vegetation season; and b.) ANPP normalized by the mean duration of growing season. Symbols with lighter color denote the data points for the CV domain, while the darker color corresponds to the data points for the CX domain. The dashed curves are hypothetical and obtained by applying a factor of $\cos \alpha_{\triangledown}$ to the ANPP for a flat horizontal surface.

23 - 5-25 do not necessarily correspond to slopes of the same magnitude. This implies that productivity does not exhibit the same pattern of distribution in the terrain as precipitation: the same rainfall depths for elements of different aspects in Figure 5-8 correspond to the same slope. It is the synthesis of rainfall and energy inputs that influences productivity at any given location. In order to compare the obtained results with the case that assumes that grass productivity is *completely* determined by precipitation and distributed with slope in the same manner, hypothetical curves are constructed (the dashed line style). These curves are obtained by applying a factor of $\cos \alpha_{\triangledown}$ to the ANPP value for a flat horizontal surface. As can be concluded from the figures, the distribution of rainfall with slope, the distribution of surface irradiance with aspect and slope, the effects of soil texture, and the interplay between vegetation-hydrology processes lead to a much more complex structure of ANPP dependence on site local characteristics.

The data points in Figures 5-23a, 5-24a, and 5-25a comprise a characteristic shape, which will be referred to in the following as the "$\epsilon$-curve". This characteristic shape,

302
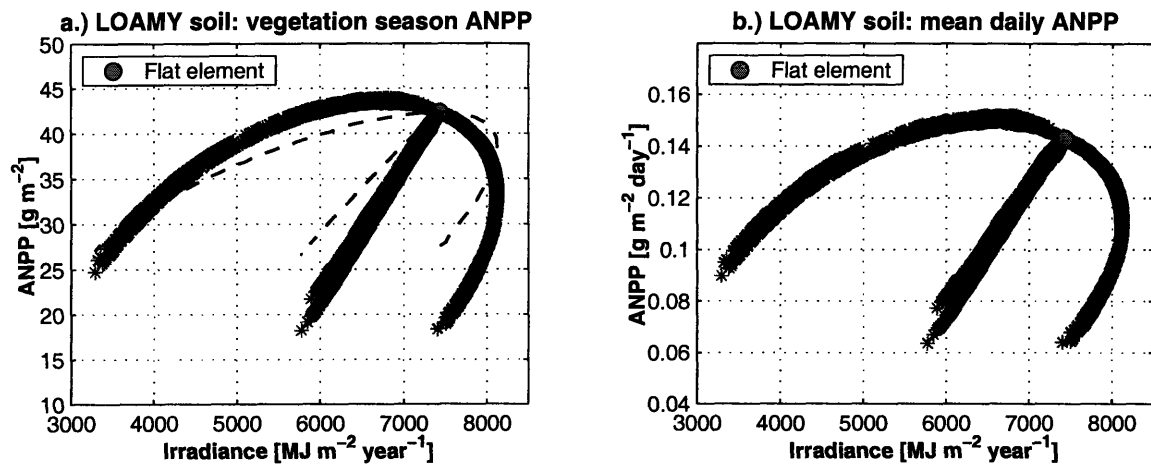
Figure 5-24: The mean simulated Above-ground Net Primary Productivity for *loamy* soil type: a.) ANPP accumulated over vegetation season; and b.) ANPP normalized by the mean duration of growing season. Symbols with lighter color denote the data points for the CV domain, while the darker color corresponds to the data points for the CX domain. The dashed curves are hypothetical and obtained by applying a factor of $\cos\alpha_\nabla$ to the ANPP for a flat horizontal surface.
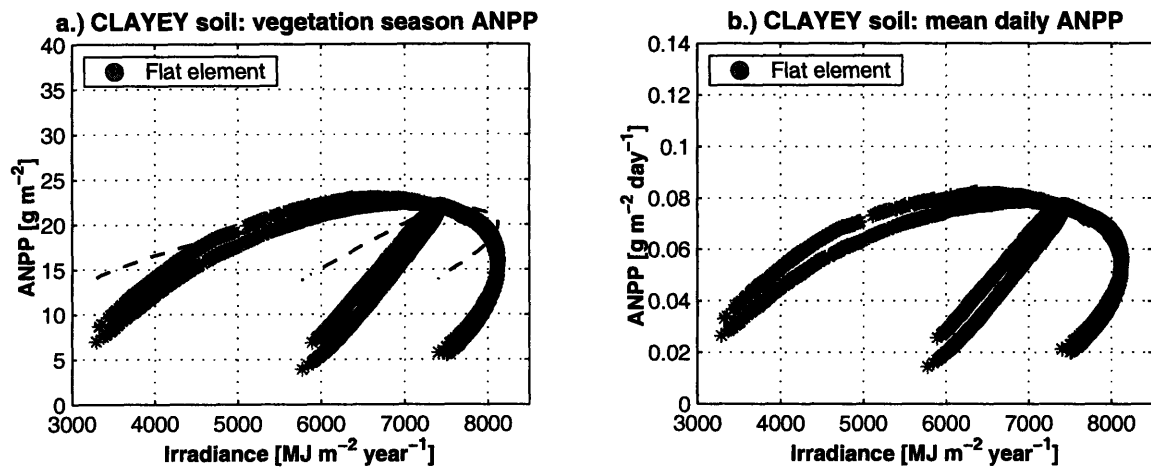


Figure 5-25: The mean simulated Above-ground Net Primary Productivity for *clayey* soil type: a.) ANPP accumulated over vegetation season; and b.) ANPP normalized by the mean duration of growing season. Symbols with lighter color denote the data points for the CV domain, while the darker color corresponds to the data points for the CX domain. The dashed curves are hypothetical and obtained by applying a factor of $\cos\alpha_\nabla$ to the ANPP for a flat horizontal surface.
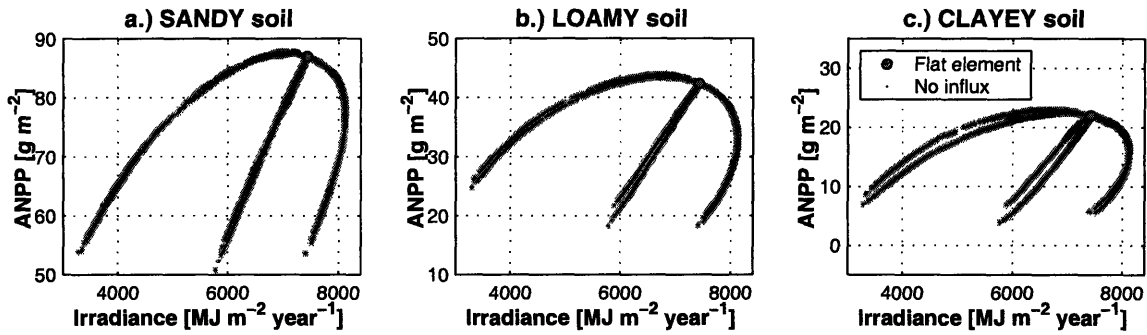
Figure 5-26: The mean simulated Above-ground Net Primary Productivity for all considered soil types. Symbols with lighter color denote the data points for the CV domain, while the darker color corresponds to the data points for the CX domain. "No influx" data points correspond to a simulation scenario in which for any given computational element, the outflux from the unsaturated zone was estimated following normal procedure, while the influx was always assigned to zero.

however, is partially an artifact of the accepted spatial discretization of the two domains. As discussed in Section 5.2.3, six cardinal aspects of the basic Voronoi element (Figure 5-1) correspond to three distinct groups of the "slope - surface irradiance" functional dependence. This results in three "surface irradiance - ANPP" curves. If site aspect were represented on a continuous basis, the space between the two enveloping curves, corresponding to north and south-facing sites, would be filled and plots in the figures would resemble tilted half-ovals filled with points.

It is evident from the figures that the relative reduction of the total rainfall depth per unit ground area, due to the *self-shading* effect of inclined surfaces (see Section 5.2), have a significant contribution to forming the "$\epsilon$-curve" shape. However, as suggested above, the relative reduction of precipitation is only one of the contributing factors. One may argue that another possible cause is the differences in the growing season durations (Figure 5-10), which determine the effective periods over which ANPP is accumulated at different topographic locations. Nonetheless, if the mean total productivity is normalized by the site mean growing season duration (Figures 5-23b, 5-24b, and 5-25b), the relationship still results in this distinctive shape with approximately the same ratio of maximum to minimum ANPP.

Clearly, in order to better understand the effect of topographic features on grass

productivity, both the *water* and *energy* aspects of hydrology-vegetation dynamics need to be considered. In the environments exhibiting excess of solar radiation, the amount of water available for plant uptake / transpiration inherently depends on the amount of energy used in the process of soil evaporation: the smaller the latter, the more favorable conditions become for vegetation. In general, unless PAR-limitation is encountered, the topographic radiative shading in such environments is favorable for vegetation function since a reduction in the incoming energy leads to smaller soil evaporation rates and, therefore, higher moisture amounts available for plant uptake. While the radiative shading is more pronounced for slopes of higher magnitude, an increase in site slope may also lead to effects that are negative for vegetation. Such effects are larger rates of surface and subsurface lateral fluxes depleting root moisture reservoir and a reduction in rainfall per unit ground area (as discussed in Section 5.2.3). Consequently, the effects resulting from higher slope magnitude can have both positive and negative implications for vegetation function.

As can be seen in Figure 5-6, the highest rate of decrease in the incoming solar radiation per unit slope angle is consistently observed for the north-facing sites. An outcome of the trade-off among the effects referred to above is an apparent association of grass maximum ANPP with sloped northerly sites. While the maximum values are identical for both domains, significant differences exist among the soil types: ANPP $= 87.7$ $g$ $m^{-2}$ at 7.74° slope angle (6931 $MJ$ $m^{-2}$ $yr^{-1}$ surface irradiance) for sandy soil; ANPP $= 43.9$ $g$ $m^{-2}$ at 8.94° slope angle (6844 $MJ$ $m^{-2}$ $yr^{-1}$ surface irradiance) for loamy soil; and ANPP $= 22.9$ $g$ $m^{-2}$ at 11.3° slope angle (6664 $MJ$ $m^{-2}$ $yr^{-1}$ surface irradiance) for clayey soil. As can be observed, the maximum ANPP for soils of finer texture is associated with larger slopes and, correspondingly, smaller incoming radiation values. It is possible that such an effect is due to larger capillary forces, characteristic for these soils. Capillary forces are responsible for the upward moisture flux caused by the surface energy partition that drives the process of soil evaporation. Consequently, a larger reduction in the energy input is required to achieve the balance among various controlling factors. Conditions for such a balance result in maximum productivity. Stronger capillarity in soils of finer texture can also explain a larger

departure of the simulated ANPP from the hypothetical curves obtained by a simple scaling of the productivity for horizontal surfaces (the dashed curves in Figures 5-23a, 5-24a, and 5-25a). The overall vegetation-hydrology dynamics in these soils are highly sensitive to the energy input and cannot be explained by a mere modification of the precipitation amount. As will be addressed in the following, this sensitivity is likely to be strongly mediated by the process of soil evaporation.

The productivity characteristics of sloped sites, which have aspects other than northerly, exhibit various behaviors. East-facing sites show a minor increase in productivity with slope, up to $1.5°$ - $4.4°$, depending on the soil type (this cannot be clearly seen in Figures 5-23 - 5-25), with a subsequent decrease. Estimated ANPP for west-facing slopes shows a continuous decrease with growing slope, although the incoming shortwave radiation becomes smaller. The grass productivity for south-facing sites, characterized by an initial increase in surface irradiance up to $24.8°$ of the site surface angle (Figure 5-6), exhibits a sharp continuous decrease with respect to the ANPP for a flat horizontal surface. In addition, the productivity for soil types of finer texture shows a larger sensitivity with respect to the actual site aspect, e.g., the difference in productivity for N-N-W and N-N-E or east- and west-facing sites is more apparent for clayey soil, rather than for sandy soil. It is necessary to recall that although sites with the aspects symmetrical with respect to the north-south axis receive essentially the same amount of solar radiation (Figure 5-6), the timing of daily maximum and relation with respect to the other hydrometeorological variables (e.g., air temperature and moisture deficit) are different.

## 5.3.2b Water balance components

For any hydrological analysis, it is essential to understand the relative magnitude of principal water balance components. As in the figures of the previous discussion that addressed grass productivity in the scope of energy and rainfall distribution in the terrain, Figure 5-27 illustrates the principal water balance components relative to the amount of annual radiation received by a site. The data points represent the mean values averaged over the 50-year simulation period. As can be inferred from the

306

figure, evapotranspiration constitutes the bulk of the annual water balance for all soil types. Evapotranspiration data perfectly follow the $\epsilon$-curve pattern with the maximum corresponding to a flat site. It is apparent in this case that evapotranspiration is completely determined by the rainfall distribution in the terrain: the simulated $\epsilon$-curve data are in excellent agreement with the hypothetical curves obtained by applying a factor of $\cos \alpha_\nabla$ to the evapotranspiration value for a flat horizontal surface (Figure 5-27, upper plots).

As mentioned previously (Section 5.3.1), one of the deficiencies of the rainfall rectangular pulse model is that the generated rainfall intensities are relatively low. Consequently, in the *base* case scenario, runoff is generated only in clayey soil and is zero for all other soil types. Due to the very high hydraulic conductivity of sandy soil, water can be lost from the root zone to deeper layers through drainage. Loamy and clayey soils both exhibit the capillary rise of moisture from the initial storage of deeper layers of the soil column for all topographic locations. This process consistently reflects the continuous moisture deficit in the grass root zone for these soil types. While the net subsurface lateral drainage is minor for all cases, it is worth noting that the site surface irradiance is irrelevant as its predictor (the plot in the lower left corner of Figure 5-27). As will be addressed in Section 6.4, site location and topographic organization upstream of a given location are the key determinants of this quantity.

Figure 5-28 illustrates major components of the total annual evapotranspiration (evaporation of intercepted water from canopy is not considered). As can be observed, while the total evapotranspiration flux is approximately the same among the soil types, its partition is significantly different. Transpiration is the dominant component for sandy soil, while bare soil evaporation is the major mechanism through which moisture escapes the unsaturated zone in clayey soil. The maximum transpiration values (Table 5.1) are associated with north-facing sites, which, in most cases, have somewhat smaller inclination than sites corresponding to the maximum ANPP, i.e., maximum ANPP does not necessarily correspond to the maximum water flux through stomata. A larger amount of biomass corresponds to denser foliage and
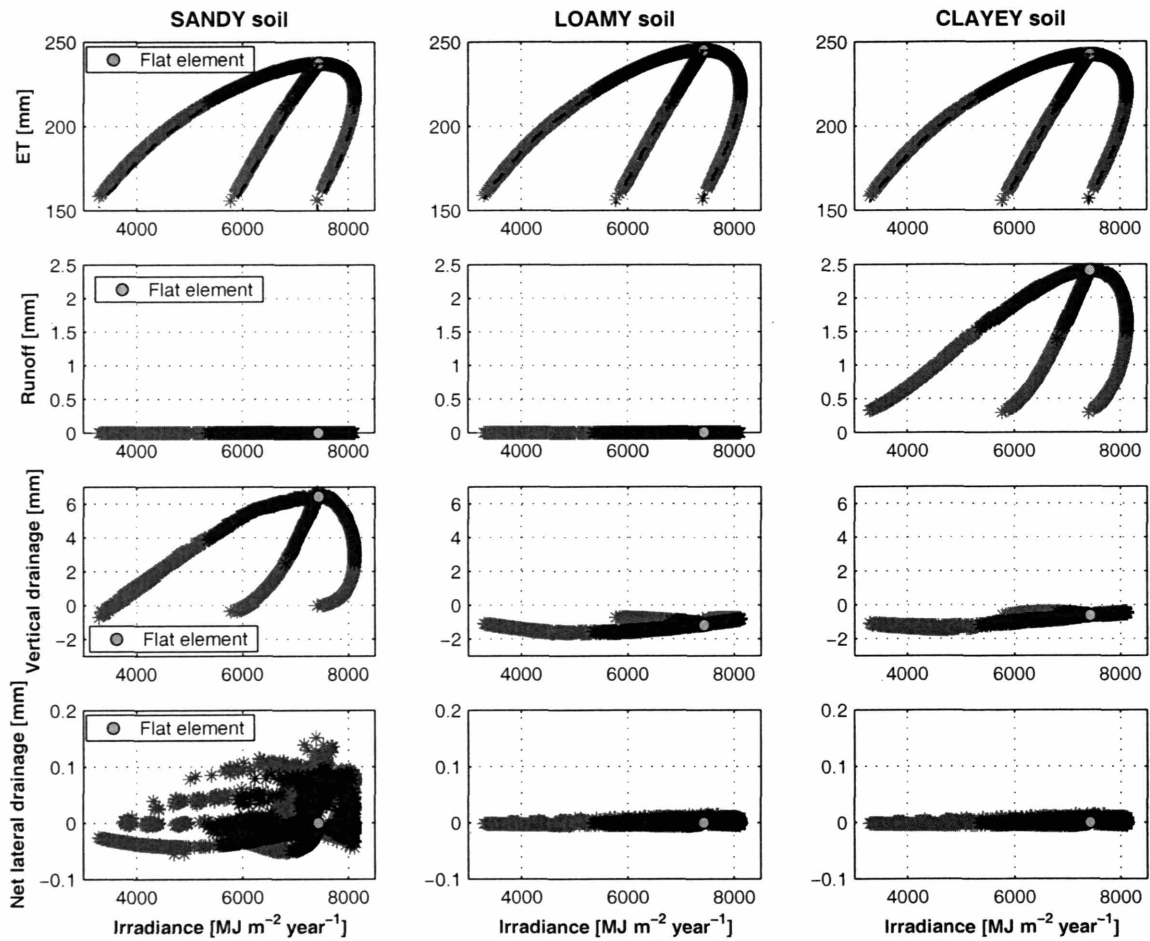
Figure 5-27: The principal mean annual water balance components for grass root zone at the element scale for all soil types. From the top - down: evapotranspiration (the sum of transpiration and soil and canopy evaporation), runoff, the net moisture exchange with deeper soil layers (drainage, if values are positive, or capillary rise, if values are negative), the net lateral exchange in the root zone (positive values imply moisture gain). The dashed curves are hypothetical and obtained by applying a factor of $\cos \alpha_{\triangledown}$ to the evapotranspiration for a flat horizontal surface. The units of depth refer to the actual inclined ground surface area.
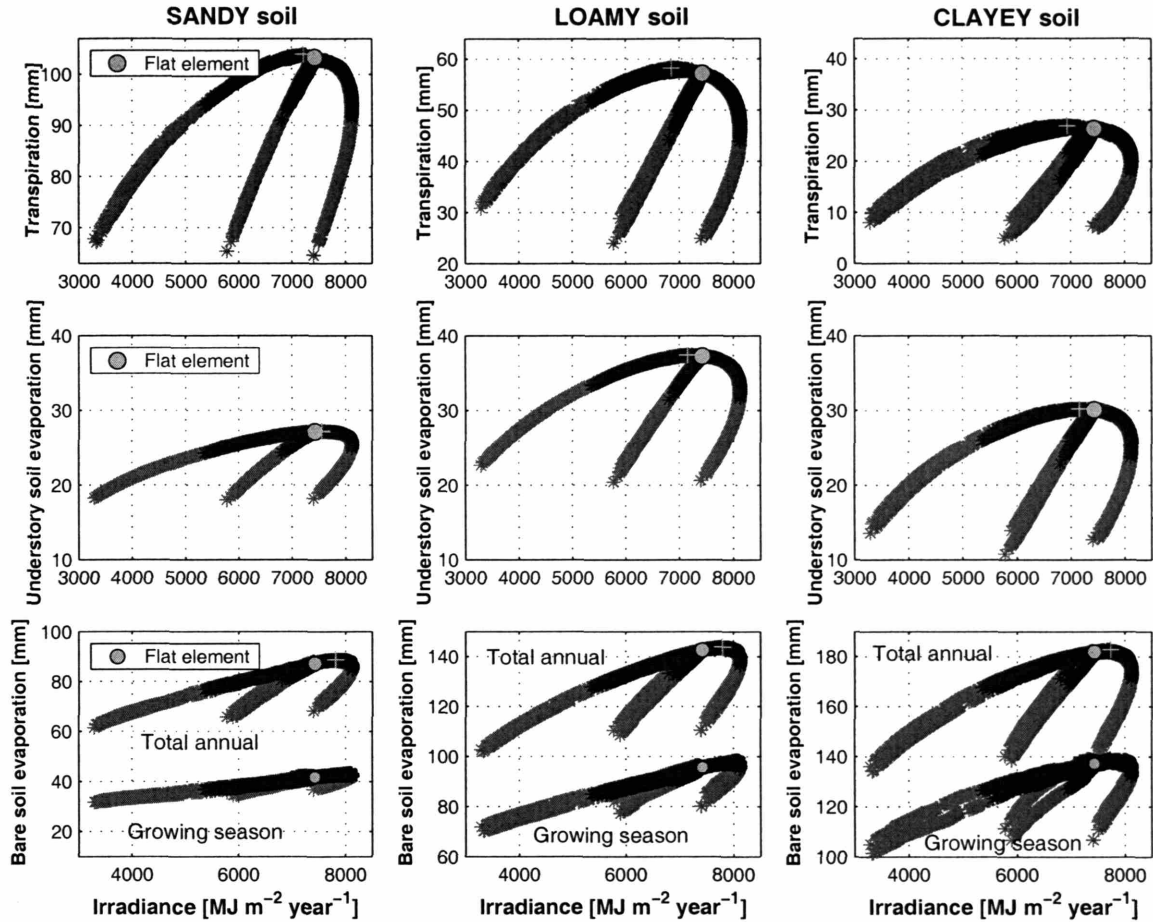
Figure 5-28: The mean annual evapotranspiration fluxes for all soil types. From the top - down: vegetation transpiration, under-canopy, and bare soil evaporation moisture fluxes (the element scale). The "+" symbols indicate the location of maximum values. The units of depth refer to the actual inclined ground surface area.

higher vegetation fraction occupied by grass within an element. Both of the latter vegetation characteristics effectively reduce the soil evaporation losses. As can be observed in Figure 5-28, sites with maximum values of soil evaporation do not coincide with the terrain locations that feature maximum transpiration. The maximum bare soil evaporation is constantly associated with south-facing slopes that receive the highest amount of solar radiation.

The evapotranspiration fluxes shown in Figure 5-28 are determined by both the site surface irradiance and precipitation, which are in turn defined by site slope and aspect. The corresponding distribution of evapotranspiration flux with slope is illus-

Table 5.1: Maximum values of evapotranspiration fluxes for sandy/loamy/clayey soil types, respectively.

|  | Maximum value [$mm$] | Site slope [°] | Aspect |
|---|---|---|---|
| **Transpiration** | 103.9 / 58.3 / 28.9 | 3.47 / 8.94 / 7.74 | NNW / NNE / NNE |
| **Under-canopy evaporation** | 27.2 / 37.4 / 30.2 | 2.40 / 4.52 / 4.52 | SSW / NNE / NNE |
| **Bare soil evaporation** | 88.7 / 143.8 / 182.8 | 8.14 / 7.85 / 6.13 | SSW / SSW / SSW |

trated in Figure 5-29 that shows both the average relative composition of the total flux (the top panel, data for sites of *all* aspects are used) as well as the fractional weights for three principal aspect directions (the bottom panel). As can be inferred from the figure, transpiration and under-canopy soil evaporation show a gradual decrease with slope (up to ∼10% of the maximum fractional weight). Accordingly, bare soil evaporation exhibits an increase with slope. Differences in the fractional composition between sites of different aspects are relatively minor, with north-facing elements featuring the highest deviations. The sites of northerly aspect also exhibit the smallest changes in the fractional weight of transpiration flux with slope.

## 5.3.2c Soil moisture and zones of favorability

It follows from the preceding discussion that certain topographic locations may favor vegetation, within the constraints of precipitation and radiation regimes. The degree of vegetation performance can be expressed through such characteristics as ANPP. It should be re-stated that no significant lateral mass exchange occurs in the *base* case scenario and all vegetation-hydrology dynamics are essentially locally driven. Correspondingly, any variable describing these local dynamics can be considered as a function of two characteristics defining site orientation in space: aspect and slope. This feature provides an opportunity for constructing a *pseudo-spatial* diagram that reflects the distribution properties of any variable in the terrain. One such diagram is based on the polar coordinate system: the distance from the central point repre-
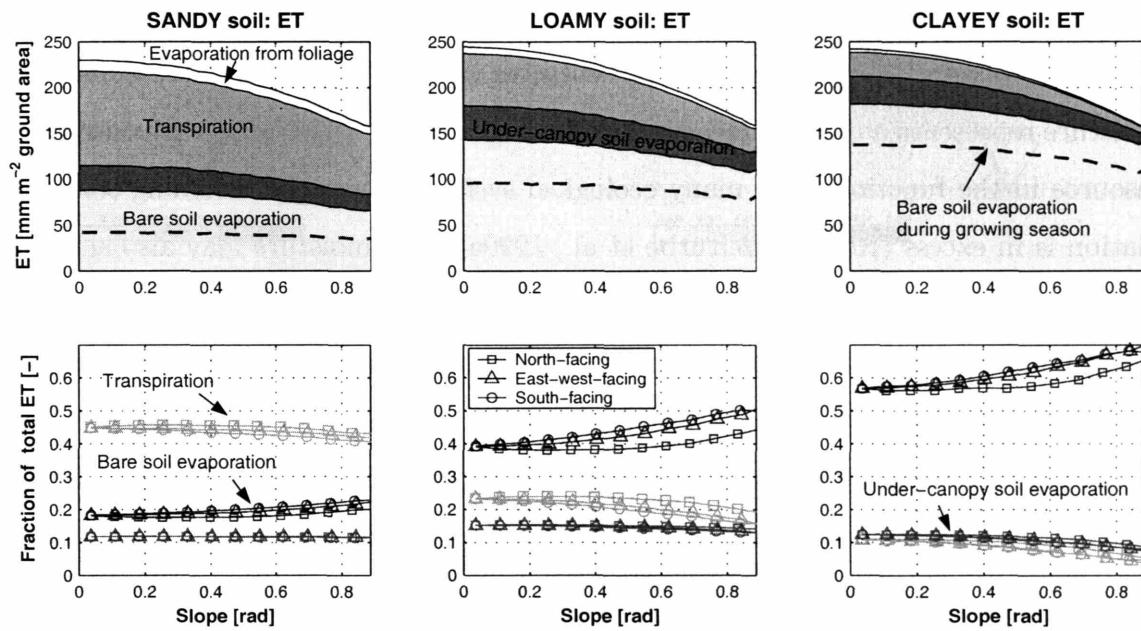
Figure 5-29: The partition of the mean annual evapotranspiration flux according to slope magnitude for all soil types. The top plots illustrate the mean relative composition of evapotranspiration flux for slopes of all aspects. The bottom plots show the fractional weights of evapotranspiration flux at sites of different aspects. The units of depth refer to the actual inclined ground surface area.

sents site slope and the clock-wise angle from the vertical line represents site aspect from north (N-E-S-W). Figure 5-30 illustrates the mean root soil moisture during the growing season using this diagram. The data points for six cardinal aspects combined for both domains are used to linearly interpolate the resulting field.

The mean root zone soil moisture in Figure 5-30 will be used for partitioning the pseudo-spatial domain into the regions of relative favorability for vegetation. These regions will be attributed to aspect-slope characteristics of the considered topographies. While the choice of favorability attribute is rather subjective, the mean root soil water content is selected as the representative variable due to several reasons. Soil moisture represents a directly measurable state quantity recognized as the controlling resource in the functioning of many ecological systems where the incoming solar radiation is in excess (Rodriguez-Iturbe et al., 1999a). Soil moisture may also act as a buffer against drought stress and, therefore, its timely availability ensures plant safety. Consequently, the mean soil moisture represents an approximate integral measure of the trade-off between the vegetation performance attributed to plant transpiration (i.e., photosynthesis and reproduction) and mortality costs of stress (Tilman, 1982). It is necessary to mention that other integral variables, such as net productivity or stress characteristics (e.g., frequency and intensity of drought-induced foliage loss), can be used for the partition procedure described below. In each case, however, the choice would be equivalently subjective since "favorability" is not a rigorously or mathematically formulated concept. *Apriori*, a representative variable needs to include the characteristics of both vegetation growth performance and stress. As will be shown in the following discussion, sites featuring the highest productivity do not necessarily correspond to locations with the minimum soil water stress characteristics. At the same time, sites with the maximum mean soil water content do not exactly coincide with locations exhibiting the highest ANPP.

The diagrams in Figure 5-30 show that the distribution of the mean root soil moisture represents a "mound", with its summit corresponding to shallow sloped sites of north-facing aspect. The simulated maximum of soil moisture is associated with slopes that exceed those corresponding to the maximum values of ANNP and
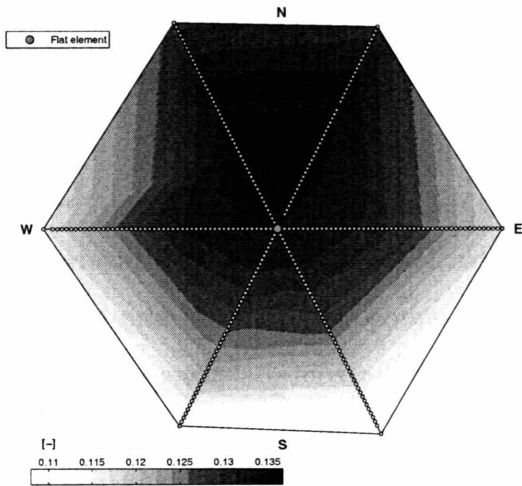
(a) SANDY soil
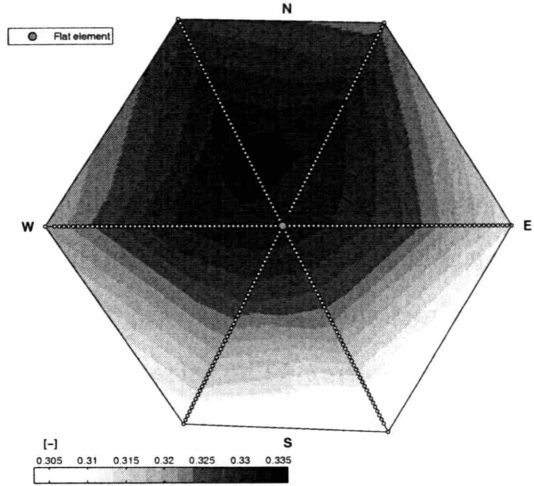


(b) LOAMY soil
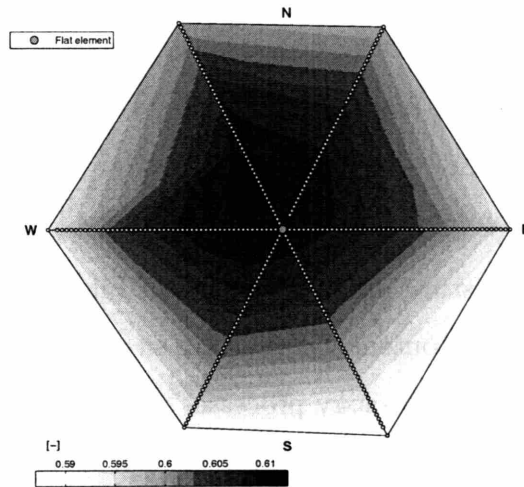


(c) CLAYEY soil

Figure 5-30: A pseudo-spatial diagram of the mean growing season root zone soil moisture shown as a two-dimensional interpolated field in polar coordinates (all soil types): the distance from the central node represents site slope and the clock-wise angle defines site aspect from north (N-E-S-W). The data for both the CX and CV domains are combined.

Table 5.2: Maximum values of the mean root zone soil moisture during growing season for sandy/loamy/clayey soil types, respectively.

| | Maximum value $[0 \div 1]$ | Site slope $[°]$ | Aspect |
|---|---|---|---|
| **Root zone SM** | 0.134 / 0.333 / 0.610 | 19.0 / 21.1 / 15.9 | NNW / NNW / NNW |

evapotranspiration fluxes (Table 5.2). The "mound" has a steeper descent towards south and a smaller gradient in the northern direction. The locations of favorability are defined here as *sites with the mean root soil water content exceeding that of a reference location.* The latter is assumed to be a flat horizontal surface not affected by the lateral effects such as radiative shading, moisture transfer in the unsaturated zone, or runon. The delineated region of relative favorability is located inside of a polygon outlined with a black solid line in subplots of Figure 5-31 with artificial points added in the N-E and S-W directions. The latter were obtained by bisecting the angle between two adjacent cardinal aspects and taking half of the slope value of the neighboring data point with soil moisture exceeding that of a horizontal surface. As can be seen, the delineated region is smallest for clayey soil that exhibits the highest soil evaporation and smallest grass productivity.

The pattern of soil moisture in the diagrams of Figure 5-30, i.e., the association of the mean root zone water content with certain sites and slopes, is due to the interplay between the vegetation-hydrology processes driven by the spatial distribution of incident radiation and rainfall. In general, given a soil type, one needs to consider the root soil moisture $\theta_{root}$ as a function of several forcing variables (no lateral mass transfer is assumed): $\theta_{root} = f\left[S_{atm} \downarrow (\zeta_\nabla, \alpha_\nabla), R(\alpha_\nabla), V_C(S_{atm} \downarrow_{vis}, \theta_{root})\right]$, where $\alpha_\nabla$ is the slope of site surface and $\zeta_\nabla$ is its aspect, $S_{atm} \downarrow$ is the global incident shortwave radiation, $S_{atm} \downarrow_{vis}$ is the PAR, $R$ is rainfall, and $V_C$ is vegetation extant at a site. $S_{atm} \downarrow_{vis}$ is assumed to be non-limiting and $\zeta_\nabla$ and $\alpha_\nabla$ are the only two independent variables in the above formulation that affect the spatial distribution of $S_{atm} \downarrow$ and $R$ in the terrain. The two latter variables are thus the key forcings, independent from the surface state (i.e., from $V_C$ and $\theta_{root}$), and it is therefore relevant for the current

(a) SANDY soil



(b) LOAMY soil



(c) CLAYEY soil
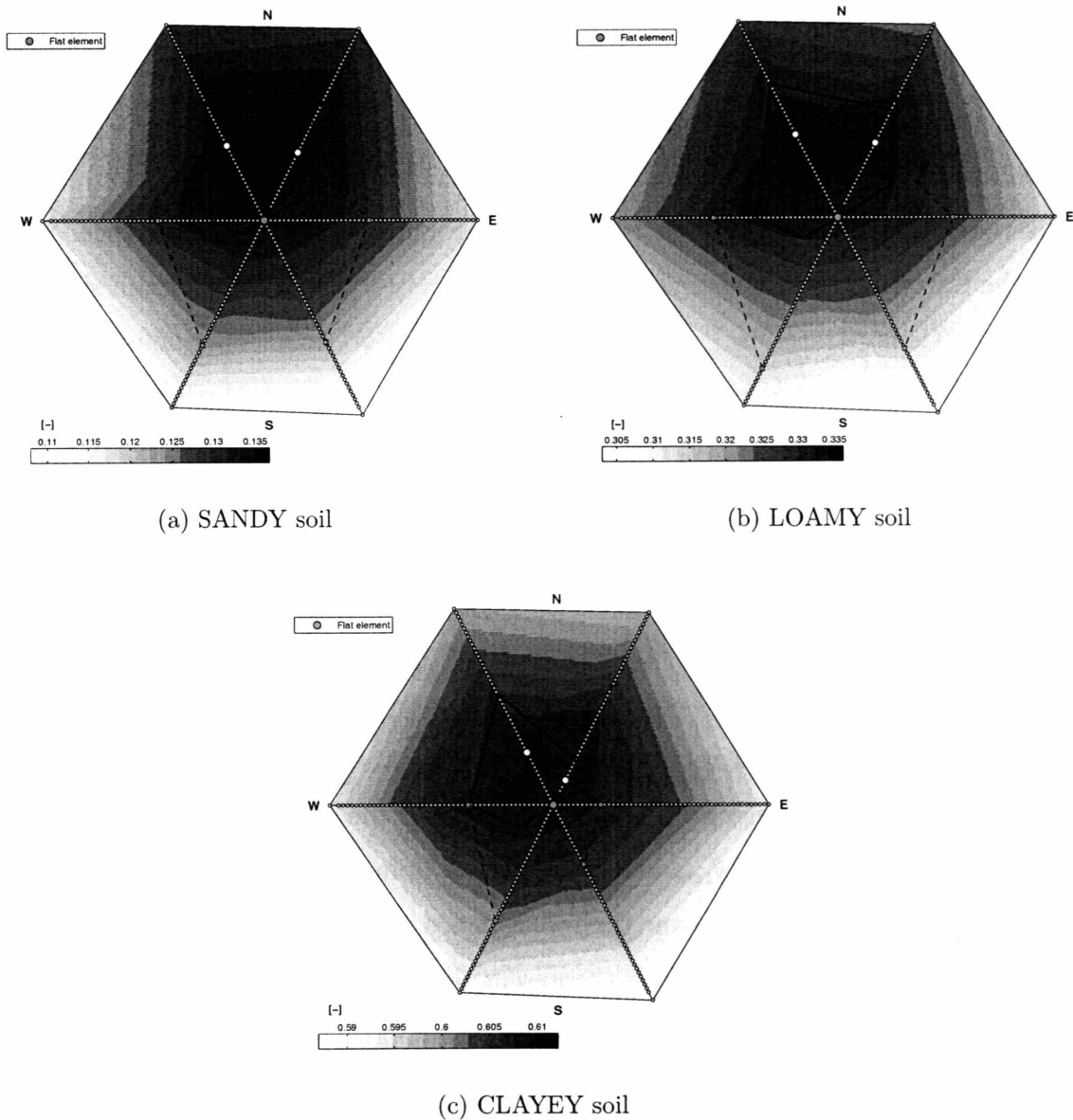
Figure 5-31: A pseudo-spatial diagram of the mean growing season root zone soil moisture shown as a two-dimensional interpolated field in polar coordinates (all soil types): the distance from the central node represents site slope and the clock-wise angle defines site aspect from north (N-E-S-W). The data for both the CX and CV domains are combined. The solid line outlines the region of relative favorability, where the mean growing season soil moisture of sloped sites is higher than that of a flat horizontal site. The dashed line outlines two regions in which either the energy (the lower area) or rainfall reduction (the upper area) plays a more significant role in the overall dynamics.

analysis to consider their relative contributions in various regions of the aspect-slope pseudo-space.

Figure 5-32 shows a two-dimensional field $\Omega \in (X, Y)$ of $\theta_{root}$ as a function of the annual global shortwave irradiance and slope (the latter variable is used as a proxy for rainfall since $R \cos \alpha_\nabla$ is the assumed precipitation projection on the terrain), where $X$ is the site slope $\alpha_\nabla$ and $Y$ is the site global annual shortwave irradiance. Note that the Cartesian coordinate system is used and only a part of the diagram shown in Figure 5-30 is illustrated in Figure 5-32, corresponding to three contiguous directions of aspect. At any initial point on the surface $\Omega \in (X, Y)$, the partial derivative of $\theta_{root}$ with respect to a chosen direction $s$ is

$$\frac{\partial \theta_{root}}{\partial s} \big|_{\Omega \in (X, Y)} = \frac{\partial \theta_{root}}{\partial X} \cos \chi + \frac{\partial \theta_{root}}{\partial Y} \sin \chi, \qquad (5.6)$$

where $\chi$ is the angle between the direction $s$ and $X$ axis. If the two components of the right-hand side of (5.6) are equal, the contributions of input radiation and rainfall to the change in the mean root soil moisture along the direction $s$ are equal. The path $s$ would therefore signify a boundary between the two regions of $\Omega$ in which the contribution to change $\theta_{root}$ along the path $s$ from either of the two hydrometeorological forcings dominates over the other. Since the mean root soil water content during growing season is assumed to represent the overall favorability of a given site to vegetation, the formulation (5.6) provides an opportunity for constructing a diagram in which the vegetation-hydrology dynamics can be attributed to a dominating influence of either of the two forcings.

*Apriori*, the peak of the "mound" shown in Figures 5-30 - 5-31 represents the point at which the contributions are equal. Hence, it should be used as an initial point for constructing the boundary that separates the two regions. However, the true peak is not contained in the simulation results since aspects are not represented on a continuous basis. Only six aspects are used and, therefore, the simulation data along each of the directions represent cross-sectional profiles of the "mound". It is assumed here, that the true maximum is located between the N-N-W and N-N-E directions

316
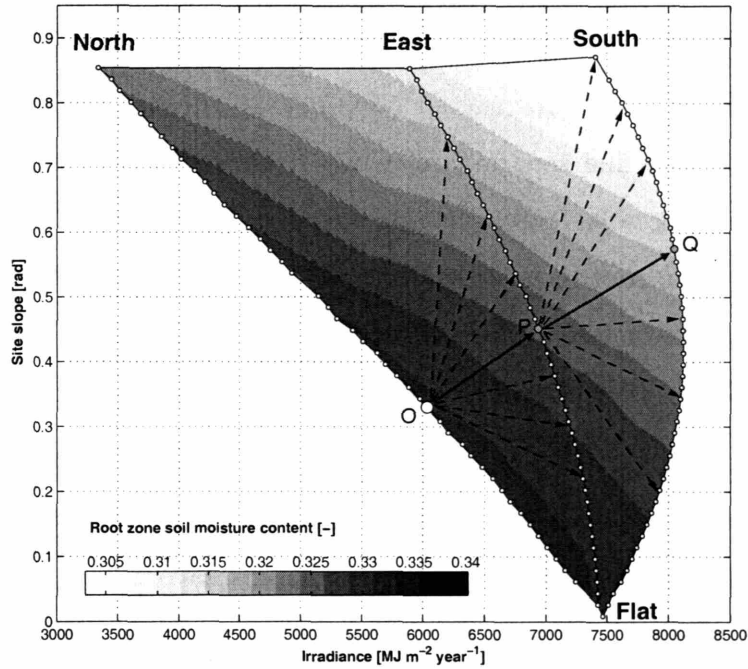
Figure 5-32: An illustration of the procedure used to partition the pseudo-spatial diagram of the mean growing season root moisture into regions where either rainfall or solar radiation dominates in their relative contribution. Site slope is used as a proxy for rainfall since $R\cos\alpha_\nabla$ is the assumed precipitation projection on the terrain. Starting at a point $O$, corresponding to a site that exhibits the maximum mean soil moisture on a slope of a given aspect (either N-N-W or N-N-E), a path is constructed to a node $P$: the direction to $P$ corresponds to an approximate equality of the partial derivatives $\frac{\partial\theta_{root}}{\partial X}\cos\chi$ and $\frac{\partial\theta_{root}}{\partial Y}\sin\chi$, where $X$ is the site slope $\alpha_\nabla$, $Y$ is the site global annual shortwave irradiance, and $\chi$ is the angle between the path $OP$ and $X$ axis. The path is selected by comparing the derivatives for all possible directions from the point $O$ (illustrated as the dashed lines). Once the point $P$ is found, a path $PQ$ is constructed using the same methodology.

(Figure 5-30), since the corresponding region exhibits the maximum reduction in the solar radiation. It is further assumed that a hypothetical path $s$ constructed from the true peak should go through the points of maximum soil moisture located in the directions of N-N-W and N-N-E aspect. These points are used in the actual procedure of constructing a path that minimizes the difference between the two right-hand side terms of (5.6). See Figure 5-32 for a visual illustration of the utilized methodology.

Figure 5-31 depicts the constructed boundary as the dashed line in each of the subplots. The dashed line separates the two regions in which either rainfall (upper area) or incoming solar energy (lower area) exhibits a more significant role in determining the mean root moisture and, therefore, overall vegetation-hydrology dynamics. Note that both forcings are referred to in the context of their change with slope (precipitation) or both aspect and slope (radiation).

Using the described methodology, an attempt is made here to conceptualize the partition of soil moisture diagrams of Figure 5-31. Regions corresponding to the characteristic integral effects of energy and water on site favorability for vegetation are identified more generically. Figure 5-33 illustrates such a conceptual sketch. The region $A$ corresponds to the slope-aspect combinations leading to conditions favorable for vegetation, i.e., dynamics at these sites result in the mean root soil moisture during growing season higher than that of a flat horizontal surface. The outlined continuous boundary of the region corresponds to the inner polygon in the soil moisture diagram of Figure 5-31, however, it is drawn as a smooth curve in Figure 5-33. The region $B$ corresponds to the slope-aspect combinations where the incoming solar energy dominates the overall dynamics. Outside of the lower half of the boundary of the region $A$, radiation imposes strong limitation on the root moisture and, therefore, is the key factor in creating unfavorable conditions for vegetation function. The boundary of the region $B$ is obtained as the union of two partition lines: one corresponds to the path of equal contribution of Figure 5-32; and the other delineates the area where the incoming radiation exceeds that of a flat surface (shown as the line with the smaller dashes in Figure 5-33). As can be seen, the latter line originates at shallow slopes with aspects somewhat deviating southward from the east (west) direction. For very
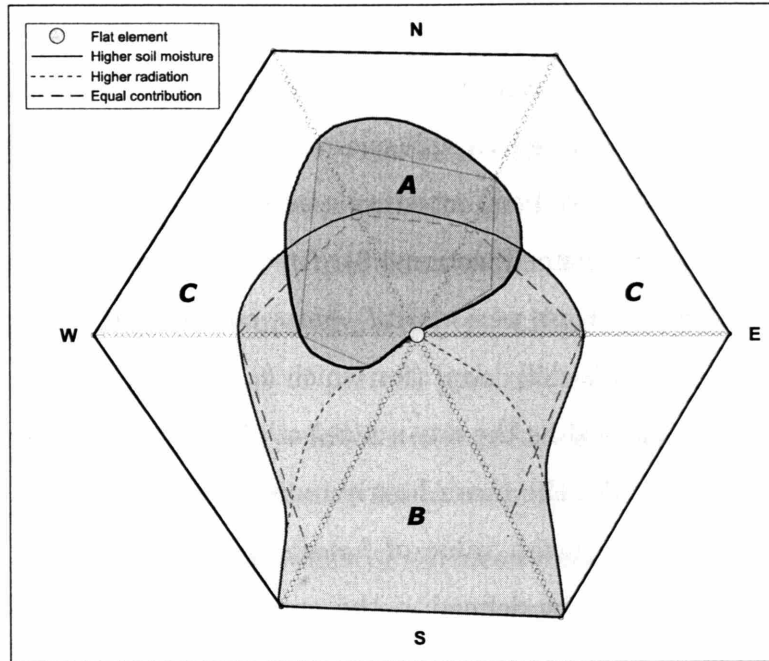
Figure 5-33: A generic partition of the slope-aspect soil moisture diagram into the regions of characteristic integral effects of energy and water on site favorability for vegetation. The region **A** includes slopes and aspects that lead to conditions favorable for vegetation. The region **B** corresponds to the area where the incoming solar energy dominates the overall dynamics, which are unfavorable to vegetation outside of the boundaries of region **A**. The region **C** corresponds to the area where precipitation dominates the overall dynamics, which are unfavorable to vegetation outside of the boundaries of region **A**.

steep slopes, the line approaches the S-S-E (S-S-W) direction (at the bottom of the plot). As above, the boundary of **B** is illustrated as an artificially smoothed curve. The region **C** corresponds to the slope-aspect combinations where the precipitation input dominates the overall vegetation-hydrology dynamics. Outside of the upper half of the boundary of the region **A**, the rainfall reduction with slope is the major reason for unfavorable conditions to vegetation.

## 5.3.2d Characterization of grass stress

In order to have a better understanding of grass dynamics, which, as was shown, are controlled by the *local* terrain features, the characteristics of water stress need to be investigated. Quantities based on the crossing properties of the root water

319

content during vegetation season are appropriate for such an analysis. For example, Ridolfi et al. (2000a) and Porporato et al. (2001) consider the structure of water stress periods, which are defined as the ones corresponding to $\theta_{root} < \theta^*$, where $\theta^*$ $[mm^3\ mm^{-3}]$ is the threshold soil moisture content for a given vegetation type at which the stomatal closure begins (Section 4.3). Among the considered quantities are: 1.) the mean duration of stress periods $\Delta T_\xi$ $[day]$ and, correspondingly, the mean duration of favorable periods $\Delta T_\varsigma$ $[day]$ (for which $\theta_{root} > \theta^*$); 2.) the mean number of stress periods $n_\xi$, expressed as the mean number of soil water downcrossings from $[\theta_{root} > \theta^*]$ to $[\theta_{root} < \theta^*]$; 3.) the mean hourly moisture deficit during stress periods $\Delta M_\xi$ $[-]$, estimated as the mean value of hourly $\frac{(\theta^* - \theta_{root})}{(\theta^* - \theta_r)}$, where $\theta_r$ $[mm^3\ mm^{-3}]$ is the residual moisture content defined as the amount of soil water that cannot be removed from soil by drainage or evapotranspiration (Section 3.7.3). As can be seen, the variable $\Delta M_\xi$ has theoretical limits of $[0 \div 1]$.

Since site slope and aspect impose essentially controlling conditions on vegetation-hydrology dynamics in the *base* case scenario, the same type of pseudo-spatial diagram as in Figure 5-30 is used to describe the distribution of stress characteristics in the two topographies. Figures 5-34, 5-35, and 5-36 illustrate the constructed diagrams for sandy, loamy, and clayey soils, respectively. The region of favorability delineated above and the boundary separating different areas of the dominant forcing (either precipitation or radiation input) are also depicted. As can be inferred from the figures, the minimum value of the mean duration of stress period can be attributed to approximately the same slope as the slope corresponding to maximum ANPP (subplots (a.) in all figures). However, the respective aspects of these two slopes are not the same, being N-N-W for the minimum duration of stress period and N-N-E for the maximum ANPP. The subplots (a.) and (b.) of Figures 5-34 - 5-36 illustrate that for soils of finer texture (loamy and clayey), there is a sharp difference among the obtained mean durations of stress period within the considered range of slopes and aspects. Same observation can be made for mean durations of favorable period. The ratio of maximum to minimum values of these quantities reaches $3 \div 5$. It appears that these extreme differences lead to the substantial variability of ANPP simulated

for these soil types (Figures 5-24 - 5-25): the ratios of maximum to minimum ANPP are of the same order of magnitude. As was observed in previously, the mean root moisture alone could not explain the significant spatial variability of ANPP. Since soil is relatively dry most of the time during the growing season, the estimated *mean* soil water content is inherently weighted towards the values representing the overall dry seasonal conditions. Consequently, site productivity characteristics need to be addressed through the properties of periods that exhibit either positive or negative effects on vegetation dynamics. As follows, the *crossing* properties of the mean root water content should be indeed suitable for these purposes.

As can be seen, the maximum values of the mean duration of favorable periods are also attributed to slopes that exhibit maximum ANPP, falling within the boundaries of the delineated regions of favorability. While this is not exactly true for sandy soil, its corresponding maximum value does not vary significantly from those one representative of the favorable region ($\sim$28 *days vs.* $\sim$26 *days*, Figure 5-34b).

The diagrams of the mean number of downcrossings or, equivalently, the mean number of stress or favorable periods (subplots (c.)), show that the maximum values are associated with south-facing slopes in sandy soils and north / west-facing slopes in soils of finer texture. Too large number of downcrossings indicates unfavorable conditions (Ridolfi et al., 2000a). However, in the case of loamy and clayey soil, such a number rather reflects the occurrence of wetting periods: the mean durations of stress periods are much higher than durations of favorable periods and, therefore, grass spends most of the growing season in a stressed state. In the case of sandy soils, the maximum value is apparently related to a combination of higher radiation values on south-facing slopes and a reduction of the actual rainfall for steeper slopes.

The mean moisture deficit, illustrated in subplots (d.), is a measure of a degree of dryness during stress periods, with higher values indicating the aggravating conditions leading to tissue damage and foliage loss. As the figures show, the minimum values of the mean moisture deficit are within the regions of favorability in most cases. For sandy soil, which represents an exception, the simulated minimum mean value does not significantly differ from those representative of the outlined region of favorability

($\sim$0.42 $vs.$ $\sim$0.45, Figure 5-34d).

Overall, it can be concluded that favorable conditions for plant function in terrain niches can be attributed to a compromise between low water stress and high productivity. This conclusion is based on the simulated distribution of stress characteristics that exhibit least extreme values at terrain locations similar to those that feature maximum ANPP (although not exactly the same). Such a trade-off between the high productivity (and, therefore, high transpiration depleting soil water reservoir) and high soil moisture (as a buffer against stress) has been previously discussed by a number of researchers (e.g., Tilman, 1982; Eagleson, 1994; Porporato et al., 2001; MacKay, 2001).

The bulk differences in stress characteristics among the soil types are illustrated in Figure 5-37. The figure shows the simulated maximum and minimum values of each of the discussed above quantities (the dashed lines) as well as their mean values representative of the delineated regions of favorability (the symbols). As can be seen in the figure, sandy soil exhibits shorter periods of stress, which, however, occur more frequently (subplots (a.) and (c.)). For soils of finer texture, grass is under stress most of the time with short, infrequent periods when the root zone is wetted above $\theta^*$. The stress periods are characterized by water deficit that, on average, is higher in sandy soil than in loamy and clayey soils. For the two latter soil types, vegetation is rather sparse and, therefore, moisture uptake is not very intense with soil evaporation depleting the soil water storage at a lower (than transpiration) rate. Notwithstanding the longer durations of stress periods, it appears that grass on these soil types is less susceptible to the negative effects of unusually long dry spells. As was demonstrated in Section 5.3.1, grass on sandy soils typically experiences dieback in the dry month of June. The reason for that is a larger amount of biomass present on sandy soils in the pre-monsoon period, as compared to loamy and clayey soils. Therefore, moisture uptake requirements are higher for vegetation on sandy soil. The unpredictable shortage of precipitation during June results in higher deficits leading to the biomass loss.

As can also be inferred from Figure 5-37, the mean values of stress characteristics

**a.) Mean duration of stress periods**

N

W      E

**Duration [day]**    S

6    8    10    12

△ Max ANPP
□ Min duration
● Flat element

**b.) Mean duration of favorable periods**

N

W      E

**Duration [day]**    S

22    24    26    28

△ Max ANPP
□ Max duration
● Flat element

**c.) Mean number of downcrossings**

N

W      E

**[#]**    S

7    8    9    10

△ Max ANPP
□ Max number
● Flat element

**d.) Mean moisture deficit**

N

W      E

**[-]**    S

0.42   0.44   0.46   0.48   0.5

△ Max ANPP
□ Min deficit
● Flat element
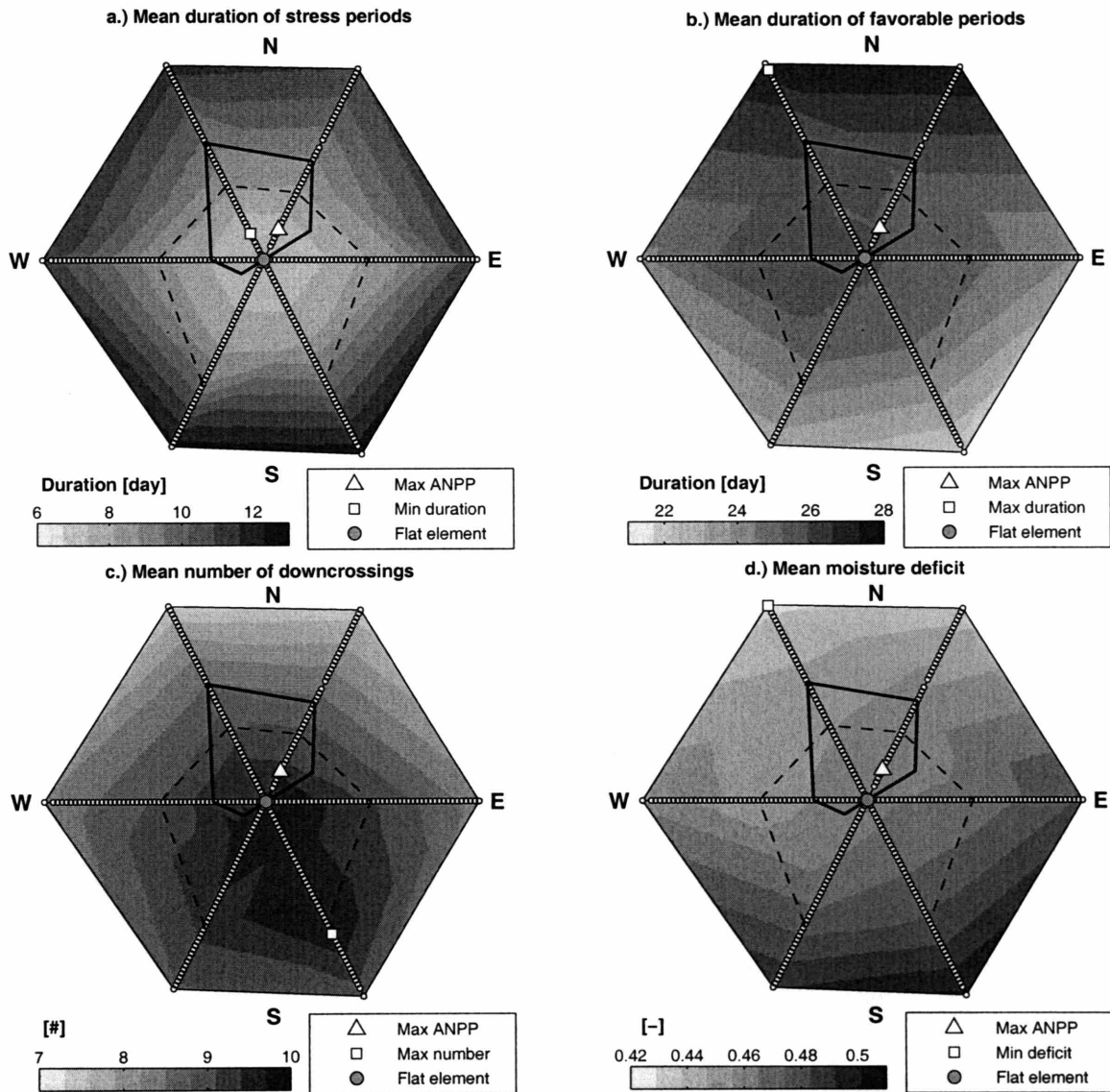
Figure 5-34: The crossing properties of the root water content during vegetation season for *sandy* soil type: a.) the mean duration of stress periods $\Delta T_\xi$; b.) the mean duration of favorable periods $\Delta T_\varsigma$; c.) the mean number of stress periods $n_\xi$; d.) the mean hourly moisture deficit during stress periods $\Delta M_\xi$.
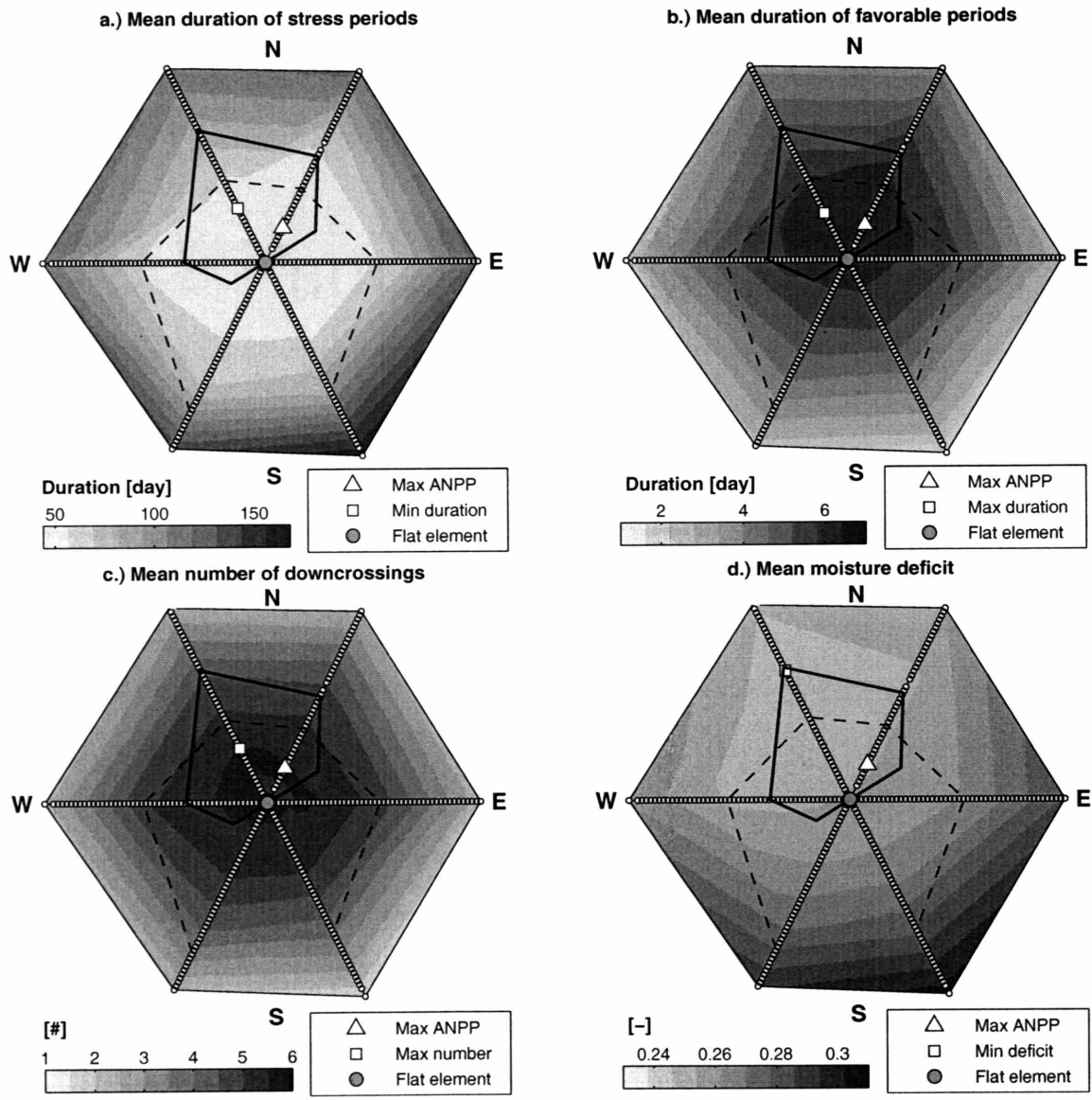
Figure 5-35: The crossing properties of the root water content during vegetation season for *loamy* soil type: a.) the mean duration of stress periods $\Delta T_\xi$; b.) the mean duration of favorable periods $\Delta T_\varsigma$; c.) the mean number of stress periods $n_\xi$; d.) the mean hourly moisture deficit during stress periods $\Delta M_\xi$.

**a.) Mean duration of stress periods**

N

W · E

S

Duration [day]

60   80   100   120   140

△  Max ANPP
□  Min duration
●  Flat element

**b.) Mean duration of favorable periods**

N

W · E

S

Duration [day]

1   2   3   4   5

△  Max ANPP
□  Max duration
●  Flat element

**c.) Mean number of downcrossings**

N

W · E

S

[#]

1   2   3   4   5   6

△  Max ANPP
□  Max number
●  Flat element

**d.) Mean moisture deficit**

N

W · E

S

[–]

0.2   0.22   0.24

△  Max ANPP
□  Min deficit
●  Flat element
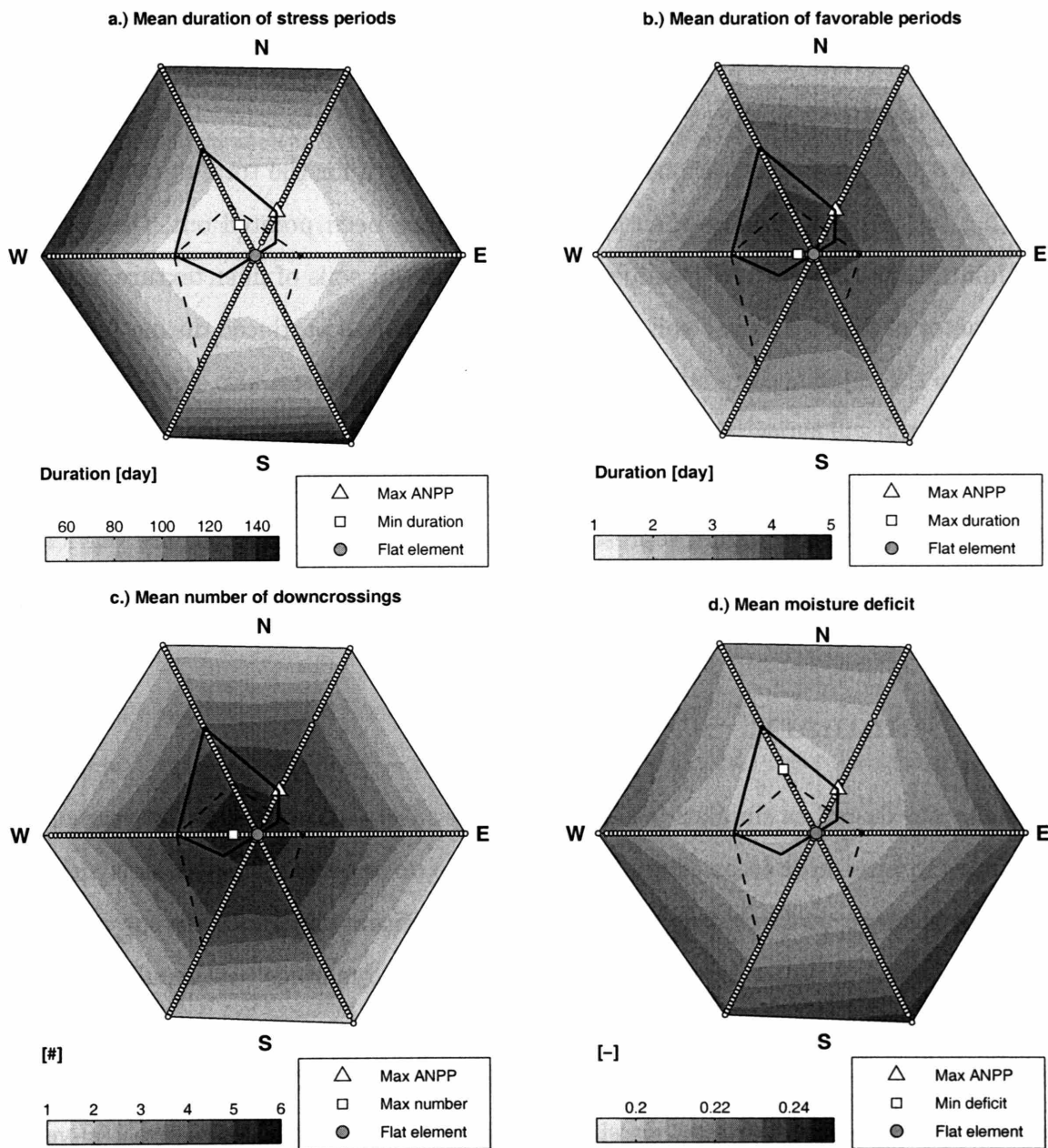
Figure 5-36: The crossing properties of the root water content during vegetation season for *clayey* soil type: a.) the mean duration of stress periods $\Delta T_\xi$; b.) the mean duration of favorable periods $\Delta T_\varsigma$; c.) the mean number of stress periods $n_\xi$; d.) the mean hourly moisture deficit during stress periods $\Delta M_\xi$.

representative of the favorability regions are within the ranges that are most favorable to vegetation. The only exception is probably the number of downcrossings for sandy soils: since the mean duration of favorable periods exceeds that of stress periods, the conditions for grass would be more favorable with a lower number of downcrossings than the estimated value.

Figure 5-38 illustrates various ANPP quantities both for the total duration of the growing season and periods when $\theta_{root} > \theta^*$. As has been pointed out, the ratio of maximum to minimum ANPP values is much higher for soils of finer texture, exceeding a factor of four for clayey soil. The fraction of biomass produced during favorable periods to the value accumulated over the entire growing season also significantly differs among the soil types. For sandy soil, most of the total ANPP (>90%) is produced during favorable periods. For loamy and clayey soils, these fractions do not exceed 15%. The mean ANPP values representative of the favorability regions are very close to the simulated maximum values.

## 5.4 Summary

This chapter describes simulations addressing the effects of topography on vegetation dynamics in semi-arid areas. The experiments are done on two small-scale synthetic domains (each is $\sim 4$ $km^2$ in area) that exhibit significant differences in the hillslope characteristics. A full range of transient vegetation dynamics are simulated for a typical annual $C_4$ grass assumed to grow in three different soil types: sandy, loamy, and clayey. The climate corresponding to Albuquerque (NM) is used as the forcing and is reproduced by the weather simulator that generates the long-term (50-year) time-series of hydrometeorological forcing variables. The flux density of incoming radiation is estimated based on the hourly Sun position and the precipitation flux is assumed to strictly follow the vertical direction. Both forcing fluxes are projected using the geometry of a receiving site. The utilized experimental design constitutes the *base* case scenario.

As discussed above, under the imposed conditions the subsurface lateral moisture
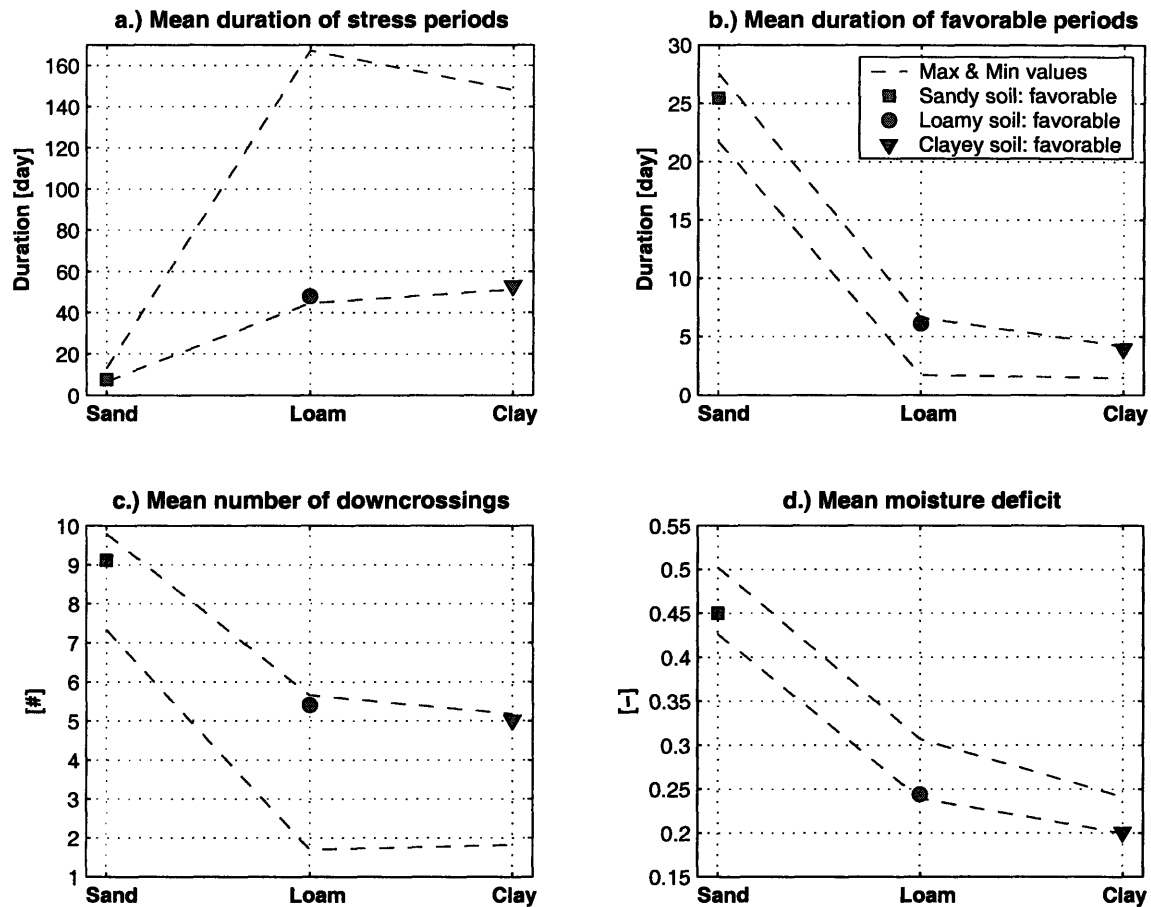
Figure 5-37: The crossing properties of the root water content during vegetation season for all soil types: a.) the mean duration of stress periods $\Delta T_\xi$; b.) the mean duration of favorable periods $\Delta T_\varsigma$; c.) the mean number of stress periods $n_\xi$; d.) the mean hourly moisture deficit during stress periods $\Delta M_\xi$. The dashed lines depict maximum and minimum values simulated for a given soil type. The symbols denote mean values for the identified regions of relative favorability.
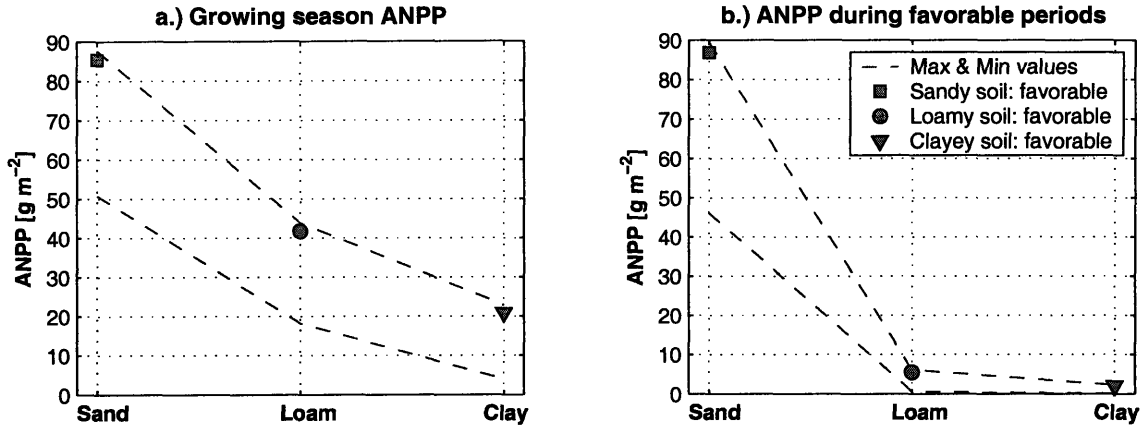
Figure 5-38: The simulated ANPP characteristics for the considered domains for: a.) the total duration of growing season and b.) periods when $\theta_{root} > \theta^*$ (referred to as the favorable periods). The dashed lines depict maximum and minimum values simulated for a given soil type. The symbols denote mean values for the identified regions of relative favorability.

exchange does not significantly affect the vegetation-hydrology dynamics and, therefore, the latter are assumed to be *spatially-independent*. The *local* terrain features, such as **aspect** and **slope**, are the key determinants of the overall dynamics at a given site. Therefore, most of the mean state variables can be simply considered as a function of these key topographic attributes. Both ANPP and water balance components, when considered as a function of site surface irradiance, which represents a convenient measure of both site aspect and slope, comprise a characteristic shape, referred to above as the "$\epsilon$-curve". The "$\epsilon$-curve" pattern is the resulting compound outcome of dynamics that involve *water* and *energy* interactions, as mediated by *vegetation* function and affected by the soil hydraulic properties.

As was shown, in conditions of the *base* case scenario certain topographic locations may favor vegetation function, as compared to a flat horizontal surface not affected by the lateral effects such as radiative shading, moisture transfer in the unsaturated zone, or runon. These locations are associated with sites of northerly aspect with surface slopes within a narrow range of magnitudes. Contributions from both the *water* and *radiation* forcing are discussed to explain the existence of these niches. Favorable conditions for plant function are attributed to a compromise between low water stress and

328

high productivity. The conclusion is drawn from the simulated spatial distribution of stress characteristics that exhibit least extreme values at terrain locations similar to those that feature maximum ANPP. Furthermore, a conceptual procedure is used to partition the aspect-slope pseudo-space into the regions of dominant influence of the forcing using the mean root moisture during growing season as a representative characteristic of site favorability to grass. In these delineated regions, either rainfall insufficiency or radiation excess impose predominant constraining conditions on grass performance.

# Chapter 6

# Sensitivity of Vegetation Dynamics to Hydrometeorological Forcing and Processes of Lateral Moisture Transfer

## 6.1 Introduction

This chapter discusses simulation results that address the sensitivity of the vegetation-hydrology dynamics described in Chapter 5, referred to below as the "*base*" case scenario. The experimental design presented in Chapter 5 is subject to modifications in the hydrometeorological forcing and processes of lateral moisture transfer. Two simulation scenarios are considered. 1.) The "*H-sensitivity*" case involves several scenarios that address variation in the *H*ydrometeorological forcing, attempting to represent the random nature of the rainfall vector (i.e., deviation of droplet pathways from the vertical) and introduce changes into the seasonal precipitation and radiation regimes. 2.) The "*R-exchange*" case that attempts to introduce *R*apid processes of lateral moisture exchange, which are governed by the high soil anisotropy ratios ($a_r \in [100 \div 1000]$), the runon mechanism allowing for re-infiltration process, and the

partial surface sealing during the growing season, leading to higher runoff generation.

## 6.2 Experimental design

The experimental design is analogous to that of the "*base*" case scenario (Section 5.2). Two landscapes, the "CX" and "CV" domains (each is $\sim 4$ $km^2$ in surface area, Section 5.2.1) are used. In total, 2,400 computational elements represent each of the synthetic topographies with the typical element dimensions of approximately 30 $m$ x 40 $m$. A generic annual $C_4$ grass is used for three different soil texture types: sandy, loamy, and clayey. No groundwater effects are considered. The total duration of simulation spans 50 years for both domains, which is assumed to be sufficient to provide consistent statistics of vegetation-hydrology dynamics. The climate of New Mexico corresponding to the location of Albuquerque is used as representative of a typical semi-arid area with a pronounced monsoon season driving most of the annual vegetation dynamics. The weather generator described in Chapter 2 is used to create consistent time-series of hydrometeorological forcing throughout the 50-year simulation period.

In the following, a number of modifications are introduced to the "*base*" case scenario that alter either hydrometeorological forcing, soil parameterization (anisotropy characteristics), or dominant processes of lateral water transfer. The modifications are detailed in each of the following sections that describe the sensitivity of results to a modified feature.

## 6.3 Sensitivity to hydrometeorological forcing

The material of this section covers the "*H-sensitivity*" case (Section 5.2) that considers several scenarios of modified hydrometeorological forcing. The scenarios include a simplified approach to representing the random nature of the rainfall vector (i.e., accounting for deviation of droplet pathways from the vertical) as well as changes in the seasonal precipitation and radiation regimes.

332

## 6.3.1 Modified projection of rainfall rate on sloped surfaces

As was shown in Section 5.2.3b, the changing precipitation intensity combined with random deviations of rain droplet pathways from the vertical may lead to equal distributions of rainfall over horizontal and inclined surfaces. Five scenarios are used that consider various values of a critical surface slope $\alpha_\nabla^o$, such that for $\alpha_\nabla \leq \alpha_\nabla^o$ the randomness in precipitation forcing leads to the same rain depth (per unit actual surface area) as for a horizontal surface. The mean annual depth for a horizontal surface is the same as in the *base* case scenario, $244 \ mm \ yr^{-1}$. The procedure assumes the following relationship:

$$
\begin{aligned}
R' &= R, & \text{if } \alpha_\nabla \leq \alpha_\nabla^o, \\
R' &= R \frac{(\cos\alpha_\nabla \cos(\alpha_\nabla - \alpha_\nabla^o) + (1 - \cos\alpha_\nabla)\cos\alpha_\nabla)}{\cos\alpha_\nabla^o (2 - \cos\alpha_\nabla^o)}, & \text{if } \alpha_\nabla > \alpha_\nabla^o,
\end{aligned} \quad (6.1)
$$

where $R \ [mm \ hr^{-1}]$ is the rainfall rate related to a unit horizontal area, $R' \ [mm \ hr^{-1}]$ is the adjusted rainfall rate for a sloped surface, and $\alpha_\nabla^o \ [rad]$ is the critical surface slope. As can be seen from (6.1), the formulation uses two cosine functions: $\cos\alpha_\nabla$ and the one lagged by $\alpha_\nabla^o$. The relative contributions from the functions are weighted, so that for $\alpha_\nabla = \pi/2$, $R' = 0$.

It is necessary to note that the procedure does not attempt to address the actual mechanisms that may lead to such a distribution of rain over inclined surfaces. Neither does the procedure consider variability of these mechanisms in time since the adjustment is applied to every storm throughout the year. The modified rainfall projection is merely assumed to be a plausible scenario in an attempt to characterize the random nature of the rainfall vector in a simplified manner. Five critical angles $\alpha_\nabla^o$ are considered: 0.1, 0.2, 0.3, 0.4, and 0.5 $[rad]$. Rainfall distribution with site slope and annual irradiance is shown in Figure 6-1.

The results for the *base* case scenario showed that in conditions of negligible lateral moisture transfer, the first moments of vegetation-hydrology variables depend only on slope and aspect. The dependence in the two domains (CX and CV) is essentially identical since the "$\epsilon$-curve" patterns overlap. In order to decrease the number of
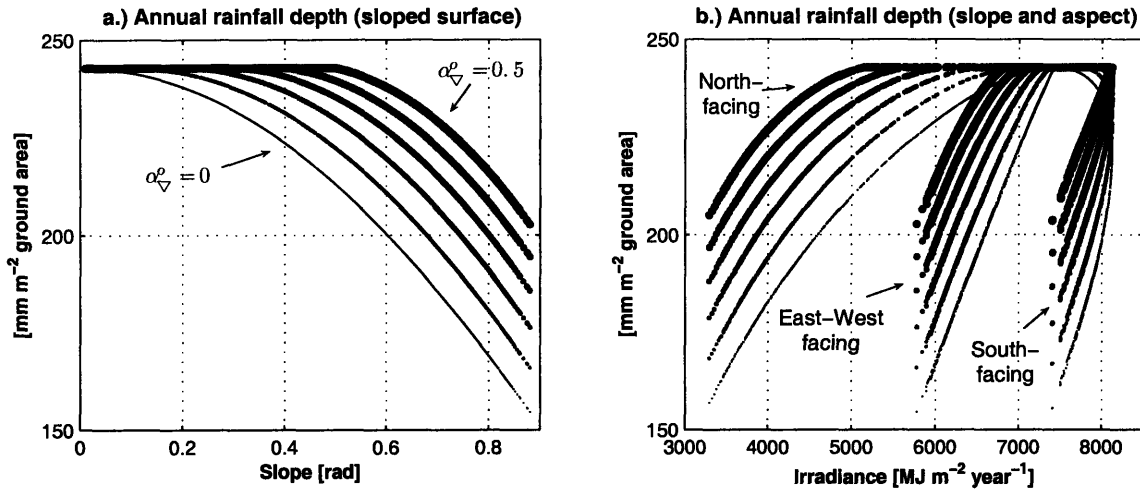
Figure 6-1: Artificially introduced adjustments to the annual rainfall depth per unit ground surface area relative to a.) site slope and b.) annual site surface irradiance (involves both site aspect and slope). Note that the units refer to actual ground surface area of computational element. The curves are obtained by applying a factor provided in (6.1) to the rainfall depth for a horizontal surface. The procedure thus assumes that there is a critical surface slope $\alpha_\nabla^o$ below which the random perturbations of the rain field lead to the same rain depth as for a horizontal surface.

required computations, the scenarios of rainfall adjustment were only used for the "CV" domain that features a substantially wider range of terrain slope magnitudes.

Figure 6-2 illustrates the results of simulations for the scenarios in the same fashion as the "$\epsilon$-curves" obtained in Section 5.3. As can be seen in the figure, the results vary among the soil types. Loamy and clayey soils exhibit a consistent change in the position and magnitude of maximum ANPP with the critical angle $\alpha_\nabla^o$. The maximum ANPP values are always associated with north-facing sites that receive less solar radiation. An opposite situation can be observed for sandy soil: while the overall grass productivity pattern changes with $\alpha_\nabla^o$, the maximum productivity is essentially insensitive to an increase in $\alpha_\nabla^o$. Only a minor change can be observed when compared to the maximum ANPP of the *base* case. This feature is further addressed in Figure 6-3 that compares the values of $\alpha_\nabla^o$ and slopes of elements with maximum simulated ANPP (their numerical values are provided in Table 6.1). As the figure shows, for loamy and clayey soils, as the critical slope $\alpha_\nabla^o$ increases, the slopes corre-

334

Table 6.1: Terrain slopes corresponding to maximum ANPP for different magnitudes of the critical surface slope $\alpha_\nabla^o$ (formulation (6.1)) for different soil types.

| Critical slope | Sandy soil | Loamy soil | Clayey soil |
|---|---|---|---|
| $\alpha_\nabla^o = 0.0\ rad$, 0.0° | 4.52° | 9.39° | 10.89° |
| $\alpha_\nabla^o = 0.1\ rad$, 5.73° | 8.94° | 15.48° | 12.81° |
| $\alpha_\nabla^o = 0.2\ rad$, 11.46° | 8.94° | 19.64° | 19.64° |
| $\alpha_\nabla^o = 0.3\ rad$, 17.19° | 8.94° | 23.18° | 23.44° |
| $\alpha_\nabla^o = 0.4\ rad$, 22.92° | 8.94° | 25.95° | 24.86° |
| $\alpha_\nabla^o = 0.5\ rad$, 28.65° | 8.94° | 28.65° | 29.00° |

sponding to locations exhibiting maximum ANPP become closer to $\alpha_\nabla^o$. This implies that the relative benefit of radiative shading by slopes of northerly aspect diminishes with growing $\alpha_\nabla^o$. It is plausible to assume that radiation, Photosynthetically Active Radiation (PAR) in particular, becomes a limiting factor in this case. The $C_4$ grass productivity for sandy soil exhibits a different pattern of behavior. The slope corresponding to a location with maximum simulated ANPP stays constant for any critical angle $\alpha_\nabla^o > 0.1\ rad$. This implies that a decrease in the incoming solar radiation due to the topographic shading does not lead to conditions more favorable than those corresponding to the location of the found constant maximum. These conditions are discussed in the following.

Figure 6-4a illustrates the mean annual cycle of ANPP simulated for a scenario with the critical angle $\alpha_\nabla^o = 0.5\ rad$ for elements of different slopes (sandy soil): $\alpha_\nabla = 0.0$, 0.156, and 0.5 $rad$. The element with $\alpha_\nabla = 0.156\ rad$ corresponds to a location exhibiting overall maximum ANPP for sandy soil (Table 6.1). It follows from the figure, that the radiative shading of topography facilitates grass dynamics during the month with the highest energy input (month of June, e.g., Figure 2-5): when compared to the cases with other slope magnitudes, ANPP is highest for the element with the surface slope $\alpha_\nabla = 0.5\ rad$. However, during the monsoon months of July through September, no significant favorable effect from terrain shading can be observed and grass performs almost equally well for all sloped sites. Furthermore,

(a) SANDY soil



(b) LOAMY soil
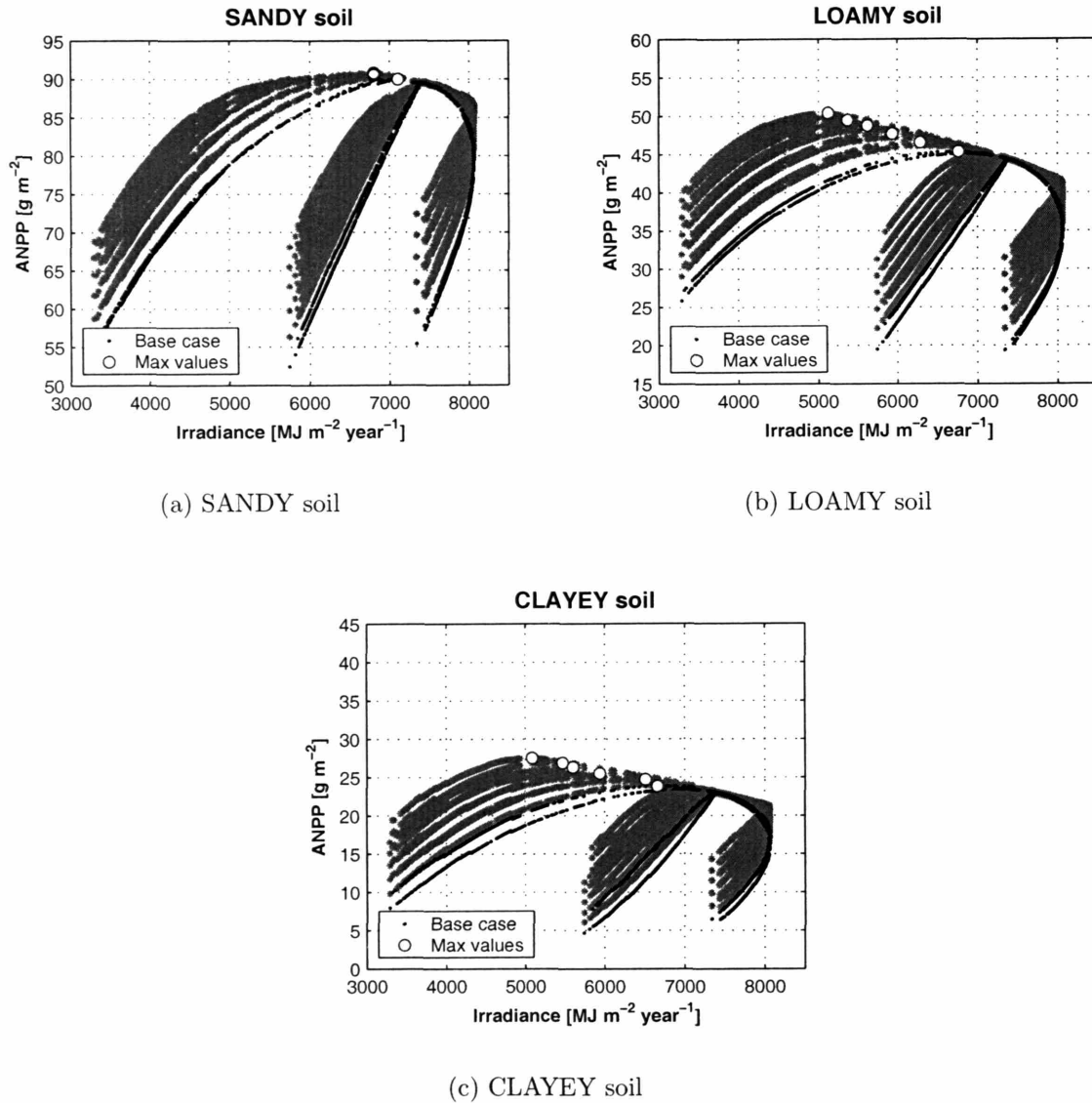


(c) CLAYEY soil

Figure 6-2: The mean simulated Above-ground Net Primary Productivity for the considered soil types for the scenario with modified projection of rainfall forcing (accounting for angle $\alpha_{\triangledown}^{o}$): a.) sandy soil; b.) loamy soil; and c.) clayey soil. The small black circles denote the data points for the *base* case scenario. The large white circles depict maximum ANPP for each considered scenario.
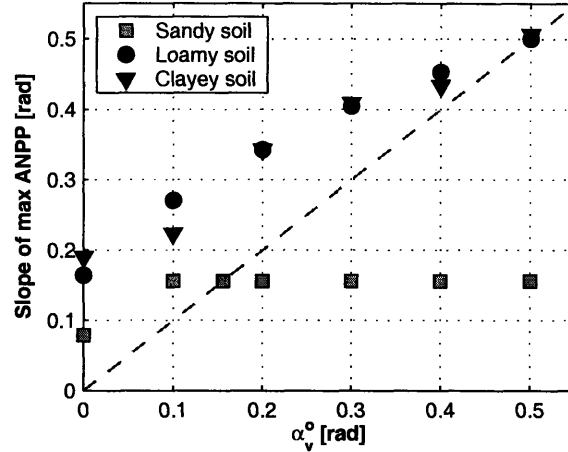
Figure 6-3: Terrain slopes corresponding to the maximum ANPP for different magnitudes of the critical surface slope $\alpha_\nabla^o$ (formulation (6.1)) for different soil types. All slopes are for sites of northerly aspect. The dashed line corresponds to the one-to-one relationship between the ordinate and abscissa angles. The benefit from radiative shading by north-facing slopes diminishes (disappears) for the data points that are closer to the dashed line (located below it).

it also appears that during early spring and late months of the fall period, radiation/PAR becomes the limiting factor for sloped surfaces and, consequently, their grass dynamics are suppressed with respect to more radiation-exposed areas.

In contrast to the ANNP dynamics for sandy soil, the productivity for soils of finer texture shows a consistent positive dependence on the degree of topographic shading. Figure 6-4b illustrates the mean annual cycle of ANPP simulated for loamy soil for elements with $\alpha_\nabla = 0.17$ and $0.5$ $rad$. The north-facing element with the surface slope $\alpha_\nabla = 0.17$ $rad$ corresponds to a location exhibiting maximum ANPP in the *base* case scenario. As can be seen in the figure, ANPP is higher for the slope of larger magnitude throughout most of the growing season except the late fall period, which can probably be also attributed to the radiation/PAR limitation. Water fluxes in the root zone are discussed in the following to interpret the above features of the annual cycles of productivity.

Figure 6-5 shows the mean annual cycles of the components of root zone water balance for the same elements as in Figure 6-4a. Figure 6-5a shows the mean monthly transpiration fluxes, which consistently resemble the ANPP cycles of Figure 6-4a, i.e.,

337
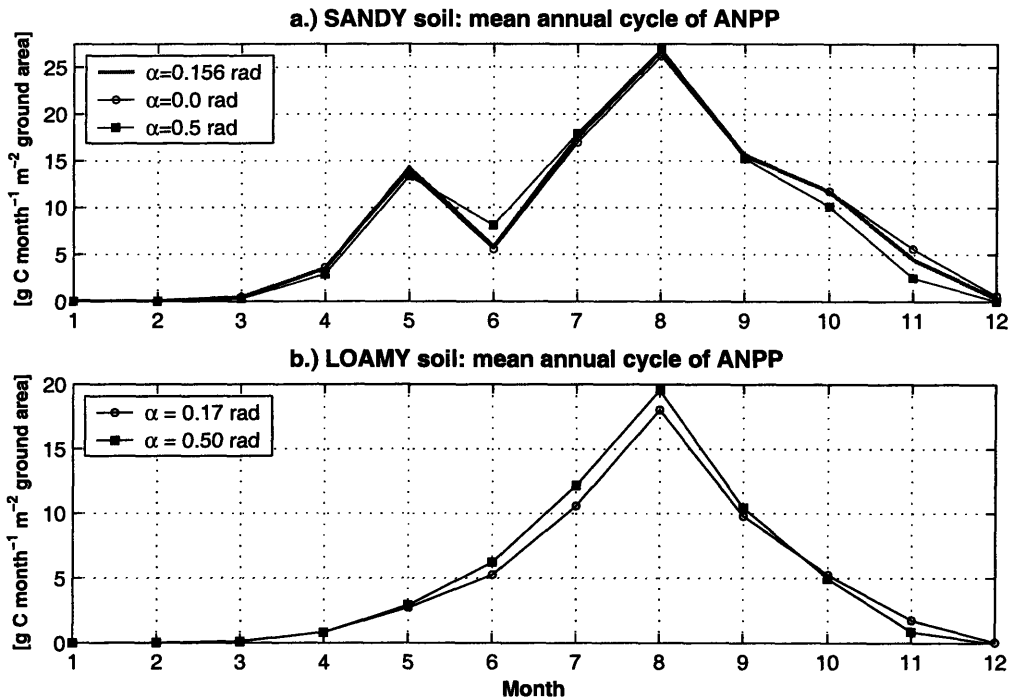
Figure 6-4: The mean annual cycles of ANPP for north-facing elements of different slope (the scenario with the critical angle $\alpha_\nabla^o = 0.5\ rad$): a.) *sandy* soil, the element with $\alpha_\nabla = 0.156\ rad$ corresponds to a location exhibiting maximum ANPP for all considered scenarios; and b.) *loamy* soil, the element with $\alpha_\nabla = 0.17\ rad$ corresponds to a location exhibiting maximum ANPP in the *base* case scenario. Note that ANPP is given in the units of gram of carbon per unit actual ground surface area.

transipiration is proportional to productivity. *Apriori*, effects from radiative shading favorable for grass dynamics should arise from decreased soil evaporation, the annual cycles of which are illustrated in Figure 6-5b. However, as can be seen in the figure, a significant decrease in soil evaporation for the element with steepest surface slope $\alpha_\nabla = 0.5$ *rad* can only be observed during winter months. A fraction of the resulting moisture excess drains from the root zone to deeper soil layers (Figure 6-5c): the drainage is higher for steeper slopes than for shallower slopes during the months of December through March. Due to weak capillary tension forces in sandy soils, only a tiny fraction of the drained excess moisture is available to vegetation during the following dry months (Figure 6-5c). A slightly better grass performance for the element with surface slope $\alpha_\nabla = 0.5$ *rad* during the month of June can thus be explained by both the terrain radiative shading effect and a somewhat wetter soil state in the preceding months. The wetter state is caused by both the smaller evaporation rates during winter and low vegetation fraction in spring, which in-turn is caused by the radiation/PAR limitation. Grass cannot perform better on steeper slopes during the months of July-September because of inability both to exploit the moisture storage below the root zone (weak capillarity of sandy soil) and to significantly decrease soil evaporation rates during that period. The latter can probably be attributed to the high water use efficiency of $C_4$ grass in any considered case, i.e., grass grows "the best it can", within the constraints of its biochemical properties and preceding history of development.

Figure 6-6 is similar to the previously discussed illustration, however, water fluxes for loamy soil are shown. As above, the transpiration cycles are consistent with the ANPP dynamics (Figure 6-6a and Figure 6-4b). The soil evaporation flux (Figure 6-6b) is smaller for the location with steeper slope ($\alpha_\nabla = 0.5$ *rad*) throughout most of the year, except during the spring period. The latter is most likely caused by the absence of vegetation and a wetter soil state because of moisture accumulation during cooler winter months. Higher drainage during the winter-early spring period, shown in Figure 6-4c, supports this statement. Consequently, during the growing season, vegetation on steeper slopes performs better due to: a.) a wetter soil state in the root
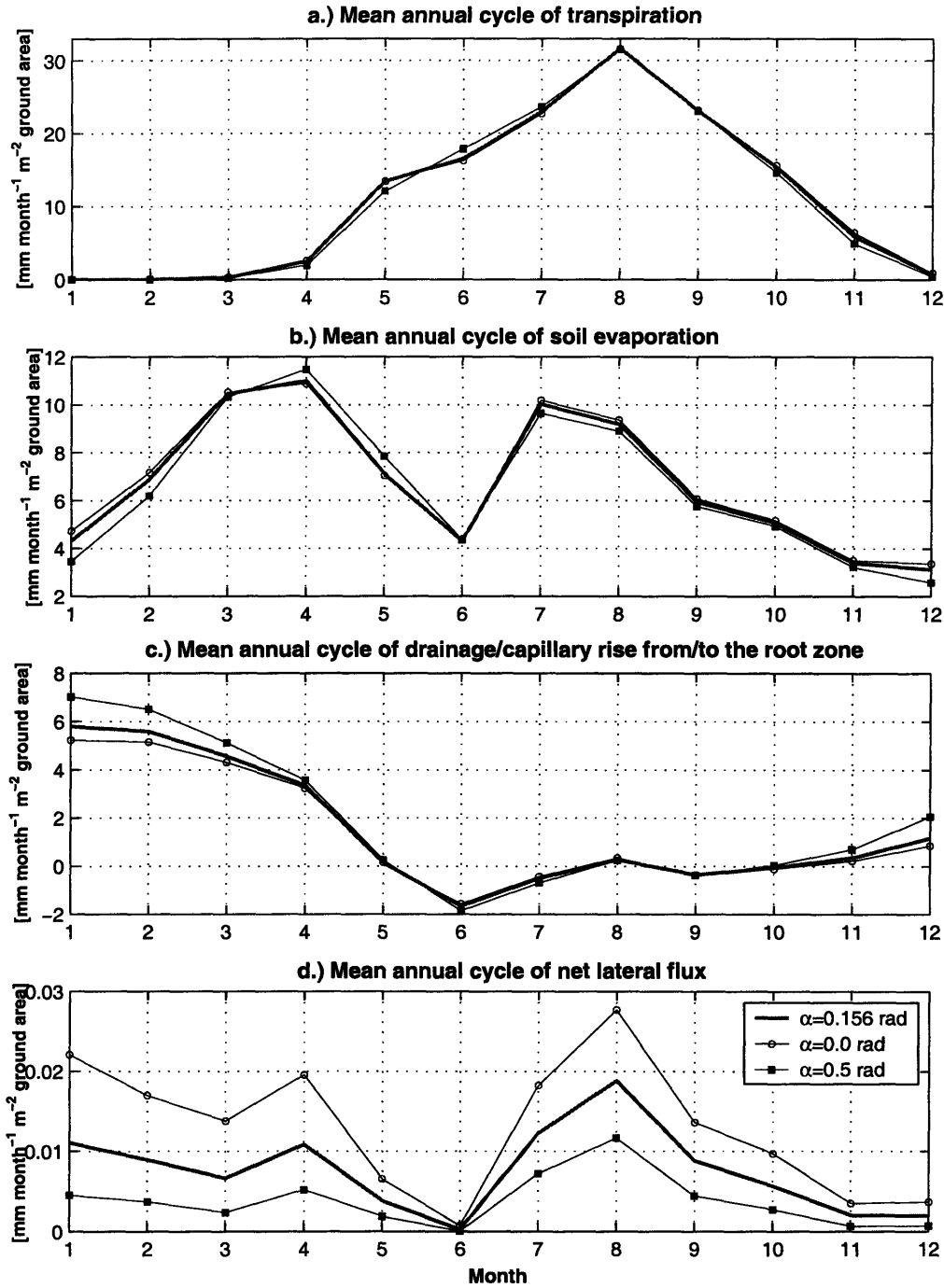
Figure 6-5: The mean annual cycles of components of root zone water balance for north-facing elements of different slope (the scenario with the critical angle $\alpha_\nabla^o = 0.5$ $rad$, $sandy$ soil case): a.) transpiration; b.) soil evaporation; c.) drainage/capillary rise from/to the root zone; and d.) net lateral flux. The element with $\alpha_\nabla = 0.156$ $rad$ corresponds to a location exhibiting maximum ANPP in all considered scenarios. Note that the fluxes are given in the units of depth per unit actual ground surface area.

zone at the beginning of the season; b.) smaller incoming radiation (terrain shading); c.) capillary rise of a larger amount of moisture drained to the storage below the root zone during cooler months (Figure 6-4c). In addition, there exists a self-fostering effect since a larger amount of grass canopy reduces the shortwave radiation reaching the understory soil surface and, therefore, effectively decreases soil evaporation.

Overall, the above discussion points out the importance of proper accounting for the actual distribution of precipitation over sloped surfaces. More research needs to be done to address the actual distribution of *hydrological* rainfall (Section 5.2.3) in complex terrain. In addition, the discussion emphasizes the important aspects of temporal relationships between energy, water, and biomass dynamics, e.g., the existence of periods of radiation limitation and excess that correspondingly affect vegetation dynamics. The presented results also unequivocally demonstrate the characteristic differences in vegetation-hydrology processes induced by soil hydraulic properties in response to the same hydrometeorological forcing.

## 6.3.2 Modified rainfall regime

The material of this section investigates the sensitivity of vegetation-hydrology dynamics observed in the *base* case scenario to alterations in the precipitation regime. As inferred from *in-situ* observations and model predictions (e.g., Houghton et al., 2001; Groisman et al., 2004), climate changes suggest variations in the frequency and size of rainfall events. To address the corresponding ecohydrological implications, the parameter values of the rainfall model (2.33)-(2.35) of Section 2.4 are modified. It is assumed that the total mean precipitation depth $\overline{P}$ [$mm$] during the most active period of the growing season, July through October, remains unchanged. $\overline{P}$ can be expressed as (Chapter 2, Section 2.4)

$$\overline{P} = \frac{\Delta T_{season}}{\mu_r + \mu_b} \left( \frac{\mu_d}{\mu_r} \mu_r \right),$$ 

(6.2)

where $\Delta T_{season}$ [$hour$] is the growing season duration. If the mean time between storms $\mu_b$ does not include the mean storm duration $\mu_r$ (i.e., taken as the mean value

341
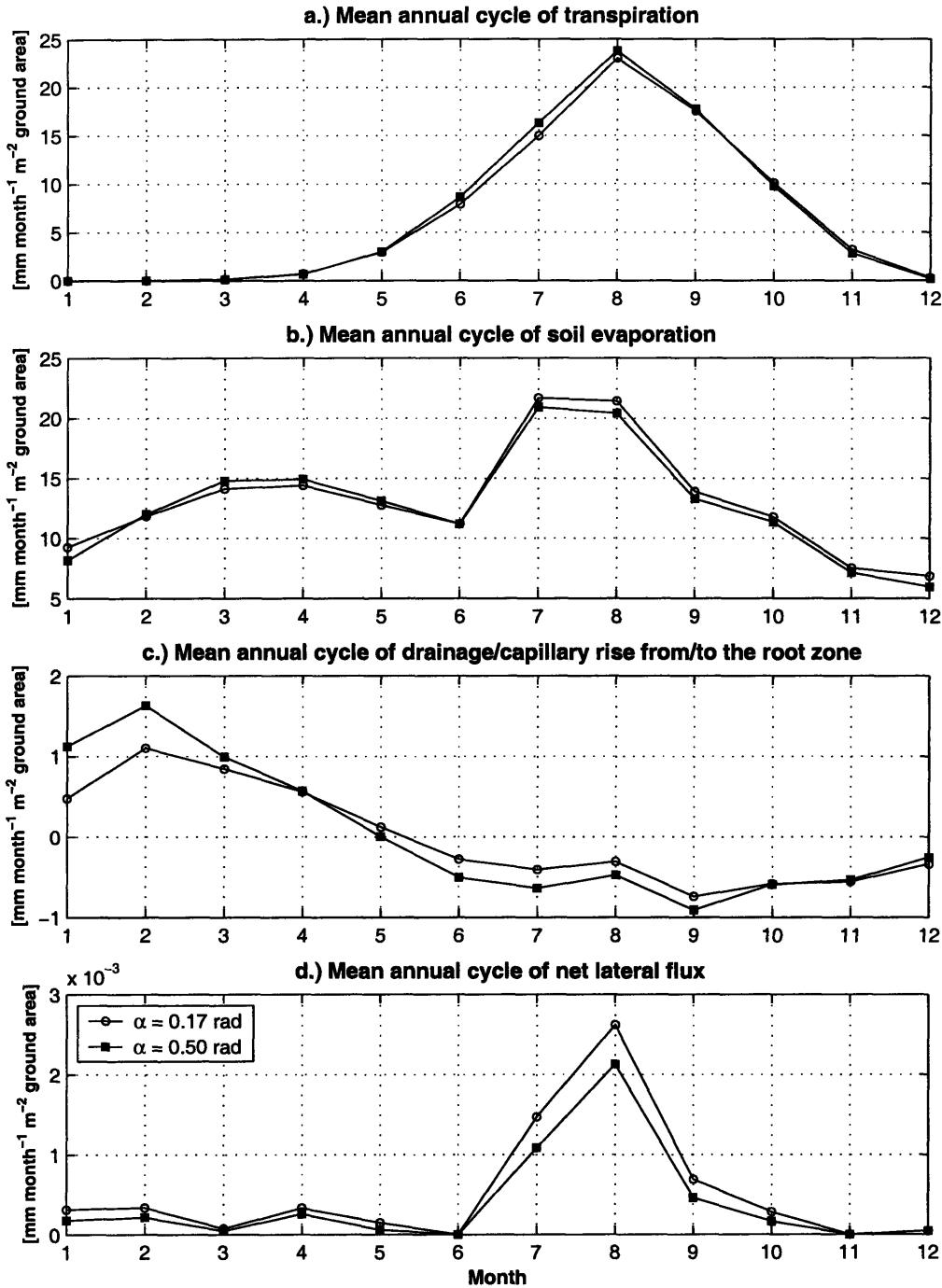
Figure 6-6: The mean annual cycles of components of root zone water balance for north-facing elements of different slope (the scenario with the critical angle $\alpha_\nabla^o = 0.5$ $rad$, $loamy$ soil case): a.) transpiration; b.) soil evaporation; c.) drainage/capillary rise from/to the root zone; and d.) net lateral flux. The element with $\alpha_\nabla = 0.17$ $rad$ corresponds to a location with maximum ANPP in the $base$ case scenario. Note that the fluxes are given in the units of depth per unit actual ground surface area.

342

of dry spells that start at the end of storm event and end at the beginning of the following event), and if the mean rate $\bar{\iota} = \frac{\mu_d}{\mu_r}$ $[mm\ hour^{-1}]$ is assumed to be constant ($\mu_d$ is the mean storm depth, Section 2.4), the above can be modified to relate $\mu_r$ and $\mu_b$:

$$\mu_r = \frac{\mu_b}{\bar{\iota}\ \frac{\Delta T_{season}}{P} - 1}.\qquad (6.3)$$

The denominator in the above equation is constant in the assumed scenario, and therefore $\mu_b$ and $\mu_r$ co-vary as $\mu'_b = C\,\mu_b$ and $\mu'_r = C\,\mu_r$, where $\mu_b$ and $\mu_r$ are the parameter values for the *base* case scenario and the constant $C$ takes values 0.5, 0.75, 1.5, 2.0, and 3.0.

Figure 6-7 illustrates the results of simulations for the considered scenarios in the same fashion as the "$\epsilon$-curves" obtained in Section 5.3. The direction of arrows indicates the change in results for successively growing mean durations of the interstorm and storm periods. As can be seen in the figure, the results strongly vary among the soil types. Loamy and clayey soils exhibit a consistent growth of the magnitude of maximum ANPP with increasing mean durations of the interstorm and storm periods. On the contrary, sandy soil shows a significant drop in productivity over the range of considered values of $\mu'_b$ and $\mu'_r$. These features are additionally illustrated in Figure 6-8 that depicts the ratio of maximum ANPP of the considered sensitivity scenarios to the maximum ANPP of the *base* case scenario. Note that $\mu'_b = 1\,\mu_b$ corresponds to the *base* case scenario.

The mean annual cycles of ANPP for sandy and loamy soils corresponding to two extreme cases of changed rainfall regime, $\mu'_b = 0.5\,\mu_b$ and $\mu'_b = 3.0\,\mu_b$, are shown in Figure 6-9. The simulated data for sloped north-facing elements that exhibited maximum ANPP in the *base* case scenario are used: for sandy soil, the element's surface slope is $\alpha_\nabla = 0.095\ rad$, and for loamy soil, $\alpha_\nabla = 0.17\ rad$. As can be seen in Figure 6-9a, the grass productivity for sandy soil drops significantly during the monsoon period if storms arrive less frequently but bring more moisture ($\mu'_b = 3.0\,\mu_b$ case). For this latter precipitation regime, grass on loamy soil shows a more complex
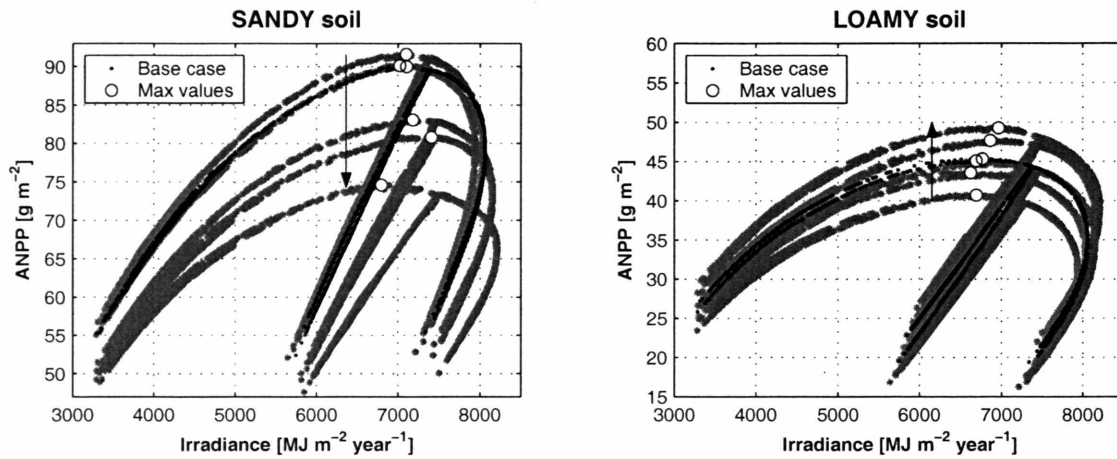
(a) SANDY soil



(b) LOAMY soil
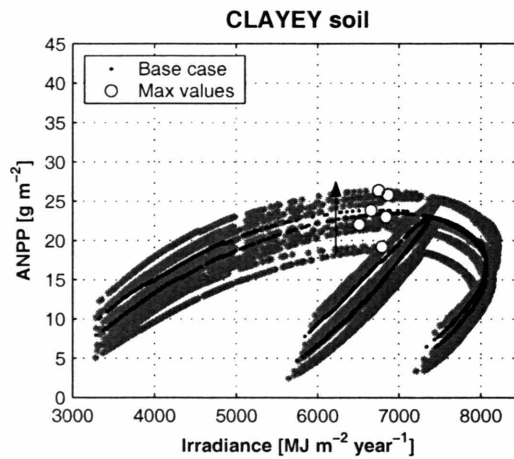


(c) CLAYEY soil

Figure 6-7: The mean simulated Above-ground Net Primary Productivity for the considered soil types for the scenario with modified rainfall arrival regime: a.) sandy soil; b.) loamy soil; and c.) clayey soil. The small black circles denote the data points for the *base* case scenario. The large white circles depict maximum ANPP for each considered scenario. The direction of arrows indicates the change in results for successively growing mean durations of interstorm and storm period, $\mu'_b$ and $\mu'_r$, respectively.
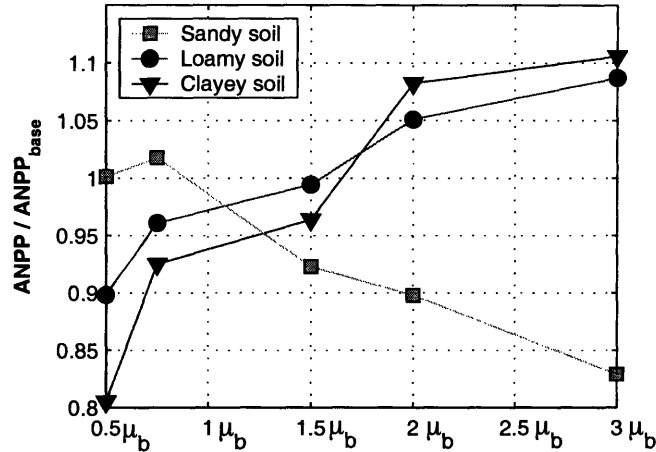
Figure 6-8: The ratios of the maximum ANPP values for considered scenarios of modified rainfall regime to ANPP value for the *base* case scenario. The considered scenarios of modified mean durations of interstorm and storm period are expressed on the horizontal axis as $\mu'_b = C\,\mu_b$, where the constant $C$ varies from 0.5 to 3.0. All data points correspond to sites of northerly aspect.

pattern of dynamics, exhibiting both higher and smaller ANPP values, as compared to the productivity cycle resulting from the contrasting storm arrival regime (i.e., more frequent arrival of storms that have smaller depths, $\mu'_b = 0.5\,\mu_b$ case). While the modification of the storm arrival regime is imposed only for the period of July through October, the discussed ANPP cycles exhibit substantial differences both in the preceding and following months of the year. This is attributed to a "carry-over" effect from the vegetation-hydrology dynamics of the period of modification. Processes affecting the soil water state introduce such memory effects into the coupled interactions. The following illustrations elucidate the actual mechanisms involved.

As can be seen in Figure 6-10, illustrating the annual cycles of essential (the net lateral drainage is excluded) water balance components for sandy soil, the transpiration cycles (Figure 6-10a) for the two rainfall regimes do not contrast as significantly as the ANPP cycles. The plausible explanation is that in the scenario of $\mu'_b = 3.0\,\mu_b$, the grass biomass accumulated after favorable wetting events experiences long periods of stress (since $\mu'_b$ is high). The stress leads to a substantial decrease in ANPP due to the respiration and foliage loss (Section 4.4.6). As opposed to ANPP, the

transiration flux depends primarily on how much biomass exists and how quickly and efficiently can vegetation respond to a precipitation event (i.e., dry spell does not lead to a decrease of an accumulated transpiration value). For the considered rainfall regimes ($\mu'_b = 0.5\,\mu_b$ and $\mu'_b = 3.0\,\mu_b$), grass states and responses to wetting periods are comparable to each other in terms of the transpiration flux.

The modified storm arrival regime has the strongest implication on the drainage from the root zone flux (Figure 6-10c). The less frequent/larger depth precipitation events lead to a significant fraction of moisture draining from the root zone. Apparently, vegetation biochemical and biophysical properties and the assumed *time-invariant* root zone profile constrain canopy development and, therefore, grass moisture uptake characteristics, leading to an inefficient water use (grass cannot uptake more soil water than it does under the above assumptions).

Figure 6-11 illustrates the principal water balance components for loamy soil. The annual cycles of drainage/capillary rise for loamy soil (Figure 6-11c) are similar to those of sandy soil, nonetheless, the losses to drainage for $\mu'_b = 3.0\,\mu_b$ scenario are significantly lower. As can also be seen in the figure, the transpiration flux for $\mu'_b = 3.0\,\mu_b$ case constantly exceeds that of $\mu'_b = 0.5\,\mu_b$ case. On the other hand, as was noted previously, the relative relationship between the ANPP cycles for the two scenarios (Figure 6-9b) is less consistent: for certain months ANPP for $\mu'_b = 0.5\,\mu_b$ case is higher than that of $\mu'_b = 3.0\,\mu_b$ case. The difference in behavior of the transpiration and ANPP cycles can be explained with similar to above arguments: less frequent but more intense storms lead to a rapid biomass accumulation and high transpiration, however, the subsequent long dry spells impose stress conditions and thus biomass losses. Therefore, in certain months the grass productivity for $\mu'_b = 3.0\,\mu_b$ case can be smaller than that of $\mu'_b = 0.5\,\mu_b$ case.

As pointed out previously, the differences between the two illustrated cases are noticeable even outside of the period with imposed changes in the rainfall regime. This feature can be clearly observed in the annual cycles of all water balance components shown in Figure 6-11. Evidently, vegetation-hydrology dynamics strongly affect the soil water state of the growing season within the period of July through October. A

346
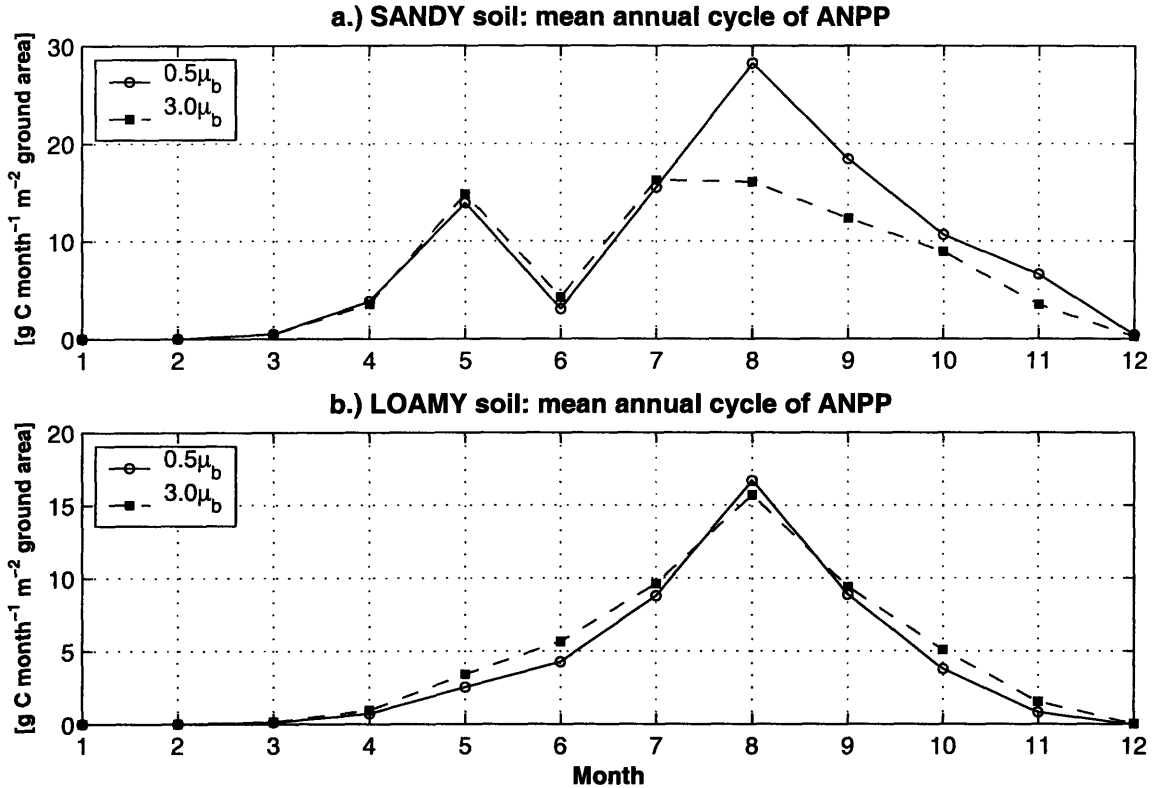
Figure 6-9: The mean annual cycles of ANPP for two rainfall regimes for north-facing elements corresponding to locations with maximum ANPP in the *base* case scenario: a.) sandy soil ($\alpha_\nabla = 0.095\ rad$); and b.) loamy soil ($\alpha_\nabla = 0.17\ rad$). Note that ANPP is given in the units of gram of carbon per unit actual ground surface area.

memory effect arises, in terms of energy and water fluxes, which lasts throughout the winter and spring months.

Overall, the above discussion stresses the complexity of response of the land-surface processes to the critical forcing variable - the growing season precipitation. The study emphasizes the critical role of soil texture type in regulating the spatial and temporal aspects of coupling between vegetation-hydrology processes. As is clearly demonstrated, the highly non-linear interactions among the biotic and abiotic components lead to a complex time-varying structure of relationships between the water and carbon fluxes.
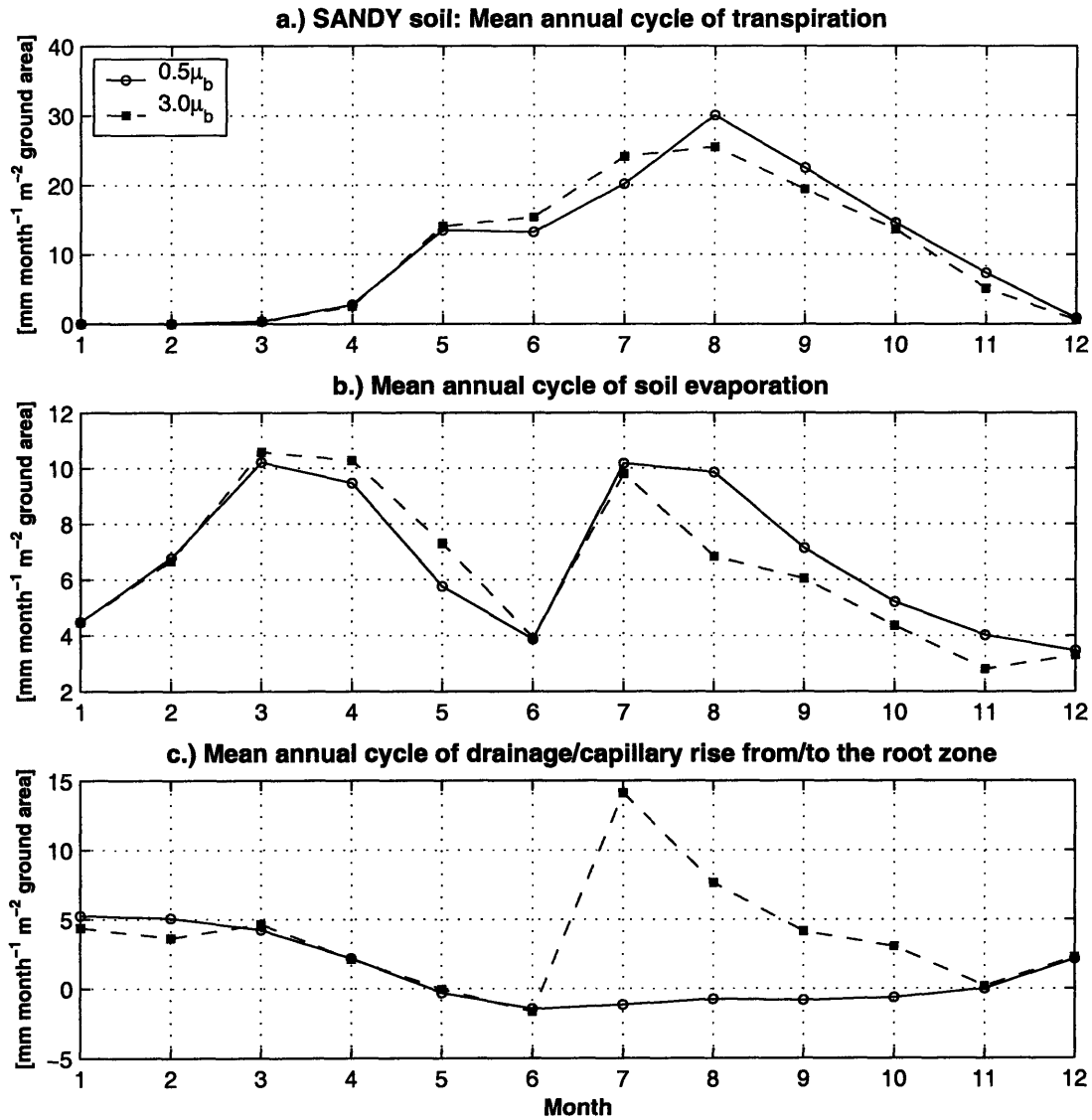
Figure 6-10: The mean annual cycles of components of root zone water balance for two rainfall regimes for a north-facing element corresponding to a location with maximum ANPP in the *base* case scenario (*sandy* soil, $\alpha_\nabla = 0.095$ *rad*): a.) transpiration; b.) soil evaporation; and c.) drainage/capillary rise from/to the root zone. Note that the fluxes are given in the units of depth per unit actual ground surface area.
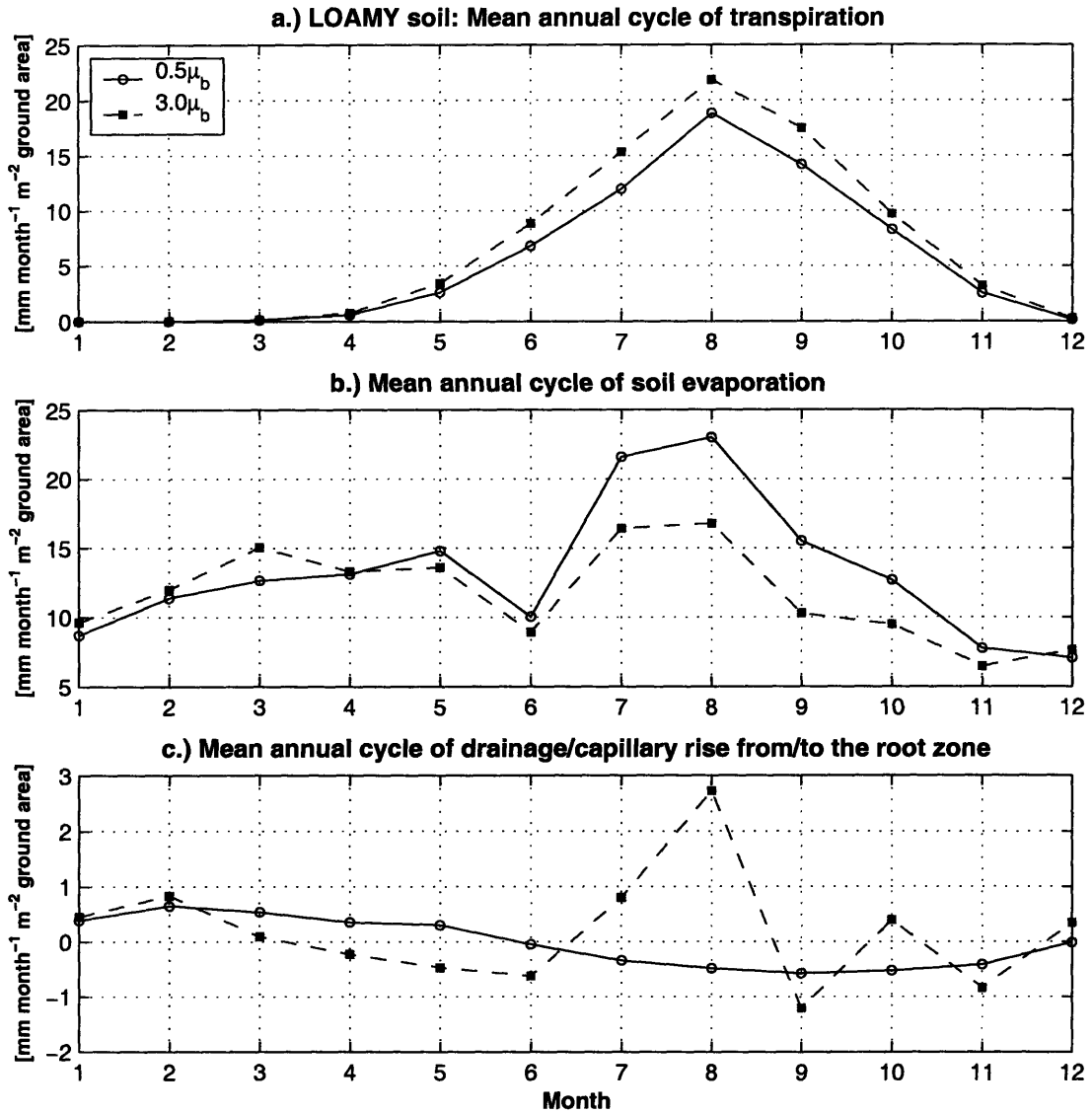
Figure 6-11: The mean annual cycles of components of root zone water balance for two rainfall regimes for a north-facing element corresponding to a location with maximum ANPP in the *base* case scenario (*loamy* soil, $\alpha_\nabla = 0.17$ *rad*): a.) transpiration; b.) soil evaporation; and c.) drainage/capillary rise from/to the root zone. Note that the fluxes are given in the units of depth per unit actual ground surface area.

349

### 6.3.3 Modified radiation regime

The material of this section investigates the sensitivity of vegetation-hydrology dynamics observed in the *base* case scenario to alterations in the solar radiation regime. The considered scenario assumes the 25% reduction in the incoming solar radiation throughout the year. The decrease is applied uniformly to both the direct and diffuse radiation components, both to the VIS and NIR bands. Figure 6-12 illustrates the results of simulations for the considered scenario in the same fashion as the "$\epsilon$-curves" obtained in Section 5.3, except that the abscissa consists of the ratio of site annual irradiance to irradiance for a flat horizontal surface. As can be inferred from the figure, a reduction in the radiation input leads to an increase in productivity (with respect to the *base* case scenario) on south-, east-, and west-facing slopes. The results for north-facing slopes differ among the soil types. Loamy and clayey soils (Figure 6-12b, c) show an increase in the productivity across a range of slope magnitudes. A decrease relative to the *base* case scenario, which indicates the radiation/PAR limitation, can only be observed at very steep slopes corresponding to smallest values on the abscissa axis. For sandy soil, the radiation/PAR limitation for sites of northerly aspect is encountered at a significantly smaller slope value (Figure 6-12a). A similar behavior was observed for the case of modified rainfall projection in Section 6.3.1, where it was attributed to suppressed vegetation dynamics during primarily the early and late growing season periods.

## 6.4 Mechanisms of rapid lateral mass exchange

As was discussed in Section 5.3.2, the lateral moisture exchange does not significantly affect the vegetation-hydrology dynamics in the *base* case scenario. Therefore, the preceding analysis considered the interaction of the vegetation-hydrology processes at the element scale as *spatially-independent*. The *local* terrain features, such as aspect and slope, were identified as the key determinants of the overall dynamics at a given site.

The material of this section covers the "*R-exchange*" case (Section 5.2), that
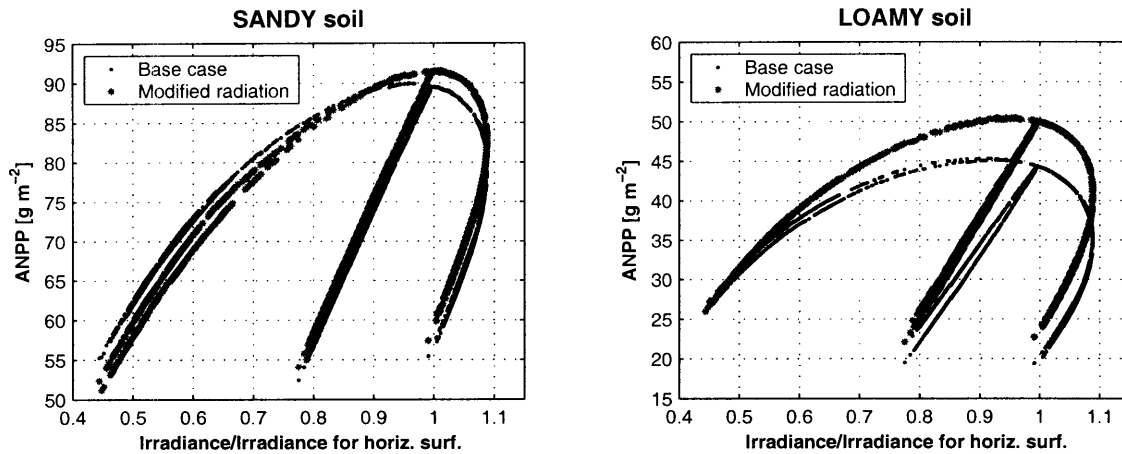
(a) SANDY soil



(b) LOAMY soil
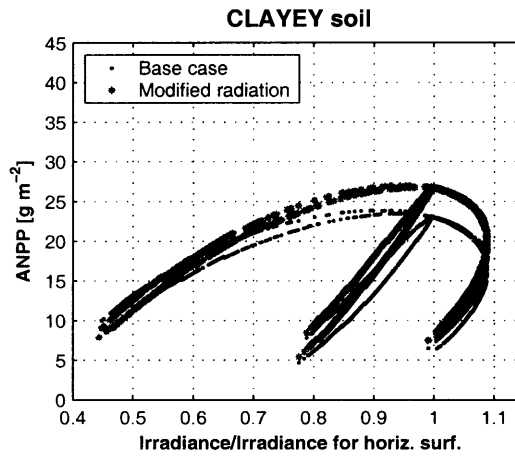


(c) CLAYEY soil

Figure 6-12: The mean simulated Above-ground Net Primary Productivity for the considered soil types for a scenario that assumes a 25% reduction in the incoming solar radiation: a.) sandy soil; b.) loamy soil; and c.) clayey soil. The ratio of the site annual irradiance to irradiance for a flat horizontal surface is used as the abscissa axis. The small black circles denote the data points for the *base* case scenario.

introduces rapid processes of the lateral moisture exchange. These are caused by assuming high soil anisotropy ratios ($a_r \in [100 \div 1000]$) and the partial sealing of the soil surface during the growing season, leading to higher runoff generation and subsequent runon/re-infiltration process at downstream locations. Thus, both the *local* and *global* terrain features determine the vegetation-hydrology interactions at any given landscape location.

## 6.4.1 Higher soil anisotropy

Figures 6-13 - 6-14 correspond to the simulation scenarios that assume soil anisotropy ratios of $a_r = 100$ and $a_r = 1000$, respectively. The figures illustrate the simulation results in the same fashion as the "$\epsilon$-curves" obtained in Section 5.3. When compared to the plots of ANPP for the *base* case scenario (Figures 5-23 - 5-25), one realizes that only the case with the anisotropy ratio $a_r = 1000$ shows significant differences in the magnitudes of grass productivity. In the case of the smaller assumed anisotropy ratio, $a_r = 100$, ANPP is somewhat modified only for more conductive sandy soil (Figure 6-13a). Consequently, it is apparent that even a relatively large assumed anisotropy value, $a_r = 100$, does not lead to any significant soil water redistribution via the subsurface lateral exchange flux (Figure 6-15). As an outcome, the productivity is not noticeably affected for all soil types. The case corresponding to $a_r = 100$ will not be considered in the following analysis, which will thus only concern the $a_r = 1000$ scenario.

It can be inferred from Figure 6-14 that very high soil anisotropy significantly affects vegetation-hydrology dynamics for all soil types. Indeed, the lateral moisture exchange leads to a spatial distribution of grass productivity noticeably different from the one obtained in the *base* case scenario (e.g., the distribution for loamy soil shown in Figure 6-16). While a similarity of the spatial pattern is significant in most of the hillslope areas, there is evidence of an increased productivity in the convergent terrain locations. Therefore, it can be concluded that along with the *local* terrain characteristics, such as aspect and slope, there exist *non-local* features of topography, such as the upstream drainage area, that significantly contribute to the vegetation

(a) SANDY soil      (b) LOAMY soil      (c) CLAYEY soil
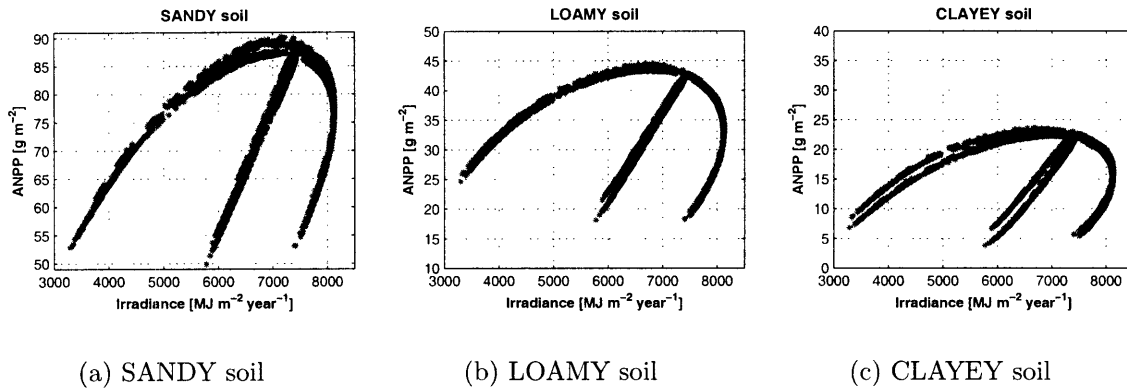
Figure 6-13: The mean simulated Above-ground Net Primary Productivity for the considered soil types with anisotropy ratio $a_r = 100$: a.) sandy soil; b.) loamy soil; and c.) clayey soil. Symbols with lighter color denote the data points for the CV domain, the darker color corresponds to the data points for the CX domain.



(a) SANDY soil      (b) LOAMY soil      (c) CLAYEY soil
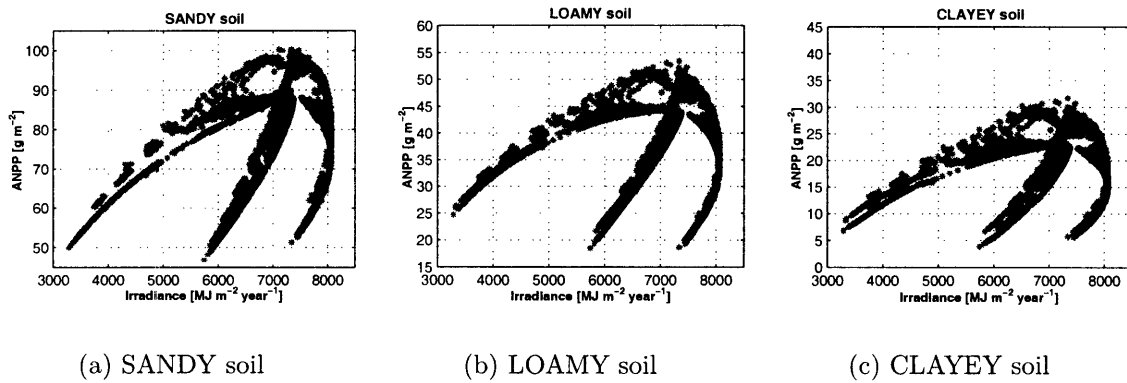
Figure 6-14: The mean simulated Above-ground Net Primary Productivity for the considered soil types with anisotropy ratio $a_r = 1000$: a.) sandy soil; b.) loamy soil; and c.) clayey soil. Symbols with lighter color denote the data points for the CV domain, the darker color corresponds to the data points for the CX domain.
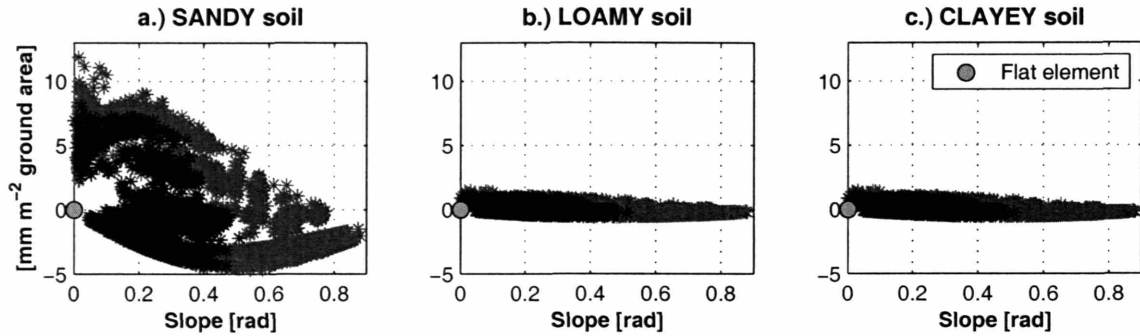
Figure 6-15: The mean simulated net lateral exchange in the root zone during a growing season for three considered soil types ($a_r = 100$ case): a.) sandy soil; b.) loamy soil; and c.) clayey soil. The positive values imply the net moisture gain, the negative values imply moisture loss. Symbols with lighter color denote the data points for the CV domain, the darker color corresponds to the data points for the CX domain.

spatio-temporal dynamics. The following analysis identifies these features.

One may observe that the pattern of association of primary productivity with the site annual irradiance, shown in Figure 6-14, strongly resembles the "$\epsilon$-curve" introduced in Section 5.3. In fact, if site productivity is considered separately for each value of the total number of upstream contributing elements ("1" corresponds to the element itself), it can be demonstrated that the $\epsilon$-shaped pattern is persistently repeated in the simulation results (Figure 6-17). As can be observed, the productivity magnitude grows downstream and the "$\epsilon$-curve" pattern becomes "noisier". Since the hydrological fluxes and soil moisture states are inherently connected to the spatial distribution of vegetation productivity, it is important to identify the primary controlling factors that lead to such a structure.

A distinction can be made between the upstream elements contributing their flow on a *global* and *contiguous* basis. The former are conventionally defined as *all* upstream elements contributing their surface-subsurface flow to a considered element. The latter are defined here as those that contribute their flow and are *immediately* contiguous to a given element, i.e., represent a complete or partial subset of contributing elements defined on the global basis. A larger number of *contiguously* contributing elements at a given location can be associated with a higher degree of terrain concav-

**a.) Base case**

**b.) Soil anisotropy a$_r$ = 1000**

ANPP [g C / sq. m ground area]
  31.59 - 33.64
  33.64 - 35.68
  35.68 - 37.73
  37.73 - 39.78
  39.78 - 41.83
  41.83 - 43.88

ANPP [g C / sq. m ground area]
  32.1 - 35.22
  35.22 - 38.34
  38.34 - 41.83
  41.83 - 44.58
  44.58 - 47.71
  47.71 - 50.83
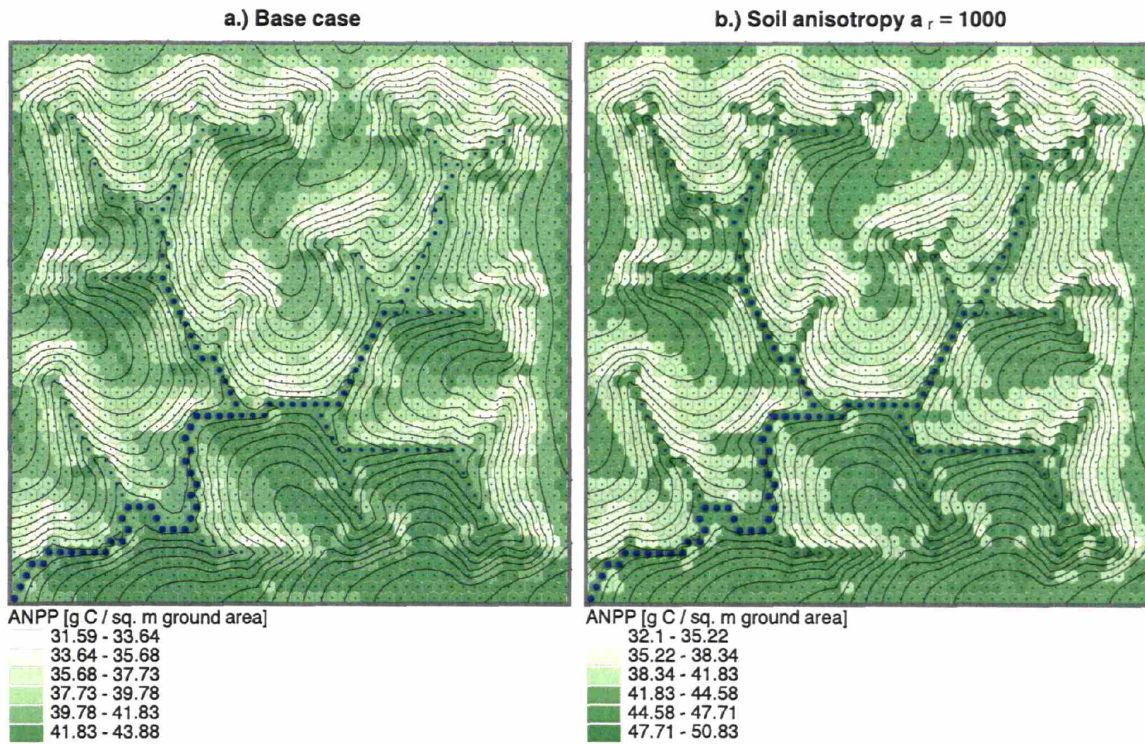
Figure 6-16: The mean annual Above-ground Net Primary Productivity simulated for C$_4$ grass on loamy soil for the CX domain: a.) the *base* case; and b.) the $a_r = 1000$ case. The units are given at the element scale and refer to the actual inclined ground surface area.
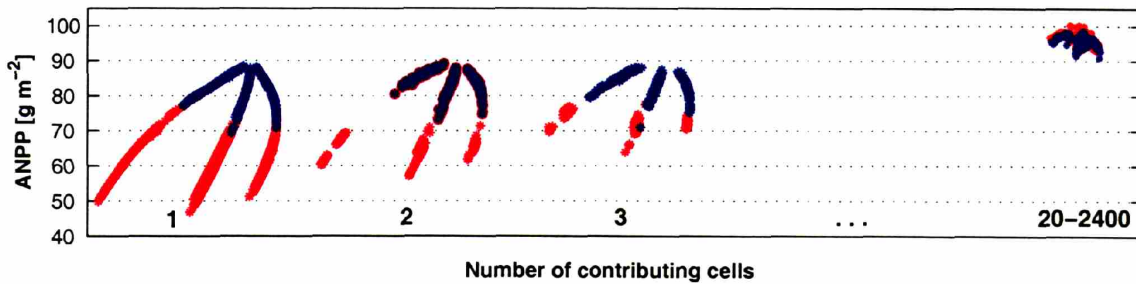


Figure 6-17: Patterns of ANPP dependence on site annual irradiance plotted for different sets of elements for sandy soil. Each set contains all elements that have the same number of upstream contributing elements ("1" corresponds to the element itself).

ity, i.e., the flow convergence at that location. The basic computational element, the Voronoi polygon (Figure 5-1), may have up to five *contiguously* contributing upstream elements (one neighboring element is always used for downstream flow routing). From the above definitions, it follows that one can define *global* and *contiguous* contributing areas.

The difference in effects of the two types of contributing areas on grass productivity is illustrated in Figure 6-18 (as well as later in Figure 6-31) that contains the data points for elements with up to 3 *globally* upstream elements. The first subplot illustrates the data points corresponding to the locations for which the number of *contiguously* contributing elements is between 0 and 1. These locations can be assumed to have **zero plan** curvature, since, at most, they receive subsurface flow through only one side of the Voronoi polygon (Figure 5-1) and discharge their flow in only one downstream direction. The second subplot shows the data points corresponding to the locations for which the number of *contiguously* contributing elements varies between 0 and 3, i.e., for each set of elements the number of *globally* and *contiguously* contributing elements is equal. The symbols of progressively larger size depict the increasing number of *globally* contributing elements.

As the figure shows, the productivity increases downstream. The rate at which the ANPP grows, however, is strongly affected by the level of local flow convergence. It can be inferred from the figure that for the same number of *globally* contributing elements (larger than one), ANPP differs for the cases shown in the two subplots: it is higher in the case of Figure 6-18b, which corresponds to locations that have a larger number of elements contributing their flow on a *contiguous* basis. This implies that the degree of local terrain concavity imposes a strong control on grass productivity. As will be shown, this effect is amplified in the simulation scenario that involves the soil surface partial sealing with runon and re-infiltration mechanisms. Another important feature of Figure 6-18 is that the $\epsilon$-shaped pattern can be consistently fitted to the data points at every downstream level for the considered range of contributing areas. This feature will be elucidated in more detail in the following analysis.

The significance of both the *global* and *contiguous* flow convergence levels is high-

SANDY soil: $a_r = 1000$

(a)
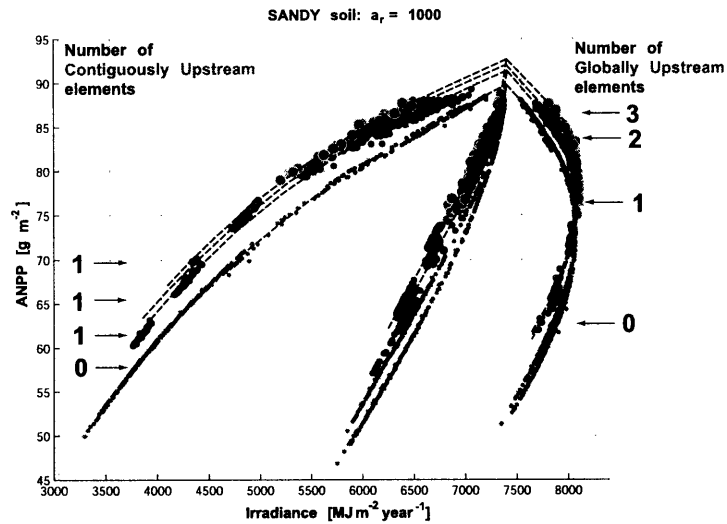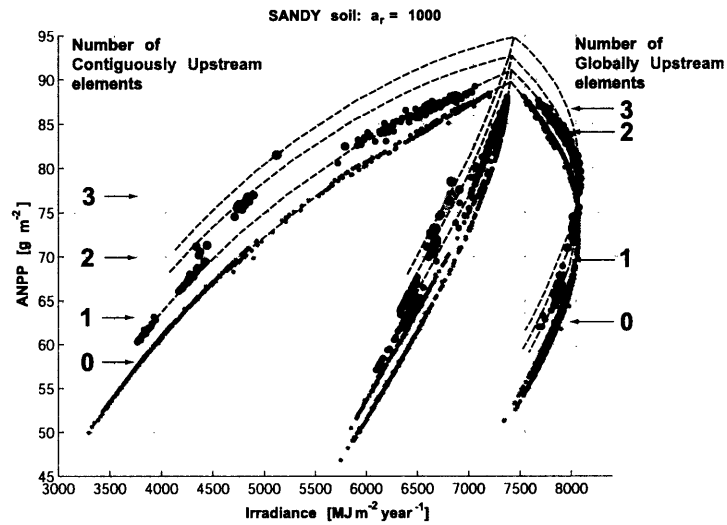
SANDY soil: $a_r = 1000$

(b)

Figure 6-18: The mean annual ANPP for sandy soil (the anisotropy ratio $a_r = 1000$ scenario). Data for elements with up to 3 *globally* upstream elements are shown: a.) the number of *contiguously* contributing elements is 0-1; and b.) the number of *contiguously* contributing elements is 0-3 (i.e., for each set of elements this number coincides with the number of *globally* contributing elements). The symbols of progressively larger size depict the increasing number of *globally* contributing elements. The dashed lines were added manually to complement and connect the data points corresponding to the same number of *globally* contributing elements.

357

**SANDY soil: scenario of $a_r$ = 1000**
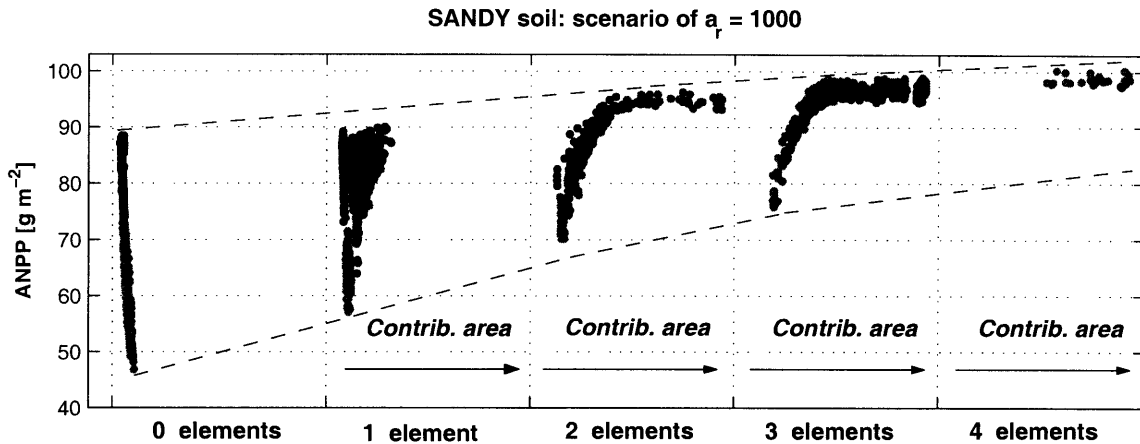
Figure 6-19: The mean annual ANPP for sandy soil (anisotropy ratio $a_r = 1000$ scenario). Data points for both domains are shown. The data are binned according to the number of *contiguously* contributing elements (0 - 4) and the increasing number reflects the growing level of local flow convergence. In each of the bins, the data points are arranged according to the *global* contributing area that grows from the left to the right.

lighted in Figure 6-19 that shows grass productivity binned according to the number of *contiguously* contributing elements (0 - 4) for a given location. In addition to that, in each of the bins the data points are arranged according to the *global* contributing area that increases from the left to the right. As the figure shows, the energy-water interactions in vegetated systems of semi-arid areas lead to a very complex structure of productivity dependence on terrain attributes. Two distinct kinds of ANPP growth, associated with the previously discussed types of contributing areas, are essentially superimposed: while grass productivity generally increases with the level of *contiguous* flow convergence, marked by the enveloping curves, a further downstream ANPP growth within each of the bins is related to the increase of the *global* contributing area. In addition to these effects, the local terrain features modifying the incoming radiation and rainfall, i.e., site aspect and slope, govern grass productivity at each point on the horizontal axis of Figure 6-19. The corresponding effects are therefore embedded into the structure of ANPP scaling with any type of contributing area, as this has already been partially illustrated in Figures 6-17 - 6-18 and will also be demonstrated in the following.

358

## 6.4.1a Analysis of data point subset # 1

In the following several examples, the analysis will be constrained to a subset of data points corresponding only to those locations that have the number of *contiguously* contributing elements ranging from 0 to 1. The number of such elements constitutes approximately 85% and 70% of the total number of computational elements in the CX and CV domains, respectively. As noted above, these locations can be assumed to have a **zero plan** curvature. The **profile** curvature of these locations can be approximately associated with a change in the local slope $(\alpha_{\bigtriangledown}^{CU} - \alpha_{\bigtriangledown})$, where $\alpha_{\bigtriangledown}^{CU}$ is the slope of upstream contributing element.

Figure 6-20 illustrates ANPP for the selected subset of data points for all considered soil types as three-dimensional plots with the horizontal axes being the surface irradiance and the *global* number of upstream contributing elements. As can be inferred from the figure, at each value of the number of upstream contributing elements, the grass productivity exhibits a pronounced dependence on site annual irradiance in the form of the "ϵ-curve" pattern. The illustration clearly indicates that in water-limited environments the water-energy interactions control vegetation-hydrology dynamics at each watershed downstream level. Consequently, the *local* terrain features, i.e., aspect and slope, are still among the key determinants of the overall dynamics at *each downstream level*. Note that so far this conclusion refers only to those locations that can be assumed to have a zero plan curvature. Note also that the rainfall projection on a sloped surface is identical to the one considered in the *base* case scenario, i.e., the factor $\cos \alpha_{\bigtriangledown}$ is used for each simulated rainfall depth applied to a horizontal plane.

If the three-dimensional plots of Figure 6-20 are rotated in a certain fashion, so that the final orientation displays annual irradiance at the plot bottom, the obtained patterns have the familiar shapes of the "ϵ-curve" (Figure 6-21). Note that these patterns combine data points for *all* considered levels of the contributing area. Such a scaling feature allows one to derive a conceptual formulation of productivity change with the contributing area. If $P_{AN}^{o}$ is the ANPP of an element with **zero** *contiguously* contributing elements (e.g., elements at the watershed boundary) and $P_{AN}^{1}$ is the ANPP of a downstream element with **one** *contiguously* contributing element, then

the following conceptual formulation can be proposed for elements with the *same aspect* and *slope*:

$$\left.\frac{P_{AN}^1}{P_{AN}^\circ}\right|_{\alpha_\nabla,\zeta_\nabla} = \left[f_1\left(\log A_T\right)\right] \times$$

$$\left[g_1\left(\alpha_\nabla^{CU}\right)\right]\left[g_2\left(\frac{\zeta_\nabla}{2}^{CU}\right)\right]\left[g_3\left(\overline{\alpha_\nabla^{GU}}\right)\right]\left[g_4\left(\overline{\frac{\zeta_\nabla}{2}^{GU}}\right)\right], \quad (6.4)$$

where $A_T = \sum_l^{N_E} A_{VR,l}/\cos\alpha_{\nabla,l}$ $[m^2]$ is the global *actual* surface area contributing to a given element, $A_{VR}$ $[m^2]$ is the Voronoi area projected on a horizontal plane (Section 3.3), $N_E$ is the total number of *globally* contributing elements, $\zeta_\nabla$ $[rad]$ is the element aspect (in clockwise or counter-clockwise direction from North, $\zeta_\nabla \in [0, \pi]$, $\zeta_\nabla = \pi$ is true southerly aspect), the index "$CU$" is used to denote all Contiguously Upstream elements, and the index "$GU$" is used to denote all Globally Upstream elements. The bar symbol implies the mean value.

A generic function in the first brackets scales grass productivity with the *actual* contributing area. The terms in the second and third brackets are the values of surface slope and aspect, respectively, for the element located *contiguously* upstream of a given location. These terms are used to account for the amount of rainfall and radiation received by the *contiguously* upstream element as well as magnitude of its subsurface flux (parameterized in the model via $\sin\alpha_\nabla$, Appendix D.2). The terms in the fourth and fifth brackets account for the amount of rainfall and radiation received by the watershed surface *globally* upstream of a given element. For example, upstream elements of southerly aspect receive more radiation, which implies higher evaporation rates. Less soil moisture is therefore available for vegetation, which is sparse and unable to quickly uptake soil water immediately after wetting events. Depending on both the magnitudes of radiation and rainfall and soil type, the net effect for vegetation productivity at downstream locations may thus be negative or positive.

In a graphical fashion similar to Figure 6-21, it can be demonstrated that the principal water balance components exhibit the same scaling properties for the considered subset of data points (i.e., for selected elements the number of *contiguously*

360

(a) SANDY soil



(b) LOAMY soil
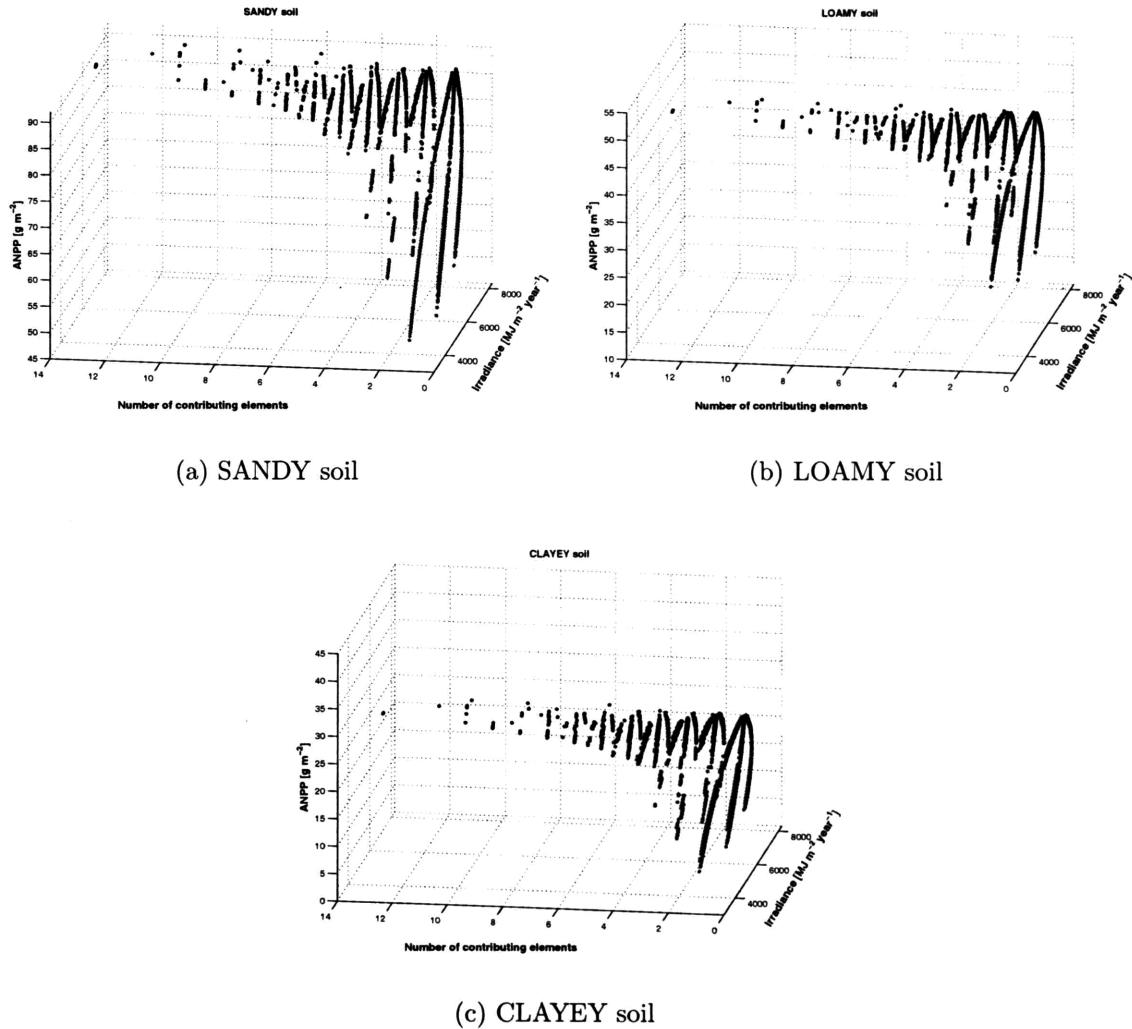


(c) CLAYEY soil

Figure 6-20: The mean annual ANPP for the considered soil types with the anisotropy ratio $a_r = 1000$: a.) sandy soil; b.) loamy soil; and c.) clayey soil. The horizontal axes are the site surface annual irradiance and the *global* number of upstream contributing elements. Only a subset of data points is shown, corresponding to those locations that have the number of *contiguously* contributing elements ranging from 0 to 1.
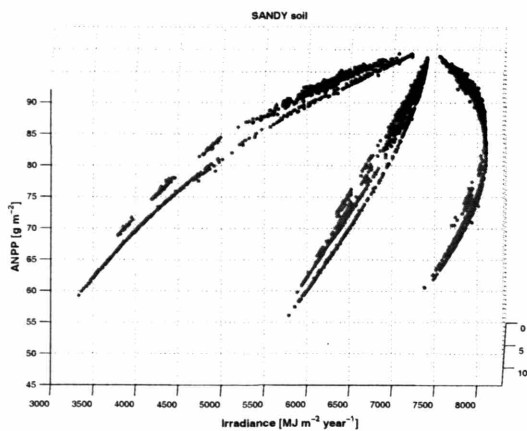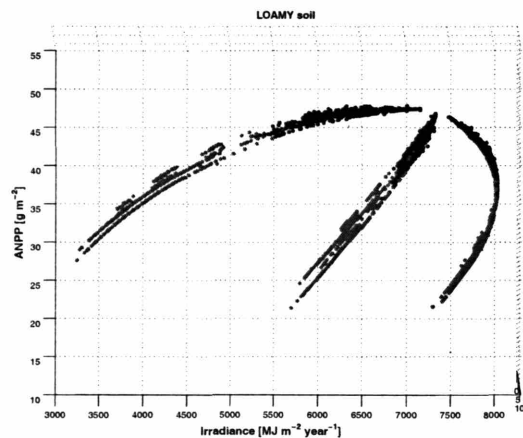
(a) SANDY soil
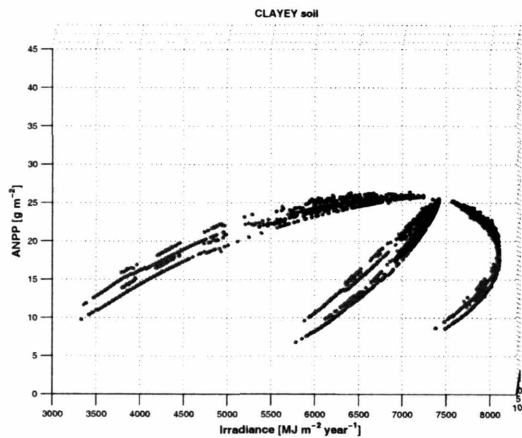


(b) LOAMY soil



(c) CLAYEY soil

Figure 6-21: The mean annual ANPP for the considered soil types with the anisotropy ratio $a_r = 1000$: a.) sandy soil; b.) loamy soil; and c.) clayey soil. The horizontal axes are the site surface annual irradiance and the *global* number of upstream contributing elements. Only a subset of data points is shown, corresponding to those locations that have the number of *contiguously* contributing elements ranging from 0 to 1. The three-dimensional plots are oriented such that the resulting pattern of data points composes the "$\epsilon$-curve".

| (a) SANDY soil | (b) LOAMY soil | (c) CLAYEY soil |
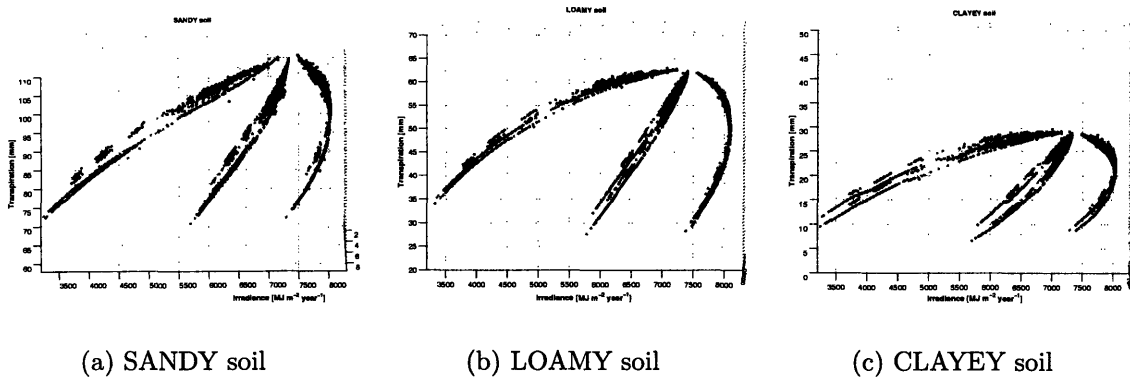
Figure 6-22: The mean annual transpiration for the considered soil types with the anisotropy ratio $a_r = 1000$: a.) sandy soil; b.) loamy soil; and c.) clayey soil. The horizontal axes are the site surface annual irradiance and the *global* number of upstream contributing elements. Only a subset of data points is shown, corresponding to those locations that have the number of *contiguously* contributing elements ranging from 0 to 1. The three-dimensional plots are oriented such that the resulting pattern of data points composes the "$\epsilon$-curve".

contributing elements ranges from 0 to 1). For example, Figure 6-22 shows the transpiration depth per unit area of sloped surface. These three-dimensional plots were rotated, so that the final orientation displays the annual irradiance at the plot bottom and obtained patterns have the shapes of the "$\epsilon$-curve". The same patterns can be obtained for the annual soil evaporation flux and drainage/capillary rise from/to the root zone (Figures 6-23 - 6-24). A very important implication of these features is that the water fluxes at different drainage locations of the terrain can be related mathematically in a manner similar to expression (6.4).

If the annual net lateral fluxes are plotted, it can be seen that the corresponding three-dimensional structures are much noisier (Figure 6-25), as compared to those obtained for the evapotranspiration fluxes and ANPP (e.g., Figure 6-20). To a certain extent, the noisy behavior can be attributed to the individual element geometry, since elements that have the same aspect and slope but different flow widths (Appendix D) would exhibit a difference in the net lateral flux. As the figure shows, the net lateral drainage is negative for most of the considered elements, which implies the annual loss of soil water to downstream elements. However, the elements that feature the positive net lateral flux, do not exhibit a substantial increase in productivity (Figure 6-20).

363

(a) SANDY soil          (b) LOAMY soil          (c) CLAYEY soil
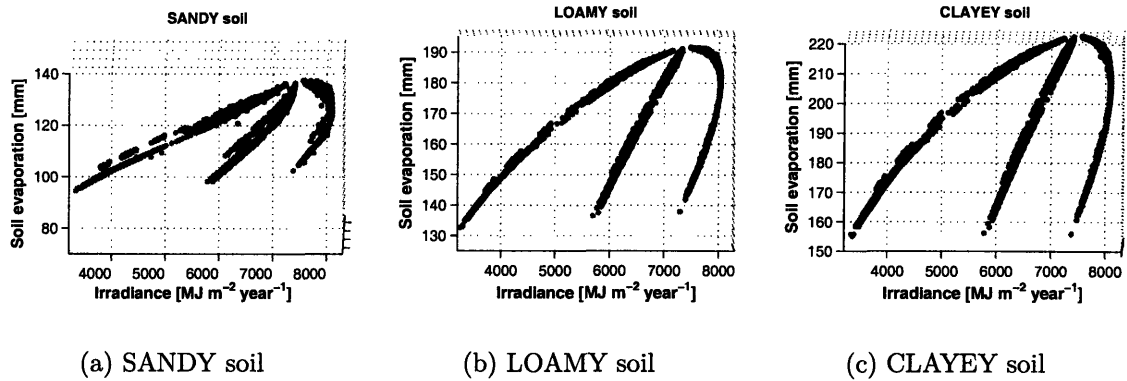
Figure 6-23: The mean annual soil evaporation for the considered soil types with the anisotropy ratio $a_r = 1000$: a.) sandy soil; b.) loamy soil; and c.) clayey soil. The horizontal axes are the site surface annual irradiance and the *global* number of upstream contributing elements. Only a subset of data points is shown, corresponding to those locations that have the number of *contiguously* contributing elements ranging from 0 to 1. The three-dimensional plots are oriented such that the resulting pattern of data points composes the "$\epsilon$-curve".



(a) SANDY soil          (b) LOAMY soil          (c) CLAYEY soil
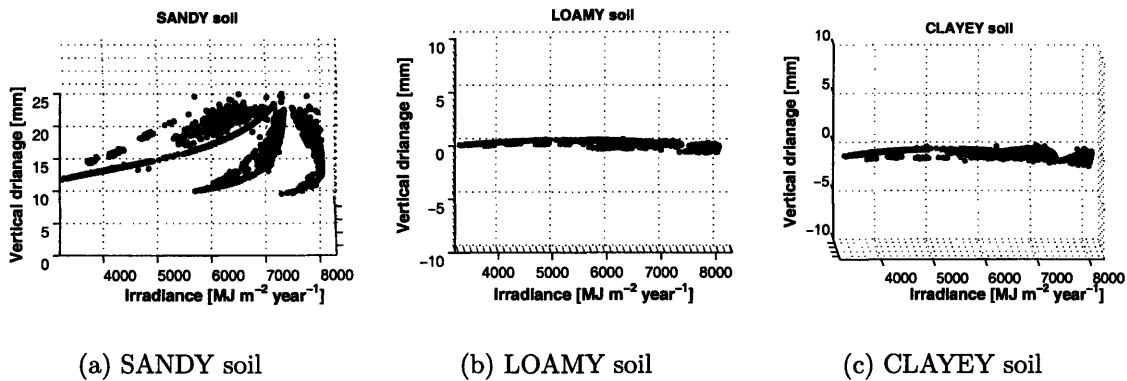
Figure 6-24: The mean annual vertical drainage for the considered soil types with the anisotropy ratio $a_r = 1000$: a.) sandy soil; b.) loamy soil; and c.) clayey soil. The horizontal axes are the site surface annual irradiance and the *global* number of upstream contributing elements. Only a subset of data points is shown, corresponding to those locations that have the number of *contiguously* contributing elements ranging from 0 to 1. The three-dimensional plots are oriented such that the resulting pattern of data points composes the "$\epsilon$-curve".

The latter fact may be related to both the magnitude of the received flux (it does not exceed more than 6% of the annual precipitation for sandy soil) and its timing (the bulk surplus of soil water during wetter periods of the early spring and late fall would not significantly affect the growing season productivity since vegetation biomass is low during these periods).

It is also relevant for the present analysis to address the characteristics of downstream distribution of the mean growing season root moisture. The result of the same procedure of rotating a three-dimensional plot, analogous to the previously discussed figures, is shown in Figure 6-26. When compared to the results of the *base* case scenario (Figure 5-30), it is evident that the absolute magnitudes are not significantly affected. However, it can also be observed in the figure that more conductive sandy soil exhibits a sharp decay of the mean soil water content with increasing slope (decreasing site irradiance) for sites of the same aspect. This can be best discerned for north-facing sites, which showed an initial growth of the mean root moisture with slope in the *base* case scenario. Such a behavior is clearly related to the process of the lateral subsurface moisture exchange that rapidly removes soil water excess not uptaken by grass roots and the downstream locations are thus favored. Another important implication is that the right-hand side of expression (6.4) can also be used to relate the mean growing season root soil water at different drainage locations of terrain.

### 6.4.1b Analysis of data point subset # 2

The next stage of this analysis considers elements that have the number of *contiguously* contributing elements **larger** than one. The number of such elements constitutes approximately 15% and 30% of the total number of computational elements in the CX and CV domains, respectively. These locations can be assumed to have the **concave plan** curvature, since they receive subsurface flow through several sides of the Voronoi polygon (Figure 5-1) and route their flow in only one downstream direction. The **profile** curvature of these locations can be approximately associated with the change in local slope, $(\overline{\alpha_{\triangledown}^{CU}} - \alpha_{\triangledown})$, where the bar implies the mean value.
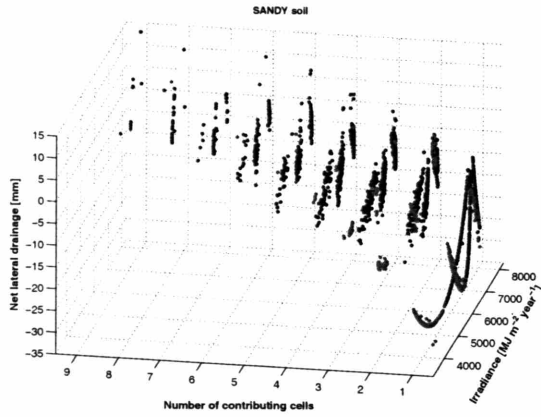
(a) SANDY soil
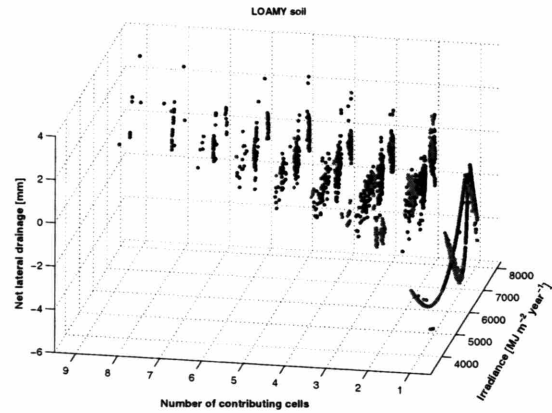


(b) LOAMY soil
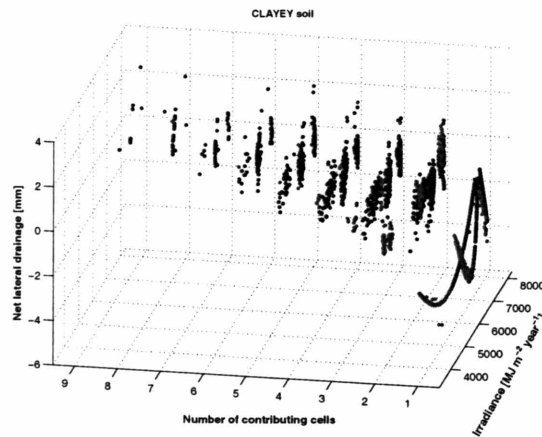


(c) CLAYEY soil

Figure 6-25: The mean annual net lateral drainage for the considered soil types with the anisotropy ratio $a_r = 1000$: a.) sandy soil; b.) loamy soil; and c.) clayey soil. The horizontal axes are the site surface annual irradiance and the *global* number of upstream contributing elements. Only a subset of data points is shown, corresponding to those locations that have the number of *contiguously* contributing elements ranging from 0 to 1.
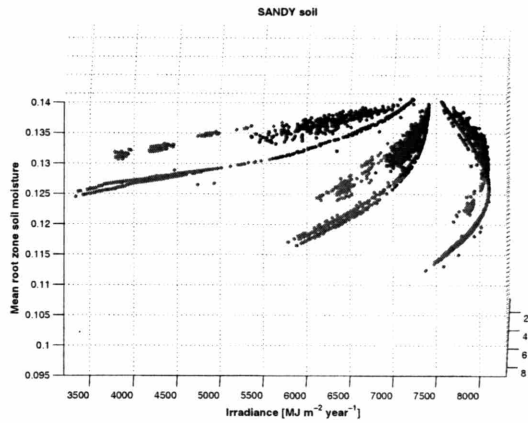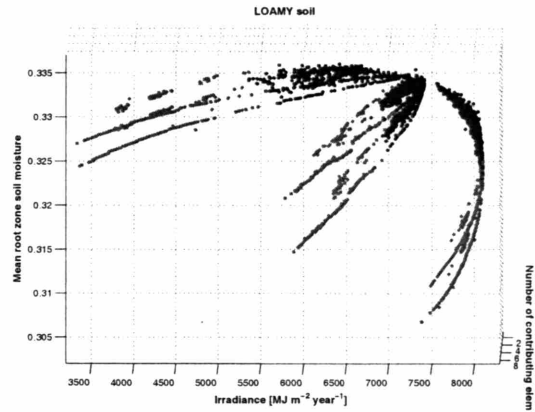
(a) SANDY soil
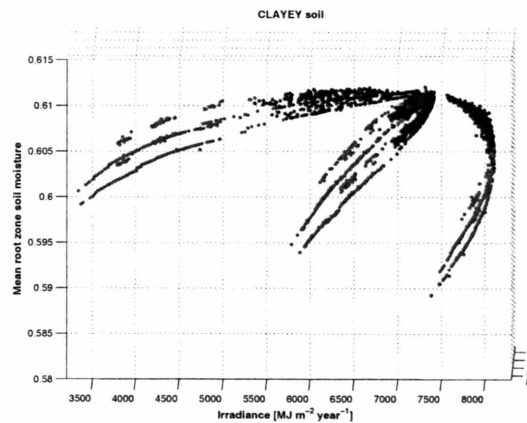


(b) LOAMY soil



(c) CLAYEY soil

Figure 6-26: The mean growing season root soil moisture for the considered soil types with the anisotropy ratio $a_r = 1000$: a.) sandy soil; b.) loamy soil; and c.) clayey soil. The horizontal axes are the site surface annual irradiance and the *global* number of upstream contributing elements. Only a subset of data points is shown, corresponding to those locations that have the number of *contiguously* contributing elements ranging from 0 to 1. The three-dimensional plots are oriented such that the resulting pattern of data points composes the "$\epsilon$-curve".
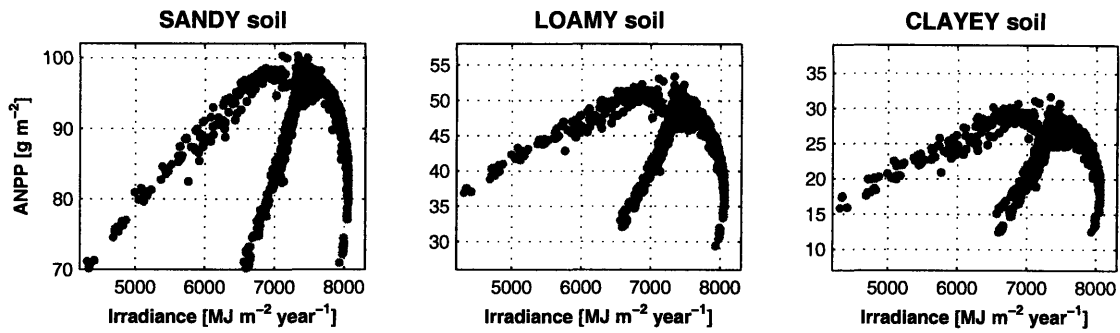
Figure 6-27: The mean simulated Above-ground Net Primary Productivity for the considered soil types with the anisotropy ratio $a_r = 1000$: a.) sandy soil; b.) loamy soil; and c.) clayey soil. Symbols with lighter color denote the data points for the CV domain, the darker color corresponds to the data points for the CX domain. Only a subset of data points is shown, corresponding to those locations that have the number of *contiguously* contributing elements exceeding 1.

Figure 6-27 illustrates ANPP for these elements. As in the previous discussion, it can be demonstrated that productivity is strongly associated with both the site annual irradiance and the contributing area. If another dimension representing the total number of *contiguously* contributing elements is added to plots shown in Figure 6-27, one can immediately realize that the pattern in each of the considered plots is, in fact, a combination of several overlapping "$\epsilon$-curves". Each of the "$\epsilon$-curves" corresponds to a certain number of *contiguously* contributing elements. Since, again, the increase of ANPP is essentially linear between these "$\epsilon$-curves", the plots can be rotated to demonstrate the energy-water controls imposed on vegetation productivity at all convergence levels of subsurface fluxes (Figure 6-28). The obtained patterns exhibit more noise, as compared to Figure 6-21. Clearly, a combination of several factors affects the composition of the observed patterns.

The principal controls that impact the above patterns are interpreted using a subset of data points corresponding to elements with **two** *contiguously* contributing elements. Note that the *global* number of upstream contributing elements strongly varies within this subset. Figure 6-29a shows productivity for the selected elements. Several data points that introduce a clear visible distortion into the "$\epsilon$-curve" are manually identified and highlighted. Figure 6-29b illustrates the distribution of the

368
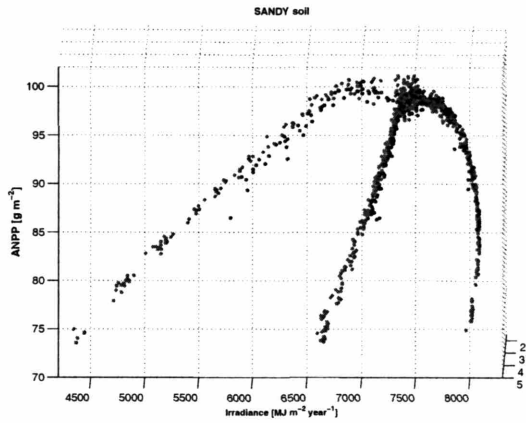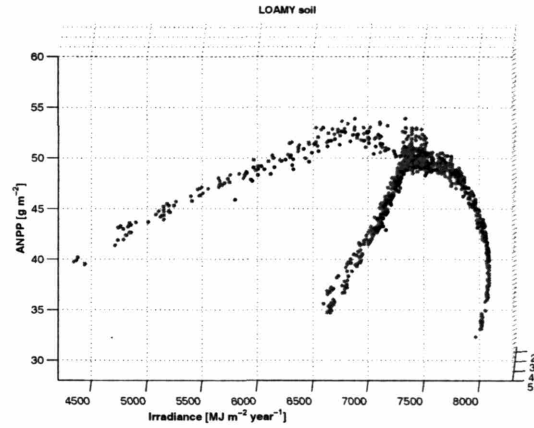
(a) SANDY soil
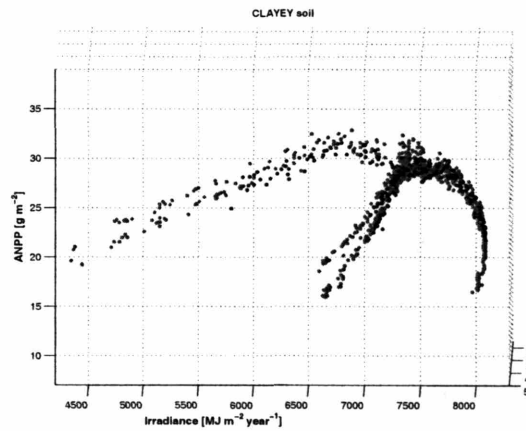


(b) LOAMY soil



(c) CLAYEY soil

Figure 6-28: The mean annual ANPP for the considered soil types with the anisotropy ratio $a_r = 1000$: a.) sandy soil; b.) loamy soil; and c.) clayey soil. The horizontal axes are the site surface annual irradiance and the *contiguous* number of upstream contributing elements. Only a subset of data points is shown, corresponding to those locations that have the number of *contiguously* contributing elements exceeding one. The three-dimensional plots are oriented such that the resulting pattern of data points composes the "$\epsilon$-curve".

natural logarithm of the global surface area $A_T$ contributing to elements versus the corresponding site annual irradiance. As can be inferred from the figure, the visible deviations of productivity from the "$\epsilon$-curve", i.e., substantially different values of ANPP for elements that have the *same aspect* and *same slope*, can be primarily attributed to the differences in the global contributing area. The discussed example is another confirmation of the significance of both the *global* and *contiguous* flow convergence levels, previously addressed in Figures 6-18 - 6-19. In order to properly account for the effects of both convergence levels, a new term needs to be added into the equation (6.4):

$$\left.\frac{P_{AN}^1}{P_{AN}^0}\right|_{\alpha_\nabla, \zeta_\nabla} = \left[f_1\left(\log A_T\right)\right]\left[f_2\left(A^{CU}\right)\right] \times$$

$$\left[g_1\left(\alpha_\nabla^{CU}\right)\right]\left[g_2\left(\frac{\zeta_\nabla}{2}^{CU}\right)\right]\left[g_3\left(\overline{\alpha_\nabla^{GU}}\right)\right]\left[g_4\left(\overline{\frac{\zeta_\nabla}{2}^{GU}}\right)\right], \quad (6.5)$$

where $f_2\left(A^{CU}\right)$ introduces an additional dependence of ANPP on the level of *contiguous* flow convergence. The above formulation therefore represents a generic relationship that can be used to relate grass productivity and, *apriori*, the components of water balance at different terrain locations for the considered simulation scenario.

Overall, the considered case of high soil anisotropy indicates that the enforced lateral water transfer in landscapes leads to a very complex structure of dependence of both the productivity and essential water balance components on terrain attributes. Nonetheless, the above discussion discriminates the characteristic controlling effects of terrain features associated with two distinct types of contributing areas, i.e., the *global* and *contiguous* flow convergence levels. Their effects are superimposed when productivity or water balance components are considered at the basin scale. In addition to these effects, the site-specific characteristics affecting the incoming radiation and rainfall further impact the vegetation-hydrology dynamics at any given combination of site *global* and *contiguous* flow convergence levels. The above discussion suggests that the combined effect of terrain attributes possesses scaling properties allowing to derive a conceptual relationship that links both the productivity and water
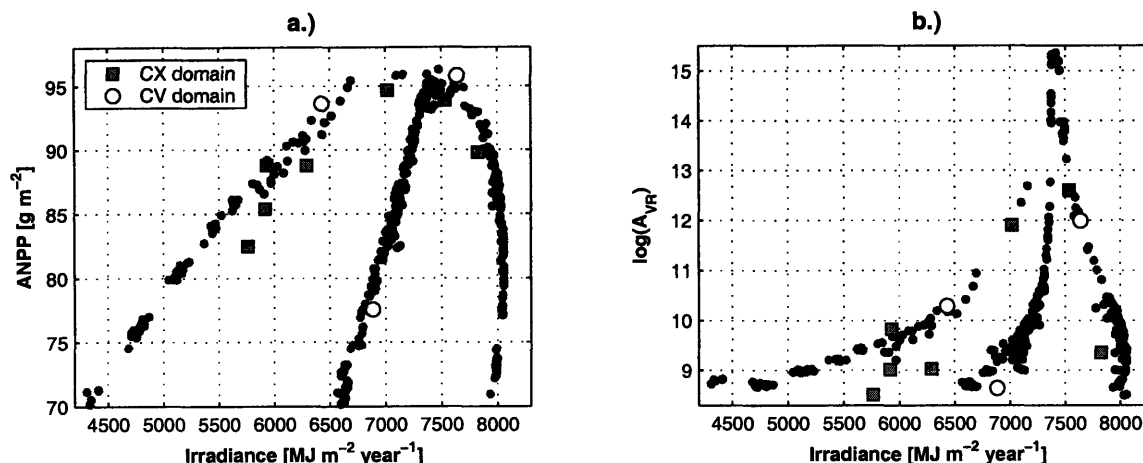
Figure 6-29: Simulation results for *sandy* soil with the anisotropy ratio $a_r = 1000$: a.) the mean simulated Above-ground Net Primary Productivity; and b.) the natural logarithm of the global surface area $A_T$ contributing to a given element. Symbols with lighter color denote the data points for the CV domain, the darker color corresponds to the data points for the CX domain. The highlighted data points introduce a clear visible distortion into the "ε-curve". Only a subset of all data points is shown, corresponding to those locations that have the number of *contiguously* contributing elements equal to two.

balance components at various landscape locations.

## 6.4.2 Surface sealing and runon

Extremely high rate of lateral moisture exchange is characteristic for systems where runon can occur. To simulate this process, it is assumed that the soil surface is partially sealed to infiltration during the monsoon months of the growing season (July, August, and September). This has been shown to be a common phenomena in arid and semi-arid areas, caused primarily by the high kinetic energy of rain droplets impacting the soil surface on exposed areas. This process leads to soil matrix compression, dispersion of soil aggregates, and therefore release of fine particles, which are drawn back into the soil pores (e.g., Moore, 1981; Poesen, 1987, 1992; Howes and Abrahams, 2003; Ludwig et al., 2005). It is assumed here that infiltration is prevented in the bare soil fraction of any given element and the corresponding fraction of rainfall depth is simply assumed to become runoff. The produced runoff is allowed

371

**a.) Base case**

**b.) Surface sealing with runon**

ANPP [g C / sq. m ground area]
31.59 - 33.64
33.64 - 35.68
35.68 - 37.73
37.73 - 39.78
39.78 - 41.83
41.83 - 43.88

ANPP [g C / sq. m ground area]
13.09 - 23.56
23.56 - 32.58
32.58 - 38.69
38.69 - 59.06
59.06 - 94.08
94.08 - 132.06
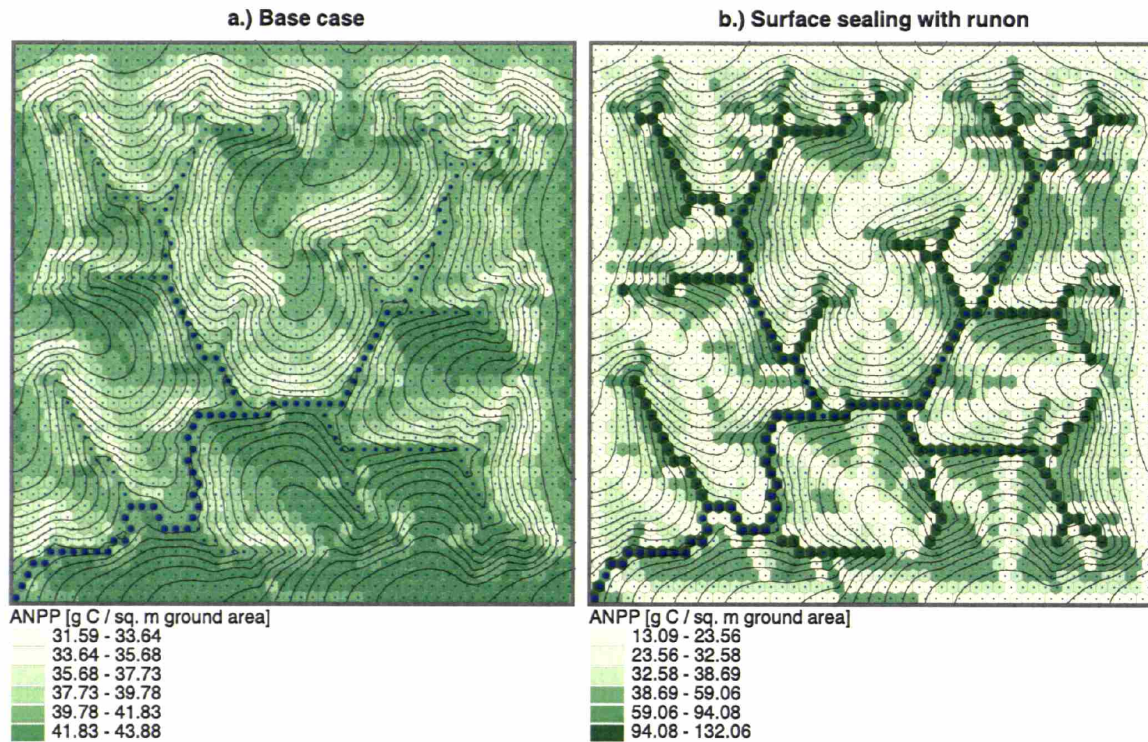
Figure 6-30: The mean annual Above-ground Net Primary Productivity simulated for $C_4$ grass on loamy soil for the CX domain: a.) the *base* case; and b.) the surface sealing with runon case. The units are given at the element scale and refer to the actual inclined ground surface area.

to re-infiltrate at downstream locations.

As can be seen in Figure 6-30, the runon scenario leads to an extremely high spatial differentiation of grass productivity. When compared to the *base* case scenario (Figure 6-30a), one can observe significantly smaller values of ANPP for the hillslope parts of the terrain and much higher values for the convergent topographic locations. Clearly, the lateral moisture redistribution causes substantial changes in the overall catchment vegetation-water-energy dynamics. *Non-local* features of topography, such as upstream drainage area and curvature, significantly contribute to the vegetation spatio-temporal dynamics.

Figure 6-31 uses the same type of plot as Figure 6-18 to illustrate the difference in effects of the *global* and *contiguous* contributing areas. The selected data points correspond to locations with up to 3 *globally* upstream elements. As the figure shows,

the rate at which ANPP grows in downstream locations, is significantly affected by the level of local flow convergence. For the same number of *globally* contributing elements (larger than one), ANPP is significantly higher when the number of elements contributing their flow on a *contiguous* basis is equal to the number of elements contributing their flow on a *global* basis. As previously discussed and can be noticed in Figure 6-31, the $\epsilon$-shaped pattern can be consistently fitted to the data points at every downstream level for the considered range of contributing areas.

The significance of both the *global* and *contiguous* flow convergence levels is further highlighted in Figure 6-32 that shows the grass productivity binned according to the number of *contiguously* contributing elements (0 - 4) for any given location. In each of the bins, the data points are arranged according to the *global* contributing area, which grows from the left to the right. As discussed previously, two distinct kinds of ANPP growth are superimposed in this type of figure: while the grass productivity generally increases with the level of *contiguous* flow convergence, marked by the enveloping curves, the ANPP growth within each of the bins is related to the increasing *global* contributing area. Additionally, as was shown for the scenario of high soil anisotropy and will be demonstrated for the runon case, the local terrain features (i.e., site aspect and slope) further control grass productivity at each level of the *global* and *contiguous* flow convergence.

Figures 6-33 and 6-34 illustrate the grass ANPP and mean growing season root soil moisture, respectively, for all considered soil types as three-dimensional plots where the horizontal axes are the surface irradiance and *global* number of upstream contributing elements. Only a subset of data points is shown corresponding to those locations that have the number of *contiguously* contributing elements ranging from 0 to 1. Similarly to the previously discussed case of high soil anisotropy, for each number of upstream contributing elements both the grass productivity and mean root moisture exhibit a pronounced dependence on site annual irradiance in the form of the "$\epsilon$-curve" pattern. Consequently, this demonstrates that notwithstanding the extreme nature of assumed lateral water redistribution, aspect and slope are still among the key determinants of the overall dynamics at *each downstream level.*
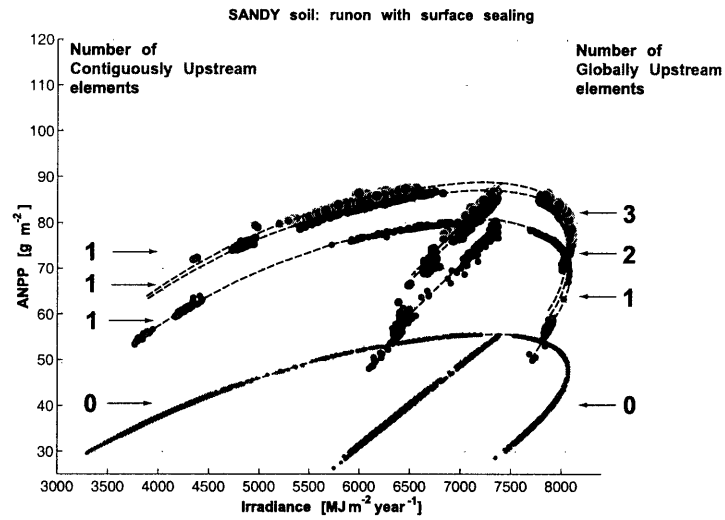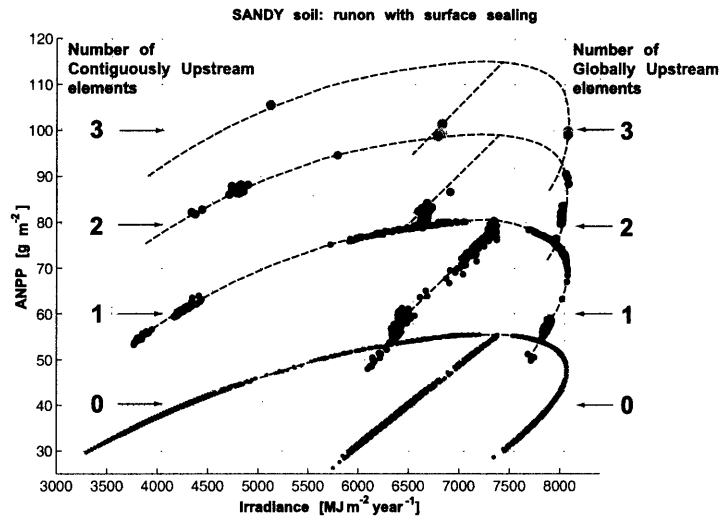
Figure 6-31: The mean annual ANPP for sandy soil (the simulation scenario involves soil surface partial sealing with runon mechanism). Data for elements with up to 3 *globally* upstream elements are shown: a.) the number of *contiguously* contributing elements is 0-1; and b.) the number of *contiguously* contributing elements is 0-3 (i.e., for each set of elements this number coincides with the number of *globally* contributing elements). The symbols of progressively larger size depict the increasing number of *globally* contributing elements. The dashed lines were added manually to complement and connect the data points corresponding to the same number of *globally* contributing elements.

374

**SANDY soil: surface sealing scenario**
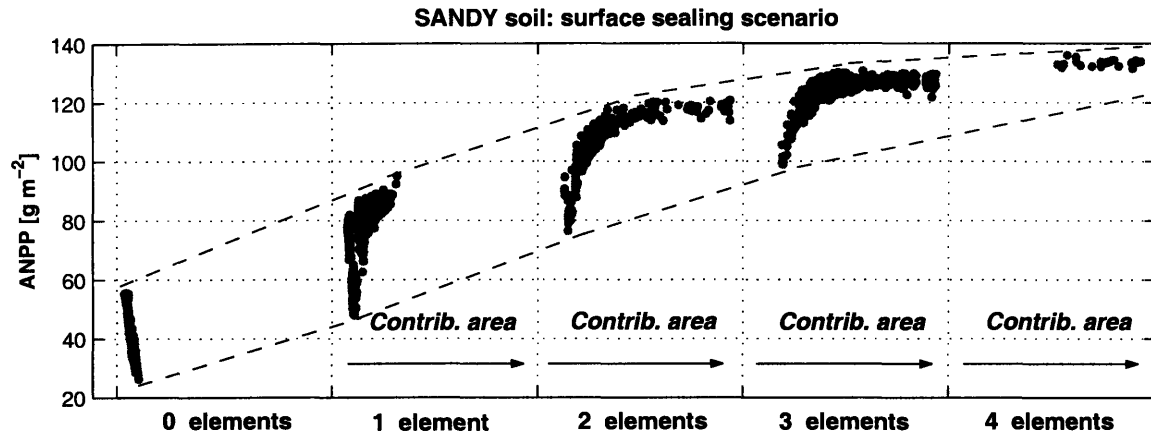
Figure 6-32: The mean annual ANPP for sandy soil (the simulation scenario involves soil surface partial sealing with runon mechanism). Data points for both domains are shown. The data are binned according to the number of *contiguously* contributing elements (0 - 4) and the increasing number reflects the growing level of local flow convergence. In each of the bins, the data points are arranged according to the *global* contributing area that grows from the left to the right.

Furthermore, it can also be demonstrated that aspect and slope control productivity and water balance components at any level of terrain concavity. Figure 6-35 illustrates the ANPP for the elements that have the number of *contiguously* contributing elements larger than one. As in the previous case of high soil anisotropy, if another dimension representing the total number of *contiguously* contributing elements is added to plots shown in Figure 6-35, one could observe that the pattern in each of the plots is, in fact, a combination of several overlapping noisy "ε-curves". Each of the "ε-curves" corresponds to a certain number of *contiguously* contributing elements. Apparently, the previously suggested formulation (6.5) that combines the controlling effects of both the *global* and *contiguous* terrain convergence levels should as well hold for the runon modeling scenario. However, as will be shown in the following example, an adjustment needs to be made to account for the additional implications of assumptions of the runon experiment.

The amount of produced grass biomass is determined by the combination of water and energy inputs at a given terrain location. According to the assumption of the simulation scenario, the amount of runoff generated at a given element is propor-
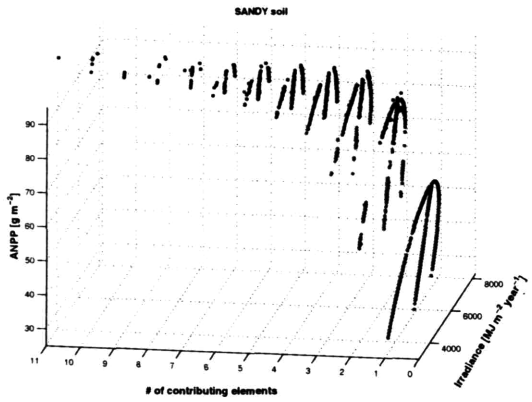
(a) SANDY soil
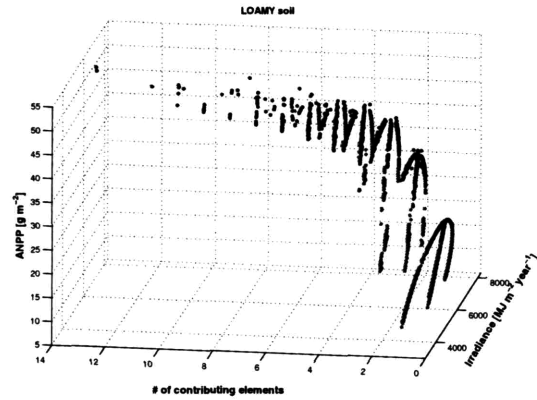


(b) LOAMY soil
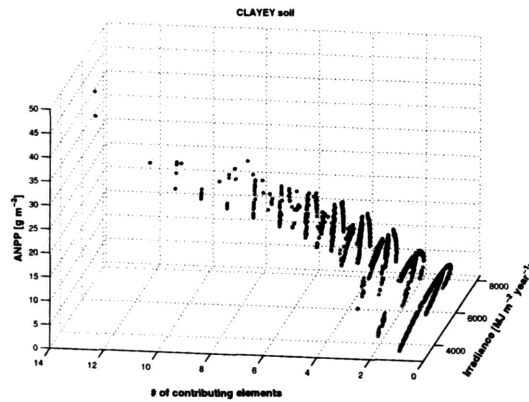


(c) CLAYEY soil

Figure 6-33: The mean annual ANPP for the considered soil types (the simulation scenario involves soil surface partial sealing with runon mechanism): a.) sandy soil; b.) loamy soil; and c.) clayey soil. The horizontal axes are the site surface annual irradiance and the *global* number of upstream contributing elements. Only a subset of data points is shown, corresponding to those locations that have the number of *contiguously* contributing elements ranging from 0 to 1.
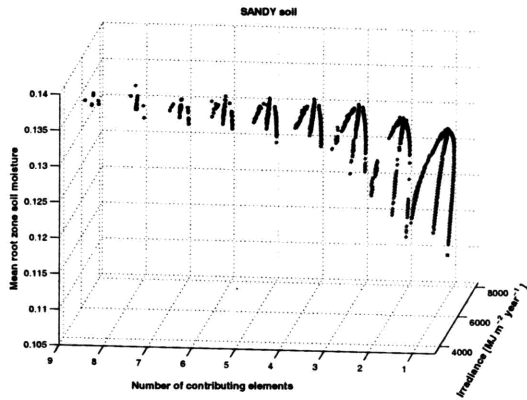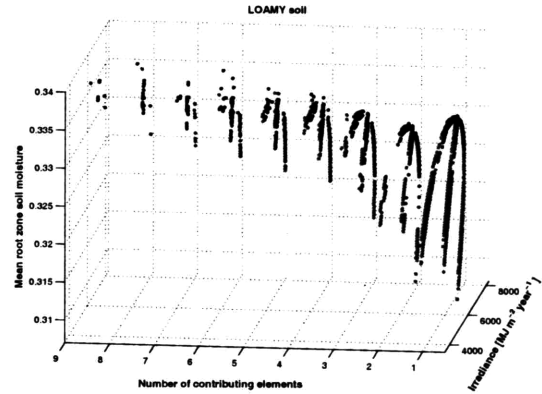
(a) SANDY soil
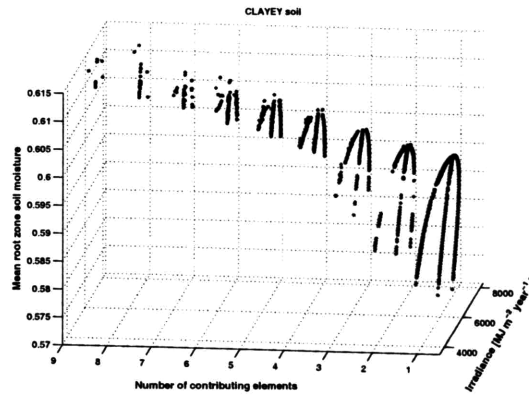


(b) LOAMY soil



(c) CLAYEY soil

Figure 6-34: The mean growing season root soil moisture for the considered soil types (the simulation scenario involves soil surface partial sealing with runon mechanism): a.) sandy soil; b.) loamy soil; c.) clayey soil. The horizontal axes are the site surface annual irradiance and the *global* number of upstream contributing elements. Only a subset of data points is shown, corresponding to those locations that have the number of *contiguously* contributing elements ranging from 0 to 1.
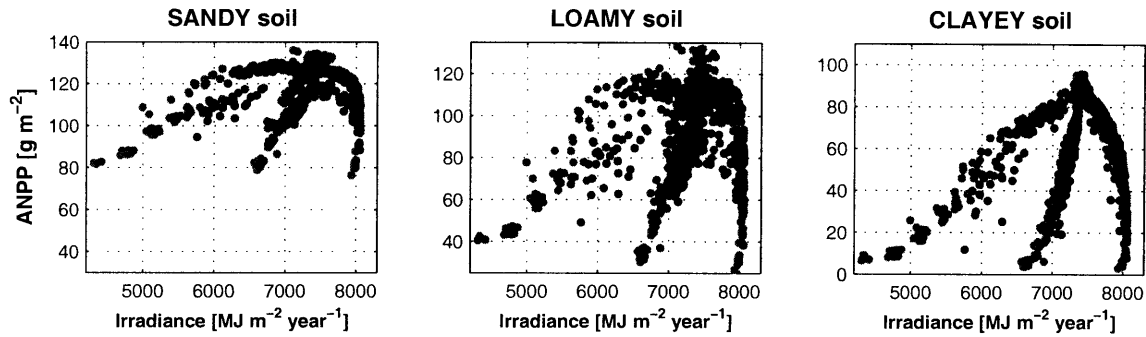
Figure 6-35: The mean simulated Above-ground Net Primary Productivity for the considered soil types (the simulation scenario involves soil surface partial sealing with runon mechanism): a.) sandy soil; b.) loamy soil; c.) clayey soil. Symbols with lighter color denote the data points for the CV domain, the darker color corresponds to the data points for the CX domain. Only a subset of data points is shown, corresponding to those locations that have the number of *contiguously* contributing elements exceeding 1.

tional to the element's fraction of bare soil, which in a water-limited environment is higher for locations with higher solar energy input. It can be shown that grass dynamics at a given site may substantially benefit if its corresponding *contiguously* contributing elements receive significantly more solar radiation than the considered site. For example, Figure 6-36 illustrates the simulation results for sandy soil for a subset of data points corresponding to the locations that have the number of *globally* contributing elements equal to one. The highlighted data points in Figure 6-36a introduce a clear distortion into the ANPP "$\epsilon$-curve". As can be seen in Figure 6-36b, some of the marked deviations in Figure 6-36a can be explained by the differences in the actual contributing area among the considered set of locations. On the other hand, it can also be concluded that the higher ANPP (relative to locations with similar aspect and slope, Figure 6-36c) for a few data points can be explained by significantly higher solar radiation input at their *contiguously* contributing elements (Figure 6-36d). Apparently, this effect is caused by the higher runoff generation at these elements. Consequently, a new term is added into the equation (6.5) to account

for this effect:

$$\left.\frac{P^1_{AN}}{P^\circ_{AN}}\right|_{\alpha_\nabla, \zeta_\nabla} = \left[f_1\left(\log A_T\right)\right]\left[f_2\left(A^{CU}\right)\right]\left[f_3\left(S^{CU}_{atm}\downarrow\right)\right] \times$$

$$\left[g_1\left(\alpha^{CU}_\nabla\right)\right]\left[g_2\left(\frac{\zeta_\nabla}{2}^{CU}\right)\right]\left[g_3\left(\overline{\alpha^{GU}_\nabla}\right)\right]\left[g_4\left(\overline{\frac{\zeta_\nabla}{2}^{GU}}\right)\right], \quad (6.6)$$

where $f_3\left(S^{CU}_{atm}\downarrow\right)$ introduces the dependence of site ANPP on radiation input in *con-tiguously* upstream contributing area. *Apriori*, the above formulation represents a generic relationship that can be used to relate **both the vegetation productivity and the components of water balance** at different terrain locations for **all considered simulation scenarios**.

Overall, the above discussion underlines the analogies with the preceding case of enforced lateral water transfer (the high soil anisotropy), found in the structure of dependence of both the grass productivity and water balance components on terrain attributes. The even more apparent superimposed controlling effects of topography features, associated with the two types of the flow convergence levels (i.e., *global* and *contiguous*) and the site-specific characteristics (i.e., aspect and slope), are emphasized. The discussed results, corresponding to extremely high lateral water transfer in the landscapes, confirm the applicability of the previously proposed generic relationship that links both the productivity and water balance components at various landscape locations.

## 6.5   Summary

This chapter discusses simulation results addressing the sensitivity of vegetation-hydrology dynamics presented in Chapter 5, referred to above as the *"base"* case scenario. The experimental design is subject to modifications in a.) the hydrometeorological forcing and b.) the processes of lateral moisture transfer.

The first set of experiments explores the impact of the random nature of the rainfall vector (i.e., deviation of droplet pathways from the vertical) as well as introduces
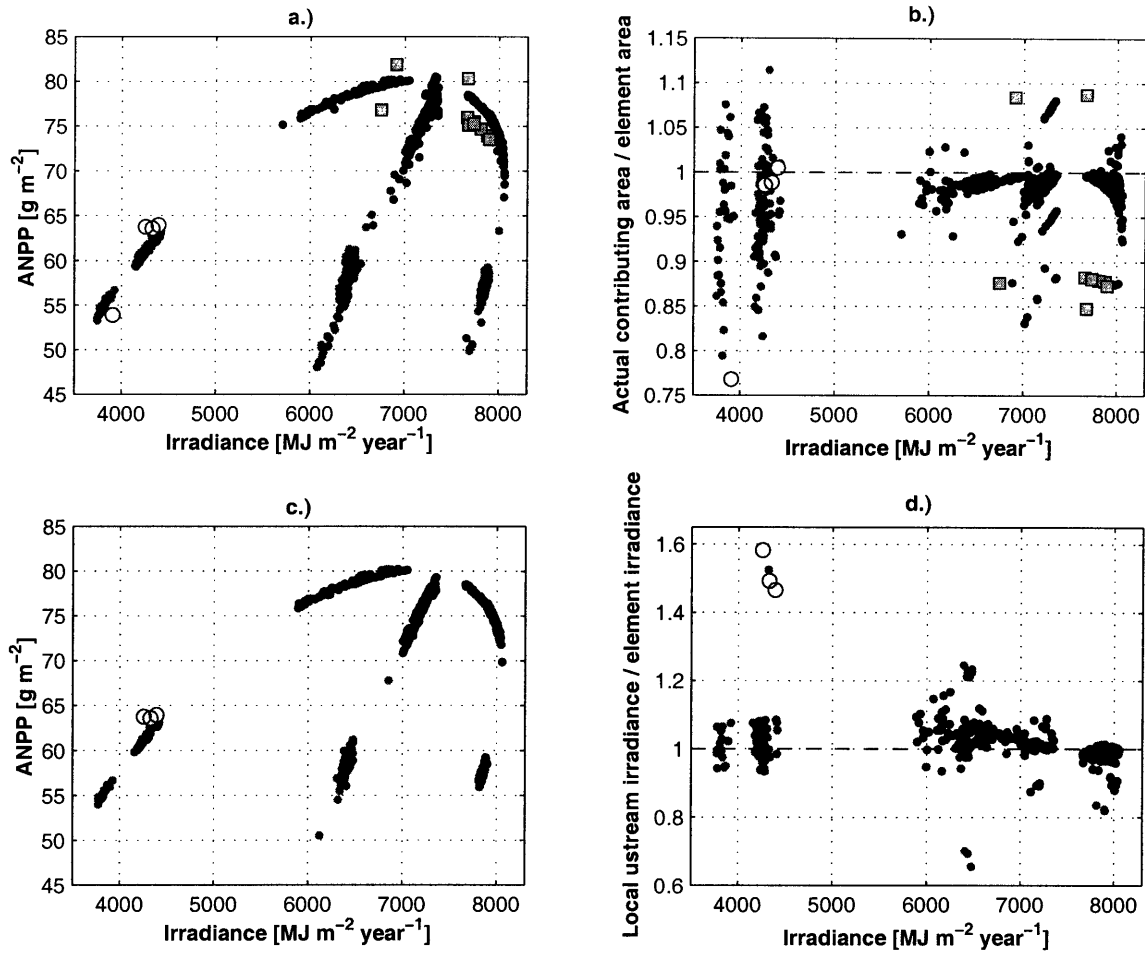
Figure 6-36: Simulation results for sandy soil for scenario that involves soil surface partial sealing with runon mechanism and re-infiltration. Only a subset of all data points is shown, corresponding to those locations that have the number of *globally* contributing elements equal to one. Symbols with lighter color denote the data points for the CV domain, the darker color corresponds to the data points for the CX domain. The highlighted data points introduce a clear distortion into the ANPP "$\epsilon$-curve": a.) the mean simulated ANPP; b.) the ratio of upstream contributing area to the element area, $A^{GU}/A_{VR}$; c.) the mean simulated ANPP excluding the data points with $A^{GU}/A_{VR} > 1.05$ and $A^{GU}/A_{VR} < 0.95$; d.) the ratio of the mean annual irradiance for *contiguously* contributing elements to the mean annual irradiance of a considered element.

artificial changes to the seasonal precipitation and radiation regimes. The discussion highlights the importance of proper accounting for the actual distribution of precipitation, i.e., the *hydrological* rainfall (Section 5.2.3), over complex terrain. Additionally, the discussion emphasizes important aspects of temporal relationships among the energy, water, and biomass dynamics, e.g., the existence of periods of radiation limitation and excess that correspondingly affect fluxes of carbon and water dynamics. The critical role of soil texture type in regulating the spatial and temporal aspects of coupling between vegetation-hydrology processes is also clearly demonstrated.

The second group of experiments introduces more rapid processes of lateral moisture exchange, as compared to the *"base"* case scenario. They are implemented through the high soil anisotropy ratios ($a_r \in [100 \div 1000]$), the runon mechanism allowing for re-infiltration process, and the partial surface sealing during growing season, leading to higher runoff-runon volumes. The cases of enforced lateral water transfer in landscapes reveal a very complex structure of dependence of both the productivity and essential water balance components on the terrain attributes. The analysis discriminates the characteristic controlling effects of terrain features associated with two distinct types of the flow convergence levels, i.e., the *global* and *contiguous*. Their effects on vegetation-hydrology dynamics at a given location are superimposed in combination with the site-specific characteristics (i.e., aspect and slope) affecting the incoming radiation and rainfall. The presented results suggest that the combined effect of terrain attributes possesses scaling properties, which allows one to propose a conceptual relationship linking both the productivity and water balance components at various landscape locations.

# Chapter 7

# Research Summary and Perspectives for Future Studies

## 7.1 Summary of results

Vegetation is an important component of terrestrial systems, playing a significant role in the processes of land-surface water and energy partition. Recent years have shown significant advances in understanding and quantitative description of interaction between vegetation and various components of climatic forcing and land-surface processes, giving rise to new subjects, such as ecohydrology. Ecosystems of arid and semi-arid areas represent a particularly interesting subject for studies, as they comprise some of the major biomes of the world often exhibiting a delicate equilibrium among their essential constituents. In these systems, water is generally considered to be the key limiting resource. The mechanisms through which water limitation affects such ecosystems are related to carbon assimilation via the control of photosynthesis and stomatal closure as well as nutrient assimilation through the control of the soil mineralization rates. Many important issues depend on the quantitative understanding of dynamics inherent to these ecosystems including human interference, climate change, environmental preservation, and proper management of resources.

While it is commonly observed that topography strongly affects the state and spatial organization of vegetation through the regulation of incoming solar radiation

and lateral redistribution of water and elements (e.g., Florinsky and Kuryakova, 1996, Franklin, 1998; Meentemeyer et al., 2001; Dirnbock et al., 2002; Kim and Eltahir, 2004; Ben Wu and Archer, 2005; Dietrich and Perron, 2006), a still largely unexplored area is how plants adjust to these regulating effects relative to their location in a landscape, what the implications are for the water balance, and whether catchment vegetation-hydrology dynamics can be generalized in the form of terrain indices. The aim of this work therefore is: 1) to develop a modeling system that incorporates *state-of-the-art* tools to represent vegetation-hydrology interactions in areas of complex terrain; and 2) to address a number of questions concerning vegetation-hydrology mechanisms in semi-arid zones. In particular, this research addresses the effects of topography on vegetation temporal function and spatial distribution.

### 7.1.1 Modeling system

The system that allows one to model dynamic vegetation in the framework of a hydrological model has been described in detail in previous chapters. This system is composed of several key components: a climate simulator, a spatially-distributed physically-based hydrological model, the *TIN-based Real-time Integrated Basin Simulator*, tRIBS (Ivanov et al., 2004a; most of the hydrological components however have been modified in this work), and a model of plant physiology and spatial dynamics, *VEGetation Generator for Interactive Evolution*, VEGGIE. The framework simulates a variety of processes that manifest numerous dynamic feedbacks among various components of the coupled vegetation-hydrology system. The following lists the key features of the developed modeling components.

1. **Climate simulator**

   - several hydrometeorological variables are generated: the incoming shortwave radiation, rainfall, air temperature and humidity, total cloud cover, and wind speed;
   - the weather simulator of Curtis and Eagleson (1982) is used as the core framework for the model (a new shortwave radiation model has been introduced; other necessary modifications have also been implemented leading to a better or more efficient representation of the simulated statistics);

- the *diurnal* (hourly) variation of hydrometeorological conditions is modeled;

- *consistent* time-series of hydrometeorological quantities are simulated: all major weather variables exhibit an agreed co-variation as the simulator captures the essential relationships among the meteorological variables of interest;

- the model is suitable for creating consistent multiple climate scenarios (e.g., dry and wet climates) in which changes in the dynamics of a certain meteorological quantity trigger corresponding changes in other related variables.

## 2. Hydrological model

- a number of *biophysical* processes are represented: absorption, reflection, and transmittance of solar shortwave radiation, absorption and emission of longwave radiation, sensible and latent heat fluxes, and ground heat flux;

- a number of *hydrological* processes are represented: precipitation interception, throughfall, and stem flow, partition of latent heat into canopy and soil evaporation, and transpiration, infiltration in a multi-layer soil, lateral water transfer in the unsaturated zone, runoff and runon;

- both vegetated (multiple vegetation types) and non-vegetated surface types are considered within a given element;

- each patch (vegetated or bare soil) constitutes a separate column upon which energy and water calculations are performed; the corresponding fractional areas are used to weight the relative contribution of each vegetation type/bare soil to the element-scale flux values;

- spatial dependencies are introduced by considering the surface (runoff-runon) and subsurface (in the unsaturated zone) moisture transfers among the elements, which affect the local dynamics via the coupled energy-water interactions;

- soil effects are accounted for by parameterizing the thermal and hydraulic properties that depend on soil's sand and clay content; soils also differ in color, which is reflected in the values of soil albedo;

- the models of biophysical processes operate at the hourly time scale, the processes of infiltration, lateral moisture transfer, and runoff (runon) use a finer time step (7.5-15 min.).

## 3. Vegetation model

- a number of *biochemical* processes are represented: photosynthesis and primary productivity, stomatal physiology, plant respiration, tissue turnover and stress-induced foliage loss, carbon allocation; vegetation phenology and plant recruitment are also simulated;

- the model allows simulation of the transient response of vegetation to hydrometeorological forcing and moisture redistribution in a natural system, while explicitly accounting for the effects of two limiting factors: water and light;

- several plant functional types can be simultaneously present in a given computational element; the above-ground competition for light is treated as the competition for available space, while the below-ground competition for water is described through the differences in plant water uptake properties and features of rooting profiles;

- a more elaborate scheme of plant competition for light, which would assume radiative shading by taller species, can be easily incorporated based on the current framework; the currently implemented approach is more suitable for arid and semi-arid areas of sparse vegetation.

The model parameterization is verified against field observations for $C_4$ grass in the semi-arid environment of central New Mexico. The results of numerical experiments provide sufficient evidence that the coupled vegetation-hydrology model is capable of producing consistent results that corroborate field-observed data. The same parameterization of $C_4$ grass was used to address the spatial aspects of vegetation-hydrology dynamics and investigate the effects of topography on vegetation dynamics in semi-arid areas.

## 7.1.2  Topography effects on vegetation and hydrology

The climate corresponding to Albuquerque (NM) was selected as representative of a semi-arid area. The weather generator was employed to generate the long-term time-series of hydrometeorological forcing variables. The experiments were done on two small-scale synthetic domains (each is $\sim 4$ $km^2$ in area) that exhibit significant differences in the hillslope characteristics. The dimensions of a typical element are approximately $30\,m \times 40\,m$. A full range of transient vegetation dynamics was simulated for a typical annual $C_4$ grass assumed to grow on three different soil types: sand, loam, and clay. The linkages between terrain attributes and patterns of $C_4$ grass productivity and water balance components were examined for conditions of negligible and significant lateral transfer of water based on 50-year long simulations.

The *base* case scenario considers isotropic soils and assumes the subsurface gravity-driven moisture flux to be the only mechanism of lateral water redistribution. This study found that under the conditions of such a scenario the moisture exchange in the domains was negligible for all soil types. Therefore, the vegetation-hydrology dynamics were assumed to be *spatially-independent*. The *local* terrain features, **aspect** and **slope**, are the key determinants of the overall dynamics at any given site. Consequently, the study argued that most of the vegetation-hydrology mean state variables could be simply considered as a function of these topographic attributes. One convenient measure of both aspect and slope is the site annual shortwave irradiance. For instance, both the Above-ground Net Primary Productivity (ANPP) and water balance components during the growing season, when considered as a function of site surface irradiance, comprised a characteristic shape referred to previously as the "$\epsilon$-curve". The "$\epsilon$-curve" pattern is the resulting compound outcome of dynamics that involve *water* and *energy* interactions, as mediated by *vegetation* function and affected by the soil hydraulic properties.

In conditions of the *base* case scenario, certain topographic locations may favor vegetation development, as compared to a flat horizontal surface not affected by the lateral effects such as radiative shading, moisture transfer in the unsaturated zone, or runon. These locations were associated with sites of northerly aspect with surface slopes within a narrow range of magnitudes. Contributions from both the *water* and *radiation* forcings were discussed to explain the existence of these niches. Favorable conditions for plant development were attributed to a compromise between low water stress and high productivity. This conclusion was drawn from the simulated spatial distribution of stress characteristics that exhibit least extreme values at terrain locations similar to those that feature maximum ANPP. Furthermore, a conceptual procedure was used to partition the aspect-slope pseudo-space into the regions of dominant influence of the forcing using the mean root moisture during growing season as a representative characteristic of site favorability to grass. In these delineated regions, either rainfall insufficiency or radiation excess impose predominant conditions on grass performance. In addition, regions of topographic "favorability" to vegetation

and regions where moisture limitation constrains its function were identified.

The sensitivity of results was further investigated relative to modifications in the meteorological forcing and the dominant mechanisms of lateral water transfer. In the first set of experiments, the impact of the random nature of the rainfall vector (i.e., deviation of droplet pathways from the vertical) was explored, highlighting the importance of proper accounting for the actual distribution of precipitation (the *hydrological* rainfall) over complex terrain. A critical slope $\alpha_\nabla^o$ was introduced to account for randomness in the precipitation forcing, such that for sites with surface slope $\alpha_\nabla \leq \alpha_\nabla^o$, the same rain depth (per unit actual surface area) was assumed as for a horizontal surface. Maximum grass productivity was still associated with north-facing sites receiving less solar radiation. While soils of finer texture (loam and clay) showed a consistent expansion of the "favorability" region with the growing $\alpha_\nabla^o$, the maximum grass productivity for sandy soil was essentially insensitive to the change in $\alpha_\nabla^o$, implying a decrease in the relative benefit of the radiative shading by slopes of northerly aspect. As was argued, Photosynthetically Active Radiation (PAR) became a limiting factor in this case.

Additionally, artificial changes to the seasonal precipitation and radiation regimes were introduced. The study further emphasized the important aspects of temporal relationships among energy, water, and biomass dynamics; for instance, the discussed simulations demonstrated the existence of periods of radiation limitation and excess that correspondingly affect vegetation dynamics. The results also unequivocally illustrated the critical role of soil texture type in regulating the spatial and temporal aspects of coupling between vegetation-hydrology processes that lead to characteristic differences in response to the same hydrometeorological forcing.

In the second set of experiments, more rapid processes of lateral moisture exchange were introduced, as compared to the *base* case scenario. They were implemented through high soil anisotropy ratios ($a_r \in [100 \div 1000]$), the runon mechanism allowing for re-infiltration process, and the partial surface sealing during growing season, leading to higher runoff-runon volumes. These cases of enforced lateral water transfer in the two landscapes revealed a very complex structure of dependence of both the

388

productivity and essential water balance components on the terrain attributes. The analysis discriminated between the characteristic controlling effects of terrain features associated with two distinct types of the flow convergence levels, i.e., the *global* and *contiguous*. At any given location, their effects on vegetation-hydrology dynamics are superimposed in combination with the site-specific characteristics (i.e., aspect and slope) that affect the incoming radiation and rainfall. The results suggest that the combined effect of terrain attributes possesses scaling properties, which allows one to propose a conceptual relationship linking both the productivity and water balance components at various landscape locations. The relationship can be expressed as a function that combines local and global terrain properties.

Overall, the results highlight the interplay among the vegetation-water-energy processes that lead to extreme non-linearity of the hydrological dynamics and complexity of the vegetation temporal function and spatial distribution in semi-arid areas. This research addresses the effects of topography in creating the niches of higher/lower favorability to vegetation and the principal factors that impact/constrain the magnitude of influence by terrain attributes.

## 7.2   Critical assumptions of the study

Any modeling study inherently contains a number of assumptions. The most critical assumptions of this work are summarized below.

1. **Climate simulator**

   - *Atmospheric radiative transfer model:* The ozone amount in the vertical column $u_o$, the spatial average regional albedo $\rho_g$, and the Angström turbidity parameters $\alpha$ and $\beta$ are all assumed to be seasonally constant. For the considered location (Albuquerque, NM), $u_o = 0.34$ *cm*, $\rho_g = 0.10$, $\alpha = 1.3$, $\beta = 0.017$. Note that only $\beta$ was considered to be a calibration parameter. Also, in the presented work, the precipitable water $w_p$ was estimated from the simulated dew point temperature, according to an empirical model of Iqbal (1983) (Appendix A). Generally, it should be obtained from measurements at meteorological stations;

   - *Shortwave radiation model - cloudiness effects:* The cloud total vertical liquid water path, *LWP*, is used in the model, which is defined as the

389

integral of the liquid water content, $LWC$, from the cloud base to the cloud top. In this work, a seasonally-varying value of $LWP$ for *overcast* conditions was used to account for the different cloud structure and origin during different periods of the year. Furthermore, it was assumed that the liquid water path for *any sky condition* can be defined as a non-parametric function of the value for overcast conditions (Section 2.3.2). The actual advantage of using $LWP$, however, is in the capability of obtaining this quantity from satellite microwave radiometry.

- *Shortwave radiation model - shading effects*: The factor that reduces the direct beam flux due to "distant-shading" from the surrounding topography, $W_{BH}$, was assumed to be equal to '1' in this work. However, $W_{BH}$ can be significantly different from unity in mountainous terrain. In order to describe such an effect, an *hourly* sun view factor needs to be estimated for each location in a given domain. Obviously, the factor needs to be seasonally-varying since the sun altitude varies throughout the year.

- *Rainfall model*: As was emphasized in the preceding chapters, one of the apparent shortcomings is that the rectangular pulse rainfall model, used to force the simulated dynamics, rarely generates precipitation events of high intensity since uniform intensity is assumed for each generated precipitation event. This leads to negligible runoff production for most natural soil types. Additionally, rain is assumed to fall in the *vertical* direction, which leads to a cosine projection of rainfall depth on a sloped surface. No random perturbations in the rainfall vector are considered.

- *Cloudiness model*: The central assumption made in the model of Curtis and Eagleson (1982) is that there is a loosely centered sub-region around the midpoint of the interstorm period in which the cloudiness process can be assumed stationary. Sometimes, passing atmospheric precipitation systems do not necessarily result in rainfall at a given location. However, the cloud cover process is obviously non-stationary during such periods. The discussed approach cannot identify such periods, which would, perhaps, require auxiliary information about cloud vertical structure and spatial information about the precipitation process. In the discussed verification results, the transition function for certain months was not adequately represented, which was partly attributed to this feature. Also, the decay coefficients, $\varsigma$ and $\gamma$, controlling the transition rates of cloudiness from the boundaries (end/beginning of precipitation events) to/from the region of "fairweather", were assumed to be equal in the this model implementation.

- *Air temperature model*: As compared to the model of Curtis and Eagleson (1982), the current formulation (equation (2.46)) of the change in the hourly air temperature excludes the terms that represent the effects of ground temperature, wind speed, and wind direction. For certain locations, where the data on the ground temperature are available or where a sudden advection of air masses may significantly contribute to the air temperature dynamics, these terms should be represented.

- *Dew temperature model*: A much simpler model (as compared to the approach of Curtis and Eagleson (1982)) of *daily* dew point temperature is implemented, based on the adjustment of the minimum daily temperature. The approach uses an *expected* value of cloudiness for the coming day to estimate an empirical adjustment factor of Kimball et al. (1997), which is applied to the minimum daily temperature. Taking into account the overall importance of proper simulation of air humidity, the simulator may need a more sound approach instead.

- *Wind speed model*: The model parameters ($\overline{W}_s$, $\sigma_s^2$, $\rho_s(1)$, and $\gamma_s$, see Section 2.8) were assumed to be time-invariant over the entire simulation period. Apparently, for some locations this constraint needs to be relaxed.

## 2. Hydrological model

- *Ground albedos*: The ground albedos are assumed to be independent of the type of incident radiation: $\alpha_{g\Lambda}^{\mu} = \alpha_{g\Lambda}$.

- *Canopy radiative transfer model*: Leaf and stem area indices, $L$ and $S$, are defined in the units of $[m^2\ leaf/stem\,area\ m^{-2}\ ground\,area]$, where *horizontal* ground area is assumed. The model, however, estimates these indices relative to the direction *normal* to the element surface. If an element is sloped, this creates a certain inconsistency. However, it can be attributed to an overall significant uncertainty concerning leaf orientation in space.

- *Soil surface and canopy resistances and energy balance*: The soil surface resistance, $r_{srf}$, assumed to take into account the impedance of the soil pores to exchanges of water vapor between the first soil layer and the immediately overlying air, is a highly empirical function of the surface soil moisture. Various forms of dependence have been suggested with no apparent advantage of one form over the other. In parameterizing heat transfer in conditions of *free convection*, a highly empirical bulk transfer coefficient is used, which has not been sufficiently tested. The understory ground and canopy heat fluxes are assumed to be independent. The aerodynamic resistance to the heat fluxes is parameterized only as a function of plant height. The amount of foliage biomass currently to not affect the aerodynamic resistance.

- *Soil temperature*: Single soil temperature $T_g$ is estimated for both bare soil and understory ground. Evidently, during day light hours, bare soil patches can be much warmer than shaded understory areas. Temperature distribution with soil depth is not computed and the root zone temperature $T_{soil}$ is assumed to be the mean value of the vector of surface temperatures $\mathbf{T_g}$ (see Section 3.6.4).

- *Canopy temperature*: The energy partition at the canopy level is based on the separate treatment of the assimilation rates and stomatal conductances for sunlit and shaded leaves. However, the same leaf temperature

is assumed for both layers, which can be a strong assumption for some environments: direct sun shine heats leaves more than the scattered light in the shade, and therefore sunlit leaves can be several degrees warmer than shaded leaves. Also, single canopy temperature is estimated although several vegetation types can be present within a given element.

- *Model of infiltration, root water uptake, and surface-subsurface exchange*: The implemented model of infiltration permits lateral moisture redistribution in the direction of steepest decent only (direction $p$ in Figure 3-1). *Gravity-driven* flow is assumed. When transpiration sinks are specified for the unsaturated zone, the root biomass profile (3.1) is assumed to be given in the direction *normal* to the element surface. While for shallow-rooted vegetation (e.g., grasses) this should not introduce significant differences with respect to the root zone specified for the *vertical* direction, the implications for deep-rooted species can be more substantial.

- *Groundwater*: No groundwater effects are considered in the current version of the model. Coupling the processes in the unsaturated zone to a groundwater module is required.

## 3. Vegetation model

- *Vegetation representation*: In order to represent the differences among various plants, the model operates with the concept of *plant functional type* (PFT). This concept allows combining species with similar characteristics into the same groups. Each vegetation patch, while co-occurring in the same element, constitutes a separate column upon which energy, water, and carbon calculations are performed.

- *Photosynthesis and stomatal resistance model*: The expression for a heuristic factor $\beta_T$ that limits photosynthesis depending on the soil moisture distribution in the root zone is a highly empirical function. Various forms of the soil moisture control of plant photosynthesis have been suggested with no apparent advantage of one form over the other. Also, several alternative methods of scaling fluxes from leaf to canopy level exist. The selected method assumes that scaling is performed when the limiting rates $J_c$, $J_e$, and $J_s$ are computed.

- *Nitrogen limitations*: Nitrogen dynamics are not accounted for in the current model implementation. However, if vegetation dynamics are addressed for a humid environment, nutrient pools of major compartments and soil will need to be considered. Since the maximum photosynthetic rate, Rubisco enzyme, electron transport rates, and respiration rate have been shown to co-vary with leaf nitrogen content, a nitrogen profile in the canopy is assumed. The central assumption is that leaf nitrogen content acclimates fully to prevailing light conditions within a canopy and is proportional to the radiation-weighted time-mean profile of PAR. A simple exponential

description of radiation attenuation is used to describe the profile of PAR with the time-mean PAR extinction coefficient $\bar{K}$ (see Section 4.4.1).

- *Stress-induced tissue loss*: Since no mechanistic model exists describing plant response to drought/cold conditions, heuristic functions of foliage loss are assumed (see Section 4.4.3). Many plants may also reduce biomass of other tissues (e.g., fine roots) in response to stress. This, however, is not represented in the current version of the model.

- *Vegetation phenology model*: For deciduous *trees and shrubs*, a period of maximum growth is assumed following dormant state. When trees/shrubs enter the maximum growth state, the preferred allocation is made to leaves. When a critical amount of foliage is attained (40-50% of the maximum LAI a given stem and root biomass can support according to equation (4.58)), vegetation transitions to normal growth stage and assimilated carbon is also allocated to sapwood and roots. Also, for consistent estimation of a number of statistics, PFTs are assumed to be in dormant state at least once a year.

- *Vegetation structural attributes*: The vegetation fraction for all species is the same as the *fractional projective cover* of canopy of an "average" individual (for grasses, only one individual is assumed), scaled to the population level for a given element. Since the vegetation fraction is also used in estimating the element-scale hydrological quantities, such as the latent heat flux/transpiration, the same fraction is simultaneously associated with the below-ground fraction of lateral spread of roots. For woody species, the stem area index $S_{ind}$ of an "average" individual is assumed to be 25% of its leaf area index $L_{ind}$. Also, dynamics of the plant height $H_v$ for woody species needs to be developed. A suitable approach is the "pipe model" of Shinozaki et al. (1964).

- *Plant recruitment, growth seedling*: As an additional mechanism to carbon uptake by existing canopy, recruitment from seeds introduces new biomass into the vegetation system. A current limitation of the model is that only *herbaceous* species can regenerate through seeds. Seed germination and seedling establishment represent functions of favorable temperatures and sufficient amounts of water at appropriate depths in the soil profile and at certain times during the year. Seed dispersal mechanisms are not considered and seeds are assumed to be present in soil in sufficient quantities to result in the new biomass corresponding to leaf area index $L = 0.0025$, which is added to the foliage pool of a given grass type during the recruitment event (the recruitment root biomass is calculated from the allometric relationship (4.58) and is added to the grass root pool).

- *Root biomass profile*: One of the major assumptions made in the model is the **time-invariance of the root distribution profile and its invariance among the soil types**. It is recognized that the root biomass distribution reflects the adaptive properties of vegetation dynamics to soil

water and temperature stress, which are characteristic for a given soil type. Consequently, the simulated grass dynamics are affected, exhibiting distinct differences among the considered soil types.

- *Competition of plant types for resources*: Only $C_4$ grass is used in the study to represent the vegetation dynamic behavior. No effects of plant interaction are therefore introduced, which could significantly modify the observed patterns. Furthermore, if several plants co-exist in the same computational domain, the model assumes that plants do not explicitly compete for light and water, i.e., the respective location of PFTs to each other and the effects of shading are not explicitly considered. Instead, these effects are accounted for in an implicit fashion. Plant water uptake properties and the characteristic features of the rooting profiles translate into PFT's differences in ability to access soil moisture and, therefore, impose the competition for available *water*. Above-ground competition for *light* is treated as the competition for available space and is determined from PFT's success to produce biomass. Obviously, the latter form of interaction among PFTs is only applicable to ecosystems with sparse vegetation, where the effects of plant shading are minimal. A more comprehensive approach to representing the competition for light in densely vegetated areas would need to explicitly consider the vertical structure of vegetation organization, i.e., representing the foliage layers of upperstory and understory species.

The net effect of most of the above assumptions should not have a significant impact on the modeled processes and major conclusions of the study. However, a comprehensive sensitivity study can be suggested. It is also highly advisable to substitute some of the heuristic/empirical formulations of the current implementation with models that feature a more solid mechanistic basis.

## 7.3   Future directions

As follows from the preceding section, the employed modeling system contains a number of assumptions. Relaxing or modifying some of them may represent a topic for fruitful research on its own. In the following, several primary potential research directions are outlined and grouped according to the nature of processes involved.

1. **Meteorological forcing**
   - *Rainfall and shortwave radiation*: A more complex model of rainfall forcing can be introduced to represent: a.) intra-storm variability of rainfall inten-

394

sity and b.) the randomness of the rainfall vector (i.e., to representation of rain directions and angles that depend on wind characteristics). A study can be suggested to address the relative role of rainfall time/space variability in facilitating/weakening niches of vegetation favorability. Also, a more comprehensive study on the impact of changes in the rainfall seasonality can be suggested.

- *Shortwave radiation*: Only *self-shading* effects of terrain on the incoming radiation were considered in the discussed study. However, the surrounding topography may also exert the effects of "distant-shading", leading to specific implications for vegetation-hydrology dynamics in certain locations of the watershed terrain. The scale of topography representation becomes an important factor in this case.

2. **Atmosphere biochemistry and climate change**

- *$CO_2$ concentration*: The present background atmospheric $CO_2$ concentration was assumed in the presented study: $c_a = 340 \times 10^{-6} P_{atm}$ $Pa$ ($P_{atm}$ is the atmospheric pressure at the ground level). A further study can be suggested to investigate the linkages between vegetation and hydrology systems in conditions of the predicted rise of the background $CO_2$ concentration.

3. **Soil biochemistry / landscape geomorphology**

- *Soil nutrients*: Since the model development was tailored to applications in arid and semi-arid areas, where water constitutes the major limiting resource, mineralization rates/nutrient supply were assumed to be directly dependent on water availability. Nutrients therefore were not tracked in the vegetation compartments. A further study can address the importance of possible nutrient limitations imposed by soil mineralization rates.

- *Soil development and geomorphological processes*: Natural landscapes represent manifestations of dynamic interactions among climatological, hydrological, vegetation, geomorphological, and soil processes. While the importance of coupling among these processes has long been recognized for studying a number of fundamental questions in geomorphology, ecohydrology, and soil science, few examples of explicit linkages exist. Furthermore, such approaches are typically over-simplified and based on heuristic rules rather than the actual description of physical processes involved. A prospective study can be suggested to focus on aspects of erosion process and landscape evolution in conditions when vegetation-water-energy-soil dynamics are directly accounted for. For example, as demonstrated in this work, hillslopes of different aspects in semi-arid areas may feature significant differences in growing season biomass and litter accumulation. While, on one hand, the apparent differences in erosion susceptibility may promote distinct hillslope evolution regimes, on the other hand, the differences in

thickness and organic content of the soil mantle may favor different plant types. Does vegetation, therefore, actively adjust landscape geomorphic processes to foster itself, thereby introducing self-sustained effects? Consequently, of extreme importance are the questions that address aspects of response/sensitivity of eco-hydro-geomorphic system to disturbances in tectonic processes.

## 4. Perched saturated zone

- *The role of impermeable soil horizon*: Soil properties have a major influence on the partitioning of rainfall into infiltration and runoff. Soils developing in semi-arid climates are characterized by the accumulation of calcium carbonate, which forms a distinct white layer of calcic horizon within a soil. Several studies have shown that the primary source of the calcium carbonate is from atmospheric dust and dissolved rainwater (Gile et al., 1961). The calcic horizon within a soil column acts as an impermeable layer to infiltrated water, which may theoretically lead to the formation of temporary perched saturated zone from storms of significant magnitude. Furthermore, limited water loss to soil lower layers may introduce additional effects in the partition of soil moisture into soil evaporation and transpiration components. The discussed study assumed 1.8 $m$ soil column with no irregularities in the conductivity profile (except for the case of surface sealing scenario) and free gravitational drainage at the column bottom. The impacts of shallow ($\sim 0.5\ m$) impermeable calcic horizon on vegetation function can be therefore addressed in future studies.

## 5. Spatial composition and plant co-existence

- *Semi-arid areas of tree-grass co-existence*: Only $C_4$ grass was used in this study. Major biomes of semi-arid areas, however, exhibit a delicate coexistence of several plant life forms: trees, shrubs, and grasses. The mechanisms that regulate the stability of such ecosystems are not fully understood and only a limited number of studies have attempted to address the problem from a numerical perspective. The following fundamental questions can be investigated in future studies: Given climate, soil, and topography, is there a preferential spatial state in the vegetation system? If so, does it possess any global properties? Are these properties invariant across different landscape geometries and soil textures? What governs the spatial composition of vegetation in water-limited ecosystems? Can coexistence of different species be explained by different water use niches? Or do natural disturbances define the natural composition?

## 6. Dynamic vegetation

- *Dynamic roots*: As pointed out previously, the root biomass distribution reflects the adaptive properties of vegetation dynamics to soil water and

temperature stress, which are characteristic for a given soil type. While this study assumed *static* root profiles, there is a potential to investigate the role of adaptive features of roots in regulating water and nutrient fluxes and whether they would significantly modify the obtained results. A study can be suggested that would feature dynamic coupling between the processes in the above- and below-ground biomass. The study would investigate the rules of adaptation of root systems to environmental stress with important implications for ecohydrological modeling.

- *Dynamic nature of plant function*: In most previous studies, vegetation has been assumed to be a static or known surface condition. Only recently the hydrologic community started gaining insight of how the dynamics of vegetation impact the seasonal, annual, inter-annual and longer-term behavior and variability of the hydrologic and energy cycles. While it is becoming more evident that vegetation is the often-ignored component, a number of open questions exist as to exactly how and when vegetation dynamics are important to be explicitly accounted for in hydrological and hydroclimatological studies: How important is a dynamic (vs. static) representation of vegetation in quantifying the response of the hydrologic and energy cycles to variability in climate? What is the role of vegetation in the partitioning of water and energy in dry and humid climates? Does vegetation attenuate/buffer or enhance the sensitivity of water and energy cycles of the land-surface to climate variability?

# Appendix A

# Clear sky atmospheric transmittances for beam and diffuse radiation

The discussed model formulates the radiative transmittances (considered for both beam and diffuse radiation) for separate atmospheric extinction layers: ozone absorption (the subscript 'O' in the following), Rayleigh scattering (the subscript 'R'), uniformly mixed gases absorption (the subscript 'G'), water vapor absorption (the subscript 'W'), and aerosol scattering and absorption (the subscript 'A'). Two bands of solar spectrum are considered: the ultraviolet (UV) / visible (VIS) band, $B_{\Lambda 1}$, [0.29 $\mu m$ ÷ 0.70 $\mu m$], where ozone absorption and molecular scattering are concentrated, and the infra-red in near and short wavelength range (NIR), $B_{\Lambda 2}$, [0.70 $\mu m$ ÷ 4.0 $\mu m$], where water and mixed gases absorptions are concentrated. The model was derived by Gueymard (1989) and reproduced here for reference.

## A.1   Direct beam irradiance

The *ozone* transmittances, $T_{Oi}$ [−], for the two considered bands are calculated as

$$T_{O1} \;=\; 1 - e^{-2.5686 + 0.6706\ln(m_o u_o)} \;,\qquad\qquad\text{(A.1)}$$

$$T_{O2} = 1.0, \tag{A.2}$$

where $u_o$ [$cm$] is the ozone amount in a vertical column and $m_o$ is the ozone mass:

$$m_o = \frac{13.5}{(181.25 \sin^2 h_\oplus + 1)^{0.5}}, \tag{A.3}$$

where $h_\oplus$ [$radian$] is the solar altitude (Section 2.3.1). Van Heuklon [1979] provides an approximation for seasonal changes of $u_o$ as a function of geographic location and day of the year. However, a constant value is used in this work equal to 0.34 [$cm$].

The transmittances corresponding to *Rayleigh scattering*, $T_{Oi}$ [$-$], are

$$T_{R1} = e^{-m_R \sigma_{R\lambda1}}, \tag{A.4}$$

$$T_{R2} = 0.999523 - 0.010274 m_R + 7.375 \times 10^{-5} m_R^2, \tag{A.5}$$

where $m_R$ is the absolute optical air mass and $\sigma_{R\lambda1}$ is the Rayleigh spectral optical thickness. The former variable is defined as

$$m_R = (p/p_0) m_{air}, \tag{A.6}$$

where $m_{air}$ is the relative air mass that depends on the solar altitude $h_\oplus$ ($h_{D\oplus}$ is used below to denote the solar altitude expressed in angular degrees):

$$m_{air} = \frac{1}{\sin h_\oplus + 0.15(h_{D\oplus} + 3.885)^{-1.253}}, \tag{A.7}$$

and ($p/p_0$) is a correction for the difference in pressures at the watershed ($p$) and sea level ($p_0$) for a given mean basin elevation $Z_{bas}$ [$m$]:

$$(p/p_0) = e^{-Z_{bas}/8434.5}. \tag{A.8}$$

The term $\sigma_{R\lambda1}$ is estimated as a function of the optical air mass $m_R$:

$$\sigma_{R\lambda1} = 1 - e^{(-0.24675 + 0.0639 \ln(1+m_R) - 0.00436 \ln^2(1+m_R))}. \tag{A.9}$$

The transmittances corresponding to the absorption effects by the uniformly *mixed gases* (mainly $O_2$ and $CO_2$), $T_{Gi}$ [−], are estimated as

$$T_{G\lambda 1} = 1,\tag{A.10}$$

$$T_{G\lambda 1} = 0.9776 - 0.0094\ln m_R - 0.0019\ln^2 m_R.\tag{A.11}$$

The *water vapor* transmittances, $T_{Wi}$ [−], are given as

$$T_{W1} = 1.0,\tag{A.12}$$

$$T_{W2} = 0.8221 - 0.0519\ln u_W - 0.0033\ln u_W,\tag{A.13}$$

where $u_W = m_W w_p$, $0.1 < u_W < 100$ [cm], $w_p$ [cm] is the precipitable water and $m_W$ is the water vapor optical mass:

$$m_W = \frac{1}{\sin h_\oplus + 0.0548(h_{D\oplus} + 2.65)^{-1.452}}.\tag{A.14}$$

The precipitable water $w_p$ can be obtained from measurements at meteorological stations. In the presented work, it is estimated from the simulated dew point temperature (Section 2.7.1) according to an empirical model of Iqbal (1983):

$$w_p = e^{0.07T_{dew}-0.075}.\tag{A.15}$$

The average *aerosol* transmittances, $T_{Ai}$ [−], are estimated for each band $i$ as

$$T_{Ai} = e^{-m_A\beta_i\lambda_{ei}^{-\alpha_i}},\tag{A.16}$$

where $m_A$ is the aerosol optical mass, $\lambda_{ei}$ is the effective wavelength for band $B_i$, and $\alpha_i$ and $\beta_i$ are the Angström turbidity parameters. The expression (A.16) is derived for $0.05 < m_A\beta < 8$ and $0.5 < \alpha < 2.5$.

Similar to water vapor, most of the aerosols are concentrated in the first two or three kilometers above sea level. Therefore, it is assumed that the aerosol optical

mass $m_A$ is equal to the water vapor optical mass, $m_W$ (A.14) (Gueymard, 1989).

The turbidity parameter $\beta$ is a function of aerosol loading of the atmosphere. It is around 0 for an ideal dust-free atmosphere, while values greater than 1 have been estimated in extremely turbid environments. Mean monthly values of $\beta$ are tabulated for various stations (Iqbal, 1983). For hourly calculations, a relationship between $\beta$ and visibility may be used since the latter is often available (Iqbal, 1983). In this work, the parameter $\beta$ is considered as one of the calibration parameters of the discussed atmospheric transmittance model and is assumed to be the same for both bands. It is also assumed to be seasonally constant.

The turbidity parameter $\alpha$ is a function of aerosol size: low values of $\alpha$ correspond to large particles and large values of $\alpha$ correspond to small particles. In most studies, however, a seasonally constant value $\alpha_1 = \alpha_2 = 1.3$ is assumed (Gueymard, 1989). This same value is also used in the following.

The effective wavelength $\lambda_{ei}$ for band $B_i$ is estimated as:

$$\lambda_{ei} \;=\; a_{i0} + a_{i1}u_A + a_{i2}u_A^2,\qquad (A.17)$$

where

$$u_A \;=\; \ln(1 + m_A\beta),\qquad (A.18)$$

$$a_{10} \;=\; 0.510941 - 0.028607\alpha_1 + 0.006835\alpha_1^2,\qquad (A.19)$$

$$a_{11} \;=\; -0.026895 + 0.054857\alpha_1 + 0.006872\alpha_1^2,\qquad (A.20)$$

$$a_{12} \;=\; 0.009649 + 0.005536\alpha_1 - 0.009349\alpha_1^2,\qquad (A.21)$$

$$a_{20} \;=\; 1.128036 - 0.0642\alpha_2 + 0.005276\alpha_2^2,\qquad (A.22)$$

$$a_{21} \;=\; -0.032851 + 0.036112\alpha_2 + 0.005066\alpha_2^2,\qquad (A.23)$$

$$a_{22} \;=\; 0.027787 + 0.064655\alpha_2 - 0.021385\alpha_2^2.\qquad (A.24)$$

As follows from the outlined above model, the following variables are required for estimation of $T_{Oi}$, $T_{Ri}$, $T_{Gi}$, $T_{Wi}$, and $T_{Ai}$: $h_\oplus$ [$radian$], $u_o$ [$cm$], $Z_{bas}$ [$m$], $w_p$ [$cm$], $\alpha$ [$-$], and $\beta$ [$-$]. As specified above, variables $u_o$ and $\alpha$ are assumed to be constant,

variable $Z_{bas}$ is estimated as the mean catchment elevation, variables $h_\oplus$ and $w_p$ are updated dynamically from the simulation of the Sun position (with respect to the central point of a given watershed, Section 2.3.1) and simulation of air humidity (Section 2.7.1), respectively. $\beta$ is assumed to be the model calibration parameter (Section 2.3.2).

## A.2   Diffuse irradiance

The diffuse irradiance at the ground level in the discussed model is estimated assuming that some fractions of Rayleigh (molecular), $B_R$, and aerosol, $B_A$, *scattered* fluxes (A.1) are directed downwards:

$$B_R = 0.5, \tag{A.25}$$

$$B_A = 1 - e^{(-0.6931 - 1.8326 \sin h_\oplus)}. \tag{A.26}$$

Both considered scattered fluxes are further assumed to undergo absorption by the aerosols (Gueymard, 1989).

The aerosol transmittances due to scattering, $T_{Asi}$, and absorption, $T_{Aai}$, are estimated as

$$T_{Asi} = e^{\omega_{Ai} \ln T_{Ai}}, \tag{A.27}$$

$$T_{Aai} = \frac{T_{Ai}}{T_{Asi}}, \tag{A.28}$$

where $\omega_{Ai}$ is the aerosol single-scattering albedo, a function of the aerosol optical characteristics, which varies with the origin of air masses and pollution levels, among other factors. Gueymard (1989) provides a set of values for different standard aerosol characteristics. These values are reproduced in Table A.1 for reference.

The sky albedo (Section 2.3.1), $\rho_{si}$, results from the reflectance of the diffuse flux emanating from the ground on the scattering layers (molecules and aerosols). It is

403

Table A.1: Band-average values of the single-scattering albedo for different types of aerosol (after Gueymard (1989)).

| Band / Aerosol type | Maritime | Rural average | Rural urban | Urban average | Urban polluted |
|---|---|---|---|---|---|
| $[0.29\ \mu m \div 0.70\ \mu m]$ | 0.965 | 0.931 | 0.865 | 0.800 | 0.667 |
| $[0.70\ \mu m \div 2.70\ \mu m]$ | 0.913 | 0.832 | 0.754 | 0.676 | 0.518 |
| $[0.29\ \mu m \div 2.70\ \mu m]$ | 0.940 | 0.883 | 0.811 | 0.740 | 0.595 |

expressed as:

$$\rho_{si} = \left[(1 - B'_R)(1 - T'_{Ri}) + (1 - B'_A)(1 - T'_{Asi})T'_{Ri}\right] T'_{Gi} T'_{Wi} T'_{Aai}. \qquad (A.29)$$

The primes in the above equations indicate that the values are computed for the effective value of the relative optical masses equal to 1.66 (Gueymard, 1989). Equations from Section A.1 are used for these purposes assuming $m_R = m_W = m_A = 1.66$.

The back-scattered diffuse flux component is a rather strong function of the spatial average regional albedo (Section 2.3.1), $\rho_g$ [−], another parameter used in the estimation of the diffuse irradiance. $\rho_g$ is assumed to be wavelength independent with typical values around 0.10-0.25 for snow-free environments. In the discussed framework, $\rho_g$ is assumed to be constant for a considered domain.

# Appendix B

# Cloud transmittances for beam and diffuse radiation

According to Stephens (1978), the optical thickness, $\tau_N$, is one of the most important parameters needed to describe the radiative properties of clouds. Approximate range for $\tau_N$ is $5 < \tau_N < 500$. By considering a set of "standard" cloud types, Stephens (1978) derives that $\tau_N$ can be approximately parameterized in terms of the effective radius of cloud-droplet size distribution, $r_e$ [$\mu m$], and liquid water path, $LWP$ [$g\ m^{-2}$]:

$$\tau_N \approx \frac{1.5\ LWP}{r_e}. \tag{B.1}$$

Liquid water path can be formally defined as the integral of the liquid water content from the cloud base to the cloud top. By considering two spectral intervals $[0.30\,\mu m \div 0.75\,\mu m]$ and $[0.75\,\mu m \div 4.0\,\mu m]$ for the set of "standard" cloud types, Stephens (1978) also derives the following relationships:

$$\log_{10}(\tau_{N1}) = 0.2633 + 1.7095\ln(\log_{10}(LWP)), \tag{B.2}$$

$$\log_{10}(\tau_{N2}) = 0.3492 + 1.6518\ln(\log_{10}(LWP)), \tag{B.3}$$

where expression (B.2) refers to the first considered spectral band, where absorption by cloud droplets is extremely small, and expression (B.3) refers to the second band,

where absorption is significant. It follows from equations (B.1), (B.2), and (B.3) that the knowledge of $LWP$ allows one to obtain an approximate estimate of $r_e$. Slingo (1989) introduced a parameterization that provided a more accurate estimate of cloud radiative properties based on $r_e$. This parameterization is used in the following.

Slingo (1989) considered four spectral bands, one in UV/VIS and three in NIR wavelength intervals: $[0.25\,\mu m \div 0.69\,\mu m]$, $[0.69\,\mu m \div 1.19\,\mu m]$, $[1.19\,\mu m \div 2.38\,\mu m]$, $[2.38\,\mu m \div 4.0\,\mu m]$ with the following respective fractions $k_j$, $j = 1, \ldots, 4$ of solar irradiance at the top of the atmosphere in each band: 0.46628316, 0.31963484, 0.180608, 0.033474. Following the parameterization of Slingo (1989), cloud transmittances and reflectances are estimated separately for each of these spectral intervals. The radiative fluxes computed for these four bands are then scaled to the two principal bands $B_{\Lambda i}$, $i = 1, \ldots, 2$, $[0.29\,\mu m \div 0.7\,\mu m]$ and $[0.70\,\mu m \div 4.0\,\mu m]$, considered in the presented framework (Section 2.3.1).

# B.1  Direct beam irradiance

For a given spectral interval, the single scattering properties of typical water clouds can be parameterized in terms of the liquid water path (provided $r_e$ is known):

$$\tau_j = LWP\left(a_j + \frac{b_j}{r_e}\right), \tag{B.4}$$

$$\tilde{\omega}_j = 1 - (c_j + d_j r_e), \tag{B.5}$$

$$g_j = e_j + f_j r_e, \tag{B.6}$$

where $\tau_i$ is the cloud optical depth, $\tilde{\omega}_i$ is the single scatter albedo, $g_i$ is the asymmetry parameter, and $a_j$, $b_j$, $c_j$, $d_j$, $e_j$, $f_j$ are the coefficients of the parameterization (provided in Table B.1). For clarity, the subscript $j$ is omitted in the following.

The transmissivity for the direct beam radiation is

$$T_{DB} = e^{\left[-(1-\tilde{\omega}f)\frac{\tau}{\sin h_\oplus}\right]}. \tag{B.7}$$

## B.2 Diffuse irradiance

Using the same notation as in B.1 and omitting the subscripts that denote a particular spectral band:

$$\beta_0 = \frac{3}{7}(1-g),\tag{B.8}$$

$$\beta(h_\oplus) = 0.5 - \frac{3\sin h_\oplus g}{4(1+g)},\tag{B.9}$$

$$f = g^2,\tag{B.10}$$

$$U_1 = \frac{7}{4},\tag{B.11}$$

$$U_2 = \frac{7}{4}\left[1 - \frac{(1-\tilde\omega)}{7\tilde\omega\beta_0}\right],\tag{B.12}$$

$$\alpha_1 = U_1[1-\tilde\omega(1-\beta_0)],\tag{B.13}$$

$$\alpha_2 = U_2\tilde\omega\beta_0,\tag{B.14}$$

$$\alpha_3 = (1-f)\tilde\omega\beta(h_\oplus),\tag{B.15}$$

$$\alpha_4 = (1-f)\tilde\omega(1-\beta(h_\oplus)),\tag{B.16}$$

$$\epsilon = \sqrt{\alpha_1^2 - \alpha_2^2},\tag{B.17}$$

$$M = \frac{\alpha_2}{\alpha_1+\epsilon},\tag{B.18}$$

$$E = e^{-\epsilon\tau},\tag{B.19}$$

$$\gamma_1 = \frac{(1-\tilde\omega f)\alpha_3 - \sin h_\oplus(\alpha_1\alpha_3 + \alpha_2\alpha_4)}{(1-\tilde\omega f)^2 - \epsilon^2\sin^2 h_\oplus},\tag{B.20}$$

$$\gamma_2 = \frac{-(1-\tilde\omega f)\alpha_4 - \sin h_\oplus(\alpha_1\alpha_4 + \alpha_2\alpha_3)}{(1-\tilde\omega f)^2 - \epsilon^2\sin^2 h_\oplus},\tag{B.21}$$

where the $U_1$ and $U_2$ are the reciprocals of the effective cosines for the diffuse upward and downward fluxes respectively, $\beta_0$ is the fraction of the scattered diffuse radiation, which is scattered into the backward hemisphere, and $\beta(h_\oplus)$ is the same for the direct radiation.

The diffuse reflectivity for diffuse incident radiation is

$$R_{DIF} = \frac{M(1-E^2)}{1-E^2 M^2},\tag{B.22}$$

Table B.1: The values of coefficients in equations B.4 - B.6 (after Slingo (1989)).

| Band | $a_j$ $[10^{-2}\,m^2\,g^{-1}]$ | $b_j$ $[\mu m\,m^2\,g^{-1}]$ | $c_j$ | $d_j$ $[\mu\,m^{-1}]$ | $e_j$ | $f_j$ $[10^{-3}\,\mu\,m^{-1}]$ |
|---|---|---|---|---|---|---|
| $[0.25\ \mu m \div 0.69\ \mu m]$ | 2.817 | 1.305 | $-5.62 \times 10^{-8}$ | $1.63 \times 10^{-7}$ | 0.829 | 2.482 |
| $[0.69\ \mu m \div 1.19\ \mu m]$ | 2.682 | 1.346 | $-6.94 \times 10^{-6}$ | $2.35 \times 10^{-5}$ | 0.794 | 4.226 |
| $[1.19\ \mu m \div 2.38\ \mu m]$ | 2.264 | 1.454 | $4.64 \times 10^{-4}$ | $1.24 \times 10^{-3}$ | 0.754 | 6.560 |
| $[2.38\ \mu m \div 4.00\ \mu m]$ | 1.281 | 1.641 | $2.01 \times 10^{-1}$ | $7.56 \times 10^{-3}$ | 0.826 | 4.353 |

the diffuse transmissivity for diffuse incident radiation is

$$T_{DIF} \;=\; \frac{E(1 - M^2)}{1 - E^2 M^2}\,, \tag{B.23}$$

and the diffuse transmissivity for direct incident radiation is

$$T_{DIR} \;=\; \left(-\gamma_2 T_{DIF} - \gamma_1 T_{DB} R_{DIF} + \gamma_2 T_{DB}\right). \tag{B.24}$$

# Appendix C

# Parameters of Canopy Radiative Transfer Model

The following parameters are obtained in Sellers (1985)[1].

$$b = 1 - \omega_\Lambda + \omega_\Lambda \beta_\Lambda$$

$$c = \omega_\Lambda \beta_\Lambda$$

$$d = \omega_\Lambda \bar{\mu} K \beta_{0,\Lambda}$$

$$f = \omega_\Lambda \bar{\mu} K (1 - \beta_{0,\Lambda})$$

$$h = \frac{\sqrt{b^2 - c^2}}{\bar{\mu}}$$

$$\sigma = (\bar{\mu} K)^2 + c^2 - b^2$$

$$u_1 = b - \frac{c}{\alpha_{g\Lambda}^\mu} \quad \text{(direct beam)} \quad \text{or} \quad u_1 = b - \frac{c}{\alpha_{g\Lambda}} \quad \text{(diffuse)}$$

$$u_2 = b - c\alpha_{g\Lambda}^\mu \quad \text{(direct beam)} \quad \text{or} \quad u_2 = b - c\alpha_{g\Lambda} \quad \text{(diffuse)}$$

$$u_3 = f + c\alpha_{g\Lambda}^\mu \quad \text{(direct beam)} \quad \text{or} \quad u_2 = f + c\alpha_{g\Lambda} \quad \text{(diffuse)}$$

$$s_1 = e^{-h(L+S)}$$

$$s_2 = e^{-K(L+S)}$$

$$p_1 = b + \bar{\mu} h$$

$$p_2 = b - \bar{\mu} h$$

---

[1] Note the error in $h_4$ in Sellers (1985).

$$p_3 = b + \bar{\mu}K$$

$$p_4 = b - \bar{\mu}K$$

$$d_1 = \frac{p_1(u_1 - \bar{\mu}h)}{s_1} - p_2(u_1 + \bar{\mu}h)s_1$$

$$d_2 = \frac{(u_2 + \bar{\mu}h)}{s_1} - (u_2 - \bar{\mu}h)s_1$$

$$h_1 = -dp_4 - cf$$

$$h_2 = \frac{1}{d_1}\left[\left(d - \frac{h_1}{\sigma}p_3\right)\frac{(u_1 - \bar{\mu}h)}{s_1} - p_2\left(d - c - \frac{h_1}{\sigma}(u_1 + \bar{\mu}K)\right)s_2\right]$$

$$h_3 = -\frac{1}{d_1}\left[\left(d - \frac{h_1}{\sigma}p_3\right)(u_1 + \bar{\mu}h)s_1 - p_1\left(d - c - \frac{h_1}{\sigma}(u_1 + \bar{\mu}K)\right)s_2\right]$$

$$h_4 = -fp_3 - cd$$

$$h_5 = -\frac{1}{d_2}\left[\frac{h_4(u_2 + \bar{\mu}h)}{\sigma s_1} + \left(u_3 - \frac{h_4}{\sigma}(u_2 - \bar{\mu}K)\right)s_2\right]$$

$$h_6 = \frac{1}{d_2}\left[\frac{h_4}{\sigma}(u_2 - \bar{\mu}h)s_1 + \left(u_3 - \frac{h_4}{\sigma}(u_2 - \bar{\mu}K)\right)s_2\right]$$

$$h_7 = \frac{c(u_1 - \bar{\mu}h)}{d_1 s_1}$$

$$h_8 = -\frac{c(u_1 + \bar{\mu}h)s_1}{d_1}$$

$$h_9 = \frac{(u_2 + \bar{\mu}h)}{d_2 s_1}$$

$$h_{10} = -\frac{s_1(u_2 - \bar{\mu}h)}{d_2}$$

The vegetation leaf and stem reflectances in VIS and NIR bands ($\alpha_\Lambda^{leaf}, \alpha_\Lambda^{stem}$), transmittances ($\tau_\Lambda^{leaf}, \tau_\Lambda^{stem}$), the departure of leaf angles from a random distribution $\chi_L$, and soil albedos for the direct beam $\alpha_{g\Lambda}^{\mu}$ and diffuse $\alpha_{g\Lambda}$ radiative flux need to be known to estimate the above parameters.

# Appendix D

# Richards infiltration model with evapotranspiration and lateral moisture exchange

## D.1 Derivation of an implicit finite-element numerical scheme with Picard iteration

The fluid flow into unsaturated soil is governed by the Richards partial differential equation (Hillel, 1980). When moisture content $\theta$ $[mm^3 \ mm^{-3}]$ is used as a dependent variable, Richards equation for a sloped surface, where the subsurface fluxes are balanced, is expressed as

$$\frac{\partial \theta}{\partial t} = \frac{\partial}{\partial z} \left( D(\theta) \frac{\partial \theta}{\partial z} - K(\theta) \cos \alpha_{\triangledown} \right), \tag{D.1}$$

where $K(\theta)$ $[mm \ hour^{-1}]$ is the unsaturated hydraulic conductivity, $D(\theta)$ $[mm^2 \ hour^{-1}]$ is the unsaturated diffusivity, $\alpha_{\triangledown}$ $[radian]$ is the slope of the soil surface (Section 2.3.1), $t$ $[hour]$ is time, and $z$ $[mm]$ denotes the *normal* to the soil's surface coordinate assumed to be positive downward. Because Richards equation is highly non-linear, analytical solution is not possible except for special cases. Numerical approximations

are typically used to solve equation (D.1). Using a backward Euler time-marching scheme, equation (D.1) can be written as

$$\frac{\theta^{n+1} - \theta^n}{\Delta t} - \frac{\partial}{\partial z}\left(D^{n+1}\frac{\partial\theta^{n+1}}{\partial z} - K^{n+1}\cos\alpha_\nabla\right) = 0, \qquad (D.2)$$

where $\theta^n$ denotes the approximate value of $\theta$ at the $n$th discrete time level $(t = t^n)$, $\Delta t = t^{n+1} - t^n$ is the time step, $D^{n+1}$ and $K^{n+1}$ denote diffusivity and hydraulic conductivity evaluated using $\theta^{n+1}$, respectively, and the solution is assumed to be known at time level $n$ and unknown at time level $n + 1$. Because $D$ and $K$ are non-linear functions of $\theta$, some linearization must be introduced into (D.2). The Picard iteration method involves sequential estimates of the unknown $\theta^{n+1}$ using the latest estimates of $D^{n+1}$ and $K^{n+1}$. If $m$ identifies the iteration level, then the Picard iteration scheme can be written as (Celia et al., 1990)

$$\frac{\theta^{n+1,m+1} - \theta^n}{\Delta t} - \frac{\partial}{\partial z}\left(D^{n+1,m}\frac{\partial\theta^{n+1,m+1}}{\partial z} - K^{n+1,m}\cos\alpha_\nabla\right) = R_P^{n+1,m}. \quad (D.3)$$

As follows from (D.3), at each iteration $D$ and $K$ are evaluated using $\theta$ at the old iteration level thus linearizing the equations. $R_P^{n+1,m}$ is the residual associated with the Picard iteration, a measure of the amount by which the temporally discretized equation fails to be satisfied by the $m$th iterative estimate $\theta^{n+1,m}$. Upon convergence in iteration, both $R_P^{n+1,m}$ and the difference in iteration $(\theta^{n+1,m+1} - \theta^{n+1,m})$ approach zero. Both of these measures are used to check the convergence of the scheme.

It is useful to recast (D.3) in terms of the $\theta$ increment at each iteration level: $\theta^{n+1,m+1} - \theta^{n+1,m} = \delta\theta^{n+1,m}$ and thus $\frac{\partial\theta^{n+1,m+1}}{\partial z} = \frac{\partial\theta^{n+1,m}}{\partial z} + \frac{\partial(\delta\theta^{n+1,m})}{\partial z}$. Equation (D.3) can be accordingly re-written as

$$\frac{\theta^{n+1,m} - \theta^n}{\Delta t} + \frac{\delta\theta^{n+1,m}}{\Delta t} - \frac{\partial}{\partial z}\left(D^{n+1,m}\left(\frac{\partial\theta^{n+1,m}}{\partial z} + \frac{\partial(\delta\theta^{n+1,m})}{\partial z}\right) - K^{n+1,m}\cos\alpha_\nabla\right) = R_P^{n+1,m}. \quad (D.4)$$

To complete the discretization, a spatial approximation is required. The finite-
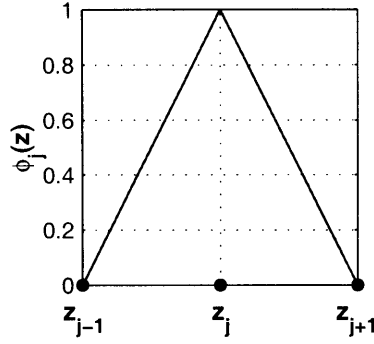
Figure D-1: Piece-wise linear Lagrange polynomial.

element method is chosen for these purposes, which assumes discretization of the domain into a number of sub-domains called elements. The elements do not necessarily have equal length, which is convenient if some part of the domain needs to be represented at a higher detail. The spatial approximation is generated by using an interpolating polynomial that approximate $\theta$ as well as $D$ and $K$:

$$\theta(z,t) = \sum_{j=1}^{N} \theta_j(t)\phi_j(z), \qquad (D.5)$$

$$K(\theta) = \sum_{j=1}^{N} K(\theta_j)\phi_j(z), \qquad (D.6)$$

$$D(\theta) = \sum_{j=1}^{N} D(\theta_j)\phi_j(z), \qquad (D.7)$$

where $\phi_j(z)$ is a basis function and $N$ is the total number of considered nodes ($N - 1$ is the total number of elements). In the following, piece-wise linear Lagrange polynomials are used as the basis functions (Figure D-1):

$$\phi_j(z) = \frac{z - z_{j-1}}{\Delta z_{j-1}}, \quad z_{j-1} \le z \le z_j$$

$$\phi_j(z) = \frac{z_{j+1} - z}{\Delta z_{j+1}}, \quad z_j \le z \le z_{j+1}$$

$$\phi_j(z) = 0, \quad \text{all other } z. \qquad (D.8)$$

By using Galerkin finite-element method, a weight function is introduced in (D.4) with the objective being to select $\theta_j(t)$ such that the residual $R_P^{n+1,m}$ is minimized.

413

This is accomplished by setting the integral of the weighted residual to zero:

$$\int_{\Omega_z} \left[ \frac{\delta\theta^{n+1,m}}{\Delta t} - \frac{\partial}{\partial z} \left( D^{n+1,m} \frac{\partial(\delta\theta^{n+1,m})}{\partial z} \right) \right] \phi_i(z) dz =$$
$$\int_{\Omega_z} \left[ -\frac{\theta^{n+1,m} - \theta^n}{\Delta t} + \frac{\partial}{\partial z} \left( D^{n+1,m} \frac{\partial\theta^{n+1,m}}{\partial z} - K^{n+1,m} \cos\alpha_\nabla \right) \right] \phi_i(z) dz, \text{(D.9)}$$

where $\phi_i(z)$ is the weight function and $\Omega_z \in [0, L]$ is the spatial domain ranging from the ground surface, $z = 0$, to the bottom of the considered soil column, $z = L$. Note that Galerkin method assumes the same functional form for the weight function as for the basis function (D.8). Integrating by parts the terms of (D.9):

$$\int_{\Omega_z} \frac{\partial}{\partial z} \left( D^{n+1,m} \frac{\partial(\delta\theta^{n+1,m})}{\partial z} \right) \phi_i(z) dz =$$
$$D^{n+1,m} \frac{\partial(\delta\theta^{n+1,m})}{\partial z} \phi_i(z) \Big|_0^L - \int_{\Omega_z} D^{n+1,m} \frac{\partial(\delta\theta^{n+1,m})}{\partial z} \frac{\partial\phi_i(z)}{\partial z} dz, \quad \text{(D.10)}$$

$$\int_{\Omega_z} \frac{\partial}{\partial z} \left( D^{n+1,m} \frac{\partial\theta^{n+1,m}}{\partial z} \right) \phi_i(z) dz =$$
$$D^{n+1,m} \frac{\partial\theta^{n+1,m}}{\partial z} \phi_i(z) \Big|_0^L - \int_{\Omega_z} D^{n+1,m} \frac{\partial\theta^{n+1,m}}{\partial z} \frac{\partial\phi_i(z)}{\partial z} dz, \quad \text{(D.11)}$$

The first term on the right side of equation (D.10) can be neglected because $\delta\theta \to 0$ as the iteration scheme converges. The first term on the right side of equation (D.11) is evaluated only at the boundaries and represents imposed boundary conditions. The term may be neglected if constant moisture values are imposed at the surface and bottom of the soil column (Neumann boundary conditions); however, it must be included when constant flux boundary conditions are imposed. In the following, $D^{n+1,m} \frac{\partial\theta^{n+1,m}}{\partial z} \phi_i(z) \Big|_0^L = [q^{n+1}\phi_i(z)] \Big|_0^L$. Re-arranging the terms of (D.9), one can obtain:

$$\int_{\Omega_z} \frac{\delta\theta^{n+1,m}}{\Delta t} \phi_i(z) dz + \int_{\Omega_z} D^{n+1,m} \frac{\partial(\delta\theta^{n+1,m})}{\partial z} \frac{\partial\phi_i(z)}{\partial z} dz =$$
$$-\int_{\Omega_z} \frac{\theta^{n+1,m} - \theta^n}{\Delta t} \phi_i(z) dz$$
$$-\int_{\Omega_z} D^{n+1,m} \frac{\partial\theta^{n+1,m}}{\partial z} \frac{\partial\phi_i(z)}{\partial z} dz$$

$$- \int_{\Omega_z} \frac{\partial K^{n+1,m}}{\partial z} \cos \alpha_\triangledown \phi_i(z) dz + \left[ q^{n+1} \phi_i(z) \right] \Big|_0^L , \qquad (D.12)$$

Substituting (D.5) - (D.7) into (D.12) results in:

$$\sum_{j=1}^N \frac{\delta \theta_j^{n+1,m}}{\Delta t} \int_0^L \phi_j(z) \phi_i(z) dz$$

$$+ \sum_{j=1}^N \delta \theta_j^{n+1,m} \sum_{l=1}^N D_l^{n+1,m} \int_0^L \phi_l(z) \frac{\partial \phi_j(z)}{\partial z} \frac{\partial \phi_i(z)}{\partial z} dz =$$

$$- \sum_{j=1}^N \frac{\theta_j^{n+1,m} - \theta_j^n}{\Delta t} \int_0^L \phi_j(z) \phi_i(z) dz$$

$$- \sum_{j=1}^N \theta_j^{n+1,m} \sum_{l=1}^N D_l^{n+1,m} \int_0^L \phi_l(z) \frac{\partial \phi_j(z)}{\partial z} \frac{\partial \phi_i(z)}{\partial z} dz$$

$$- \sum_{l=1}^N K_l^{n+1,m} \cos \alpha_\triangledown \int_0^L \frac{\partial \phi_l(z)}{\partial z} \phi_i(z) dz + \left[ q^{n+1} \phi_i(z) \right] \Big|_0^L , \qquad (D.13)$$

If a consistent approximation of the temporal derivative is used (sometimes referred as the "$L1$ scheme"), the terms of the above equation can be integrated (Zarba, 1988) using the definition of the basis functions (D.8) to obtain:

$$\sum_{j=1}^N \frac{\delta \theta_j^{n+1,m}}{\Delta t} \int_{\Omega_z} \phi_j(z) \phi_i(z) dz = \delta \theta_{i-1}^{n+1,m} \frac{\Delta z_{i-1}}{6 \Delta t} +$$

$$\delta \theta_i^{n+1,m} \frac{(\Delta z_{i-1} + \Delta z_i)}{3 \Delta t} +$$

$$\delta \theta_{i+1}^{n+1,m} \frac{\Delta z_i}{6 \Delta t} , \qquad (D.14)$$

$$\sum_{j=1}^N \frac{(\theta_j^{n+1,m} - \theta_j^n)}{\Delta t} \int_{\Omega_z} \phi_j(z) \phi_i(z) dz = (\theta_{i-1}^{n+1,m} - \theta_{i-1}^n) \frac{\Delta z_{i-1}}{6 \Delta t} +$$

$$(\theta_i^{n+1,m} - \theta_i^n) \frac{(\Delta z_{i-1} + \Delta z_i)}{3 \Delta t} +$$

$$(\theta_{i+1}^{n+1,m} - \theta_{i+1}^n) \frac{\Delta z_i}{6 \Delta t} . \qquad (D.15)$$

As can be seen, using the time-consistent approximation leads to the temporal derivatives that are distributed in space around nodes $i - 1$, $i$, and $i + 1$. The other terms

of (D.13) are obtained in a similar fashion:

$$\sum_{j=1}^{N} \delta\theta_j^{n+1,m} \sum_{l=1}^{N} D_l^{n+1,m} \int_0^L \phi_l(z) \frac{\partial \phi_j(z)}{\partial z} \frac{\partial \phi_i(z)}{\partial z} dz =$$

$$\frac{1}{2} \left[ -\frac{D_{i-1}^{n+1,m} + D_i^{n+1,m}}{\Delta z_{i-1}} \right] \delta\theta_{i-1}^{n+1,m} +$$

$$\frac{1}{2} \left[ \frac{D_{i-1}^{n+1,m}}{\Delta z_{i-1}} + D_i^{n+1,m} \left( \frac{1}{\Delta z_{i-1}} + \frac{1}{\Delta z_i} \right) + \frac{D_{i+1}^{n+1,m}}{\Delta z_i} \right] \delta\theta_i^{n+1,m} +$$

$$\frac{1}{2} \left[ -\frac{D_{i+1}^{n+1,m} + D_i^{n+1,m}}{\Delta z_i} \right] \delta\theta_{i+1}^{n+1,m} , \qquad \text{(D.16)}$$

$$\sum_{j=1}^{N} \theta_j^{n+1,m} \sum_{l=1}^{N} D_l^{n+1,m} \int_0^L \phi_l(z) \frac{\partial \phi_j(z)}{\partial z} \frac{\partial \phi_i(z)}{\partial z} dz =$$

$$\frac{1}{2} \left[ -\frac{D_{i-1}^{n+1,m} + D_i^{n+1,m}}{\Delta z_{i-1}} \right] \theta_{i-1}^{n+1,m} +$$

$$\frac{1}{2} \left[ \frac{D_{i-1}^{n+1,m}}{\Delta z_{i-1}} + D_i^{n+1,m} \left( \frac{1}{\Delta z_{i-1}} + \frac{1}{\Delta z_i} \right) + \frac{D_{i+1}^{n+1,m}}{\Delta z_i} \right] \theta_i^{n+1,m} +$$

$$\frac{1}{2} \left[ -\frac{D_{i+1}^{n+1,m} + D_i^{n+1,m}}{\Delta z_i} \right] \theta_{i+1}^{n+1,m} , \qquad \text{(D.17)}$$

$$\sum_{l=1}^{N} K_l^{n+1,m} \cos\alpha_{\triangledown} \int_0^L \frac{\partial \phi_l(z)}{\partial z} \phi_i(z) dz = \frac{K_{i+1}^{n+1,m} - K_{i-1}^{n+1,m}}{2} \cos\alpha_{\triangledown} , \quad \text{(D.18)}$$

From the above derivations, one can obtain a complete time-consistent numerical approximation of Richards equation that uses Picard iteration. For convenience, the numerical scheme below considers only interior nodes (boundary nodes will be considered later):

$$\left[ \frac{\Delta z_{i-1}}{6\Delta t} - \frac{D_{i-1}^{n+1,m} + D_i^{n+1,m}}{2\Delta z_{i-1}} \right] \delta\theta_{i-1}^{n+1,m} +$$

$$\left[ \frac{\Delta z_{i-1} + \Delta z_i}{3\Delta t} + \frac{1}{2} \left( \frac{D_{i-1}^{n+1,m}}{\Delta z_{i-1}} + D_i^{n+1,m} \left( \frac{1}{\Delta z_{i-1}} + \frac{1}{\Delta z_i} \right) + \frac{D_{i+1}^{n+1,m}}{\Delta z_i} \right) \right] \delta\theta_i^{n+1,m} +$$

$$\left[ \frac{\Delta z_i}{6\Delta t} - \frac{D_{i+1}^{n+1,m} + D_i^{n+1,m}}{2\Delta z_i} \right] \delta\theta_{i+1}^{n+1,m} =$$

$$-(\theta_{i-1}^{n+1,m} - \theta_{i-1}^{n})\frac{\Delta z_{i-1}}{6\Delta t} - (\theta_{i}^{n+1,m} - \theta_{i}^{n})\frac{(\Delta z_{i-1} + \Delta z_i)}{3\Delta t} - (\theta_{i+1}^{n+1,m} - \theta_{i+1}^{n})\frac{\Delta z_i}{6\Delta t}$$

$$+\frac{1}{2}\left[\frac{D_{i-1}^{n+1,m} + D_{i}^{n+1,m}}{\Delta z_{i-1}}\right]\theta_{i-1}^{n+1,m}$$

$$-\frac{1}{2}\left[\frac{D_{i-1}^{n+1,m}}{\Delta z_{i-1}} + D_{i}^{n+1,m}\left(\frac{1}{\Delta z_{i-1}} + \frac{1}{\Delta z_i}\right) + \frac{D_{i+1}^{n+1,m}}{\Delta z_i}\right]\theta_{i}^{n+1,m}$$

$$+\frac{1}{2}\left[\frac{D_{i+1}^{n+1,m} + D_{i}^{n+1,m}}{\Delta z_i}\right]\theta_{i+1}^{n+1,m} - \frac{K_{i+1}^{n+1,m} - K_{i-1}^{n+1,m}}{2}\cos\alpha_{\triangledown}. \tag{D.19}$$

As noted above, the time-consistent approximation results in temporal derivatives that are distributed in space. Celia et al. (1990) and others identified this distribution of mass as the source of oscillations that are present in the solution. The oscillations in the solution can be eliminated or greatly reduced in size by employing a temporal lumping scheme (Bouloutas, 1989). The lumping scheme that is used in the presented modeling framework is the $L2$ scheme of Milly (1985). The $L2$ scheme modifies the terms of (D.14)-(D.15) as

$$\sum_{j=1}^{N}\frac{\delta\theta_{j}^{n+1,m}}{\Delta t}\int_{\Omega_z}\phi_j(z)\phi_i(z)dz \simeq$$

$$\frac{\delta\theta_{i}^{n+1,m}}{\Delta t}\int_{\Omega_z}\phi_i(z)dz = \delta\theta_{i}^{n+1,m}\frac{(\Delta z_{i-1} + \Delta z_i)}{2\Delta t}, \tag{D.20}$$

$$\sum_{j=1}^{N}\frac{(\theta_{j}^{n+1,m} - \theta_{j}^{n})}{\Delta t}\int_{\Omega_z}\phi_j(z)\phi_i(z)dz \simeq$$

$$\frac{(\theta_{i}^{n+1,m} - \theta_{i}^{n})}{\Delta t}\int_{\Omega_z}\phi_i(z)dz = (\theta_{i}^{n+1,m} - \theta_{i}^{n})\frac{(\Delta z_{i-1} + \Delta z_i)}{2\Delta t}. \tag{D.21}$$

The effect of the lumping scheme is to diagonalize the temporal matrix. The final numerical scheme with $L2$ lumping can be written for interior nodes as

$$\left[-\frac{D_{i-1}^{n+1,m} + D_{i}^{n+1,m}}{\Delta z_{i-1}}\right]\delta\theta_{i-1}^{n+1,m}+$$

$$\left[\frac{\Delta z_{i-1} + \Delta z_i}{\Delta t} + \left(\frac{D_{i-1}^{n+1,m}}{\Delta z_{i-1}} + D_{i}^{n+1,m}\left(\frac{1}{\Delta z_{i-1}} + \frac{1}{\Delta z_i}\right) + \frac{D_{i+1}^{n+1,m}}{\Delta z_i}\right)\right]\delta\theta_{i}^{n+1,m} +$$

$$\left[-\frac{D_{i+1}^{n+1,m} + D_{i}^{n+1,m}}{\Delta z_i}\right]\delta\theta_{i+1}^{n+1,m} =$$

$$-(\theta_{i}^{n+1,m} - \theta_{i}^{n})\frac{(\Delta z_{i-1} + \Delta z_i)}{\Delta t}$$

$$+ \left[ \frac{D_{i-1}^{n+1,m} + D_i^{n+1,m}}{\Delta z_{i-1}} \right] \theta_{i-1}^{n+1,m}$$

$$- \left[ \frac{D_{i-1}^{n+1,m}}{\Delta z_{i-1}} + D_i^{n+1,m} \left( \frac{1}{\Delta z_{i-1}} + \frac{1}{\Delta z_i} \right) + \frac{D_{i+1}^{n+1,m}}{\Delta z_i} \right] \theta_i^{n+1,m}$$

$$+ \left[ \frac{D_{i+1}^{n+1,m} + D_i^{n+1,m}}{\Delta z_i} \right] \theta_{i+1}^{n+1,m} - \left( K_{i+1}^{n+1,m} - K_{i-1}^{n+1,m} \right) \cos \alpha_\nabla . \qquad (D.22)$$

Using the *constant flux* (Dirichlet) boundary conditions for $[q^{n+1}\phi_i(z)] \big|_0^L$ from (D.12), the numerical scheme (D.22) can be written for the boundary nodes as

$i = 1:$

$$\left[ \frac{\Delta z_1}{\Delta t} + \frac{D_1^{n+1,m} + D_2^{n+1,m}}{\Delta z_1} \right] \delta\theta_1^{n+1,m} + \left[ -\frac{D_1^{n+1,m} + D_2^{n+1,m}}{\Delta z_1} \right] \delta\theta_2^{n+1,m} =$$

$$-(\theta_1^{n+1,m} - \theta_1^n)\frac{\Delta z_1}{\Delta t}$$

$$- \left[ \frac{D_1^{n+1,m} + D_2^{n+1,m}}{\Delta z_1} \right] \theta_1^{n+1,m} + \left[ \frac{D_1^{n+1,m} + D_2^{n+1,m}}{\Delta z_1} \right] \theta_2^{n+1,m}$$

$$- \left( K_2^{n+1,m} + K_1^{n+1,m} \right) \cos \alpha_\nabla + 2\, q_{infl} , \qquad (D.23)$$

$i = N:$

$$\left[ -\frac{D_{N-1}^{n+1,m} + D_N^{n+1,m}}{\Delta z_{N-1}} \right] \delta\theta_{N-1}^{n+1,m} + \left[ \frac{\Delta z_{N-1}}{\Delta t} + \frac{D_{N-1}^{n+1,m} + D_N^{n+1,m}}{\Delta z_{N-1}} \right] \delta\theta_N^{n+1,m} =$$

$$-(\theta_N^{n+1,m} - \theta_N^n)\frac{\Delta z_{N-1}}{\Delta t}$$

$$+ \left[ \frac{D_{N-1}^{n+1,m} + D_N^{n+1,m}}{\Delta z_{N-1}} \right] \theta_{N-1}^{n+1,m} - \left[ \frac{D_{N-1}^{n+1,m} + D_N^{n+1,m}}{\Delta z_{N-1}} \right] \theta_N^{n+1,m}$$

$$+ \left( K_{N-1}^{n+1,m} + K_N^{n+1,m} \right) \cos \alpha_\nabla - 2\, q_{rech}^{n+1,m} , \qquad (D.24)$$

where $q_{infl}$ $[mm\ hour^{-1}]$ is the flux at the upper boundary (soil's surface), which may include direct rainfall, drainage from the canopy, dew moisture, and melted snow water; $q_{rech}^{n+1,m}$ $[mm\ hour^{-1}]$ is the outflux from the soil column from the bottom node and is assumed to be the gravitational drainage only: $q_{rech}^{n+1,m} = K_N^{n+1,m} \cos \alpha_\nabla$.

The system of algebraic equations generated by writing equations (D.22)-(D.24) for each node can be written as

$$A^{n+1,m}\, \delta\theta^{n+1,m} = B^{n+1,m} , \qquad (D.25)$$

418

where $A^{n+1,m}$ is a tridiagonal Picard iteration matrix and $B^{n+1,m}$ is a finite-element approximation of the governing equation (D.1) evaluated at iteration level $m$. As a result, the right hand side of (D.22) provides a measure of the failure of the $m$th iterate to solve the finite-element equation. The vector $B^{n+1,m}$ can thus be thought of as a residual and is used as the convergence criterion for the iteration scheme. The difference between the soil moisture at successive iteration levels, $\delta\theta^{n+1,m}$, is also used as a convergence criterion.

## D.2 Evapotranspiration and lateral moisture exchange

The system of equations (D.22)-(D.24) can be used to simulate infiltration in areas where both the net subsurface lateral exchange in the unsaturated zone and evapotranspiration flux are zero. The former condition can hold for some sections of planar hillslopes, located sufficiently away from the boundaries, and the latter can be true for certain hydrometeorological conditions and vegetation states. When one needs to consider a domain of an arbitrary geometrical configuration, subject to a variety of possible hydrometeorological and vegetation states, such conditions are rare and a more general formulation of (D.22)-(D.24) is required. This can be achieved by adding the corresponding sink/source terms into the formulation for each node of the soil column:

$$A^{n+1,m}\,\delta\theta^{n+1,m} \;\;=\;\; B^{n+1,m} - 2\,E^{n+1} + 2\,(q_{in}^{n+1} - q_{out}^{n+1,m})\,, \qquad (\text{D.26})$$

where $E^{n+1}$ $[mm\ hour^{-1}]$ is a sink corresponding to evapotranspiration flux, $q_{in}^{n+1}$ $[mm\ hour^{-1}]$ is a source due to subsurface influx, and $q_{out}^{n+1,m}$ $[mm\ hour^{-1}]$ is a sink due to lateral drainage. The subscript '$n+1$' used for subsurface influx and evapotranspiration implies that these terms are pre-defined and do not change during the iteration step. The lateral drainage, $q_{out}^{n+1,m}$, however, is iteratively computed based on $\theta^{n+1,m}$. An estimation methodology for each of the terms follows.

## D.2a Lateral outflux

Spatially-distributed hydrological models typically operate on three-dimensional domains that are discretized into computational elements in a certain fashion. When a control-volume approach is used to estimate the subsurface dynamics, a single three-dimensional element is considered at a time. Mass transfer between the elements is used to relate the local subsurface dynamics to the dynamics that occur upstream of a given element. For the control-volume approach, the down slope outflux from the node $i$ of (D.22)-(D.24) for a soil that exhibits anisotropy *parallel* to the slope (Philip, 1991) can be approximated with a *gravity-driven flow* as

$$q_{out,i}^{n+1,m} = a_r K_i^{n+1,m} \sin \alpha_\nabla \Delta z_i' q_D', \qquad (D.27)$$

where $a_r$ $[-]$ is the anisotropy ratio between the parallel and normal to the slope hydraulic conductivities and:

$$\Delta z_i' = \frac{\Delta z_i}{2}, \quad i = 1, \qquad (D.28)$$

$$\Delta z_i' = \frac{\Delta z_{i-1} + \Delta z_i}{2}, \quad 1 < i < N, \qquad (D.29)$$

$$\Delta z_i' = \frac{\Delta z_{i-1}}{2}, \quad i = N, \qquad (D.30)$$

$$q_D' = \frac{W_{VR} \cos \alpha_\nabla}{A_{VR}}, \qquad (D.31)$$

where $W_{VR}$ $[mm]$ is the width of the interface through which the subsurface flow occurs (the Voronoi flow width, Section 3.3) and $A_{VR}$ $[mm^2]$ is the surface area of the considered element projected on a horizontal plane (the Voronoi area). As can be seen, $\Delta z_i' q_D'$ is a conversion factor that is used to obtain the consistent mass flow rate units $[mm \ hour^{-1}]$. The total down slope outflux from the considered element, $Q_{S\,out}$ $[mm^3 \ hour^{-1}]$, is obtained at the end of the simulation time step via the summation of the gravity-driven flow components at various depths of the unsaturated zone:

$$Q_{S\,out} = \frac{A_{VR}}{\cos \alpha_\nabla} \sum_i^N q_{out,i}^{n+1}. \qquad (D.32)$$

## D.2b Lateral influx

Since several upstream elements may contribute their flow to a single downstream cell, the subsurface unsaturated lateral influx $Q_{Sin}$ $[mm\ hour^{-1}]$ into a given element can generally be expressed as

$$Q_{Sin} = \frac{\cos \alpha_{\triangledown}}{A_{VR}} \sum_{l}^{N_{VR}} Q_{Sout,l},$$  (D.33)

where $N_{VR}$ is the total number of contributing upstream elements. Since $Q_{Sin}$ is simply a bulk quantity, it has to be distributed along the soil profile to obtain the sources terms for (D.22)-(D.24). It is assumed in the presented modeling framework that the subsurface influx into a given element is distributed with depth *in a similar fashion as the profile of hydraulic conductivities at the time step* $(t-1)$, i.e., preceding the iteration:

$$q_{in,i}^{n+1} = Q_{Sin} \frac{K_i^n \Delta z_i'}{K^{n'}},$$  (D.34)

where $K^{n'} = \sum_{i}^{N} K_i^n \Delta z_i'$. The above assumption states that for a given element the moisture influx into the soil column would be higher in the areas of higher unsaturated hydraulic conductivity and smaller in the areas where the hydraulic conductivity is relatively smaller.

## D.2c Evapotranspiration

Soil evaporation is simply a sink term for the first node, $(i = 1)$, of the soil profile:

$$E_1 = \sum_{k}^{N_V} E_{g,k}^{veg}\ f_{v,k} + \left(1 - \sum_{k}^{N_V} f_{v,k}\right) E_g^{bare},$$  (D.35)

where $f_{v,k}$ $[-]$ is a vegetation fraction of the $k$th plant functional type present in a given element (Section 4.4.8), $N_V$ is the total number of vegetation types present in the element, $E_{g,k}^{veg}$ $[mm\ hour^{-1}]$ is the under-canopy soil evaporation from the $k$th vegetated fraction (Section 3.6.3b), and $E_g^{bare}$ $[mm\ hour^{-1}]$ is the evaporation from

bare soil (Section 3.6.3a).

Transpiration flux represents sink terms distributed with depth according to the fractional root biomass profile $r_{i,k}$ [−], $i = 1 \ldots I_{root,k}$ of the $k$th vegetation type present in the element (Section 3.4, note that $\sum_{i}^{I_{root,k}} r_{i,k} = 0.95$). Since the soil moisture profile $\theta(z)$ from the time step $(t - 1)$ is used to estimate the transpiration flux $E_{T,k}^{veg}$ (Section 3.6.3b), the transpiration factor $\beta_T(z)$ [−] is also used to obtain the terms $E_i$ [$mm\ hour^{-1}$], $i = 1 \ldots I_{root,k}$:

$$E_i = \sum_{k}^{N_V} E_{T,k}^{veg} \frac{\beta_{T,i,k}\ r_{i,k}}{\beta_{T,k}}\ f_{v,k}\,, \qquad (D.36)$$

where

$$\beta_{T,i,k} = \max\left[0,\ \min\left(1,\ \frac{\theta_i - \theta_{w,k}}{\theta_k^* - \theta_{w,k}}\right)\right]\,, \quad \text{if } T_{soil} > 273.15\,, \qquad (D.37)$$

$$\beta_{T,i,k} = 0.01\,, \qquad\qquad\qquad\qquad \text{if } T_{soil} \le 273.15\,, \qquad (D.38)$$

$$\beta_{T,k} = \sum_{i}^{I_{root,k}} \beta_{T,i,k}\ r_{i,k}\,, \qquad (D.39)$$

where $\theta_{w,k}$ [$mm^3\ mm^{-3}$] is the wilting point, $\theta_k^*$ [$mm^3\ mm^{-3}$] is the threshold soil moisture contents of the $k$th vegetation type (Section 4.3) and $T_{soil}$ is estimated according to Section 3.6.4 (used to constrain transpiration if soil temperature drops below the freezing point).

## D.2d Root zone drainage and capillary rise

Besides the contributions from evapotranspiration and lateral drainage in the soil moisture balance, it is also important to know the net moisture exchange at the bottom of the root zone. Moisture drainage and, therefore, water loss may occur when there is water excess in the root zone. Capillary rise is characteristic for situations when the root zone is drier than deeper soil layers: the root zone gains moisture in this case. The net flux [$mm\ hour^{-1}$] is estimated by the following integration:

$$Q_{D\,out} = (\Omega_1 - 2\,q_{infl}) + \frac{(\theta_i^{n+1} - \theta_i^n)\Delta z_1}{\Delta t} +$$

422

$$\sum_{i=2}^{I_{root}} \Omega_i + \frac{(\theta_i^{n+1} - \theta_i^n)(\Delta z_{i-1} + \Delta z_i)}{\Delta t} \, , \tag{D.40}$$

where $I_{root} \leq N$, $\Omega_1$ is the right-hand side of equation (D.23) and $\Omega_i$ is the right-hand side of equation (D.22). If $Q_{D\,out}$ is positive, it represents drainage. In the opposite case, it represents capillary rise.

# References

[1] Aguiar, R., and Collares-Pereira, M. (1992). TAG - a Time-Dependent, Autoregressive, Gaussian model for generating synthetic hourly radiation, *Solar Energy*, 49(3): 167-174.

[2] Ahmed, J. (1974). *Optimization of water-use efficiency in crop production systems by dynamic simulation of crop behavior under stochastic regimes*. Ph.D. Thesis, Texas A&M University, College Station, TX, USA.

[3] Ambroise, B. (1995). Topography and the water cycle in a temperate middle mountain environment - the need for interdisciplinary experiments, *Agricultural and Forest Meteorology*, 73(3-4): 217-235.

[4] Arora, V.K. (2002). Modeling vegetation as a dynamic component in soil-vegetation-atmosphere transfer schemes and hydrological models, *Reviews of Geophysics*, 40(2): 3-1 - 3-26.

[5] Arora, V.K., and Boer, G.J. (2002). A GCM-based assessment of the global moisture budget and the role of land-surface moisture reservoirs in processing precipitation, *Climate Dynamics*, 20(1): 13-29.

[6] Arora, V.K., and Boer, G.J. (2005). A parameterization of leaf phenology for the terrestrial ecosystem component of climate models, *Global Change Biology*, 11(1): 39-59.

[7] Arya, S.P. (2001). *Introduction to Micrometeorology*. 2nd ed. Academic Press, New York, NY, USA, 420 pp.

[8] Avissar, R. (1998). Which type of soil-vegetation-atmosphere transfer scheme is needed for general circulation models: a proposal for a higher-order scheme, *Journal of Hydrology*, 213(1-4): 136-154.

[9] Ball, J.T., Woodrow, I.E., and Berry, J.A. (1987). A model predicting stomatal conductance and is contribution to the control of photosynthesis under different environmental conditions. In: J. Biggins (Editor), *Progress in Photosynthesis Research*. Martinus Nijhoff, Zoetermeer, The Netherlands, pp. 221-224.

[10] Balzter, H., Braun, P.W., and Kohler, W. (1998). Cellular automata models for vegetation dynamics, *Ecological Modelling*, 107(2-3): 113-125.

[11] Band, L.E., Patterson, P., Nemani, R., and Running, S.W. (1993). Forest ecosystem processes at the watershed scale - incorporating hillslope hydrology, *Agricultural and Forest Meteorology*, 63(1-2): 93-126.

[12] Band, L.E., Peterson, D.L., Running, S.W., Coughlan, J., Lammers, R., Dungan, J., and Nemani, R. (1991). Forest ecosystem processes at the watershed scale - basis for distributed simulation, *Ecological Modelling*, 56(1-4): 171-196.

[13] Becker, S. (2001). Calculation of direct solar and diffuse radiation in Israel, *International Journal of Climatology*, 21(12): 1561-1576.

[14] Ben Wu, X., and Archer, S.R. (2005). Scale-dependent influence of topography-based hydrologic features on patterns of woody plant encroachment in savanna landscapes, *Landscape Ecology*, 20(6): 733-742.

[15] Benjamin, J.R., and Cornell, C.A., (1970). *Probability, Statistics and Decision for Civil Engineers*. McGraw-Hill, New York, NY, USA.

[16] Bernacchi, C.J., Singsaas, E.L., Pimentel, C., Portis, A.R., and Long, S.P. (2001). Improved temperature response functions for models of Rubisco-limited photosynthesis, *Plant Cell and Environment*, 24(2): 253-259.

[17] Beven, K., and Germann, P. (1982). Macropores and water-flow in soils, *Water Resources Research*, 18(5): 1311-1325.

[18] Beven, K.J. (1986). Runoff production and flood frequency in catchments of order n: an alternative approach. In: V.K. Gupta, et al. (Editor), *Scale problems in hydrology*. Kluwer Acad. Publ., Dordecht, The Netherlands, pp. 107-131.

[19] Beven, K.J., and Kirkby, M.J. (1979). Physically based, variable contributing area model of basin hydrology, *Hydrol. Sci. Bull. Sci. Hydrol.*, 24(1): 43-69.

[20] Beyschlag, W., Lange, O.L., and Tenhunen, J.D. (1986). Photosynthesis and water relations of the Mediterranean evergreen sclerophyll *Arbutus unedo L.* throughout the year at a site in Portugal. 1. Diurnal courses of $CO_2$ gas-exchange and transpiration under natural conditions, *Flora*, 178(6): 409-444.

[21] Blocken, B., Carmeliet, J., and Poesen, J. (2005). Numerical simulation of the wind-driven rainfall distribution over small-scale topography in space and time, *Journal of Hydrology*, 315(1-4): 252-273.

[22] Bonan, G.B. (1995). Land-atmosphere interactions for climate system models - coupling biophysical, biogeochemical, and ecosystem dynamical processes, *Remote Sensing of Environment*, 51(1): 57-73.

[23] Bonan, G.B. (1996). *A land surface model (LSM version 1.0) for ecological, hydrological, and atmospheric studies: technical description and user's guide.* NCAR Technical Note NCAR/ TN-417, NCAR, Boulder, CO, USA.

[24] Bonan, G.B., Levis, S., Kergoat, L., and Oleson, K.W. (2002). Landscapes as patches of plant functional types: An integrating concept for climate and ecosystem models, *Global Biogeochemical Cycles*, 16(2).

[25] Bouloutas, E.T. (1989). *Improved numerical methods for modeling flow and transport processes in partially saturated porous media.* Ph.D. Thesis, Massachusetts Institute of Technology, Cambridge, MA, USA.

[26] Bowling, L.C., Storck, P., and Lettenmaier, D.P. (2000). Hydrologic effects of logging in western Washington, United States, *Water Resources Research*, 36(11): 3223-3240.

[27] Bras, R.L. (1990). *An Introduction to Hydrologic Science.* Addison-Wesley-Longman, Reading, MA, USA, 643 pp.

[28] Bronstert, A. (1999). Capabilities and limitations of detailed hillslope hydrological modelling, *Hydrological Processes*, 13(1): 21-48.

[29] Brooks, R.H., and Corey, A.T. (1964). *Hydraulic properties of porous media.* Hydrological Paper 3, Colorado State University, Fort Collins, CO, USA.

[30] Brown, B.G., Katz, R.W., and Murphy, A.H. (1984). Time-series models to simulate and forecast wind-speed and wind power, *Journal of Climate and Applied Meteorology*, 23(8): 1184-1195.

[31] Brutsaert, W. (1982). *Evaporation into the atmosphere: theory, history, and applications.* D. Reidel Publ. Co., Dordecht, The Netherlands.

[32] Bryan, J.G. (1964). *Short range hour-by-hour forecast of temperature by projecting the characteristic curve with constants fitted to immediately preceding data.* Unpublished report, The Travelers Research Center, Inc., Hartford, CT, USA.

[33] Bugmann, H. (2001). A review of forest gap models, *Climatic Change*, 51(3-4): 259-305.

[34] Buishand, T.A. (1978). Some remarks on use of daily rainfall models, *Journal of Hydrology*, 36(3-4): 295-308.

[35] Burdine, N.T. (1953). Relative permeability calculations from pore size distributions data, *Journal of Petroleum Technology*, 5: 71-78.

[36] Campbell, D.I. (1989). Energy-balance and transpiration from tussock grassland in New-Zealand, *Boundary-Layer Meteorology*, 46(1-2): 133-152.

[37] Carlin, J., and Haslett, J. (1982). The probability-distribution of wind power from a dispersed array of wind turbine generators, *Journal of Applied Meteorology*, 21(3): 303-313.

[38] Caylor, K.K., Manfreda, S., and Rodriguez-Iturbe, I. (2005). On the coupled geomorphological and ecohydrological organization of river basins, *Advances in Water Resources*, 28(1): 69-86.

[39] Celia, M.A., Bouloutas, E.T., and Zarba, R.L. (1990). A general mass-conservative numerical solution for the unsaturated flow equation, *Water Resources Research*, 26(7): 1483-1496.

[40] Chia, E., and Hutchinson, M.F. (1991). The beta-distribution as a probability model for daily cloud duration, *Agricultural and Forest Meteorology*, 56(3-4): 195-208.

[41] Chin, E.H. (1977). Modeling daily precipitation occurrence process with Markov-Chain, *Water Resources Research*, 13(6): 949-956.

[42] Choudhury, B.J., and Monteith, J.L. (1988). A 4-layer model for the heat-budget of homogeneous land surfaces, *Quarterly Journal of the Royal Meteorological Society*, 114(480): 373-398.

[43] Collatz, G.J., Ball, J.T., Grivet, C., and Berry, J.A. (1991). Physiological and environmental regulation of stomatal conductance, photosynthesis and transpiration - a model that includes a laminar boundary-layer, *Agricultural and Forest Meteorology*, 54(2-4): 107-136.

[44] Collatz, G.J., Ribas-Carbo, M., and Berry, J.A. (1992). Coupled photosynthesis-stomatal conductance model for leaves of C4 plants, *Australian Journal of Plant Physiology*, 19(5): 519-538.

[45] Cordova, J.R., and Bras, R.L. (1981). Physically-based probabilistic models of infiltration, soil moisture, and actual evapotranspiration, *Water Resources Research*, 17(1): 93-106.

[46] Cox, P.M., Betts, R.A., Bunton, C.B., Essery, R.L.H., Rowntree, P.R., and Smith, J. (1999). The impact of new land surface physics on the GCM simulation of climate and climate sensitivity, *Climate Dynamics*, 15(3): 183-203.

[47] Cox, P.M., Huntingford, C., and Harding, R.J. (1998). A canopy conductance and photosynthesis model for use in a GCM land surface scheme, *Journal of Hydrology*, 213(1-4): 79-94.

[48] Crawford, R.M.M. (1989). Studies in plant survival. Ecological case histories to plant adaptation to adversity, *Studies in Ecology, Volume 11*. Blackwell Scientific Publications, Oxford, U.K.

[49] Crawley, M.J. (1986). *Plant Ecology*. Blackwell Scientific Publications, Oxford, U.K.

[50] Curtis, D.C., and Eagleson, P.S. (1982). *Constrained Stochastic Climate Simulation*. Technical Report 274, Massachusetts Institute of Technology, Department of Civil and Environmental Engineering, Ralph M. Parsons Laboratory, Cambridge, MA, USA.

[51] Dai, Y.J., Dickinson, R.E., and Wang, Y.P. (2004). A two-big-leaf model for canopy temperature, photosynthesis, and stomatal conductance, *Journal of Climate*, 17(12): 2281-2299.

[52] de Pury, D.G.G., and Farquhar, G.D. (1997). Simple scaling of photosynthesis from leaves to canopies without the errors of big-leaf models, *Plant Cell and Environment*, 20(5): 537-557.

[53] De Vries, D.A. (1963). Thermal properties of soils. In: W.R. van Wijk (Editor), *Physics of Plant Environment*. John Wiley, New York, NY, USA.

[54] Dickinson, R.E. (1983). Land surface processes and climate surface albedos and energy balance, *Advances in Geophysics*, 25: 305-353.

[55] Dickinson, R.E. (2000). How coupling of the atmosphere to ocean and land helps determine the timescales of interannual variability of climate, *Journal of Geophysical Research-Atmospheres*, 105(D15): 20115-20119.

[56] Dickinson, R.E., Henderson-Sellers, A., and Kennedy, P.J. (1993). *Biosphere-atmosphere transfer scheme (BATS) version 1E as coupled to the NCAR Community Climate Model.* Technical report NCAR/TN-387+STR, National Center for Atmospheric Research, Boulder, CO, USA.

[57] Dickinson, R.E., Shaikh, M., Bryant, R., and Graumlich, L. (1998). Interactive canopies for a climate model, *Journal of Climate*, 11(11): 2823-2836.

[58] Dietrich, W.E., and Perron, J.T. (2006). The search for a topographic signature of life, *Nature*, 439(7075): 411-418.

[59] Dietrich, W.E., Wilson, C.J., Montgomery, D.R., McKean, J., and Bauer, R. (1992). Erosion thresholds and land surface morphology, *Geology*, 20(8): 675-679.

[60] Dirnbock, T., Hobbs, R.J., Lambeck, R.J., and Caccetta, P.A. (2002). Vegetation distribution in relation to topographically driven processes in southwestern Australia, *Applied Vegetation Science*, 5(1): 147-158.

[61] D'Odorico, P., Ridolfi, L., Porporato, A., and Rodriguez-Iturbe, I. (2000). Preferential states of seasonal soil moisture: The impact of climate fluctuations, *Water Resources Research*, 36(8): 2209-2219.

[62] Dunne, T., and R. D. Black (1970). Partial area contributions to storm runoff in a small new England watershed, *Water Resour. Res.*, 6(5): 1296-1311.

[63] Eagleson, P.S. (1978). Climate, soil, and vegetation. A series of papers: Parts 1-7. *Water Resources Research*, 14(5): 705-776.

[64] Eagleson, P.S. (1982). Ecological optimality in water-limited natural soil-vegetation systems. 1. Theory and hypothesis, *Water Resources Research*, 18(2): 325-340.

[65] Eagleson, P.S. (1994). The evolution of modern hydrology (from watershed to continent in 30 years), *Advances in Water Resources*, 17(1-2): 3-18.

[66] Eagleson, P.S. (2002). *Ecohydrology: Darwinian Expression of Vegetation Form and Function.* Cambridge University Press, Cambridge, U.K., 496 pp.

[67] Eagleson, P.S., and Segarra, R.I. (1985). Water-limited equilibrium of savanna vegetation systems, *Water Resources Research*, 21(10): 1483-1493.

[68] Eltahir, E.A.B. (1996). Role of vegetation in sustaining large-scale atmospheric circulations in the tropics, *Journal of Geophysical Research-Atmospheres*, 101(D2): 4255-4268.

[69] Evans, G.C. (1972). *The quantitative analysis of plant growth.* Blackwell Scientific Publications, Oxford, U.K., 734 pp.

[70] Falls, L.W. (1974). Beta-distribution - statistical model for world cloud cover, *Journal of Geophysical Research*, 79(9): 1261-1264.

[71] Famiglietti, J.S., and Wood, E.F. (1991). Evapotranspiration and runoff from large land areas, *Land Surface-Atmosphere Interaction: Observations, Models and Analysis.* Kluwer Academic, Norwell, MA, USA, pp. 179-204.

[72] Famiglietti, J.S., and Wood, E.F. (1994). Multiscale modeling of spatially-variable water and energy-balance processes, *Water Resources Research*, 30(11): 3061-3078.

[73] Farouki, O.T. (1981). *Thermal Properties of Soils.* CRREL Monograph 81-1, United States Army Cold Regions Research and Engineering Laboratories, Hanover, NH, USA, pp. 134.

[74] Farquhar, G.D., and S. VonCaemmerer (1982). Modelling of photosynthetic response to environmental conditions. In: O.L. Lange, P.S. Nobel, C.B. Osmond and H. Ziegler (Editors), *Encyclopedia of plant physiology. Physiological Plant Ecology II.* Springer-Verlag, Berlin, Germany, pp. 550-587.

[75] Farquhar, G.D., Caemmerer, S.V., and Berry, J.A. (1980). A biochemical model of photosynthetic $CO_2$ assimilation in leaves of C-3 species, *Planta*, 149(1): 78-90.

[76] Fernandez-Illescas, C.P., Porporato, A., Laio, F., and Rodriguez-Iturbe, I. (2001). The ecohydrological role of soil texture in a water-limited ecosystem, *Water Resources Research*, 37(12): 2863-2872.

[77] Field, C., and H. A. Mooney (1986). The photosynthesis-nitrogen relationship in wild plants. In: T.J. Givnish (Editor), *On the economy of plant form and function.* Cambridge University Press, Cambridge, UK.

[78] Florinsky, I.V., and Kuryakova, G.A. (1996). Influence of topography on some vegetation cover properties, *Catena*, 27(2): 123-141.

[79] Foley, J.A., Levis, S., Costa, M.H., Cramer, W., and Pollard, D. (2000). Incorporating dynamic vegetation cover within global climate models, *Ecological Applications*, 10(6): 1620-1632.

[80] Foley, J.A., Prentice, I.C., Ramankutty, N., Levis, S., Pollard, D., Sitch, S., and Haxeltine, A. (1996). An integrated biosphere model of land surface processes, terrestrial carbon balance, and vegetation dynamics, *Global Biogeochemical Cycles*, 10(4): 603-628.

[81] Fourcade, H.G. (1942). Some notes on the effects of the incidence of rain on the distribution of rainfall over the surface of unlevel ground, *Transactions of the Royal Society of South-Africa*, 29(3): 235-254.

[82] Franklin, J. (1998). Predicting the distribution of shrub species in southern California from climate and terrain-derived variables, *Journal of Vegetation Science*, 9(5): 733-748.

[83] Friedlingstein, P., Joel, G., Field, C.B., and Fung, I.Y. (1999). Toward an allocation scheme for global terrestrial carbon models, *Global Change Biology*, 5(7): 755-770.

[84] Friend, A.D., Schugart, H.H., and Running, S.W. (1993). A physiology-based gap model of forest dynamics, *Ecology*, 74(3): 792-797.

[85] Friend, A.D., Stevens, A.K., Knox, R.G., and Cannell, M.G.R. (1997). A process-based, terrestrial biosphere model of ecosystem dynamics (Hybrid v3.0), *Ecological Modelling*, 95(2-3): 249-287.

[86] Gabriel, R., and Neuman, J. (1962). A Markov chain model for daily rainfall occurrence at Tel Aviv, Israel, *Q. J. R. Meteorol, Soc.*, 88: 90-95.

[87] Gile, L.H. (1961). A classification of calcium horizons in the soils of a desert region, Dona Ana County, New Mexico, *Soil Science Society of America Proc.*, pp. 52-61.

[88] Goudrian, J. (1977). *Crop Meteorology: A Simulation Study.* PUDOC - Centre for Agricultural Publishing and Documentation, Wageningen, The Netherlands, 249 pp.

[89] Grace, R.A., and Eagleson, P.S. (1967), A model for generating synthetic sequences of short-time interval depths, Proceed. International Hydrologic Symposium, Fort Collins, Colorado, USA, pp. 268-276.

[90] Grayman, W.M., and Eagleson, P.S. (1969). *Streamflow record length for modeling catchment dynamics.* Technical Report 114, Massachusetts Institute of Technology, Department of Civil and Environmental Engineering, Ralph M. Parsons Laboratory, Cambridge, MA, USA.

[91] Green, P.J., and Sibson, R. (1978). Computing Dirichlet tessellations in plane, *Computer Journal*, 21(2): 168-173.

[92] Groisman, P.Y., Knight, R.W., Karl, T.R., Easterling, D.R., Sun, B.M., and Lawrimore, J.H. (2004). Contemporary changes of the hydrological cycle over the contiguous United States: Trends derived from in situ observations, *Journal of Hydrometeorology*, 5(1): 64-85.

[93] Gueymard, C. (1989). A 2-band model for the calculation of clear sky solar irradiance, illuminance, and photosynthetically active radiation at the earth's surface, *Solar Energy*, 43(5): 253-265.

[94] Guswa, A.J., Celia, M.A., and Rodriguez-Iturbe, I. (2002). Models of soil moisture dynamics in ecohydrology: A comparative study, *Water Resources Research*, 38(9).

[95] Hamilton, E.L. (1954). *Rainfall sampling on rugged terrain*. Tech. Bull. U.S. Dep. Agric. 1096, USDA, Washington, DC, USA, pp. 41.

[96] Hanson, C.L., Cumming, K.A., Woolhiser, D.A., and Richardson, C.W. (1994). *Microcomputer program for daily weather simulations in the contiguous USA*. Agricultural research service ARS-114, USDA, Washington, DC, USA, pp. 38.

[97] Hanson, C.L., and Johnson, G.L. (1998), GEM (Generation of Weather elements for Multiple Applications): Its application in areas of complex terrain, hydrology, water resources and ecology in headwaters Proc. HeadWater '98 Conf., Meran, Italy.

[98] Haslett, J., and Raftery, A.E. (1989). Space-time modeling with long-memory dependence - assessing Ireland's wind power resource, *Applied Statistics-Journal of the Royal Statistical Society Series C*, 38(1): 1-50.

[99] Haxeltine, A., and Prentice, I.C. (1996). BIOME3: An equilibrium terrestrial biosphere model based on ecophysiological constraints, resource availability, and competition among plant functional types, *Global Biogeochemical Cycles*, 10(4): 693-709.

[100] Hennessey, J.P. (1977). Some aspects of wind power statistics, *Journal of Applied Meteorology*, 16(2): 119-128.

[101] Hillel, D. (1980). *Fundamentals of soil physics*. Academic Press, New York, NY, USA, 413 pp.

[102] Hogg, E.H., Price, D.T., and Black, T.A. (2000). Postulated feedbacks of deciduous forest phenology on seasonal climate patterns in the western Canadian interior, *Journal of Climate*, 13(24): 4229-4243.

[103] Houghton, J.T., Ding, Y., Griggs, D.J., Noguer, M., Linden, P.J.v.d., Dai, X., Maskell, K., and Johnson, C.A. (Editors) (2001). IPCC Working Group I Third Assessment Report: *Climate Change 2001: The Scientific Basis.* Cambridge University Press, New York, NY.

[104] Howard, A.D. (1994). A detachment-limited model of drainage-basin evolution, *Water Resources Research*, 30(7): 2261-2285.

[105] Howes, D.A., and Abrahams, A.D. (2003). Modeling runoff and runon in a desert shrubland ecosystem, Jornada Basin, New Mexico, *Geomorphology*, 53(1-2): 45-73.

[106] Hutjes, R.W.A., Kabat, P., Running, S.W., Shuttleworth, W.J., Field, C., Bass, B., Dias, M., Avissar, R., Becker, A., Claussen, M., Dolman, A.J., Feddes, R.A., Fosberg, M., Fukushima, Y., Gash, J.H.C., Guenni, L., Hoff, H., Jarvis, P.G., Kayane, I., Krenke, A.N., Liu, C., Meybeck, M., Nobre, C.A., Oyebande, L., Pitman, A., Pielke, R.A., Raupach, M., Saugier, B., Schulze, E.D., Sellers, P.J., Tenhunen, J.D., Valentini, R., Victoria, R.L., and Vorosmarty, C.J. (1998). Biospheric aspects of the hydrological cycle - Preface, *Journal of Hydrology*, 213(1-4): 1-21.

[107] Ingestad, T., and Lund, B.B. (1986). Theory and techniques for steady state mineral nutrition and growth of plants, *Scandinavian Journal of Forest Research*, 1: 439-453.

[108] Iqbal, M. (1983). *An Introduction to Solar Radiation.* Academic Press, Toronto, Ontario, Canada, 390 pp.

[109] Ivanov, V.Y., Vivoni, E.R., Bras, R.L., and Entekhabi, D. (2004a). Catchment

hydrologic response with a fully distributed triangulated irregular network model, *Water Resources Research*, 40(11).

[110] Ivanov, V.Y., Vivoni, E.R., Bras, R.L., and Entekhabi, D. (2004b). Preserving high-resolution surface and rainfall data in operational-scale basin hydrology: a fully-distributed physically-based approach, *Journal of Hydrology*, 298(1-4): 80-111.

[111] Jackson, R.B., Canadell, J., Ehleringer, J.R., Mooney, H.A., Sala, O.E., and Schulze, E.D. (1996). A global analysis of root distributions for terrestrial biomes, *Oecologia*, 108(3): 389-411.

[112] Jarvis, P.G., and T. A. Mansfield (1981). *Stomatal Physiology*. Cambridge University Press, Cambridge, U.K., 295 pp.

[113] Jeltsch, F., Milton, S.J., Dean, W.R.J., and VanRooyen, N. (1996). Tree spacing and coexistence in semiarid savannas, *Journal of Ecology*, 84(4): 583-595.

[114] Jeltsch, F., and Wissel, C. (1994). Modeling dieback phenomena in natural forests, *Ecological Modelling*, 75: 111-121.

[115] Keane, R.E., Morgan, P., and W., R.S. (1996). *FIRE-BGC - A mechanistic ecological process model for simulating fire succession on coniferous forest landscapes of the Northern Rocky Mountains*. USDA Forest Research Service Paper INT-RP-484, Ogden, UT, USA, pp. 122.

[116] Kim, C.P., Salvucci, G.D., and Entekhabi, D. (1999). Groundwater-surface water interaction and the climatic spatial patterns of hillslope hydrological response, *Hydrology and Earth System Sciences*, 3(3): 375-384.

[117] Kim, Y., and Eltahir, E.A.B. (2004). Role of topography in facilitating coexistence of trees and grasses within savannas, *Water Resources Research*, 40(7).

[118] Kimball, J.S., Running, S.W., and Nemani, R. (1997). An improved method for estimating surface humidity from daily minimum temperature, *Agricultural and Forest Meteorology*, 85(1-2): 87-98.

[119] Kinyamario, J.I., and Imbamba, S.K. (1992). Savanna at Nairobi National Park, Nairobi. In: S.P. Long, M.B. Jones and M.J. Roberts (Editors), *Primary Productivity of Grass Ecosystems of the Tropics and Sub-Tropics*. Chapman & Hall, Pdastow, Cornwall, U.K., pp. 25-69.

[120] Knorr, W. (2000). Annual and interannual $CO_2$ exchanges of the terrestrial biosphere: process-based simulations and uncertainties, *Global Ecology and Biogeography*, 9(3): 225-252.

[121] Kondo, J., and Ishida, S. (1997). Sensible heat flux from the earth's surface under natural convective conditions, *Journal of the Atmospheric Sciences*, 54(4): 498-509.

[122] Kramer, P.J. (1983). *Water Relations of Plants*. Academic Press, London, U.K., 489 pp.

[123] Krinner, G., Viovy, N., de Noblet-Ducoudre, N., Ogee, J., Polcher, J., Friedlingstein, P., Ciais, P., Sitch, S., and Prentice, I.C. (2005). A dynamic global vegetation model for studies of the coupled atmosphere-biosphere system, *Global Biogeochemical Cycles*, 19(1).

[124] Kucharik, C.J., Foley, J.A., Delire, C., Fisher, V.A., Coe, M.T., Lenters, J.D., Young-Molling, C., Ramankutty, N., Norman, J.M., and Gower, S.T. (2000). Testing the performance of a Dynamic Global Ecosystem Model: water balance, carbon balance, and vegetation structure, *Global Biogeochemical Cycles*, 14(3): 795-825.

[125] Kumler, M.P. (1994). An intensive comparison of triangulated irregular networks (TINs) and digital elevation models (DEMs), *Cartographica, Monograph 45*, 31(2): 48pp.

[126] Laio, F., Porporato, A., Ridolfi, L., and Rodriguez-Iturbe, I. (2001a). Plants in water-controlled ecosystems: active role in hydrologic processes and response

to water stress - II. Probabilistic soil moisture dynamics, *Advances in Water Resources*, 24(7): 707-723.

[127] Laio, F., Porporato, A., Fernandez-Illescas, C.P., and Rodriguez-Iturbe, I. (2001b). Plants in water-controlled ecosystems: active role in hydrologic processes and response to water stress - IV. Discussion of real cases, *Advances in Water Resources*, 24(7): 745-762.

[128] Landsberger, J.J. (1986). *Physiological Ecology of Forest Production*. Academic Press, London, U.K., 198 pp.

[129] Leung, L.R., and Wigmosta, M.S. (1999). Potential climate chance impacts on mountain watersheds in the Pacific Northwest, *Journal of the American Water Resources Association*, 35(6): 1463-1471.

[130] Leuning, R. (1995). A critical appraisal of a combined stomatal-photosynthesis model for C-3 plants, *Plant Cell and Environment*, 18(4): 339-355.

[131] Leuning, R., Dunin, F.X., and Wang, Y.P. (1998). A two-leaf model for canopy conductance, photosynthesis and partitioning of available energy. II. Comparison with measurements, *Agricultural and Forest Meteorology*, 91(1-2): 113-125.

[132] Levine, J.B., and Salvucci, G.D. (1999). Equilibrium analysis of groundwater-vadose zone interactions and the resulting spatial distribution of hydrologic fluxes across a Canadian prairie, *Water Resources Research*, 35(5): 1369-1383.

[133] Levis, S., Bonan, G. B., Vertenstein, M., and Oleson, K. W. (2004). *The Community Land Model's Dynamic Global Vegetation Model (CLM-DGVM): Technical description and user's guide*. Technical Note NCAR/TN-459+IA, NCAR, Boulder, CO, USA.

[134] Levitt, J. (1980). *Response of plants to environmental stresses*. 2nd ed., Vol. I. Academic Press, New York, NY, USA, 497 pp.

[135] Ludeke, M.K.B. (1994). The Frankfurt biosphere model: a global process-oriented model of seasonal and long-term $CO_2$ exchange between terrestrial ecosystems and the atmosphere. I. Model description and illustrative results for cold deciduous and boreal forests, *Climate Research*, 4(2): 143-166.

[136] Ludwig, J.A., Wilcox, B.P., Breshears, D.D., Tongway, D.J., and Imeson, A.C. (2005). Vegetation patches and runoff-erosion as interacting ecohydrological processes in semiarid landscapes, *Ecology*, 86(2): 288-297.

[137] Maass, A., Hufschmidt, M.M., Dorfman, R., Thomas, H.A., Jr., Marglin, S.A., and Fair, G.M. (1962). *Design of water-resources systems*. Harvard University Press, Cambridge, MA, USA, 620 pp.

[138] Mackay, D.S. (2001). Evaluation of hydrologic equilibrium in a mountainous watershed: incorporating forest canopy spatial adjustment to soil biogeochemical processes, *Advances in Water Resources*, 24(9-10): 1211-1227.

[139] Mackay, D.S., and Band, L.E. (1997). Forest ecosystem processes at the watershed scale: dynamic coupling of distributed hydrology and canopy growth, *Hydrological Processes*, 11(9): 1197-1217.

[140] Martin, P. (1992). EXE - a climatically sensitive model to study climate change and $CO_2$ enhancement effects on forests, *Australian Journal of Botany*, 40(4-5): 717-735.

[141] Martinez-Mena, M., Albaladejo, J., and Castillo, V.M. (1998). Factors influencing surface runoff generation in a Mediterranean semi-arid environment: Chicamo watershed, SE Spain, *Hydrological Processes*, 12(5): 741-754.

[142] McKean, J.A., Dietrich, W.E., Finkel, R.C., Southon, J.R., and Caffee, M.W. (1993). Quantification of soil production and downslope creep rates from cosmogenic Be-10 accumulations on a hillslope profile, *Geology*, 21(4): 343-346.

[143] Meentemeyer, R.K., Moody, A., and Franklin, J. (2001). Landscape-scale patterns of shrub-species abundance in California chaparral - the role of topographically mediated resource gradients, *Plant Ecology*, 156(1): 19-41.

[144] Milly, P.C.D. (1985). A mass-conservative procedure for time-stepping in models of unsaturated flow, *Advances in Water Resources*, 8(1): 32-36.

[145] Moore, I.D. (1981). Effect of surface sealing on infiltration, *Transactions of the ASAE*, 24(6): 1546-1552.

[146] Nicks, A.D., and Gander, G.A. (1993). *Using CLIGEN to stochastically generate climate data inputs to WEPP and other water resources models*. USGS Water resources investigations Rep. 93-4018, USGS, Denver, CO, USA, pp. 443.

[147] Nicks, A.D., and Gander, G.A. (1994), CLIGEN: A weather generator for climate inputs to water resource and other models, Proceedings Fifth Int. Conf. Computers in Agric., Amer. Soc. Agric. Eng., Orlando, FL, USA, pp. 903-909.

[148] Norman, J.M. (1993). Scaling processes between leaf and canopy levels. In: J. Ehleringer and C. Field (Editors), *Scaling Physiological Processes: Leaf to Globe*. Academic Press, New York, New York, USA, pp. 41-76.

[149] Oleson, K., Dai, Y., Bonan, G., Bosilovich, M., Dickinson, R., Dirmeyer, P., Hoffman, F., Houser, P., Levis, S., Niu, G.-Y., Thornton, P., Vertenstein, M., Yang, Z.-L., and Zeng, X. (2004). *Technical Description of the Community Land Model (CLM)*. Technical Note NCAR/TN-461+STR, NCAR, Boulder, CO, USA.

[150] Olseth, J.A., Skartveit, A., and Zou, H. (1995). Spatially continuous mapping of solar resources in a complex high latitude topography, *Solar Energy*, 55(6): 475-485.

[151] Pacala, S.W., Canham, C.D., Saponara, J., Silander, J.A., Kobe, R.K., and Ribbens, E. (1996). Forest models defined by field measurements: estimation, error analysis and dynamics, *Ecological Monographs*, 66(1): 1-43.

[152] Pacala, S.W., Canham, C.D., and Silander, J.A. (1993). Forest models defined by field-measurements. 1. The design of a Northeastern forest simulator, *Canadian Journal of Forest Research-Revue Canadienne De Recherche Forestiere*, 23(10): 1980-1988.

[153] Palacios-Velez, O.L., and Cuevas-Renaud, B. (1986). Automated river-course, ridge and basin delineation from digital elevation data, *Journal of Hydrology*, 86(3-4): 299-314.

[154] Parlange, M.B., and Katz, R.W. (2000). An extended version of the Richardson model for simulating daily weather variables, *Journal of Applied Meteorology*, 39(5): 610-622.

[155] Peng, C.H. (2000). From static biogeographical model to dynamic global vegetation model: a global perspective on modelling vegetation dynamics, *Ecological Modelling*, 135(1): 33-54.

[156] Peng, C.H., Liu, J.X., Dang, Q.L., Apps, M.J., and Jiang, H. (2002). TRIPLEX: a generic hybrid model for predicting forest growth and carbon and nitrogen dynamics, *Ecological Modelling*, 153(1-2): 109-130.

[157] Penning De Vries, F.W.T. (1975). Cost of maintenance processes in plant-cells, *Annals of Botany*, 39(159): 77-92.

[158] Peters, D.P.C. (2000). Climatic variation and simulated patterns in seedling establishment of two dominant grasses at a semi-arid-arid grassland ecotone, *Journal of Vegetation Science*, 11(4): 493-504.

[159] Philip, J.R. (1991). Hillslope infiltration - planar slopes, *Water Resources Research*, 27(1): 109-117.

[160] Pielke, R.A. (2001). Influence of the spatial distribution of vegetation and soils on the prediction of cumulus convective rainfall, *Reviews of Geophysics*, 39(2): 151-177.

[161] Poesen, J.W.A. (1987). The role of slope angle in surface seal formation. In: V. Gardiner (Editor), *International Geomorphology 1986. Part II.*. Wiley, Chichester, UK, pp. 437-448.

[162] Poesen, J.W.A. (1992). Mechanisms of overland-flow generation and sediment production on loamy sand soils and sandy soils with and without rock fragments. In: A.J. Parsons and A.D. Abrahams (Editors), *Overland Flow: Hydraulics and Erosion Mechanics.* UCL Press, London, UK, pp. 275-305.

[163] Poiani, K.A., and Johnson, W.C. (1993). A spatial simulation-model of hydrology and vegetation dynamics in semi-permanent prairie wetlands, *Ecological Applications,* 3(2): 279-293.

[164] Porporato, A., Laio, F., Ridolfi, L., and Rodriguez-Iturbe, I. (2001). Plants in water-controlled ecosystems: active role in hydrologic processes and response to water stress - III. Vegetation water stress, *Advances in Water Resources,* 24(7): 725-744.

[165] Porporato, A., and Rodriguez-Iturbe, I. (2002). Ecohydrology - a challenging multidisciplinary research perspective, *Hydrological Sciences Journal-Journal Des Sciences Hydrologiques,* 47(5): 811-821.

[166] Press, W.H., Teukolsky, S.A., Vetterling, W.T., and Flannery, B.P. (1999). *Numerical Recipes in C. The Art of Scientific Computing.* 2nd ed. Cambridge University Press.

[167] Priestley, C.H.B., and Taylor, R.J. (1972). On the assessment of surface heat flux and evaporation using large-scale parameters, *Mon. Weather Rev.,* 100: 81-92.

[168] Protopapas, A.L., and Bras, R.L. (1988). State-space dynamic hydrological modeling of soil-crop-climate interactions, *Water Resources Research,* 24(10): 1765-1779.

[169] Protopapas, A.L., and Bras, R.L. (1993). Effects of weather variability and soil

parameter uncertainty on the soil crop climate system, *Journal of Climate*, 6(4): 645-656.

[170] Protopapas, A.L., and L., B.R. (1986). *A model of plant growth and its relation to moisture and solute transport in the soil.* Technical Report 309, Massachusetts Institute of Technology, Department of Civil and Environmental Engineering, Ralph M. Parsons Laboratory, Cambridge, MA, USA.

[171] Ragab, R., Bromley, J., Rosier, P., Cooper, J.D., and Gash, J.H.C. (2003). Experimental study of water fluxes in a residential area: 1. Rainfall, roof runoff and evaporation: the effect of slope and aspect, *Hydrological Processes*, 17(12): 2409-2422.

[172] Rawls, W.J., Brakensiek, D.L., and Saxton, K.E. (1982). Estimation of soil-water properties, *Transactions of the ASAE*, 25(5): 1316-1320.

[173] Remund, J., Kunz, S., and Lang, R. (1999). *Solar engineering handbook. METEONORM: Global meteorological database for solar energy and applied climatology.* Meteotest, Bern, Switzerland.

[174] Restrepo-Posada, P.J., and Eagleson, P.S. (1982). Identification of independent rainstorms, *Journal of Hydrology*, 55(1-4): 303-319.

[175] Richardson, C.W. (1981). Stochastic simulation of daily precipitation, temperature, and solar radiation, *Water Resources Research*, 17(1): 182-190.

[176] Richardson, C.W., and D.A., W. (1984). *WGEN: A model for generating daily weather variables.* Publication ARS-8, USDA Agricultural Research Service, Washington, DC, USA, pp. 83.

[177] Ridolfi, L., D'Odorico, P., Porporato, A., and Rodriguez-Iturbe, I. (2000a). Duration and frequency of water stress in vegetation: an analytical model, *Water Resources Research*, 36(8): 2297-2307.

[178] Ridolfi, L., D'Odorico, P., Porporato, A., and Rodriguez-Iturbe, I. (2000b). Impact of climate variability on the vegetation water stress, *Journal of Geophysical Research-Atmospheres*, 105(D14): 18013-18025.

[179] Ridolfi, L., D'Odorico, P., Porporato, A., and Rodriguez-Iturbe, I. (2003). Stochastic soil moisture dynamics along a hillslope, *Journal of Hydrology*, 272(1-4): 264-275.

[180] Rodriguez-Iturbe, I. (2000). Ecohydrology: A hydrologic perspective of climate-soil-vegetation dynamics, *Water Resources Research*, 36(1): 3-9.

[181] Rodriguez-Iturbe, I., Porporato, A., Ridolfi, L., Isham, V., and Cox, D.R. (1999a). Probabilistic modelling of water balance at a point: the role of climate, soil and vegetation, *Proceedings of the Royal Society of London Series a-Mathematical Physical and Engineering Sciences*, 455(1990): 3789-3805.

[182] Rodriguez-Iturbe, I., D'Odorico, P., Porporato, A., and Ridolfi, L. (1999b). On the spatial and temporal links between vegetation, climate, and soil moisture, *Water Resources Research*, 35(12): 3709-3722.

[183] Rodriguez-Iturbe, I., Entekhabi, D., and Bras, R.L. (1991). Nonlinear dynamics of soil-moisture at climate scales. 1. Stochastic analysis, *Water Resources Research*, 27(8): 1899-1906.

[184] Rodriguez-Iturbe, I., Porporato, A., Laio, F., and Ridolfi, L. (2001). Plants in water-controlled ecosystems: active role in hydrologic processes and response to water stress - I. Scope and general outline, *Advances in Water Resources*, 24(7): 695-705.

[185] Ross, J. (1975). Radiative transfer in plant communities. In: J.L. Monteith (Editor), *Vegetation and the atmosphere*. Academic Press, London, New York, and San Francisco, pp. 13-55

[186] Running, S.W., and Coughlan, J.C. (1988). A general-model of forest ecosystem

processes for regional applications. 1. Hydrologic balance, canopy gas-exchange and primary production processes, *Ecological Modelling*, 42(2): 125-154.

[187] Running, S.W., and Hunt, E.R., Jr. (1993). Generalization of a forest ecosystem process model for other biomes, BIOME-BGC, and an application for global-scale models. In: J.R. Ehleringer and C. Field (Editors), *Scaling Physiological Processes: Leaf to Globe*. Academic Press, San Diego, CA, USA, pp. 141-158.

[188] Rutter, A.J., Kershaw, K.A., Robins, P.C., and Morton, A.J. (1971). A predictive model of rainfall interception in forests. 1. Derivation of the model from observation in a plantation of Corsican pine, *Agric. Meteorol.*, 9: 367-384.

[189] Rutter, A.J., Morton, A.J., and Robins, P.C. (1975). Predictive model of rainfall interception in forests. 2. Generalization of model and comparison with observations in some coniferous and hardwood stands, *Journal of Applied Ecology*, 12(1): 367-380.

[190] Saeki, T. (1961). Inter-relationship between leaf amount, light distribution, and total photosynthesis in a plant community, *Botanic Magazine*, 11: 235-241.

[191] Salter, M.G., Franklin, K.A., and Whitelam, G.C. (2003). Gating of the rapid shade-avoidance response by the circadian clock in plants, *Nature*, 426(6967): 680-683.

[192] Salvucci, G.D., and Entekhabi, D. (1995). Hillslope and climatic controls on hydrologic fluxes, *Water Resources Research*, 31(7): 1725-1739.

[193] Sariahmed, A., and Kisiel, C.C. (1968), Synthesis of sequences of summer thunderstorm volumes for the Atterbury watershed in the Tucson area, Proc. Int. Assoc. Hydrol. Sci. Symp. on Use of Analog and Digital Computers in Hydrology, pp. 439-447.

[194] Scanlon, B.R., Levitt, D.G., Reedy, R.C., Keese, K.E., and Sully, M.J. (2005). Ecological controls on water-cycle response to climate variability in deserts, *Pro-*

ceedings of the National Academy of Sciences of the United States of America, 102(17): 6033-6038.

[195] Scholes, R.J., and Walker, B.H. (1993). An African Savanna: Synthesis of the Nylsvley Study. Cambridge University Press, Cambridge, U.K., 318 pp.

[196] Sellers, P.J. (1985). Canopy reflectance, photosynthesis and transpiration, International Journal of Remote Sensing, 6(8): 1335-1372.

[197] Sellers, P.J., Berry, J.A., Collatz, G.J., Field, C.B., and Hall, F.G. (1992). Canopy reflectance, photosynthesis, and transpiration. 3. A reanalysis using improved leaf models and a new canopy integration scheme, Remote Sensing of Environment, 42(3): 187-216.

[198] Sellers, P.J., Randall, D.A., Collatz, G.J., Berry, J.A., Field, C.B., Dazlich, D.A., Zhang, C., Collelo, G.D., and Bounoua, L. (1996a). A revised land surface parameterization (SiB2) for atmospheric GCMs. 1. Model formulation, Journal of Climate, 9(4): 676-705.

[199] Sellers, P.J., Los, S.O., Tucker, C.J., Justice, C.O., Dazlich, D.A., Collatz, G.J., and Randall, D.A. (1996b). A revised land surface parameterization (SiB2) for atmospheric GCMs. 2. The generation of global fields of terrestrial biophysical parameters from satellite data, Journal of Climate, 9(4): 706-737.

[200] Sellers, W.D. (1965). Physical Climatology. University of Chicago Press, Chicago, IL, USA, 272 pp.

[201] Seyfried, M.S., Schwinning, S., Walvoord, M.A., Pockman, W.T., Newman, B.D., Jackson, R.B., and Phillips, E.M. (2005). Ecohydrological control of deep drainage in arid and semiarid regions, Ecology, 86(2): 277-287.

[202] Sharon, D. (1980). Distribution of hydrologically effective rainfall incident on sloping ground, Journal of Hydrology, 46(1-2): 165-188.

447

[203] Sharon, D., and Arazi, A. (1997). The distribution of wind-driven rainfall in a small valley: an empirical basis for numerical model verification, *Journal of Hydrology*, 201(1-4): 21-48.

[204] Shinozaki, K., Yoda, K., Hozumi, K., Kira, T. (1964). A quantitative analysis of plant form: the pipe model theory. I. Basic analyses., *Japanese Journal of Ecology*, 14: 97-105.

[205] Shuttleworth, W.J. (1979). *Evaporation*. Institute of Hydrology Report 56, Wallingford, U.K.

[206] Shuttleworth, W.J. (1992). Evaporation. In: D.R. Maidment (Editor), *Handbook of Hydrology*. McGraw-Hill, Inc., New York, NY, USA, pp. 4.1-4.53.

[207] Sitch, S., Smith, B., Prentice, I.C., Arneth, A., Bondeau, A., Cramer, W., Kaplan, J.O., Levis, S., Lucht, W., Sykes, M.T., Thonicke, K., and Venevsky, S. (2003). Evaluation of ecosystem dynamics, plant geography and terrestrial carbon cycling in the LPJ dynamic global vegetation model, *Global Change Biology*, 9(2): 161-185.

[208] Sivapalan, M., Beven, K., and Wood, E.F. (1987). On hydrologic similarity. 2. A scaled model of storm runoff production, *Water Resources Research*, 23(12): 2266-2278.

[209] Slingo, A. (1989). A GCM parameterization for the shortwave radiative properties of water clouds, *Journal of the Atmospheric Sciences*, 46(10): 1419-1427.

[210] Slingo, A., and Schrecker, H.M. (1982). On the shortwave radiative properties of stratiform water clouds, *Quarterly Journal of the Royal Meteorological Society*, 108(456): 407-426.

[211] Smith, R.E., and Schreiber, H.A. (1973). Point processes of seasonal thunderstorm rainfall. 1. Distribution of rainfall events, *Water Resources Research*, 9(4): 871-884.

[212] Smith, T.M., Shugart, H.H., and Woodward, F.I. (1997). *Plant functional types: their relevance to ecosystem properties and global change*, International Geosphere-Biosphere Programme Book Series, Vol. 1. Cambridge University Press, 369 pp.

[213] Spitters, C.J.T. (1986). Separating the diffuse and direct component of global radiation and its implications for modeling canopy photosynthesis. 2. Calculation of canopy photosynthesis, *Agricultural and Forest Meteorology*, 38(1-3): 231-242.

[214] Stephens, G.L. (1978). Radiation profiles in extended water clouds. 2. Parameterization schemes, *Journal of the Atmospheric Sciences*, 35(11): 2123-2132.

[215] Stieglitz, M., Rind, D., Famiglietti, J., and Rosenzweig, C. (1997). An efficient approach to modeling the topographic control of surface hydrology for regional and global climate modeling, *Journal of Climate*, 10(1): 118-137.

[216] Storck, P., Bowling, L., Wetherbee, P., and Lettenmaier, D. (1998). Application of a GIS-based distributed hydrology model for prediction of forest harvest effects on peak stream flow in the Pacific Northwest, *Hydrological Processes*, 12(6): 889-904.

[217] Storey, H.C., and Hamilton, E.L. (1943). A comparative study of rain-gages, *Trans. Amer. Geophys. Union*(24): 133-141.

[218] Taiz, L., and Zeiger, E. (2002). *Plant Physiology*. 3rd ed. Sinauer Associates, Inc., Sunderland, MA, USA, 690 pp.

[219] Tan, C.S., and Black, T.A. (1976). Factors affecting the canopy resistance of a Douglas-Fir forest, *Boundary Layer Meteorology*, 10: 475-488.

[220] Tilman, D. (1982). *Resource competition and community structure*. Princeton University Press, Princeton, New Jersey, USA, 296 pp.

[221] Todorovic, P. (1968). *A mathematical study of precipitation phenomena*. Rep. CER 67-68PT65, Eng. Res. Center, Colorado State University, Fort Collins, CO, USA.

[222] Todorovic, P., and Yevjevich, V. (1969). *Stochastic processes of precipitation.* Colo. State Univ. Hydrol. Pap. 35, Fort Collins, CO, USA, pp. 1-161.

[223] Tucker, G.E., and Bras, R.L. (2000). A stochastic approach to modeling the role of rainfall variability in drainage basin evolution, *Water Resources Research,* 36(7): 1953-1964.

[224] Tucker, G.E., Lancaster, S.T., Gasparini, N.M., and Bras, R.L. (2001). The Channel-Hillslope Integrated Landscape Development (CHILD) Model. In: R.S. Harmon and W.W. Doe (Editors), *Landscape Erosion and Sedimentation Modeling.* Kluwer Press, New York, NY, USA, pp. 349-388.

[225] Turner, N.C., Schulze, E.D., and Gollan, T. (1985). The responses of stomata and leaf gas exchange to vapor pressure deficits and soil-water content. 2. In the mesophytic herbaceous species *Helianthus Annuus, Oecologia,* 65(3): 348-355.

[226] Van Heuklon, T.K. (1979). Estimating atmospheric ozone for solar-radiation models, *Solar Energy,* 22(1): 63-68.

[227] van Wijk, M.T., and Rodriguez-Iturbe, I. (2002). Tree-grass competition in space and time: Insights from a simple cellular automata model based on ecohydrological dynamics, *Water Resources Research,* 38(9).

[228] VanShaar, J.R., Haddeland, I., and Lettenmaier, D.P. (2002). Effects of land-cover changes on the hydrological response of interior Columbia River basin forested catchments, *Hydrological Processes,* 16(13): 2499-2520.

[229] Verseghy, D.L., McFarlane, N.A., and Lazare, M. (1993). CLASS - a Canadian Land-Surface Scheme for GCMs. 2. Vegetation model and coupled runs, *International Journal of Climatology,* 13(4): 347-370.

[230] Vertessy, R.A., Hatton, T.J., Benyon, R.G., and Dawes, W.R. (1996). Long-term growth and water balance predictions for a mountain ash (*Eucalyptus regnans*) forest catchment subject to clear-felling and regeneration, *Tree Physiology,* 16(1-2): 221-232.

[231] Vieux, B.E. (1988). *Finite element analysis of hydrologic response areas using geographic information systems.* Ph.D. Thesis, Michigan State University, East Lansing, MI, USA.

[232] Vivoni, E.R., Ivanov, V.Y., Bras, R.L., and Entekhabi, D. (2004). Generation of triangulated irregular networks based on hydrological similarity, *Journal of Hydrologic Engineering*, 9(4): 288-302.

[233] Walker, B.H. (1994). Landscape to regional-scale responses of terrestrial ecosystems to global change, *Ambio*, 23(1): 67-73.

[234] Walker, B.H., and Steffen, W.L. (1997). The terrestrial biosphere and global change: implications for natural and managed ecosystems. A synthesis of GCTE and related research, *Conservation Ecology*. IGBP Science Stockholm, pp. 31.

[235] Walko, R.L., Band, L.E., Baron, J., Kittel, T.G.F., Lammers, R., Lee, T.J., Ojima, D., Pielke, R.A., Taylor, C., Tague, C., Tremback, C.J., and Vidale, P.L. (2000). Coupled atmosphere-biophysics-hydrology models for environmental modeling, *Journal of Applied Meteorology*, 39(6): 931-944.

[236] Wang, G.L., and Eltahir, E.A.B. (2000). Biosphere-atmosphere interactions over West Africa. II: Multiple climate equilibria, *Quarterly Journal of the Royal Meteorological Society*, 126(565): 1261-1280.

[237] Wang, J., and Bras, R.L. (1999). Ground heat flux estimated from surface soil temperature, *Journal of Hydrology*, 216(3-4): 214-226.

[238] Wang, Y.P., and Jarvis, P.G. (1990). Description and validation of an array model - MAESTRO, *Agricultural and Forest Meteorology*, 51(3-4): 257-280.

[239] Wang, Y.P., and Leuning, R. (1998). A two-leaf model for canopy conductance, photosynthesis and partitioning of available energy I: Model description and comparison with a multi-layered model, *Agricultural and Forest Meteorology*, 91(1-2): 89-111.

[240] Waring, R.H., Schroeder, P.E., and Oren, R. (1982). Application of the pipe model-theory to predict canopy leaf-area, *Canadian Journal of Forest Research-Revue Canadienne De Recherche Forestiere*, 12(3): 556-560.

[241] Warrach, K., Stieglitz, M., Mengelkamp, H.T., and Raschke, E. (2002). Advantages of a topographically controlled runoff simulation in a soil-vegetation-atmosphere transfer model, *Journal of Hydrometeorology*, 3(2): 131-148.

[242] Watson, F.G.R., Grayson, R.B., Vertessy, R.A., and McMahon, T.A. (1998). Large-scale distribution modelling and the utility of detailed ground data, *Hydrological Processes*, 12(6): 873-888.

[243] Watson, F.G.R., Vertessy, R.A., and Grayson, R.B. (1999). Large-scale modelling of forest hydrological processes and their long-term effect on water yield, *Hydrological Processes*, 13(5): 689-700.

[244] Wiegand, T., Milton, S.J., and Wissel, C. (1995). A simulation-model for a shrub ecosystem in the semi-arid Karoo, South-Africa, *Ecology*, 76(7): 2205-2221.

[245] Wigmosta, M.S., Leung, L.R., and Rykiel, E.J. (1995). Regional modelling of climate-terrestrial ecosystem interactions, *Journal of Biogeography*, 22(2-3): 453-465.

[246] Wigmosta, M.S., Vail, L.W., and Lettenmaier, D.P. (1994). A distributed hydrology-vegetation model for complex terrain, *Water Resources Research*, 30(6): 1665-1679.

[247] Wilks, D.S., and Wilby, R.L. (1999). The weather generation game: a review of stochastic weather models, *Progress in Physical Geography*, 23(3): 329-357.

[248] Williams, C.A., and Albertson, J.D. (2005). Contrasting short- and long-timescale effects of vegetation dynamics on water and carbon fluxes in water-limited ecosystems, *Water Resources Research*, 41(6).

[249] Wilson, E.G., and Hillerty, M.M. (1932). Distribution of Chi Square, *Proc. Natl. Acad. Sci.*, 17: 684-688.

[250] Wolfram, S. (1983). Statistical-mechanics of cellular automata, *Reviews of Modern Physics*, 55(3): 601-644.

[251] Wolfram, S. (1984). Universality and complexity in cellular automata, *Physica D*, 10(1-2): 1-35.

[252] Woolhiser, D.A. (1992). Modeling daily precipitation - progress and problems. In: A.T. Walden and P. Guttorp (Editors), *Statistics in the Environmental and Earth Sciences*. Edward Arnold, Londond, U.K., pp. 71-89.

[253] Xue, Y.K. (1997). Biosphere feedback on regional climate in tropical north Africa, *Quarterly Journal of the Royal Meteorological Society*, 123(542): 1483-1515.

[254] Zarba, R.L. (1988). *A numerical investigation of unsaturated flow*. M.S. Thesis, Cambridge, MA, USA.